

MULTISCALE MECHANICS AND STRUCTURAL DESIGN OF PERIODIC CELLULAR MATERIALS

by

Mostafa S.A. Elsayed

Department of Mechanical Engineering

McGill University, Montreal

October 2010

A thesis submitted to McGill University

in partial fulfilment of the requirements for the degree of

Doctor of Philosophy

© Mostafa S.A. Elsayed, 2010

To the souls of my parents
Fawzeya (1930-1990) & Saleh (1925-2006)

Intellectual growth should commence at birth and cease only at death.

Albert Einstein, 1879- 1955

Many times a day I realize how much my own life is built on the labours of my fellowmen, and how earnestly I must exert myself in order to give in return as much as I have received.

Albert Einstein, 1879- 1955

ABSTRACT

A periodic cellular material, also known as lattice material, is a periodic, reticulated micro-truss structure made up of a large number of elements; it is generated by tessellating a unit cell, composed of a small number of elements, in an infinite periodicity. Lattice materials are used to expand the properties of the solid material from which they are constructed to ranges of properties that depend on the lattice cell geometry, besides the material relative density, $\bar{\rho}$. The development of lattice materials results in expanding the materials selection design space, thereby providing tailored materials for advanced engineering applications.

Recent progress on this new family of materials has led to a classification which categorizes lattice materials into two groups, namely, bending dominated and stretching dominated. The former contains lattice materials that collapse by the local bending of their microscopic constituents, generating mechanical properties that are far from optimal. The latter includes lattice cell topologies that collapse by the stretching of their cell elements, giving a much higher stiffness and strength per unit mass. Despite this recent research advance in the understanding of the failure mechanics of lattice materials, important challenges need to be addressed. i) To date, the current approaches for modeling infinite periodic lattice structures are applicable to certain lattice topologies only. A robust, automated, analytical procedure to characterize the mechanical properties of a lattice material with an arbitrary microscopic topology is missing. ii) The strategy followed in literature to shape the cross-sections of slender cell elements into circular shapes, results in a local buckling failure of the lattice elements. To avoid this collapse, researchers have proposed to increase the cross-section size of the microscopic elements; this resistance increase, however, occurs at the expense of the material weight. iii) A stretching dominated lattice material offers mechanical properties that are remarkably better than a bending dominated material. Its structure consisting of fully triangulated topologies might yet contain several redundant members that bring about undesired extra weight as well as non-conformal and non-morphing structural behavior.

The work reported in this thesis aims at improving the current multiscale mechanics models as well as the structural analysis tools for the design of lattice materials. Three main contributions that help to address the issues mentioned above arise from this thesis.

- (i) A systematic, matrix based, procedure for the theoretical modeling and characterization of lattice materials with arbitrary cell topologies is presented, with the goal of integrating it with an iterative routine to tailor the material properties. To this end, the *Bloch*-wave method and the *Cauchy-Born* hypothesis are applied, respectively, to model periodic wave-functions and to homogenize the microscopic properties of the lattice infinite periodic microstructure that generates the material effective properties. Stiffness selection charts are presented for pin- and rigid-jointed architectures of lattice materials to help designers select the best lattice topology for a given engineering application.
- (ii) Multiscale design charts of lattice materials are developed to enable designers to determine simultaneously the micro- and the macro-scale geometric parameters that meet prescribed requirements as well as enhance the specific load carrying capacity of a lattice structure. The criterion used to develop these charts is to impose the coincidence between the elastic buckling and the material yielding failures at different length scales. The cross-section design method of shape transformers is used to determine the best cross-section shape and size of the microscopic cell elements as well as of the macroscopic members.
- (iii) Finally, a new class of lattice materials is proposed, namely, tensegrity lattice material, which has a stretching dominated behavior with less redundancy than a typical stretching dominated topology. This class of lattice materials can support all modes of macroscopic loadings due to the lattice non-linear geometrical stiffness resistance that is associated with first-order, infinitesimal, periodic, internal mechanisms.

Keywords: Cellular Materials; Lattice Material; Cellular Solids; Hybrid Materials; Honeycombs; Lattice Structures; Periodic Structure; Micro-trusses; Tensegrity Structures; Tensegrity Lattice Materials; Tensegrity Lattice Structures; Pre-stress; Mechanisms; *Bloch's* theorem; Dummy-Node Rule; Dummy-Node Scheme; *Cauchy-Born* Hypothesis; Shape transformers; Efficiency of Cross-sections; Multiscale Mechanics.

RÉSUMÉ

Les matériaux cellulaires périodiques, aussi connus sous le nom de matériaux réseaux, sont constitués d'un grand nombre d'éléments de micro-treillis réticulés qui sont assemblés de manière périodique ; ils sont construits en assemblant un grand nombre de cellules composées d'un petit nombre d'éléments pour former un pavé dont la périodicité peut être infinie. Les matériaux réseaux servent à modifier les propriétés des matériaux solides qui les constituent selon la topologie des cellules ou la densité relative, $\bar{\rho}$. Le développement des matériaux réseaux permet d'élargir la gamme de matériaux pouvant servir dans la conception d'applications avancées.

Les progrès récents dans cette nouvelle famille de matériaux ont mené à leur regroupement dans deux catégories: les matériaux dominés par le fléchissement et ceux dominés par l'étirement. Les premiers contiennent des matériaux réseaux qui s'affaissent par le fléchissement localisé de leurs cellules, conduisant à des propriétés qui ne sont pas optimales. Les derniers contiennent une topologie de cellules qui s'affaissent par l'étirement de leurs éléments, produisant ainsi une plus grande résistance par unité de masse. Malgré les avancées récentes dans la compréhension du mécanisme d'affaiblissement des matériaux réseaux, certains défis importants demeurent. i) Les modèles existants de structures réseaux périodiques sont applicables à certaines topologies seulement. Une procédure robuste, automatisée et analytique pour caractériser les propriétés mécaniques des matériaux réseaux ayant une topologie microscopique arbitraire doit être développée. ii) La stratégie utilisée dans la littérature pour former la section transversale d'éléments de cellule minces en formes circulaires mène à un affaiblissement des éléments du treillis par gondolement. Pour éviter cet affaiblissement, les chercheurs ont proposé d'augmenter la taille de la section transversale des éléments microscopiques. Cependant, cette augmentation de la résistance se fait au détriment du poids du matériau. iii) Les matériaux réseaux qui sont dominés par l'étirement offrent des propriétés mécaniques très supérieures à celles des matériaux dominés par le fléchissement. Leur structure, constituée uniquement de topologies triangulaires, pourrait toutefois contenir plusieurs membres superflus qui ajoutent un poids indésirable et un comportement structurel qui ne se conforme pas aisément.

Le travail décrit dans cette thèse a pour but d'améliorer les modèles mécaniques existants à plusieurs échelles ainsi que les outils d'analyse structurelle servant à la conception de matériaux réseaux. Les trois contributions principales de cette thèse, abordant les problématiques mentionnées plus haut, sont les suivantes:

- (i) Une procédure systématique basée sur les matrices est présentée pour la modélisation et la caractérisation des matériaux réseaux possédant une topologie cellulaire arbitraire. Cette procédure peut être intégrée à une routine itérative pour ajuster les propriétés d'un matériau. La méthode ondulatoire de *Bloch* et l'hypothèse de *Cauchy-Born* sont appliquées, respectivement, pour modéliser les fonctions d'ondes périodiques et pour homogénéiser les propriétés microscopiques de la microstructure périodique des treillis, responsable des propriétés effectives du matériau. Des tableaux de sélection de la dureté sont présentés pour des architectures de matériaux réseaux à joints rigides ou à boulons. Ces tableaux permettent de choisir la meilleure topologie de treillis pour une application donnée.
- (ii) Des tableaux de conception multi-échelle pour les matériaux réseaux sont développés pour permettre aux concepteurs d'établir simultanément les paramètres géométriques microscopiques et macroscopiques qui satisfont aux exigences prescrites et qui améliorent la capacité de charge de la structure en treillis. Le critère utilisé pour développer ces tableaux est que le gonflement élastique doit coïncider avec l'affaiblissement du matériau par écoulement à toutes les échelles de longueur. La méthode de transformation de formes est utilisée afin de définir la meilleure forme pour la section transversale, la taille des éléments cellulaires microscopiques, ainsi que celle des membres macroscopiques.
- (iii) Finalement, une nouvelle classe de matériaux réseaux est proposée pour les matériaux dont le comportement est dominé par l'étirement et qui ont moins de membres superflus que les matériaux typiquement dominés par l'étirement. Cette classe de matériaux peut soutenir tous les modes de chargement macroscopiques grâce à la résistance géométrique non linéaire du treillis qui provient de mécanismes périodiques infinitésimaux du premier ordre.

ACKNOWLEDGEMENTS

Working as a Ph.D. student at McGill University was a magnificent as well as a challenging experience to me. In all these years, many people were instrumental directly or indirectly in shaping up my academic career. It was hardly possible for me to thrive in my doctoral work without the precious support of those personalities. Here is a small tribute to all those people. First of all, I wish to thank my supervisor Professor Damiano Pasini for introducing me to the world of cellular solids. It was only due to his valuable guidance, cheerful enthusiasm and ever-friendly nature that I was able to complete my research work in a respectable manner. My special thanks to Professor Jorge Angeles (McGill University) and Professor A. Srikantha Phani (University of British Columbia) for their valuable discussions and for providing me valuable references that remarkably helped me in my work. My thanks also extend to Professor Francois Barthelat (McGill University) for his valuable discussions during my experimental work. I would like to thank Professor Larry Lessard and Professor Pascal Hubert (McGill University) for giving me access to the facilities in the structures and composite materials laboratory necessary to perform my experiments. My thanks extend towards Ing. Eric Lavoie of the Experimental Laboratory of the Hydro-Quebec Research Institute in Varennes, Canada where the specimens necessary for my experimental work were manufactured, for his technical assistance during the manufacturing process. Many thanks also to Mrs Joyce Nault, the graduate secretary in the Mechanical engineering department at McGill University, for her help in all the administrative matters that was necessary for my work at McGill University.

I would like to thank the National Sciences and Engineering Research Council of Canada (NSERC), The faculty of Engineering at McGill University and Mr Les Vadasz for providing the financial support for my research project through, the NSERC/D3 fellowship, the McGill Engineering Doctoral Award (MEDA) and Les Vadasz Doctoral Award, respectively.

I wish to thank my sisters Azza and Salwa and my brother-in-law Nader for their constant support and encouragement in all my professional endeavours. Finally, I wish to express my gratitude to my wife "Mayada" for her continuous emotional and moral supports.

CLAIM OF ORIGINALITY

The author claims the originality¹ of the main ideas and research results reported in this thesis, the most significant being listed below:

- The development of a systematic matrix based procedure for the classification and characterization of lattice materials.
- The Dummy Node Rule (DNR) and the Dummy Node Scheme (DNS) for the static analysis of pin-jointed lattice structures and materials.
- The development of the comprehensive (material and geometrical) stiffness Characteristics of periodic lattice structures and materials.
- Introducing the structuring concepts of Periodicity Induced Stability (PIS) and Periodicity Induced Tensegrity (PIT).
- Introducing and characterizing the Tensegrity Lattice Materials (TLM) as a new class of open cell cellular solids.
- The development of multiscale design charts of macroscopic mechanical members manufactured of lattice materials.
- Integrating the concept of cross-sectional shape transformers into the design process of lattice materials.

¹Some of the reported results have in part been published in (Elsayed, M.S.A. and Pasini, D., 2009; 2010a; 2010b).

PUBLICATIONS ARISING FROM THIS THESIS

Refereed Journal Papers

1. **Mostafa S.A. Elsayed** and Damiano Pasini, “Analysis of the Elastostatic Specific Stiffness of 2D Stretching-Dominated Lattice Materials”, *Journal of Mechanics of Materials*, Vol. 42, 7, pp. 709-725. (2010a).
2. **Mostafa S.A. Elsayed** and Damiano Pasini, “Multiscale Structural Design of Columns Made of Regular Octet-Truss Lattice Material”, *International Journal of Solids and Structures* Vol. 47, 14-15, pp. 1764-1774, (2010b).
3. **Mostafa S.A. Elsayed**, Pasini D., "Mechanics of 2D Pin Jointed Lattice Structures", *AES Technical Reviews, Part B: International Journal of Advances in Mechanics and Applications of Industrial Materials*, Vol. 1, 1, pp. 83 – 91, (2009).
4. **Mostafa S.A. Elsayed** and Damiano Pasini, “Stiffness Properties of Rigid-Jointed Periodic Cellular Solids”, Submitted to the *International Journal of Solids and Structures*, Manuscript Number: IJSS-D-10-00777. (2010c).
5. **Mostafa S.A. Elsayed** and Damiano Pasini, “Comprehensive Stiffness of Prestressed Periodic Structures and Cellular Materials”, Submitted to the *Journal of Materials Science and Engineering A*, Manuscript Number: MSEA-S-10-04036. (2010d).

Refereed Conference Papers

1. **Mostafa S.A. Elsayed** and Damiano Pasini “Theoretical and Experimental Characterization of the $3^4.6$ 2D Lattice Material”. *ASME 2010 International Design Engineering Technical Conferences & Computers and Information in Engineering Conference IDETC/CIEC* August, 15-18, 2010, Montreal, Qc, Canada.
2. **Mostafa S.A. Elsayed** and Damiano Pasini “Structural Performance Analysis and Characterization of Novel 2D Stretching Dominated Infinite Lattice Materials”, *ASME 2009 International Design Engineering Technical Conferences & Computers and Information in Engineering Conference IDETC/CIE*, Aug 30- Sept 2, 2009, San Diego, California, USA.
3. **Mostafa S.A. Elsayed**, Hébert Clément, and Damiano Pasini “Structural Analysis of Pin Jointed Lattice Structures”. *Third International Conference on Advances and Trends in Engineering Materials and their Applications AES-TEMA 2009*. McGill University, July 6-10 2009.

4. **Mostafa S.A. Elsayed** and Damiano Pasini “Multi-Scale Model of the Effective Properties of the Octet-Truss Lattice Material”, AIAA Technical Conferences, Victoria, BC, Canada, September 10-12, 2008.

Technical Reports

1. **Mostafa S.A. Elsayed**, "The *Bloch's* Theorem". McGill University, Technical Report No. TR-MDOG-09-01 (2009).

TABLE OF CONTENTS

CHAPTER 1. Introduction.....	1
1.1 Lattice Materials.....	3
1.2 Problem Statement.....	5
1.3 Research Objectives.....	6
1.4 Thesis Outline.....	7
CHAPTER 2. Literature Review.....	8
2.1 Introduction.....	8
2.2 Statics of Truss-Like Finite Structures.....	8
2.2.1 Determinacy Analysis and Classification of Pin-Jointed Finite Structures.....	8
2.2.2 Pre-Stressed Mechanisms.....	11
A. Tensegrity Structures: A Class of Pre-Stressed Finite Structures.....	13
A.1 The Concept of Tensegrity.....	13
A.1.1 Definition of a Tensegrity Structure.....	13
A.2 Statics of Tensegrity Structures.....	16
2.3 Statics of Infinite Periodic Lattice Structures and Materials.....	17
2.3.1 Geometrical Classification of Periodic Lattice Structures.....	18
A. Planar Lattice Structures.....	18
B. Spatial Lattice Structures.....	19
2.3.2 Determinacy Analysis and Classification of Infinite Periodic Lattice Structure.....	19
2.3.3 Effective Mechanical Properties of Cellular Materials.....	24
2.3.4 <i>Bloch</i> -Wave Method.....	27
A. The <i>Bloch</i> 's Theorem.....	27
A.1 The <i>Bloch</i> 's Theorem and its Applications in Solid State Physics.....	28
A.2 <i>Bloch</i> 's Theorem in Continuum Mechanics.....	29
A.3 Statement of the <i>Bloch</i> 's Theorem in Continuum Mechanics.....	30
A.4 Applications of the <i>Bloch</i> 's Theorem in the Literature of Periodic Structures and Lattice Materials.....	31
2.4 Concluding Remarks Emerging From the Literature.....	33
CHAPTER 3. Determinacy Analysis and Classification of Pin-Jointed Infinite Periodic Lattice Structures.....	34
3.1 Introduction.....	34

3.2 Equilibrium and Kinematic Matrix Systems of Unit Cell Finite Structures.....	34
3.2.1 Definition of the Unit Cell of a Lattice Structure.....	34
A. Node Bases Group.....	35
B. Bar Bases Group.....	36
3.2.2 Equilibrium System of the Unit Cell Finite Structure.....	36
3.2.3 Kinematic System.....	37
3.2.4 Duality of the Kinematic and the Equilibrium Matrices.....	38
3.3 Determinacy Analysis of the Finite Structure of the Unit Cell.....	38
3.3.1 Four Fundamental Subspaces.....	39
3.4 Stiffening Effect of States of Self Stress.....	40
3.4.1 The Necessary Condition for First-Order Infinitesimal Mechanisms: The Product Force Vector Approach.....	40
A. Mode (i) of Structural Response.....	41
B. Mode (ii) of Structural Response.....	41
B.1 Product Force Vector Analysis.....	42
B.2 Global State of Self-Stress.....	43
B.2.1 Vector of Linear Combination Constants γ	43
B.2.2 Vector of Imposed Elongations e_0	44
C. Combined Response of the Structure.....	45
3.4.2 The Sufficient Condition for First-Order Infinitesimal Mechanisms: The Definiteness of the stress tensor Quadratic Form.....	46
3.5 Determinacy Analysis of the Infinite Periodic Structure.....	47
3.5.1 Direct Translational Bases.....	47
3.5.2. Direct Translational Vector.....	47
3.5.3. Position Vectors.....	47
3.5.4. Direct Lattice.....	48
3.5.5 Reciprocal Lattice.....	48
3.5.6 <i>Bloch's</i> Theorem.....	49
A. <i>Bloch</i> -Wave-Function.....	49
B. Wave-Functions Transformation Matrices.....	50
3.6 Stiffening Effect of Periodic States of Self-Stress to Periodic states of Internal Mechanisms.....	53

3.6.1 The Necessary Condition for First-Order Infinitesimal Mechanisms: The Product Force Vector Approach.....	53
A. Mode (i) of Infinite Periodic Structural Response.....	54
B. Mode (ii) of Infinite Periodic Structural Response.....	54
B.1 Product Force Vector Analysis of Infinite Periodic Structures.....	55
C. Combined Response of the Infinite Periodic Lattice.....	56
3.6.2 The Sufficient Condition for First-Order Infinitesimal Mechanisms: The Definiteness of the Stress Tensor Quadratic Form.....	56
3.6.3 Stiffening Effect of Periodic States of Self-Stress to Periodic States of Internal Mechanisms at wave-number $\omega = (0,0)$	57
3.7 The Dummy Node Rule for the Analysis of Pin-Jointed Periodic Lattice Structures.....	59
3.7.1. Extending the Mathematical Description of the Unit Cell.....	60
A. Lattice Bases.....	61
A.1 Dummy Node Bases Group.....	61
A.2 Node Bases Group.....	61
A.3 Bar Bases Group.....	62
3.7.2 The Dummy Node Rule.....	62
A. Proof of the DNR.....	63
3.7.3 The Application of the Dummy Node Rule for the Determinacy Analysis of Lattice Structure: The Dummy Node Scheme.....	66
A. Proof of the Validity of the Elimination Scheme.....	68
A.1 Equilibrium Analysis.....	68
A.2 Kinematic Analysis.....	70
3.8 Classification of Pin-Jointed Infinite Periodic Lattice Structures.....	72
3.9 Conclusion.....	72
CHAPTER 4. Effective Elastic and Strength Properties of Pin-Jointed Lattice Materials.....	75
4.1 Introduction.....	75
4.2 Relative Density of 2D Lattice Material.....	76
4.3 Effective Elastic Properties of 2D Lattice Materials.....	76
4.3.1 Macroscopic Strain Generated by Microscopic Mechanisms.....	76

A. <i>Cauchy-Born</i> Hypothesis.....	76
4.3.2 Microscopic Element Deformations in Terms of Macroscopic Strain Field.....	78
4.3.3 Macroscopic Strain Energy Density: Material Elastic Moduli.....	80
4.4 Effective Strength Properties of Lattice Materials.....	81
4.4.1 Plastic Yield Strength.....	83
4.4.2 Elastic Buckling Strength.....	84
4.5 Lattice Materials Stiffness Selection Design Charts.....	85
4.6 Conclusion.....	85
CHAPTER 5. Multiscale Structural Design of Columns made of Regular Octet-Truss	
Lattice Material.....	89
5.1 Introduction.....	89
5.2 Description of the Regular Octet-Truss Cell.....	90
5.3 Geometric Variables.....	90
5.4 Modeling the Effective Properties of the Octet-Truss Lattice Material.....	94
5.4.1. Relative Density.....	95
5.4.2. Elastic Properties.....	95
5.4.3 Strength Properties.....	96
A. Plastic Yield Strength.....	96
B. Elastic Buckling Strength.....	97
5.5 Collapse Surfaces.....	100
5.5.1 Yield Collapse.....	100
5.5.2 Buckling Collapse Surfaces.....	102
5.6 Examples.....	103
5.6.1 Example 1.....	103
5.6.2 Example 2.....	104
5.7 Design Charts for the Regular Octet-Truss Lattice Material.....	107
5.8. Multiscale Design of an Axially Loaded Macroscopic Member.....	109
5.8.1 Design Chart for Macroscopic Strut.....	109
5.8.2 Multiscale Design Charts.....	112
5.9 Conclusion.....	113
CHAPTER 6. Experimental Characterization of the $3^4.6$ 2D Lattice Material.....	115

6.1 Introduction.....	115
6.2 Design of Specimens.....	115
6.2.1 Design of the Microscopic Cell Element.....	117
6.2.2 Design of the Specimen Macroscopic Dimension.....	118
6.2.3 Design of the Specimen Thickness.....	119
6.3 Theoretical Mechanical Properties of the Designed Lattice Material.....	121
6.4 Experimental Set-up and Instrumentation.....	122
6.5 Tests and Test Results.....	124
6.5.1 Compression Test.....	124
6.5.2 Tension Test.....	126
6.5.3 Shear Test.....	127
6.6 Discussion.....	128
6.7 Conclusion.....	130
CHAPTER 7. Stiffness Properties of Rigid-Jointed Micro-Structured Lattice Materials.....	132
7.1 Introduction.....	132
7.2 Equilibrium and Kinematic Systems of Unit Cell Rigid-Jointed Finite Structure.....	133
7.3 Stiffness System of Unit Cell Rigid-Jointed Finite Structure.....	135
7.4 Stiffness System of Rigid-Jointed Infinite Lattice Structure.....	138
7.5 The Homogenization Process of the Stiffness Properties of Periodic Microstructure: The Macroscopic Stiffness of Lattice Material.....	141
7.5.1 <i>Cauchy-Born</i> Hypothesis.....	141
7.5.2 Microscopic Nodal Deformations in Terms of Macroscopic Strain Field.....	142
7.5.3 Homogenized Macroscopic Stiffness of Lattice Material.....	144
7.6 Application of the Developed Methodology to Thirteen 2D Lattice Topologies.....	145
7.6.1 Effectiveness of Nodal Rigidity.....	148
7.7 Anisotropy of Lattice Material.....	151
7.8 Discussion and Concluding Remarks.....	157
CHAPTER 8. Comprehensive Stiffness and Classification of Periodic Lattice Materials and Structures.....	158
8.1 Introduction.....	158
8.2 Comprehensive Stiffness System of Unit Cell Finite Structure.....	160
8.2.1 Comprehensive Stiffness of bar and frame Elements.....	161
A. Comprehensive Stiffness of a Bar element: an Element in a Pin-Jointed Lattice	

Structure.....	161
B. Comprehensive Stiffness of a Frame element: an Element in Rigid-Jointed Lattice Structure.....	163
8.3 Macroscopic Stiffness of Lattice Material: the Homogenization Process of the Stiffness Properties of the Microscopic Lattice Structure.....	167
8.4 Classification of Lattice Material.....	168
8.5 Effectiveness of the Geometrical Stiffness and its Contribution to the Lattice Material Stiffness Resistance.....	171
8.5.1 The Kagome Lattice Material.....	171
8.5.2 The $3^3.4^2$ Lattice Material.....	173
8.6 Conclusion.....	175
CHAPTER 9. Conclusions and Future work.....	177
9.1 Conclusions.....	177
9.2 Suggestions for Future Work.....	180
BIBLIOGRAPHY.....	182
Appendix A. Bravais Lattices.....	196
A.1. 2D Bravais Lattices.....	196
A.1.1. List of 2D Bravais Lattices.....	196
A.2. 3D Bravais Lattices.....	198
A.2.1. List of 3D Bravais Lattices.....	198
Appendix B. Definitions and Concepts of Solid State Physics and Quantum Mechanics Necessary for the Statement and Proof of the <i>Bloch's</i> Theorem.....	201
B.1 The Observable- Operators in Quantum Mechanics.....	201
B.2 The Schrödinger equation.....	201
B.3 The Translation Operator T_R	203
B.4 The Wave-function, $\psi(x,t)$	204
B.4.1 Properties of the wave-function, $\psi(x,t)$	204
Appendix C. The <i>Bloch's</i> theorem in Solid State Physics.....	206
C.1 The <i>Bloch's</i> Theorem.....	206
C.2 First Proof of the <i>Bloch's</i> theorem.....	206
C.3 Second Proof of the <i>Bloch's</i> theorem.....	209
Appendix D Mathematical Representation of Lattice Assemblies.....	211

D.1 Atomic Structure and Symmetries.....	211
D.1.1 Primitive Unit Cell.....	212
A. Bravais Lattices.....	213
B. Wigner-Seitz Primitive Cell.....	214
D.1.2 Conventional Unit Cells.....	214
D.1.3 Lattices with Basis.....	214
D.2 Reciprocal Lattice.....	215
D.3 Brillouin Zones.....	217
D.4 Point Group Symmetry and its application to the reduction of the first Brillouin Zone..	218
D.4.1 Point Group Theory of Lattice Symmetries.....	219
A. Mathematical Group.....	219
A.1 The Cyclic Group.....	220
A.1.1 The n^{th} Root of Unity C_n	220
A.2 The dihedral group D_n	221
APPENDIX E. Determinacy Analysis of 2D Infinite Lattice Structures: Applications.....	223
E.1 Square Lattice Structure.....	223
E.2 Lattice Structure with Schlafl symbol of $3^3.4^2$	228
E.2.1 Unit Cell Equilibrium System.....	228
E.2.2 Determinacy Analysis of Unit Cell Finite Structure.....	230
E.2.3 Infinite Lattice Determinacy Analysis.....	230
E.2.4 Stiffening Effect of Periodic States of Self-Stress to Periodic Internal Mechanisms.	232
E.3 Kagome Lattice Structure.....	235
E.3.1 Determinacy Analysis of Unit Cell A of the Kagome Lattice Structure.....	235
E.3.2 Determinacy Analysis of the Infinite Kagome Lattice Structure.....	238
E.3.3 Stiffening Effect Analysis of the Kagome Lattice at Wave-Number.....	249
E.3.4 Stiffening Effect Analysis of the Kagome Lattice at Wave-Number.....	251
E.4 Determinacy Analysis of the Kagome Lattice at Wave-Number $\omega = (0,0)$	253
E.5 Summary of the Determinacy Analysis Results of the 19 Lattice Topologies.....	257
APPENDIX F. Effective Elastic and Strength Properties of Pin-Jointed Lattice Materials:	
Applications.....	265
F.1 Characterization of the Semi-Double-Braced Square Lattice.....	265
F.2 Characterization of the $3^4.6$ Lattice Material.....	273

F.3 Double Hexagonal Triangulation (DHT).....	276
F.4 Full Triangulation (3^6).....	276
F.5 Hexagonal Honeycombs.....	277
F.6 Kagome Lattice.....	277
F.7 Square Lattice.....	278
F.8 Semi-Uni-Braced Square Lattice.....	278
F.9 Uni- Braced Square Lattice.....	278
F.10 Double- Braced Square Lattice.....	278
Appendix G. Elastic Properties of Rigid Jointed 2D Lattice Materials: Applications.....	280
G.1 Example.....	280
G.2 Square Lattice Material.....	285
G.3 Kagome Lattice Material.....	286
G.4 Lattice Material with Schläfli Symbol of $3^3.4^2$	286
G.5 Lattice Material with Schläfli Symbol of $3^4.6$	287
G.6 Double Hexagonal Triangulation (DHT) Lattice Material.....	288
G.7 Semi-Uni- Braced Square (SUBS) Lattice Material.....	288
G.8 Triangular- Triangular (TT) Lattice Material.....	289
G.9 Semi-Double Braced Square (SDBS) Lattice Material.....	290
G.10 Uni- Braced Square (UBS) Lattice Material.....	290
G.11 Double-Braced Square (DBS) Lattice Material.....	291
G.12 Patched Kagome' Lattice Material.....	292
G.13 Semi-Hexagonal Triangulation (SHT) Lattice Material.....	293
Appendix H. Comprehensive Stiffness Properties of 2D Pin- and Rigid-Jointed Lattice Materials: Application.....	294
H.1 Square Lattice Material.....	294
H.2 The $3^3.4^2$ Lattice Material.....	296
H.3 Triangular Lattice Material.....	298
H.4 Lattice Material with Schläfli Symbol of $3^3.4^2$	298
H.5 Lattice Material with Schläfli Symbol of $3^4.6$	299
H.6 Double Hexagonal Triangulation (DHT) Lattice Material.....	300
H.7 Semi-Uni- Braced Square (SUBS) Lattice Material.....	301

H.8 Triangular- Triangular (TT) Lattice Material.....	302
H.9 Semi-Double Braced Square (SDBS) Lattice Material.....	303
H.10 Uni- Braced Square (UBS) Lattice Material.....	303
H.11 Double-Braced Square (DBS) Lattice Material.....	304
H.12 Patched Kagome Lattice Material.....	305
H.13 Semi-Hexagonal Triangulation (SHT) Lattice Material.....	306
H.14 Kagome lattice material.....	307

LIST OF FIGURES

1.1 Material selection chart-Materials' density versus Young's modulus property space.....	1
1.2 Different types of monolithic and hybrid materials.....	2
1.3 Filling gaps in a metal selection chart by mapping properties of Aluminum alloy through the development of aluminum cellular solids (Foams and Lattice Materials).....	3
1.4 Microstructure of cellular materials.....	4
1.5 Examples of recent applications of lattice materials.....	4
2.1 Different types of 2D frameworks.....	10
2.2 Example of a purest tensegrity structure.....	15
2.3 Examples of classes 1, 2 and 3 of tensegrity structures.....	15
2.4 2D regular lattice structures.....	18
2.5 2D semi-regular lattice structures.....	20
2.6 2D other lattice structures.....	21
2.7 3D polyhedral cells.....	22
2.8 Examples of Double Layered Grids.....	22
2.9 Structure of a unit cell of the regular octet-truss lattice material.....	22
3.1 (a) Kagome lattice structure; (b) Cell envelope; (c) Unit cell.....	35
3.2 Three node equilibrium in pin-jointed structure.....	37
3.3 Three node kinematics in pin-jointed structure.....	38
3.4 A generic unit cell with its periodic displacement boundary conditions.....	50
3.5 (a) Lattice structure; (b) Cell envelope; (c) Unit cell A; (d) Unit cell B without dummy nodes; (e) Unit cell B with dummy nodes.....	60
3.6 A lattice structure (left) and the assembly of three unit cells (right) that are tessellated in the direction of the horizontal translational basis.....	64
4.1 The relative Young's modulus in the x direction of the stretching dominated lattice material versus its relative density.....	86
4.2 The relative Young's modulus in the y direction of the stretching dominated lattice material versus its relative density.....	87
4.3 The relative Shear modulus of the stretching dominated lattice material versus its relative density.....	88
5.1 Structure of a unit cell of the regular octet-truss lattice material.....	91
5.2 Multiscale geometrical details of macroscopic member manufactured of lattice material.....	92

5.3 Variation of the shape transformers of the cross-section area and second moment of area for different cross-section shapes.....	93
5.4 Variation of the lattice material relative density with respect to cross-section efficiency and to area shape transformer.....	99
5.5 Elastic and plastic collapse surfaces of the octet-truss lattice material evaluated for the relative direct stresses and normalized with respect to the material relative density.....	102
5.6 Efficiencies of different cross-section shapes at specified $\psi_A=0.6$	105
5.7 Elastic and plastic collapse surfaces and the effect of cross-section efficiency on the structural performance.....	106
5.8 Design chart of the microscopic architecture of 2D lattice materials.....	110
5.9 Design chart of mechanical members loaded in axial compression.....	112
6.1 (a) Specimens in the manufacturing work space (b) The A2 EMB system.....	116
6.2 Parametric detailed dimensioning of the microscopic and the macroscopic constituents of a lattice material specimen.....	117
6.3 Shear specimen mounted into the three rail shear fixture and installed into the test machine	119
6.4 CAD drawing of the test specimens along with loading directions.....	121
6.5 Schematic drawing of the test set-up.....	123
6.6 Experimental set-up and instrumentation.....	123
6.7 Compression test.....	124
6.8 A ruptured x -oriented compression specimen.....	125
6.9 Compression test results-(a) x - oriented specimens (b) y - oriented specimens.....	126
6.10 Tension specimens-(a) Tension specimen, y -oriented, with the holding plates (b) Ruptured, x -oriented, tension specimen.....	127
6.11 Tension test results-(a) x - oriented specimens (b) y - oriented specimens.....	128
6.12 Shear test results.....	129
7.1 A frame element along with all internal and external forces and deformations fields.....	134
7.2 Generic unit cell with its periodic equilibrium boundary conditions.....	139
7.3 Relative Young's modulus in the horizontal direction versus relative density of selected 2D lattice materials.....	146
7.4 Relative Young's modulus in the vertical direction versus relative density of selected 2D lattice materials.....	147
7.5 Relative shear modulus versus relative density of selected 2D lattice materials.....	148

7.6 Contribution percentage of the microscopic bending stiffness of microscopic cell elements to the macroscopic Young's modulus in the horizontal direction of the lattice material versus the material relative density.....	149
7.7 Contribution percentage of the microscopic bending stiffness of microscopic cell elements to the macroscopic Young's modulus in the vertical direction of the lattice material versus the material relative density.....	150
7.8 Contribution percentage of the microscopic bending stiffness of microscopic cell elements to the macroscopic shear modulus versus the material relative density.....	151
7.9 Infinitesimal stress field of lattice material.....	152
7.10 Polar plot of the variation of the Young's modulus of lattice material in the x - direction with the angle $\theta \in [0^\circ, 360^\circ]$ for material relative.....	154
7.11 Polar plot of the variation of the Young's modulus of lattice material in the y - direction with the angle $\theta \in [0^\circ, 360^\circ]$ for material relative.....	155
7.12 Polar plot of the variation of the shear modulus of lattice material in the xy - direction with the angle $\theta \in [0^\circ, 360^\circ]$ for material relative density.....	156
8.1 Statically and kinematically indeterminate framework.....	159
8.2 Bar element (left) and frame element (right) along with nodal degrees of freedom.....	162
8.3 Variation of the elastic moduli of the Kagome lattice material with the nominal strain of the solid material.....	172
8.4 Variation of the shear moduli of the $3^3.4^2$ lattice material with the nominal strain of the solid material.....	174
8.5 Comparison of the elastic moduli of the Kagome and the $3^3.4^2$ lattice materials.....	

LIST OF TABLES

2.1 Classes of pin-jointed structures.....	11
2.2 Common cell topologies considered in the literature of lattice material.....	23
3.1 Classes of infinite periodic lattice structures.....	72
3.2 Classification of 2D infinite periodic lattice structures.....	73
6.1 Height of tension and compression specimens.....	118
6.2 Width of the tension and compression specimens.....	119
6.3 Summary of the compression test results.....	125
6.4 Summary of the tension test results.....	127
6.5 Summary of the shear test results.....	128
6.6 Comparison between the theoretical and the experimental characterization results.....	131
8.1 Classification of lattice materials.....	169
8.2 Classification of lattice materials.....	170

CHAPTER 1

Introduction

One of the main objectives in engineering design is the selection of the optimum material for a given application. A number of optimization techniques have been developed for this purpose. An excellent technique to scan candidate materials for given functional requirements and geometry is the creation of material selection charts (Ashby, M.F., 2005). Fig (1.1) shows a material selection chart developed for the Young's modulus and density. Such chart helps selecting the material with the optimum stiffness (or compliance) for a specific application.

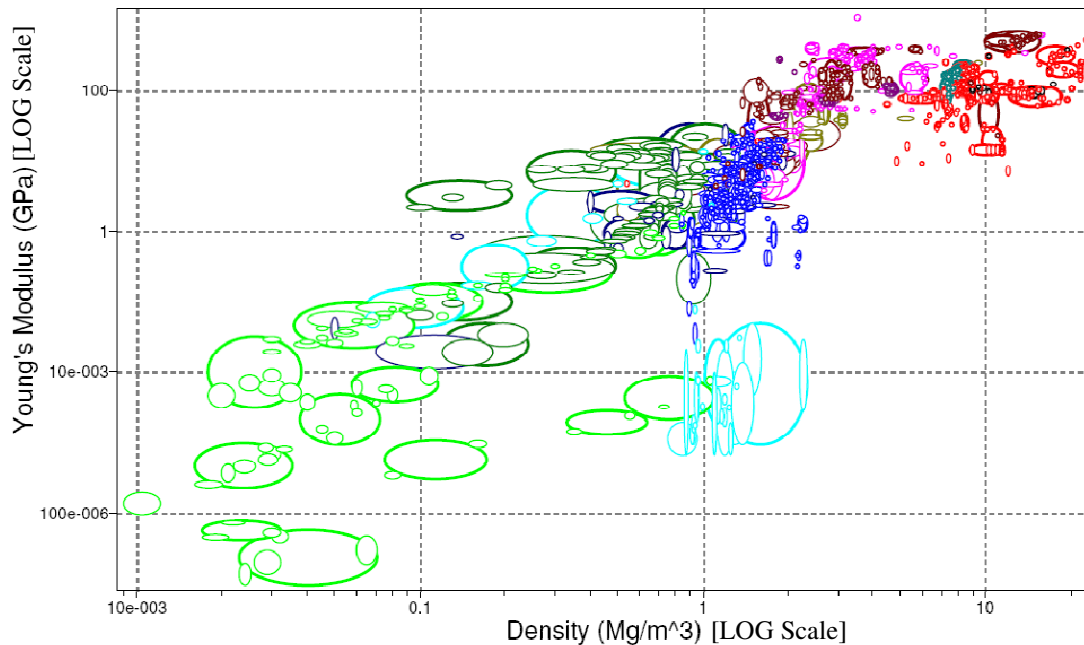


Fig (1.1) Material selection chart- Materials' density versus Young's modulus property space

As shown in Fig (1.1), the design space in a material selection chart is discontinuous. A material is generally described by the coordinates of a point. Materials falling within the same class cluster together in the same boundaries forming a bubble-like region. However, gaps exist where no material can achieve certain properties. Filling those gaps and finding alternative materials are among the main motives of material scientists and engineers.

Several methods were proposed to develop new materials, such as metal alloys and polymers. Among those, there are methods attempting to integrate a material with either air, or fluid or a

combination of solid materials to allow the superposition or interpolation of their properties. Such materials are referred to as Hybrid Materials (Ashby, M.F., 2005). Examples of hybrid materials include composites, sandwich and cellular materials. Fig (1.2) shows the five families of monolithic materials and the different types of hybrid materials.

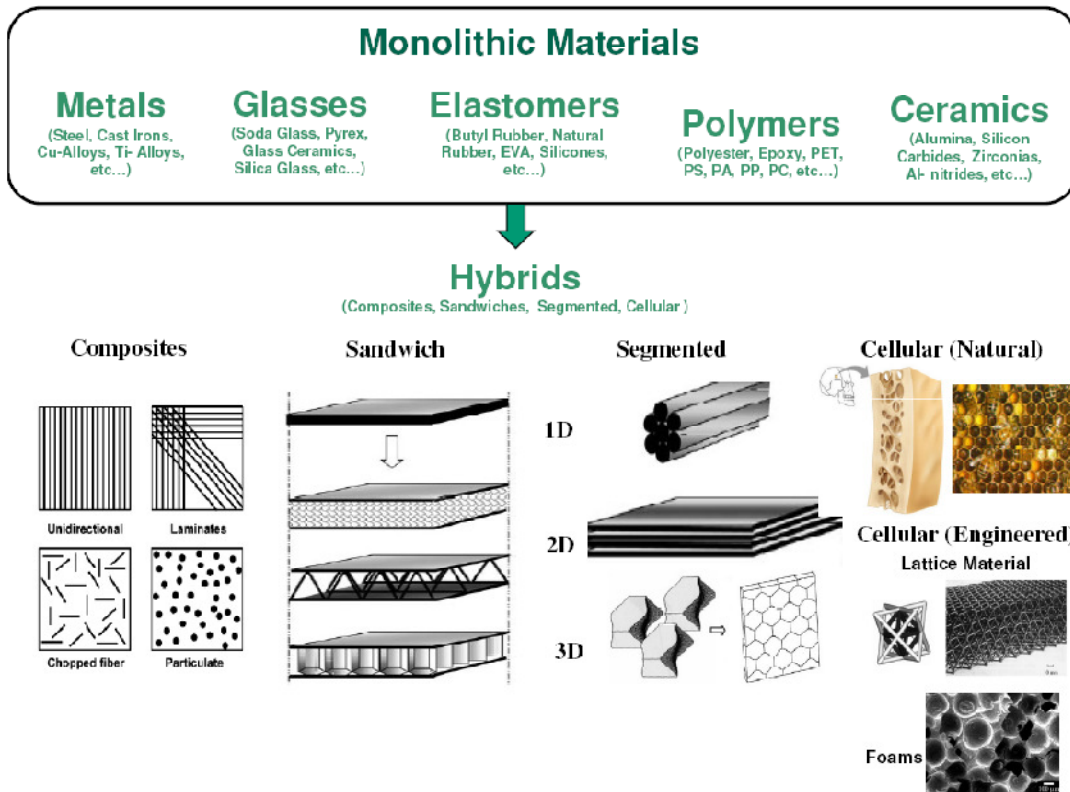


Fig (1.2) Different types of monolithic and hybrid materials

A cellular material can be considered as a structured material whose building blocks are the material cells. When a solid material is structured into a cellular material with microscopic architecture, the single valued material property expands to assume a range that depends on the cellular material microscopic topology, besides the relative density, $\bar{\rho}$, of the cellular material.

An example of mapping material properties to populate empty gaps of a material selection chart is shown in Fig (1.3). Here, an aluminum alloy is shaped into a cellular solid with augmented material properties that occupy new regions of the material chart. These new materials result in expanding the material design space, thereby providing tailored advanced materials for new applications.

Cellular materials are found in nature, such as wood, bees' honeycombs, trabecular bones. Engineered cellular materials are generally classified into foams and lattice materials (Deshpande,

V.S., et.al. 2001a). Foam is mostly produced by the introduction of gas bubbles into a melt (Gibson, L. J. and Ashby, M. F., 1997).

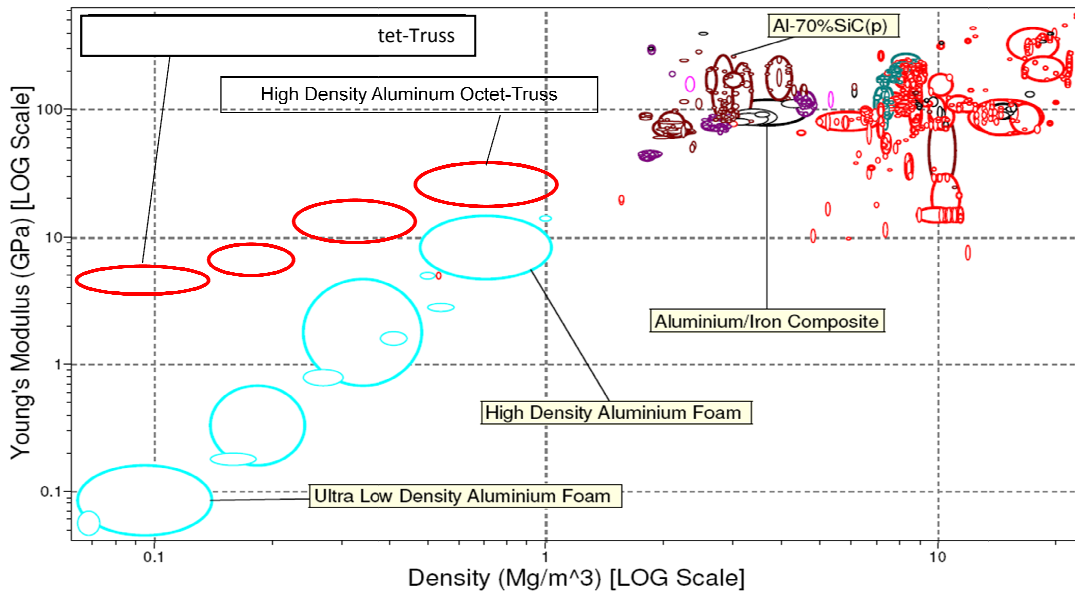


Fig. (1.3) Filling gaps in a metal selection chart by mapping properties of Aluminum alloy through the development of aluminum cellular solids (Foams and Lattice Materials) (Elsayed, M.S.A., Pasini, D., 2008)

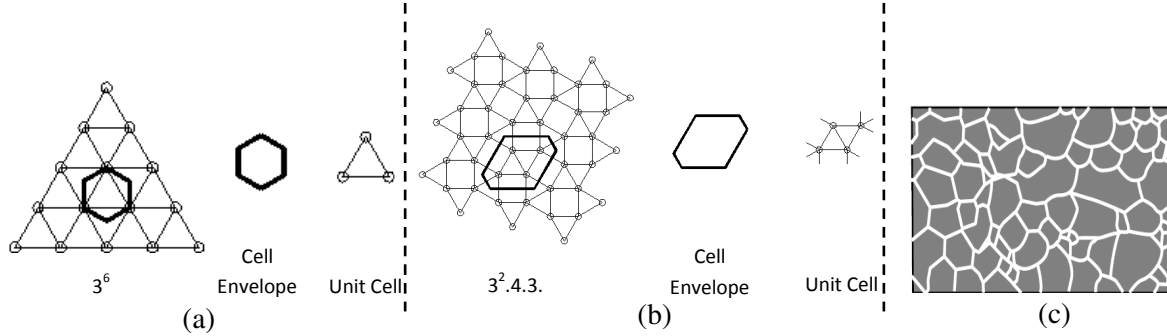
Microscopic structural analysis shows that foams have a random cellular structure and a low nodal connectivity at the cell vertices, typically three to four elements connectivity at a node, as shown in Fig (1.4c). The random cellular structure results in a less controllability of the foam properties and the low nodal connectivity results in a microscopic bending dominated failure mode, where the microscopic cells eventually collapse by the local bending of their walls. These features generate mechanical properties that are far from optimal.

1.1 Lattice Materials

A lattice material can be defined as a periodic, reticulated micro-truss structure made up of a large number of elements; it is generated by tessellating a unit cell, composed of a few number of elements, in an infinite periodicity, either in a two or three-dimensional spaces (Fleck, N.A., et.al., 2010).

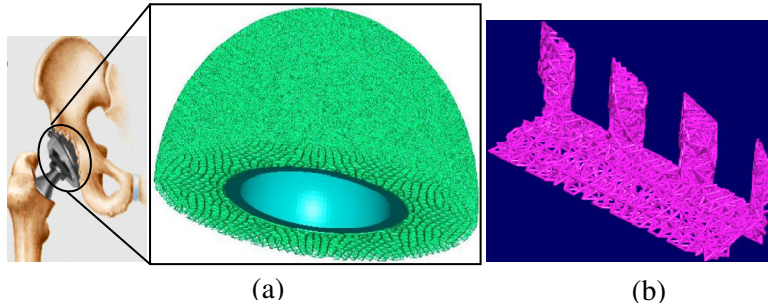
Figures (1.4a) and (1.4b) show the microstructures of two examples of planar lattice materials along with their unit cell finite structures and cell envelopes. A cell envelope is a virtual entity in a periodic lattice structure that represents the structural periodicity.

The main advantage of lattice materials over foams is the precise control of its microstructure. This has made them strong candidates for many applications in the biomedical, aerospace and automotive sectors. Fig (1.5) shows two examples of the use of lattice material in biomedical and aerospace engineering (Hongqing V. W., 2005).



(a) Triangular 2D lattice structure; (b) 2D lattice structure with topology of Schlegli symbol $3^2.4.3$; (c) Foam

Fig (1.4) Microstructure of cellular materials



(a) Hip replacement mechanisms (b) Turbine blades

Fig (1.5) Examples of recent applications of lattice materials (Hongqing V. W., 2005)

The precise control of the lattice material microstructure allows generating materials with tailored properties and controlled nodal connectivity. Controlling the nodal connectivity enables the development of a type of lattice material that collapses by the stretching of its cell members, giving a much higher stiffness and strength per unit mass. This type is known as a stretching dominated lattice material. For instance, structural analysis of the stretching dominated lattice material shows that its stiffness and strength scale up with the densities ratio of the lattice material to the solid material, $\bar{\rho}$, where the solid material is the material used to manufacture the lattice material. On the other hand, the stiffness and strength of the bending dominated lattice materials are governed, respectively, by $\bar{\rho}^2$ and $\bar{\rho}^{3/2}$ (Gibson, L. J. & Ashby, M. F., 1997). The different

scaling laws have a strong impact on the strength and stiffness of the material. For example, at $\bar{\rho} = 0.01$, the stretching dominated lattice material is hundred times stiffer and ten times stronger than the bending dominated counterpart.

1.2 Problem Statement

There are several open research issues within the scope of the static response analysis and characterization of lattice materials that need to be addressed. The following summarizes the research issues that this thesis aims to address.

- (i) To distinguish between the bending dominated and the stretching dominated lattice materials, it is required to analyze the static and the kinematic determinacy states of the pin-jointed version of the lattice microstructure. It is also required to search for any modes of macroscopic strain field developed by inextensional microscopic mechanisms within the lattice microstructure. The determinacy analysis of finite pin-jointed frameworks is well established in literature, as the state of the art survey illustrates in the second chapter of this thesis. An accurate prediction of the performance of lattice materials requires extending the determinacy analysis of finite structures to account for pin-jointed infinite periodic structures. Such an analysis was performed in literature, although the method bears a few shortcomings. For example, the analysis of Hutchinson (2004), using the *Bloch*-wave method, focused mainly on a special type of topology where the cell elements of the unit cells are all contained within their cell envelope, as no elements extend between adjacent unit cells, such as the topology of the triangular lattice shown in Fig (1.4a). On the other hand, the characterization of topologies, such as the $3^2.4.3$ lattice (Fig (1.4b)), using the *Bloch*-wave method represents a challenge since the unit cell does not contain any nodes on the cell envelope to retrieve the lattice periodicity. Thus a robust analytical procedure to characterize lattice materials with any arbitrary microscopic cell topology needs to be developed.
- (ii) To date, no study has investigated the interactions between the periodic states of self-stress and the periodic internal mechanisms developed within an infinite lattice structure. Thus, the contribution of the periodic states of self-stress to the comprehensive stiffness of lattice materials in the form of non-linear geometrical stiffness remains an open issue.
- (iii) A few number of lattice topologies develop a stretching dominated behavior. Stretching dominated lattice materials are mostly structured as a combination of fully triangulated topologies in 2D or 3D. Often, these cell topologies generate highly redundant microstructures that hold many limitations, including extra weight, non-conformal and non-

morphing behavior of the material. The search for new stretching dominated lattice concepts which are less redundant than the current stretching dominated lattice materials needs to be explored.

- (iv) The microscopic members of a stretching dominated lattice material are generally loaded in axial tension or compression; this load distribution triggers instability, which might involve elastic buckling failure. In the literature, current methods proposed the design of slender microscopic cell elements with circular solid cross-sections only, which resulted in collapse modes that are dominated by local buckling. To increase buckling resistance, the size of the cell member cross-sections, i.e. the relative density of the lattice, is increased at the expense of the weight of the material. Multiscale strategies that enable simultaneously selecting the micro- and the macro-scale cross-sectional shape parameters of the members of the lattice material need to be developed.

1.3 Research Objectives

- (i) Develop a robust, automated, matrix-based procedure for the determinacy analysis and characterization of periodic lattice structures and materials. The procedure must be able to model and characterize a lattice material with any arbitrary unit cell topology.
- (ii) Validate the developed theoretical modeling procedure by conducting experimental studies.
- (iii) Investigate the stiffening effect of the periodic states of self-stress on the periodic internal mechanisms and use the results of this analysis to classify infinite periodic lattice structures.
- (iv) Formulate the non-linear geometrical stiffness generated by the states of self-stress, especially in lattice structures that involve microscopic internal mechanisms.
- (v) Assess the impact of the microscopic geometrical stiffness of lattice structures to the macroscopic, homogenized, stiffness characteristics of lattice materials.
- (vi) Search for new lattice material concepts that have a stretching dominated behavior, yet less redundant than the typical stretching dominated topologies, available in literature.
- (vii) Generate multiscale design charts for the simultaneous optimum selection of the micro- and the macro-scale geometric parameters that can meet prescribed design requirements as well as enhance the specific load carrying capacity of lattice structures. Resort to the cross-section design method of the shape transformers to model cross-section shape and size of the microscopic cell elements as well as the macroscopic members manufactured of lattice material.

1.4 Thesis Outline

The thesis is organized in nine chapters. After this introduction, chapter two reviews the literature on the effective properties of cellular solids. The effect of the states of self-stress on the macroscopic performance of lattice materials and structures is outlined. The literature of pre-stressed mechanisms and tensegrity structures are also reviewed where the recent developments as well as the open areas of research are presented. Research questions emerging from the state of the art on this subject are given to motivate the rest of this thesis. In chapter three, the determinacy analysis of periodic infinite structures is conducted where the stiffening effect of the periodic states of self-stress on the periodic internal mechanisms is investigated. Chapter four presents an automated, robust, matrix-based, procedure for the analysis and characterization of pin-jointed lattice materials. In chapter five, the multiscale design of columns made of 3D octet-truss lattice material is addressed. In this chapter, the efficiencies of the cell element cross-sections of the lattice material are considered among the design parameters. The chapter presents multiscale design charts which can be used by designers to select the macroscopic and the microscopic attributes of columns manufactured of octet-truss lattice material. To verify the methodology developed in chapter four, we conduct in chapter six an experimental study that characterizes the elastic properties of the 2D triangular-hexagonal lattice material with the Schläfli symbol of $3^4.6$ cell topology. We manufactured titanium alloy specimens with $3^4.6$ topology of lattice material and conducted quasi-static tests to determine its elastic moduli and compare them with the results obtained in chapter four. In chapter seven, the elastic properties of rigid-jointed lattice materials are characterized where the bending stiffness of the microscopic cell elements are considered along with their axial stiffness. The comprehensive stiffness of lattice materials and structures are characterized in chapter eight where the geometrical stiffness developed by the geometrical non-linearity of lattice structures is computed and superimposed to the structure's material stiffness. The comprehensive stiffness computations are used for the classification of lattice materials. The thesis ends in chapter nine with a set of conclusions and suggestions for future work.

CHAPTER 2

Literature Review

2.1 Introduction

This chapter reviews the literature on the determinacy analysis and characterization of finite as well as infinite periodic lattice structures. Different approaches to determine the effective mechanical properties of cellular solids are discussed. Fundamental topics on pre-stressed mechanisms and tensegrity structures are also reviewed with the goal of demonstrating the significance of the concept of states of self-stress in developing the geometrical stiffness of finite frameworks and highlighting their potential significance in enhancing the performance of infinite periodic lattice structures and materials. Additional open areas of research in the literature of lattice structures and materials are detailed including sizing and shaping of cell element cross-sections of lattice structures and materials. The chapter concludes with a list of open, un-resolved issues that motivate the remainder of this thesis.

We start with the statics of pin-jointed finite structures before extending the review to the infinite periodic lattice structures.

2.2 Statics of Truss-Like Finite Structures

2.2.1 Determinacy Analysis and Classification of Pin-Jointed Finite Structures

The mechanical behavior of pin-jointed frameworks is largely governed by their determinacy state in the form of static and kinematic determinacy. The static determinacy is used to determine the different modes of states of self-stress experienced by a structure. A state of self-stress is defined as a vector of element forces generated within an unloaded framework. On the other hand, the kinematic determinacy is used to determine the different modes of mechanisms experienced by a pin-jointed structure. The modes of mechanisms include the rigid-body motions and the states of internal mechanisms; here the states of internal mechanisms are considered as the different modes of structural deformations that are conducted with undeformed elements. While many structural frameworks are designed and manufactured with rigid-joints, the performance of pin-jointed frameworks is an excellent guide to predict the performance of their rigid-jointed versions (Pellegrino, S., Calladine, C. R., 1986; Hoff, N.J. and Fernandez-Sintes, J., 1980; Parkes, E.W., 1974; Timoshenko, S.P. and Young, D.H., 1965).

Maxwell (Maxwell, J.C., 1864) set a rule for the minimum number of bars necessary for a pin-jointed framework to be kinematically determinate, namely, "simply-stiff" structure; these minimum numbers of bars are, $(2j-3)$ and $(3j-6)$ in 2D and 3D frameworks, respectively, where j is the number of nodes within a framework. A framework with less number of bars than the minimum condition of Maxwell is a mechanism, unless its nodes are set to be rigid. In this case the framework behavior is bending dominated as the structural failure is dominated by the bending stresses in its constituents. If the number of bars is more than the minimum condition of Maxwell, then the structure is over constrained, namely, "over-stiff" structure. Simply-stiff and over-stiff structures are kinematically determinate frameworks which have a stretching dominated behavior as the failure mode is dominated by the axial stress of the structural constituents. Even if simply- and over-stiff frameworks are manufactured as rigid-jointed, which introduce secondary bending stresses into their elements, the structural failure is still dominated by axial stresses; thus these structures are still classified as stretching dominated.

Examples of such kind of frameworks are shown in Fig (2.1). Fig (2.1a) is a mechanism that can resist a loading once its nodes are set to rigid, as shown in Fig (2.1b), where the structure becomes bending dominated. Fig (2.1c) shows a pin-jointed simply-stiff structure which can support any loading and is classified as stretching dominated. Even with rigid nodes (Fig (2.1d)) introducing secondary bending stresses into the structural constituents, the framework is still classified as stretching dominated.

Part A of Fig (2.1e) shows an over-stiff structure that contains a redundant element in the diagonal, while part B shows a mechanism. According to Maxwell's rule (Maxwell, J.C., 1864), combining part A and B of Fig (2.1e) apparently generates a simply-stiff structure; however, this is not the case, as part B remains a mechanism. Calladine (Calladine, C. R., 1978) and Pellegrino (Pellegrino, S., Calladine, C. R., 1986; Pellegrino, S., 1993) reviewed the linear-algebraic basis of Maxwell's rule. As a result, they reformulated the problem to obtain the generalization of Maxwell's rule, which includes information about the states of self-stress and the states of internal mechanisms within the framework.

The analysis of the frameworks shown in Figs (2.1e) and (2.1f) using the generalized Maxwell's rule shows that each of these structures contains one internal mechanism and one state of self-stress. However, according to Maxwell's rule the structure of Fig (2.1f) is a mechanism that cannot support any loading. This is not the case as the static equilibrium of the external load, F , and the elements axial load, t_0 , can be expressed as:

$$F = \frac{2t_0}{L_0} \Delta + \frac{EA}{L_0^3} \Delta^3 \quad (2.1)$$

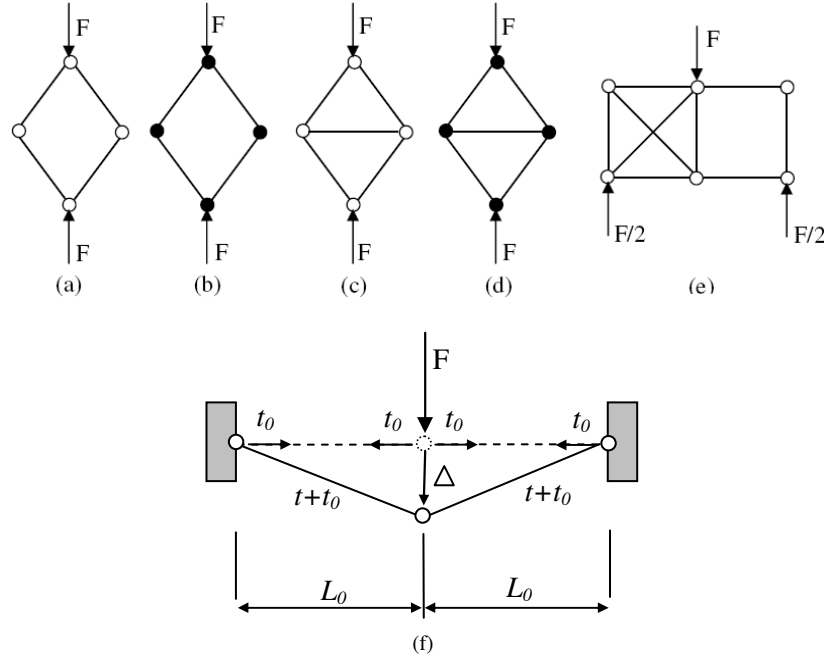


Fig (2.1) Different types of 2D frameworks

where Δ is the structural deformation, t_0 is a pre-stress in the elements, E is the material Young's modulus, A the elements cross-sectional area and L_0 is the elements' initial length. The result of eqn (2.1) indicates that the structure in Fig (2.1f) supports external loading, which qualifies this structure as a "pre-stressed mechanism".

A statically and kinematically indeterminate framework is a pin-jointed structure with states of self-stress and states of internal mechanisms; while some of those internal mechanisms generate a kinematic mobility that allows finite displacements with every additional external load increment (e.g. the framework of Fig (2.1e)), other types are unique as the structure encounters only first order infinitesimal displacement accompanied by higher order strains (e.g. the framework of Fig (2.1f)). Such kinds of structures are pre-stressable and can be found in many engineering and natural systems (Kuznetsov, E.N., 1997; Tilbert, G., 2002). Examples of pre-stressed engineering systems include cable systems (e.g. cable nets), tensegrity frameworks, pneumatic domes and fabric roofs.

Table (2.1) shows four types of pin-jointed structures found in engineering problems (Pellegrino, S., 1992; Pellegrino, S., 1988). For structures of type four, further analysis is required to investigate the stiffening effect of the states of self-stress on the states of internal mechanisms.

This study would allow discriminating between bending dominated structures (e.g. the structure shown in Fig (2.1e)) and pre-stressed mechanisms (e.g. the structure shown in Fig (2.1f)).

Table (2.1) Classes of pin-jointed structures

Type	# of modes of states of self-stress (s)	# of modes of states of internal mechanisms (m)	Description	Class
I	$s = 0$	$m = 0$	Statically & kinematically determinate	Simply-stiff (Stretching dominated)
II	$s = 0$	$m > 0$	Statically determinate & kinematically indeterminate	Mechanism (Bending dominated)
III	$s > 0$	$m = 0$	Statically indeterminate & kinematically determinate	Over-stiff (Stretching dominated)
IV	$s > 0$	$m > 0$	Statically & kinematically indeterminate	Mechanism (Bending dominated or qualified as pre-stressed mechanism)

2.2.2 Pre-Stressed Mechanisms

Pre-stressed mechanisms are common assemblies in structural engineering. Widespread types include pneumatic domes, cable systems and cable nets, fabric roofs and tensegrity structures. As shown in §2.2.1, pre-stressed mechanisms are statically and kinematically indeterminate structures. Static analysis of pre-stressed mechanisms finds its roots in the works of Mohr (1885), Maxwell (1864) and Levi-Civita and Amaldi (1930), Calladine (1982), Calladine and Pellegrino (1986; 1991), Volokh and Vilnay (1997) and Kuznetsov (1997; 2000).

Pellegrino and Calladine (1986) reported a methodology to verify the pre-stressability of statically and kinematically indeterminate frameworks. They derived the equilibrium and the kinematic systems of pin-jointed finite structures and used the fundamental subspaces of the kinematic and the equilibrium matrices to investigate the existence of any states of self-stress and states of internal mechanisms. They also developed a methodology to recognize the states of rigid-body motions and distinguish them from internal mechanisms for structures that are not constrained into a foundation. To study the stiffening effect of the states of self-stress on the internal mechanisms they developed the product force vector approach. The product force vector is the vector of nodal forces developed in the new geometrical configuration of the structure after undergoing the inextensional deformations generated by the internal mechanisms. The work of Pellegrino and Calladine (1986) was criticized by Kuznetsov (1989) who showed that the stiffening effect developed by the product force vector is just a necessary but not sufficient

condition for the structure to impart a positive definite stiffness; positive or semi-positive definiteness of the stiffness matrix is a sufficient condition to qualify an internal mechanisms into a first-order infinitesimal mechanisms. This drawback in the work of Pellegrino and Calladine (1986) was addressed later by the same authors (Calladine, C. R., and Pellegrino, S. (1991)), who set a matrix-based algorithm to distinguish between first-order infinitesimal mechanisms, higher order mechanisms and finite mechanisms. They formulated a generalized state of self-stress as a linear combination of the individual states of self-stress experienced by the structure. They conducted an iterative algorithm to determine the linear combination constants necessary to generate the generalized state of self-stress which is capable of imparting positive or semi-positive definiteness of the geometrical stiffness of the structure. Further remarks on the topic can be found in Calladine and Pellegrino (1991; 1992).

Kuznetsov (1997) investigated statically and kinematically indeterminate frameworks. He developed an algorithm for the resolution of any applied load to a structure into two orthogonal components. One component is resisted by the determinate part of the structure while the other part is resisted by the geometrical stiffness developed by the structure's geometrical non-linearity. Other approaches (Guest 2006; Livesley, R. K., 1975; Connelly, R., Whiteley, W., 1996) used a generalized methodology by analyzing the comprehensive stiffness of a structure to investigate the stiffening effect of the states of self-stress on the internal mechanisms. The comprehensive stiffness of a structure is the superposition of the structure's material stiffness and geometrical stiffness. Guest (2006) developed a simple unified approach to derive the comprehensive/tangent stiffness of pre-stressed pin-jointed finite structures. He also reviewed the different approaches available in literature to derive the comprehensive stiffness of pre-stressed structures including: the conventional energy based methods (Livesley, R. K., 1975; Bickford, W. B., 1998; Reddy, J. N., 2002; McGuire, W., 2000; Cook, R.D., et. al., 2001), Rigidity theory and pre-stress stability method (Connelly, R., Whiteley, W., 1996) and the method of Pellegrino and Calladine (1986). Guest (2006) showed that the method of Pellegrino and Calladine (1986) is a special case of the other approaches as the geometrical stiffness is developed if the structure experiences inextensional deformations developed by first-order infinitesimal mechanisms.

In this thesis, we are particularly interested in tensegrity structures, as a class of pre-stressed mechanisms. We will employ this concept to develop a new class of periodic structures and lattice materials. The following is a review on the statics of tensegrity structures.

A. Tensegrity Structures: A Class of Pre-Stressed Finite Structures

This section presents the evolution of the concept of tensegrity and describes the statics of tensegrity structures.

A.1 The Concept of Tensegrity

The concept of tensegrity has received a great attention among scientists and engineers in many fields and relative applications. Wroldsen (2007) in his PhD thesis gives a detailed description of the origin of the concept of tensegrity. In the early 19th century, the Russians constructivists were the first to introduce this concept. Gough (1998) provided details of some of the Russian constructivists in what is called the spatial constructions. She provided details of the work of Karl Ioganson (1890-1929) and other Russians in the field of tensegrity structures. The North American literature of tensegrity is a controversy between Snelson and Buckminster Fuller. This controversy has been discussed in several papers by Sadao (1996), Snelson (1996) and Emmerich (1996) to name a few. The concept of tensegrity structure was first introduced as a form of an artwork by Snelson in 1948 (Snelson, 1965). Later, Buckminster Fuller, after recognizing the engineering relevance of this concept, introduced the term “tensegrity”, to describe the integration of struts within a net of strings (Fuller, 1962; Fuller, 1976).

Independently, David Georges Emmerich (1925-1996) investigated the same concept in France in the late 1950s and early 1960s. He named it as "self-tensioning structures". Emmerich investigated these ideas and developed several double-layer structures while experimenting different ways of interconnecting the basic elements (Emmerich, 1966).

D’Estree Sterk (2003; 2006) presented tensegrity structures as a possible building envelope for responsive architecture as the term "responsive architecture" was introduced by Negroponte (1975) for buildings that are able to change form in order to respond to green architecture requirements. In aerospace, the concept of tensegrity is used in building lightweight deployable structures; a review of such kind of structures can be found in Tilbert (2002). In the field of robotics, biologically motivated tensegrity robots are examples of the use of the concept of tensegrity (Skelton and Sultan, 1997; 2003; Aldrich et al., 2003a; 2003b).

A.1.1 Definition of a Tensegrity Structure

Different definitions and structuring techniques are introduced in the literature of tensegrity structures. In 1927, Buckminster Fuller introduced several geometries wherein the concept pre-

stressability is incorporated in the form of rigid bodies, in compression, stabilized by a network of strings in tension. The compressed rigid bodies were generally a set of rods that touch among each other. He introduced also the geodesic domes as a type of tension structures where the tension strings were attached to more than one node on the rods other than their ends, (Sadao, 1996).

In 1948 Snelson introduced an art form, which later described as the purest possible class of tensegrity structures, where the rigid bodies were a discontinuous set of thin rods, in compression, stabilized by a continuous network of strings, in tension. The rigid rods were not touching one another, and the strings were only attached at the two nodes of the rods, (Snelson, 1965), as shown in Fig (2.2).

To this point, the term tensegrity was not yet introduced, later, Buckminster Fuller, after recognizing the engineering relevance of this concept, introduced the term “tensegrity”, to describe the integration of struts within a net of strings (Fuller, 1962; Fuller, 1976).

In 1976 Pugh described the mechanical principle of tensegrity structures with an analogy to balloons. The inside pressure of the balloon is higher than that of the surrounding medium, and is pushing in the outward direction against the balloon surface. The elastic balloon is then deformed outwards until static equilibrium is reached between internal air pressure and external pressure from the balloon skin and the surrounding medium (Pugh, 1976).

In 1994, Hanaor defined a tensegrity structure as an internally pre-stressed, free-standing pin-jointed network, in which the cables or tendons are tensioned against a system of bars or struts, (Hanaor, 1994). This wide definition included the early works of Buckminster Fuller as tensegrity structures. It is worth mentioning here, that this definition did not put any restrictions about the compression elements being forming a discontinuous set of rigid compressed rods, in contrast to a previous definition. Skelton et al. (2001a) supported this definition by presenting the term "Class k" to distinguish the different types of tensegrity structures included in this broader definition of Hanaor (1994). Their definition is “A Class k tensegrity structure is a stable tensegrity structure with a maximum of k compressive members connected at the node(s)”. Examples of classes 1, 2 and 3 tensegrity structures are shown in Fig (2.3). However, in 2003, Motro proposed a very strict definition for a tensegrity structures; he stated that “a tensegrity systems are spatial reticulate systems in a state of self-stress; all their elements have a straight middle fibre and are of equivalent size; tensioned elements have no rigidity in compression and constitute a continuous set. Compressed elements constitute a discontinuous set; each node receives one and only one compressed element” (Motro, 2003). This definition includes only the purest tensegrity structures,

similar to the one introduced by Snelson in 1948 and exclude earlier structures introduced by Fuller.



Fig (2.2) Example of a purest tensegrity structure introduced by Snelson (1965)

This definition is very strict, that is why many researchers disagreed with some of its aspects. For example, Wroldsen (2007) disagreed about the statement that all the elements of a tensegrity structure should have a straight middle fibre and be of equivalent size. Motro's definition is also in conflict with former definitions of tensegrity frameworks. For example, Hanaor (1988) invented the double layer tensegrity grids where some rods were touching at the nodes, and still defined them as tensegrity structures.

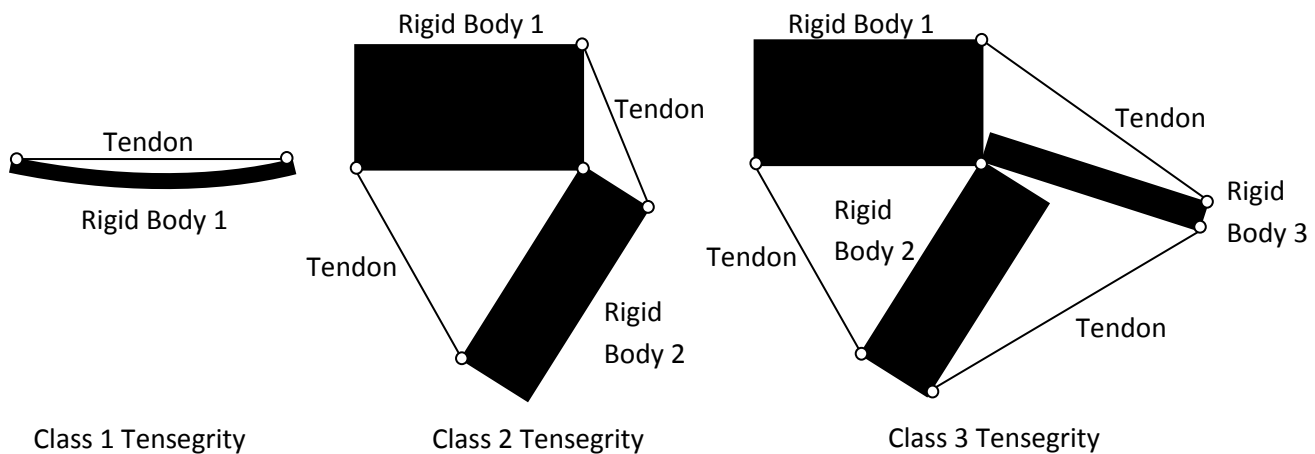


Fig (2.3) Examples of classes 1, 2 and 3 of tensegrity structures introduced by Skelton et al. (2001a)

So far, all definitions agree upon the fact that a tensegrity structure is a self-standing pre-stressed mechanism, i.e. no boundary conditions are necessary to stabilize any internal mechanism. There is also consensus about the absence of compression stiffness in tension elements, strings or tendons. However, Calladine (1978) replaced the tension strings by a set of rigid bars, similar to the compression elements, and used a matrix based technique to study the determinacy of the structure and the effect of the pre-stress on the inherent internal mechanisms within the framework (Calladine, 1978). According to the assumption of Calladine, the definition of a tensegrity structure can be generalized to include any self-standing structure that has internal mechanisms stabilized by pre-stressing.

A.2 Statics of Tensegrity Structures

Calladine (1978) applied Maxwell's rule (Maxwell, 1864) on the calculation of the equilibrium and stiffness of frames to investigate the statics of tensegrity structures. Calladine (1978) demonstrated examples in which the structure has fewer elements than what is required from Maxwell's rule, but yet it is not a mechanism. These exceptions were described by Maxwell, who concluded that the stiffness of these frames were of inferior order. The state of self-stress of tensegrity structures make them statically and kinematically indeterminate with infinitesimal mechanisms, which means that infinitesimal changes in geometry are possible without changing the length of any members (Calladine, 1978, Sultan, 2006).

Tarnai (1980) also researched pin-jointed tower structures with cyclic symmetry through Maxwell's rule (1864). He established conditions for kinematic and static indeterminacies of these structures by observing the rank of the equilibrium matrix. He proved that both the kinematic and static indeterminacies were independent of the number of stages, and how these properties were separated, in his tower structures. Pellegrino and Calladine (1986) and Calladine and Pellegrino (1991) elaborated on the findings of Calladine (1978) and examined the physical significance of the vector subspaces of the equilibrium matrix for pin-jointed structures being both kinematically and statically indeterminate. They developed a matrix-based algorithm to distinguish between first order infinitesimal mechanisms and higher order infinitesimal, or finite, mechanisms. Hanaor (1988) presented a unified algorithm for analysis and optimal pre-stress design of pre-stressed pin-jointed structures. The proposed algorithm is based on the flexibility method of structural analysis. The algorithm is used on both i) geometrically rigid (kinematically determinate) and statically indeterminate (Statically redundant) structures, where pre-stress is caused by to the lack of fit, and ii) kinematically indeterminate (not geometrically rigid) and statically indeterminate

(statically redundant) structures with infinitesimal mechanisms, where pre-stress is needed for geometric integrity. The latter category includes tensegrity structures. He also emphasized how the pre-stress could increase the load bearing capacity of certain structures. Hanaor (1992) provided guidelines for the design of double layer tensegrity domes. Although this analysis is linear and only valid for small displacements, it still provides useful information for design purposes and experimental work.

Murakami (2001), Murakami and Nishimura (2001a) and Murakami and Nishimura (2001b) developed equations within a finite framework for both static and dynamic analysis of tensegrity structures using three-dimensional theory of elasticity for large deformations. They conducted modal analysis of pre-stressed configurations to characterize the infinitesimal modes.

Motro et al. (1986) presented some results from an experimental study of linear dynamics of a structure consisting of three rods and nine strings where the dynamic characteristics were found from the harmonic excitation of nodes. Several aspects have been investigated by Motro and co-workers; examples include self-stressability (Kebiche et al., 1999), form-finding (Vassart and Motro, 1999, Zhang et al., 2006) and design algorithms (Quirrant et al., 2003) of tensegrity structures.

Oppenheim and Williams (2000) examined the effects of geometric stiffening, the nonlinear force-displacement relationship, observed when tensegrity structures are subject to perturbation forces. They concluded that such structures could be relatively soft in the vicinity of the static equilibrium.

Skelton et al. (2001c) and Skelton (2005) presented a theory for Class 1 structures from momentum and force considerations. De Oliveira (2005) developed a general theory for Class k structures from energy considerations. De Oliveira (2006) presented simulation results from a comparison study of different formulations.

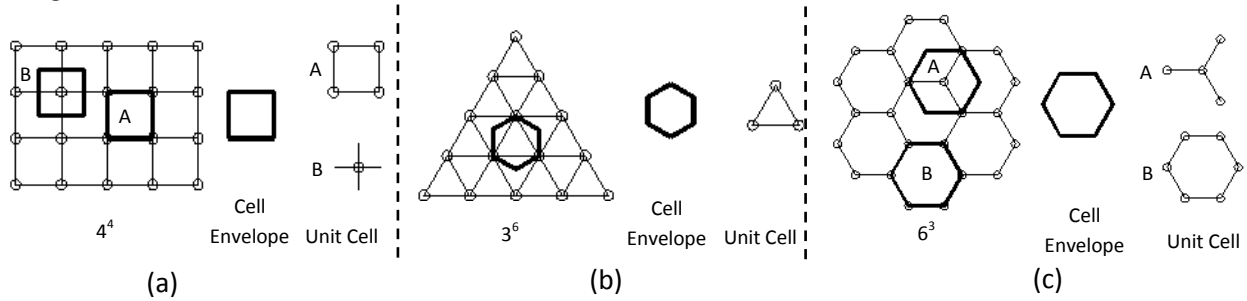
2.3 Statics of Infinite Periodic Lattice Structures and Materials

Throughout this thesis we will use the two terms "*lattice materials*" and "*lattice structures*". A *lattice material* is a lattice structure with global macroscopic length scale much larger than that of its microscopic constituents. In particular, the wavelength of any loading applied to a lattice material is much larger than that of the length of its microscopic elements. On the other hand, a *lattice structure* is subjected to loadings of wavelengths that are comparable to the lengths of its constituents.

2.3.1 Geometrical Classification of Periodic Lattice Structures

A. Planar Lattice Structures

The topologies of a 2D lattice structure are generally classified as regular, semi-regular and others (Cundy and Rolett, 1961; Frederickson, 1997; Lockwood and Macmillan, 1978). A regular lattice is composed of a unique regular polygon type, which can only be a triangle, a square, or a hexagon, as shown in Figure (2.4). In the semi-regular lattices, more than one regular polygon is used to tessellate the plane. There are eight topologies for the semi-regular lattices, as shown in Figure (2.5).



a- Square- 4^4 b- Triangular- 3^6 c- Hexagonal- 6^3

Fig (2.4) 2D regular lattice structures

An example of a semi-regular lattice is the "triangular-hexagonal" lattice, which is known as the Kagome lattice (Syozzi, 1972; Hyun and Torquato, 2002), shown in Fig (2.5a). In the regular and the semi-regular lattices, all nodes of a lattice are constrained to have the same connectivity, where the connectivity represents the number of elements connected at a node. By relaxing this constraint, an infinite number of 2D lattice topologies can be generated. In Figure (2.6) we show only eight topologies of other lattice structures.

The features of the constant nodal connectivity in the regular and the semi-regular lattice structures have been used to classify the lattices (Cundy and Rolett, 1961; Frederickson, 1997; Lockwood and Macmillan, 1978). For example, the Schläfli symbols (Cundy and Rolett, 1961) were introduced to name the lattice by a series of numbers describing the order of the regular polygons around a lattice node. For instance, the square, the triangular and the hexagonal lattices are named respectively, as 4^4 , 3^6 and 6^3 . The notion of 3^6 indicates that there are six (6) regular triangular (3) polygons successively surrounding each lattice node. Each of Figs (2.4a), (2.4c) and (2.5a) illustrates two types of unit cells that can be used for the tessellation of the same lattice structures.

B. Spatial Lattice Structures

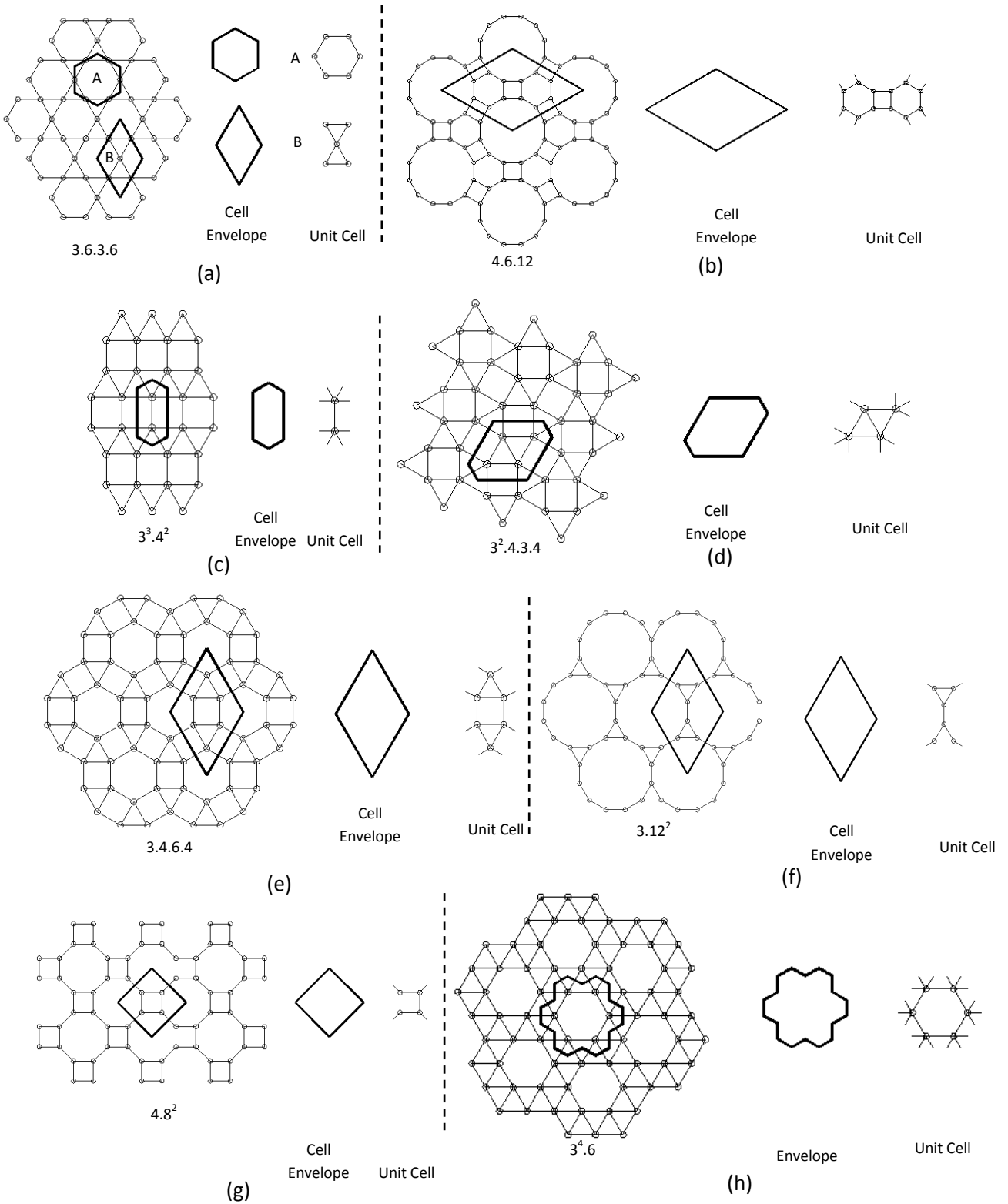
Spatial lattice structures can be constructed by tessellating polyhedra to fill the space. There are nine fundamental polyhedra, shown in Fig (2.7), of which only two, the cube and the rhombic dodecahedra, can be tessellated to fill the space and generate regular spatial lattice structure (Gibson and Ashby 1997). Other lattice structures can be constructed using combinations of different polyhedra. For example, a combination between the tetrahedra and the octahedra is used to generate the concept of octet-truss lattice (Deshpande et al. 2001a), shown in Fig (2.9).

Restricting the periodicity of the 3D lattice to a finite set of cells in the out of plane direction generates the layered grids, such as the double layered grids (Kollar and Hegedus, 1985; Lan, 1984; Wright, 1965). Double layered grids occupy a plate like structure; they are composed of two layers of planar lattice material parallel to one another and connected by a set of bars and nodes forming a lattice core. Examples of double layered grids are shown in Fig (2.8). One of the famous double layered grids is the Kagome Double Layered Grid (KDLG). For details about the KDLG, the reader is referred to (Hutchinson, R. G., 2004).

In table (2.2) we show a summary of the common cell topologies considered in the literature of lattice material. Most of the topologies in Table (2.2) are bending dominated. It is also found that most of the topologies considered in literature have square or hexagonal symmetry in 2D and cubic symmetry in 3D (Christensen, R.M., 2000).

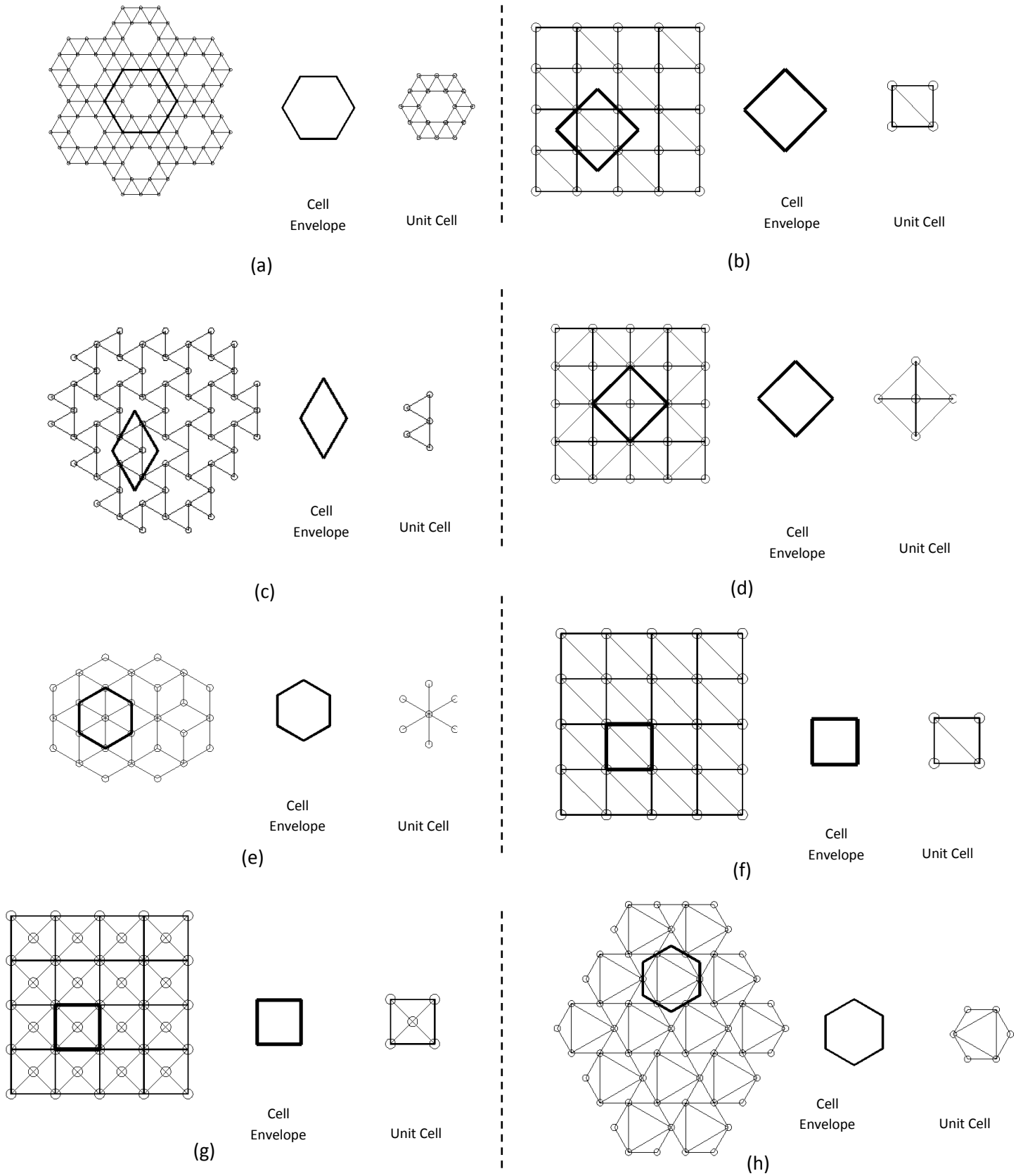
2.3.2 Determinacy Analysis and Classification of Infinite Periodic Lattice Structure

As explained in §2.2.1, the generalized Maxwell's rule, derived by Calladine (Calladine, C. R., 1978) and Pellegrino (Pellegrino, S., Calladine, C. R., 1986; Pellegrino, S., 1993), can be used to obtain an accurate prediction of the determinacy state of finite structures. However, the analysis of periodic lattice materials requires extending the model to an infinite structure. Such an extension was proposed by Deshpande et. al. (2001b) who examined the pin-jointed mechanics of a restricted set of infinite-periodic lattice topologies. They considered only topologies wherein the nodes are similarly situated, i.e. the framework appears the same and in the same orientation regardless of the viewpoint. In 2D, these are the regular square and triangular lattices; in 3D, this set includes the regular octet-truss. The generalized Maxwell's rule, was used to prove that the necessary but not sufficient nodal connectivity, Z , of a structure to be stretching dominated is $Z=4$ and $Z=6$ in 2D and 3D, respectively.



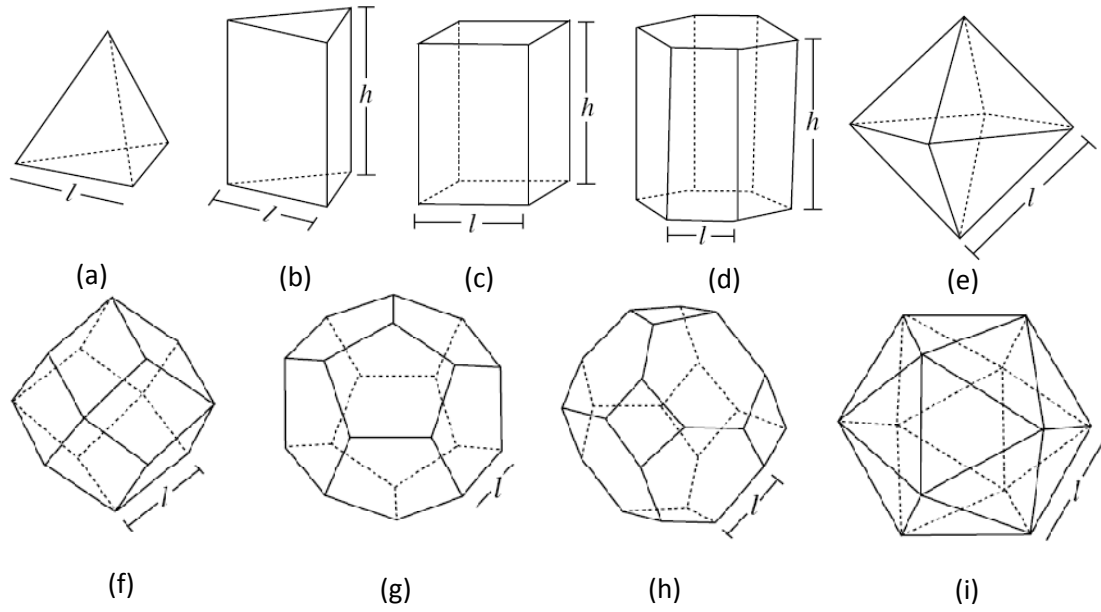
a- Kagome- 3.6.3.6 b- 4.6.12 c- 3³.4² d- 3².4.3.4 e- 3.4.6.4 f- 3.12² g- 4.8² h- 3⁴.6

Fig (2.5) 2D semi-regular lattice structures



a- Double Hexagonal Triangulation; b- Semi-Uni- Braced Square (SUBS); c- Triangular-Triangular d- Semi-Double- Braced Square; e- Equilaterals- Hexagon; f- Uni- Braced Square; g- Double- Braced Square; h- Patched Kagome

Fig (2.6) 2D other lattice structures



(a) Tetrahedron, (b) Triangular prism, (c) Square prism, (d) Hexagonal prism, (e) Octahedron, (f) Rhombic dodecahedron, (g) Dodecahedron (h) Truncated octahedron, and (i) Icosahedron

Fig (2.7) 3D polyhedral cells (Deshpande et al., 2001b)

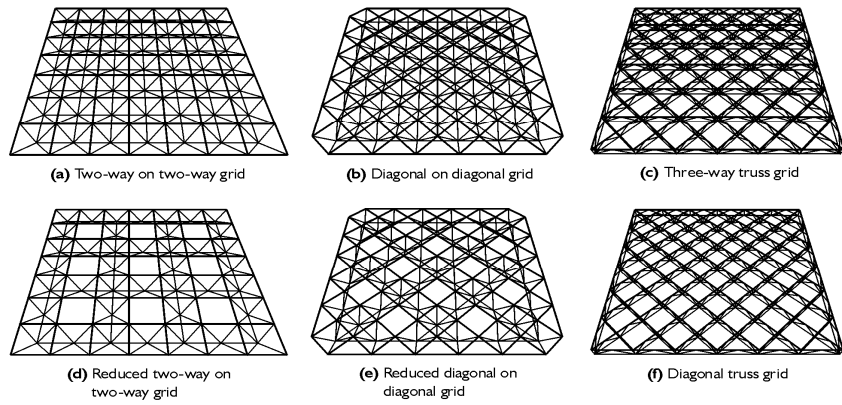


Fig (2.8) Examples of Double Layered Grids (DLG) (Makowski, Z S, 1981)

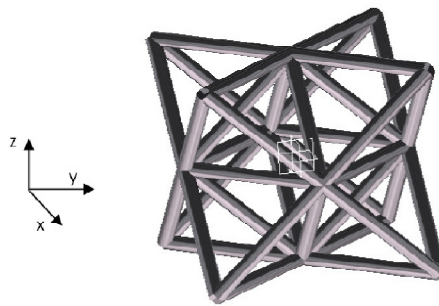
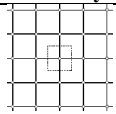
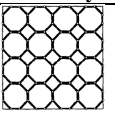
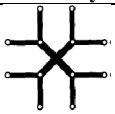
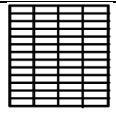
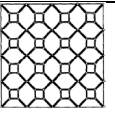
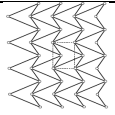
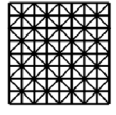
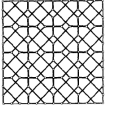
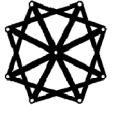
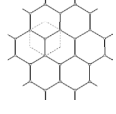
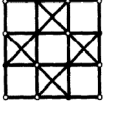
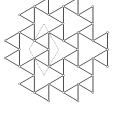
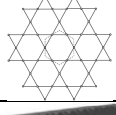

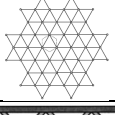
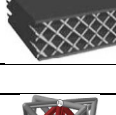
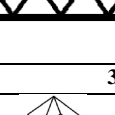
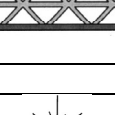
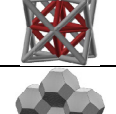
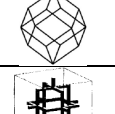
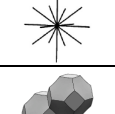
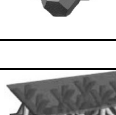
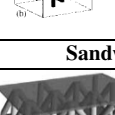
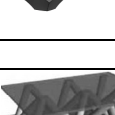
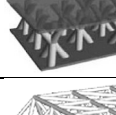
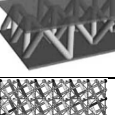
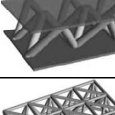
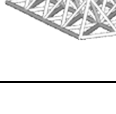
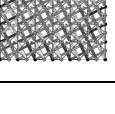
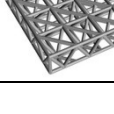


Fig. (2.9) Structure of a unit cell of the regular octet-truss lattice material

On the other hand, the sufficient nodal connectivity was proven to be $Z=6$ and $Z=12$ in 2D and 3D, respectively. For double-layered grids, they found that the sufficient nodal connectivity is $Z=9$.

Table (2.2) Common cell topologies considered in the literature of lattice material

2D Lattice Topologies								
Cell Geometry	Cell Name	Reference	Cell Geometry	Cell Name	Reference	Cell Geometry	Cell Name	Reference
	Square (Pack of cells)	Alethea, 2004; Côté, et.al., 2006		Optimized Ground Truss (Pack of cells)	Sigmund, 1994		Optimized Ground Truss (single cell)	Sigmund, 1994
	Rectangular (Pack of cells)	Alethea, 2004		Optimized Ground Truss (Pack of cells)	Sigmund, 1994		Negative Poisson's ratio (Pack of cells)	Sigmund, 1994
	Mixed (square-triangle) (Pack of cells)	Alethea, 2004		Optimized Ground Truss (Pack of cells)	Sigmund, 1994		Negative Poisson's ratio (single cell)	Sigmund, 1994
	Hexagonal (Pack of cells)	Christensen, 2000		Optimized Ground Truss (Pack of cells)	Sigmund, 1994		Triangular-Triangular (Pack of cells)	Hutchinson, 2004
	Kagome (Pack of cells)	Christensen, 2000		Star (Pack of cells)	Christensen, 2000		Triangular (Pack of cells)	Hutchinson, 2004
	Diamond lattice	Côté, et.al., 2006		Truss triangular plate	Evans, E.G., et.al., 2001		Truss triangular plate	Prud'homme, C., et.al., 2002
3D Lattice Topologies								
	Octet-truss	Deshpande, et.al., 2001		Circumferential cubic packing	Thomas, 2005		Radial Cubic packing	Hongqing, V.W., 2005
	Weaire-Phelan cell (2 cells pack)	Weaire & Phelan, 1994		Simplest foam model	Gibson, & Ashby, 1997		Kelvin cell (2 Cell pack)	Kelvin, 1887
Sandwich and Layered Grids								
	KDLG	Wallach & Gibson, 2001		Tetrahedral Core	Wallach & Gibson, 2001		Pyramid	Wallach & Gibson, 2001
	Tetrahedral Block	Wicks & Hutchinson, 2001		Tensegrity double layered grid	Quirant J, et.al., 2003		Lattice block material	Fan, H.L., et.al., 2008

Hutchinson (2004) and Hutchinson and Fleck (2006) considered the determinacy analysis of infinite lattice structures subjected to a periodic node-displacement field. They showed that some microscopic lattice structures can experience microscopic internal mechanisms that do not appear at the macroscopic level, thus the lattice material is still classified as stretching dominated.

However, they did not investigate the stiffening effect of the microscopic states of self-stress on the microscopic internal mechanisms.

The stiffening effect of states of self-stress on the internal mechanisms is investigated on small scale of finite structures in what is called pre-stressed mechanisms; however, no study considered such analysis for infinite periodic structures.

2.3.3 Effective Mechanical Properties of Cellular Materials

The analysis and characterization of foams were conducted long earlier than for lattice materials. Initial studies on foams assumed that their mechanical properties are linearly dependent on the relative density, an assumption that was later proved inaccurate. A good understanding of the mechanical properties of foams was given by Gent and Thomas (1959) and Patel and Finnie (1970). Based on the solid materials used to manufacture the cellular material, three classes of cellular materials exist in literature, namely, ceramic, polymers and metals (Ashby, M.F., 2010). Polymeric cellular materials, especially two-dimensional honeycombs, are extensively investigated in literature (Gibson and Ashby 1997) with a detailed description of the thermal, mechanical and electrical properties of foams. Foaming of metals (Davis NG, et. al., 2001; Körner, C., 2008) led to an in-depth study of their mechanical properties and their possible applications (Ashby et al. 2000; Colombo and Scheffler 2005; Shwartz et al. 1998; Banhart et al. 1999, 2001; Banhart and Fleck 2003). Similar studies are applied to the ceramic foams (Brezny and Green 1989; Huang and Gibson 1991a,b, 1993; Vedula et al., 1998a,b).

The advantages of periodic lattice materials over foams were elaborated by Evans et.al. (2001). These advantages were proven experimentally by Deshpande et.al. (2001a), Deshpande and Fleck (2001), Wallach and Gibson (2001), Chiras et al. (2002) and Wang et al. (2003).

Through continuum mechanics, Kollar and Hegedus (1985) examined the homogenization of the effective properties of lattice materials, where the mechanical response of the microstructure of the material is averaged or "smeared -out" over the macroscopic length scale of the lattice.

Bardenhagen and Triantafyllidis (1994), Schraad and Triantafyllidis (1997a; 1997b) and Triantafyllidis and Bardenhagen (1996) explored the effective response of lattice materials subjected to macroscopic strain gradients. Hassani and Hinton (1998a; 1998b; 1998c) presented variation and finite element solution techniques for the homogenization and the topology optimization of the effective properties of some composites with ordinary periodic geometries.

Different approaches are used in literature for modelling the effective properties of lattice materials, including, the linear and the non-linear Cauchy continua, the micro-polar continua, finite difference and *Bloch*-wave methods.

Askar and Cakmak (1968) considered the double-braced square lattice topology; in particular they studied its static and dynamic responses. The lattice was assumed as a set of masses lumped at the nodes that are linked by flexible, extensible, unshearable linearly-elastic beams connecting the nearest neighbours and the second nearest neighbours. They used this model to derive the strain energy density of the lattice, where the static and the kinematic functions of the node degrees of freedoms are derived using first-order Taylor series expansion. Finally, they differentiated the strain energy density with respect to the strain gradients to obtain the effective work-conjugate. Banks and Sokolowski (1968) followed a similar method to obtain the effective "couple stress" continuum (Koiter, 1964) of a 2D rectangular lattice. The methods of Askar and Cakmak (1968) and Banks and Sokolowski (1968) were criticized by Bazant and Christensen (1972), as they considered only the first-order terms in the Taylor series expansions (Abramowitz, M., Stegun, I. A. 1970; Thomas, G.B.; Finney, R. L. 1996; Greenberg, M. 1998) of the static and kinematic functions of the nodal degrees of freedom. In the work of Bazant and Christensen (1972), they considered rectangular planar lattice under initial stress to show certain second-order Taylor series terms should be kept for the calculation of the effective strain energy density function. These second-order terms were converted to first-order using the divergence theorem (Stewart, J., 2008; Byron, F., Fuller, R., 1992). Bazant and Christensen (1972) used the beam-column equations (Cross, 1932; Horne and Merchant, 1965; Livesley, 1975; Livesley and Chandler, 1956) to model the microscopic cell elements, for which they obtained the micro-polar effective moduli. It is found that the effective stiffness derived by Bazant and Christensen (1972) may lose its positive definiteness conditions under certain initial lattice loadings. This drawback was considered in Bazant and Christensen (1973).

Renton (1984) analyzed beam-like mechanical members made of pin-jointed spatial lattice materials. He used the finite difference approach for such analysis as he applied the finite-difference calculus to the linearly elastic stiffness matrix of the truss element within each unit cell. The node deformations were assumed as a series of characteristic deformation modes in the form of a finite polynomials and complex exponentials. After applying the unit cell boundary conditions, the element tension forces were derived for the following elastic properties characterization. This approach was applied to beam-like structures with square, triangle, and tetrahedron-based unit cells.

Sigmund (1994) used topology optimization to develop lattice materials with prescribed semi-positive definite constitutive tensors. He called the problem as an inverse problem involving the search of a material with given homogenized coefficients; this problem required finding the interior topology of a base cell that minimizes compliance while meeting volume constraints defined by the prescribed constitutive parameters. Other researchers developed lattice materials with negative Poisson's ratio (Phan-Tien and Karihaloo, 1994).

Schraad and Triantafyllidis (1997a) investigated the scale and imperfection effects on the macroscopic properties of a non-linearly elastic, pin-jointed, periodic, planar lattice structure of finite size. They applied the method of Bardenhagen and Triantafyllidis (1994) and proved that the macroscopic moduli of lattice materials are independent of the scale of the unit cell to the macroscopic length of the lattice if a uniform macroscopic strain field is applied.

Hohe and Becker (1999) and Hohe et al. (1999) computed the effective elastic stiffness properties of rigid-jointed lattice materials by applying uniform, macroscopically, symmetric stress and strain constraints to the unit cell stiffness matrix. They also studied the anisotropic behavior of the lattice material by showing how the elastic moduli vary with the lattice orientation.

Christensen (2000) reviewed the linear elastic stiffness properties of common lattice materials.

Numerical topology optimization techniques were used by Hyun and Torquato (2002) to generate optimally stiff 2D lattice materials; they showed that the Kagome and the full triangulated topologies satisfies the upper Hashin-Shtrikman bounds (Hashin and Shtrikman, 1962) in the low relative density limit.

Deshpande et al. (2001a) investigated the effective elastic stiffness and collapse mechanisms of the octet-truss lattice materials. Deshpande and Fleck (2001) investigated the collapse of sandwich beams with octet-truss core using three-point bending approach. General topological design rules have been presented in Evans et al. (2001) for truss-core lattice materials. Brittain et al. (2001) described the manufacture, testing and analysis of tetrahedral lattice structure with macroscopic dimensions on the order of one centimeter and microscopic dimensions on the order of millimeters. They used soft lithography, electrochemical plating and welding, and various folding and die-stamping operations to manufacture beam-like lattice structures. The performance of the manufactured structure was evaluated using four-point bending tests (Hollenberg, G. W., et al., 1971), through which the effective flexural rigidity and the effective shear rigidity of the material were measured. Brittain et al. (2001) found that their non-optimized tetrahedral lattice beam was much less stiff than an optimized box beam of the same weight and material, and its maximum load capacity was also lower. Chiras et al. (2002) used a similar analysis to interpret

their finite-element modeling and experimental testing of investment cast, tetragonal-truss core sandwich panels. They found that the stiffness and strength of tetragonal core truss panel are near-optimal in comparison with the octet-truss core sandwich beams analyzed by Deshpande and Fleck (2001), and their results agreed with the analytical results given by Ashby et al. (2000), Deshpande et al. (2001a), Deshpande and Fleck (2001) and Wicks and Hutchinson (2001). Chiras et al. (2002) found also that the truss sandwich panel response is asymmetric: the trusses in tension exhibit strain hardening behavior while truss in compression exhibit strain softening behavior due to plastic buckling of the core members.

Although the aforementioned research works were successful in characterizing most of the effective properties of lattice materials, little was known about the periodic collapse mechanisms of pin-jointed versions of lattice materials. Such analysis was conducted using the *Bloch*-wave method.

2.3.4 Bloch-Wave Method

The *Bloch*-wave method is based on the *Bloch's* theorem (Grosso, G. and Pastori-Parravincini, G., 2000). Since the *Bloch's* theorem is used extensively in this thesis for modelling and characterization of periodic lattice structures and lattice materials, the literature of this theorem is detailed thoroughly in the following sections.

A. The *Bloch's* Theorem

The mathematical representation of periodic structures, detailed in Appendix D, is used in this thesis to describe periodic waves propagating through infinite lattice structures using the *Bloch's* theorem.

The *Bloch's* theorem finds its roots in the field of solid-state physics of metals. It was first introduced to describe the transport of electron particles within the crystal structure of a solid; later it was used to obtain a solution of the Schrödinger equation that models wave-functions of the electron particles (Altmann, S. L., 1991; Brillouin, L., 1946; Cantrell, C. D., 2000; Grosso, G. and Pastori-Parravincini, G., 2000; Jones, W. and March, N. H., 1973). Although grounded in the literature of solid-state physics, the *Bloch's* theorem is extensively used in the field of continuum mechanics, as detailed by the work presented in § 2.3.4(A.2).

A.1 The *Bloch's* Theorem and its Applications in Solid State Physics

The historical progress of the theories dealing with the transport properties in metals and its correlation with the material electrical characteristics can be reported as follows. Three years after Thomson's discovery of the electron in 1897, Drude suggested that the electron transport properties of metals might be understood by assuming that their electrons are free and in thermal equilibrium with their atoms, in what was called the free electron gas theory (Ashcroft, N., Mermin, N., 1976). This theory was refined by Lorentz (Ashcroft, N., Mermin, N., 1976). Assuming that the mean free path of electrons was limited by collisions, where the mean free path of an electron is the distance that the electron passes between two successive collisions with other electrons, Lorentz was able to derive Ohm's law for the electrical conductivity. He also obtained the ratio of the thermal to electrical conductivity in excellent agreement with experiments. This ratio, divided by the absolute temperature, is called the Wiedemann-Franz ratio and had been recognized to be universal fifty years earlier (Altmann, S. L., 1991).

The free electron gas theory, however, had two major shortcomings. First, it predicted a large component of the specific heat of a metal which was not observed experimentally. Second, the comparison of the theory with experimental data indicated that the mean free path of the electrons became extremely large at low temperatures; for this phenomenon the model offered no justification (Altmann, S. L., 1991).

In 1928, Sommerfeld revised Lorentz's formulations by using quantum statistics, which solved the above problem; the specific heat was predicted without losing the description of the transport properties. This theory remains at the basis of the understanding of most transport properties of metals and semiconductors (Altmann, S. L., 1991). Sommerfeld's model assumed that the free electrons, also called the valence electrons, within a metal behave as gas particles in vacuum. The resistivity of the metal is computed based on the mean free path which is determined by statistical mechanics, through which the distance between two successive electron scatterings is calculated. This measure represents the distance an electron travels within the metal before two successive collisions with other electrons. In this model, however, the structure of the lattice was not taken into account (Brillouin, L., 1946).

Although the free electron gas theory was successful in explaining many fundamental phenomena in solid state physics, it failed explaining the disagreement of the predictions of metal resistivity at low temperatures with their experimental measurements.

At about the same time, in 1928, Houston and Bloch solved the quantum-mechanical wave equation for electrons in a regular periodic structure. They found that the mean free paths are

arbitrarily large if there were no defects in the periodicity, thereby putting the free-electron theory on a firm basis (Cantrell, C. D., 2000).

Felix Bloch in his "Reminiscences of Heisenberg and the early days of quantum mechanics" (1976) (Grosso, G. and Pastori-Parravicini, G., 2000) explained how his investigation of the theory of conductivity in metal led to what is now known as the *Bloch's* Theorem. He considered wave-functions in a one-dimensional periodic potential and used Fourier analysis to find that the wave differed from the plane wave of free electrons only by a periodic modulation. He concluded that scattering of electrons is caused not by the lattice itself but by defects in the lattice, due to either thermal fluctuation and/or to impurities. At low temperatures, electron mean free paths in metals should increase up to a limit that is set by the density of the impurity. This behavior is observed experimentally and supports Bloch's framework (Brillouin, L., 1946).

For the statement and proof of the *Bloch's* theorem in solid-state physics the reader is referred to appendix C.

A.2 *Bloch's* Theorem in Continuum Mechanics

A closer look at the literatures of the *Bloch's* theorem in solid-state physics one can find a close analogy with the dynamics boundary value problems in continuum mechanics. A similar formulation to the wave-function assumed by the *Bloch's* theorem, as a solution for the Schrödinger equation presented by F. Bloch in 1928, was proposed by Rayleigh 1887. Rayleigh, in his paper (Ashcroft, N., Mermin, N., 1976) on the vibration of strings excited by a time-varying tension and on the propagation of waves through a medium endowed with a periodic structure, set forth all the basic aspects of *Floquet* theorem (Marder, Michael P., 2000) and *Bloch's* theorem (F. Bloch, Dec. 1976) for periodic structures. He explained the phenomenon of selective wave reflection, i.e., why a periodic structure transmits certain waves while totally reflecting others. Rayleigh (Lord Rayleigh., 1887) then considered the equation of vibrating string with periodic mass density per unit length. This equation has the form:

$$T \frac{\partial^2 w(x,t)}{\partial x^2} = \left(m_0 + m_1 \cos\left(\frac{2\pi x}{l}\right) + m_2 \cos\left(\frac{4\pi x}{l}\right) + \dots \right) \frac{\partial^2 w(x,t)}{\partial t^2} \quad (2.2)$$

where T is the tension, l is the distance over which the mass density is periodic, x is the spatial coordinate along the periodic length of the string and t is the time. Assuming a simple harmonic motion of the form:

$$w(x,t) = \bar{w}(x) e^{i\alpha t} \quad (2.3a)$$

Or

$$w(x, t) = \bar{w}(x) \{A \sin(\omega t) + B \cos(\omega t)\} \quad (2.3b)$$

The governing equation for the spatial part $\bar{w}(x)$ can be put in the form of Hill's equation (Hill, G.W., 1886) as:

$$\frac{d^2 \bar{w}}{d\xi^2} + (\Theta_0 + 2\Theta_1 \cos(2\xi) + 2\Theta_2 \cos(4\xi) + \dots) \bar{w} = 0 \quad (2.4)$$

Where $\xi = \pi x/l$ and $\Theta_0 = (\omega^2 m_0 l^2)/(\pi^2 T)$, $2\Theta_k = (\omega^2 m_k l^2)/(\pi^2 T)$ and $k=1, 2, \dots$

Following Hill, Rayleigh assumed a particular solution of the form:

$$\bar{w}(\xi) = e^{ic\xi} \sum_{n=-\infty}^{\infty} b_n e^{2in\xi} \quad (2.5)$$

where in the uniform mass limit, $c = \pm\sqrt{\Theta_0}$, which is the Floquet solution (Marder, Michael P., 2000) with a characteristic exponent ic .

A comparison between the wave-function formulation proposed by Bloch as a solution for the Schrödinger equation and the one dimensional periodic solution proposed by Hill and Rayleigh in dynamics problem of continuum mechanics, one can find they are similar. The *Floquet-Bloch* theorem (Bloch, F., 1928; Floquet, G., 1883) discusses and shows this similarity, first given in a one-dimensional setting by Floquet and later rediscovered by Bloch and generalized to any periodic structure in one, two or three-dimensional spaces. The basis of the two theories is a mathematical concept, where an assumption of a perfectly periodic medium is set forth. A solution is assumed having a spatial term multiplied by a periodic term, which describes the periodicity of a perfectly periodic structural reciprocal space. The reciprocal space is the Fourier transform of the wave-function representing the solution in its reciprocal space.

In the past 30 years, the *Bloch's* theorem has been widely accepted and regularly used in continuum mechanics problems as an alternative framework to the finite-difference methods.

A.3 Statement of the *Bloch's* Theorem in Continuum Mechanics

In continuum mechanics, the *Bloch's* theorem may be stated as follows (Hutchinson R.G., 2004): any spatially-periodic discrete field, ψ , (defined over a periodic structure made up of discrete unit

cells) may be decomposed into a summation of characteristic modes, $\psi\left(\vec{r} + \vec{R}, \omega\right)$, where \vec{r} is

the discrete position vector (basis) over the lattice unit cell, ω is the discrete wave vector and \vec{R} is the Bravais lattice position vector. Group theory (Armstrong, M. A., 1988; Hill, V. E., 2000; Aschbacher, M., 2000; James, G. and Liebeck, M., 2001) may be used to show that these modes are given by:

$$\psi\left(\vec{r} + \vec{R}, \omega\right) = \psi\left(\vec{r}, \omega\right) e^{2\pi i \omega \vec{R}} \quad (2.6)$$

where $\psi\left(\vec{r}, \omega\right)$ is periodic over the unit cell while the exponential term, $e^{2\pi i \omega \vec{R}}$, represents the

“long” wavelength (i.e. over a large, integer number of unit cell multiples) modulation of

$\psi\left(\vec{r} + \vec{R}, \omega\right)$ parameterized by the wave vector ω . Alternatively, this may be proved using

Fourier analysis (Iorio, R. J. and De Magalhaes Iorio, V., 2001; Stein, E. M. and Shakarchi, R., 2003).

A.4 Applications of the *Bloch's* Theorem in the Literature of Periodic Structures and Lattice Materials

An example of the applications of the *Bloch*-wave methods in continuum mechanics is the analysis of Anderson (Anderson, M. S., 1981; 1983) on the buckling of periodic, reticulated cylindrical shells. Anderson (1981) calculated the variation of axial buckling load for a macroscopic structure on the form of an iso-grid cylinder. This lattice structure was previously analyzed by Forman & Hutchinson (1970) (Thompson, J. M. T., Hunt, G. W., 1983) using finite difference methods. The key point for the application of the *Bloch's* theorem in continuum mechanics is that the two analysis procedures of Anderson and Forman and Hutchinson yielded the same results. Furthermore, the analogy of the formalisms between the *Bloch's* theorem and Rayleigh formalisms emphasizes the validity of the use of the Bloch-wave methods for the applications of continuum mechanics in periodic mediums.

Anderson and Williams (1986) extended the approach of Anderson (1981) to the buckling and natural vibration of any lattice structure having repetitive geometry and loading. Their pin and rigid-jointed analyses of the 3D hexahedral lattice plate agreed with the earlier work of Noor et al. (1978) using finite element methods and the equivalent, continuum-plate hypothesis.

The *Bloch's* theorem was also employed in the dynamic analysis of periodic structures. Mead (1973; 1996) used the *Floquet-Bloch* theorem, the one-dimensional version of the *Bloch's* theorem, to analyze the in-plane and out-of-plane vibration behavior in stiffened panels. Triantafyllidis and Schnaidt (Triantafyllidis, N. and Schraad, M. W., 1998; Triantafyllidis, N. and Schnaidt, W. C., 1993) analyzed the elastic stability of a planar, rigid-jointed square lattice material. Using the beam-column form of the Euler-Bernoulli beam stiffness matrix (Affan, A., 1987; Timoshenko, S. P. and Young, D. H., 1945), they first considered the primitive unit cell as a finite structure of rigid-joints and elastic beams. To convert this finite problem to the desired problem of periodic, infinite extent, they then made the assumption that the nodal (rigid-joint), infinitesimal displacement field (including rotations) could be represented using *Bloch's* theorem. Thus, the generalized displacement field was taken as doubly-periodic over the entire lattice. In 2006, Phani, et.al. (2006) used the *Bloch's* theorem to study the wave propagation in two dimensional infinite lattices. They determined the frequency band-gaps for different two dimensional lattice topologies. Phani and Fleck (2008) investigated the phenomenon of elastic boundary layers under quasi-static loading using the *Floquet-Bloch* formalism for two-dimensional, isotropic, periodic lattices.

Hutchinson (2004) and Hutchinson and Fleck (2006) characterized the effective elastic, plastic and buckling properties of pin and rigid-jointed lattice materials using the *Bloch-waves* method. First they formulated the static and the kinematic systems of the pin-jointed structure of the unit cell of the lattice material and used the *Bloch's* theorem to describe the periodic propagation of the nodal and the elements static and kinematic wave-functions. These functions were employed to reduce the derived systems of the unit cell into the irreducible forms of the infinite lattice. Once the irreducible static and kinematic systems are computed, they derived the states of self-stress and the states of internal mechanisms associated with each wave-number generated from the irreducible Brillouin zone of the reciprocal space of the infinite lattice structure (Brillouin, L., 1946). They used the *Cauchy-Born* hypothesis (Bhattacharya, K., 2003; Ericksen, J. L., 1984; Pitteri, M., & Zanzotto, G., 2003; Maugin, G. A., 1992; Born, M., & Huang, K., 1954) to homogenize the microscopic lattice response due to the effect of an assumed uniform macroscopic strain field applied to the lattice. Using this method, they derived an explicit expression of the microscopic element deformations in terms of the macroscopic strain field which are employed to derive the macroscopic strain energy density. By applying *Castigliano's* theorem (Wempner, G.A., 1981), they derived the effective, averaged, macroscopic properties of several 2D lattice topologies with pin- and rigid-joints.

Although the method of Hutchinson (2004) and Hutchinson and Fleck (2006) was successful in predicting the different modes of states of self-stress and the states of internal mechanisms, they did not explore the interaction between these static and kinematic modes; in addition the possible effects on the lattice macroscopic performance in the form of geometrical, non-linear, behavior were not considered. Their method was successful in characterizing simple topologies where all cell elements are included within the cell envelope (e.g. topologies of Figs (2.4a,b,c)); their work also did not include a robust matrix analysis procedure for lattice materials that are constructed of unit cells that have cell elements intersecting their envelopes not at their end nodes but extending between adjacent unit cells (e.g. topologies of Figs (2.5b,c,d,e,f,g,h)).

2.4 Concluding Remarks Emerging From the Literature

From the aforementioned literature review, it is concluded that:

1. The stiffening effect of the states of self-stress on the states of internal mechanisms in infinite periodic lattice structures is still an open area of research. So far, no study looked at this concept applied to lattice materials. This requires investigating the contribution of the states of self-stress to the comprehensive stiffness of lattice structures and materials through the formulation of the geometrical stiffness, especially for the static and kinematic indeterminate topologies.
2. The work of Hutchinson (2004) and Hutchinson and Fleck (2006) are meritorious in characterizing lattice materials and providing a deep understanding on the different modes of the static and kinematic indeterminacy. However, the development of a systematic, automated, matrix-based algorithm that can be applied to any arbitrary microscopic lattice topology needs to be addressed.
3. Recent advances in rapid prototyping and rapid manufacturing technologies (Kruth, et.al., 2005; Rochus, et.al., 2007; Waterman and Dickens, 1994) encourages extending the structuring of lattice materials to include cell member cross-sections. Sizing and shaping of the lattice material cell member cross-sections are not considered yet in literature (Fleck, N.A., et. al., 2010; Ashby, M.F, 2010). However, few researchers examined experimentally the effect of using hollow cylindrical cross-sections on the effective properties of lattice material manufactured at the meso/macro scales (Douglas T. Q. & Haydn N.G. W., 2005). No design methodology has been proposed so far in this area.

CHAPTER 3

Determinacy Analysis and Classification of Pin-Jointed Infinite Periodic Lattice Structures

3.1 Introduction

In this chapter, we present a systematic, matrix-based, procedure for the determinacy analysis of periodic lattice structures with any arbitrary cell topology. We consider the lattice as a periodic micro-truss structure with pin-jointed members. Matrix methods of linear algebra are used for the determinacy analysis where the fundamental subspaces of the equilibrium or the kinematic matrices are computed to determine the states of self-stress and the states of internal mechanisms. For lattice topologies with unit cells that have microscopic cell elements intersecting their envelopes not at their end nodes but extending between adjacent unit cells, we develop the Dummy Node Rule (DNR). The stiffening effect of the periodic states of self-stress on the periodic internal mechanisms is assessed using the product force vector approach and the definiteness of the stress matrix developed by first-order, infinitesimal, periodic, internal mechanisms. The proposed analysis technique is applied to 19 2D lattice topologies, whereas their determinacy analysis results are used for their classification. Infinite, periodic, lattice structures are classified into three classes, namely, stretching dominated, bending dominated and tensegrity lattice structures. The proposed analysis presented in this chapter can be easily extended to 3D lattice topologies.

3.2 Equilibrium and Kinematic Matrix Systems of Unit Cell Finite Structures

We first define the parameters of the unit cell, the building block of periodic lattice structures, before reviewing its equilibrium and kinematics matrix systems, necessary for the determinacy analysis, as proposed by Calladine and Pellegrino (1986).

3.2.1 Definition of the Unit Cell of a Lattice Structure

In continuum mechanics, a periodic lattice structure can be characterized by adopting the notions of crystal physics (Grosso and Pastori-Parravicini, 2000). The crystal structure is generally described by its lattice and its crystal bases. The lattice is represented by the cell envelope which defines the structure periodicity.

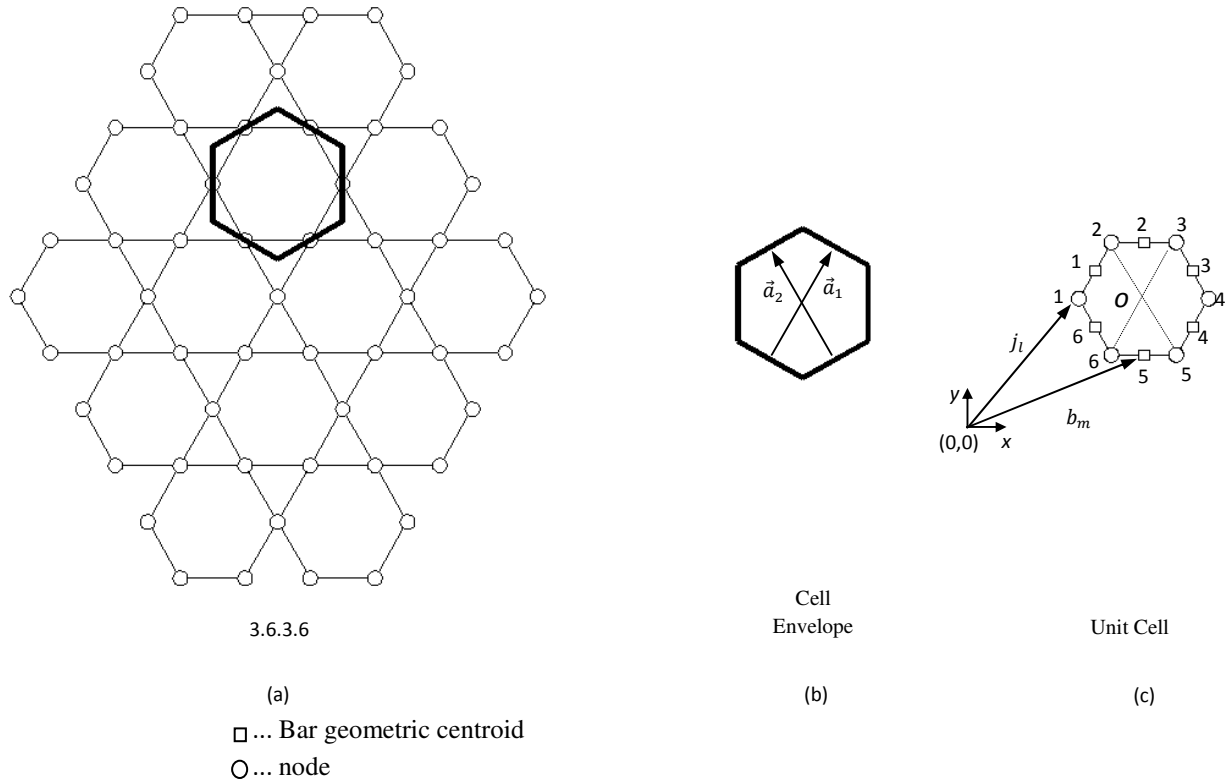


Fig (3.1) (a) Kagome lattice structure; (b) Cell envelope; (c) Unit cell

Fig (3.1a) shows the Kagome lattice structure along with its unit cell and the cell envelope. The lattice structure is shown by the thin lines while the cell envelope is shown by the thick lines. The cell envelope, shown in Fig (3.1b), is the geometrical property of the lattice used to fill the plane in a periodic fashion. To ensure a proper tessellation, which contains no gaps and overlaps, the cell envelope should exhibit a minimum level of symmetry, as defined by the Bravais lattice symmetry (Brillouin, 1946). Here, the cell envelope is a regular hexagon which represents the hexagonal symmetry of the Kagome lattice structure.

The structure of the unit cell, enclosed within the cell envelope, consisting of a set of bars connected between a set of nodes, shown in Fig (3.1c), can be represented by two groups, namely, the node bases group and the bar bases group.

A. Node Bases Group

The node bases group, G_N , is the mathematical group that contains the position vectors of all nodes in the unit cell $\exists G_N \equiv \{j_1, \dots, j_l, \dots, j_j\}$, where j_l is the position vector of node l and

$l \in \{1, 2, \dots, j\}$. j is the total number of nodes within the unit cell structure.

B. Bar Bases Group

The bar bases group, G_B , is the mathematical group that contains the position vectors of all bars in the unit cell $\exists G_B \equiv \{b_1, \dots, b_m, \dots, b_b\}$, where b_m is the position vector of the geometric centroid of bar m where $m \in \{1, 2, \dots, b\}$. b is the total number of bars within the unit cell.

3.2.2 Equilibrium System of the Unit Cell Finite Structure

The static equilibrium system of a structure that has b elements connected between j nodes is represented by:

$$\mathbf{A}t = f \quad (3.1)$$

where $\mathbf{A} \in R^{nj \times b}$, $n=2$ in 2D and $n=3$ in 3D, is a Jacobian matrix with entries of the direction cosines that transforms the vector of tension forces of the structural elements $t \in R^b$ to the vector of the nodal forces $f \in R^{nj}$ (Kuznetsov, E. N., 1997; 2000).

Consider only three nodes, i, j and k that are connected by two bars a and b , as shown the framework in Fig (3.2). For node “ i ”, the equilibrium of its forces with the force of element “ a ”, t_a , is given by:

$$\begin{bmatrix} \frac{(r_{ix} - r_{jx})}{l_a} \\ \frac{(r_{iy} - r_{jy})}{l_a} \end{bmatrix} \begin{bmatrix} t_a \end{bmatrix} = \begin{bmatrix} f_{ixa} \\ f_{iya} \end{bmatrix} \quad (3.2)$$

where f_{ixa} and f_{iya} are, respectively, the x and the y components of the portion of the force of node “ i ” that is in equilibrium with the axial force in element “ a ”. Similarly, the distribution of axial force t_a to the node “ j ” is formulated as:

$$\begin{bmatrix} \frac{(r_{jx} - r_{ix})}{l_a} \\ \frac{(r_{jy} - r_{iy})}{l_a} \end{bmatrix} \begin{bmatrix} t_a \end{bmatrix} = \begin{bmatrix} f_{jxa} \\ f_{jya} \end{bmatrix} \quad (3.3)$$

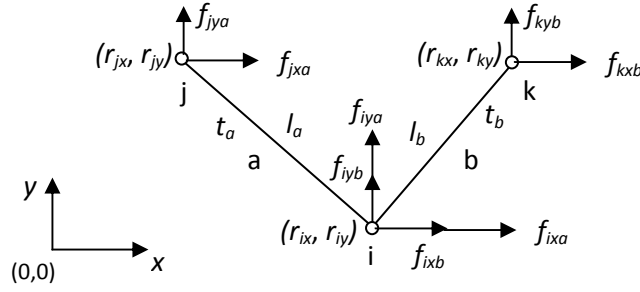


Fig (3.2) Three node equilibrium in pin-jointed structure

Equations (3.2) and (3.3) can be assembled in matrix form as:

$$\begin{bmatrix} \frac{(r_{ix} - r_{jx})}{l_a} \\ \frac{(r_{iy} - r_{jy})}{l_a} \\ \frac{(r_{jx} - r_{ix})}{l_a} \\ \frac{(r_{jy} - r_{iy})}{l_a} \end{bmatrix} [t_a] = \begin{bmatrix} f_{ixa} \\ f_{iya} \\ f_{jxa} \\ f_{jya} \end{bmatrix} \quad (3.4)$$

The same formulation can be generated to other elements and nodes. The final assembled system is the equilibrium system of the pin-jointed framework.

3.2.3 Kinematic System

The kinematic system of a framework that consists of b bars and j nodes can be formulated as:

$$\mathbf{B}d = e \quad (3.5)$$

where $\mathbf{B} \in R^{b \times nj}$, $n = 2$ in 2D and $n = 3$ in 3D, is a Jacobian matrix of entries of direction cosines that transforms the vector of nodal displacements $d \in R^{nj}$ to the vector of element deformations $e \in R^b$ (Kuznetsov, E. N., 1997; 2000).

Element “a” of the pin-jointed framework, shown in Fig (3.3), is connected between the two nodes i and j; the compatibility equation of this element can be formulated as:

$$(r_{ix} - r_{jx})d_{ix} + (r_{iy} - r_{jy})d_{iy} + (r_{jx} - r_{ix})d_{jx} + (r_{jy} - r_{iy})d_{jy} = l_a e_a \quad (3.6a)$$

which can be arranged in matrix form as:

$$\begin{bmatrix} (r_{ix} - r_{jx}) & (r_{iy} - r_{jy}) & (r_{jx} - r_{ix}) & (r_{jy} - r_{iy}) \end{bmatrix} \begin{bmatrix} d_{ix} \\ d_{iy} \\ d_{jx} \\ d_{jy} \end{bmatrix} = l_a e_a \quad (3.6b)$$

where e_a is the axial deformation in element “a”.

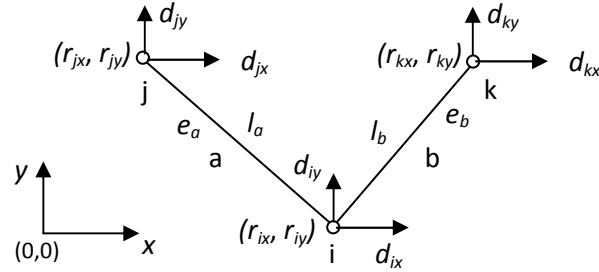


Fig (3.3) Three node kinematics in pin-jointed structure

The same compatibility relation can be written for all framework elements and assembled in what is called the kinematic system of the pin-jointed framework.

3.2.4 Duality of the Kinematic and the Equilibrium Matrices

By applying the Principle of Virtual Work (Timoshenko and Young, 1945) to the unit cell structure we obtain:

$$f^T \cdot \delta l = t^T \cdot \delta e \quad (3.7)$$

where the superscript T denotes the algebraic transpose of a vector and δ is the virtual displacement increment. Substituting eqns (3.1) and (3.5) into eqn (3.7), results in:

$$t^T \mathbf{A}^T \delta l = t^T \mathbf{B} \delta l \quad (3.8)$$

which leads to the following relation:

$$\mathbf{B} = \mathbf{A}^T \quad (3.9)$$

To evaluate the determinacy state of the unit cell finite structure, we examine the four fundamental vector subspaces of the equilibrium matrix, as described below.

3.3 Determinacy Analysis of the Finite Structure of the Unit Cell

The determinacy state of a pin-jointed framework can be evaluated by computing the four fundamental subspaces of the equilibrium or the kinematic matrices (Pellegrino & Calladine (1986).

3.3.1 Four Fundamental Subspaces

The four fundamental subspaces of the equilibrium matrix are defined as:

1. $\text{Row}(\mathbf{A})$: the row space of the equilibrium matrix represents the basis for the equilibrium bar tension vectors t without self-stress, where $\dim(\text{Row}(\mathbf{A})) = r_A$ as r_A is the rank of the equilibrium matrix.
2. $\text{Col}(\mathbf{A})$: the column space of the equilibrium matrix represents the basis for the equilibrium external force vectors f , where $\dim(\text{Col}(\mathbf{A})) = r_A$.
3. $\text{Null}(\mathbf{A})$: the null space of the equilibrium matrix represents the basis for all bar tensions t in equilibrium with $f = 0$, i.e. the modes of states of self-stress. The states of self-stress are the modes of element tension forces developed in a framework with zero external loading. The number of states of self-stress, s , are given by $\dim(\text{Null}(\mathbf{A})) = b - r_A = s$, as b is the number of columns within the equilibrium matrix or simply the number of bars within the finite framework.
4. $\text{Null}(\mathbf{A}^T)$: Kinematically, this subspace is composed of all modes of “inextensional” nodal displacements d compatible with $e = 0$ since $\text{Null}(\mathbf{A}^T) = \text{Null}(\mathbf{B})$; the number of all mechanisms m is given by $m = \dim(\text{Null}(\mathbf{A}^T)) = nj - r_A$, as j is the number of nodes within the framework and $n = 2$ in 2D and $n = 3$ in 3D. On the other hand, the number of internal mechanisms, im , is given as $im = m - rm$, where rm is the number of rigid-body modes for structures that are not constrained into a foundation where $rm = 3$ in 2D and $rm = 6$ in 3D.

Details about the above four fundamental subspaces can be found in Pellegrino & Calladine (1986). Pellegrino (1993) redefined the four fundamental subspaces using the technique of the singular value decomposition (Horn, R. A., et. Al., 1985; 1991; Strang G., 1998).

It is worth mentioning here that the states of mechanisms computed from the null space of the kinematic matrix include both modes of rigid-body motion and modes of internal mechanisms. The rigid-body mechanisms arise as the structure of the unit cell is not constrained into a foundation. To distinguish between the rigid-body mechanisms and the internal mechanisms, Pellegrino & Calladine (1986) presented a simple strategy that is applicable for any finite framework. Interested readers are referred to (Pellegrino, S., Calladine, C. R., 1986).

The next step is to investigate the stiffening effect of states of self-stress to the states of internal mechanisms.

3.4 Stiffening Effect of States of Self Stress

Stable statically and kinematically indeterminate pin-jointed structures are qualified as pre-stressed mechanisms. As described in Chapter two, pre-stressed mechanisms are common assemblies in structural engineering, e.g. pneumatic domes, cable systems and cable nets, fabric roofs and tensegrity structures. Tensegrity structures are unique type among the pre-stressed mechanisms as the kinematic indeterminacy in the form of internal mechanisms is tightened-up by the modes of self-stress, triggered by their infinitesimal displacements, generating a self-standing structure without any external supports.

Calladine and Pellegrino (1986) developed the product force vector approach to examine the stiffening effect of the states of self-stress to first-order infinitesimal mechanisms; an approach that was proven a necessary but not sufficient to classify the kinematic indeterminacy as first-order infinitesimal mechanisms (Kuznetsov, E.N., 1989). Calladine and Pellegrino (1991) modified the product force vector approach to test the positive definiteness of a quadratic form that is computed using the states of self-stress and the states of internal mechanisms within the pin-jointed assembly. They proved that a positive definite quadratic form is a sufficient condition to qualify an internal mechanism as a first-order infinitesimal mechanism. This approach is followed in this thesis and shown in the following section.

3.4.1 The Necessary Condition for First-Order Infinitesimal Mechanisms: The Product Force Vector Approach

A statically and kinematically indeterminate pin-jointed framework responds to external loading by two modes: (i) in the first mode, the structure bar tension forces, t , increase by δt which implies that the structure carry the external loading with a minor geometrical changes; (ii) in the second mode, the structure deforms in an inextensional manner under constant stress until the structure geometry changes to a new balanced configuration. A combined response of the two modes is dependent on the external loading. Kuznetsov (1997) developed a methodology to resolve external load into two orthogonal modes whereas each mode triggers one of the above structural responses.

Consider a structure subjected to two orthogonal modes of external loading $f^{(i)} \in R^{nj}$ and $f^{(ii)} \in R^{nj}$ as j is the number of nodes of the framework with $n = 2$ in 2D and $n = 3$ in 3D. Also, assume that the structural response to these two external loading is $d^{(i)}$ and $d^{(ii)}$, respectively. In

the following we analyse the structural response to each of these two modes as well as the analysis of their combined response.

A. Mode (i) of Structural Response

Similar to eqn (3.1), the equilibrium system of a structure, composed of b bars, connected between j nodes and subjected to a loading $f^{(i)}$, is formulated as:

$$\mathbf{A}t = f^{(i)} \quad (3.10)$$

where $f^{(i)} \in R^{nj}$ is the vector of external forces applied to the nodes of the framework. Since mode $f^{(i)}$ of the external loading triggers only mode (i) of the structural response, then, any redundant bar in the structure provides zero resistance to the external loading. The different vectors corresponding to the redundant elements in the structure are grounded in the column space of the equilibrium matrix, the non-pivotal columns of the equilibrium matrix, \mathbf{A} . The non-pivotal modes in the column space of the equilibrium matrix can be determined by evaluating the reduced row echelon form (Strang G., 1998) of the equilibrium matrix and determining its pivot columns. Other non-pivotal columns correspond to the redundant bars within the structure. Since the redundant bars generate zero loading resistance, then, the non-pivotal columns can be eliminated to generate the matrix system:

$$\hat{\mathbf{A}}t = f^{(i)} \quad (3.11)$$

where $\hat{\mathbf{A}} \in R^{nj \times (b-s)}$ is the truncated equilibrium matrix that is developed by eliminating the non-pivotal columns of the equilibrium matrix, corresponding to redundant elements in the structure. The entries in the tension force vector, t , that correspond to those redundant elements are also eliminated to generate the truncated vector t .

B. Mode (ii) of Structural Response

A structure that has internal mechanisms, if loaded by an external loading, $f^{(ii)}$, that is not in the column space of its equilibrium matrix, excites the modes of internal mechanisms, mode (ii) of structural response. The structure undergoes inextensional deformations, under constant axial forces in its bars, until it changes configuration to a new balanced position. The response of Mode (ii) is obtained through the product force vector analysis.

B.1 Product Force Vector Analysis

The inextensional deformation of pin-jointed structure that has im states of internal mechanisms can be formulated as:

$$d = \mathbf{D}\beta \quad (3.12)$$

$d \in R^{nj}$ is the generalized inextensional deformation vector experienced by the structure.

$\mathbf{D} \in R^{nj \times im}$ is a matrix with the im states of internal mechanisms concatenated into its columns. j

is the number of nodes within the structure. $\beta \in R^{im}$ is a vector of arbitrary constants used to develop a linear combination of the different modes of internal mechanisms.

Consider the framework shown in Fig (3.3), for which the static equilibrium of node i in its original configuration can be formulated as:

$$\begin{bmatrix} \frac{r_{ix} - r_{jx}}{l_a} \\ \frac{r_{iy} - r_{jy}}{l_a} \end{bmatrix} \begin{bmatrix} t_a \end{bmatrix} + \begin{bmatrix} \frac{r_{ix} - r_{kx}}{l_b} \\ \frac{r_{iy} - r_{ky}}{l_b} \end{bmatrix} \begin{bmatrix} t_b \end{bmatrix} = \begin{bmatrix} f_{ix} \\ f_{iy} \end{bmatrix} \quad (3.13)$$

If the structure of Fig (3.3) undergoes a mechanism motion which displaces its nodes by (d_{qx}, d_{qy}) , where d_{qx} and d_{qy} are the nodal displacements in the x and y directions, respectively and $q \in \{i, j, k\}$, then, the static equilibrium of node i can thus be written as:

$$\left\{ \begin{bmatrix} \frac{r_{ix} - r_{jx}}{l_a} \\ \frac{r_{iy} - r_{jy}}{l_a} \end{bmatrix} + \begin{bmatrix} \frac{d_{ix} - d_{jx}}{l_a} \\ \frac{d_{iy} - d_{jy}}{l_a} \end{bmatrix} \right\} \begin{bmatrix} t_a \end{bmatrix} + \left\{ \begin{bmatrix} \frac{r_{ix} - r_{kx}}{l_b} \\ \frac{r_{iy} - r_{ky}}{l_b} \end{bmatrix} + \begin{bmatrix} \frac{d_{ix} - d_{kx}}{l_b} \\ \frac{d_{iy} - d_{ky}}{l_b} \end{bmatrix} \right\} \begin{bmatrix} t_b \end{bmatrix} = \begin{bmatrix} f_{ix} \\ f_{iy} \end{bmatrix} \quad (3.14)$$

Subtracting eqn (3.13) from eqn (3.14) generates the product force vector as:

$$\begin{bmatrix} p_{ix} \\ p_{iy} \end{bmatrix} = \begin{bmatrix} \frac{d_{ix} - d_{jx}}{l_a} \\ \frac{d_{iy} - d_{jy}}{l_a} \end{bmatrix} \begin{bmatrix} t_a \end{bmatrix} + \begin{bmatrix} \frac{d_{ix} - d_{kx}}{l_b} \\ \frac{d_{iy} - d_{ky}}{l_b} \end{bmatrix} \begin{bmatrix} t_b \end{bmatrix} \quad (3.15)$$

where p_{ix} and p_{iy} are the product force vector components of node i in the x and y directions, respectively. Similar computations are generated for other nodes within the structure and the resulting product force vectors of all nodes are recast into a column vector of dimension $2j$ in 2D or $3j$ in 3D. Similar computations can also be generated for other modes of internal mechanisms. All columns of product force vectors are concatenated together as the columns of the product force vector matrix, \mathbf{PFV} . The generalized product force vector, PFV , can be formulated as:

$$PFV = \mathbf{PFV}\beta = f^{(ii)} \quad (3.16)$$

This derivation of the product force vector is based on a single state of self-stress. For structures that possess more than one state of self-stress a linear combination of the different modes of states of self-stress is developed in what we call the global state of self-stress.

B.2 Global State of Self-Stress

The vector of tension forces of the structural elements can be expressed as:

$$t = t_f + \mathbf{SS}\gamma = t_f + S_G \quad (3.17)$$

where $t_f \in R^b$ is the vector of axial forces in the structural elements that are developed by the nodal applied external forces f . $\mathbf{SS} \in R^{b \times s}$ is the states of self-stress matrix which is formed by concatenating the modes of the structural states of self-stress into the columns of the \mathbf{SS} matrix as s is the number of states of self-stress in the structure. $\gamma \in R^s$ is a vector of arbitrary constants which is used to generate a linear combination of the structural states of self-stress.

A global state of self-stress, S_G , is expressed as:

$$S_G = \mathbf{SS}\gamma \quad (3.18)$$

as S_G is the linear combination of all modes of states of self-stress within the structure.

B.2.1 Vector of Linear Combination Constants, γ

The vector of linear combination constants is evaluated by imposing the orthogonality condition that the vector of element deformations, e , is orthogonal to the null space of the equilibrium matrix, A (Pellegrino, S., 1990). This orthogonality condition is formulated as:

$$\mathbf{SS}^T e = 0 \quad (3.19)$$

It is worth mentioning the following point. As the null space of the equilibrium matrix, \mathbf{A} , generating the states of self-stress, is identical to the left-null space of the kinematic matrix, \mathbf{B} , generating modes of elements deformation, then, this orthogonality condition is a natural property of the structures as the subspaces of the equilibrium matrix in the form of the null space and the left-null space are naturally orthogonal in engineering structures (Pellegrino, S., 1993).

The element deformation vector, e , can be expressed as:

$$e = e_0 + \mathbf{F}t \quad (3.20)$$

where $e_0 \in R^b$ is the vector of imposed axial element deformation generated in the redundant elements of the structure due to heating, misfit or pre-stressing of the structure using technologies of active and adaptive members (Sener, M., et.al., 1994). \mathbf{F} is a flexibility diagonal matrix that is formulated as:

$$\mathbf{F}(i, i) = \frac{l_i}{EA_i} \quad (3.21)$$

where l_i and A_i are, respectively, the length and the cross-sectional area of element i and E is the solid material Young's modulus. The solid material is the material used to manufacture the structure. Assume the length of bar elements of the structure can be expressed in terms of a reference length, L , as:

$$l_k = c_k L \quad (3.22)$$

where c_k is a constant that depends on the geometry of the structure and $k \in \{1, \dots, b\}$. b is the number of elements within the structure. Considering a unified cross-sectional area of all elements in the structure and substituting eqn (3.22) into eqn (3.21) results in:

$$\mathbf{F}(k, k) = \left(\frac{L}{EA} \right) c_k \quad \text{or} \quad \mathbf{F} = \left(\frac{L}{EA} \right) \mathbf{F}_c \quad (3.23)$$

where $\mathbf{F}_c(k, k) = c_k$.

Substituting eqn (3.17) into eqn (3.20), then substituting the result into eqn (3.19) and rearranging, results in:

$$\gamma = -(\mathbf{SS}^T \mathbf{FSS})^{-1} \mathbf{SS}^T (e_0 + \mathbf{F}t_f) \quad (3.24)$$

Considering only the axial forces developed by the imposed elongations, e_0 , modifies eqn (3.24) into:

$$\gamma = -(\mathbf{SS}^T \mathbf{FSS})^{-1} \mathbf{SS}^T e_0 \quad (3.25)$$

B.2.2 Vector of Imposed Elongations, e_0

The imposed elongations are applied to the redundant elements in the structure. The redundant elements are determined by computing the reduced row echelon form (Strang G., 1998) of the equilibrium matrix and determining the non-pivotal columns. Once the non-pivotal columns in the equilibrium matrix are determined, the vector of imposed elongations, $e_0 \in R^b$, is formulated as:

$$e_0(i) = \varepsilon_0 c_i L \quad (3.26a)$$

where ε_0 is a nominal strain assumed in the redundant elements which is used to control the level of tension field within the structure. For the purpose of the determinacy analysis we consider $\varepsilon_0 = 1$. $e_0(i)$ is the i^{th} entry of the imposed elongation vector, e_0 , $i \in \{1, \dots, r\}$ and the r 's are indices of the redundant elements in the unit cell structure. Other indices corresponding to pivotal elements in the equilibrium matrix are set equal to zero in the imposed elongation vector, e_0

Assuming a reference length of unity, $L = 1$, eqn (3.26a) can be written as:

$$e_0(i) = \varepsilon_0 c_i \quad \text{or} \quad e_0 = \varepsilon_0 e_c \quad (3.26b)$$

where $e_c \in R^b$ is a vector with entries, corresponding to redundant elements, of topological

constants, c 's, defined in eqn (3.22). Other entries in $e_c \in R^b$ are set to zero.

Substituting eqn (3.25) into eqn (3.18) generates the global state of self-stress as:

$$S_G = -\mathbf{SS}(\mathbf{SS}^T \mathbf{FSS})^{-1} \mathbf{SS}^T e_0 \quad (3.27)$$

The global state of self-stress can be used to generate the product force vector.

C. Combined Response of the Structure

The combined response of the structure can be computed by the superposition of the two modes of structural response, mode (i) and mode (ii). This can be done by adding eqn (3.11) and eqn (3.16) which results in:

$$\left[\begin{array}{c} \hat{\mathbf{A}} \\ \mathbf{PFV} \end{array} \right] \left[\begin{array}{c} \hat{t} \\ \beta \end{array} \right] = \mathbf{A}_{\text{aug}} \left[\begin{array}{c} \hat{t} \\ \beta \end{array} \right] = f^{(i)} + f^{(ii)} \quad (3.28)$$

where \mathbf{A}_{aug} is the augmented equilibrium matrix that includes the bases of the statically determinate framework and the modes of the product force vector developed by the different modes of inextensional deformations.

The augmented equilibrium matrix can be used for the determinacy analysis of the structure in its new configuration, i.e. after undergoing the inextensional deformation to the new balanced configuration. This can be done by computing the four fundamental subspaces of the augmented equilibrium matrix, as explained in § 3.3.1. An empty null space of the transpose of the augmented equilibrium matrix ($\dim(\text{null}(\mathbf{A}_{\text{aug}}^T) = 0)$) indicates that the states of self-stress are

capable of stiffening the internal mechanisms. This is the necessary but not sufficient condition to classify the internal mechanisms as first-order infinitesimal mechanisms.

3.4.2 The Sufficient Condition for First-Order Infinitesimal Mechanisms: The Definiteness of the stress tensor Quadratic Form

Consider a structure that possesses im states of internal mechanisms and one state of self-stress. Calladine and Pellegrino (1991) showed that the actual force developed is given by the product force vector, $PFV = \mathbf{PFV}[\beta]$ whereas a linear combination of the im internal mechanisms is actuated. The work done during this inextensional deformation is given by:

$$W = \frac{1}{2} \beta^T \mathbf{D}^T \mathbf{PFV} \beta \quad (3.29)$$

which can be written as:

$$W = \frac{1}{2} \beta^T \mathbf{Q} \beta \quad (3.30)$$

where $\mathbf{Q} = \mathbf{D}^T \mathbf{PFV}$ is a symmetric matrix. Guest (2006) indicated that the matrix \mathbf{Q} is a reduced form of the stress matrix, a subset of the geometrical stiffness of the structure, where motion is restricted to only inextensional internal mechanisms.

A sufficient condition for first-order infinitesimal mechanisms can be stated as:

$$\beta^T \mathbf{Q} \beta > 0 \quad (3.31)$$

In other words, the matrix \mathbf{Q} has to be positive definite to impart a positive stiffness to any internal mechanism in the structure. A simple test for positive definiteness is that the Eigen values of the matrix \mathbf{Q} should be all positive.

For structures that possess s states of self-stress, the sufficient condition for first-order infinitesimal mechanisms, eqn (3.31), is modified to:

$$\beta^T \left(\sum_{i=1}^s \mathbf{Q}_i \gamma_i \right) \beta > 0 \quad (3.32)$$

where $\mathbf{Q}_i = \mathbf{D}^T \mathbf{PFV}_i$, \mathbf{PFV}_i and γ_i are, respectively, the symmetric reduced stress matrix, the product force vector matrix and the vector of linear combination constants that are computed at the i^{th} state of self-stress as $i \in \{1, \dots, s\}$. Assuming that $\gamma_i \in [-1, 1] - \{0\} \forall i \in \{1, \dots, s\}$, (Calladine and Pellegrino, 1991), a simple code can be written to check the existence of a global positive

definite matrix on the form of $\mathbf{Q}_G = \sum_{i=1}^s \mathbf{Q}_i \gamma_i$. A global positive definite matrix, \mathbf{Q}_G , is a sufficient condition to classify the internal mechanisms as first-order infinitesimal mechanisms.

3.5 Determinacy Analysis of the Infinite Periodic Structure

We apply the *Bloch's* theorem, as described by Hutchinson (2004), for the determinacy analysis of the infinite lattice structure. To do so, we first define the set of parameters necessary to describe the propagation of a periodic wave-function through an infinite lattice structure.

3.5.1 Direct Translational Bases

The lattice translational symmetry primitive bases, \vec{a}_k , are referred to as the direct translational bases. These translational bases are used to tessellate the unit cell that fills the space under translational symmetry. The direct translational bases are feature of the unit cell envelope which demonstrates the axes through which the unit cell is tessellated to fill the space.

3.5.2. Direct Translational Vector

A direct translational vector, expressed as a linear combination of the direct translational bases, is used to translate the reference unit cell to any other cell in the lattice space. This is represented by the primitive lattice vector spanned over a set of cells in the lattice space and is defined as:

$$\vec{R} = \sum_{k=1}^n m_k \vec{a}_k \quad (3.33)$$

where m_k is any set of integers and n is the dimensional space of the lattice ($n = 2$ in 2D and $n = 3$ in 3D).

3.5.3. Position Vectors

The position vectors of bars and nodes of the whole lattice structure can be expressed as a function of the bar and the node bases, defined with reference to the unit cell envelope in addition to the direct translational vector as:

$$\begin{aligned} p_l &= j_l + \vec{R} = j_l + \sum_{k=1}^n m_k \vec{a}_k \quad \forall l \in \{1, \dots, J\}, \\ q_m &= b_m + \vec{R} = b_m + \sum_{k=1}^n m_k \vec{a}_k \quad \forall m \in \{1, \dots, B\}, \\ k &\in \{1, \dots, n\}, n = 2 \text{ in } 2D \text{ and } n = 3 \text{ in } 3D \text{ and } m_k \in \mathbb{Z} \end{aligned} \quad (3.34)$$

where p_l and q_m are the node and the bar position vectors, respectively. J and B are, respectively, the numbers of independent nodes and bars within the reference unit cell. The independent set of bases is defined in § 3.5.4.

3.5.4. Direct Lattice

The direct lattice is the set of independent bar and node bases, over the reference unit cell envelope, spanned over the infinite periodic lattice structure by their position vectors. To determine this independent set of bar and node vectors over the reference unit cell, we verify whether a vector V_{i-l} is dependent on a vector V_i over one unit cell period through the relation:

$$V_{i-l} = V_i + \sum_{k=1}^n x_k \vec{a}_k \quad (3.35)$$

where $x_k \in \{-1, 0, 1\}$ is a unit translation vector, If V_{i-l} and V_i belong to the node position vectors, then $V_i \equiv j_l$ & $i \equiv l \in \{1, \dots, J\}$ and if they belong to the bar position vectors, then $V_i \equiv b_m$ & $i \equiv m \in \{1, \dots, B\}$. The dependency information is used later to modify the wave-function over the reference unit cell to generate the periodic wave-function over the infinite lattice.

3.5.5 Reciprocal Lattice

The reciprocal lattice is itself a Bravais lattice introduced to describe the lattice in terms of primitive vectors. The advantage of resorting to the reciprocal lattice is to discretize the continuous space of the lattice into a discrete summation of modes at which the lattice performance can be examined. The reciprocal lattice can be represented by the primitive vectors

\vec{b}_1 and \vec{b}_2 , which are defined as:

$$\vec{b}_i \cdot \vec{a}_j = 2\pi \delta_{ij} \quad (3.36)$$

where \vec{a}_j and \vec{b}_i are the direct and the reciprocal lattice bases, respectively, and $i, j \in \{1, 2\}$ in 2D or $i, j \in \{1, 2, 3\}$ in 3D. δ_{ij} is the Kronecker delta symbol that satisfies:

$$\delta_{ij} = \begin{cases} 0 & \text{for } i \neq j \\ 1 & \text{for } i = j \end{cases} \quad (3.37)$$

Thus, the translational vectors of the reciprocal lattice are defined as:

$$\omega = \omega_1 \vec{b}_1 + \omega_2 \vec{b}_2 \quad \forall \omega_1, \omega_2 \in [0,1) \subset \mathcal{Q} \quad (3.38)$$

where ω_1 and ω_2 are the covariant components of ω with respect to the basis \vec{b}_1 and \vec{b}_2 and \mathcal{Q} is the set of all rational numbers. ω_1 and ω_2 are derived from the irreducible first Brillouin zone of the reciprocal lattice in agreement with the *Bloch's* theorem (Hutchinson, R.G., 2004; Elsayed, M.S.A., 2009), described in § 3.5.6.

3.5.6 Bloch's Theorem

The *Bloch's* theorem is used to extend the analysis of the unit cell to the unbounded periodic lattice.

A. Bloch-Wave-Function

The *Bloch's* theorem is applied to define the propagation of a wave-function over the infinite lattice structure. For nodal deformation function, the generalized nodal displacement vectors $d(p_l, \omega) \in C^2$, where C is the set of all complex numbers, can be expressed over the entire lattice as a wave-function of the form:

$$d(p_l, \omega) = d\left(j_l + \vec{R}, \omega\right) = d(j_l, \omega) e^{2\pi i \omega \vec{R}} \quad \forall l \in \{1, 2, \dots, J\} \quad (3.39a)$$

where J is the number of independent nodes within the unit cell envelope, $p_l = j_l + \vec{R}$ is the position vector of any node throughout the lattice and \vec{R} is the Bravais cell vector of any unit cell through the entire lattice.

Similarly, for bar deformation function, the generalized bar deformation vectors $e(q_m, \omega) \in C^2$ can be expressed over the entire lattice as a wave-function of the form:

$$e(q_m, \omega) = e\left(b_m + \vec{R}, \omega\right) = e(b_m, \omega) e^{2\pi i \omega \vec{R}} \quad \forall m \in \{1, 2, \dots, B\} \quad (3.39b)$$

where B is the number of independent bars within the unit cell envelope and $q_m = b_m + \vec{R}$ is the position vector of any bar throughout the entire lattice.

To obtain the reduced forms of the kinematic and the equilibrium equations using the generalized equations of wave-functions, transformation matrices are defined for finite wave-functions to

generate the periodic wave-functions over the entire infinite lattice. This procedure makes use of the periodic boundary conditions defined over the unit cell (Langley, 1993; Langley, et.al., 1997).

B. Wave-Functions Transformation Matrices

Applying the *Bloch's* theorem to the generic unit cell, shown in Fig (3.4), we obtain:

$$\begin{aligned}
 q_R &= e^{\mu_x} q_L \\
 q_T &= e^{\mu_y} q_B \\
 q_{RB} &= e^{\mu_x} q_{LB} \\
 q_{LT} &= e^{\mu_y} q_{LB} \\
 q_{RT} &= e^{\mu_x + \mu_y} q_{LB}
 \end{aligned} \tag{3.40}$$

where q is a generic nodal or element function, such as force and deformation, and T, B, L and R denote top, bottom, left and right, respectively. μ_x and μ_y are the wave-numbers, derived from the reciprocal space of the lattice and the dependency information of the nodes, and are expressed as:

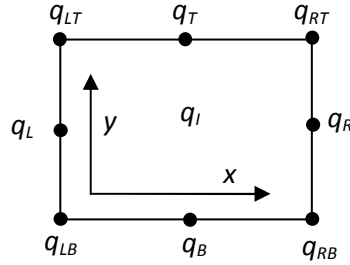


Fig (3.4) A generic unit cell with its periodic displacement boundary conditions

$$\mu_x = 2\pi\omega_1 i, \quad \mu_y = 2\pi\omega_2 i \tag{3.41}$$

where i is the complex number, $i = \sqrt{-1}$. Eqn (3.40) can be arranged in matrix form as:

$$\begin{bmatrix} q_I \\ q_B \\ q_T \\ q_L \\ q_R \\ q_{LB} \\ q_{RB} \\ q_{LT} \\ q_{RT} \end{bmatrix} = \begin{bmatrix} I & 0 & 0 & 0 \\ 0 & I & 0 & 0 \\ 0 & Ie^{\mu_y} & 0 & 0 \\ 0 & 0 & I & 0 \\ 0 & 0 & Ie^{\mu_x} & 0 \\ 0 & 0 & 0 & I \\ 0 & 0 & 0 & Ie^{\mu_x} \\ 0 & 0 & 0 & Ie^{\mu_y} \\ 0 & 0 & 0 & Ie^{\mu_x + \mu_y} \end{bmatrix} \begin{bmatrix} q_I \\ q_B \\ q_L \\ q_{LB} \end{bmatrix}, \quad \text{or } q = \mathbf{T}\tilde{q} \quad (3.42)$$

where \mathbf{T} is the transformation matrix from the primitive cell degrees of freedom to the reduced cell degrees of freedom.

The transformation matrices for the element deformations and the nodal displacements wave-functions are given by:

$$e = \mathbf{T}_e \tilde{e} \quad (3.43a)$$

$$d = \mathbf{T}_d \tilde{d} \quad (3.43b)$$

where \tilde{e} and \tilde{d} are the element deformations and nodal displacements reduced vectors (periodic wave-function), respectively. \mathbf{T}_e and \mathbf{T}_d are the transformation matrices, used to transform, respectively, the full vectors of the element deformations and the nodal displacements to their reduced forms.

To obtain the transformation matrix, \mathbf{T} , for a set of vectors, $V \in C^n$, we implement the following steps. If all vectors are independent, then V can be written as:

$$V = \mathbf{I} \cdot V \quad (3.44)$$

where $\mathbf{I} \in R^{n \times n}$ is a unit square matrix. On the other hand, if some vectors are dependent vectors, then eqn (3.44) can be modified as:

$$V = \mathbf{T} \cdot V_{ind} \quad (3.45)$$

where V_{ind} is the set of independent vectors. Here, \mathbf{T} is a modification of \mathbf{I} . Assume that the vector with the order n_1 in the set, V , is dependent on the vector with the order n_2 . Then, to modify \mathbf{I} , the column number n_1 in \mathbf{I} has to be eliminated, and the element in matrix \mathbf{I} with the index $\mathbf{I}(n_1, n_2)$ has to be modified to:

$$\mathbf{T}(n_1, n_2) = e^{2\pi i \left(\hat{\omega}_1 x_1 + \hat{\omega}_2 x_2 \right)} \quad (3.46)$$

where $\hat{x}_1, \hat{x}_2 \in \{1, 0, -1\}$ according to the vectors dependency relation developed by eqn (3.35).

This process requires that the dependent vectors are arranged in a descending order during the column elimination process to avoid column order swap.

By substitution of eqn (3.43) into the kinematic system of the finite truss, $\mathbf{B}\mathbf{d} = \mathbf{e}$, we obtain:

$$\mathbf{B}\mathbf{T}_d\tilde{\mathbf{d}} = \mathbf{T}_e\tilde{\mathbf{e}} \quad (3.47)$$

The transformation matrix \mathbf{T}_e is a complex non-square matrix, which can be inverted by

multiplying it by the transpose of its conjugate (the Hermitian transpose), \mathbf{T}_e^H such that:

$$\mathbf{T}_e^H \mathbf{B}\mathbf{T}_d\tilde{\mathbf{d}} = \mathbf{T}_e^H \mathbf{T}_e\tilde{\mathbf{e}} \quad (3.48)$$

The multiplication of a complex matrix by its Hermitian transpose generates the following block real matrix, \mathbf{B}_e :

$$\mathbf{T}_e^H \mathbf{T}_e = \mathbf{B}_e \quad (3.49)$$

Substituting eqn (3.49) into eqn (3.48) and inverting the real block matrix \mathbf{B}_e results in:

$$\mathbf{B}_e^{-1} \mathbf{T}_e^H \mathbf{B}\mathbf{T}_d\tilde{\mathbf{d}} = \tilde{\mathbf{e}} \quad (3.50)$$

Thus, from eqn (3.50), the reduced kinematic matrix can be expressed as:

$$\tilde{\mathbf{B}} = \mathbf{B}_e^{-1} \mathbf{T}_e^H \mathbf{B}\mathbf{T}_d \quad (3.51)$$

Using eqn (3.51), the irreducible form of the equilibrium system of infinite periodic lattice structure can be formulated as:

$$\left(\mathbf{B}_e^{-1} \mathbf{T}_e^H \mathbf{B}\mathbf{T}_d \right)^T \tilde{\mathbf{t}} = \tilde{\mathbf{f}} \quad \text{or} \quad \tilde{\mathbf{A}}\tilde{\mathbf{t}} = \tilde{\mathbf{f}} \quad (3.52)$$

where $\tilde{\mathbf{t}}$ and $\tilde{\mathbf{f}}$ are, respectively, the irreducible wave-functions representing the axial bar forces and the nodal forces of the infinite lattice structure.

The determinacy state of the infinite lattice can be analyzed by computing the four fundamental subspaces of the reduced kinematic or equilibrium matrices of the infinite lattice structure. The four fundamental subspaces determine the independent sets of periodic mechanisms and periodic states of self-stress. This process is performed at the different wave-vectors (ω_1, ω_2) that are computed from the reciprocal lattice irreducible first Brillouin zone (Brillouin, 1953).

The information obtained from the four fundamental vector subspaces play an important role in the classification of infinite periodic lattice structure. It has been demonstrated that periodic structures cannot be statically and kinematically determinate (Guest and Hutchinson, 2003). A lattice structure that has a kinematically determinate ($im=0$) and statically indeterminate ($s>0$)

periodic architecture is classified as stretching dominated. On the other hand, periodic lattice structures with statically determinate ($s=0$) and kinematically indeterminate ($im>0$) periodic architectures are classified as bending dominated. For lattice structures with statically and kinematically indeterminate ($s>0$ and $im>0$) periodic architecture, a further analysis (§ 3.6) is required to verify the stiffening effect of the periodic states of self-stress on the periodic states of internal mechanisms. If the periodic states of self-stresses stiffen the periodic states of internal mechanisms at all wave-numbers, then the periodic structure is classified as a tensegrity lattice structure; if this is not the case, then the periodic structure is a bending-dominated.

It is important to note that, although the determinacy analysis and the classification of periodic infinite structures gives an insight into the lattice microscopic performance in the form of element redundancy, inextensional collapse mechanisms as well as the role of the periodic states of self-stress in stiffening the periodic internal mechanisms. However, such analysis finds its importance in a periodic structure subjected to loadings of wavelengths comparable to the lengths of its microscopic elements. In the case of a lattice material, a further study is required for the analysis and the classification of the material. Such analysis is conducted in chapter eight of this thesis.

We developed an in-house MATLAB code that use point group symmetry to determine the irreducible first Brillouin zone and compute the wave-numbers of periodic lattice structures with any arbitrary cell geometry. We integrated this code with our analysis routines that we use throughout this thesis to analyse and characterize different lattice structures and materials.

3.6 Stiffening Effect of Periodic States of Self-Stress to Periodic states of Internal Mechanisms

In this section we investigate the necessary and the sufficient conditions for the stiffening effect of periodic states of self-stress to the periodic states of internal mechanisms in infinite periodic lattice structures.

3.6.1 The Necessary Condition for First-Order Infinitesimal Mechanisms: The Product Force Vector Approach

In this section, we follow the same approach applied to finite frameworks, § 3.4.1. Consider an infinite periodic lattice structure that is subjected to two modes of external loading $\tilde{f}^{(i)} \in C^{nJ}$ and $\tilde{f}^{(ii)} \in C^{nJ}$ as J is the number of independent nodes within the unit cell of the infinite lattice and $n = 2$ in 2D and $n = 3$ in 3D. Assume that the structural response to these two external loadings is

$\tilde{d}^{(i)}$ and $\tilde{d}^{(ii)}$, respectively. In the following we present the analysis of these two modes of structural responses as well as the analysis of their combination.

A. Mode (i) of Infinite Periodic Structural Response

The equilibrium system of the irreducible form of an infinite periodic lattice structure, subjected to a loading $\tilde{f}^{(i)}$, is formulated, similar to eqn (3.52), as:

$$\tilde{\mathbf{A}}\tilde{\mathbf{t}} = \tilde{\mathbf{f}}^{(i)} \quad (3.53)$$

where $\tilde{\mathbf{A}} \in C^{nJ \times B}$ is the irreducible form of the equilibrium matrix; B is the number of independent bars within the unit cell of the lattice. $\tilde{\mathbf{t}} \in C^B$ is the reduced vector of axial forces in the independent bars and $\tilde{\mathbf{f}}^{(i)} \in C^{nJ}$ is the reduced vector of external forces applied to the independent nodes within the unit cell.

Since $\tilde{f}^{(i)}$ triggers only mode (i) of the infinite lattice response as the redundant bars in the lattice provide zero resistance to the external loading, accordingly, we develop the truncated equilibrium system of the lattice as:

$$\hat{\tilde{\mathbf{A}}}\hat{\tilde{\mathbf{t}}} = \hat{\tilde{\mathbf{f}}}^{(i)} \quad (3.54)$$

where the modes in the column space of the reduced equilibrium matrix, $\tilde{\mathbf{A}}$, corresponding to the redundant elements are eliminated by determining the non-pivotal elements in the matrix using

the reduced row echelon form (Strang G., 1998). Here, $\hat{\tilde{\mathbf{A}}} \in C^{nJ \times (B-s)}$ is the truncated reduced equilibrium matrix of the infinite periodic structure and s is the number of periodic states of self-stress at a specified wave-number. Also, the entries in $\tilde{\mathbf{t}}$ corresponding to the redundant elements

are eliminated to develop the truncated vector, $\hat{\tilde{\mathbf{t}}}$.

B. Mode (ii) of Infinite Periodic Structural Response

Similar to what we explained for finite structures, an infinite periodic structure that has periodic internal mechanisms, if loaded by an external loading, $\tilde{f}^{(ii)}$, that is not in the column space of its equilibrium matrix, excites the modes of periodic internal mechanisms, mode (ii) of the lattice response, and the lattice undergoes inextensional deformations, under constant axial forces in its

bars, until the lattice changes configuration to a new balanced position. The response of mode (ii) is derived using the product force vector analysis.

B.1 Product Force Vector Analysis of Infinite Periodic Structures

The first step in this analysis is to compute the reduced, global, periodic state of self-stress which is expressed as:

$$\tilde{S}_G = \tilde{S} \tilde{S} \tilde{\gamma} \quad (3.55)$$

where \tilde{S}_G , \tilde{S} and $\tilde{\gamma}$ are, respectively, the reduced, global, periodic state of self-stress, the reduced periodic state of self-stress matrix and the reduced vector of linear combination constants. The reduced vector of linear combination constants can be computed as:

$$\tilde{\gamma} = - \left(\begin{matrix} \tilde{S}^T & \tilde{F} \tilde{S} \end{matrix} \right)^{-1} \begin{matrix} \tilde{S}^T \\ \tilde{e}_0 \end{matrix} \quad (3.56)$$

where \tilde{F} and \tilde{e}_0 are, respectively, the diagonal reduced flexibility matrix, expressed as shown in eqn (3.23), and the reduced imposed elongation vector which is computed in the same manner as shown in § 3.4.1 (B.2.2). Substituting eqn (3.56) into eqn (3.55), results in the reduced global state of self-stress.

The second step in the analysis is to expand the reduced modes of mechanisms and the global states of self-stress to generate, respectively, the kinematical displacements of all nodes and the tension forces of all elements within the unit cell. This computation is formulated as:

$$\mathbf{D} = \mathbf{T}_d \tilde{\mathbf{D}} \quad (3.57)$$

$$S_G = \mathbf{T}_e \tilde{S}_G \quad (3.58)$$

where \mathbf{T}_d and \mathbf{T}_e are the nodal and the element transformation matrices, given in eqns (3.43).

The expanded modes of mechanisms along with the expanded global state of self-stress are used to formulate the set of product force vectors corresponding to each individual mechanism. The developed product force vectors are concatenated into the product force vector matrix, \mathbf{PFV} . The product force vector matrix is then reduced to the irreducible product force vector matrix, $\tilde{\mathbf{PFV}}$, representing the product force vectors of the infinite lattice structure, which is formulated as:

$$\tilde{\mathbf{PFV}} \tilde{\beta} = \mathbf{T}_d^T \mathbf{PFV} \beta \quad (3.59)$$

where $\tilde{\beta} \in R^{im}$ is a reduced vector of linear combination constants that is used primarily to generate a global reduced internal mechanism as a linear combination of all modes of internal mechanisms within the infinite lattice structure.

C. Combined Response of the Infinite Periodic Lattice

The combined response of the structure can be computed by the superposition of the two modes of structural response, mode (i) and mode (ii). This can be done by adding eqn (3.54) and eqn (3.59) which results in:

$$\left[\begin{array}{c} \hat{\tilde{\mathbf{A}}} \\ \tilde{\mathbf{P}}\mathbf{F}\mathbf{V} \end{array} \right] \left[\begin{array}{c} \hat{\tilde{t}} \\ \tilde{\beta} \end{array} \right] = \tilde{\mathbf{A}}_{\text{aug}} \left[\begin{array}{c} \hat{\tilde{t}} \\ \tilde{\beta} \end{array} \right] = \tilde{f}^{(i)} + \tilde{f}^{(ii)} \quad (3.60)$$

where $\tilde{\mathbf{A}}_{\text{aug}}$ is the augmented reduced equilibrium matrix that includes the bases of the statically determinate periodic lattice structure and the modes of the periodic product force vector developed by the different modes of inextensional periodic internal mechanisms.

Finally, four fundamental subspaces of the augmented reduced equilibrium matrix, $\tilde{\mathbf{A}}_{\text{aug}}$, is computed to determine any periodic internal mechanisms. An empty null space of the transpose of the augmented reduced equilibrium matrix ($\dim(\text{null}(\tilde{\mathbf{A}}_{\text{aug}}^T) = 0)$) indicates that the periodic states of self-stress are capable of stiffening the periodic internal mechanisms and this is the necessary but not sufficient condition to classify the periodic internal mechanisms as first-order infinitesimal periodic mechanisms.

Similar computations can be conducted at the other wave-numbers to investigate the tightening-up of the periodic internal mechanisms at the different wave-numbers.

3.6.2 The Sufficient Condition for First-Order Infinitesimal Mechanisms: The Definiteness of the Stress Tensor Quadratic Form

Similar to the analysis given in § 3.4.2, in infinite lattice structure that possesses im periodic states of internal mechanisms and one periodic state of self-stress, a linear combination of the reduced product force vectors can be given as:

$$\tilde{P}\mathbf{F}\mathbf{V} = \mathbf{P}\mathbf{F}\mathbf{V} \tilde{\beta} \quad (3.61)$$

and the work done during this inextensional deformation is given by:

$$\tilde{W} = \frac{1}{2} \tilde{\beta}^T \tilde{\mathbf{D}}^T \mathbf{P} \mathbf{F} \mathbf{V} \tilde{\beta} \quad (3.62)$$

which can be written as:

$$\tilde{W} = \frac{1}{2} \tilde{\beta}^T \tilde{\mathbf{Q}} \tilde{\beta} \quad (3.63)$$

where $\tilde{\mathbf{Q}} = \tilde{\mathbf{D}}^T \mathbf{P} \mathbf{F} \mathbf{V}$ is a symmetric matrix.

Accordingly, a sufficient condition for first-order infinitesimal periodic mechanisms can be stated as:

$$\tilde{\beta}^T \tilde{\mathbf{Q}} \tilde{\beta} > 0 \quad (3.64)$$

For multiple periodic state of self-stress case, the sufficient condition is modified to:

$$\tilde{\beta}^T \left(\sum_{i=1}^s \tilde{\mathbf{Q}}_i \tilde{\gamma}_i \right) \tilde{\beta} > 0 \quad \tilde{\gamma}_i \in [-1, 1] - \{0\} \quad \forall i \in \{1, \dots, s\} \quad (3.65)$$

where $\tilde{\mathbf{Q}}_i = \tilde{\mathbf{D}}^T \mathbf{P} \mathbf{F} \mathbf{V}_i$ as $i \in \{1, \dots, s\}$ and s is the number of periodic states of self-stress at a

specific wave-number. The global reduced stress matrix is expressed as $\tilde{\mathbf{Q}}_G = \sum_{i=1}^s \tilde{\mathbf{Q}}_i \tilde{\gamma}_i$. It is

important to note that the matrix $\tilde{\mathbf{Q}}_G$ is a complex matrix. A sufficient condition for a complex matrix to be a positive definite is that the Eigen values of the Hermetian part of the complex

matrix are all positive. The Hermetian part of the matrix $\tilde{\mathbf{Q}}_G$ is computed as $\frac{1}{2} \left[\tilde{\mathbf{Q}}_G + (\tilde{\mathbf{Q}}_G)^H \right]$.

3.6.3 Stiffening Effect of Periodic States of Self-Stress to Periodic States of Internal

Mechanisms at wave-number $\omega = (0,0)$

Computation of the left-null space of the reduced equilibrium matrix, $\tilde{\mathbf{A}}$, at wave-number $\omega = (0,0)$, generates a set of modes representing the infinite lattice periodic mechanisms at that specific wave-number. Two of those modes of mechanisms are translational rigid-body motion and the others are internal mechanisms. In order to have a correct computation of the states of self-stress that are associated with the internal mechanisms, the modes of the rigid-body motions have to be eliminated from the row space of the reduced equilibrium matrix and the states of self-stress have to be re-computed based on the resulting new equilibrium matrix. The new computed states of self-stress are the accurate states associated with the internal mechanisms which can be

used to check the tightening-up of the lattice at wave-number $\omega = (0,0)$. To distinguish between the modes of mechanisms, we use the product force vector approach. First, we compute the reduced product force vector matrix associated with the set of reduced states of self-stress and the reduced mechanisms at wave-number $\omega = (0,0)$. Second, we determine the non-pivotal columns in the reduced equilibrium matrix and we generate the truncated reduced equilibrium matrix at wave-number $\omega = (0,0)$. We augment the reduced product force vector matrix and the truncated reduced equilibrium matrix to generate the augmented reduced equilibrium matrix, $\tilde{\mathbf{A}}_{\text{aug}}$. The reduced row echelon form of the matrix $\tilde{\mathbf{A}}_{\text{aug}}^T$ is computed to determine the non-pivotal modes, representing the set of mechanisms after applying the stiffening effect of the global state of self-stress, along with their indices. If the number of the computed mechanisms is reduced to two, then these modes are rigid-body mechanisms and the rest of mechanisms are internal mechanisms that are stiffened by the global state of self-stress. However, if the number of the computed mechanisms is greater than two an additional filtration step is required to distinguish between the rigid body mechanisms and the non-stiffened internal mechanisms.

If the number of independent nodes within the unit cell is J , then, two modes of rigid body mechanisms can be defined for the infinite lattice as:

$$\begin{aligned} \tilde{d}_x(2(i-1)+1) &= 1 \\ \tilde{d}_x(2(i-1)+2) &= 0 \\ \tilde{d}_y(2(i-1)+1) &= 0 \\ \tilde{d}_y(2(i-1)+2) &= 1 \end{aligned} \quad \text{and } i \in \{1, \dots, J\} \quad (3.66)$$

where \tilde{d}_x and \tilde{d}_y are the rigid-body mechanisms in the x and the y directions, respectively. The modes of mechanism that are independent of the two modes of rigid-body mechanisms, defined in eqn (3.66), are the internal mechanisms while the dependent modes are the rigid-body mechanisms. The indices of these modes of rigid-body mechanisms are determined and their corresponding rows in the reduced equilibrium matrix are eliminated to form the matrix $\tilde{\tilde{\mathbf{A}}}$. Again the null space of this new reduced equilibrium matrix is computed and the resulting periodic states of self-stress are used to form the final global periodic state of self-stress and the stiffening effect analysis has to be repeated by the new computed periodic state of self-stress.

Infinite periodic lattice structures that have unit cells with all their elements enclosed within their cell envelope can be directly analysed using the aforementioned proposed analysis technique.

However, lattice topologies that have unit cells with elements extending between adjacent unit cells, such as those shown in Fig (2.5b-h), require extending the analysis to include the Dummy Node Rule which we present in the next section.

3.7 The Dummy Node Rule for the Analysis of Pin-Jointed Periodic Lattice Structures

An accurate prediction of the microscopic behavior of periodic lattice structures using the *Bloch*-wave method requires the retrieving of all the periodicity information of the kinematic and the static wave-functions within the cell envelope. Lattice structures constructed of unit cells that involve elements extending between adjacent unit cells do not possess the full periodicity information within the configuration of their unit cells; this occurrence (Figs. 2.5b-h) represents a challenge for the current methods of analysis. To solve this, a new rule, namely, the Dummy Node Rule (DNR) is presented in this section. The definition of the DNR is based on the *Bloch*'s theorem applied to a unit step periodicity across the unit cell envelope assuming that the wave-function is propagating with a constant amplitude and without any phase change, i.e. at wave-number $\omega = (0,0)$.

A simplified scheme for the application of the DNR in modelling a wave-function over the finite structure of a unit cell is presented, namely, the Dummy Node Scheme (DNS). The DNS is a simple and straight forward method that can be used to generate the unit cell kinematic and equilibrium matrices that are employed in the analysis of the infinite lattice structures. It is also used in the application of the *Cauchy-Born* hypothesis (Bhattacharya, K., 2003; Ericksen, J. L., 1984; Pitteri, M., & Zanzotto, G., 2003; Maugin, G. A., 1992; Born, M., & Huang, K., 1954) necessary for the homogenization process of the microscopic characteristics of lattice structures, as will be shown in chapter four.

The first step in the DNS is to introduce dummy nodes at the intersection points between the cell envelope and the elements extending between adjacent unit cells. These dummy nodes are treated as part of the finite structure of the unit cell which is used to derive the static and the kinematic analytical models of the unit cell finite structure. In this step, the DNS establishes the kinematic and the equilibrium periodic relationships of the wave-function propagating across the dummy nodes and also across the microscopic elements connected to those dummy nodes.

The statement of the DNR requires extending the mathematical description of the unit cell to account for the dummy nodes.

3.7.1. Extending the Mathematical Description of the Unit Cell

The DNR requires extending the unit cell parameters, defined earlier in §3.2.1, to account for the dummy nodes, namely, the dummy node bases group. These lattice parameters are shown in details in Fig (3.5) and briefly defined hereafter.

Fig (3.5) shows a 2D square lattice structure which is used here as a paradigm for the analysis. The lattice structure, in Fig (3.5), is demonstrated by the thin lines while the cell envelopes are demonstrated by the thick lines. Unit cells A and B, shown in Figs (3.5c) and (3.5d), respectively, can be used to generate the square lattice by infinite 2D tessellation. Unit cell A is a traditional cell, where all the cell elements are included within its envelope. Employing unit cell A for the determinacy analysis and characterization of the square lattice using the method developed earlier in this chapter is straightforward.

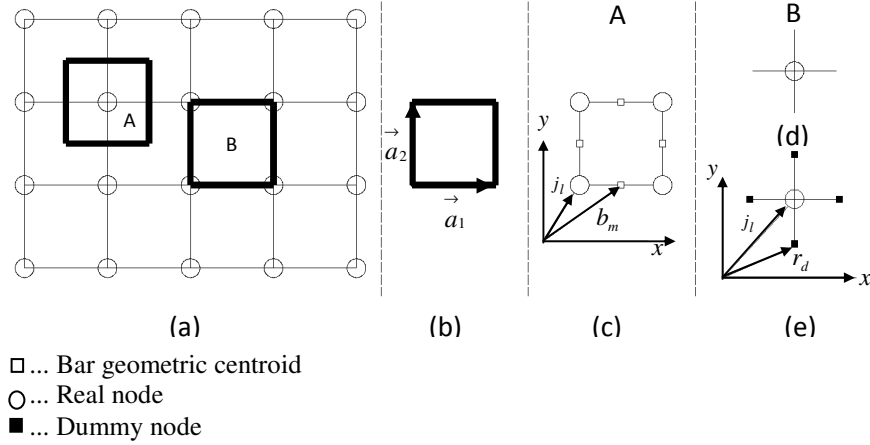


Fig (3.5) (a) Lattice structure; (b) Cell envelope; (c) Unit cell A; (d) Unit cell B without dummy nodes; (e) Unit cell B with dummy nodes

Unit cell B is an alternative unit cell that can be also used to generate the square lattice. However, using unit cell B for the determinacy analysis and characterization of the square lattice by applying the *Bloch*-wave method is challenging as the structure of the unit cell does not have any nodes that lay on the envelope. We analyze the square lattice using the two unit cells and show at the end of this section that they generate similar results which demonstrates the accuracy of the DNR and the DNS.

The bar and the node bases are represented by their position vectors. For this purpose, a Cartesian coordinate system is defined for each unit cell in the square lattice, with its origin located at the left- bottom node of unit cell A and at the only real node of unit cell B. A length of unity is assumed for all microscopic cell elements of the square lattice.

A. Lattice Bases

The set of bases representing the physical lattice structure contains two groups, namely, the node bases group and the bar bases group (Elsayed, M.S.A. and Pasini, D., 2010b; Hutchinson R.G., 2004). In the current study, another group that contains the bases of the dummy nodes is introduced, as explained in section A.1.

A.1 Dummy Node Bases Group

In lattice structures constructed of unit cells that have cell elements intersecting their envelopes not at their end nodes but extending between adjacent unit cells, hypothetical dummy nodes are introduced at the intersection points between the microscopic cell elements and the cell envelope, as shown in Fig (3.5e).

The dummy node bases group, G_D , is the mathematical group that contains the position vectors $r_d \equiv j_d$ of all the dummy nodes within a unit cell, where $d \in \{1, \dots, D\}$ and D is the number of dummy nodes within a unit cell. For unit cells A and B of the square lattice, the dummy node bases groups are formulated respectively as: $G_D^A = \Phi$, where Φ is the empty group and $G_D^B = \{(-0.5, 0), (0, 0.5), (0.5, 0), (0, -0.5)\}$.

The superscripts A and B indicate parameters of unit cells A and B, respectively.

A.2 Node Bases Group

The node bases group, G_N , is the mathematical group that contains the position vectors of all nodes in the unit cell. In a unit cell that contains only real nodes, such as unit cell A, shown in Fig (3.5c), $G_N \equiv \{j_1, \dots, j_l, \dots, j_j\}$, where j_l is the position vector of node l and $l \in \{1, 2, \dots, j\}$. j is the total number of nodes within the unit cell structure. If the unit cell contains dummy nodes, such as unit cell B shown in Fig (3.5e), then, $G_N \equiv \{j_1, \dots, j_l, \dots, j_j\} \cup G_D$.

For unit cells A and B of the square lattice, the node bases groups are formulated, respectively, as:

$$G_N^A = \{(0, 0), (0, 1), (1, 1), (1, 0)\} \text{ and } G_N^B = \{(0, 0), (-0.5, 0), (0, 0.5), (0.5, 0), (0, -0.5)\}.$$

A.3 Bar Bases Group

The bar bases group, G_B , is the mathematical group that contains the position vectors of all the bars in the unit cell. In a unit cell that contains only real nodes, $G_B \equiv \{b_1, \dots, b_m, \dots, b_b\}$, where b_m is the position vector of the geometric centroid of a bar m with $m \in \{1, 2, \dots, b\}$. b is the total number of bars within the unit cell structure that are connected between real nodes. In a unit cell that contains dummy nodes, then, $G_B \equiv \{b_1, \dots, b_m, \dots, b_b\} \cup G_D$, as the position vectors of the dummy nodes are coincident with the position vectors of the bars connected to them. Accordingly, it is evident that the dummy node bases group is always defined as a subset of the node bases group and the bar bases group.

For unit cells A and B of the square lattice, the bar bases groups are formulated, respectively, as:

$$G_B^A = \{(0, 0.5), (0.5, 1), (1, 0.5), (0.5, 0)\} \text{ and } G_B^B = \{(-0.5, 0), (0, 0.5), (0.5, 0), (0, -0.5)\}.$$

These unit cell parameters are used to generate the equilibrium and the kinematic systems of the unit cell using the DNS which is based on the definition of the DNR.

3.7.2 The Dummy Node Rule

In a periodic lattice structure, constructed by tessellating a unit cell composed of bar bases group G_B , node bases group G_N and dummy node bases group $G_D \subset G_N$, \forall independent bar element n , with position vector $b_n \in G_B$, which is connected between independent dummy node j , with position vector $j_j \equiv b_n \in G_D$, and real node l , with position vector $j_l \in G_N$, \exists a dependent bar element m , with position vector $b_m \in G_B$, that is connected between dependent dummy node i , with position vector $j_i \equiv b_m \in G_D$, and real node k , with position vector $j_k \in G_N$, such that:

$$j_i = j_j + \lambda \vec{a}_k \quad (a)$$

$$b_m = b_n + \lambda \vec{a}_k \quad (b)$$

$$\hat{n}_m = \hat{n}_n \quad (c)$$

$$t_m = -t_n e^{2\lambda\pi i \omega} \quad (d)$$

$$e_m = e_n e^{2\lambda\pi i \omega} = e_{m1} + e_{n2} e^{2\lambda\pi i \omega} = e_{m2} + e_{n1} e^{2\lambda\pi i \omega} \quad (e)$$

$$f_i = -f_j e^{2\lambda\pi i\omega} \quad (f)$$

$$d_i = d_j e^{2\lambda\pi i\omega} \quad (g)$$

$$d_i = (d_l e^{2\lambda\pi i\omega} - d_k) \frac{\|j_i - j_k\|}{\|j_l + \lambda a_k - j_k\|} \quad (h)$$

$$d_j = (d_l - d_k e^{-2\lambda\pi i\omega}) \frac{\|j_l - j_j\|}{\|j_l + \lambda a_k - j_k\|} \quad (i)$$

where \vec{a}_k is the direct translational basis of the lattice, $\lambda \in \{1, -1\}$ is a unit integer that defines the dummy nodes periodicity relation across the cell envelope. λ is a subset of \hat{x}_k , defined in eqn (3.35); \hat{n} , t , f , d and e denote, respectively, a unit vector in the direction of an element, an element tension force, nodal force, nodal displacement and an element axial deformation. The subscripts i, j, m , and n denote, respectively, dummy node i , dummy node j , element m and element n . On the other hand, the subscripts $m1$ and $m2$ denote, respectively, the portion of element m included within the reference unit cell envelope and the portion of element m out of the reference unit cell envelope. Similarly, subscripts, $n1$ and $n2$ denote, respectively, the portion of element n out of the reference unit cell envelope and the portion of element n included within the reference unit cell envelope. ω is a wave-number derived from the irreducible first Brillouin zone of the lattice and i appearing in the exponential power is the complex number $i = \sqrt{-1}$. It is noted that, due to the translational symmetry of the lattice, the dummy nodes are always introduced in pairs where, within a pair, the two dummy nodes are mutually, periodically, dependent on one another with one-step integer translation, as defined by eqn (3.35).

A. Proof of the DNR

For the proof of the DNR, we examine the lattice topology shown in Fig (3.6). After the proof we resume the analysis of the square lattice structure shown in Fig (3.5) at which we apply the DNS to derive the equilibrium and the kinematic systems of the lattice unit cells.

Consider elements m and n in the three-unit cell assembly of the lattice structure shown in Fig (3.6). Element m is connected to node k , located on the borders between unit cells I and II, and to node p that belongs to unit cell III. Element n connected to node q belongs to unit cell I, and to node l belongs to unit cell II. The envelope of unit cell II intersects elements m and n at nodes i

and j , respectively, where i and j are dummy nodes that we introduce at the intersection points. Node i divides element m into two segments $m1$ and $m2$ of length L_{m1} and L_{m2} , respectively. On the other hand, node j divides element n into two segments $n1$ and $n2$ of length L_{n1} and L_{n2} , respectively. Elements m and n carry internal tension forces t_m and t_n , respectively. The portions of the nodal forces that are in balance with the tension forces in elements m and n are denoted as f_r where $r \in \{i, j, k, l, p, q\}$. f_r is a two dimensional vector that has two components in the x and the y Cartesian coordinate directions.

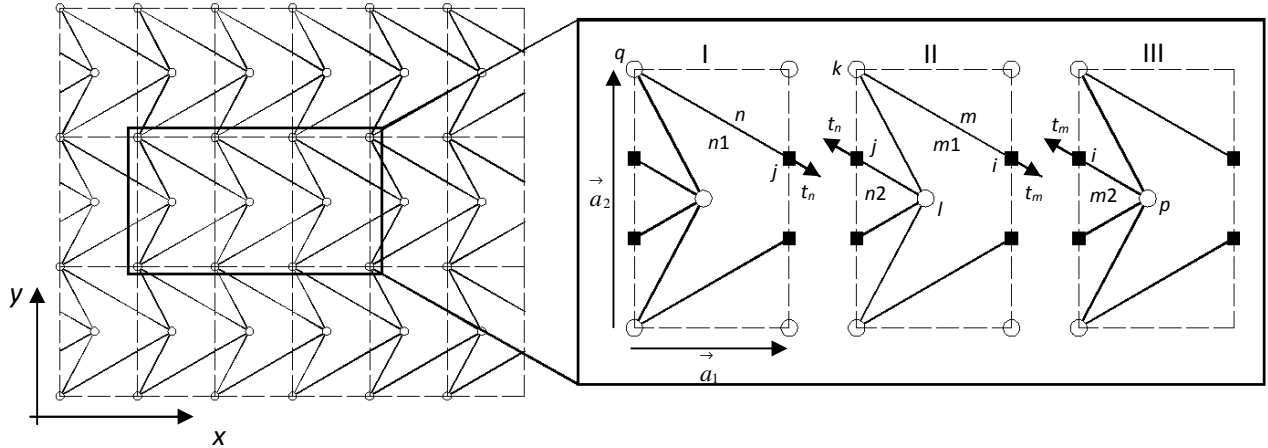


Fig (3.6) A lattice structure (left) and the assembly of three unit cells (right) that are tessellated in the direction of the horizontal translational basis. The structural elements are presented by the continuous lines and the cell envelopes are presented by the dashed lines.

Real structural nodes are presented as (O) and the dummy nodes are presented as (■)

Geometrical inspection of the three cells assembly in Fig (3.6) shows that element m is periodically dependent on element n . Accordingly, eqns (a-c) of the DNR are proven directly, where:

$$\vec{j}_i = \vec{j}_j + \vec{a}_1 \quad (3.67)$$

$$\vec{b}_m = \vec{b}_n + \vec{a}_1 \quad (3.68)$$

$$\hat{n}_m = \hat{n}_n \quad (3.69)$$

The value of λ in eqn (a) of the DNR is decided upon the dependency relation between the two dummy nodes, which is equivalent to \hat{x}_k defined by eqn (3.35).

Using the bar dependency relation defined in eqn (3.68), the *Bloch's* theorem can be applied to define the wave-functions propagating across the microscopic cell elements in the form of the tension forces and the axial deformations. The tension forces and the axial deformations of elements m and n are expressed as:

$$t_m = t_n e^{2\pi i \omega} \quad (3.70)$$

$$e_{m1} = e_{n1} e^{2\pi i \omega} \quad (3.71)$$

$$e_{m2} = e_{n2} e^{2\pi i \omega} \quad (3.72)$$

By splitting the three-unit cells assembly into separate cells, as shown in Fig (3.6), applying the conditions of static equilibrium, and considering the static equilibrium of unit cell II, we can write eqn (3.70) as:

$$t_m = -t_n e^{2\pi i \omega} \quad (3.73)$$

which proves eqn (d) of the DNR. Adding the left and the right hand sides of eqn (3.71) to the left and the right hand sides of eqn (3.72) in an alternative manner, results in eqn (e). Eqn (e) of the DNR is necessary for the computation of the strain energy density, necessary for the stiffness computation of the homogenized lattice material.

From Fig (3.6), it can be deduced that nodes k and p are dependent on nodes q and l , respectively, such that:

$$j_k = j_q + \vec{a}_1 \quad (3.74)$$

$$j_p = j_l + \vec{a}_1 \quad (3.75)$$

Using the dependency relations, defined in eqns (3.74) and (3.75), the *Bloch's* theorem can be applied to describe the wave-functions propagating across the nodes. Considering also the anti-periodic constraints necessary for the static equilibrium of the lattice, the nodal forces and the nodal displacements of nodes k and q , and nodes p and l are related as:

$$f_k = -f_q e^{2\pi i \omega} \quad (3.76)$$

$$f_p = -f_l e^{2\pi i \omega} \quad (3.77)$$

$$d_k = d_q e^{2\pi i \omega} \quad (3.78)$$

$$d_p = d_l e^{2\pi i \omega} \quad (3.79)$$

Rearranging eqns (3.76) and (3.77), eqn (f) of the DNR can be derived. Similarly, the rearrangement of eqns (3.78) and eqn (3.79) yields eqn (g) of the DNR.

Equations (h) and (i) express the displacements of the dummy nodes as a linear interpolation of the displacements of the real nodes within the unit cell envelope. For instance, the displacement of the dummy node j is expressed in eqn (i) of the DNR as a linear interpolation of the displacements of nodes l and k . As shown in § 3.7.3, the degrees of freedom associated with the dummy nodes are eliminated from the derived matrix systems. However, it is necessary to derive all types of structural response by using the parameters given within the unit cell envelope, which is the notion of modelling lattice structures by considering only the unit cell.

3.7.3 The Application of the Dummy Node Rule for the Determinacy Analysis of Lattice Structure: The Dummy Node Scheme

In this section, the DNR is applied to the determinacy analysis of lattice structures. Here, a method is developed as a simple and straightforward scheme for the application of the DNR, which we name the DNS. In particular, DNS is used to obtain the equilibrium and the kinematic systems of unit cell finite structure.

To derive the equilibrium and the kinematic systems of unit cells that have cell elements extending between adjacent unit cells involves the following steps:

Step 1: Hypothetical dummy nodes are defined at the intersection points between the microscopic cell elements, extending between neighbouring unit cells, and the cell envelope. The kinematic and the equilibrium matrices of the finite microstructure are then formulated to take into account the dummy nodes.

Step 2: Once the kinematic and the equilibrium systems are formulated, the degrees of freedom associated with the hypothetical dummy nodes are eliminated from the generated matrices.

The degrees of freedom associated with the dummy nodes appear in: (i) the row space of the equilibrium matrix, also in (ii) the column space of the kinematic matrix. To eliminate the degrees of freedom associated with the dummy nodes, all modes in the row space of the equilibrium matrix and the column space of the kinematic matrix that are associated with the dummy nodes are eliminated. The same elimination technique is applied to the nodal force and the nodal displacement vectors.

For the square lattice structure, shown in Fig (3.5), the equilibrium and the kinematic systems of the finite structure of unit cell A are formulated as:

$$\begin{bmatrix} 0 & 0 & 0 & -1 \\ -1 & 0 & 0 & 0 \\ 0 & -1 & 0 & 0 \\ 1 & 0 & 0 & 0 \\ 0 & 1 & 0 & 0 \\ 0 & 0 & 1 & 0 \\ 0 & 0 & 0 & 1 \\ 0 & 0 & -1 & 0 \end{bmatrix} \begin{bmatrix} t_1 \\ t_2 \\ t_3 \\ t_4 \end{bmatrix}^A = \begin{bmatrix} f_{1x} \\ f_{1y} \\ f_{2x} \\ f_{2y} \\ f_{3x} \\ f_{3y} \\ f_{4x} \\ f_{4y} \end{bmatrix}^A, \quad \begin{bmatrix} 0 & 0 & 0 & -1 \\ -1 & 0 & 0 & 0 \\ 0 & -1 & 0 & 0 \\ 1 & 0 & 0 & 0 \\ 0 & 1 & 0 & 0 \\ 0 & 0 & 1 & 0 \\ 0 & 0 & 0 & 1 \\ 0 & 0 & -1 & 0 \end{bmatrix}^T \begin{bmatrix} e_1 \\ e_2 \\ e_3 \\ e_4 \end{bmatrix}^A = \begin{bmatrix} d_{1x} \\ d_{1y} \\ d_{2x} \\ d_{2y} \\ d_{3x} \\ d_{3y} \\ d_{4x} \\ d_{4y} \end{bmatrix}^A \quad (3.80)$$

The equilibrium and the kinematic systems of unit cell B are formulated as:

$$\begin{bmatrix} 1 & 0 & -1 & 0 \\ 0 & -1 & 0 & 1 \\ \boxed{-1 & 0 & 0 & 0} \\ \boxed{0 & 0 & 0 & 0} \\ \boxed{0 & 0 & 0 & 0} \\ \boxed{0 & 1 & 0 & 0} \\ \boxed{0 & 0 & 1 & 0} \\ \boxed{0 & 0 & 0 & 0} \\ \boxed{0 & 0 & 0 & 0} \\ \boxed{0 & 0 & 0 & -1} \end{bmatrix} \begin{bmatrix} t_1 \\ t_2 \\ t_3 \\ t_4 \end{bmatrix}^B = \begin{bmatrix} f_{1x} \\ f_{1y} \\ \boxed{f_{d1x}} \\ \boxed{f_{d1y}} \\ \boxed{f_{d2x}} \\ \boxed{f_{d2y}} \\ \boxed{f_{d3x}} \\ \boxed{f_{d3y}} \\ \boxed{f_{d4x}} \\ \boxed{f_{d4y}} \end{bmatrix}^B, \quad \begin{bmatrix} 1 & 0 & -1 & 0 \\ 0 & -1 & 0 & 1 \\ \boxed{-1 & 0 & 0 & 0} \\ \boxed{0 & 0 & 0 & 0} \\ \boxed{0 & 0 & 0 & 0} \\ \boxed{0 & 1 & 0 & 0} \\ \boxed{0 & 0 & 1 & 0} \\ \boxed{0 & 0 & 0 & 0} \\ \boxed{0 & 0 & 0 & 0} \\ \boxed{0 & 0 & 0 & -1} \end{bmatrix}^T \begin{bmatrix} d_{1x} \\ d_{1y} \\ \boxed{d_{d1x}} \\ \boxed{d_{d1y}} \\ \boxed{d_{d2x}} \\ \boxed{d_{d2y}} \\ \boxed{d_{d3x}} \\ \boxed{d_{d3y}} \\ \boxed{d_{d4x}} \\ \boxed{d_{d4y}} \end{bmatrix}^B = \begin{bmatrix} e_1 \\ e_2 \\ e_3 \\ e_4 \end{bmatrix}^B \quad (3.81)$$

The second step is the elimination of all degrees of freedom associated with the dummy nodes. The modes associated with the dummy nodes in the kinematic and the equilibrium systems are surrounded by the dotted rectangles shown in eqn (3.81). This process yields eqn (3.81) to the form:

$$\begin{bmatrix} 1 & 0 & -1 & 0 \\ 0 & -1 & 0 & 1 \\ 0 & 0 & 0 & 0 \\ 0 & 0 & 0 & -1 \end{bmatrix} \begin{bmatrix} t_1 \\ t_2 \\ t_3 \\ t_4 \end{bmatrix} = \begin{bmatrix} f_{1x} \\ f_{1y} \end{bmatrix}, \quad \begin{bmatrix} 1 & 0 \\ 0 & -1 \\ -1 & 0 \\ 0 & 1 \end{bmatrix} \begin{bmatrix} d_{1x} \\ d_{1y} \end{bmatrix} = \begin{bmatrix} e_1 \\ e_2 \\ e_3 \\ e_4 \end{bmatrix} \quad (3.82)$$

Equation (3.82) represents the equilibrium and the kinematic systems of the finite structure of unit cell (B), shown in Fig (3.5d). The dependency relations of the real node bases and also those of the bar bases are then derived to be used along with the definition of the *Bloch's* theorem to express the irreducible forms of the matrix systems of eqn (3.82). The irreducible forms of the equilibrium and the kinematic systems of unit cells A and B, developed for the infinite square lattice structure, are used to predict the lattice behavior at different wave-numbers as the wave-

numbers are derived from the irreducible first Brillouin zone of the reciprocal lattice. It is realized that the analysis using the two unit cells identically predicts the microscopic performance of the infinite periodic square lattice structure which is classified as a bending dominated lattice structure. This result illustrates the accuracy of the DNR and the DNS. Examples for the application of this methodology are reported in Appendix E.

A. Proof of the Validity of the Elimination Scheme

Consider the two elements, m and n in the three-unit cells assembly of the lattice structure shown in Fig (3.6). A unit vector in the direction of elements m and n can be written as:

$$\hat{n}_m = \frac{j_i - j_k}{L_{m1}} = \frac{j_p - j_i}{L_{m2}} = \frac{j_p - j_k}{L_m} \quad (3.83)$$

$$\hat{n}_n = \frac{j_j - j_q}{L_{n1}} = \frac{j_l - j_j}{L_{n2}} = \frac{j_l - j_q}{L_n} \quad (3.84)$$

A.1 Equilibrium Analysis

Consider segment $m1$ of element m , the static equilibrium of forces of nodes k and i with the tension force in the element t_m can be formulated as:

$$\begin{bmatrix} -\hat{n}_m \\ \hat{n}_m \end{bmatrix} t_m = \begin{bmatrix} f_k \\ f_i \end{bmatrix} \quad (3.85)$$

Similarly, consider segment $m2$ of element m , the static equilibrium of forces of nodes i and p with the tension force in the element t_m can be expressed as:

$$\begin{bmatrix} -\hat{n}_m \\ \hat{n}_m \end{bmatrix} t_m = \begin{bmatrix} f_i \\ f_p \end{bmatrix} \quad (3.86)$$

The assembly of eqns (3.85) and (3.86) into one matrix system results in:

$$\begin{bmatrix} -\hat{n}_m \\ \hat{n}_m - \hat{n}_m \\ \hat{n}_m \end{bmatrix} t_m = \begin{bmatrix} -\hat{n}_m \\ 0 \\ \hat{n}_m \end{bmatrix} t_m = \begin{bmatrix} f_k \\ f_i \\ f_p \end{bmatrix} \quad (3.87)$$

From eqn (3.87) one can realize that the coefficients of the dummy node, i , are set to zero, which enables the elimination of the node from the matrix system, which results in:

$$\begin{bmatrix} -\hat{n}_m \\ \hat{n}_m \\ n_m \end{bmatrix} t_m = \begin{bmatrix} f_k \\ f_p \end{bmatrix} \quad (3.88)$$

The same reasoning can be applied to element n , where the equilibrium of the nodal forces of nodes q , l and j with the element tension force t_n can be expressed respectively in eqns (3.89) and (3.90) as:

$$\begin{bmatrix} -\hat{n}_n \\ \hat{n}_n \\ n_n \end{bmatrix} t_n = \begin{bmatrix} f_q \\ f_j \end{bmatrix} \quad (3.89)$$

$$\begin{bmatrix} -\hat{n}_n \\ \hat{n}_n \\ n_n \end{bmatrix} t_n = \begin{bmatrix} f_j \\ f_l \end{bmatrix} \quad (3.90)$$

The assembly of eqns (3.89) and (3.90) in one matrix system results in:

$$\begin{bmatrix} -\hat{n}_n \\ \hat{n}_n \\ n_n \end{bmatrix} t_n = \begin{bmatrix} f_q \\ f_l \end{bmatrix} \quad (3.91)$$

Now, we consider only the equilibrium of the portions of elements m and n that are included within the envelope of cell II. Those are segment $m1$ of element m and segment $n2$ of element n . Using the DNR, the static relations of dummy nodes i and j and elements m and n at wave-number $\omega = (0,0)$ can be formulated as:

$$\hat{n}_m = \hat{n}_n, \quad t_m = -t_n \quad \text{and} \quad f_i = -f_j \quad (3.92)$$

Now, consider the equilibrium of segment $m1$ of element m , formulated in eqn (3.85), and the equilibrium of segment $n2$ of element n (eqn (3.90)). The assembly of eqns (3.85) and (3.90) in one matrix system results in:

$$\begin{bmatrix} -\hat{n}_m & 0 \\ \hat{n}_m & 0 \\ 0 & -\hat{n}_n \\ 0 & n_n \end{bmatrix} \begin{bmatrix} t_m \\ t_n \end{bmatrix} = \begin{bmatrix} f_k \\ f_i \\ f_j \\ f_l \end{bmatrix} \quad (3.93)$$

Applying the conditions of eqn (3.92), results in:

$$\begin{bmatrix} -\hat{n}_m \\ \hat{n}_m \\ n_m \\ \hat{n}_n \\ -n_n \end{bmatrix} t_m = \begin{bmatrix} f_k \\ f_i \\ f_j \\ f_l \end{bmatrix}_{t_m = -t_n}, \quad \begin{bmatrix} -\hat{n}_m \\ \hat{n}_m \\ n_m - \hat{n}_n \\ -n_n \end{bmatrix} t_m = \begin{bmatrix} f_k \\ f_i \\ f_l \end{bmatrix}_{f_i = -f_j}, \quad \begin{bmatrix} -\hat{n}_m \\ 0 \\ \hat{n}_m \\ -n_m \end{bmatrix} t_m = \begin{bmatrix} f_k \\ f_i \\ f_l \end{bmatrix}_{\hat{n}_m = \hat{n}_n} \quad (3.94)$$

where the subscript denotes the applied condition. Finally the matrix system of eqn (3.94) is reduced to:

$$\begin{bmatrix} \hat{n}_m \\ -\hat{n}_m \\ \hat{n}_m \end{bmatrix} t_m = \begin{bmatrix} \hat{n}_m & 0 \\ 0 & \hat{n}_m \end{bmatrix} \begin{bmatrix} t_m \\ t_n \end{bmatrix} = \begin{bmatrix} f_k \\ f_l \end{bmatrix} \quad (3.95)$$

which is equivalent to the elimination of the degrees of freedom of the dummy nodes i and j from the matrix system. It should be noted that the matrix system obtained in eqn (3.95) is identical to the results obtained in eqn (3.88) and eqn (3.91).

A.2 Kinematic Analysis

Consider segment $m1$ of element m ; the kinematic compatibility of displacements of nodes k and i with the deformation of the element portion, e_{m1} can be written as:

$$\begin{bmatrix} \hat{n}_m & -\hat{n}_m \end{bmatrix} \begin{bmatrix} d_k \\ d_i \end{bmatrix} = e_{m1} \quad (3.96)$$

Similarly for segment $m2$ of element m , the kinematic compatibility of displacements of nodes i and j with the deformation of the element portion, e_{m2} can be formulated as:

$$\begin{bmatrix} \hat{n}_m & -\hat{n}_m \end{bmatrix} \begin{bmatrix} d_i \\ d_p \end{bmatrix} = e_{m2} \quad (3.97)$$

The assembly of eqns (3.96) and (3.97) into one matrix system results in:

$$\begin{bmatrix} \hat{n}_m & \hat{n}_m & \hat{n}_m & -\hat{n}_m \end{bmatrix} \begin{bmatrix} d_k \\ d_i \\ d_i \\ d_p \end{bmatrix} = \begin{bmatrix} \hat{n}_m & 0 & -\hat{n}_m \end{bmatrix} \begin{bmatrix} d_k \\ d_i \\ d_p \end{bmatrix} = e_{m1} + e_{m2} = e_m \quad (3.98)$$

From eqn (3.98) one can realize that the coefficients of the dummy node, i , are set to zero, which enables the elimination of the node from the matrix system that results in:

$$\begin{bmatrix} \hat{n}_m & -\hat{n}_m \end{bmatrix} \begin{bmatrix} d_k \\ d_p \end{bmatrix} = e_m \quad (3.99)$$

The same reasoning can be applied to element n , where the kinematic compatibility of the displacements of nodes q , l and j with the element deformation, e_n can be expressed respectively in eqns (3.100) and (3.101) as:

$$\begin{bmatrix} \hat{n}_n & -\hat{n}_n \end{bmatrix} \begin{bmatrix} d_q \\ d_j \end{bmatrix} = e_{n1} \quad (3.100)$$

$$\begin{bmatrix} \hat{n}_n & -\hat{n}_n \end{bmatrix} \begin{bmatrix} d_j \\ d_l \end{bmatrix} = e_{n2} \quad (3.101)$$

The assembly of eqns (3.100) and (3.101) into one matrix system results in:

$$\begin{bmatrix} \hat{n}_n & -\hat{n}_n \end{bmatrix} \begin{bmatrix} d_q \\ d_l \end{bmatrix} = e_n \quad (3.102)$$

Now, we consider only the kinematic compatibility of the portions of elements m and n that are included within the envelope of cell II. Those are segment $m1$ of element m and segment $n2$ of element n .

Using the DNR the kinematic relations of dummy nodes i and j and elements m and n at wave-number $\omega = (0,0)$ can be formulated as:

$$e_{m1} + e_{n2} = e_{m2} + e_{n1} = e_m = e_n \text{ and } d_i = d_j \quad (3.103)$$

Consider the kinematic compatibility of segment $m1$ of element m , given in eqn (3.96), and the kinematic compatibility of segment $n2$ of element n , given in eqn (3.101), the assembly of these two eqns in one matrix system results in:

$$\begin{bmatrix} \hat{n}_m & -\hat{n}_m & \hat{n}_n & -\hat{n}_n \end{bmatrix} \begin{bmatrix} d_k \\ d_i \\ d_j \\ d_l \end{bmatrix} = e_{m1} + e_{n2} \quad (3.104)$$

Applying the conditions of eqn (3.103), results in:

$$\begin{bmatrix} \hat{n}_m & \hat{n}_n - \hat{n}_m & -\hat{n}_n \end{bmatrix} \begin{bmatrix} d_k \\ d_i \\ d_l \end{bmatrix}_{d_i=d_j} = \begin{bmatrix} \hat{n}_m & 0 & -\hat{n}_n \end{bmatrix} \begin{bmatrix} d_k \\ d_i \\ d_l \end{bmatrix}_{\substack{\hat{n}_m = \hat{n}_n \\ n_m = n_n}} = e_m \quad (3.105)$$

where the subscript denotes the applied condition. Finally the matrix system of eqn (3.105) is reduced to:

$$\begin{bmatrix} \hat{n}_m & -\hat{n}_n \end{bmatrix} \begin{bmatrix} d_k \\ d_l \end{bmatrix} = e_m \quad (3.106)$$

which is equivalent to the elimination of the degrees of freedom of dummy nodes i and j from the matrix system.

The previous analysis shows that the application of the DNS helps significantly to simplify the matrix computation of lattice structures. Failure of eliminating the degrees of freedom associated

with the dummy nodes results in inaccurate results as the analysis is carried out for pin-jointed lattice structure.

In the determinacy analysis of infinite periodic lattice structures, the DNS is employed to derive the equilibrium and the kinematic systems of the unit cell finite structure. Once the equilibrium and the kinematic systems of the unit cell are established, the technique described in §3.5 is applied to the real structure of the unit cell, including only the real nodes and bars, of the unit cell to generate the irreducible equilibrium and kinematic systems of the infinite lattice structures.

3.8 Classification of Pin-Jointed Infinite Periodic Lattice Structures

Infinite periodic lattice structures are classified into three classes, namely, Stretching Dominated Lattice Structure (SDLS), Bending Dominated Lattice Structure (BDLS) and Tensegrity Lattice Structure (TLS), as shown in table (3.1). This classification is based on the determinacy state of the infinite lattice and the stiffening effect of the periodic states of self-stress to the periodic internal mechanisms.

We apply the determinacy analysis procedure, developed in this chapter, to the nineteen lattice topologies, shown in Figs (2.4), (2.5) and (2.6) and we classify them in light of their determinacy state after checking the stiffening effect of the periodic states of self-stress to the periodic internal mechanisms. The determinacy analysis results are reported in Appendix E.

Table (3.1) Classes of infinite periodic lattice structures

	Static determinacy	Kinematic determinacy	Stiffening effect	Class
I	$s > 0$	$m = 0$	-	SDLS
II	$s = 0$	$m > 0$	-	BDLS
III	$s > 0$	$m > 0$	No	
IV	$s > 0$	$m > 0$	Yes	TLS

The nineteen lattice topologies are classified in table (3.2) based on their determinacy analysis results, reported in Appendix E. Two lattice topologies out of the nineteen are classified as Tensegrity Lattice Structures, namely, the $3^3.4^2$ lattice, shown in Fig (2.5c), and the Equilaterals-Hexagon (EH) lattice, shown in Fig (2.6e).

3.9 Conclusion

A systematic, matrix-based, procedure for the determinacy analysis of periodic structures with any arbitrary cell topology using the *Bloch*-wave method has been presented. A new rule, namely, the Dummy Node Rule supported by the Dummy Node Scheme, has been proposed to simplify

the analysis of infinite periodic structures that have unit cells with cell elements extending between adjacent unit cells. The stiffening effect of the periodic states of self-stress to the periodic internal mechanisms has been assessed using the Product Force Vector approach and the definiteness of the stress matrix developed by first-order, infinitesimal, periodic, internal mechanisms. The proposed analysis technique has been applied to 19 2D lattice topologies whereas their determinacy analysis results are used for their classification. Numeric results of this analysis are reported in Appendix E where the steps of the analysis for the square, the Kagome and the $3^3.4^2$ lattice topologies are demonstrated in details.

Table (3.2) Classification of 2D infinite periodic lattice structures

Lattice Topology	Class	Lattice Topology	Class
Square (Fig (2.4a))	BDLS	$3^4.6$ (Fig (2.5h))	SDLS
Triangular (Fig (2.4b))	SDLS	DHT (Fig (2.6a))	SDLS
Hexagonal (Fig (2.4c))	BDLS	SUBS (Fig (2.6b))	BDLS
Kagome (Fig (2.5a))	BDLS	TT (Fig (2.6c))	SDLS
4.6.12 (Fig (2.5b))	BDLS	SDBS (Fig (2.6d))	SDLS
$3^3.4^2$ (Fig (2.5c))	TLS	EH (Fig (2.6e))	TLS
$3^2.4.3.4$ (Fig (2.5d))	SDLS	UBS (Fig (2.6f))	SDLS
3.4.6.4 (Fig (2.5e))	BDLS	DBS (Fig (2.6g))	SDLS
3.12^2 (Fig (2.5f))	BDLS	PK (Fig (2.6h))	SDLS
4.8^2 (Fig (2.5g))	BDLS		

It is found that the infinite Kagome lattice structure has a bending dominated behavior as the lattice experiences a periodic internal mechanism at wave-number $\omega = (0.5,0)$ that is not tightened-up by any periodic state of self-stress. This result, however, is different than the classification of the Kagome lattice material whereas the Kagome lattice material. Kagome lattice material is classified in literature (Elsayed, MSA and Pasini, D., 2010; Hutchinson RG, 2004) as stretching dominated lattice material as the collapse internal mechanism, computed at wave-number $\omega = (0.5,0)$, vanishes at the macroscale as the microscopic properties of the lattice are smeared-out by homogenization. Details about this analysis are given in chapters four and eight of this thesis. We show in chapter four, that the pin-jointed, infinite, periodic, structure of the Kagome lattice, gains its stability when it is handled as a lattice material, i.e. when it is used in manufacturing mechanical elements with macroscopic length scale much larger than those of its microscopic constituents as well as loaded by macroscopic loadings with wavelengths much larger than those of its elements; a phenomenon that we named Periodicity Induced Stability (PIS).

It has been found that there are three types of infinite, periodic, lattice structures, namely, stretching dominated, bending dominated and tensegrity lattice structures. Two lattice topologies out of the selected nineteen are classified as Tensegrity Lattice Structures (TLS), as shown in table (3.2).

CHAPTER 4

Effective Elastic and Strength Properties of Pin-Jointed Lattice Materials

4.1 Introduction

This chapter presents a matrix-based procedure to characterize the effective specific stiffness and strength properties of 2D lattice materials with any arbitrary cell topology. Unlike previous works, the current study automates the analysis process to include lattice materials whose unit cell has elements extending between adjacent unit cells and thus intersecting their envelopes. The main challenge in the analysis of this periodic lattice structures is that the unit cell does not have the full information concerning its nodal kinematic and static periodicity. For this reason, we employ the DNR, developed in chapter three, which enables the analysis of lattice material with any cell topology.

The lattice material is considered here as a pin-jointed infinite micro-truss structure. The *Cauchy-Born* hypothesis (Bhattacharya, K., 2003; Born, M., & Huang, K., 1954; Maugin, G. A., 1992; Pitteri, M., et.al., 2003; Ericksen, J. L., 1984) is used to homogenize the lattice material elastic properties by formulating the microscopic lattice nodal deformations in terms of a macroscopic, hypothetical, homogeneous, strain field applied to the material as assumed by the *Cauchy-Born* hypothesis. This formulation, in turn, is used to express the microscopic element deformations in terms of the macroscopic strain field, from which the material macroscopic stiffness properties are derived. In this process, the DNS is a necessary step to construct the nodal periodicity within the unit cell, which is used to apply the *Cauchy-Born* kinematic Boundary condition to the nodal deformation wave-functions. The developed characterization method is applied to ten lattice topologies, five of which have unit cells with a square Bravais lattice symmetry and the other five have unit cells with a hexagonal Bravais lattice symmetry. Finally, charts representing the relative elastic moduli of the stretching-dominated lattice materials versus its relative density are developed. These charts assist in the selection of the best topology of a stretching-dominated lattice material for a given application that requires a material with specific stiffness properties. The analysis is conducted here for 2D lattice materials; however the methodology can be simply extended to include 3D lattice materials.

4.2 Relative Density of 2D Lattice Material

Assuming that the mass of the boundary elements of a unit cell, i.e. elements lying on the cell envelope, are divided equally among the neighbouring cells, then, the relative density of the 2D lattice material can be expressed as:

$$\bar{\rho} = \frac{\rho_L}{\rho} = C_T^\rho \left(\frac{H}{L} \right) \quad (4.1)$$

where C_T^ρ is a constant depending on the topology of the 2D lattice material, H and L are, respectively, the in-plane thickness and the length of a reference cell element. ρ_L and ρ are the densities of the lattice material and the solid material, respectively; where the solid material is the material used in manufacturing the lattice material.

4.3 Effective Elastic Properties of 2D Lattice Materials

4.3.1 Macroscopic Strain Generated by Microscopic Mechanisms

As described in Chapter three, the *Bloch's* theorem allows characterizing mechanisms corresponding to periodic nodal displacement fields. To examine the macroscopic strain field generated by periodic mechanisms, we resort to the *Cauchy-Born* hypothesis (Bhattacharya, K., 2003; Born, M., & Huang, K., 1954; Maugin, G. A., 1992; Pitteri, M., et.al., 2003; Ericksen, J. L., 1984).

A. *Cauchy-Born* Hypothesis

From the definition of the *Cauchy-Born* hypothesis (Hutchinson R.G., 2004), the infinitesimal displacement field of a periodic node in a lattice structure can be formulated as:

$$d\left(j_l + \vec{R}, \vec{\epsilon}\right) = d(j_l, \vec{\epsilon} = 0) + \vec{\epsilon} \cdot \vec{R} \quad (4.2)$$

Where $\vec{\epsilon}$ is an assumed homogeneous macroscopic strain field applied to the lattice material along a set of unit cells spanned by the vector \vec{R} . $d(j_l, \vec{\epsilon} = 0)$ is the periodic displacement field of node j_l . Assume that the periodic nodes defined by the position vectors j_l and $j_l + \vec{R}$, are the two periodic nodes i and j within a lattice structure, then, eqn (4.2) can be formulated in matrix form as:

$$\begin{bmatrix} u_i \\ v_i \end{bmatrix} = \begin{bmatrix} u_j \\ v_j \end{bmatrix} + \begin{bmatrix} \varepsilon_{11} & \varepsilon_{12} \\ \varepsilon_{21} & \varepsilon_{22} \end{bmatrix} \begin{bmatrix} x_i - x_j \\ y_i - y_j \end{bmatrix} \quad \text{in 2D} \quad (4.3)$$

where u and v are the nodal displacement components in the x and y directions, respectively, and node i is the dependent node, while node j is the independent node. In terms of the engineering strain (Renton, J.D., 2002), eqn (4.3) can be reformulated as:

$$\begin{bmatrix} u_i \\ v_i \end{bmatrix} = \begin{bmatrix} u_j \\ v_j \end{bmatrix} + \begin{bmatrix} \varepsilon_{11} & \frac{1}{2}\varepsilon_{12} \\ \frac{1}{2}\varepsilon_{21} & \varepsilon_{22} \end{bmatrix} \begin{bmatrix} x_i - x_j \\ y_i - y_j \end{bmatrix} \quad \text{in 2D} \quad (4.4)$$

which in turn can be expressed as:

$$\begin{bmatrix} u_i \\ v_i \end{bmatrix} = \begin{bmatrix} u_j \\ v_j \end{bmatrix} + \begin{bmatrix} (x_i - x_j) & 0 & \frac{1}{2}(y_i - y_j) \\ 0 & (y_i - y_j) & \frac{1}{2}(x_i - x_j) \end{bmatrix} \begin{bmatrix} \varepsilon_{11} \\ \varepsilon_{22} \\ \varepsilon_{21} \end{bmatrix} \quad (4.5)$$

or $d_i = d_j + \mathbf{E}\bar{\varepsilon}$

Equation (4.5) is the kinematic boundary condition of the *Cauchy-Born* hypothesis. Applying this boundary condition to the unit cell nodal displacement vector, d , results in:

$$d = \mathbf{T}_d \tilde{d} + \mathbf{E}\bar{\varepsilon} \quad (4.6)$$

where \mathbf{T}_d is the nodal transformation matrix, formulated in eqn (3.43b), that transforms the nodal displacement vector of the unit cell, d , to the periodic reduced vector of nodal displacements of the infinite lattice, \tilde{d} .

Substituting eqn (4.6) into the kinematic system of the unit cell (eqn (3.5)) results in:

$$\mathbf{B}\{\mathbf{T}_d \tilde{d} + \mathbf{E}\bar{\varepsilon}\} = e \quad (4.7)$$

Where \mathbf{B} and e are, respectively, the kinematic matrix and the vector of element deformations of the unit cell finite structure.

Substituting eqn (3.43a) into eqn (4.7) and inverting \mathbf{T}_e , results in:

$$\tilde{\mathbf{B}}\tilde{d} + \tilde{\mathbf{E}}\bar{\varepsilon} = \tilde{e} \quad (4.8)$$

Where $\tilde{\mathbf{B}} = (\mathbf{B}_e)^{-1} \mathbf{T}_e^H \mathbf{B} \mathbf{T}_d$ is identical to the reduced kinematic matrix of the infinite lattice at wave-number $\omega = (0,0)$, and $\tilde{\mathbf{E}} = (\mathbf{B}_e)^{-1} \mathbf{T}_e^H \mathbf{B} \mathbf{E}$.

From eqn (4.6) one can realize that the *Cauchy-Born* kinematic boundary condition is applied to the kinematic compatibility system of the lattice microstructure to express an explicit relation between the microscopic nodal displacements and a homogeneous, averaged, macroscopic strain

field, $\bar{\epsilon}$. A key parameter to establish this relation is the existence of the complete information of nodal periodicity within the unit cell envelope. The *Cauchy-Born* hypothesis cannot be applied to the kinematic compatibility relations of unit cells such as those shown in Fig (2.5b-h) without resorting to the DNS. This is described by the steps below.

Step 1: Hypothetical dummy nodes are introduced at the intersection points between the microscopic cell elements that extend between neighbouring unit cells, and the cell envelope. These dummy nodes are used to generate the kinematic and the equilibrium matrices of the finite microstructure of the unit cell, as described in chapter (3).

Step 2: The unit cell bases dependency check, formulated in eqn (3.35), is applied to the total group of node bases (including the dummy nodes) to determine the dependent and the independent set of nodes.

Step 3: the dependency relations generated in step 2, is now used to apply the *Cauchy-Born* kinematic boundary condition to the kinematic system of the unit cell generated in step 1. This results in a formulation similar to eqn (4.7).

Distributing the bracket in eqn (4.7), results in:

$$\underbrace{\mathbf{B}\mathbf{T}_d}_{1}\tilde{d} + \underbrace{\mathbf{B}\mathbf{E}\bar{\epsilon}}_2 = e \quad (4.9)$$

where $\mathbf{B}\mathbf{T}_d\tilde{d} \in R^{\dim(e) \times \dim(\tilde{d})}$ and $\mathbf{B}\mathbf{E}\bar{\epsilon} \in R^{\dim(e) \times 3}$. The first term in the left hand side of eqn (4.9) includes the degrees of freedom associated with the dummy nodes.

Step 4: the degrees of freedom associated with the hypothetical dummy nodes, in term (1) of eqn (4.9), are eliminated from the matrix systems in the same manner as described in § (3.7.3).

Step 5: Substituting eqn (3.43a) into eqn (4.9) and inverting T_e , results in:

$$\begin{aligned} & \underbrace{(\mathbf{B}_e)^{-1}\mathbf{T}_e^H \mathbf{B}\mathbf{T}_d}_{1}\tilde{d} + \underbrace{(\mathbf{B}_e)^{-1}\mathbf{T}_e^H \mathbf{B}\mathbf{E}\bar{\epsilon}}_2 = \tilde{e} \\ & \text{or } \underbrace{\tilde{\mathbf{B}}\tilde{d}}_1 + \underbrace{(\mathbf{B}_e)^{-1}\mathbf{T}_e^H \mathbf{B}\mathbf{E}\bar{\epsilon}}_2 = \tilde{e} \end{aligned} \quad (4.10)$$

Equation (4.10) is the complete reduced kinematic system representing the infinite lattice structure.

4.3.2 Microscopic Element Deformations in Terms of Macroscopic Strain Field

Equation (4.10) is a matrix system that expresses the periodic element deformations in terms of the macroscopic strain field, $\bar{\epsilon}$, and the periodic nodal displacements, \tilde{d} . This matrix system is

rearranged to express the periodic element deformations in terms of the macroscopic strain field and independent on the periodic nodal displacement field, \tilde{d} . This is done by generating the following augmented matrix:

$$\left[\underbrace{\left((\mathbf{B}_e)^{-1} \mathbf{T}_e^H \mathbf{B} \mathbf{T}_d \right)}_1 \middle| \underbrace{\left((\mathbf{B}_e)^{-1} \mathbf{T}_e^H \mathbf{B} \mathbf{E} \right)}_2 \middle| \underbrace{(\mathbf{I})}_3 \right] \quad (4.11)$$

In (4.11), \mathbf{I} is a unit square matrix with dimension equal to $\dim(\tilde{e})$. The next step is to find the reduced row echelon form of the matrix expressed in (4.11) and collect the rows in the sub matrices (2) and (3) that correspond to zero rows in the sub matrix (1). This process generates the two matrices $\tilde{\mathbf{E}}$ and $\tilde{\mathbf{I}}$, which are used to write the following expression:

$$[0]\tilde{d} + \tilde{\mathbf{E}}\bar{\epsilon} = \tilde{\mathbf{I}}\tilde{e} \quad \text{or} \quad \tilde{\mathbf{E}}\bar{\epsilon} = \tilde{\mathbf{I}}\tilde{e} \quad (4.12)$$

The matrix system generated in eqn (4.12) is used to find an explicit expression of the element deformations in terms of the macroscopic strain field. This can be obtained by inverting the matrix $\tilde{\mathbf{I}}$. To invert the matrix $\tilde{\mathbf{I}}$, we resort to the Moore-Penrose pseudo-inverse technique that depends on generating the Singular Value Decomposition (Pellegrino, S., 1993; Horn, Roger A. 1985; 1991; Strang G., 1998) of the matrix $\tilde{\mathbf{I}}$ as:

$$\tilde{\mathbf{I}} = \mathbf{S} \cdot \mathbf{V} \cdot \mathbf{D}^H \quad (4.13)$$

The singular value decomposition of a matrix $\tilde{\mathbf{I}} \in R^{m \times n}$ generates the diagonal matrix $\mathbf{V} \in R^{m \times n}$, which contains the non-negative Eigenvalues of matrix $\tilde{\mathbf{I}}$; the square unitary matrix $\mathbf{S} \in R^{m \times m}$ and the conjugate transpose matrix \mathbf{D}^H . The Moore-Penrose pseudo-inverse of the matrix $\tilde{\mathbf{I}}$, is then formulated as:

$$(\tilde{\mathbf{I}})^{-1} = (\mathbf{D})(\tilde{\mathbf{V}})^{-1}(\mathbf{S})^H \quad (4.14)$$

where the term $(\tilde{\mathbf{V}})^{-1}$ is formulated by: (i) eliminating the rows and the columns of matrix \mathbf{V} that have zero diagonal values, and then (ii) obtaining the reciprocal of the diagonal entries of the matrix resulting from (i).

Multiplying eqn (4.14) to both sides of eqn (4.12), results in the following expression of the element deformations in terms of the macroscopic strain field:

$$\tilde{e} = \left((\tilde{\mathbf{I}})^{-1} \tilde{\mathbf{E}} \right) \bar{\epsilon} \quad \text{or} \quad \tilde{e} = \mathbf{M} \bar{\epsilon} \quad (4.15)$$

Computing the null space of matrix \mathbf{M} , gives the independent modes of macroscopic strain field generated with inextensional microscopic element deformations. An empty null space of matrix \mathbf{M} indicates that the lattice material can support all macroscopic modes of strain fields. In other words, the material does not collapse by periodic mechanisms or any special modes of macroscopic loading.

Finally, the deformations of all elements in the unit cell can be expressed by substituting eqn (4.15) into eqn (3.43a) as:

$$e = \mathbf{T}_e \mathbf{M} \bar{\epsilon} \quad (4.16)$$

4.3.3 Macroscopic Strain Energy Density: Material Elastic Moduli

The macroscopic strain energy density of a lattice can be averaged by considering the element deformations of a unit cell with b bars which is defined as (Hutchinson, R. G. & Fleck, N.A., 2006):

$$W = \frac{1}{2} \bar{\sigma} : \bar{\epsilon} = \frac{1}{2|\mathbf{Y}|} \sum_{k=1}^b t_k e_k \quad (4.17)$$

where $|\mathbf{Y}|$ is the unit cell area, t_k is the tension force in the k^{th} bar element. $\bar{\sigma}$ and $\bar{\epsilon}$ are the macroscopic stress and strain fields, respectively. Since the lattice structure considered in the current analysis is a pin-jointed structure, then, the bar elements of the unit cell carry only axial loads. Accordingly, the tension force in a bar element, k , can be expressed as

$$t_k = (EA/L)e_k \quad (4.18)$$

where E is the Young's modulus of the solid material, A is the cross-sectional area of the bar element, and L is the bar length. Substituting eqn (4.18) into eqn (4.17) results in:

$$W = \frac{1}{2} \bar{\sigma} : \bar{\epsilon} = \frac{EA}{2L|\mathbf{Y}|} \sum_{k=1}^b e_k^2 \quad (4.19)$$

Substituting eqn (4.16) into eqn (4.19) results in:

$$W = \frac{1}{2} \bar{\sigma} : \bar{\epsilon} = \frac{EA}{2L|\mathbf{Y}|} \sum_{k=1}^b \left(\mathbf{M}(k, :) \bar{\epsilon} \right)^2 \quad (4.20)$$

where $\mathbf{M}(k, :)$ is the k^{th} row in the matrix \mathbf{M} . Using eqn (4.20), the macroscopic fourth order stiffness tensor of the lattice material can be computed as:

$$k_{ijij} = \frac{\partial^2 W}{\partial \bar{\epsilon}_{ii} \partial \bar{\epsilon}_{jj}} \quad (4.21)$$

where i and $j \in \{1, \dots, n\}$ and $n=2$ or $n=3$ in 2D or 3D, respectively.

Once the macroscopic stiffness tensor is computed, the macroscopic compliance matrix can be obtained by inverting the stiffness matrix, where $\mathbf{C}_L = \mathbf{K}_L^{-1}$ is the linearly elastic, fourth-order, compliance tensor of the lattice material.

For a general anisotropic material the compliance tensor is given by:

$$\begin{bmatrix} \varepsilon_{xx} \\ \varepsilon_{yy} \\ \varepsilon_{xy} \end{bmatrix} = \begin{bmatrix} C_{xxxx} & C_{xxyy} & C_{xxxy} \\ C_{yyxx} & C_{yyyy} & C_{yyxy} \\ C_{xyxx} & C_{xyyy} & C_{xyxy} \end{bmatrix} \begin{bmatrix} \sigma_{xx} \\ \sigma_{yy} \\ \sigma_{xy} \end{bmatrix} \quad \text{or} \quad \bar{\varepsilon} = \mathbf{C}_L \bar{\sigma} \quad (4.22)$$

The compliance tensor can be used to compute the lattice material elastic moduli as:

$$\begin{aligned} (E_L)_{xx} &= \frac{1}{C_{xxxx}} \\ (E_L)_{yy} &= \frac{1}{C_{yyyy}} \\ (v_L)_{yx} &= -\frac{C_{xxxy}}{C_{xxyy}} \\ (v_L)_{xy} &= -\frac{C_{yyxy}}{C_{yyxx}} \\ G_L &= \frac{1}{C_{xyxy}} \end{aligned} \quad (4.23)$$

Where E_L , v_L and G_L are, respectively, the Young's modulus, the Poisson's ratio and the shear modulus of the lattice material.

4.4 Effective Strength Properties of Lattice Materials

From eqn (4.16), a relationship between the microscopic cell element deformations and the macroscopic strain field is developed as:

$$e = \mathbf{T}_e \mathbf{M} \bar{\varepsilon} = \mathbf{M}_G \bar{\varepsilon} \quad (4.24)$$

where \mathbf{M}_G is a compatibility matrix that transforms the macroscopic strain vector, $\bar{\varepsilon}$, into the microscopic cell element deformation vector, e . Multiplying eqn (4.24) by matrix \mathbf{M}_L , generates a relationship between the microscopic cell element strain vector, ε_μ , and the macroscopic strain field as:

$$\mathbf{M}_L e = \varepsilon_\mu = \mathbf{M}_L \mathbf{M}_G \bar{\varepsilon} \quad (4.25)$$

where \mathbf{M}_L is a $\dim(e) \times \dim(e)$ diagonal matrix with element $\mathbf{M}_L(q,q)=1/L_q$, L_q is the length of the element q and $q \in \{1, \dots, b\}$, b is the number of elements within the unit cell. The multiplication of the Young's modulus of the solid material, E , to the matrix \mathbf{M}_L generates the constitutive law of linear bar elements, with unit cross-sectional areas, that comprise the microscopic lattice structure within the unit cell.

Since the lattice material considered here is modelled as a micro-truss with pin-jointed bar elements, the microscopic strain induced in the cell elements, ε_μ , is an axial strain field along the axes of the cell elements that are manufactured of solid material. Multiplying both sides of eqn (4.25) by the Young's modulus of the solid material, E , generates the microscopic cell element stress vector as:

$$\boldsymbol{\sigma}_\mu = E\varepsilon_\mu = E\mathbf{M}_L\mathbf{M}_G\bar{\boldsymbol{\varepsilon}} \quad (4.26)$$

By substituting eqn (4.22) into eqn (4.26), the microscopic stress field, σ_μ , can be expressed in terms of the macroscopic stress field, $\bar{\boldsymbol{\sigma}}$, as:

$$\sigma_\mu = E\mathbf{M}_L\mathbf{M}_G\mathbf{C}_L\bar{\boldsymbol{\sigma}} \quad (4.27)$$

Considering eqn (4.1), the matrix system in eqn (4.27) can be expressed as:

$$\sigma_\mu = \frac{1}{\bar{\rho}} \boldsymbol{\Lambda} \bar{\boldsymbol{\sigma}} \quad (4.28)$$

where $\boldsymbol{\Lambda}$ is a matrix in which the values of its entries depend on the topology of the unit cell as well as the deformations of the microscopic cell elements. The matrix system in eqn (4.28) can be expanded as:

$$\begin{bmatrix} \sigma_\mu^1 \\ \sigma_\mu^2 \\ \cdot \\ \cdot \\ \sigma_\mu^B \end{bmatrix} = \frac{1}{\bar{\rho}} \begin{bmatrix} \Lambda_{xx}^1 & \Lambda_{yy}^1 & \Lambda_{xy}^1 \\ \Lambda_{xx}^2 & \Lambda_{yy}^2 & \Lambda_{xy}^2 \\ \cdot & \cdot & \cdot \\ \cdot & \cdot & \cdot \\ \Lambda_{xx}^B & \Lambda_{yy}^B & \Lambda_{xy}^B \end{bmatrix} \begin{bmatrix} \sigma_{xx} \\ \sigma_{yy} \\ \sigma_{xy} \end{bmatrix} \quad (4.29)$$

Equation (4.29) is used to derive the strength properties of the lattice material. By applying three distinct stress fields, $[\sigma_{xx} \ 0 \ 0]^T$, $[0 \ \sigma_{yy} \ 0]^T$ and $[0 \ 0 \ \sigma_{xy}]^T$ to the lattice, we obtain the critical macroscopic strength of the lattice material as:

$$\sigma_L^{cr} = \frac{\sigma_\mu^{cr}}{\max(\boldsymbol{\Lambda}(:,i))} \bar{\rho} = C_\sigma(i) \sigma_\mu^{cr} \bar{\rho} \quad (4.30)$$

where $i \in \{1,2,3\}$, $(\sigma_L^{cr})_{xx} = \sigma_L^{cr}$ at $i=1$, $(\sigma_L^{cr})_{yy} = \sigma_L^{cr}$ at $i=2$ and $(\sigma_L^{cr})_{xy} = \sigma_L^{cr}$ at $i=3$. $(\sigma_L^{cr})_{xx}$ and $(\sigma_L^{cr})_{yy}$ are the lattice material critical direct strength in the x and the y directions, respectively. $(\sigma_L^{cr})_{xy}$ is the lattice material critical shear strength in the x - y plane. $C_\sigma(i)$ is a constant that depends on the topology of the 2D lattice material and the deformations of the microscopic cell elements.

In eqn (4.30), σ_μ^{cr} is dependent on the microscopic failure mode of the material. Since the microscopic elements of the pin-jointed lattice materials are subjected only to either tension or compression, then there are two possible failure modes: plastic yielding or instability elastic buckling, governed by the microscopic element slenderness ratio.

4.4.1 Plastic Yield Strength

If the plastic yielding of the microscopic cell elements is the dominant failure mode, then, the microscopic critical strength is equal to $\sigma_\mu^{cr} = \sigma_{ys}$, where σ_{ys} is the solid material yield strength. The lattice material macroscopic plastic yield strength is expressed as:

$$\sigma_L^y = \frac{\sigma_{ys}}{\max(\Lambda(:,i))} \bar{\rho} \quad (4.31)$$

where $(\sigma_L^y)_{xx} = \sigma_L^y$ at $i=1$, $(\sigma_L^y)_{yy} = \sigma_L^y$ at $i=2$ and $(\sigma_L^y)_{xy} = \sigma_L^y$ at $i=3$. Where $(\sigma_L^y)_{xx}$ and $(\sigma_L^y)_{yy}$ are the macroscopic direct yield strengths of the lattice material in the x and y directions, respectively. $(\sigma_L^y)_{xy}$ is the macroscopic yield shear strength in the x - y plane of the lattice material.

Dividing both sides of eqn (4.31) by σ_{ys} generates the relative macroscopic yield strengths of the lattice material as:

$$\bar{\sigma}_L^y = \frac{\sigma_L^y}{\sigma_{ys}} = \frac{1}{\max(\Lambda(:,i))} \bar{\rho} = C^y(i) \bar{\rho} \quad (4.32)$$

where $C^y(i) = \frac{1}{\max(\Lambda(:,i))}$ is a constant that depends on the microscopic topology of the lattice material and the deformation of the microscopic elements.

4.4.2 Elastic Buckling Strength

The Euler critical buckling load of an axially loaded member in compression is:

$$P_{cr} = c^2 \frac{\pi^2 EI}{L^2} \quad (4.33)$$

where E is the Young's modulus of the material, I is the smallest second moment of area of the member cross-section, L is the length of the member and c is a factor that depends on the rotational stiffness of the member end boundaries. For a pin jointed element at which the rotation is freely allowed, $c=1$. If the rotation is totally prohibited by a fixed boundary conditions, then $c=2$. In practice, the value of the factor c of a lattice material is between 1 and 2. We consider the factor $c=1$, for the lattice material is assumed as a pin-jointed micro-truss.

The critical buckling strength of a microscopic cell element loaded in compression can be computed by dividing eqn (4.33) by the cross-section area of the element which results in:

$$\sigma_{\mu}^b = \frac{P_{cr}}{A} = \frac{\pi^2 EI}{L^2 A} \quad (4.34)$$

Considering 2D lattice materials constructed of microscopic cell elements with rectangular cross-sections and by substituting eqn (4.1) into eqn (4.34), results in:

$$\sigma_{\mu}^b = \frac{P_{cr}}{A} = \left(\frac{\pi^2}{12} \right) (E) \left(\frac{\bar{\rho}}{C_T^{\rho}} \right)^2 \quad (4.35)$$

Considering the microscopic critical buckling strength as the dominant failure mode of the 2D lattice material, then the macroscopic critical buckling strength of the 2D lattice material can be formulated by substituting eqn (4.35) into the term of σ_{μ}^b in eqn (4.30) which results in:

$$\sigma_L^b = \left(\frac{\pi^2}{12 (C_T^{\rho})^2 \max(\Lambda(:, i))} \right) (E) (\bar{\rho})^3 \quad (4.36)$$

Where $(\sigma_L^b)_{xx} = \sigma_L^b$ at $i=1$, $(\sigma_L^b)_{yy} = \sigma_L^b$ at $i=2$ and $(\sigma_L^b)_{xy} = \sigma_L^b$ at $i=3$. $(\sigma_L^b)_{xx}$ and $(\sigma_L^b)_{yy}$ are the lattice material direct critical buckling strength in the x and y directions, respectively, on the other hand, $(\sigma_L^b)_{xy}$ is the lattice material shear critical buckling strength in the x - y plane. Dividing both sides of eqn (4.36) by the solid material yield strength, results in the lattice material macroscopic relative critical buckling strength as:

$$\sigma_L^b = \left(\frac{\pi^2}{12(C_F^\rho)^2 \max(\Lambda(:,i))} \right) \left(\frac{E}{\sigma_{ys}} \right) (\bar{\rho})^3 \quad (4.37)$$

It can be deduced from eqn (4.37) that the relative critical buckling strength of the 2D lattice material is not only a function of the relative density of the lattice material but also of the solid material strength and elastic properties.

The accuracy of employing the DNS in the application of the *Cauchy-Born* hypothesis is verified analytically as we consider a lattice topology that can be characterized by two candidate unit cells, namely, the Semi-Double-Braced square lattice, shown in Fig (2.6d). One unit cell requires the application of the DNS as it contains elements intersecting the cell envelope; the other has all of its elements contained within the envelope, thus there is no need to apply the DNS. The characterization processes using the two unit cells generate similar results which verify the accuracy of the DNS. Details of this example are reported in Appendix F.

4.5 Lattice Materials Stiffness Selection Design Charts

The stiffness analysis procedure, described above, is carried out for the lattice topologies shown in Figs (2.4a,b,c), (2.5a,h) and (2.6a,b,d,f,g) and the results are reported in Appendix F. The resulting stiffness properties are plotted on charts representing the relative elastic moduli of the stretching-dominated lattice materials versus its relative density. These charts assist in the selection of the best topology of stretching-dominated lattice materials for given applications that require materials with specific stiffness properties. The final results are shown below.

4.6 Conclusion

This chapter has described a systematic matrix-based procedure for the specific stiffness and strength characterization of lattice materials with any arbitrary topology. This procedure is efficient for the automation of the characterization process of complex microscopic topologies. The procedure has been applied in details to two lattice topologies of which one has a square Bravais lattice symmetry and the other has a hexagonal Bravais lattice symmetry. The stiffness characterization process is applied to other eight lattice materials and the elastic moduli of the stretching dominated topologies are plotted on design charts that can help in the selection process of lattice materials that generate specific stiffness required by certain applications. It is found that the lattice materials with cell topologies, shown in Fig (2.6b) and (2.6d) exhibit 11 % increase of the specific stiffness compared to the Kagome and the full triangulation lattice materials. On the

other hand, the lattice material with cell topology shown in Fig (2.6g) shows 17 % improvement in the specific shear modulus compared to the Kagome and the full triangulation lattice materials.

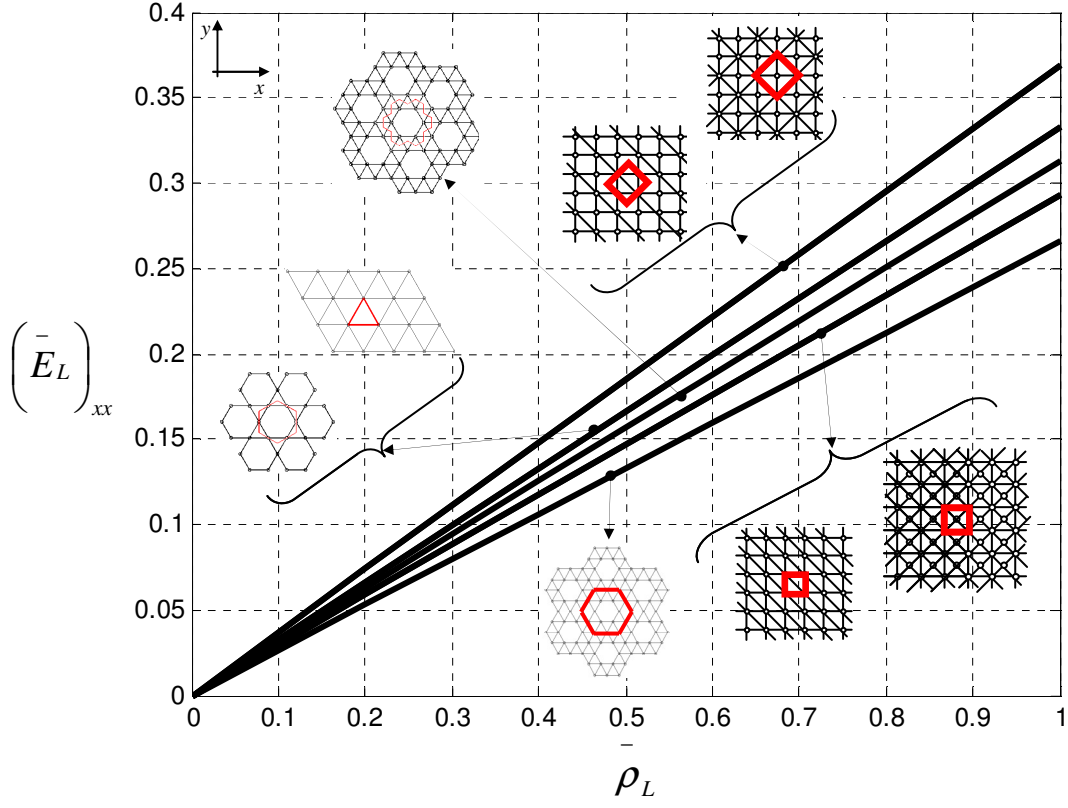


Fig (4.1) The relative Young's modulus in the x direction of the stretching dominated lattice material versus its relative density

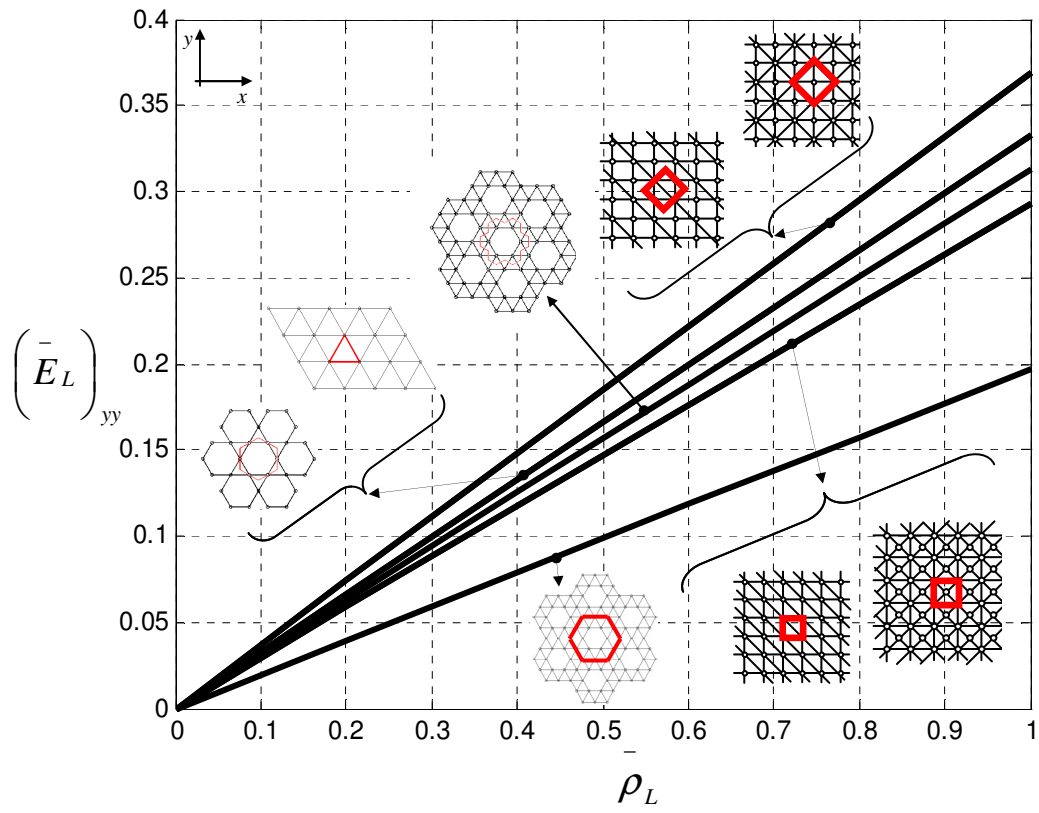


Fig (4.2) The relative Young's modulus in the y direction of the stretching dominated lattice material versus its relative density

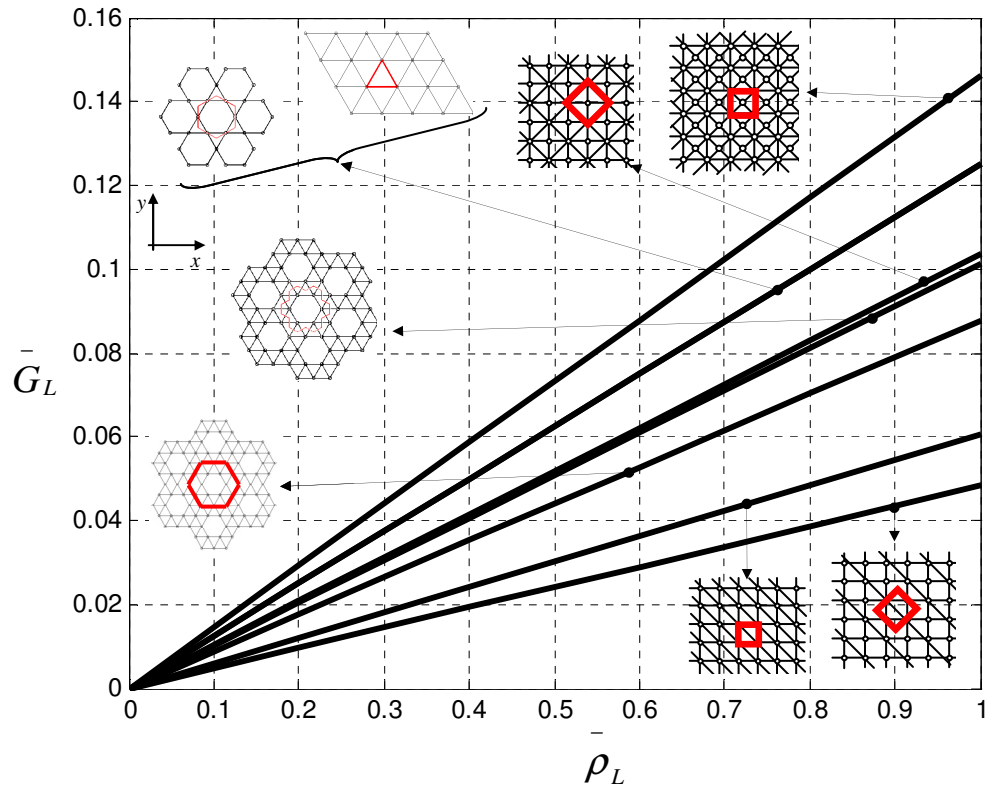


Fig (4.3) The relative Shear modulus of the stretching dominated lattice material versus its relative density

CHAPTER 5

Multiscale Structural Design of Columns made of Regular Octet-Truss Lattice Material

5.1 Introduction

This chapter focuses on the structural design of the microscopic architecture of a lattice material with regular octet-truss cell topology and on the multiscale design of an axially loaded member manufactured of this type of cellular solid. The rationale followed here hinges on the coincidence of the failure modes of a stretching dominated lattice material, which experiences two types of microscopic failure modes, namely, elastic buckling and plastic yielding. A lattice material that fails by the elastic buckling of its cell elements without reaching the plastic yielding is far from optimum, since the element becomes unstable without fulfilling its potential yield resistance, where the element fails in the elastic region at a loading lower than the load inducing its plasticity. To improve this behavior, researchers found critical values of the relative densities for different cell topologies at which the buckling failure of the cell elements can be avoided (Fan, et.al., 2008). Such strength improvement was achieved at the expense of the lattice material density, which therefore had to be increased, as the cell element's slenderness ratio was decreased by either lowering its length or by scaling up its radius of gyration. However, no attention to the potential of shaping the cross-section was considered. So far, studies on lattice material have considered microscopic cell elements with circular solid cross-sections. A few studies have investigated experimentally the behavior of lattice material with cylindrical hollow cross-sections (Wadley, 2002). Due to recent development in micro manufacturing technologies, namely rapid prototyping and rapid manufacturing (Kruth, et.al., 2005; Rochus, et.al., 2007; Waterman and Dickens, 1994), shaping microscopic structural elements in more efficient geometries has become feasible. Such progress on the manufacturing process encourages exploiting the potential of shaping and sizing the cross-sections of the cell elements to increase the lattice material strength. This chapter examines the impact of shaping the cell element cross-sections of the lattice material on its structural performance. We resort to recent studies that have investigated the effect of cross-section geometry on the performance of macroscale structures under different loading (Pasini, 2007; Pasini, et.al., 2003; Pasini, et.al., 2006). We first illustrate that enhancing the cell elements' buckling resistance by shaping their cross-sections allows the design of low density lattice

material that fail by plastic yielding rather than buckling and, thus, fully exploit the material strength. Then, we examine an axially loaded member manufactured of octet-truss lattice material with the aim of fully exploiting its load carrying capacity. For this purpose, the structural member is optimized by imposing the coincidence between three failure modes, namely, the local buckling (buckling of the microscopic cell elements), global buckling (buckling of the macroscopic structure) and the plastic yielding of the lattice material. Design charts are developed to enable a multiscale design of a macroscale member subjected to axial compression and manufactured of regular octet-truss lattice material. The charts help compare and select simultaneously the micro and the macro structural design parameters.

5.2 Description of the Regular Octet-Truss Cell

This work focuses on a lattice material with regular octet-truss cell topology. Fig (5.1) shows the microscopic topology of a unit cell of the lattice material examined here. The unit cell can be viewed as a regular octahedron core that is surrounded by eight regular tetrahedrons distributed on its eight faces. The cell has a Face Centered Cube (FCC) lattice structure with cubic symmetry generating a material with an isotropic behavior (Renton, 2002); its nodes are similarly situated with 12 cell elements connectivity at each node.

Determinacy analysis of the pin-jointed version of this microscopic topology shows that this unit cell is statically and kinematically determinate. However, when the unit cell is tessellated to generate the periodic material, the resulting microstructure becomes highly redundant and statically indeterminate, a feature common to all stretching dominated cell topologies (Guest, et.al., 2003).

In literature, works on the octet-truss lattice material consider the geometry of each cell element as uniform along their length and with circular solid cross-section. It has been demonstrated that a lattice material that fully exploits the yield strength of the cell elements can be designed at the expenses of its relative density (Fan, 2008). As a result, the lattice material density must be increased to critical values, under which the cell elements buckle. In this work, we circumvent this strategy. Rather than increasing the material density, we chose to strengthen the buckling resistance of each cell element by shaping its cross-sections into a more efficient geometry.

5.3 Geometric Variables

To model the effective properties of the regular octet-truss lattice material, we define a range of modeling parameters. Fig (5.2) shows the geometrical details of a macroscopic mechanical

member that is hierarchically parameterized and manufactured of a lattice material. On the microscale, three parameters S , D and D_0 are defined for a cell element cross-section of an arbitrary shape and size, where S , D and D_0 are, respectively, the shape, the envelope, and the envelope of a reference square.

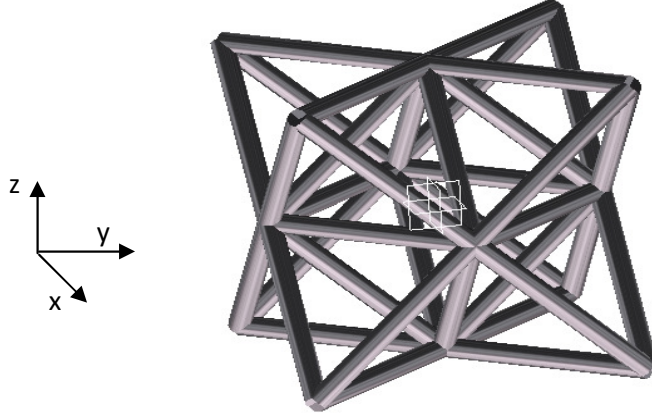


Fig. (5.1) Structure of a unit cell of the regular octet-truss lattice material

To model the efficiency of a cross-section, dimensionless parameters, named as shape transformers, can be defined to classify shapes into families and classes as well as to describe their geometrical properties (Pasini, 2007).

For example, the shape transformers of the area and of the second moment of area of a cross-section are defined as:

$$\psi_A = \frac{A}{A_D} \quad (5.1a)$$

$$\psi_I = \frac{I}{I_D} \quad (5.1b)$$

where ψ_A and ψ_I are, respectively, the area and the second moment of area shape transformers; A and I are, respectively, the area and the second moment of area of an arbitrary cross-section and A_D and I_D are the area and the second moment of area of the cross-section envelope, respectively.

Shape transformers can be used to define the cross-section efficiencies of alternative shapes for given loading requirements. For example, the cross-section geometric efficiency, λ , controlling the bending stiffness and the elastic buckling can be defined as:

$$\lambda = \frac{\psi_I}{\psi_A} \quad (5.2)$$

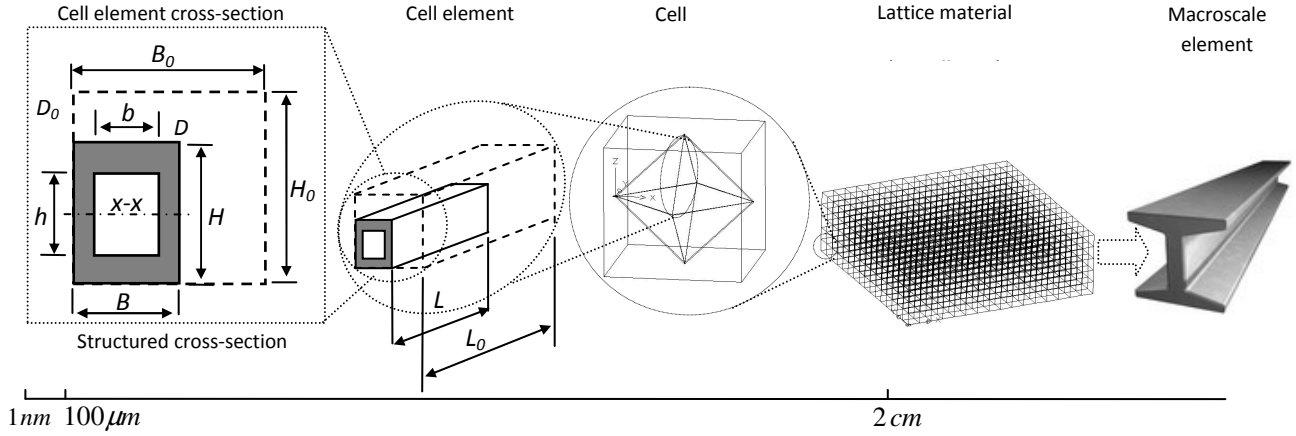


Fig. (5.2) Multiscale geometrical details of macroscopic member manufactured of lattice material

On the other hand, the effect of scaling the cross-section size is governed by two dimensionless multipliers, u and v , where u and v scale, respectively, the width B_0 and the height H_0 of the reference square envelope, D_0 , to the required dimensions of the cross-section. As a result, u and v can be expressed as:

$$u = \frac{B}{B_0} \quad (5.3a)$$

$$v = \frac{H}{H_0} \quad (5.3b)$$

where B and H are, respectively, the width and the height of the cross-section envelope. Using eqns (5.1) and (5.3), the area and the second moment of area of a cross-section can be expressed as:

$$A = \psi_A uv A_0 \quad (5.4a)$$

$$I = \psi_I uv^3 I_0 \quad (5.4b)$$

where A_0 and I_0 are, respectively, the area and the second moment of area of the reference square. For the shape of the cross-section, shown in Fig (5.2), the shape transformers of the second moment of area and that of the area, ψ_I and ψ_A , can be expressed as:

$$\psi_I = 1 - cd^3 \quad (5.5a)$$

$$\psi_A = 1 - cd \quad (5.5b)$$

where $c=b/B$ and $d=h/H$ and $0 \leq c \leq 1$ and $0 \leq d \leq 1$. By using eqns (5.5), the cross-section efficiency is expressed as:

$$\lambda = \frac{1 - cd^3}{1 - cd} \quad (5.6)$$

A change of c and d in the interval of $[0,1]$ results in values of ψ_I and ψ_A in the range of $[0,1]$ while λ range is $[1,3]$. Similar formulation can be expressed for different shape classes, e.g. ellipses and diamonds (Pasini, 2007; Pasini, et.al., 2003; Pasini, et.al., 2006).

The limiting curves that show the variation of ψ_I and ψ_A with the variation of the two parameters c and d is plotted in Fig (5.3) for the three cross-section shapes considered in this study.

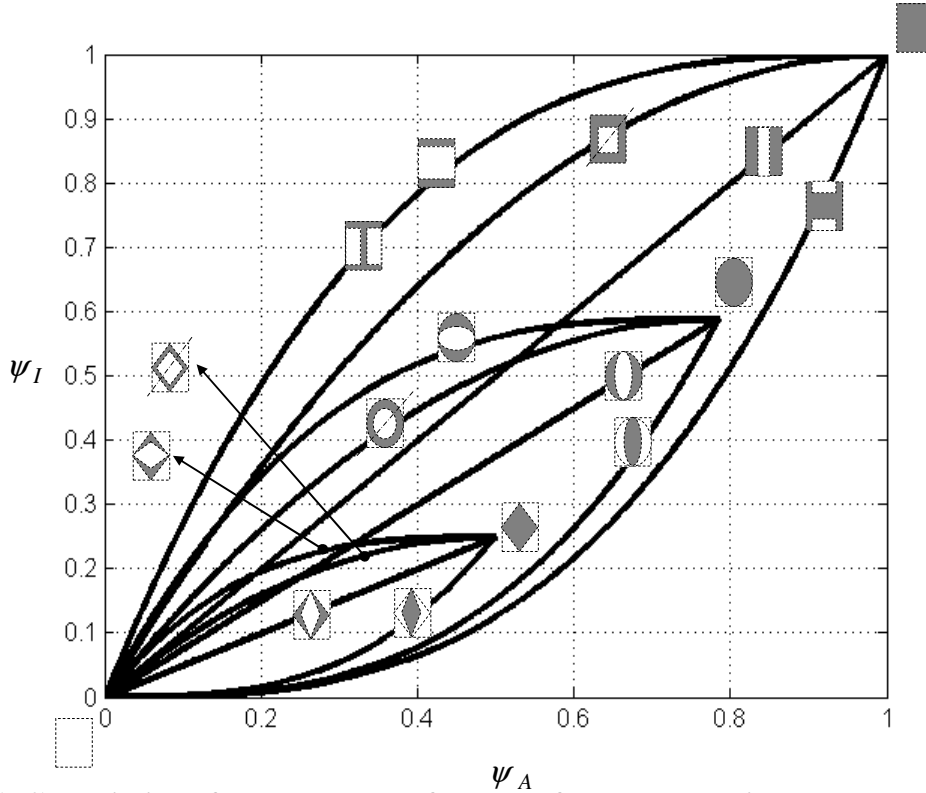


Fig (5.3) Variation of the shape transformers of the cross-section area and second moment of area for different cross-section shapes

In Fig (5.3), the bending efficiency necessary to assess the bending and the buckling resistance of a cross-section can be evaluated by computing the tangent of the angle formed by the line extending from the origin of the graph to the point representing the shape of each cross-section.

The buckling resistance of the microscopic cell element of the lattice material is governed by the radius of gyration, r_g , of the element cross-section, besides by its length. The radius of gyration is linked to the second moment of area by the expression:

$$I = A r_g^2 \quad (5.7)$$

To express eqn (5.7) in terms of the shape transformers, we substitute eqns (5.4) and (5.5) into eqn (5.7) and use eqn (5.2) to obtain the following expression (Pasini, et.al., 2003):

$$r_g^2 = \lambda v^2 r_{g0}^2 \quad (5.8)$$

where r_{g0} is the radius of gyration of the reference cross-section.

In addition to modeling the cross-section geometry, we introduce also another parameter, s , which models the length L of the cell element with respect to the length L_0 of a reference prismatic element. Similar to u and v , this scaling multiplier is expressed as:

$$s = \frac{L}{L_0} \quad (5.9)$$

Expressions (5.1) to (5.9) are used in this work to model the geometrical properties at the micro and macroscopic scales of the structure. To distinguish between scales' parameters, we use throughout the whole chapter the subscript “ e ” for the microscopic parameters and “ G ” for the macroscopic ones.

5.4 Modeling the Effective Properties of the Octet-Truss Lattice Material

In this section, the effective properties of the regular octet-truss lattice material are formulated as a function of the shape properties of the cell element cross-sections. Cross-sections with double symmetry with respect to their principal axes are examined. The properties considered include the material density, the elastic and the strength properties and the material collapse surfaces. For comparison, we report here also the formulations of the regular octet-truss lattice material found in literature (Deshpande, et.al., 2001), where the cell element geometry of the lattice material is assumed to be uniform with circular solid cross-section. The properties of previous models are identified here with the suffix “ a ”; whereas the suffix “ b ” is used for our models, which are governed by the parameters presented in § 5.3. It is assumed that the solid material, used in manufacturing the lattice material is elastic-perfectly plastic and has an isotropic behavior with a Poisson's ratio of $\nu_0 = 1/3$.

5.4.1. Relative Density

If we assume that the mass of the boundary elements of the unit cell are divided equally among the neighbouring cells, then the relative density of the regular octet-truss lattice material can be expressed as:

$$\bar{\rho}_{La} = \frac{\rho_{La}}{\rho} = \left(6\pi\sqrt{2}\right)\left(\frac{a_e}{L_e}\right)^2 \quad (5.10a)$$

$$\bar{\rho}_{Lb} = \frac{\rho_{Lb}}{\rho} = \left(6\sqrt{2}\right)\left(\frac{A_{e0}}{L_{e0}^2}\right)\left(\frac{\psi_{eA}u_e v_e}{s_e^2}\right) \quad (5.10b)$$

where a_e is the radius of the cell element cross-section. $\bar{\rho}_L$ is the relative density of the lattice material, ρ_L is the density of the lattice material and ρ is the density of the solid material used to manufacture the lattice material.

5.4.2. Elastic Properties

The regular octet-truss cell geometry has a cubic symmetry, which generates a material with isotropic properties (Renton, 2002). The compliance matrix of an isotropic material can be expressed as:

$$\mathbf{C} = \frac{1}{E_L} \begin{bmatrix} 1 & -\nu_L & -\nu_L & 0 & 0 & 0 \\ -\nu_L & 1 & -\nu_L & 0 & 0 & 0 \\ -\nu_L & -\nu_L & 1 & 0 & 0 & 0 \\ 0 & 0 & 0 & 2(1+\nu_L) & 0 & 0 \\ 0 & 0 & 0 & 0 & 2(1+\nu_L) & 0 \\ 0 & 0 & 0 & 0 & 0 & 2(1+\nu_L) \end{bmatrix} \quad (5.11)$$

where ν_L and E_L are, respectively, the lattice material Poisson's ratio and Young's modulus.

By using the direct stiffness method, the relative Young's modulus of the octet-truss lattice material can be expressed as:

$$\bar{E}_{La} = \frac{E_{La}}{E} = \frac{2\pi\sqrt{2}}{3}\left(\frac{a_e}{L_e}\right)^2 \quad (5.12a)$$

$$\bar{E}_{Lb} = \frac{E_{Lb}}{E} = \frac{2\sqrt{2}}{3}\left(\frac{A_{e0}}{L_{e0}^2}\right)\left(\frac{\psi_{eA}u_e v_e}{s_e^2}\right) \quad (5.12b)$$

where E_L , \bar{E}_L and E are respectively, the Young's modulus of the lattice material, the relative Young's modulus of the lattice material and the Young's modulus of the solid material.

Combining eqns (5.12a) to eqn (5.10a) and eqns (5.12b) to eqn (5.10b) results in:

$$\bar{E}_L = \frac{E_L}{E} = \frac{1}{9} \bar{\rho}_L \quad (5.13)$$

The Poisson's ratio of the regular octet-truss lattice material is found to be $\nu_L = 1/3$. Therefore, the full compliance matrix of the regular octet-truss lattice material can be formulated as:

$$\mathbf{C} = \frac{1}{E \bar{\rho}_L} \begin{bmatrix} 9 & -3 & -3 & 0 & 0 & 0 \\ -3 & 9 & -3 & 0 & 0 & 0 \\ -3 & -3 & 9 & 0 & 0 & 0 \\ 0 & 0 & 0 & 24 & 0 & 0 \\ 0 & 0 & 0 & 0 & 24 & 0 \\ 0 & 0 & 0 & 0 & 0 & 24 \end{bmatrix} \quad (5.14)$$

The relative shear modulus, \bar{G}_L , and the relative bulk modulus, $\bar{\kappa}_L$, of the regular octet-truss lattice material can then be expressed as:

$$\bar{G}_L = \frac{G_L}{G} = \left(\frac{E_L}{2(1+\nu_L)} \right) / G = \frac{\bar{\rho}_L}{9} \quad (5.15)$$

$$\bar{\kappa}_L = \frac{\kappa_L}{\kappa} = \left(\frac{E_L}{3(1-2\nu_L)} \right) / \kappa = \frac{\bar{\rho}_L}{9} \quad (5.16)$$

where G and κ are, respectively, the shear and the bulk moduli of the solid material.

Equations (5.13), (5.15) and (5.16), show that the elastic properties of the regular octet-truss lattice material are independent of the geometrical attributes of the cell elements. It can be realized that the ratio of the relative elastic moduli to the relative density is “1/9”, a constant that depends on the topology of the regular octet-truss cell.

5.4.3 Strength Properties

A. Plastic Yield Strength

By using the direct stiffness method, axial and shear yield strengths of the regular octet-truss lattice material can be formulated as:

$$\bar{\sigma}_{yLa} = \frac{\sigma_{yLa}}{\sigma_{y0}} = \pi\sqrt{2}\left(\frac{a_e}{L_e}\right)^2 \quad (5.17a)$$

$$\bar{\tau}_{yLa} = \frac{\tau_{yLa}}{\tau_{y0}} = \frac{\pi}{\sqrt{2}}\left(\frac{a_e}{L_e}\right)^2 \quad (5.17b)$$

$$\bar{\sigma}_{yLb} = \frac{\sigma_{yLb}}{\sigma_{y0}} = \sqrt{2}\left(\frac{A_{e0}}{L_{e0}^2}\right)\left(\frac{\psi_{eA}u_e v_e}{s_e^2}\right) \quad (5.18a)$$

$$\bar{\tau}_{yLb} = \frac{\tau_{yLb}}{\tau_{y0}} = \sqrt{2}\left(\frac{A_{e0}}{L_{e0}^2}\right)\left(\frac{\psi_{eA}u_e v_e}{s_e^2}\right) \quad (5.18b)$$

where σ_{y0} and σ_{yL} are the direct yield strengths of the solid material and the lattice material, respectively. τ_{y0} and τ_{yL} are the shear yield strengths of the solid material and the lattice material, respectively.

Combining eqns (5.17a) and (5.18a) into eqn (5.10a) as well as combining eqns (5.17b) and (5.18b) into eqn (5.10b) give:

$$\bar{\sigma}_{yL} = \frac{\sigma_{yL}}{\sigma_{y0}} = \frac{1}{6}\bar{\rho}_L \quad (5.19a)$$

$$\bar{\tau}_{yL} = \frac{\tau_{yL}}{\tau_{y0}} = \frac{1}{6}\bar{\rho}_L \quad (5.19b)$$

where $\tau_{yL} = \frac{1}{2}\sigma_{yL}$ and $\tau_{y0} = \frac{1}{2}\sigma_{y0}$ are obtained from the Mohr's circle of an isotropic material in pure shear.

Equations (5.19) shows that, also the yield strength properties of the regular octet-truss lattice material are independent of the cell elements geometry where the ratio of lattice material relative direct and shear strengths to its relative density is a constant.

B. Elastic Buckling Strength

The Euler critical buckling load of an axially loaded member in compression is expressed as:

$$P_{cr} = k^2 \frac{\pi^2 E I}{L^2} \quad (5.20)$$

where E is the Young's modulus of the material, I is the smallest second moment of area of the member cross-section, L is the length of the member and k is a factor that depends on the

rotational stiffness of the member end boundaries. For a pin jointed element where joint rotation is freely allowed, $k = 1$. If the rotation is fully constrained by fixed boundary conditions, then $k = 2$. In practice, the value of the factor k of a stretching dominated lattice material is between 1 and 2. We idealize the octet-truss lattice material as a pin jointed micro-truss structure with $k = 1$, which is a safe design assumption.

Equations (5.8-5.9) along with eqn (5.20) are used to express the critical buckling stress of the regular octet-truss lattice material as:

$$\frac{\sigma_{ea}^{cr}}{\sigma_{y0}} = \left(\frac{2\pi^3\sqrt{2}}{3} \right) \left(\frac{E}{\sigma_{y0}} \right) \left(\frac{a_e}{L_e} \right)^4 \quad (5.21a)$$

$$\frac{\sigma_{eb}^{cr}}{\sigma_{y0}} = \left(\pi^2\sqrt{2} \right) \left(\frac{r_{eg0}^2 A_{e0}}{L_{e0}^4} \right) \left(\frac{E}{\sigma_{y0}} \right) \left(\frac{\psi_{el} u_e v_e^3}{s_e^4} \right) \quad (5.21b)$$

where σ_e^{cr} and σ_e are, respectively, the relative critical buckling strength and the critical buckling strength of the regular octet-truss lattice material.

By combining eqns (5.21a) to (5.10a), and (5.21b) to (5.10b), eqns (5.21) can be modified as:

$$\frac{\sigma_{ea}^{cr}}{\sigma_{y0}} = \left(\frac{\pi}{54\sqrt{2}} \right) \left(\frac{E}{\sigma_{y0}} \right)^{-2} \rho_L \quad (5.22a)$$

$$\frac{\sigma_{eb}^{cr}}{\sigma_{y0}} = \left(\frac{\pi^2}{36\sqrt{2}} \right) \left(\frac{r_{eg0}^2}{A_{e0}} \right) \left(\frac{E}{\sigma_{y0}} \right) \left(\frac{\lambda_e}{\psi_{eA}} \right) \left(\frac{v_e}{u_e} \right)^{-2} \rho_L \quad (5.22b)$$

From eqn (5.22a), it can be seen that the critical buckling strength of the lattice material with uniform cell elements of a circular solid cross-section is a function of the material relative density as well as the solid material properties. On the other hand, eqn (5.22b) shows that, in lattice materials with shaped cell element cross-sections, the critical buckling strength is also a function of the geometrical attributes of the cell element cross-section.

To avoid failure by buckling, we impose the condition:

$$\sigma_e^{cr} \geq \sigma_{yL} \quad (5.23)$$

Substituting eqns (5.17a) and (5.22a) into inequality (5.23) gives:

$$\rho_{La} \geq \left(\frac{6\sqrt{2}}{\pi} \right) \left(\frac{\sigma_{y0}}{E} \right) \quad (5.24)$$

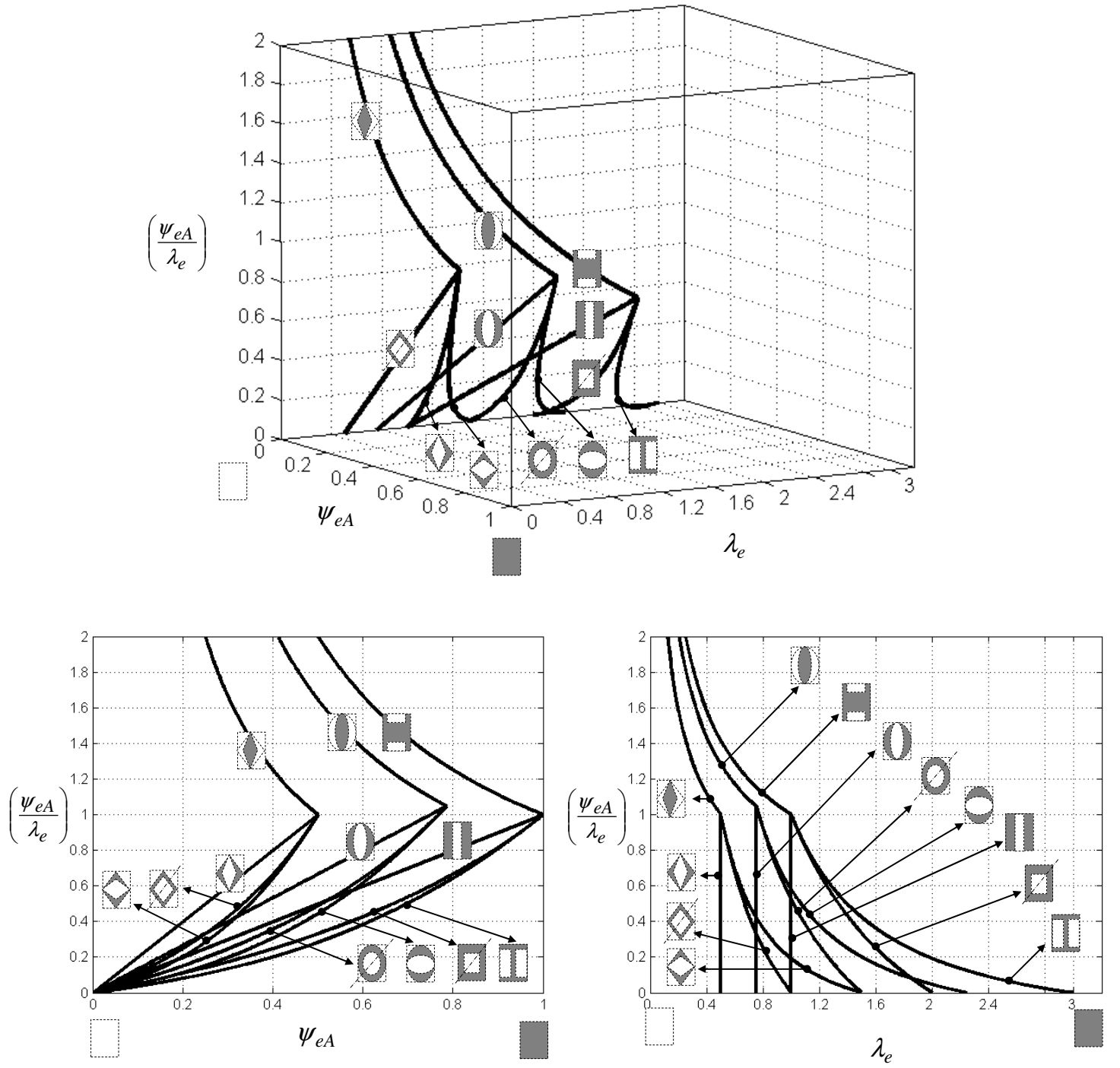


Fig (5.4) Variation of the lattice material relative density with respect to cross-section efficiency and to area shape transformer

The equality form of expression (5.24) is the critical relative density, $\bar{\rho}_{La}^*$, of the regular octet-truss lattice material with circular solid cell element cross-sections. As formulated, $\bar{\rho}_{La}^*$ is only a

function of the solid material properties. The geometrical attributes of the cell element are included together with the cell topology properties in the constant $\left(\frac{6\sqrt{2}}{\pi}\right)$.

To formulate the critical relative density, $\bar{\rho}_{Lb}^*$, as a function of the geometrical properties of the cell element cross-section, we combine eqn (5.18a) and (5.22b) with inequality (5.23), and write:

$$\bar{\rho}_{Lb}^* = \left(\frac{6\sqrt{2}}{\pi^2}\right) \left(\frac{A_{e0}}{r_{eg0}^2}\right) \left(\frac{\sigma_{y0}}{E}\right) \left(\frac{u_e}{v_e}\right) \left(\frac{\psi_{eA}}{\lambda_e}\right) \quad (5.25)$$

The contribution of the shape of the cell element cross-section can be isolated by rearranging eqn (5.25) as:

$$\frac{\bar{\rho}_{Lb}^*}{\left(\frac{6\sqrt{2}}{\pi^2}\right) \left(\frac{A_{e0}}{r_{eg0}^2}\right) \left(\frac{\sigma_{y0}}{E}\right) \left(\frac{u_e}{v_e}\right)} = \left(\frac{\psi_{eA}}{\lambda_e}\right) \quad (5.26)$$

The effect of the cross-section efficiency and area shape transformer on the lattice material critical relative density is shown in Fig (5.4), where eqn (5.26) was plotted for the three shape families (rectangular, elliptical and diamond) considered in this work. For a given area shape transformer, ψ_{eA} , each family of cross-section shapes generates its own specific trend of critical relative density which provides the minimum critical density that minimizes eqn (5.26). From Fig (5.4), we gather that for the whole range of ψ_{eA} the family of the rectangles has the potential to minimize $\frac{\psi_{eA}}{\lambda_e}$ better than the other shapes.

5.5 Collapse Surfaces

A lattice material subjected to static loading encounters four types of collapses, namely, plastic yielding (strength failure), elastic buckling (instability failure), creep (deformation increase under constant loading) and relaxation (load carrying capacity decrease under constant deformations). In the following analysis, strength and stability collapses are examined.

5.5.1 Yield Collapse

The elements of a stretching dominated lattice material are always loaded axially, either in tension or compression. Unlike the collapse surfaces of solid materials (Beer, et.al., 1981) which, in the

case of ductile materials, are based on combined stresses derived from the Mohr's circle in the form of maximum shear stresses, e.g. Trisca, or the maximum distortion energy, e.g. the Von Mises; the yield collapse of the stretching dominated lattice material is based on axial yielding of microscopic cell elements through load transformation from the macroscopic stress field into the microscopic elements. If we assume that each microscopic element of the octet-truss lattice material has a slenderness ratio that prevents buckling, then all the cell members will fail by plastic yielding. Following the approach of Deshpande, et.al., 2001, we consider a load case where the regular octet-truss cell is loaded by two forces in the x and the z principal directions, as shown in Fig (5.1). If the yield strength, σ_{y0} , is the same in tension and compression, the elastic yielding collapse surface in the x - z plane can be formulated as:

$$\left| \frac{\sigma_{xxa}}{\sigma_{y0}} \right| + \left| \frac{\sigma_{zza}}{\sigma_{y0}} \right| \leq 2\pi\sqrt{2} \left(\frac{a_e}{L_e} \right)^2 \quad (5.27a)$$

$$\left| \frac{\tau_{xza}}{\sigma_{y0}} \right| + \left| \frac{\sigma_{zza}}{2\sigma_{y0}} \right| \leq \pi\sqrt{2} \left(\frac{a_e}{L_e} \right)^2 \quad (5.27b)$$

$$\left| \frac{\sigma_{xxb}}{\sigma_{y0}} \right| + \left| \frac{\sigma_{zzb}}{\sigma_{y0}} \right| \leq 2\sqrt{2} \left(\frac{A_{e0}}{L_{e0}^2} \right) \left(\frac{\psi_e A_e u_e v_e}{s_e^2} \right) \quad (5.27c)$$

$$\left| \frac{\tau_{xzb}}{\sigma_{y0}} \right| + \left| \frac{\sigma_{zzb}}{2\sigma_{y0}} \right| \leq \sqrt{2} \left(\frac{A_{e0}}{L_{e0}^2} \right) \left(\frac{\psi_e A_e u_e v_e}{s_e^2} \right) \quad (5.27d)$$

Combining eqn (5.10a) to (5.27a) and (5.27b) as well as eqn (5.10b) to (5.27c) and (5.27d), then, the plastic yielding collapse surfaces of the regular octet-truss lattice material can be formulated as:

$$\left| \frac{\sigma_{xx}}{\sigma_{y0}} \right| + \left| \frac{\sigma_{zz}}{\sigma_{y0}} \right| \leq \frac{1}{3} \rho_L \quad (5.28a)$$

$$\left| \frac{\tau_{xz}}{\sigma_{y0}} \right| + \left| \frac{\sigma_{zz}}{2\sigma_{y0}} \right| \leq \frac{1}{6} \rho_L \quad (5.28b)$$

From eqns (5.28), it can be deduced that for the regular octet-truss lattice material the ratios of the plastic collapse stresses to the relative density are independent of the cell elements geometry.

5.5.2 Buckling Collapse Surfaces

Assume that the regular octet-truss cell is loaded by two forces in the x and z principal directions, as shown in Fig (5.1), then, the critical buckling collapse surfaces in the x - z plane can be formulated as:

$$\left| \frac{\sigma_{xxa}^{cr}}{\sigma_{y0}} \right| + \left| \frac{\sigma_{zza}^{cr}}{\sigma_{y0}} \right| \leq \left(\frac{\sqrt{2}\pi}{54} \right) \left(\frac{E_0}{\sigma_{y0}} \right)^{-2} \rho_L \quad (5.29a)$$

$$\left| \frac{\tau_{xza}^{cr}}{\sigma_{y0}} \right| + \left| \frac{\sigma_{zza}^{cr}}{2\sigma_{y0}} \right| \leq \left(\frac{\pi}{54\sqrt{2}} \right) \left(\frac{E_0}{\sigma_{y0}} \right)^{-2} \rho_L \quad (5.29b)$$

$$\left| \frac{\sigma_{xxb}^{cr}}{\sigma_{y0}} \right| + \left| \frac{\sigma_{zzb}^{cr}}{\sigma_{y0}} \right| \leq \left(\frac{\pi^2}{18\sqrt{2}} \right) \left(\frac{r_{eg0}^2}{A_{e0}} \right) \left(\frac{E}{\sigma_{y0}} \right) \left(\frac{\lambda_e}{\psi_{eA}} \right) \left(\frac{v_e}{u_e} \right)^{-2} \rho_L \quad (5.29c)$$

$$\left| \frac{\tau_{xzb}^{cr}}{\sigma_{y0}} \right| + \left| \frac{\sigma_{zzb}^{cr}}{2\sigma_{y0}} \right| \leq \left(\frac{\pi^2}{36\sqrt{2}} \right) \left(\frac{r_{eg0}^2}{A_{e0}} \right) \left(\frac{E}{\sigma_{y0}} \right) \left(\frac{\lambda_e}{\psi_{eA}} \right) \left(\frac{v_e}{u_e} \right)^{-2} \rho_L \quad (5.29d)$$

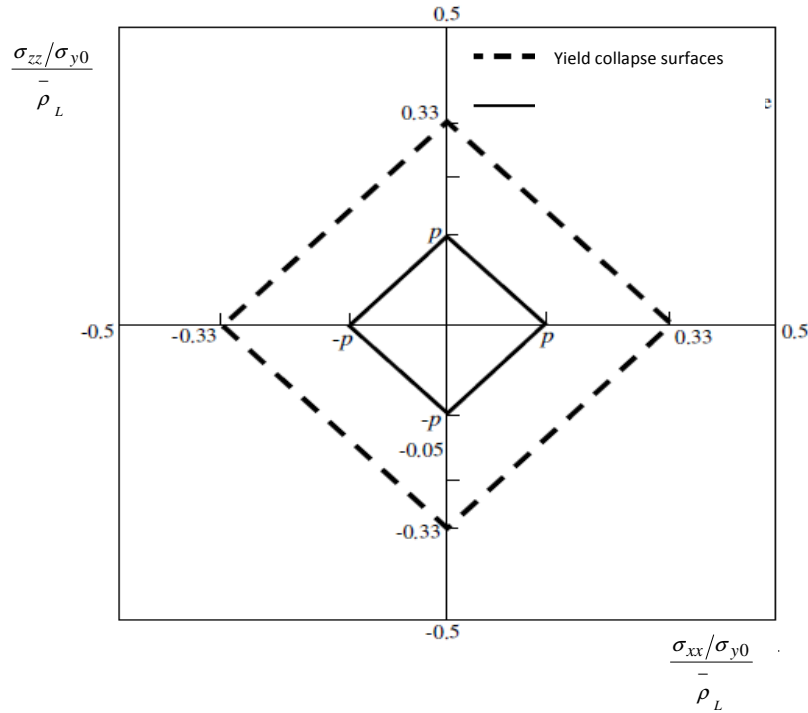


Fig (5.5) Elastic and plastic collapse surfaces of the octet-truss lattice material evaluated for the relative direct stresses and normalized with respect to the material relative density

By normalizing eqns (5.28a), (5.29a) and (5.29c) with respect to the relative density of the lattice material, we can express the collapse surfaces as:

Yield (for a circular and a generic cross-section)

$$\left| \frac{\sigma_{xx}}{\sigma_{y0}} \right| \left/ \frac{\rho_L}{\rho_L} \right| + \left| \frac{\sigma_{zz}}{\sigma_{y0}} \right| \left/ \frac{\rho_L}{\rho_L} \right| \leq \frac{1}{3} \quad (5.30a)$$

Buckling (for a circular cross-section)

$$\left| \frac{\sigma_{xxa}^{cr}}{\sigma_{y0}} \right| \left/ \frac{\rho_L}{\rho_L} \right| + \left| \frac{\sigma_{zza}^{cr}}{\sigma_{y0}} \right| \left/ \frac{\rho_L}{\rho_L} \right| \leq \left(\frac{\sqrt{2}\pi}{54} \right) \left(\frac{E}{\sigma_{y0}} \right) \rho_L \quad (5.30b)$$

Buckling (for a generic cross-section)

$$\left| \frac{\sigma_{xxb}^{cr}}{\sigma_{y0}} \right| \left/ \frac{\rho_L}{\rho_L} \right| + \left| \frac{\sigma_{zzb}^{cr}}{\sigma_{y0}} \right| \left/ \frac{\rho_L}{\rho_L} \right| \leq \left(\frac{\pi^2}{18\sqrt{2}} \right) \left(\frac{r_{eg0}^2}{A_{e0}} \right) \left(\frac{E}{\sigma_{y0}} \right) \left(\frac{\lambda_e}{\psi_{eA}} \right) \left(\frac{v_e}{u_e} \right) \rho_L \quad (5.30c)$$

The relative direct stresses normalized with respect to the material relative density are plotted in Fig (5.5).

For octet-truss lattice material with cell elements of circular solid cross-sections, the parameter “ p ”, which represents the relative strength to the relative density ratio, is expressed as:

$$p_a = \left(\frac{\sqrt{2}\pi}{54} \right) \left(\frac{E}{\sigma_{y0}} \right) \rho_L \quad (5.31a)$$

For a generic cell element cross-sections, the parameter p is expressed as:

$$p_b = \left(\frac{\pi^2}{18\sqrt{2}} \right) \left(\frac{r_{eg0}^2}{A_{e0}} \right) \left(\frac{E}{\sigma_{y0}} \right) \left(\frac{\lambda_e}{\psi_{eA}} \right) \left(\frac{v_e}{u_e} \right) \rho_L \quad (5.31b)$$

The impact of shaping cell element cross-sections on the strength to mass ratio of the lattice material is shown in the following examples.

5.6 Examples

5.6.1 Example 1

Consider an octet-truss lattice material with relative density of $\rho_L = 0.0174$ that is manufactured of steel AISI L2 (tempered at 205°C) which has compressive yield strength of 1835 MPa, a Young’s modulus of 210 GPa and a density of 7940 kg/m³. Starting with a preliminary design, the structural performance of the lattice material is compared in two scenarios:

a) The lattice material has cell elements of circular solid cross-sections of radius $a_e=0.2557$ mm and length $L_e=10$ mm. If these values are substituted into eqn (5.31a), we obtain $p_a = 0.164$.

b) The lattice material has generic cell elements with geometrical attributes that have the values of $u_e=2.5$, $v_e=s_e=1$, $L_{e0}=10$ mm, $A_{e0}=0.4107$ mm², $r_{e0}=0.185$ mm, and $\psi_{eA}=0.2$. Similarly, substituting these values into eqn (5.31b) gives $p_b = 0.129\lambda_e$.

Assume that the generic cross-sections have efficiency $\lambda_e = 1$, then, the lattice material in both cases (a) and (b) fails by elastic buckling. However, as explained in the previous sections, an axially loaded structure that fails by buckling is far from optimum since the material fails before reaching its yielding strength, therefore, we optimize our design by increasing the buckling resistance until it coincides with the plastic yield strength. In the case of the circular solid cross-sections, this strategy results in increasing the relative density of the lattice material from 0.0174 to 0.035. On the other hand, in the case of cell element with generic cross-sections, the relative density of the material can be left constant, while the shape of the cross-section can be tuned to generate an efficiency of $\lambda_e = 2.56$. This value can be provided by a cross-section of the rectangular family with a geometry described, for example, by $c=1$ and $d=0.849$. As a result, shaping the cell element cross-sections of the regular octet-truss lattice material with $\lambda_e = 2.56$

increases the stress carrying capacity of the material from $(\sigma/\sigma_{y0})/\bar{\rho}_L = 0.164$ to

$(\sigma/\sigma_{y0})/\bar{\rho}_L = 0.33$ and reduces the structural weight of 50%.

5.6.2 Example 2

In this second example, the effect of changing the efficiency of alternative cell element cross-sections on the collapses surfaces is investigated. In particular, the cross-section efficiency of the cell elements is optimized in order to increase the buckling resistance until it reaches the material yielding.

Assume a solid material with yield strain $\varepsilon_{y0}=0.05$, and assume that the cross-section geometry of the cell elements is described by $A_{e0}=4$ μm², $u_e=v_e=1$, and has shape properties of $\psi_{eA}=0.6$ and element length $L_e=1$ cm. Using the derived expressions, from previous section that characterize the lattice material properties, those properties can be computed as:

Relative density

$$\bar{\rho}_L = \frac{\rho_L}{\rho} = 6\sqrt{2} \left(\frac{\psi_A A_{D0} u v}{L_e^2} \right) = 0.203 \quad (5.32a)$$

Plastic collapse surface

$$\left| \frac{\sigma_{xx}}{\sigma_{y0}} \right| + \left| \frac{\sigma_{zz}}{\sigma_{y0}} \right| \leq 0.0676 \quad (5.32b)$$

Elastic buckling collapse surface

$$\left| \frac{\sigma_{xxb}^{cr}}{\sigma_{y0}} \right| + \left| \frac{\sigma_{zzb}^{cr}}{\sigma_{y0}} \right| \leq 0.0445\lambda_e \quad (5.32c)$$

As expected, eqn (5.32c) depends on the cell element cross-section efficiency, λ_e , of the lattice material. Resorting to the cross-section selection chart, shown in Fig (5.6), the efficiency of alternative cross-section shapes can be computed.

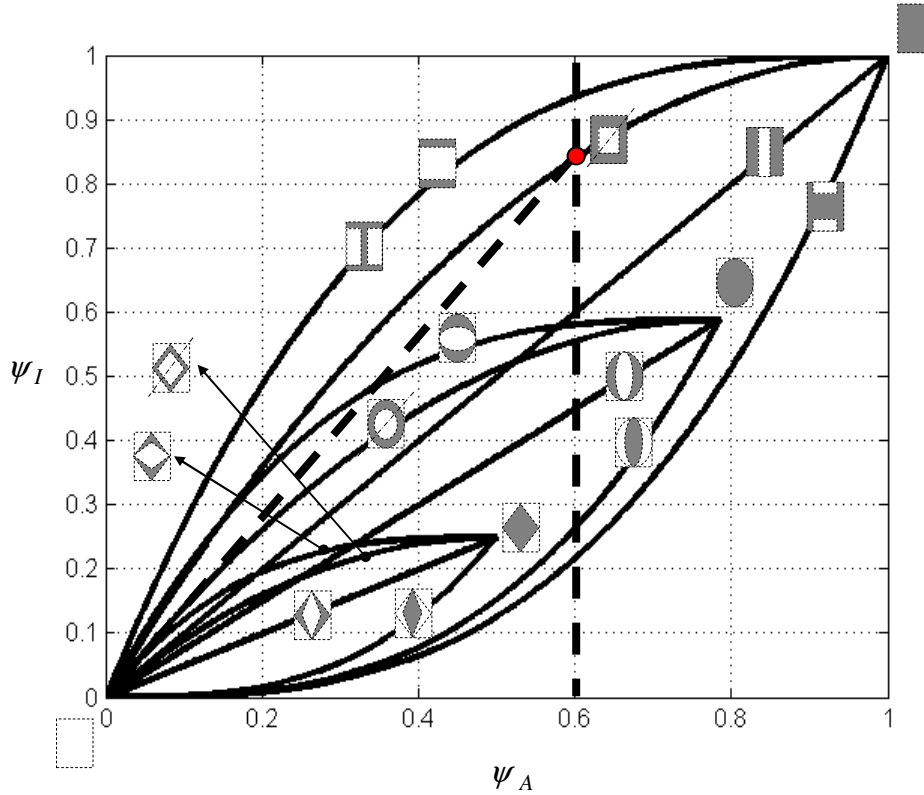


Fig (5.6) Efficiencies of different cross-section shapes at specified $\psi_A=0.6$

In Fig (5.6), we prescribed the area shape transformer ($\psi_{eA}=0.6$) which contributes to the lattice material density. The condition $\psi_{eA}=0.6$ is illustrated by the dashed vertical line that intersects the limiting curves of the alternative cross-section shapes available. The cross-section efficiency, λ_e , is simply the slope of a segment connecting a point to the origin of the chart.

If we determine the value of the efficiency, λ_e , of the cross-section that is selected from Fig (5.6) and substitute it into eqn (5.32c), then, the collapse surfaces can be obtained (Fig (5.7)) for the cross-sections meeting the requirement $\psi_{eA}=0.6$.

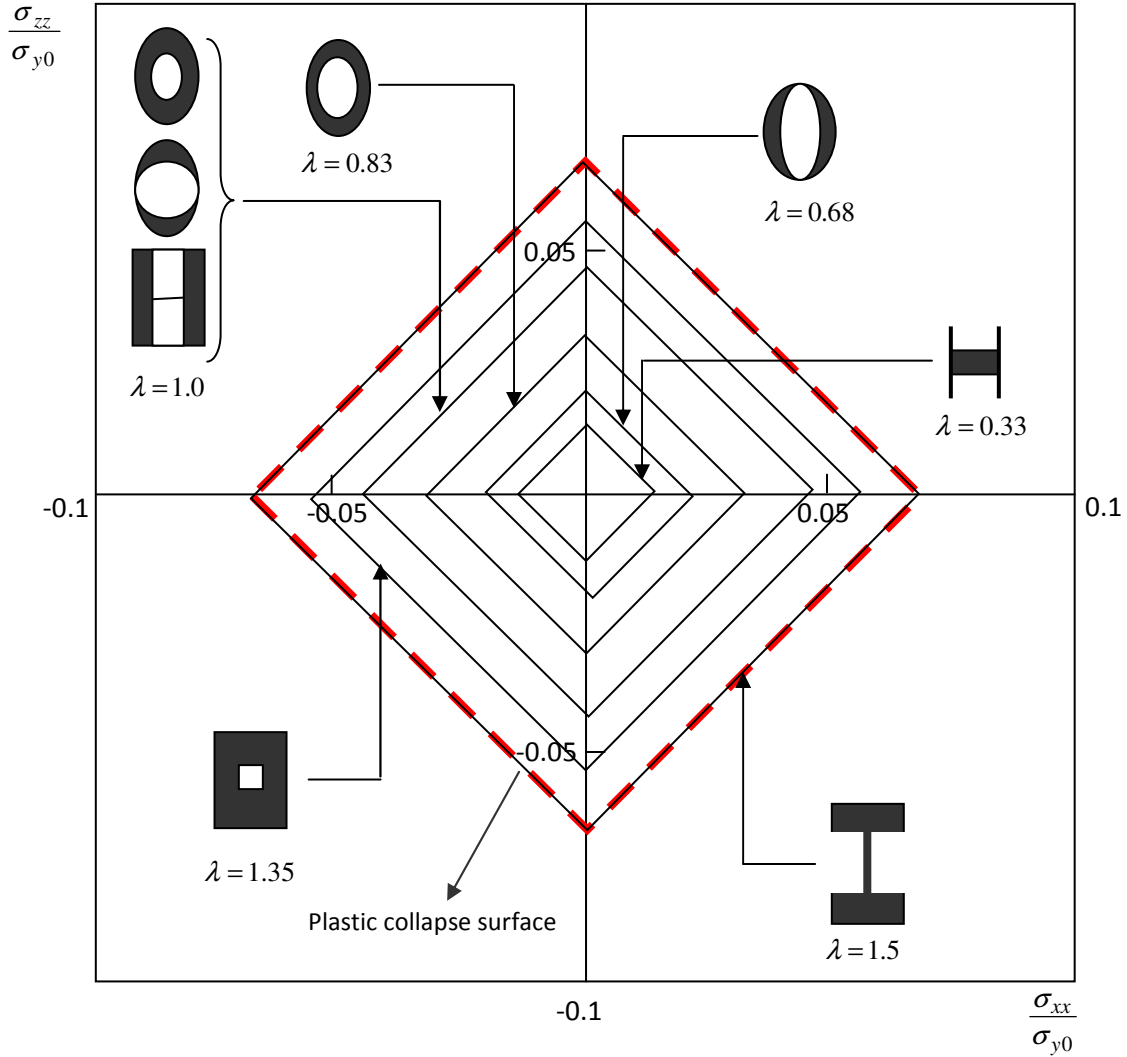


Fig. (5.7) Elastic and plastic collapse surfaces and the effect of cross-section efficiency on the structural performance

In Fig (5.7), the plastic yielding collapse surfaces are superimposed to the elastic buckling collapse surfaces of the lattice material under the load case corresponding to two direct stresses in

the x - z plane. Fig (5.7) shows four failure modes corresponding to Mode I= $\left(+\frac{\sigma_{xx}^{cr}}{\sigma_{y0}}, +\frac{\sigma_{zz}^{cr}}{\sigma_{y0}} \right)$,

$$\text{Mode II}=\left(+\frac{\sigma_{xx}^{cr}}{\sigma_{y0}}, -\frac{\sigma_{zz}^{cr}}{\sigma_{y0}} \right), \text{Mode III}=\left(-\frac{\sigma_{xx}^{cr}}{\sigma_{y0}}, -\frac{\sigma_{zz}^{cr}}{\sigma_{y0}} \right) \text{ and Mode VI}=\left(-\frac{\sigma_{xx}^{cr}}{\sigma_{y0}}, +\frac{\sigma_{zz}^{cr}}{\sigma_{y0}} \right).$$

The optimum lattice material is obtained when the elastic buckling resistance is increased until it is equal to the yielding failure strength (Ashby, 2005; Weaver and Ashby, 1997). In this example, such a criterion is achieved at $\lambda_e = 1.5$, which can be satisfied, for example, by a rectangular cross-section with $c=1$ and $d=0.48$. Although higher efficiencies can be obtained, no increase in the structural performance can be achieved, as for $\lambda_e > 1.5$ the plastic yielding will dominate the failure mode.

Whereas prescribed in this example, the cell element length will be considered design variable in the next sections.

5.7 Design Charts for the Regular Octet-Truss Lattice Material

In this section, a design chart is developed to help selecting the microscopic attributes of the regular octet-truss lattice material that best minimize its relative density for a given strength requirement σ_L . Here, the cell element length multiplier, s_e , as well as the shape of a double symmetry cross-section are considered as design variables.

For the purpose of developing such a chart, we formulate the problem in optimization terms as follows:

$$\begin{aligned} \text{Minimize} \quad & \bar{\rho}_L \\ \text{With respect to} \quad & s_e \text{ and } \psi_{eA} \\ \text{Subject to} \quad & \sigma_e^{cr} = \sigma_{yL} = \sigma_L \\ & \text{and } u_e/v_e \geq 1 \end{aligned} \tag{5.33}$$

The equality constraint (5.33) is imposed to use the material strength to its maximum extent. Before plotting the chart, we rearrange in three steps the expressions of the objective function

$\bar{\rho}_L$ and the constraint $\sigma_e^{cr} = \sigma_{yL}$. The goal is to make them functions solely of the geometric

variables of the cell element, which include the cell element length multiplier, s_e , and the cross-section efficiency λ_e .

Step 1) s_e is reformulated by substituting eqns (5.18a) and (5.21b) into eqn (5.33), which results in the expression:

$$s_e = \left(\pi \left(\frac{r_{eg0}}{L_{e0}} \right) (v_e) \sqrt{\left(\frac{E}{\sigma_{y0}} \right) \lambda_e} \right) \quad (5.34)$$

In eqn (5.34), the cell element length multiplier is controlled by the cell element cross-section shape through $\sqrt{\lambda_e}$. For convenience, we redefine s_e with the following parameter Ω_e as:

$$\Omega_e := \left(\left(\frac{L_{e0}}{r_{eg0}} \right) s_e \right) / \left(\pi v_e \sqrt{\frac{E}{\sigma_{y0}}} \right) = \sqrt{\lambda_e} \quad (5.35)$$

Step 2) The octet-truss lattice material yield strength σ_{yL} is expressed as a function of Ω_e and ψ_{eA} . Here, eqn (5.35) is used to reformulate s_e in terms of Ω_e and to substitute the result into eqn (5.18a) which is rewritten as:

$$\bar{\sigma}_{yL} = \frac{\sigma_{yL}}{\sigma_{y0}} = \left(\frac{\sqrt{2}}{\pi^2} \right) \left(\frac{A_{e0}}{r_{eg0}^2} \right) \left(\frac{\sigma_{y0}}{E} \right) \left(\frac{\psi_{eA}}{\Omega_e^2} \right) \left(\frac{u_e}{v_e} \right) \quad (5.36)$$

By rearranging eqn (5.36), the contribution of the cell element geometry to the strength of the lattice material can be isolated, and σ_{yL} can be redefined as:

$$\sigma_{yL}^* := \frac{\sigma_{yL}}{\left(\frac{\sqrt{2}}{\pi^2} \right) \left(\frac{A_{e0}}{r_{eg0}^2} \right) \left(\frac{\sigma_{y0}}{E} \right) \left(\frac{u_e}{v_e} \right)} = \left(\frac{\psi_{eA}}{\Omega_e^2} \right) \quad (5.37)$$

Step 3) Finally, the objective function, $\bar{\rho}_L$, is expressed in terms of the design variables. From eqn (5.35), s_e is expressed in terms of Ω_e and the resulting expression is substituted into eqn (5.10b) which is given by:

$$\bar{\rho}_L = C_e \frac{\psi_{eA}}{\Omega_e^2} \quad (5.38)$$

where $C_e = \left(\frac{6\sqrt{2}}{\pi^2} \right) \left(\frac{A_{e0}}{r_{eg0}^2} \right) \left(\frac{1}{v_e^2} \right) \left(\frac{\sigma_{y0}}{E} \right)$. As noted previously, eqn (5.38), similarly to eqn (5.36),

is dependent on $\frac{\psi_{eA}}{\Omega_e^2}$ through the coefficient C_e .

The previous relations are now plotted into the design chart shown in Fig (5.8). The lightest lattice materials that minimize $\frac{\psi_{eA}}{\Omega_e^2}$ in eqn (5.38) are the solutions displayed at the left-top corner. The black lines, which guide the choice of Ω_e , represent the cell element lengths, eqn (5.35), of different cross-section shapes. Iso-stress contours σ_{yL}^* , eqn (5.37), are also superimposed to help the designer to select the best cell element cross-section shape and its length for a given σ_L requirement.

Since σ_L is specified by the problem, eqn (5.37) is used to determine σ_{yL}^* , after having scaled the element cross-section with a value of u_e/v_e that meets the strength requirement. Although a specific ratio of u_e/v_e can be generated by an infinite combinations of values of u_e and v_e , in practice the maximum dimension of the cubic envelope of the microscopic octet-truss lattice cell must be limited by the minimum dimensions of the structure at the macroscopic scale.

5.8. Multiscale Design of an Axially Loaded Macroscopic Member

The chart presented in the previous section helps design the lattice material at the microscale. In this section, the design of a real macroscopic pin jointed strut manufactured of octet-truss lattice material is examined. The structure is subjected to a compressive force F with octet-truss lattice material properties ρ_L (density), E_L (Young's modulus) and σ_{yL} (yield strength). The lattice material is manufactured of a solid material that has density, ρ , Young's modulus, E , and yield strength, σ_{y0} . As mentioned in § 5.3, the macroscale parameters are specified by the subscript G .

§ 5.8.1 examines the design chart for a macro-scale strut; § 5.8.2 present the multiscale design of the strut, which involves the simultaneous use of both the micro and macroscale design charts.

5.8.1 Design Chart for Macroscopic Strut

Similar to the previous section, we pose the design problem of the strut under compressive force F as follows:

$$\begin{aligned}
&\text{Minimize} && m \\
&\text{With respect to} && s_G \text{ and } \psi_{GA} \\
&\text{Subject to} && s_f \sigma = \sigma_{yL} \leq \sigma_G^{cr} \\
&&& u_G \geq v_G
\end{aligned}$$

where m is the mass of the macroscopic structure, s_G is the strut length multiplier, σ_{yL} is the yield point of the strut, s_f is a design safety factor and σ is the axial stress generated by the external force F . To plot the macroscopic structure design chart, we rearranged the above expression in three steps.

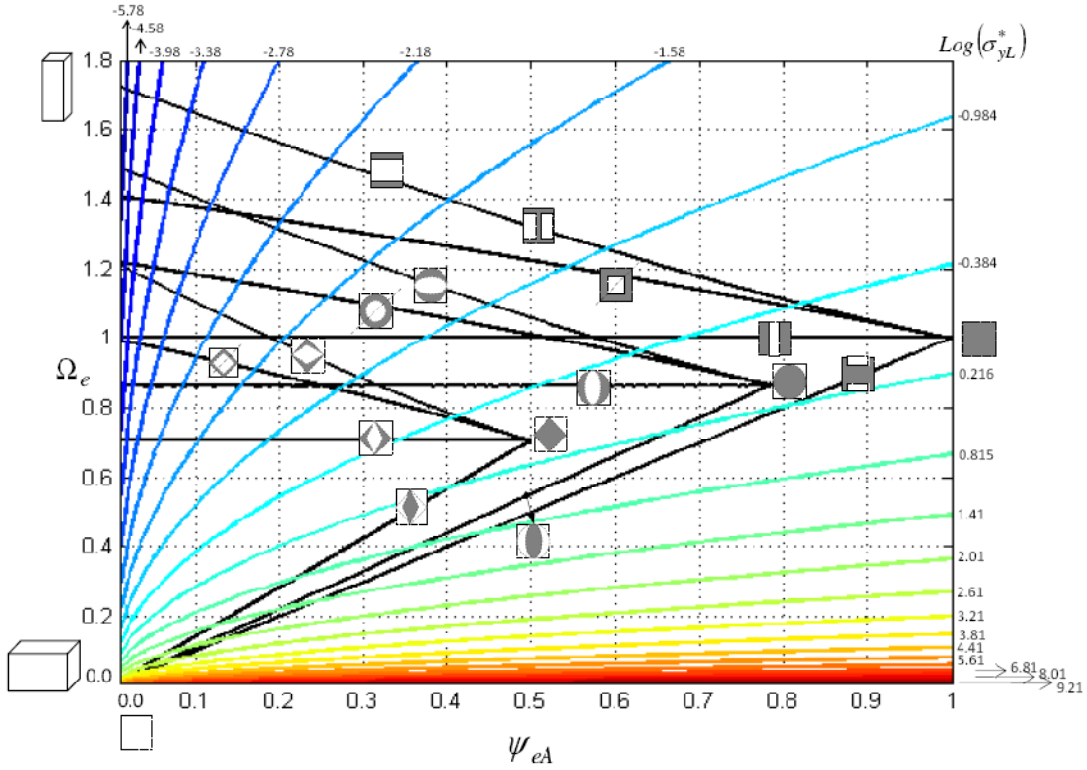


Fig (5.8) Design chart of the microscopic architecture of 2D lattice materials

Step 1) Similar to the microscopic cell element length multiplier, s_e , the macroscopic strut length multiplier, s_G , is formulated as:

$$s_G \leq (\pi) \left(\frac{r_{Gg0}}{L_{G0}} \right) (v_G) \sqrt{\left(\frac{2}{3} \right) \frac{E}{\sigma_{y0}}} \lambda_G \quad (5.39)$$

Now, eqn (5.39) is rearranged to isolate the macroscopic cross-section geometrical parameters where a new expression of s_G is redefined as:

$$\Omega_G := \frac{s_G}{\left(\pi \left(\frac{r_{Gg0}}{L_{G0}}\right) (v_G) \sqrt{\left(\frac{2}{3}\right) \left[\frac{E}{\sigma_{y0}}\right]}} \leq \sqrt{\lambda_G} \quad (5.40)$$

Step 2) To avoid the yielding of the macroscopic strut under the compressive loading, F , the yield constraint $s_f \sigma = \sigma_{yL}$, is written as a function of the external force, F , such that:

$$s_f \frac{F}{A_G} = \frac{s_f F}{A_{G0} \psi_G u_G v_G} = \sigma_{yL} \quad (5.41)$$

Isolating v_G in eqn (5.40), and substituting its expression into eqn (5.41) results in:

$$\sigma_{yL} := \frac{s_f F \pi \sqrt{\left(\frac{2}{3}\right) \frac{E}{\sigma_{y0}}} \Omega_G}{\left(\frac{L_{G0}}{r_{Gg0}}\right) A_{G0} s_G u_G \psi_{GA}} \quad (5.42)$$

In eqn (5.42), the cross-section shape contribution is isolated and the strut yielding point is redefined as:

$$\sigma_G^* = \frac{\left(\frac{L_{G0}}{r_{Gg0}}\right) A_{G0} s_G}{s_f F \pi \sqrt{\left(\frac{2}{3}\right) \frac{E}{\sigma_{y0}}}} (u_G) (\sigma_{yL}) = \frac{\Omega_G}{\psi_{GA}} \quad (5.43)$$

Step 3) The objective function, m , is expressed in terms of the design variables as:

$$m = C_G \bar{\rho}_L \Omega_G \psi_{GA} \quad (5.44)$$

where $C_G = \left(\pi \sqrt{\frac{2}{3}}\right) (A_{G0} r_{Gg0}) \left(\rho_0 \sqrt{\frac{E}{\sigma_{y0}}}\right) (u_G v_G^2)$.

Figure (5.9) visualizes the macroscopic design chart that can be used to select the best geometrical attributes of a strut in axial compression for a given macroscopic loading. In Fig (5.9), the black lines are the plots of eqn (5.40), obtained for different cross-section shapes. They represent the correspondent strut length multiplier, s_G , which is determined from Ω_G through eqn (5.40), after the cross-section height is scaled with the value of v_G that meets the load requirement. In

addition, eqn (5.43) is plotted in Fig (5.9) to represent iso-stress lines that intersect the curves Ω_G .

From this chart, the designer can select the best element length and cross-section shape of the macroscopic strut.

Next section shows how to combine Fig (5.8) and (5.9) for a multiscale design of a lattice structural member.

5.8.2 Multiscale Design Charts

We consider a multiscale design problem which involves the optimization of a column manufactured of octet-truss lattice material at both the micro and the macro scales. The design requirements are set at the structure as well material level. At the column level, the length, L_G , the external load, F , and the design safety factor, s_f , are prescribed; while at the material scale the requirements include the solid material properties of the yield strength, σ_{y0} , the Young's modulus, E , and the density, ρ . For the reference element, the baseline of the geometric parameters are r_{eg0} , A_{e0} and L_{e0} at the microscale and L_{G0} , r_{Gg0} and A_{G0} at the macroscale.

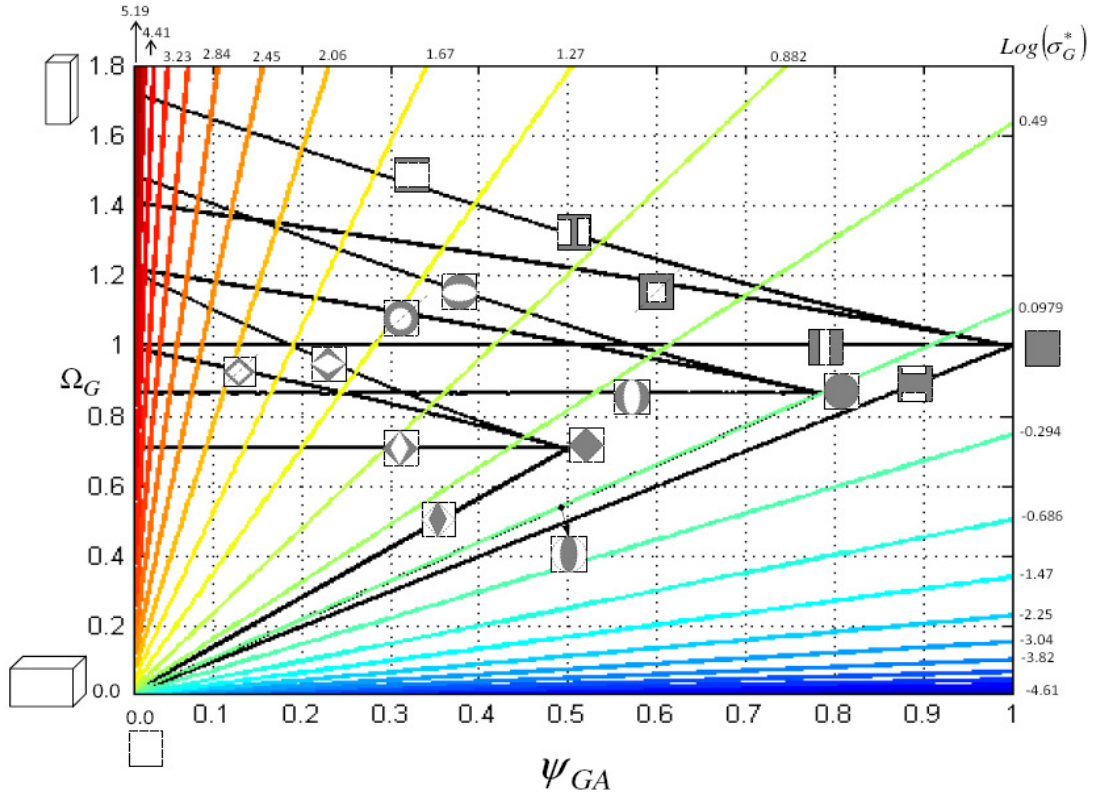


Fig (5.9) Design chart of mechanical members loaded in axial compression

In this problem, the objective of fully exploiting the material strength at each length scale requires the design of a column in which the three failure modes, namely, the local buckling σ_e^{cr} (buckling of the microscopic cell elements), global buckling σ_G^{cr} (buckling of the macroscopic structure) and the plastic yielding failure of the strut σ_{yL} , occur simultaneously, i.e. $\sigma_e^{cr} = \sigma_{yL} = \sigma_G^{cr}$. The rationale behind is the following: if any of the three failure modes dominates the structural failure, any performance enhancement that shifts the other two failure modes to higher limits will not contribute to the global structural performance (Weaver and Ashby, 1997). Based on this criterion, we now combine the charts shown in Fig (5.8) and Fig (5.9) to design a column made out of regular octet-truss lattice material.

At the macroscale, we first determine the column length multiplier, $s_G = L_G/L_{G0}$, from which we calculated Ω_G through eqn (5.40), after scaling the cross-section with v_G to meet the load requirement. When Ω_G is obtained, the cross-section shape of the strut can be selected in Fig (5.9) for different values of the constraint σ_{GyL}^* . Substituting the selected σ_{GyL}^* into eqn (5.43) allows obtain the plastic strength σ_{yL} that will be used as an input in Fig (5.8) for the design of the lattice material. σ_{yL} is then used in Fig (5.8) to determine σ_{eyL}^* through eqn (5.37), after scaling the cell-element cross-section with the appropriate u_e/v_e , as explained in § 5.7. The obtained value σ_{eyL}^* corresponds to an iso-stress line, whose intersections with Ω_e define the cell element multiplier of the lattice. The criterion to use when moving along such an iso-stress line is that of minimizing the mass of the structure, i.e. minimizing the density of the lattice material. As described in eqn (5.38), the lattice materials that best minimize $\frac{\psi_{eA}}{\Omega_e^2}$ are the solutions displayed at the left-top corner of Fig (5.8).

5.9 Conclusion

Under compression, a column manufactured of regular solid material experiences two types of failure modes, namely, the global buckling and the yield failure. A lattice material column, on the other hand, may also fail for either the local buckling or yielding of its microscopic cell element. To fully exploit the strength of a strut made of lattice material, the global buckling and the yielding failures must occur simultaneously with the microscopic failure modes. To achieve this,

this chapter presented multiscale design charts for the selection of the geometric properties for both the cell elements and the column cross-section. The charts help to gain insight into the impact that the structural geometry at both the micro and macroscale has on the overall resistance of the column.

CHAPTER 6

Experimental Characterization of the 3⁴.6 2D Lattice Material

6.1 Introduction

Lattice materials have been extensively studied over the last decade. Among these studies, experimental investigations of cellular solids provided a deep understanding of the material mechanical behavior (Xiaogang Chen¹, et.al., 2008a; 2008b; Queheillalt, D. T., Wadley, H. N.G., 2005; Maiti, S. K., et.al., 1984; Zhou¹, Q., Mayer, R.R., 2002; Gibson, L. J. , 1989; Parsons, R.T., 2009; Andrews, E.W., et.al., 1999; Hinnerichs, T.D., et.al., 2006). It is found that the material performance under dynamic loading dramatically changes compared to the one under static loading, as the effect of the strain rate on the material response is significant. Thus for static applications, quasi-static characterization, at which the material is loaded by a strain rate in the order of 10^{-3} , is always recommended (Lee, S., et.al., 2006).

In this chapter, the effective elastic properties of the 3⁴.6 lattice material are characterized experimentally. A detailed description of the design procedure of the test specimens is presented. Three quasi-static tests are performed, namely, uniaxial tension, uniaxial compression and pure shear. The comparison of the experimental data to the theoretical results, calculated following the procedure described in chapter four, shows that the former are in good agreement with the latter. The maximum error obtained of 15.2% is acceptable according to the literature on experimental studies of cellular solids (Ashby, M., et.al., 2000). This result verifies the fidelity of the characterization methodology presented in chapters three and four.

6.2 Design of Specimens

To determine the material fourth order stiffness constants in the x , y and xy directions, three types of tests are performed on the 3⁴.6 lattice material: uniaxial tension, uniaxial compression and pure shear. By inspecting the microstructure of the 3⁴.6 lattice material, shown in Fig (E.2h), one can realize that the lattice has different geometrical orientations in the x and y directions. Accordingly, two types of specimens are designed for the tension and the compression tests. The first type is x -oriented, with orientation similar to that shown in Fig (E.2h); the second type is y - oriented, which is a 90° rotation about the z - axis in Fig (E.2h).

The rapid manufacturing facility at the Hydro-Quebec Research Institute in Varennes, Canada (Hydro-Quebec Research Institute, 2009), was used to manufacture the test specimens. The

facility is powered by the A2 Arcam Electron Beam Melting (EBM) system (Arcam AB[®], 2010a), shown in Fig (6.1b). The A2 Arcam EBM system is provided by Arcam AB[®]. EBM is a type of additive manufacturing of metal parts where the parts are manufactured by melting metal powder layer-by-layer using a beam of electrons in a high vacuum chamber. EBM is one of the rapid manufacturing technologies. For details about the EBM technology and other rapid manufacturing technologies, the reader is referred to references (Kruth, J.P., et.al., 2005; Waterman, N. A., Dickens, P., 1994; Rochus, P., et.al., 2007).

To manufacture the specimens by the EBM system, a Stereolithography (STL) CAD file for the designed specimens was prepared using AutoCAD2010 and imported into the A2 EBM system interfacing software. A snapshot of the interfacing software screen showing the designed specimens in the manufacturing workspace is shown in Fig (6.1a).

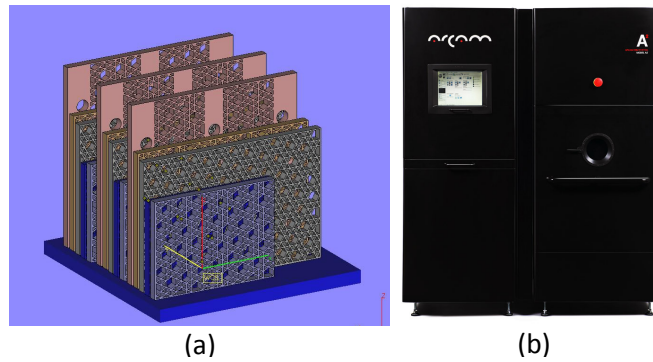


Fig (6.1) (a) Specimens in the manufacturing work space (b) The A2 EMB system provided by ARCAM AB[®]

The Ti6Al4V ELI Titanium Alloy is the solid material used for manufacturing the specimens. Based on tensile coupon test results provided by ARCAM AB[®] (Ti6Al4V ELI Titanium Alloy, 2010b), solid parts made of Ti6Al4V ELI Titanium Alloy and manufactured by EBM have a yield strength of $\sigma_{ys} = 940 \text{ MPa}$, ultimate strength of $\sigma_{us} = 990 \text{ MPa}$ and a modulus of elasticity of $E = 120 \text{ GPa}$.

Fig (6.2) shows the dimensions required to fully parameterize the lattice material specimens. Two envelopes are shown in Fig (6.2). The first is the cell envelope which is a feature of the periodic lattice structure. The cell envelope is defined to tessellate the unit cell to the infinite lattice (also shown in Fig (E.2h)). The second is the size envelope, which is defined here in order to compute the distance occupied by the unit cell in the x and the y directions. We annotate the dimensions of the size envelope as B_c and H_c in the x and the y directions, respectively.

On the other hand, L_e , H_e and B_e are, respectively, the cell element length, the cell element cross-section in-plane thickness and the cell element cross-section out of plane depth. Finally, H_s , B_s

and t_s are, respectively, the specimen height, the specimen width and the specimen thickness. It should be noted that the depth of the specimen, t_s , is equal to the microscopic cell element out of plane depth, B_e .

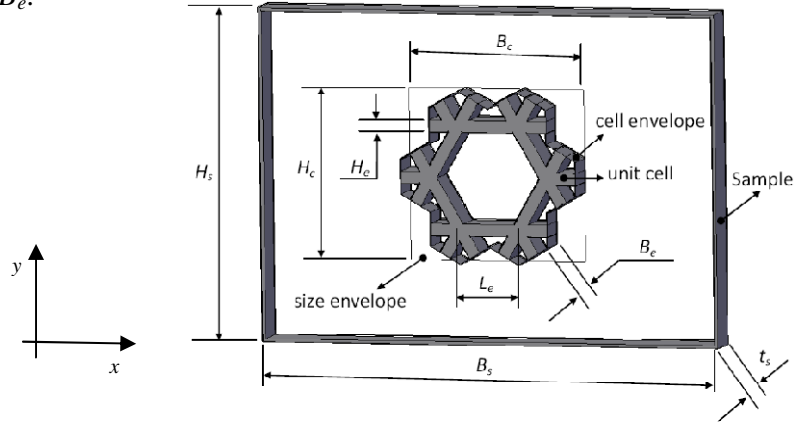


Fig (6.2) Parametric detailed dimensioning of the microscopic and the macroscopic constituents of a lattice material specimen

6.2.1 Design of the Microscopic Cell Element

For the design of the $3^4.6$ lattice material, the dimensions of the microscopic cell elements are computed by following the approach reported in chapter 5. This approach optimizes the lattice material by generating a coincidence between three failure modes, namely, microscopic elastic buckling failure of the cell elements, lattice material plastic yielding failure and the macroscopic elastic buckling failure of the specimen. The approach also goes further by considering sizing and shaping of the cell element cross-sections to minimize the weight of the lattice material. The design is based on elastic perfectly plastic solid material as post yielding failure is not considered in the current study. We start by assuming that the lattice material has microscopic cell elements with solid rectangular cross-sections. The in-plane thickness is assumed to be $H_e = 1 \text{ mm}$.

Although shaping the geometry of the cell element cross-sections enhances the lattice material performance in the form of higher strength to weight ratio, simple rectangular geometry of cell element cross-sections are used here as we are mainly interested in validating our theoretical analysis technique developed in chapters 3 and 4.

The length of the microscopic elements is computed to impose a coincidence between the two microscopic failure modes, namely, the plastic yielding of the solid material and the elastic local buckling of the microscopic elements. Following the approach developed in chapter 5, to avoid buckling of the microscopic cell elements, its length is obtained as:

$$L_e = \left(\frac{\pi}{2\sqrt{3}} \right) H_e \sqrt{\frac{E}{\sigma_{ys}}} \quad (6.1)$$

By substituting $H_e = 1 \text{ mm}$, $E = 120 \text{ GPa}$ and $\sigma_{ys} = 940 \text{ MPa}$ into eqn (6.1), the length of the microscopic cell element can be computed as $L_e = 10.24 \text{ mm}$. Using a dimensional safety factor of 2 and rounding the results to the nearest integer, the final length of the microscopic cell element is approximately $L_e = 5 \text{ mm}$. Using the length of the microscopic cell element, the dimensions of the size envelope can be computed as $B_c = 15.00 \text{ mm}$ and $H_c = 14.43 \text{ mm}$ for the x - oriented lattice. For the y - oriented lattice, the dimensions of the size envelope are $H_c = 15.00 \text{ mm}$ and $B_c = 14.43 \text{ mm}$.

6.2.2 Design of the Specimen Macroscopic Dimension

To compute the specimen height, H_s , we resort to the ASTM standards Designations C363- 00 and C364- 99, and estimate the height of the tension and the compression specimens as shown in table (6.1).

Table (6.1) Height of tension and compression specimens

	Specimen Height	
	x - Oriented	y - Oriented
Tension	144 mm	150 mm
Compression	73 mm	76 mm

The ratio of the specimen size to the cell size affects the measurement of the mechanical properties of the cellular materials (Ashby, M., et.al., 2000). In uniaxial tension or uniaxial compression tests, the upper and the lower ends of the specimen are in contact with the loading grips while the sides of the specimen are free. As a result, the cells, which are close to the sides of a specimen, contribute less to its load carrying capacity, which also results in less contribution to the overall stiffness and strength of the material. It is found that the measured values of the stiffness and the strength of the tested cellular materials increase with the ratio of the specimen size to the cell size. It is determined empirically (Ashby, M., et.al., 2000) that for uniaxial loading, in either tension or compression, the width of the specimens should be at least seven times the cells size ($B_s \geq 7B_c$). This enables the computation of the specimen widths as shown in the table (6.2).

Table (6.2) Width of the tension and compression specimens

	Specimen Width	
	x- Oriented	y- Oriented
Tension	105 mm	101 mm
Compression	105 mm	101 mm

For the shear test, we use the standard three-rail shear method (ASTM Standards, D 4255/D 4255M- 01), as shown in Fig (6.3). Since the sides of the shear specimen are all clamped into the stiff three-rail fixture, which produces a stiffening effect by contributing into the lattice material boundary stiffness, experiments have shown that the boundary stiffening effect becomes negligible when the ratio of the specimen size to the cell size is greater than 3 ($B_s \geq 3B_c$) (Ashby, M., et.al., 2000).



Fig (6.3) Shear specimen mounted into the three rail shear fixture and installed into the test machine

This enables the computation of the lattice material width on each side of the three-rail shear fixture to be 42 mm. The height of the shear specimen is constrained by the height of the three-rail fixture to 140 mm.

6.2.3 Design of the Specimen Thickness

The compression specimen has the critical thickness since it is subjected to an elastic, global, macroscopic buckling failure. The thickness of the compression specimen is obtained by imposing

a coincidence between the two macroscopic failure modes, namely, the plastic yielding of the lattice material and the elastic global buckling of the specimen.

Two simple cases are considered here: a column with a rectangular solid cross-section under compressive loading and a thin plate with rectangular cross-section under distributed compressive loading or pure shearing. The thickness of the compressive specimen is computed by considering it first as a column and then as a plate; the higher dimensions between the two is selected to avoid any geometric instability.

For a column, made of lattice material, with length, H_s , and a rectangular solid cross-section of width, B_s , and thickness, t_s , the Euler critical buckling stress is defined as (Megson, T.H.G., 2003):

$$\sigma_{cr} = c^2 \frac{\pi^2 E_L}{12} \left(\frac{t_s}{H_s} \right)^2 \quad (6.2)$$

where the constant c is dependent on the column end boundary conditions.

For thin plates with rectangular solid cross-section and subjected to a compressive distributed loading, the critical buckling stress of the plate is expressed as (Howard, D. Curtis, 1997):

$$\sigma_{cr} = C \frac{\pi^2 E_L}{12(1-\nu_L^2)} \left(\frac{t_s}{B_s} \right)^2 \quad (6.3)$$

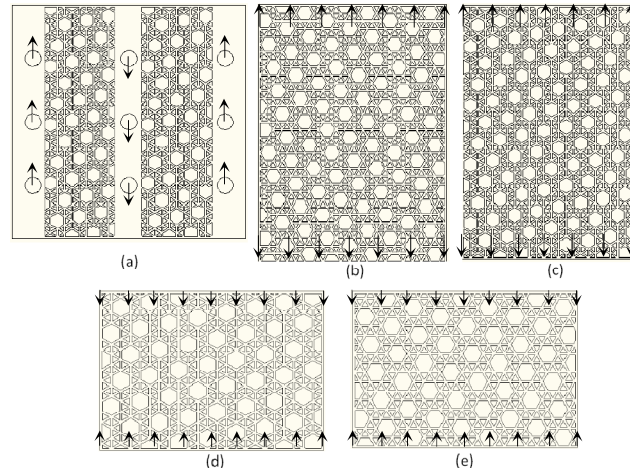
where ν_L and E_L are the macroscopic lattice material Poisson's ratio and Young's modulus, respectively. C is a constant that depends on the plate boundary conditions: the Poisson's ratio of the lattice material and the plate aspect ratio (plate length to width ratio). The Poisson's ratio for the 3⁴.6 lattice topology is computed in § 4.5.2 as $(\nu_L)_{xy} = (\nu_L)_{yx} = 0.5434$.

Imposing the coincidence between the macroscopic buckling stress, σ_{cr} , and the lattice material yield strength, σ_L^y , using the equality constraint ($\sigma_{cr} = \sigma_L^y$), results in the following expression of the thickness for the compression specimen:

$$t_s = \begin{cases} \left(\frac{2}{c\pi} \right) H_s \sqrt{3C^y(i)C_{xxxx} \left(\frac{\sigma_{ys}}{E} \right)} & \text{For Column} \\ \left(\frac{2}{\pi} \right) B_s \sqrt{\frac{3C^y(i)C_{xxxx}}{C} \left(1 - \left(\frac{C_{xyyy}}{C_{xxxx}} \right)^2 \right) \left(\frac{\sigma_{ys}}{E} \right)} & \text{For thin Plate} \end{cases} \quad (6.4)$$

where C_{xxxx} and C_{xyyy} are the fourth order compliance constants of the lattice material, as shown in eqn (4.22). $C^y(i)$ is the i lattice material strength constant computed in eqn (4.32). The boundary condition constants for pinned-pinned columns and pinned-free- pinned-free plates with aspect ratio of 0.695 are commonly found in literature (e.g. Howard, D. Curtis, (1997)) as $c=1$ and $C=4.9$.

Substituting the computed values into eqn (6.4), gives a thickness of the compression specimen of $t_s = 6.20mm$. This value is considered a nominal thickness for all specimens.



(a) Shear (b) Tension, x - oriented (c) Tension y - oriented (d) Compression y - oriented (e) Compression x - oriented

Fig (6.4) CAD drawing of the test specimens along with loading directions

Using the computed dimensions of the microscopic and the macroscopic constituent of the test specimens, an STL CAD file is generated for five models, namely, shear specimen, x - oriented and y - oriented compression specimens and the same for the tension specimens, as shown in Fig (6.4). The STL file was provided to the rapid manufacturing facility of the Hydro-Quebec Research Institute in Varennes, Canada, where fifteen specimens were manufactured, three for each specimen design.

6.3 Theoretical Mechanical Properties of the Designed Lattice Material

Using the theoretical geometric details of the designed lattice material, used in creating the STL CAD file, the relative density of the material is then computed as:

$$\bar{\rho} = \frac{\rho_L}{\rho} = 2.4744 \left(\frac{H_e}{L_e} \right) = 0.495 \quad (6.5)$$

Using the value of the relative density, the stiffness and strength properties of the designed lattice material can be computed as:

$$\mathbf{K}_L = E_s \bar{\rho} \begin{bmatrix} 0.44 & 0.24 & 0 \\ 0.24 & 0.44 & 0 \\ 0 & 0 & 0.10 \end{bmatrix} = \begin{bmatrix} 26.39 & 14.34 & 0 \\ 14.34 & 26.39 & 0 \\ 0 & 0 & 6.027 \end{bmatrix} GPa \quad (6.6)$$

$$\sigma_L^y = \begin{bmatrix} 0.20 \\ 0.25 \\ 0.13 \end{bmatrix} \sigma_{ys} \bar{\rho} = \begin{bmatrix} 96.71 \\ 114.80 \\ 59.03 \end{bmatrix} MPa \quad (6.7)$$

The compliance matrix is computed as:

$$\mathbf{C}_L = \frac{1}{E_s \bar{\rho}} \begin{bmatrix} 3.19 & -1.73 & 0 \\ -1.73 & 3.19 & 0 \\ 0 & 0 & 9.85 \end{bmatrix} = \begin{bmatrix} 0.05 & -0.03 & 0 \\ -0.03 & 0.05 & 0 \\ 0 & 0 & 0.17 \end{bmatrix} GPa^{-1} \quad (6.8)$$

From the compliance properties in eqn (6.8), the elastic moduli of the lattice material can be written as:

$$E_{xxxx} = \frac{1}{C_{xxxx}} = 18.60 GPa, E_{yyyy} = \frac{1}{C_{yyyy}} = 18.60 GPa, E_{xxyy} = G = \frac{1}{C_{xxyy}} = 6.00 GPa \quad (6.9)$$

These values of the stiffness and strength are compared with the results obtained from the experiments.

It should be noted that the A2 EBM system, provided by ARCAM AB[®], has a model-to-part accuracy of ± 0.20 mm per 100 mm range models (Arcam AB[®] Setting the standard for Additive Manufacturing, 2010c). This tolerance is verified experimentally where the in-plane thickness of the microscopic cell elements of the manufactured specimens are found as: $H_e = 1 \pm 0.01$ mm.

6.4 Experimental Set-up and Instrumentation

A schematic drawing of the full experimental set-up is shown in Fig (6.5); while Fig (6.6) shows the instrumentation used for the testing at McGill University.

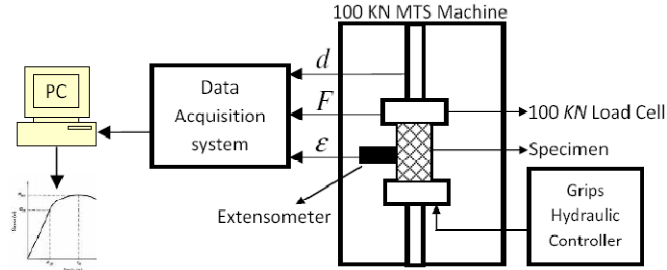
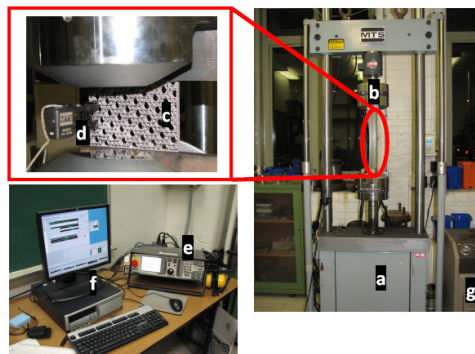


Fig (6.5) Schematic drawing of the test set-up

The experimental set-up is composed of the MTS[®] hydraulic tensile test machine; a load cell, model MTS 647 Hydraulic Wedge Grip, with maximum capacity of 100 kN that is attached to the upper axis of the MTS machine; a hydraulic controller, model MTS 685 hydraulic grip supply controller, that governed the operation of the grips of the load cell as well as the lower grips installed on the lower axis of the MTS machine to hold or release specimens or fixtures; an extensometer, model 632-31E-24, attached to the specimens to measure the axial strain; a data acquisition system, model MTS FLEX Test SE, that receives the inputs of three channels transferring the measurements of the load cell forces, the extensometer strain and the crosshead displacement; and a computer connected to the data acquisition system through the FLEX Test SE Station Manager interface software (version 3.5C 1815).



(a) 100 kN MTS machine (b) load cell (c) specimen (d) extensometer (e) data acquisition system (f) computer (g) grips hydraulic controller

Fig (6.6) Experimental set-up and instrumentation

To avoid the inertia effect (Song, B., 2007) and the strain rate dependency of the results (Krempel, E., Khan, F, 2003; Sarsfield, H., et.al., 2007; El-Magd, E., et.al., 2003), quasi-static tests are considered for the current study where a strain rate of the order of $10^{-3} s^{-1}$ is adopted (Lee, S., et. Al., 2006).

6.5 Tests and Test Results

6.5.1 Compression Test

Fig (6.7) shows a compression specimen during the test. Rather than holding the specimen by the upper and the lower grips of the MTS machine, which resembles fixed boundary conditions, we insert the upper and the lower flat faces of the specimen between the flat faces of hard steel, thick plates that are held horizontally by the grips of the MTS machine at 2000 psi. The compression specimen is then compressed between the two plates.

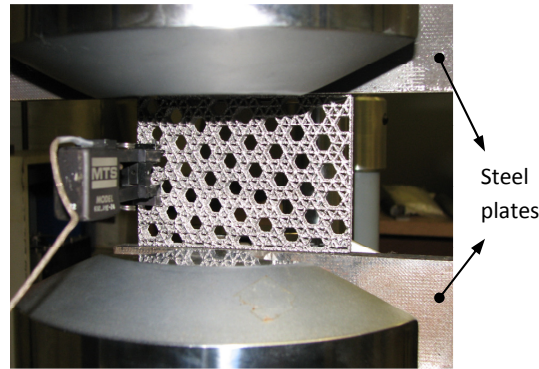


Fig (6.7) Compression test

This assembly resembles pin jointed boundary conditions, since the ends of the specimen are free to rotate while its vertical movement is controlled by the grips motion and its horizontal movement is constrained by the friction force between the specimen and the steel plate surfaces. This is similar to the boundary conditions used in the theoretical analysis to compute the critical thickness of the specimen that prevents buckling.

To measure the axial strain, the extensometer is connected to the specimen as shown in Fig (6.7). The test is performed at crosshead speed of 0.5 mm/min. This speed applies a strain rate of $1.14 \times 10^{-4} \text{ s}^{-1}$ for the x - oriented specimens and $1.11 \times 10^{-4} \text{ s}^{-1}$ for the y - oriented specimens. Three measurements, namely, the axial strain, the load cell force and the crosshead displacement, are transferred via three analog channels into the data acquisition system which digitizes the data and transfers it into a computer through the FLEX Test SE Station Manager interface software where the data is saved into a file of DAT format. The test runs until the rupture of the specimens, as shown in Fig (6.8).

The DAT file is then post processed in MATLAB (The MathworksTM) where a simple code is developed to compute the nominal stress, σ_N , and to plot the stress strain diagram.

The nominal stress is computed as:

$$\sigma_N(t) = \frac{F(t)}{A_0} \quad (6.10)$$

where t is the time, $F(t)$ is the load cell force, and A_0 is the initial cross-section area of the specimen which is expressed as:

$$A_0 = B_s t_s \quad (6.11)$$

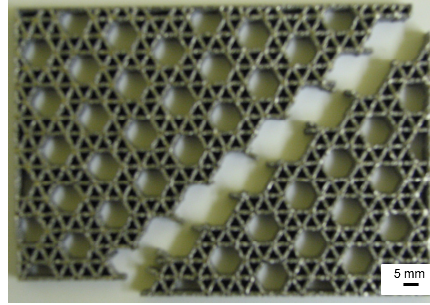


Fig (6.8) A ruptured x -oriented compression specimen

The test is performed for six specimens, three of which are x - oriented, whereas the others are y - oriented. Figs (6.9a) and (6.9b) show the test results. Since the plots do not clearly show the yield point of the lattice material, the yield strength is determined by the offset method (Beer, F.P., Johnston, E.R., 1981). In this method, the yield strength at 0.2% offset is obtained by drawing a line parallel to the straight part of the stress-strain curve, through the point of strain that is equal to $\varepsilon = 0.002$. The parallel line intersects the stress-strain curve at the point of 0.2% offset yield strength. The strength and the stiffness results are summarized in table (6.3). For each experiment set, the mean, \bar{x} and the standard deviation, std , are calculated.

Table (6.3) Summary of the compression test results

	x- oriented		y- oriented	
Specimen	$(\sigma_L^y)_{xx}$ (MPa)	E_{xxxx} (GPa)	$(\sigma_L^y)_{yy}$ (MPa)	E_{yyyy} (GPa)
1	108.4	20.3	129.7	21.5
2	111.8	22.7	129.7	21.9
3	105.3	20.8	114.4	20.9
\bar{x}	108.5	21.3	126.6	21.4
std	2.7	1.1	7.2	0.4

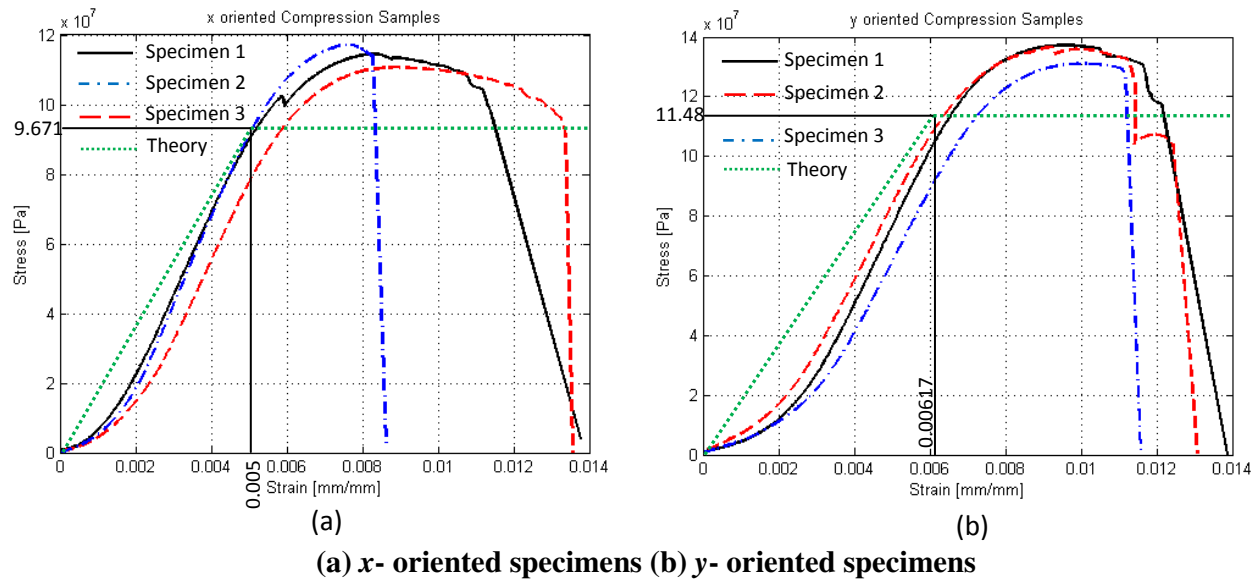


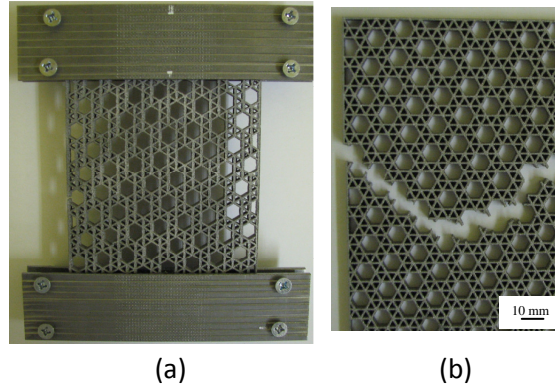
Fig (6.9) Compression test results

6.5.2 Tension Test

Since the width of the grip wedges of the MTS machine is small compared to the width of the tension specimens, four plates, with rough surfaces and with width larger than that of the tension specimens, are manufactured of hard steel and are used to hold the tension specimens, as shown in Fig (6.10a). The grips then hold the specimens by applying the pressure force over the plates to distribute the load uniformly along the width of the specimens. The steel plates at each end of the tension specimens hold a depth of 20 mm; accordingly, the gauge lengths of the tension specimens become 104 mm for the x - oriented specimens and 110 mm for the y - oriented ones. The same procedure described for the compression test is followed here. The test is performed at a crosshead speed of 0.5 mm/min. This speed applies a strain rate of $8.01 \times 10^{-5} \text{ s}^{-1}$ for the x - oriented specimens and $7.58 \times 10^{-5} \text{ s}^{-1}$ for the y - oriented specimens. The tension test is performed until rupture of the specimens, as shown in Fig (6.10b). The nominal stress, σ_N , is computed from the generated data using eqn (6.10) and the stress strain diagrams are generated for 3 sets of data of the x - oriented specimens, Fig (6.11a), and other three sets of data of the y - oriented specimens, Fig (6.11b).

Tensile yield strengths are considered as the maximum stresses achieved in the stress-strain diagrams of Fig (6.11). The stiffness of the specimens in tension is computed as the average slope

of each curve in Fig (6.11). The strength and the stiffness results are summarized in table (6.4), where the mean and the standard deviations of the data are also given.



(a) Tension specimen, y-oriented, with the holding plates (b) Ruptured, x- oriented, tension specimen

Fig (6.10) Tension specimens

Table (6.4) Summary of the tension test results

	<i>x</i> - oriented		<i>y</i> - oriented	
Specimen	$(\sigma_L^y)_{xx}$ (MPa)	E_{xxxx} (GPa)	$(\sigma_L^y)_{yy}$ (MPa)	E_{yyyy} (GPa)
1	111.0	19.9	123.5	19.7
2	107.2	18.4	126.2	19.7
3	106.2	18.4	124.4	19.7
\bar{x}	108.1	18.9	124.7	19.7
<i>std</i>	2.1	0.7	1.1	0

6.5.3 Shear Test

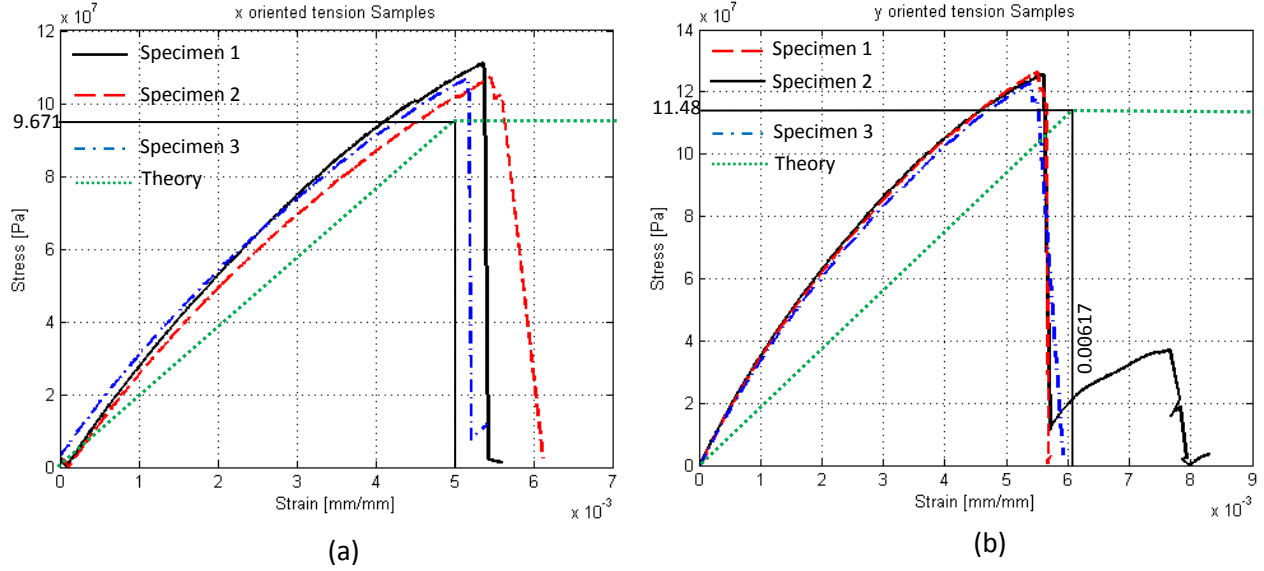
The standard three-rail shear method (ASTM Standards, D 4255/D 4255M- 01) is used to perform the shear test, as shown in Fig (6.3). The shear specimen is mounted into the three-rail shear fixture and sand paper is placed between the specimens and the fixture surfaces to increase the friction and prevent slipping. The fixture is then mounted into the grips of the MTS machine where the specimen is loaded at a crosshead speed of 0.5 mm/min. An average shear strain rate is considered which is computed as the crosshead speed divided by the width of the lattice material.

This generates an average shear strain rate of 1.98×10^{-4} rad/s . The test is continued until the rupture of the specimen. The generated data is post processed to generate the stress- strain diagram as shown in Fig (6.12) where the nominal stress is calculated as:

$$\sigma_N(t) = \frac{F(t)}{A_{0s}} \quad (6.12)$$

where A_{0s} is the initial shear area of the specimen which is computed as:

$$A_{0s} = 2H_s t_s \quad (6.13)$$



(a) x- oriented specimens (b) y- oriented specimens

Fig (6.11) Tension test results

The yield strength is considered as the maximum stress reached in the three tests of Fig (6.12) and the stiffness of the specimens is considered as the average slope of the curves of Fig (6.12).

Finally, the data are summarized in table (6.5) along with their respective statistical information.

Table (6.5) Summary of the shear test results

Specimen	τ_L^y (MPa)	G (GPa)
1	68.4	6.3
2	66.4	6.3
3	65.5	7.7
\bar{x}	66.7	6.8
std	1.2	0.7

6.6 Discussion

A comparison between the theoretical results and the mean values of the experimental results is presented in table (6.6). The percentage error is computed as the difference between the experimental and the theoretical results divided by the value of the theoretical result.

Table (6.6) shows that the theoretical analysis predicts lower values for the stiffness and the strength when compared to the experimental results. It is shown that the maximum percentage error obtained is 15.2%, which is an acceptable error in the experimental studies on cellular solids (Ashby, M., et.al. 2000).

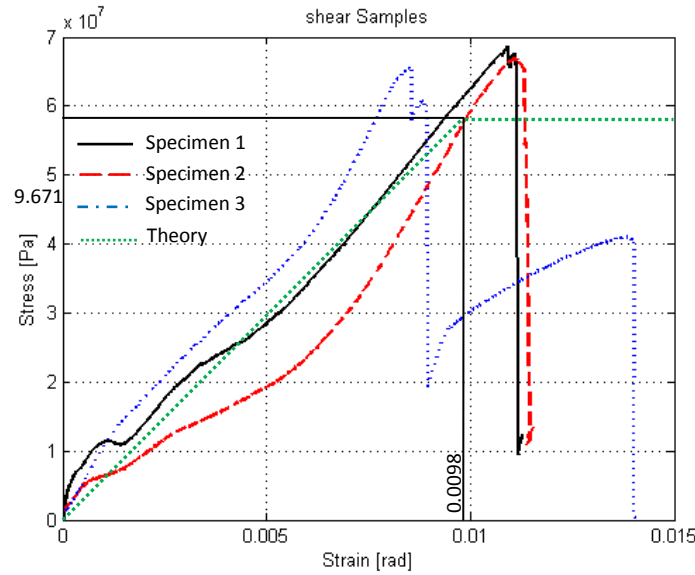


Fig (6.12) Shear test results

Error propagation in experimental studies has different sources (Dieck, R.H., 1997). For instance, in the experimental characterization of foams, error propagation is largely affected by the uncertainty in defining the material microscopic attributes due to the foam stochastic microstructure (Ramamurty, U., Paul, A., 2003). On the other hand, lattice materials are produced with an exact periodic microstructure; therefore, it is expected that other reasons have contributed to the propagation of the reported errors in the current study. For instance, the theoretical results are obtained by considering the lattice material as a microscopic pin-jointed truss structure. This assumption implies that the axial stiffness of the microscopic cell elements is the only stiffness considered in the model. However, in practice, a lattice material component is manufactured as a rigid-jointed reticulated structure, which implies that the bending stiffness of the microscopic elements contributes to the overall material stiffness and strength, even if the material microstructure is kinematically determinate. Moreover, the mechanical properties of the Ti6Al4V ELI Titanium Alloy are expected to be a function of the manufacturing parameters of the rapid manufacturing technique used to build the specimens. These manufacturing parameters in turn have their effect on the phase content and grain size of the solid material microstructure. For

instance, Engel and Bourell (Engel, B. and Bourell, D.L., 2000) investigated the effect of the processing parameters used in the preparation of the Titanium alloy powder that is used in the selective laser sintering (SLS), a technique of additive manufacturing. They found that pre-treatment of titanium powder alloy has a significant effect on the SLS results. Without pre-treatment, titanium alloy powder flows poorly and creates a balling effect that includes the formation of molten cluster masses developed from the laser exposure during the SLS process, rather than wetting and joining together the molten powder between the current and the previous layers. Mechanical parts produced using such powder are expected to have poor surface finish, poor mechanical properties, and low density due to the large porosity. The theoretical models developed in chapter 4 of this thesis did not consider the effect of the EBM manufacturing parameters. This idealization is expected to contribute to the propagation of the reported errors in table (6.6). Lastly, the current study considered only three specimens per each test; by increasing the number of specimens, it is expected that the computed error percentage would be reduced. Further investigations are recommended to determine the impact of the selected manufacturing technique on the solid material properties and predict the expected errors due to the assumptions made in the theoretical models.

6.7 Conclusion

The effective mechanical properties of a novel 2D lattice topology, with the Schläfli symbol $3^4.6$, have been characterized experimentally. The effective mechanical properties include the effective stiffness and the effective uniaxial and pure shear strength properties. The theoretical and the experimental results are compared and showed good agreement. This result verifies the theoretical model developed in chapter 4.

Further theoretical and experimental investigations are required to interpret the unclear post yielding behavior of the material. The $3^4.6$ lattice material has shown some ductility during the compression test, as illustrated by the plateau part of the curve in Fig (6.9), whereas the tensile test shows a clear brittle behaviour, as illustrated in Fig (6.11) by the sudden rupture of the specimens. Additional analysis is also required to characterize both theoretically and experimentally the material collapse surfaces. To experimentally characterize the collapse surfaces of the lattice material, it is recommended to manufacture and test three sets of lattice material specimens. The first set should be designed to fail in the elastic-buckling-dominated regime, the second set should be designed to fail in the buckling-yielding boundary regime and the third set in the plastic-dominated regime. The theoretical models should be validated for each

one of these failure modes; the microscopic failure mechanisms should also be investigated and interpreted with respect to the material macroscopic collapse regimes.

Table (6.6) Comparison between the theoretical and the experimental characterization results

		Theoretical	Experimental	Error (%)
Compression	$(\sigma_L^y)_{xx} \text{ (MPa)}$	96.7	108.5	12.2
	$(\sigma_L^y)_{yy} \text{ (MPa)}$	114.8	126.6	10.3
	$E_{xxxx} \text{ (GPa)}$	18.6	21.3	14.3
	$E_{yyyy} \text{ (GPa)}$	18.6	21.4	15.2
Tension	$(\sigma_L^y)_{xx} \text{ (MPa)}$	96.7	108.1	11.8
	$(\sigma_L^y)_{yy} \text{ (MPa)}$	114.8	124.7	8.6
	$E_{xxxx} \text{ (GPa)}$	18.6	18.9	1.5
	$E_{yyyy} \text{ (GPa)}$	18.6	19.7	5.9
	$\tau_L^y \text{ (MPa)}$	59.0	66.7	13.0
	$G \text{ (GPa)}$	6.0	6.8	12.2

Furthermore, it is necessary to determine the material principal stresses and their relation to the lines of ruptures depicted in Figs (6.8) and (6.10b) for the compression and the tension tests, respectively. The compression test specimen, shown in Fig (6.8), had a rupture line inclined 45° with respect to the direction of loading; on the other hand, the tensile test specimen, shown in Fig (6.10b), had a V-shaped rupture line. Preliminary analysis for such behaviors in hexagonal honeycombs was investigated recently by Joshi, et.al. (Shraddha Joshi, et.al., 2010). They experimentally studied the damage of hexagonal honeycombs under in-plane shear loading. Five different hexagonal meso-structures were experimentally investigated using polycarbonate (PC) coupon samples. The samples were manufactured using 3D printing, a technique of rapid prototyping. Effective shear stress-strain curves of the PC honeycomb coupons were generated for each shear test. They showed that the failure modes of the PC honeycombs changed primarily with both the cell wall thickness and the principal load directionality within the lattice material.

CHAPTER 7

Stiffness Properties of Rigid-Jointed Micro-Structured Lattice Materials

7.1 Introduction

Microscopically architected lattice materials are mainly manufactured as rigid-jointed frameworks with elements loaded in both axial and bending modes. Although a stretching dominated lattice mainly fails by axial stresses, its microscopic constituents still experience secondary bending stresses developed during the material deformation. Thus, an accurate prediction of the lattice material stiffness properties is obtained by modelling the material as a rigid-jointed, periodic, framework.

Several numerical and analytical approaches were developed to model the effective properties of rigid-jointed lattice materials (Timoshenko, S.P., Gere, J.M., 1961). Most numerical approaches approximated the performance of lattice materials by studying the response of a finite structure in the form of a unit cell or a finite cluster of cells. Modelling the characteristics of lattice materials using analytical continuum models are also presented; these approaches, however, yield to unacceptable results once the in-plane bending of the lattice microscopic element, associated with its rigid-jointed architecture, are considered in the analysis (Noor, A.K. and Nemeth, M.P., 1980). To overcome this difficulty, a micro-polar continuum model is used to characterize lattice materials (Bazant, Z.P., Christensen, M., 1972; Noor, A.K. and Nemeth, M.P., 1980; Eringen, A.C., 1968; Eringen, A.C., 1966). Recently, the *Bloch's* theorem is used to model the propagation of equilibrium and kinematic wave-functions through infinite periodic structures which are employed to predict the homogenized stiffness and strength properties of rigid-jointed lattice materials (Hutchinson R.G., 2004).

In this chapter, we present a matrix-based methodology to model and characterize the stiffness properties of lattice materials with rigid-jointed microstructure. The microscopic members of the unit cell are modelled as frame elements which are used to derive the stiffness system of the unit cell microstructure. This stiffness system is employed to predict the stiffness behavior of the periodic lattice structure where the Kinematic and the equilibrium wave-functions, propagating through the infinite lattice, are modelled using the *Bloch's* theorem. A modified *Cauchy-Born* kinematic boundary condition is used to express the microscopic nodal deformations in terms of a

homogeneous macroscopic strain field applied to the lattice material. After calculating the nodal forces and deformations, the principle of virtual work and the Hill-Mandel principle of macro-homogeneity are used to derive the homogenized stiffness of the material. The Bond-stress and strain orthogonal transformations are applied to a homogenized infinitesimal stress field within the lattice to evaluate the stiffness anisotropy emerging in the lattice material. In the second part of this chapter, the proposed procedure is applied to 13 planar lattice topologies to obtain closed-form expressions of their material stiffness and elastic properties which are reported in Appendix G. Charts representing the relative elastic moduli of the lattice material versus its relative density are developed which can be used as design charts that assist in the selection of the best lattice topology for a given stiffness requirement. Furthermore, polar coordinate maps are generated to capture the anisotropic behavior of the selected lattice topologies. The effectiveness of the bending stiffness of the microscopic members of the lattice on the homogenized elastic properties of the stretching dominated lattice topologies is also examined.

7.2 Equilibrium and Kinematic Systems of Unit Cell Rigid-Jointed Finite Structure

To derive the equilibrium system of a finite rigid-jointed truss like structure, we first consider a linearly elastic, straight frame element, k , connected between nodes i and q (Fig (7.1)). To demonstrate the internal forces and deformations fields, the element is sectioned at A-A into two segments, I and II. Two Cartesian coordinate systems are defined in Fig (7.1). The first coordinate system, $x_1 - y_1$, is local to element k with the " x_1 -axis" in the same direction of the neutral axis of the element and " y_1 -axis" is perpendicular to the " x_1 -axis". The other coordinate system is the global coordinate system x - y with the x - and the y -axes in the horizontal and the vertical directions, respectively. The x_1 -axis is oriented by an angle α in the counter clock wise direction from the x -axis.

The static equilibrium of segment I of element k can be written as:

$$\begin{bmatrix} -1 & 0 & 0 \\ 0 & -1 & 0 \\ 0 & -l_k/2 & -1 \end{bmatrix} \begin{bmatrix} P_k \\ V_k \\ M_k \end{bmatrix} = \begin{bmatrix} f_{ix_1} \\ f_{iy_1} \\ m_i \end{bmatrix} \quad (7.1)$$

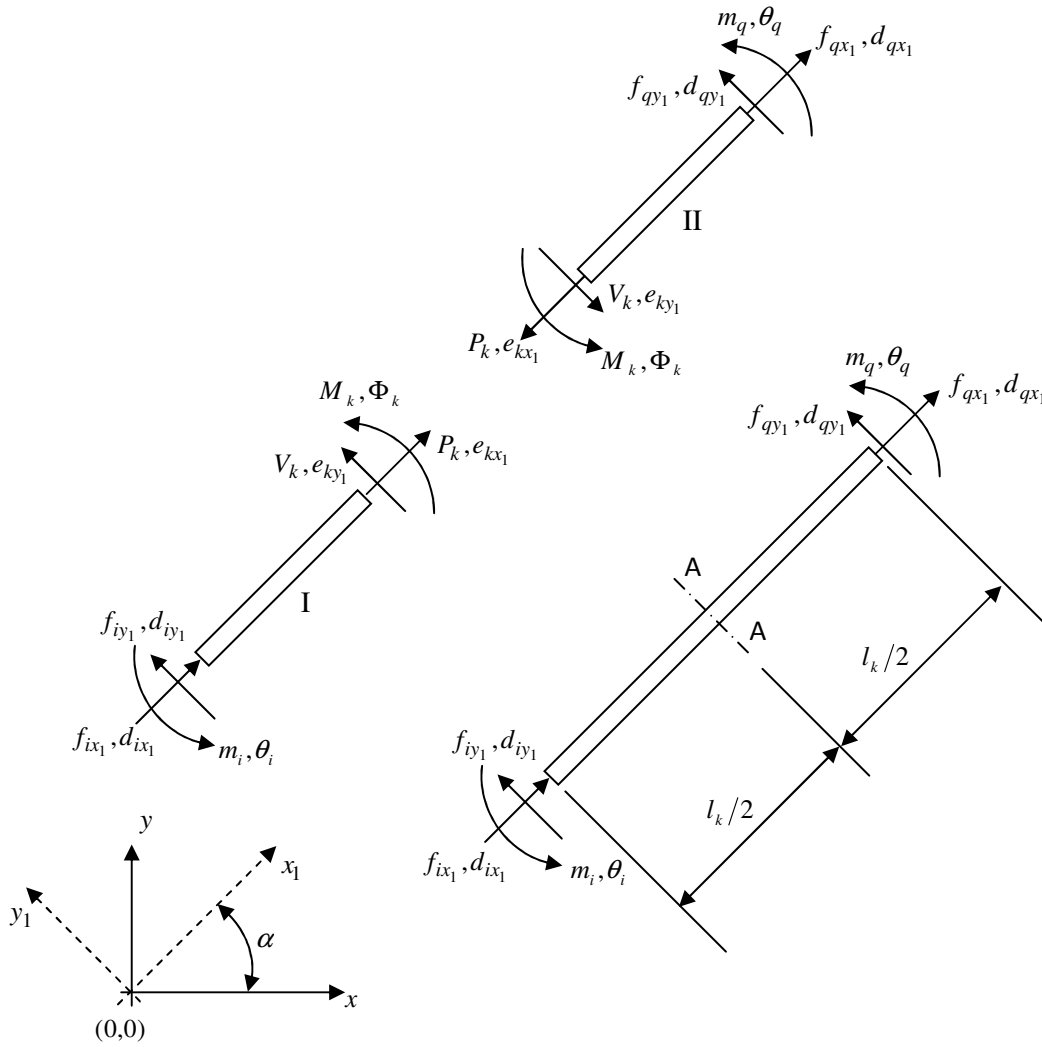


Fig (7.1) A frame element along with all internal and external forces and deformations fields

where P_k , V_k , M_k and l_k are respectively, the internal axial and shear forces, the internal bending moment and the length of element k , where $k \in \{1, \dots, b\}$. On the other hand, f_{ix_1} and f_{iy_1} are the forces acting on node i in the x_1 and y_1 directions respectively; m_i is the bending moment acting on node i where $i \in \{1, \dots, j\}$.

Similarly, the static equilibrium of segment II in element k is given by:

$$\begin{bmatrix} 1 & 0 & 0 \\ 0 & 1 & 0 \\ 0 & -l_k/2 & 1 \end{bmatrix} \begin{bmatrix} P_k \\ V_k \\ M_k \end{bmatrix} = \begin{bmatrix} f_{qx_1} \\ f_{qy_1} \\ m_q \end{bmatrix} \quad (7.2)$$

where f_{qx_1} and f_{qy_1} are the forces acting on node q in the x_1 and y_1 directions respectively. m_q is the bending moment acting on node q .

The assembly of eqn (7.1) and eqn (7.2) into one matrix system results in:

$$\begin{bmatrix} -1 & 0 & 0 \\ 0 & -1 & 0 \\ 0 & -l_k/2 & -1 \\ 1 & 0 & 0 \\ 0 & 1 & 0 \\ 0 & -l_k/2 & 1 \end{bmatrix} \begin{bmatrix} P_k \\ V_k \\ M_k \end{bmatrix} = \begin{bmatrix} f_{ix_1} \\ f_{iy_1} \\ m_i \\ f_{qx_1} \\ f_{qy_1} \\ m_q \end{bmatrix} \quad \text{or} \quad \mathbf{A}_k^l t_k = f_k^l \quad (7.3)$$

Equation (7.3) is the equilibrium system of element k derived in its local coordinate system ($x_1 - y_1$). \mathbf{A}_k^l and f_k^l are, respectively, the equilibrium matrix and the nodal force vectors of element k in the local coordinate system ($x_1 - y_1$). t_k is element k internal forces vector.

Recalling eqn (3.9), representing the duality relation between the equilibrium and the kinematic matrices of frameworks, and considering eqn (7.3), the kinematic system of the frame element shown in Fig (7.1) can be expressed in the local coordinate system ($x_1 - y_1$) as:

$$\begin{bmatrix} -1 & 0 & 0 & 1 & 0 & 0 \\ 0 & -1 & -l_k/2 & 0 & 1 & -l_k/2 \\ 0 & 0 & -1 & 0 & 0 & 1 \end{bmatrix} \begin{bmatrix} d_{ix_1} \\ d_{iy_1} \\ \theta_i \\ d_{qx_1} \\ d_{qy_1} \\ \theta_q \end{bmatrix} = \begin{bmatrix} e_{k1} \\ e_{k2} \\ \Phi_k \end{bmatrix} \quad \text{or} \quad \mathbf{B}_k^l d_k^l = e_k \quad (7.4)$$

where \mathbf{B}_k^l and d_k^l are, respectively, the kinematic matrix and the nodal deformation vector of element k in the local coordinate system ($x_1 - y_1$), and e_k is element k internal deformation vector. e_{k1} , e_{k2} and Φ_k are element k axial, lateral and bending deformations, respectively.

7.3 Stiffness System of Unit Cell Rigid-Jointed Finite Structure

The stiffness system of a structure that has b elements connected between j nodes is expressed as:

$$\mathbf{K}d = f \quad (7.5)$$

where $\mathbf{K} \in R^{nj \times nj}$ is the stiffness matrix of the structure that relates its nodal deformation vector, $d \in R^{nj}$, to the applied force vector, $f \in R^{nj}$ (McCormac, J.C., 2006).

The internal forces of a framework, composed of b elements, can be related to its internal deformations through the relation:

$$t = Ce \quad (7.6)$$

where $\mathbf{C} \in R^{b \times b}$ is the constitutive diagonal matrix that relates the vector of element forces, $t \in R^b$, to the vector of element deformations, $e \in R^b$.

Recalling eqns (3.1) and (3.5), representing, respectively, the equilibrium and the kinematic systems of a framework, and considering eqns (7.5) and (7.6), the following relation can be established between the stiffness, the equilibrium, the kinematic and the constitutive matrices as:

$$\mathbf{K} = \mathbf{ACB} \quad (7.7)$$

On the other hand, the constitutive law that relates the internal forces and the internal deformations of a linear frame element, k , can be expressed as:

$$\begin{bmatrix} P_k \\ V_k \\ M_k \end{bmatrix} = \begin{bmatrix} EA/l_k & 0 & 0 \\ 0 & 12EI/l_k^3 & 0 \\ 0 & 0 & EI/l_k \end{bmatrix} \begin{bmatrix} e_{kx_1} \\ e_{ky_1} \\ \Phi_k \end{bmatrix} \quad (7.8)$$

where E is the Young's modulus of the solid material, A is the cross-sectional area of the frame element.

Substituting eqns (7.3), (7.4) and (7.8) into eqn (7.7), the stiffness system of a linearly elastic frame element k can be expressed as:

$$\begin{bmatrix} \frac{EA}{l_k} & 0 & 0 & -\frac{EA}{l_k} & 0 & 0 \\ 0 & \frac{12EI}{l_k^3} & \frac{6EI}{l_k^2} & 0 & -\frac{12EI}{l_k^3} & \frac{6EI}{l_k^2} \\ 0 & \frac{6EI}{l_k^2} & \frac{4EI}{l_k} & 0 & -\frac{6EI}{l_k^2} & \frac{2EI}{l_k} \\ -\frac{EA}{l_k} & 0 & 0 & \frac{EA}{l_k} & 0 & 0 \\ 0 & -\frac{12EI}{l_k^3} & -\frac{6EI}{l_k^2} & 0 & \frac{12EI}{l_k^3} & -\frac{6EI}{l_k^2} \\ 0 & \frac{6EI}{l_k^2} & \frac{2EI}{l_k} & 0 & -\frac{6EI}{l_k^2} & \frac{4EI}{l_k} \end{bmatrix} \begin{bmatrix} d_{ix_1} \\ d_{iy_1} \\ \theta_i \\ d_{qx_1} \\ d_{qy_1} \\ \theta_q \end{bmatrix} = \begin{bmatrix} f_{ix_1} \\ f_{iy_1} \\ m_i \\ f_{qx_1} \\ f_{qy_1} \\ m_q \end{bmatrix} \quad \text{or } \mathbf{K}_k^l d_k^l = f_k^l \quad (7.9)$$

where \mathbf{K}_k^l is the linearly elastic stiffness matrix of element k . The stiffness matrix system of eqn (7.9) can be reformulated as:

$$\begin{aligned}
& \left\{ \frac{EA}{l_k} \begin{bmatrix} 1 & 0 & 0 & -1 & 0 & 0 \\ 0 & 0 & 0 & 0 & 0 & 0 \\ 0 & 0 & 0 & 0 & 0 & 0 \\ -1 & 0 & 0 & 1 & 0 & 0 \\ 0 & 0 & 0 & 0 & 0 & 0 \\ 0 & 0 & 0 & 0 & 0 & 0 \end{bmatrix} + \frac{EI}{l_k^3} \begin{bmatrix} 0 & 0 & 0 & 0 & 0 & 0 \\ 0 & 12 & 6l_k & 0 & -12 & 6l_k \\ 0 & 6l_k & 4l_k^2 & 0 & -6l_k & 2l_k^2 \\ 0 & 0 & 0 & 0 & 0 & 0 \\ 0 & -12 & -6l_k & 0 & 12 & -6l_k \\ 0 & 6l_k & 2l_k^2 & 0 & -6l_k & 4l_k^2 \end{bmatrix} \right\} \begin{bmatrix} d_{ix_1} \\ d_{iy_1} \\ \theta_i \\ d_{qx_1} \\ d_{qy_1} \\ \theta_q \end{bmatrix} = \begin{bmatrix} f_{ix_1} \\ f_{iy_1} \\ m_i \\ f_{qx_1} \\ f_{qy_1} \\ m_q \end{bmatrix} \\
& \text{or } \{ \mathbf{K}_{k_l}^{bar} + \mathbf{K}_{k_l}^{beam} \} d_k^l = f_k^l
\end{aligned} \tag{7.10}$$

where $\mathbf{K}_{k_l}^{bar}$ and $\mathbf{K}_{k_l}^{beam}$ are the element axial and bending stiffness matrices, respectively, as

$$\mathbf{K}_k^l = \mathbf{K}_{k_l}^{bar} + \mathbf{K}_{k_l}^{beam}.$$

The length of the microscopic cell elements can be expressed in terms of a reference length, L , as:

$$l_k = s_k L \tag{7.11}$$

where s_k is a constant that depends on the geometry of the unit cell and $k \in \{1, \dots, b\}$. b is the number of elements within the unit cell.

Substituting eqn (7.11) into eqn (7.10), assuming a unit reference length, results in:

$$\left\{ EA \begin{bmatrix} \frac{1}{s_k} & 0 & 0 & -\frac{1}{s_k} & 0 & 0 \\ 0 & 0 & 0 & 0 & 0 & 0 \\ 0 & 0 & 0 & 0 & 0 & 0 \\ -\frac{1}{s_k} & 0 & 0 & \frac{1}{s_k} & 0 & 0 \\ 0 & 0 & 0 & 0 & 0 & 0 \\ 0 & 0 & 0 & 0 & 0 & 0 \end{bmatrix} + EI \begin{bmatrix} 0 & 0 & 0 & 0 & 0 & 0 \\ 0 & \frac{12}{s_k^3} & \frac{6}{s_k^2} & 0 & -\frac{12}{s_k^3} & \frac{6}{s_k^2} \\ 0 & \frac{6}{s_k^2} & \frac{4}{s_k} & 0 & -\frac{6}{s_k^2} & \frac{2}{s_k} \\ 0 & 0 & 0 & 0 & 0 & 0 \\ 0 & -\frac{12}{s_k^3} & -\frac{6}{s_k^2} & 0 & \frac{12}{s_k^3} & -\frac{6}{s_k^2} \\ 0 & \frac{6}{s_k^2} & \frac{2}{s_k} & 0 & -\frac{6}{s_k^2} & \frac{4}{s_k} \end{bmatrix} \right\} \begin{bmatrix} d_{ix_1} \\ d_{iy_1} \\ \theta_i \\ d_{qx_1} \\ d_{qy_1} \\ \theta_q \end{bmatrix} = \begin{bmatrix} f_{ix_1} \\ f_{iy_1} \\ m_i \\ f_{qx_1} \\ f_{qy_1} \\ m_q \end{bmatrix} \tag{7.12}$$

Formulation similar to eqn (7.12) can be generated to other elements which can then be assembled in a global matrix system. The final assembled system is the stiffness system of the rigid-jointed microscopic structure of the unit cell. In order to assemble the stiffness systems of the individual cell element into the global matrix system of the structure, the nodal degrees of freedom of the element have to be transformed from the element local coordinate system, $(x_1 - y_1)$, to the global coordinate system $(x - y)$ using the counter clockwise rotation defined by the orthogonal affine transformation as:

$$\begin{bmatrix} d_{ix} \\ d_{iy} \\ \theta_i \\ d_{qx} \\ d_{qy} \\ \theta_q \end{bmatrix} = \begin{bmatrix} \cos(\alpha) & -\sin(\alpha) & 0 & 0 & 0 & 0 \\ \sin(\alpha) & \cos(\alpha) & 0 & 0 & 0 & 0 \\ 0 & 0 & 1 & 0 & 0 & 0 \\ 0 & 0 & 0 & \cos(\alpha) & -\sin(\alpha) & 0 \\ 0 & 0 & 0 & \sin(\alpha) & \cos(\alpha) & 0 \\ 0 & 0 & 0 & 0 & 0 & 1 \end{bmatrix} \begin{bmatrix} d_{ix_1} \\ d_{iy_1} \\ \theta_i \\ d_{qx_1} \\ d_{qy_1} \\ \theta_q \end{bmatrix} \text{ or } d_k = \mathbf{Q}d_k^l \quad (7.13)$$

where d_k and d_k^l are the nodal deformation vectors of element k in the global, $(x-y)$, and the local, $(x_1 - y_1)$, coordinate systems, respectively. \mathbf{Q} is the counter clockwise rotational orthogonal transformation matrix. Similar transformation can be applied to the nodal forces as:

$$f_k = \mathbf{Q}f_k^l \quad (7.14)$$

where f_k and f_k^l are the nodal forces in the global and the local coordinate systems, respectively. This kind of transformation is a unitary transformation where \mathbf{Q} is a unitary matrix (Strang G., 1998). To express the local nodal forces in terms of the global nodal forces, the matrix, \mathbf{Q} , in eqn (7.14) has to be inverted. The inverse of a real unitary matrix is its transpose. Therefore, eqns (7.13) and (7.14) can be formulated as:

$$f_k^l = \mathbf{Q}^T f_k \quad (7.15)$$

$$d_k^l = \mathbf{Q}^T d_k \quad (7.16)$$

where \mathbf{Q}^T is the transpose of matrix \mathbf{Q} .

Substituting eqns (7.15) and (7.16) into eqn (7.12), the stiffness system of the cell element in the global coordinate system $(x-y)$ is expressed as:

$$\mathbf{K}_k d_k = \{\mathbf{K}_k^{bar} + \mathbf{K}_k^{beam}\} d_k = \mathbf{Q} \{\mathbf{K}_{k_l}^{bar} + \mathbf{K}_{k_l}^{beam}\} \mathbf{Q}^T d_k = f_k \quad (7.17)$$

where $\mathbf{K}_k^{bar} = \mathbf{Q} \mathbf{K}_{k_l}^{bar} \mathbf{Q}^T$ and $\mathbf{K}_k^{beam} = \mathbf{Q} \mathbf{K}_{k_l}^{beam} \mathbf{Q}^T$ are, respectively, element k global axial and bending stiffness matrices.

The assembled global stiffness system of the unit cell finite structure is formulated as:

$$\mathbf{K}d = \{\mathbf{K}^{bar} + \mathbf{K}^{beam}\}d = f \quad (7.18)$$

7.4 Stiffness System of Rigid-Jointed Infinite Lattice Structure

The *Bloch's* theorem is used here to generate the irreducible form of the stiffness system of the unit cell. This irreducible form is the stiffness representation of the infinite lattice structure.

Similar to the approach found in (Elsayed, M.S.A. & Pasini, D., 2010b; Hutchinson R.G., 2004), we first generate the transformation matrices necessary to transform the equilibrium and the kinematic wave-functions of the unit cell to its periodic irreducible forms by apply the *Bloch's* theorem.

Recalling eqn (3.42), the kinematic transformation system is expressed as:

$$\begin{bmatrix} q_I \\ q_B \\ q_T \\ q_L \\ q_R \\ q_{LB} \\ q_{RB} \\ q_{LT} \\ q_{RT} \end{bmatrix} = \begin{bmatrix} I & 0 & 0 & 0 \\ 0 & I & 0 & 0 \\ 0 & Ie^{\mu_y} & 0 & 0 \\ 0 & 0 & I & 0 \\ 0 & 0 & Ie^{\mu_x} & 0 \\ 0 & 0 & 0 & I \\ 0 & 0 & 0 & Ie^{\mu_x} \\ 0 & 0 & 0 & Ie^{\mu_y} \\ 0 & 0 & 0 & Ie^{\mu_x + \mu_y} \end{bmatrix} \begin{bmatrix} q_I \\ q_B \\ q_L \\ q_{LB} \end{bmatrix}, \quad \text{or } q = \mathbf{T} \tilde{q} \quad (7.19)$$

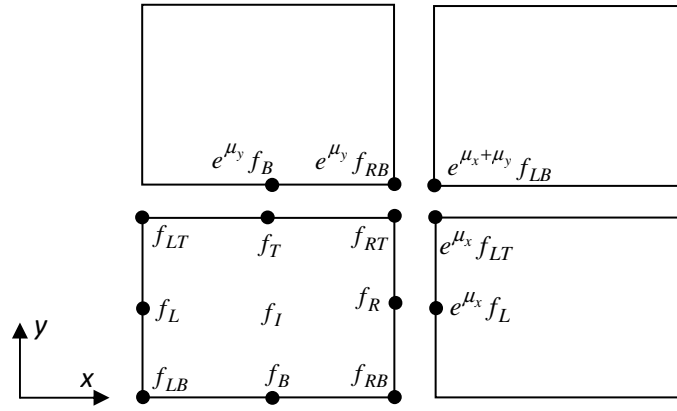


Fig (7.2) Generic unit cell with its periodic equilibrium boundary conditions

where \mathbf{T} is the transformation matrix from the primitive cell degrees of freedom to the reduced cell degrees of freedom. q is a generic nodal or element deformation functions, and T , B , L and R denote top, bottom, left and right, respectively. μ_x and μ_y are the wave-numbers, derived from the reciprocal space of the lattice along with the dependency relations of the nodes and elements bases. The transformation matrices for the nodal displacements wave-functions are obtained such that:

$$d = \mathbf{T} \tilde{d} \quad (7.20)$$

where \tilde{d} is the element deformations and the nodal displacements reduced vectors (periodic wave-function), respectively.

The same concept, used to derive the kinematic transformation matrix, can be applied to generate the equilibrium transformation matrix that takes into account the anti-periodic constraints necessary for the static equilibrium of the lattice.

For the cluster of four generic unit cells shown in Fig (7.2), the application of the *Bloch's* theorem allows writing the following relations:

$$f_R + e^{\mu_x} f_L = 0, \quad f_T + e^{\mu_y} f_B = 0,$$

$$f_{RT} + e^{\mu_x} f_{LT} + e^{\mu_y} f_{RB} + e^{\mu_x + \mu_y} f_{LB} = 0 \quad (7.21)$$

Equation (7.21) can be arranged in matrix form as:

$$\begin{bmatrix} f_I \\ f_B \\ f_L \\ f_{LB} \end{bmatrix} = \begin{bmatrix} I & 0 & 0 & 0 & 0 & 0 & 0 & 0 & 0 \\ 0 & I & Ie^{\mu_y} & 0 & 0 & 0 & 0 & 0 & 0 \\ 0 & 0 & 0 & I & Ie^{\mu_x} & 0 & 0 & 0 & 0 \\ 0 & 0 & 0 & 0 & 0 & I & Ie^{\mu_x} & Ie^{\mu_y} & Ie^{\mu_x + \mu_y} \end{bmatrix} \begin{bmatrix} f_I \\ f_B \\ f_T \\ f_L \\ f_R \\ f_{LB} \\ f_{RB} \\ f_{LT} \\ f_{RT} \end{bmatrix} = 0 \quad (7.22)$$

$$\text{or } \tilde{f} = \mathbf{T}^H f = 0$$

where \mathbf{T}^H is the Hermitian (the conjugate transpose) of the transformation matrix \mathbf{T} .

The transformation matrices are generated by accounting for the dependency relations of the bars and the nodes bases, as expressed by eqn (3.35).

Eqns (7.20) and (7.22) are substituted into the stiffness system of the unit cell, eqn (7.5), to derive its periodic reduced form as:

$$\tilde{\mathbf{K}} \tilde{d} = \tilde{f} \quad (7.23)$$

where $\tilde{\mathbf{K}}$ is the reduced stiffness matrix of the infinite lattice structure, expressed as:

$$\tilde{\mathbf{K}} = \mathbf{T}^H \mathbf{K} \mathbf{T} \quad (7.24)$$

7.5 The Homogenization Process of the Stiffness Properties of Periodic Microstructure: The Macroscopic Stiffness of Lattice Material

The stiffness properties of the microscopic lattice structure are homogenized to generate the effective macroscopic stiffness properties of the lattice material. This is done by using the *Cauchy-Born* hypothesis (Bhattacharya, K., 2003; Born, M., & Huang, K., 1954; Maugin, G. A., 1992; Pitteri, M., et.al., 2003; Ericksen, J. L., 1984).

7.5.1 *Cauchy-Born* Hypothesis

From the definition of the *Cauchy-Born* hypothesis (Bhattacharya, K., 2003), the infinitesimal displacement field of a periodic node in a lattice structure can be formulated as:

$$d\left(j_l + \vec{R}, \bar{\varepsilon}\right) = d\left(j_l, \bar{\varepsilon} = 0\right) + \bar{\varepsilon} \cdot \vec{R} \quad (7.25)$$

where $d(j_l, \bar{\varepsilon} = 0)$ is the periodic displacement field of node j_l . Assume that the periodic nodes

defined by the position vectors j_l and $j_l + \vec{R}$, are the two rigid nodes i and j within a lattice structure, then, eqn (7.25) can be formulated in matrix form as:

$$\begin{bmatrix} d_{ix} \\ d_{iy} \\ \theta_i \end{bmatrix} = \begin{bmatrix} d_{jx} \\ d_{jy} \\ \theta_j \end{bmatrix} + \begin{bmatrix} \varepsilon_{xx} & \varepsilon_{xy} \\ \varepsilon_{yx} & \varepsilon_{yy} \\ 0 & 0 \end{bmatrix} \begin{bmatrix} x_i - x_j \\ y_i - y_j \end{bmatrix} \quad \text{in 2D} \quad (7.26)$$

where u and v are the node displacement field components in the x and y directions, respectively, and node i is the dependent node, while node j is the independent node. In terms of engineering strain (Renton, J.D., 2002), eqn (7.26) can be reformulated as:

$$\begin{bmatrix} d_{ix} \\ d_{iy} \\ \theta_i \end{bmatrix} = \begin{bmatrix} d_{jx} \\ d_{jy} \\ \theta_j \end{bmatrix} + \begin{bmatrix} \varepsilon_{xx} & \frac{1}{2}\varepsilon_{xy} \\ \frac{1}{2}\varepsilon_{yx} & \varepsilon_{yy} \\ 0 & 0 \end{bmatrix} \begin{bmatrix} x_i - x_j \\ y_i - y_j \end{bmatrix} \quad \text{in 2D} \quad (7.27)$$

which in turn can be expressed as:

$$\begin{bmatrix} d_{ix} \\ d_{iy} \\ \theta_i \end{bmatrix} = \begin{bmatrix} d_{jx} \\ d_{jy} \\ \theta_j \end{bmatrix} + \begin{bmatrix} (x_i - x_j) & 0 & \frac{1}{2}(y_i - y_j) \\ 0 & (y_i - y_j) & \frac{1}{2}(x_i - x_j) \\ 0 & 0 & 0 \end{bmatrix} \begin{bmatrix} \varepsilon_{xx} \\ \varepsilon_{yy} \\ \varepsilon_{xy} \end{bmatrix} \quad (7.28)$$

$$\text{or } d_i = d_j + \mathbf{E} \bar{\varepsilon}$$

Applying this boundary condition to the unit cell node displacement vector, d , results in:

$$d = \mathbf{T} \tilde{d} + \mathbf{E} \bar{\varepsilon} \quad (7.29)$$

Equation (7.29) is the rigid-jointed modified kinematic boundary condition of the *Cauchy-Born* hypothesis.

Substituting eqn (7.29) into the stiffness system of the unit cell (eqn (7.18)) results in:

$$\mathbf{K} \left\{ \mathbf{T} \tilde{d} + \mathbf{E} \bar{\varepsilon} \right\} = \left\{ \mathbf{K}^{bar} + \mathbf{K}^{beam} \right\} \left\{ \mathbf{T} \tilde{d} + \mathbf{E} \bar{\varepsilon} \right\} = f \quad (7.30)$$

Multiplying both sides of eqn (7.30) by the Hermetian of the transformation matrix, \mathbf{T}^H , and substituting eqn (7.22) into the outcome, results in:

$$\mathbf{T}^H \mathbf{K} \left\{ \mathbf{T} \tilde{d} + \mathbf{E} \bar{\varepsilon} \right\} = \mathbf{T}^H \left\{ \mathbf{K}^{bar} + \mathbf{K}^{beam} \right\} \left\{ \mathbf{T} \tilde{d} + \mathbf{E} \bar{\varepsilon} \right\} = \mathbf{T}^H f = \tilde{f} = 0 \quad (7.31)$$

Rearranging eqn (7.31), results in:

$$\mathbf{T}^H \left\{ \mathbf{K}^{bar} + \mathbf{K}^{beam} \right\} \mathbf{T} \tilde{d} = -\mathbf{T}^H \left\{ \mathbf{K}^{bar} + \mathbf{K}^{beam} \right\} \mathbf{E} \bar{\varepsilon} \quad (7.32)$$

Equation (7.32) can be split into two matrix systems as:

$$\tilde{\mathbf{K}}^{bar} \tilde{d} = -\mathbf{T}^H \mathbf{K}^{bar} \mathbf{E} \bar{\varepsilon} \quad (7.33)$$

$$\tilde{\mathbf{K}}^{beam} \tilde{d} = -\mathbf{T}^H \mathbf{K}^{beam} \mathbf{E} \bar{\varepsilon} \quad (7.34)$$

where $\tilde{\mathbf{K}}^{bar} = \mathbf{T}^H \mathbf{K}^{bar} \mathbf{T}$ and $\tilde{\mathbf{K}}^{beam} = \mathbf{T}^H \mathbf{K}^{beam} \mathbf{T}$ are the axial (bar) and bending (beam) stiffness matrices, respectively.

7.5.2 Microscopic Nodal Deformations in Terms of Macroscopic Strain Field

The microscopic nodal deformation can be computed in terms of the macroscopic strain field using eqns (7.33) and (7.34). This can be done by multiplying both sides of eqns (7.33) and (7.34)

by the inverse of the stiffness matrices. However, the microscopic stiffness matrices contain, in their column and row spaces, two modes of translational rigid body motion, as the lattice is not constrained into a foundation. The column and the row spaces of the stiffness matrices might contain also other modes associated with microscopic mechanisms within the lattice structure. In order to compute the inverse of the stiffness matrices, all modes related to rigid body motion as well as those modes related to internal mechanisms have to be eliminated from the column and the row spaces of the stiffness matrices. This can be done by computing the reduced row echelon

form (Strang G., 1998) of the two matrices $\tilde{\mathbf{K}}^{bar}$ and $\tilde{\mathbf{K}}^{beam}$, then determine the non-pivotal modes in the row and the column spaces. A simple elimination strategy can be conducted as follows: assume that a non-pivotal mode is determined with the index np in the stiffness matrix $\tilde{\mathbf{K}}^{bar}$, then, all the values in the row and the column of the stiffness matrix with the index np have

to be set to zero while the diagonal value has to be set to unity; i.e. $\tilde{\mathbf{K}}^{bar}(:, np) = \tilde{\mathbf{K}}^{bar}(np, :) = 0$

and $\tilde{\mathbf{K}}^{bar}(np, np) = 1$. On the other hand, all the values in the row with the rank np in the right hand side matrix of eqns (7.33) and (7.34) have to be set to zero. Once the elimination process is complete, the stiffness matrices can be inverted and an expression of the microscopic nodal displacements in terms of the assumed macroscopic strain field can be written as:

$$\tilde{d}_{bar} = - \left(\tilde{\mathbf{K}}_{red}^{bar} \right)^{-1} \left(\mathbf{T}^H \mathbf{K}^{bar} \mathbf{E} \right)_{red} \bar{\boldsymbol{\varepsilon}} \quad (7.35)$$

$$\tilde{d}_{beam} = - \left(\tilde{\mathbf{K}}_{red}^{beam} \right)^{-1} \left(\mathbf{T}^H \mathbf{K}^{beam} \mathbf{E} \right)_{red} \bar{\boldsymbol{\varepsilon}} \quad (7.36)$$

where \tilde{d}_{bar} and \tilde{d}_{beam} are, respectively, the microscopic nodal deformations corresponding to the

axial and the bending stiffness resistances. $\tilde{\mathbf{K}}_{red}^{bar}$ and $\tilde{\mathbf{K}}_{red}^{beam}$ are, respectively, the bar and the beam reduced stiffness matrices generated after eliminating modes associated with the rigid body motions and the internal microscopic mechanisms from the stiffness matrices.

The generalized deformation of all nodes within the unit cell can be computed by substituting eqns (7.35) and (7.36) into eqn (7.29), which results in:

$$d_{bar} = \tilde{\mathbf{T}} d_{bar} + \mathbf{E} \bar{\boldsymbol{\varepsilon}} = \left\{ -\mathbf{T} \left(\tilde{\mathbf{K}}_{red}^{bar} \right)^{-1} \left(\mathbf{T}^H \mathbf{K}^{bar} \mathbf{E} \right)_{red} + \mathbf{E} \right\} \bar{\boldsymbol{\varepsilon}} = \mathbf{M}_{bar}^d \bar{\boldsymbol{\varepsilon}} \quad (7.37)$$

$$d_{beam} = \tilde{\mathbf{T}} d_{beam} + \mathbf{E} \bar{\boldsymbol{\varepsilon}} = \left\{ -\mathbf{T} \left(\tilde{\mathbf{K}}_{red}^{beam} \right)^{-1} \left(\mathbf{T}^H \mathbf{K}^{beam} \mathbf{E} \right)_{red} + \mathbf{E} \right\} \bar{\boldsymbol{\varepsilon}} = \mathbf{M}_{beam}^d \bar{\boldsymbol{\varepsilon}} \quad (7.38)$$

Expression of the generalized microscopic nodal forces in terms of the macroscopic strain field can be computed by direct substitution of eqns (7.37) and (7.38) into the stiffness system of the unit cell presented in eqn (7.18), which results in:

$$f_{bar} = \mathbf{K}^{bar} d_{bar} = \mathbf{K}^{bar} \left\{ -\mathbf{T} \left(\tilde{\mathbf{K}}_{red}^{bar} \right)^{-1} \left(\mathbf{T}^H \mathbf{K}^{bar} \mathbf{E} \right)_{red} + \mathbf{E} \right\} \bar{\boldsymbol{\varepsilon}} = \mathbf{M}_{bar}^f \bar{\boldsymbol{\varepsilon}} \quad (7.39)$$

$$f_{beam} = \mathbf{K}^{bar} d_{beam} = \mathbf{K}^{bar} \left\{ -\mathbf{T} \left(\tilde{\mathbf{K}}_{red}^{beam} \right)^{-1} \left(\mathbf{T}^H \mathbf{K}^{beam} \mathbf{E} \right)_{red} + \mathbf{E} \right\} \bar{\boldsymbol{\varepsilon}} = \mathbf{M}_{beam}^f \bar{\boldsymbol{\varepsilon}} \quad (7.40)$$

7.5.3 Homogenized Macroscopic Stiffness of Lattice Material

The generalized nodal forces and deformations, formulated in the previous section, are used to derive the rigid-jointed lattice material macroscopic stiffness properties using the principle of the virtual work (Timoshenko, S. P., & Young, D. H., 1945) and the *Hill-Mandel* principle (Maugin, G. A., 1992) of macro-homogeneity which results in:

$$\mathbf{K}_L^{bar} = \left(\frac{EA}{2|Y|} \right) \left(\left(\mathbf{M}_{bar}^f \right)^T \left(\mathbf{M}_{bar}^d \right) \right) \quad (7.41)$$

$$\mathbf{K}_L^{beam} = \left(\frac{EI}{2|Y|} \right) \left(\left(\mathbf{M}_{beam}^f \right)^T \left(\mathbf{M}_{beam}^d \right) \right) \quad (7.42)$$

where $|Y|$ is the unit cell in-plane area. \mathbf{K}_L^{bar} and \mathbf{K}_L^{beam} are, respectively, the lattice material homogenized, fourth order, axial and bending stiffness tensors.

Recalling eqn (4.1), the relative density of a 2D lattice material is given by:

$$\bar{\rho} = \frac{\rho_L}{\rho} = C_T^\rho \left(\frac{H}{L} \right) \quad (7.43)$$

where C_T^ρ is a constant depends on the geometry of the unit cell. Considering an out of plane depth of the 2D lattice equal to a unit length, a cell element reference length of unit length, $L=1$, and substituting eqns (7.43) into eqns (7.41) and (7.42) result in:

$$\mathbf{K}_L^{bar} = \left(\frac{E}{2|Y|} \right) \left(\frac{\rho_L}{C_T^\rho} \right) \left(\left(\mathbf{M}_{bar}^f \right)^T \mathbf{M}_{bar}^d \right) \quad (7.44)$$

$$\mathbf{K}_L^{beam} = \left(\frac{E}{2|Y|} \right) \left(\frac{\rho_L}{C_T^\rho} \right)^3 \left(\left(\mathbf{M}_{beam}^f \right)^T \mathbf{M}_{beam}^d \right) \quad (7.45)$$

Once the macroscopic stiffness tensor is computed, the macroscopic compliance matrix can be obtained by inverting the stiffness matrix, where $\mathbf{C}_L = \mathbf{K}_L^{-1}$ is the linearly elastic fourth order compliance tensor of the lattice material which is used to compute the lattice material elastic moduli.

7.6 Application of the Developed Methodology to Thirteen 2D Lattice Topologies

The methodology presented above is now applied to 13 lattice topologies. Their closed form expressions of the stiffness matrix along with its elastic moduli and Poisson's ratios are included in Appendix G. Charts representing the relative elastic moduli of the lattice material versus its relative density are developed in Figs (7.3- 7.5). These charts assist the selection of the best topology of a lattice material for a given application that requires a material with specific stiffness properties.

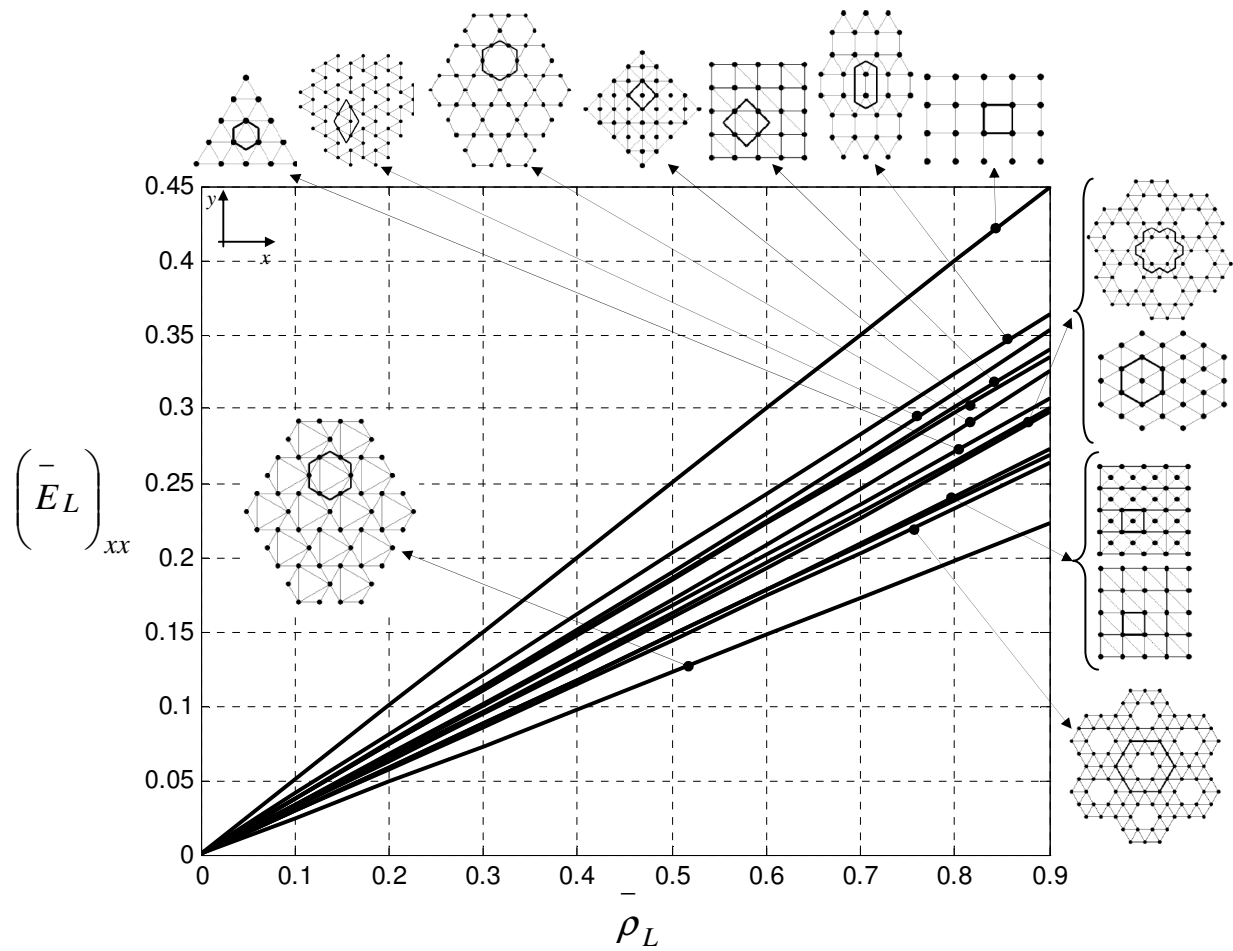


Fig (7.3) Relative Young's modulus in the horizontal direction versus relative density of selected 2D lattice materials

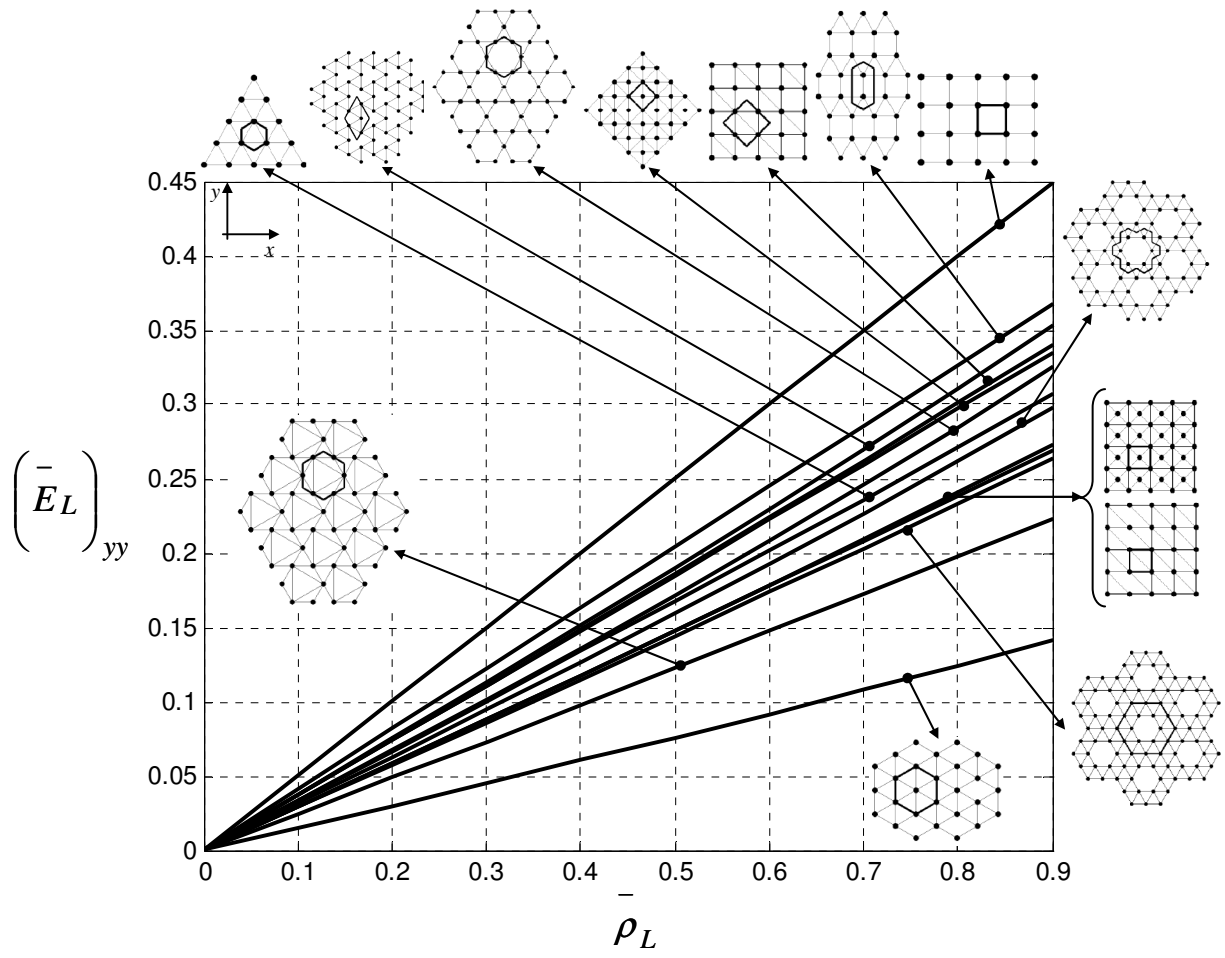


Fig (7.4) Relative Young's modulus in the vertical direction versus relative density of selected 2D lattice materials

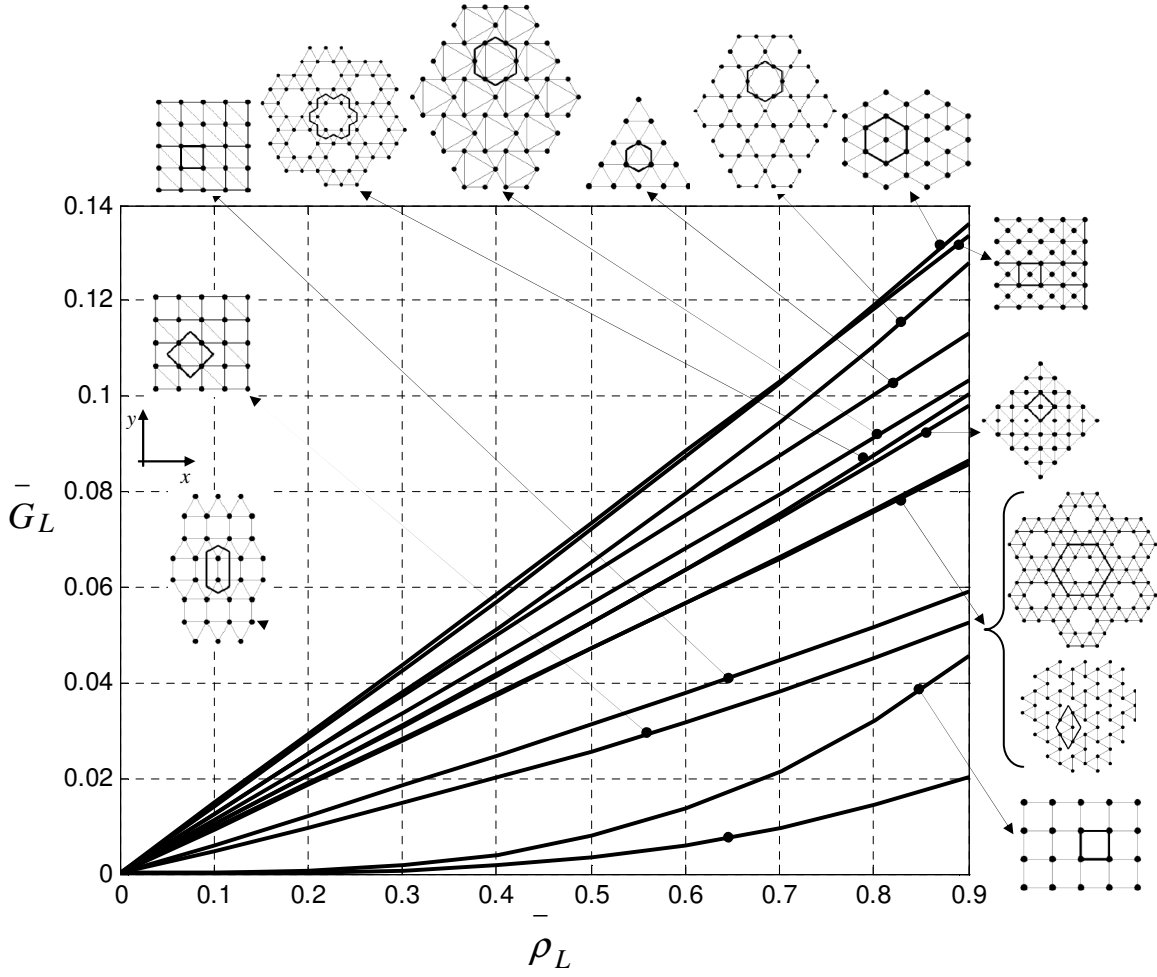


Fig (7.5) Relative shear modulus versus relative density of selected 2D lattice materials

7.6.1 Effectiveness of Nodal Rigidity

The effectiveness of the nodal rigidity of the microscopic lattice on the stiffness characteristics of the stretching dominated lattice topologies is examined here. The contribution of the bending stiffness of the microscopic cell elements to the macroscopic stiffness of the lattice material is assessed by the relations:

$$\left(\Delta \bar{E}_L \right)_{xx} = 100 \left(\left(\bar{E}_L \right)_{xx} - \left(\bar{E}_L^{bar} \right)_{xx} \right) / \left(\bar{E}_L \right)_{xx} [\%] \quad (7.46)$$

$$\left(\Delta \bar{E}_L \right)_{yy} = 100 \left(\left(\bar{E}_L \right)_{yy} - \left(\bar{E}_L^{bar} \right)_{yy} \right) / \left(\bar{E}_L \right)_{yy} [\%] \quad (7.47)$$

$$\Delta \bar{G}_L = 100 \left(\frac{\bar{G}_L - \bar{G}_L^{bar}}{\bar{G}_L} \right) [\%] \quad (7.48)$$

The above relations are plotted in Figs (7.6-7.8). The results show that the closer the topology to the full triangulation, the less the contribution of the microscopic bending stiffness to the homogenized macroscopic stiffness of the lattice material.

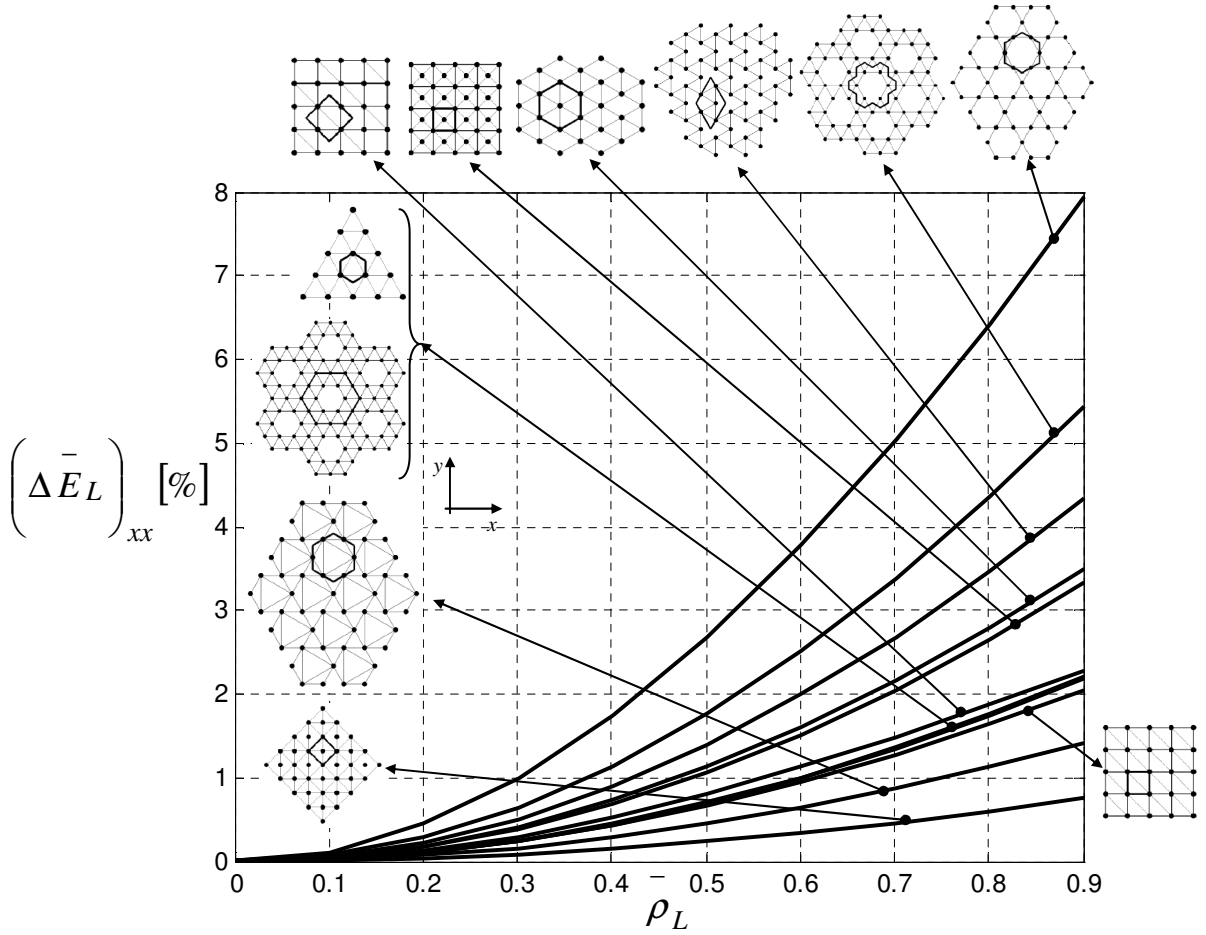


Fig (7.6) Contribution percentage of the microscopic bending stiffness of microscopic cell elements to the macroscopic Young's modulus in the horizontal direction of the lattice material versus the material relative density

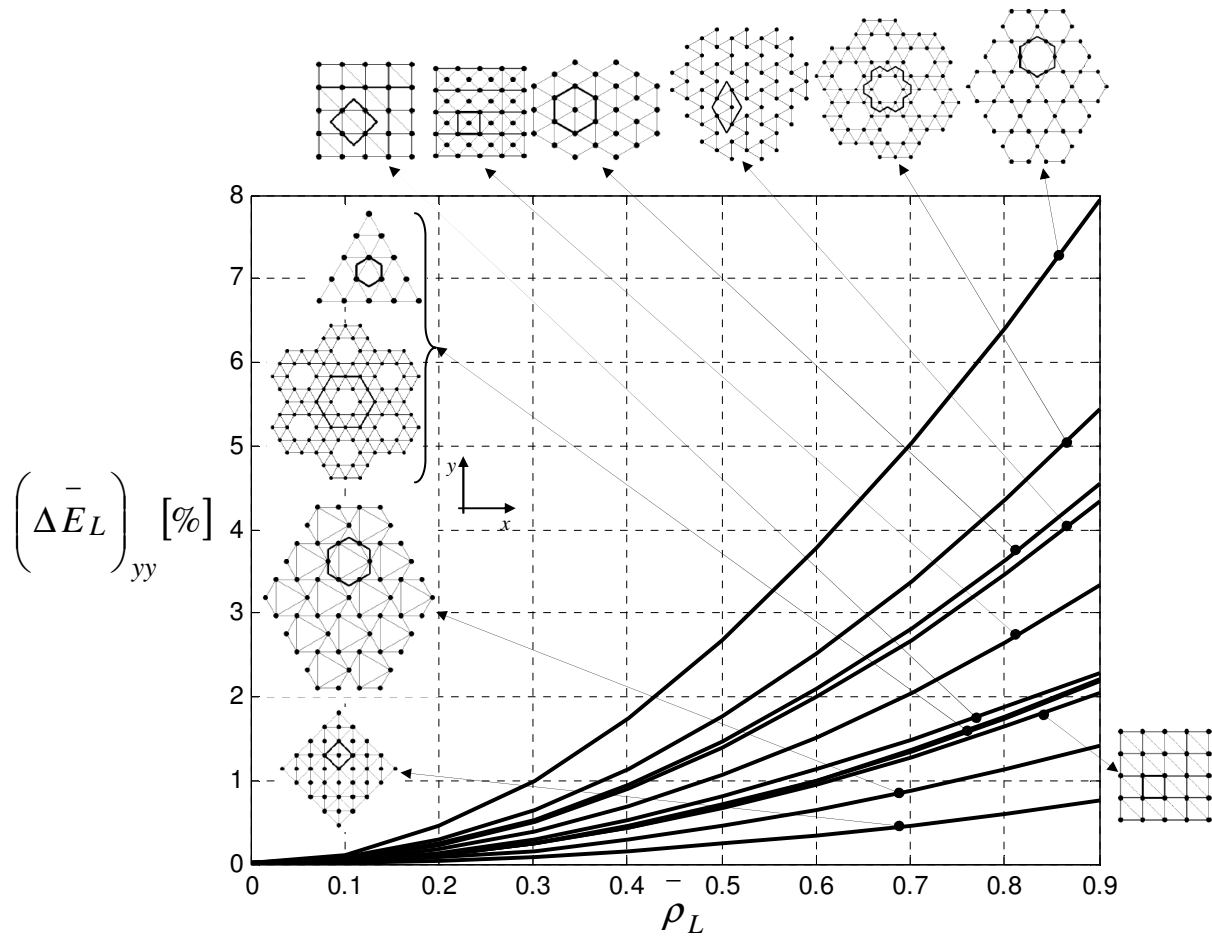


Fig (7.7) Contribution percentage of the microscopic bending stiffness of microscopic cell elements to the macroscopic Young's modulus in the vertical direction of the lattice material versus the material relative density

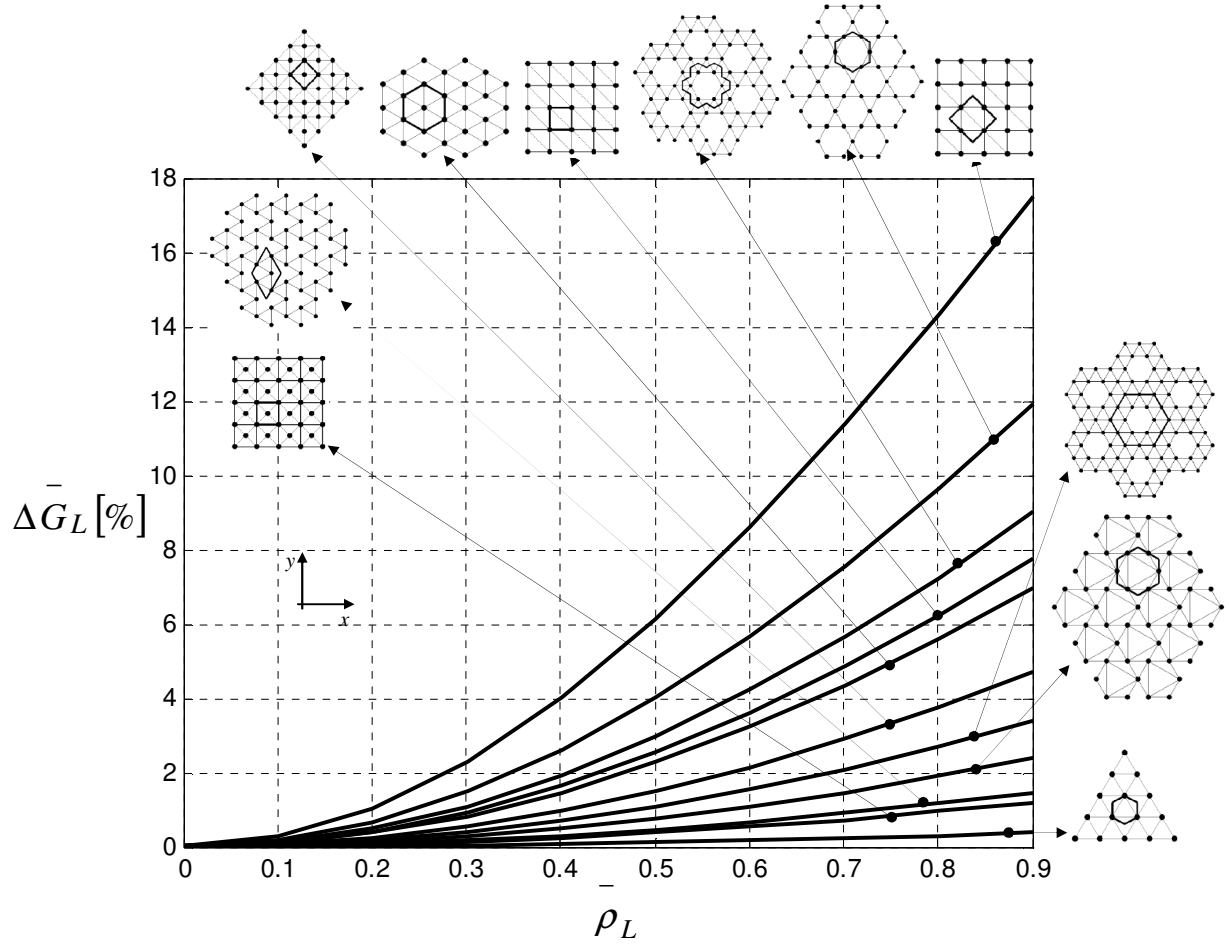


Fig (7.8) Contribution percentage of the microscopic bending stiffness of microscopic cell elements to the macroscopic shear modulus versus the material relative density

7.7 Anisotropy of Lattice Material

Fig (7.9) illustrates the infinitesimal stress field of a lattice material considered here to examine the anisotropic behavior of the homogenized stiffness characteristics of the material. The 2D

infinitesimal stress field $(\sigma_x, \sigma_y, \tau_{xy})$ is transformed counter clockwise by an angle

$\theta \in [0^\circ, 360^\circ]$ to a new stress field $(\sigma_{x_\theta}, \sigma_{y_\theta}, \tau_{x_\theta y_\theta})$. An efficient technique to convert the

material elastic properties from the $(x - y)$ coordinates to the $(x_\theta - y_\theta)$ coordinates is the use of the Bond-stress and strain transformation matrices (AULD, B. A., 1990; Hoffmeister, B. K., 2000; Bond, W. L., 1943; Hearmon, R. F. S., 1946; Bin, L., 2010). The linearly elastic stress field in the $(x - y)$ coordinates can be related to the strain field in the same coordinate system by

Hooke's law such that:

$$\sigma = \mathbf{K}\varepsilon \quad (7.49)$$

where K is the fourth order, linearly elastic, stiffness tensor.

As demonstrated by Bond, the stress field in the $(x - y)$ coordinates, σ , can be transformed to a stress field in the $(x_\theta - y_\theta)$ coordinates, σ_θ , using the Bond-Stress Transformation matrix, M_σ , such that:

$$\sigma_\theta = \mathbf{M}_\sigma \sigma \quad (7.50)$$

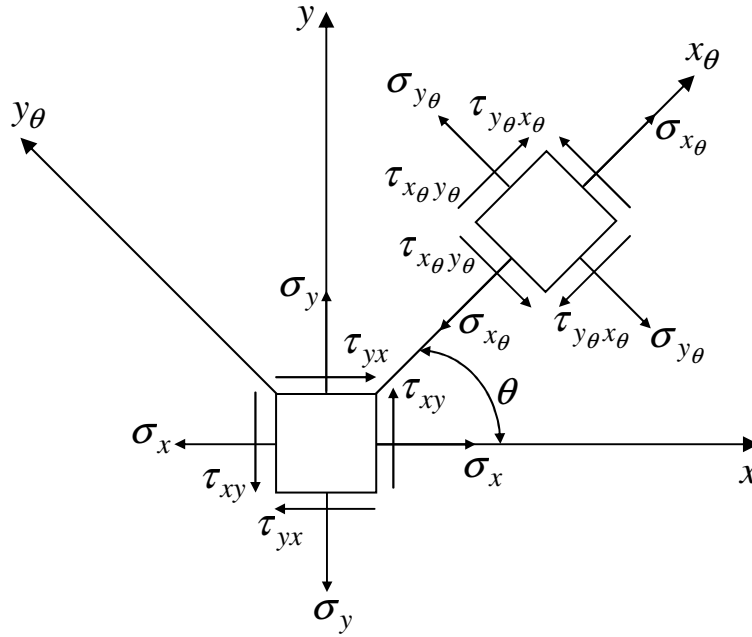


Fig (7.9) Infinitesimal stress field of lattice material

The 2D Bond-Stress Transformation matrix is given by:

$$\mathbf{M}_\sigma = \begin{bmatrix} \cos^2(\theta) & \sin^2(\theta) & \sin(2\theta) \\ \sin^2(\theta) & \cos^2(\theta) & -\sin(2\theta) \\ -0.5\sin(2\theta) & 0.5\sin(2\theta) & \cos(2\theta) \end{bmatrix} \quad (7.51)$$

Similarly, the corresponding strain field in the $(x - y)$ coordinates, ε , can be transformed to a strain field in the $(x_\theta - y_\theta)$ coordinates, ε_θ , using the Bond-Strain Transformation matrix, M_ε , such that:

$$\varepsilon_\theta = \mathbf{M}_\varepsilon \varepsilon \quad (7.52)$$

Inverting the matrices in eqns (7.50) and (7.52) and substituting the results into eqn (7.60), results in:

$$\sigma_{\theta} = \mathbf{M}_{\sigma} \mathbf{K} \mathbf{M}_{\varepsilon}^{-1} \varepsilon_{\theta} \quad (7.53)$$

The above results in:

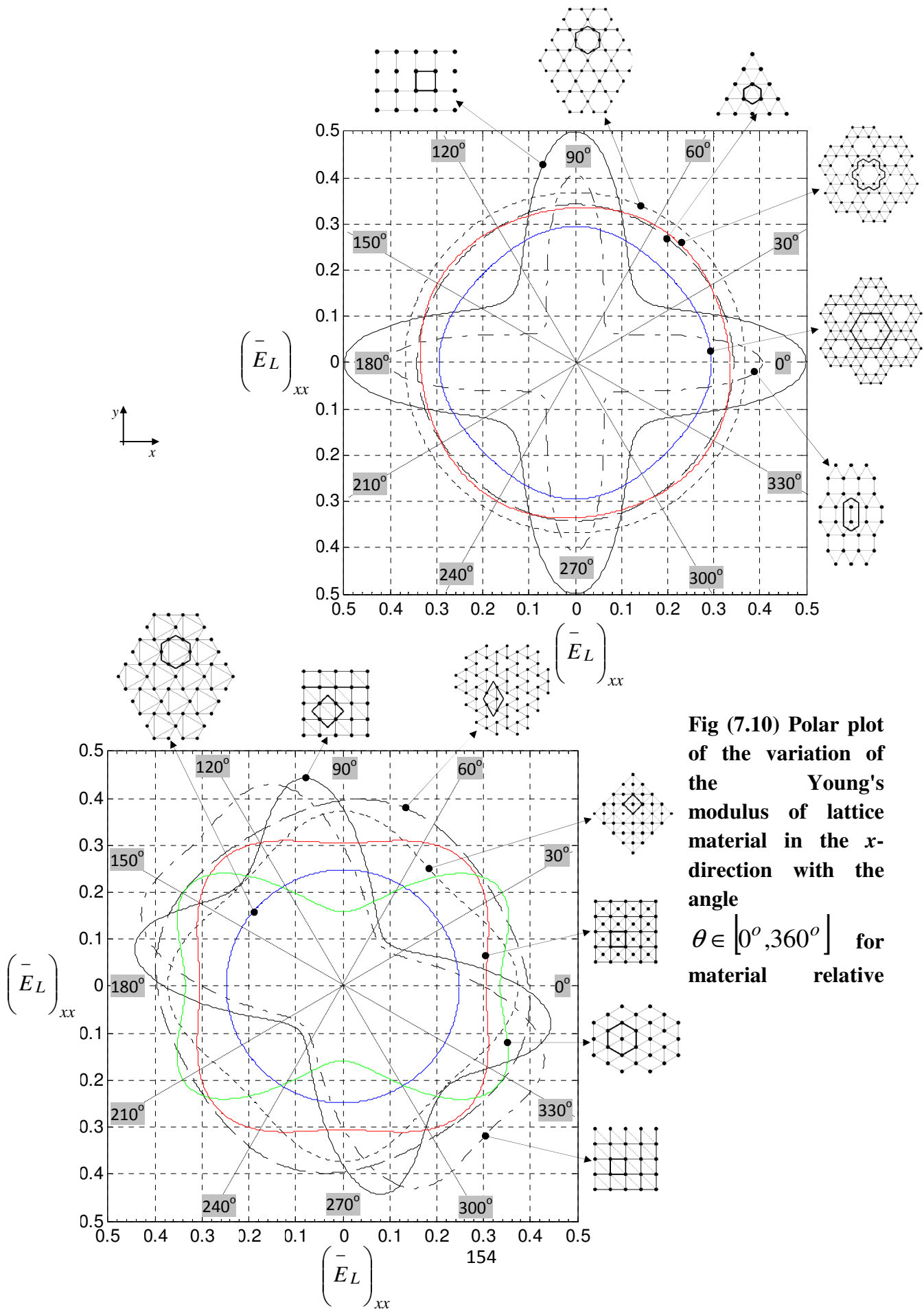
$$\mathbf{M}_{\varepsilon}^{-1} = \mathbf{M}_{\sigma}^T \quad (7.54)$$

where \mathbf{M}_{σ}^T is the transpose of \mathbf{M}_{σ} .

Substituting eqn (7.54) into eqn (7.53), results in:

$$\mathbf{K}_{\theta} = \mathbf{M}_{\sigma} \mathbf{K} \mathbf{M}_{\sigma}^T \quad (7.55)$$

If we set the material relative density as unity, i.e. $\bar{\rho}_L = 1$, for the 13 topologies, we can plot 2D polar charts (Figs. 10-12) illustrating the variation of the Young's moduli in the x_{θ} and y_{θ} directions as well as the shear modulus in the $x_{\theta}y_{\theta}$ direction. The results of the elastic properties of the rigid-jointed lattice are given in Appendix G for the 13 topologies examined in this chapter.



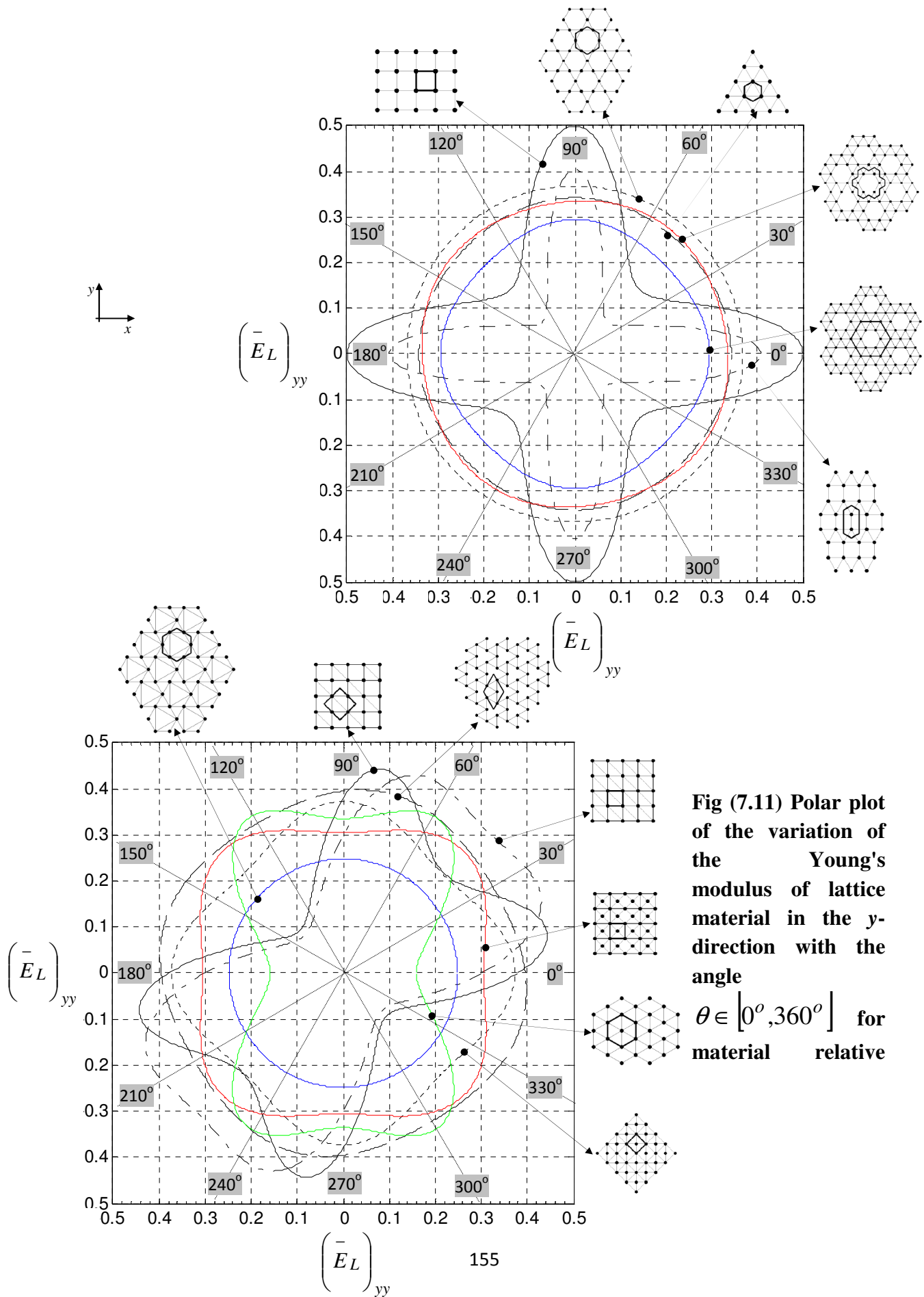


Fig (7.11) Polar plot of the variation of the Young's modulus of lattice material in the y-direction with the angle $\theta \in [0^\circ, 360^\circ]$ for material relative

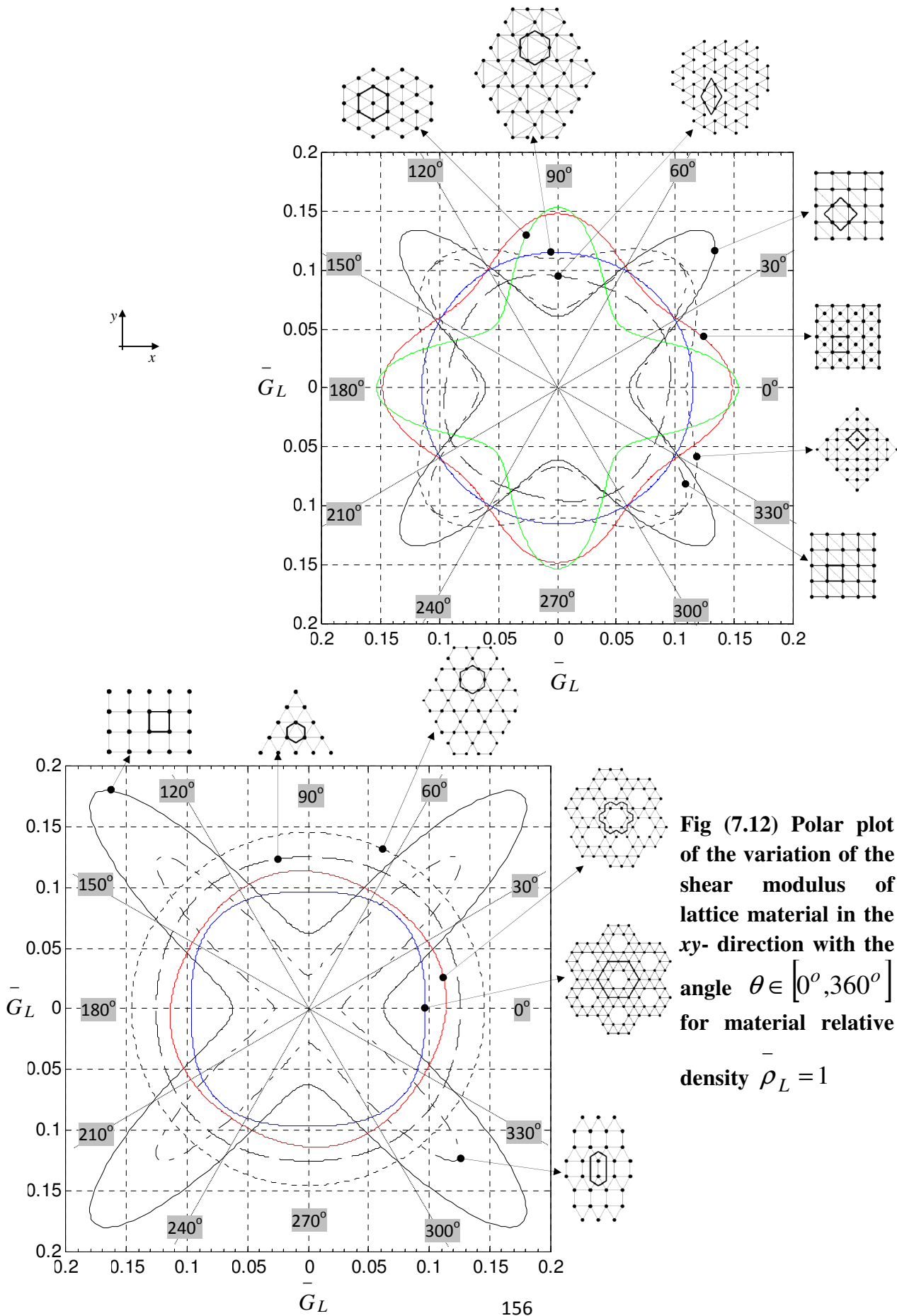


Fig (7.12) Polar plot of the variation of the shear modulus of lattice material in the xy -direction with the angle $\theta \in [0^\circ, 360^\circ]$ for material relative density $\bar{\rho}_L = 1$

7.8 Discussion and Concluding Remarks

This chapter has presented a theoretical approach to calculate the elastic properties of micro-truss lattice materials with rigid-jointed architecture. Closed form expressions of the elastic moduli, Poisson's ratios and relative densities have been obtained for 13 lattice topologies (Appendix G). The results for each topology have been plotted into selection charts that illustrate the variation of the elastic moduli of the lattice material with respect to their relative density.

The chapter has also examined the bending stiffness contribution that the microscopic constituents of stretching dominated lattice material provide to the homogenized macroscopic stiffness of the material. The main outcome of this analysis, plotted in Figs (7.6-7.8), has shown that the closer the microscopic topology of the stretching dominated lattice material to the full triangulation, the less the microscopic bending stiffness contribution of the micro-truss members. The contribution is negligible for lattice structures that possess no microscopic internal mechanisms in their pin-jointed versions of micro-truss (Elsayed, M.S.A., Pasini, D., 2010b). On the other hand, it is found that the Kagome lattice has constituent members, whose bending resistant contribute up to 8% to the overall direct stiffness of the material. This is the highest contribution among the selected topologies. Although the semi-uni-braced square lattice topology has internal mechanisms, the bending stiffness contribution of its microscopic constituents is limited to 2.1%. The reason for this is that uni-directional loading in either x - and/or y - directions (see appendix G) of the pin-jointed version of the semi-uni-braced square lattice does not excite its internal mechanism. On the other hand, the contribution of the bending stiffness Fig (7.8) of the microscopic constituents to the homogenized shear stiffness is 17.5% for the semi-uni-braced square lattice since this topology has microscopic internal mechanisms that are excited by shear macroscopic loadings. Finally this work has studied the anisotropic behavior of the lattice material by analysing the transformation of the material elastic properties through an angle $\theta \in [0^\circ, 360^\circ]$. Results for the selected topologies are illustrated in the polar plots of Figs (7.10-7.12) which shows their elastic moduli sensitivity to the change of load direction. The analysis and design charts developed in this chapter help to gain insight into the lattice topology that can be selected to best meet prescribed stiffness requirements. The charts help to explore the potential that these hybrid materials have in filling the gaps emerging in the material properties charts. Other plots have been presented to estimate the errors between theoretical results of pin-jointed micro-trusses and their real behavior, generally obtained through experiments. Finally, polar maps have been generated to reveal the anisotropic behavior of the selected micro-truss.

CHAPTER 8

Comprehensive Stiffness and Classification of Periodic Lattice Materials and Structures

8.1 Introduction

Two types of nonlinearities are encountered in structural analysis, namely, material and geometrical nonlinearities. The former is developed due to the nonlinear elastic, plastic and/or viscoelastic behavior of the material. The latter starts once the structural deformations exceed the infinitesimal limit at which the deformations are sufficiently large to generate a change in the initial geometry of the structure. In this case, the equilibrium system of the deformed structure cannot be assumed to be equal to its original undeformed state, as supposed by the theory of linear elasticity; rather it must be formulated in its deformed configuration. The modified equilibrium system is expressed by an additional term, namely the geometrical stiffness.

The geometrical stiffness can emerge due to both compressive and tensile loads acting on the constituent members of a structure. When developed by compression in the structural constituents, the overall stiffness of the structure reduces to the bifurcation point where the structure fails by buckling. On the other hand, a geometrical stiffness developed by tensile loading of the structural constituents results in an enhanced loading resistance.

Whereas geometrical nonlinearities are present, although often negligible in the responses of any structure, their effect becomes significant in kinematically indeterminate, under-constrained, frameworks. A kinematically indeterminate framework is a pin-jointed structure with internal mechanisms, i.e. alternative modes of structural deformations are encountered with undeformed elements. Some of these internal mechanisms generate finite displacements at each increment of the external load; other mechanisms are unique as the structure encounters only first order infinitesimal mechanisms accompanied by higher order strains. Such kinds of structures are prestressable and can be found in several natural and engineering systems (Kuznetsov, E.N., 1997; Tilbert, G., 2002), e.g. cable systems (e.g. cable nets), tensegrity frameworks, pneumatic domes and fabric roofs.

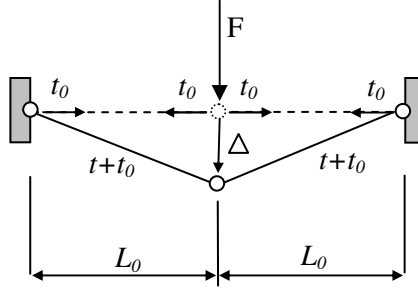


Fig (8.1) Statically and kinematically indeterminate framework

Example of a pre-stressable structure is shown in Fig (8.1). The determinacy analysis of the finite framework, shown in Fig (8.1), shows that this structure contains one internal mechanism and one state of self-stress. The static equilibrium between the external load, F , and the element axial forces, t_0 , is expressed as:

$$F = \frac{2t_0}{L_0} \Delta + \frac{EA}{L_0^3} \Delta^3 \quad (8.1)$$

where Δ is the structural deformation, t_0 is a pre-stress in the elements, E is the material Young's modulus, A the element cross-sectional areas and L_0 is the element initial lengths. The initial stress in the elements can be formulated as:

$$t_0 = \frac{EA}{L_0} \delta_0 \quad (8.2)$$

where δ_0 is the initial axial deformation of an element. Substituting eqn (8.2) into eqn (8.1), results in:

$$F = \frac{EA}{L_0^2} \left(2\delta_0 \Delta + \frac{1}{L_0} \Delta^3 \right) \quad (8.3)$$

For unit length elements, $L_0 = 1$, one can find that a pre-stressed structure bears an external loading greater by one order of magnitude than its counterpart supported by the un-prestressed structures. As per eqn (8.3), the external loading is proportional to $\delta_0 \Delta$ if the initial stress of $t_0 > 0$. On the other hand, with no initial stress, $t_0 = 0$, the external load is proportional to Δ^3 . This simple example demonstrates the significance of the geometrical resistance initiated by the axial pre-stressing of the constituents of a statically and kinematically indeterminate framework.

From literature (Mohr, O., 1885; Maxwell, J.C., 1864; Levi-Civita, T., Amaldi, U., 1930; Calladine, C.R., 1982; Pellegrino, S., Calladine, C.R., 1986; Calladine, C.R., Pellegrino, S., 1991; Volokh, K.Yu., Vilnay, O., 1997; Kuznetsov, E. N., 2000; Deshpande, V. S., et.al., 2001a; Hutchinson R.G., 2004), it appears that many efforts are established in the analysis of the determinacy state of finite and infinite frameworks. However, the impact of the determinacy state on the static response of the structures in the form of comprehensive stiffness characteristics has been only investigated on finite frameworks (Guest, S., 2006; Pellegrino, S., Calladine, C.R., 1984; Connelly, R., Whiteley, W., 1996; Sener, M., et.al., 1994; Pellegrino, S., 1992; 1990; 1988).

The current chapter extends the literature of this topic to model the comprehensive stiffness of an infinite periodic structure where the material stiffness characteristics are generalized to account for the geometrical non-linearity of periodic frameworks. The analysis is conducted on pin- and rigid-jointed periodic architectures. The resulting geometrical stiffness is used along with the material stiffness to obtain the comprehensive stiffness of the lattice structure. With particular emphasis on lattice materials, the chapter presents the derivation of their homogenized comprehensive, fourth order, stiffness tensor, from which the Poisson's ratios and the elastic moduli of the lattice material are derived. Examples of deriving the comprehensive stiffness properties of lattice materials with square and $3^3.4^2$ lattice topologies are presented Appendix H to demonstrate and explain numerically the steps of the analysis. The comprehensive stiffness of pin-jointed lattice materials is used for their classification. Finally, the effectiveness of the geometrical stiffness in enhancing the stiffness resistance of lattice material is analysed where the contribution of the geometrical stiffness to the comprehensive stiffness of the Kagome and the $3^3.4^2$ lattice materials is demonstrated at different levels of nominal strains of the solid material.

8.2 Comprehensive Stiffness System of Unit Cell Finite Structure

In the following, we start by formulating the comprehensive stiffness system of the finite structure of the unit cell before generalizing it to include the comprehensive stiffness of the infinite structure of the lattice. Finally, the infinite stiffness characteristics are homogenized to derive the macroscopic stiffness properties of the lattice material.

The stiffness system of a structure that has b elements connected between j nodes is presented in eqn (7.5). To account for the geometrical stiffness, eqn (7.5) is modified as:

$$(\mathbf{K}_E + \mathbf{K}_G)d = f \quad (8.4)$$

where $\mathbf{K}_E \in R^{nj \times nj}$ and $\mathbf{K}_G \in R^{nj \times nj}$ are the material and the geometrical stiffness matrices, respectively.

8.2.1 Comprehensive Stiffness of bar and frame Elements

Different approaches exist in the literature to derive the comprehensive stiffness characteristics of finite structures with pin- and rigid-jointed architectures. Guest (2006) presented a unified derivation for the comprehensive stiffness of pin-jointed finite structures. On the other hand, many introductory text books on structural analysis (McCormac, J.C., 2006; Przemieniecki, J. S., 1968; Livesley, R. K., 1975; Bickford, W. B., 1998; Reddy, J. N., 2002; McGuire, W., 2000; Cook, R.D., 2001) present a pin- as well as a rigid-jointed conventional geometrical stiffness derivations and formulations using the energy method. Pellegrino and Calladine (Pellegrino, S., Calladine, C.R., 1984; 1986) developed an approach based on the product force vector analysis. They considered a finite pin-jointed structure where the geometrical stiffness is only employed, as a special case, whenever there is an inextensional internal mechanism excited. Another approach is based on the theory of rigidity (Connelly, R., Whiteley, W., 1996) where the stability of the prestressed structures is discussed.

In this chapter, we follow the traditional formulation developed by Cook, et.al. (2001). We start by deriving the comprehensive stiffness matrices of each individual element within the finite structure before assembling them together in one global matrix system, which represents the comprehensive stiffness of the finite structure of the unit cell.

A. Comprehensive Stiffness of a Bar element: an Element in a Pin-Jointed Lattice Structure

Consider the linearly elastic, uniform and straight bar element, k , connected between nodes i and q , shown in Fig (8.2a). The bar element is oriented in the $(x_1 - y_1)$ local coordinate system, where the x_1 - axis is coincident with the bar neutral axis.

The axial strain in the bar is determined using the following large-deflection strain-displacement equation:

$$\varepsilon_{x_1 x_1} = \frac{\partial e_{kx_1}}{\partial x_1} + \frac{1}{2} \left(\frac{\partial e_{ky_1}}{\partial x_1} \right)^2 \quad (8.5)$$

where e_{kx_1} and e_{ky_1} are, respectively, the axial and the lateral linear displacements along the bar element in its local coordinate system.

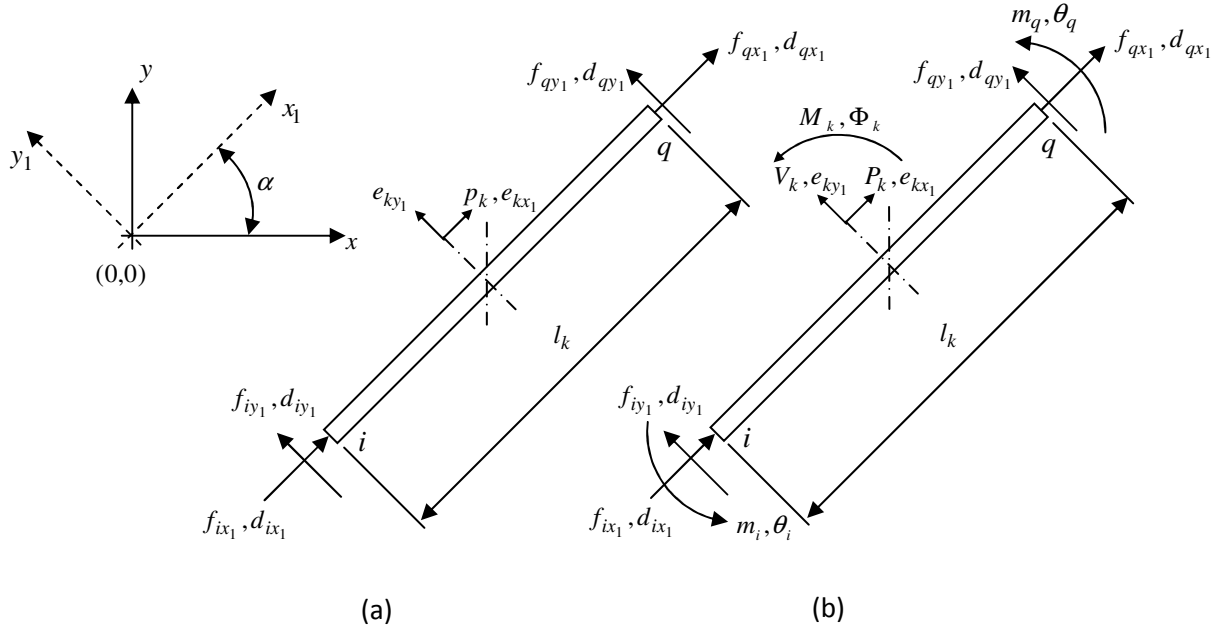


Fig (8.2) Bar element (left) and frame element (right) along with nodal degrees of freedom

The bar deformations are linearly related to the nodal deformations using the assumed shape-functions, as follows:

$$\begin{bmatrix} e_{kx1} \\ e_{ky1} \end{bmatrix} = \begin{bmatrix} 1-\xi & 0 & \xi & 0 \\ 0 & 1-\xi & 0 & \xi \end{bmatrix} \begin{bmatrix} d_{ix1} \\ d_{iy1} \\ d_{qx1} \\ d_{qy1} \end{bmatrix} \quad (8.6)$$

where $\xi = x_1/l_k$.

The strain energy, U_k , stored in a linearly elastic, uniform and straight bar element can be expressed as:

$$U_k = \frac{AE}{2} \int_0^{l_k} (\epsilon_{x_1 x_1})^2 dx_1 \quad (8.7)$$

Substituting eqn (8.6) into eqn (8.5), substituting the result into eqn (8.7) and neglecting higher-order terms (terms with power four), result in:

$$U_k = \frac{AE}{2l_k} (d_{ix1}^2 - 2d_{ix1} d_{qx1} + d_{qx1}^2) + \frac{AE}{2l_k^2} (d_{qx1} - d_{ix1}) (d_{iy1}^2 - 2d_{iy1} d_{qy1} + d_{qy1}^2) \quad (8.8)$$

The axial force in the bar element can be expressed as:

$$P_k = \frac{AE}{l_k} (d_{qx1} - d_{ix1}) \quad (8.9)$$

Substituting eqn (8.9) into eqn (8.8) gives:

$$U_k = \frac{AE}{2l_k} (d_{ix_1}^2 - 2d_{ix_1} d_{qx_1} + d_{qx_1}^2) + \frac{P_k}{2l_k} (d_{iy_1}^2 - 2d_{iy_1} d_{qy_1} + d_{qy_1}^2) \quad (8.10)$$

Using *Castigliano's* theorem (Renton, J.D., 2002), the nodal force-displacement relation, representing the bar element stiffness system, can be written as:

$$\frac{EA}{l_k} \begin{bmatrix} 1 & 0 & -1 & 0 \\ 0 & 0 & 0 & 0 \\ -1 & 0 & 1 & 0 \\ 0 & 0 & 0 & 0 \end{bmatrix} \begin{bmatrix} d_{ix_1} \\ d_{iy_1} \\ d_{qx_1} \\ d_{qy_1} \end{bmatrix} + \frac{P_k}{l_k} \begin{bmatrix} 0 & 0 & 0 & 0 \\ 0 & 1 & 0 & -1 \\ 0 & 0 & 0 & 0 \\ 0 & -1 & 0 & 1 \end{bmatrix} \begin{bmatrix} d_{ix_1} \\ d_{iy_1} \\ d_{qx_1} \\ d_{qy_1} \end{bmatrix} = \begin{bmatrix} f_{ix_1} \\ f_{iy_1} \\ f_{qx_1} \\ f_{qy_1} \end{bmatrix} \quad (8.11)$$

$$\text{or} \quad \left({}^l_p \mathbf{K}_{kE}^{bar} + {}^l_p \mathbf{K}_{kG}^{bar} \right) d_k^l = f_k^l \quad (8.12)$$

where ${}^l_p \mathbf{K}_{kE}^{bar}$ and ${}^l_p \mathbf{K}_{kG}^{bar}$ are, respectively, bar k material and geometrical stiffness matrices in the bar local coordinate system. The letters p , l , E and G correspond to pin-jointed, local coordinate, material and geometrical, respectively. $k \in \{1, \dots, b\}$ where b is number of elements in the unit cell.

The length of the bar can be expressed in terms of a reference length, L , as:

$$l_k = c_k L \quad (8.13)$$

where c_k is a constant that depends on the geometry of the unit cell.

Considering a reference length of unity and substituting eqn (8.13) into eqn (8.11) result in:

$$EA \begin{bmatrix} \frac{1}{c_k} & 0 & -\frac{1}{c_k} & 0 \\ 0 & 0 & 0 & 0 \\ -\frac{1}{c_k} & 0 & \frac{1}{c_k} & 0 \\ 0 & 0 & 0 & 0 \end{bmatrix} \begin{bmatrix} d_{ix_1} \\ d_{iy_1} \\ d_{qx_1} \\ d_{qy_1} \end{bmatrix} + P_k \begin{bmatrix} 0 & 0 & 0 & 0 \\ 0 & \frac{1}{c_k} & 0 & -\frac{1}{c_k} \\ 0 & 0 & 0 & 0 \\ 0 & -\frac{1}{c_k} & 0 & \frac{1}{c_k} \end{bmatrix} \begin{bmatrix} d_{ix_1} \\ d_{iy_1} \\ d_{qx_1} \\ d_{qy_1} \end{bmatrix} = \begin{bmatrix} f_{ix_1} \\ f_{iy_1} \\ f_{qx_1} \\ f_{qy_1} \end{bmatrix} \quad (8.14)$$

B. Comprehensive Stiffness of a Frame element: an Element in Rigid-Jointed Lattice Structure

Following the above procedure, the comprehensive stiffness of a linearly elastic, uniform and straight frame element, k , connected between nodes i and q of a rigid-jointed structure (Fig (8.2b)) can be written, neglecting the shear strain contribution to the stiffness, as:

$$\begin{aligned}
& \frac{EA}{l_k} \begin{bmatrix} 1 & 0 & 0 & -1 & 0 & 0 \\ 0 & 0 & 0 & 0 & 0 & 0 \\ 0 & 0 & 0 & 0 & 0 & 0 \\ -1 & 0 & 0 & 1 & 0 & 0 \\ 0 & 0 & 0 & 0 & 0 & 0 \\ 0 & 0 & 0 & 0 & 0 & 0 \end{bmatrix} \begin{bmatrix} d_{ix_1} \\ d_{iy_1} \\ \theta_i \\ d_{qx_1} \\ d_{qy_1} \\ \theta_q \end{bmatrix} + \frac{EI}{l_k^3} \begin{bmatrix} 0 & 0 & 0 & 0 & 0 & 0 \\ 0 & 12 & 6l_k & 0 & -12 & 6l_k \\ 0 & 6l_k & 4l_k^2 & 0 & -6l_k & 2l_k^2 \\ 0 & 0 & 0 & 0 & 0 & 0 \\ 0 & -12 & -6l_k & 0 & 12 & -6l_k \\ 0 & 6l_k & 2l_k^2 & 0 & -6l_k & 4l_k^2 \end{bmatrix} \begin{bmatrix} d_{ix_1} \\ d_{iy_1} \\ \theta_i \\ d_{qx_1} \\ d_{qy_1} \\ \theta_q \end{bmatrix} + \\
& \frac{P_k}{l_k} \begin{bmatrix} 0 & 0 & 0 & 0 & 0 & 0 \\ 0 & \frac{6}{5} & \frac{l_k}{10} & 0 & -\frac{6}{5} & \frac{l_k}{10} \\ 0 & \frac{l_k}{10} & \frac{2}{15}l_k^2 & 0 & -\frac{l_k}{10} & -\frac{l_k^2}{30} \\ 0 & 0 & 0 & 0 & 0 & 0 \\ 0 & -\frac{6}{5} & -\frac{l_k}{10} & 0 & \frac{6}{5} & -\frac{l_k}{10} \\ 0 & \frac{l_k}{10} & -\frac{l_k^2}{30} & 0 & -\frac{l_k}{10} & \frac{2}{15}l_k^2 \end{bmatrix} \begin{bmatrix} d_{ix_1} \\ d_{iy_1} \\ \theta_i \\ d_{qx_1} \\ d_{qy_1} \\ \theta_q \end{bmatrix} = \begin{bmatrix} f_{ix_1} \\ f_{iy_1} \\ m_i \\ f_{qx_1} \\ f_{qy_1} \\ m_q \end{bmatrix} \quad (8.15)
\end{aligned}$$

$$\text{or} \quad \left({}^l_r\mathbf{K}_{kE}^{bar} + {}^l_r\mathbf{K}_{kE}^{beam} + {}^l_r\mathbf{K}_{kG}^{frame} \right) d_k^l = f_k^l \quad (8.16)$$

where ${}^l_r\mathbf{K}_{kE}^{bar}$, ${}^l_r\mathbf{K}_{kE}^{beam}$ and ${}^l_r\mathbf{K}_{kG}^{frame}$ are the axial stiffness, the bending stiffness and the geometrical stiffness of the frame element. The subscript r corresponds to rigid-jointed. For details about the derivation of eqn (8.15), the reader is referred to (Cook, R.D., et.al., 2001). Considering a reference length of unity and substituting eqn (8.13) into eqn (8.15), we obtain:

$$\begin{aligned}
& EA \begin{bmatrix} \frac{1}{c_k} & 0 & 0 & -\frac{1}{c_k} & 0 & 0 \\ 0 & 0 & 0 & 0 & 0 & 0 \\ 0 & 0 & 0 & 0 & 0 & 0 \\ -\frac{1}{c_k} & 0 & 0 & \frac{1}{c_k} & 0 & 0 \\ 0 & 0 & 0 & 0 & 0 & 0 \\ 0 & 0 & 0 & 0 & 0 & 0 \end{bmatrix} \begin{bmatrix} d_{ix_1} \\ d_{iy_1} \\ \theta_i \\ d_{qx_1} \\ d_{qy_1} \\ \theta_q \end{bmatrix} + EI \begin{bmatrix} 0 & 0 & 0 & 0 & 0 & 0 \\ 0 & \frac{12}{c_k^3} & \frac{6}{c_k^2} & 0 & -\frac{12}{c_k^3} & \frac{6}{c_k^2} \\ 0 & \frac{6}{c_k^2} & \frac{4}{c_k} & 0 & -\frac{6}{c_k^2} & \frac{2}{c_k} \\ 0 & 0 & 0 & 0 & 0 & 0 \\ 0 & -\frac{12}{c_k^3} & -\frac{6}{c_k^2} & 0 & \frac{12}{c_k^3} & -\frac{6}{c_k^2} \\ 0 & \frac{6}{c_k^2} & \frac{2}{c_k} & 0 & -\frac{6}{c_k^2} & \frac{4}{c_k} \end{bmatrix} \begin{bmatrix} d_{ix_1} \\ d_{iy_1} \\ \theta_i \\ d_{qx_1} \\ d_{qy_1} \\ \theta_q \end{bmatrix} + \\
& P_k \begin{bmatrix} 0 & 0 & 0 & 0 & 0 & 0 \\ 0 & \frac{6}{5c_k} & \frac{1}{10} & 0 & -\frac{6}{5c_k} & \frac{1}{10} \\ 0 & \frac{1}{10} & \frac{2}{15}c_k & 0 & -\frac{1}{10} & -\frac{c_k}{30} \\ 0 & 0 & 0 & 0 & 0 & 0 \\ 0 & -\frac{6}{5c_k} & -\frac{1}{10} & 0 & \frac{6}{5c_k} & -\frac{1}{10} \\ 0 & \frac{1}{10} & -\frac{c_k}{30} & 0 & -\frac{1}{10} & \frac{2}{15}c_k \end{bmatrix} \begin{bmatrix} d_{ix_1} \\ d_{iy_1} \\ \theta_i \\ d_{qx_1} \\ d_{qy_1} \\ \theta_q \end{bmatrix} = \begin{bmatrix} f_{ix_1} \\ f_{iy_1} \\ m_i \\ f_{qx_1} \\ f_{qy_1} \\ m_q \end{bmatrix} \quad (8.17)
\end{aligned}$$

Equations (8.12) and (8.16) can be applied to each element of the unit cell for pin- and rigid-jointed lattices, respectively, before assembling them into the global matrix system of the stiffness of the whole finite structure. In order to assemble the stiffness systems of the individual cell elements into the global matrix system of the unit cell structure, the nodal degrees of freedom of the element have to be transformed from the element local coordinate system, $(x_1 - y_1)$, into the global coordinate system $(x - y)$ using, the counter clockwise rotation, orthogonal transformation, see § 7.3 for the orthogonal transformation of degrees of freedoms of frame elements. For a bar element, the orthogonal transformation matrix is formulated as:

$$\begin{bmatrix} d_{ix} \\ d_{iy} \\ d_{qx} \\ d_{qy} \end{bmatrix} = \begin{bmatrix} \cos(\alpha) & -\sin(\alpha) & 0 & 0 \\ \sin(\alpha) & \cos(\alpha) & 0 & 0 \\ 0 & 0 & \cos(\alpha) & -\sin(\alpha) \\ 0 & 0 & \sin(\alpha) & \cos(\alpha) \end{bmatrix} \begin{bmatrix} d_{ix_1} \\ d_{iy_1} \\ d_{qx_1} \\ d_{qy_1} \end{bmatrix} \quad \text{or} \quad d_k = \mathbf{Q} d_k^l \quad (8.18)$$

Using the transformation matrices, the comprehensive stiffness systems of the bar and the frame elements in the global coordinate system $(x - y)$ are formulated in eqns (8.19a) and (8.19b), respectively, as:

$${}_p \mathbf{K}_{kC}^{bar} d_k = ({}_p \mathbf{K}_{kE}^{bar} + {}_p \mathbf{K}_{kG}^{bar}) d_k = \mathbf{Q} ({}_p^l \mathbf{K}_{kE}^{bar} + {}_p^l \mathbf{K}_{kG}^{bar}) \mathbf{Q}^T d_k = f_k \quad (8.19a)$$

where ${}_p\mathbf{K}_{kE}^{bar} = \mathbf{Q}({}_p\mathbf{K}_{kE}^{bar})\mathbf{Q}^T$ and ${}_p\mathbf{K}_{kG}^{bar} = \mathbf{Q}({}_p\mathbf{K}_{kG}^{bar})\mathbf{Q}^T$ are, respectively, bar element k global axial and geometrical stiffness matrices.

$${}_r\mathbf{K}_{kC}d_k = ({}_r\mathbf{K}_{kE}^{bar} + {}_r\mathbf{K}_{kE}^{beam} + {}_r\mathbf{K}_{kG}^{frame})d_k = \mathbf{Q}({}_r\mathbf{K}_{kE}^{bar} + {}_r\mathbf{K}_{kE}^{beam} + {}_r\mathbf{K}_{kG}^{frame})\mathbf{Q}^T d_k = f_k \quad (8.19b)$$

where ${}_r\mathbf{K}_{kE}^{bar} = \mathbf{Q}({}_r\mathbf{K}_{kE}^{bar})\mathbf{Q}^T$, ${}_r\mathbf{K}_{kE}^{beam} = \mathbf{Q}({}_r\mathbf{K}_{kE}^{beam})\mathbf{Q}^T$ and ${}_r\mathbf{K}_{kG}^{frame} = \mathbf{Q}({}_r\mathbf{K}_{kG}^{frame})\mathbf{Q}^T$ are, respectively, frame element k global axial, bending and geometrical stiffness matrices.

The assembled global stiffness system of the pin-jointed and the rigid-jointed unit cell finite structures are formulated, respectively, as:

$${}_p\mathbf{K}_C d = \{ {}_p\mathbf{K}_E^{bar} + {}_p\mathbf{K}_G^{bar} \} d = f \quad (8.20a)$$

$${}_r\mathbf{K}_C d = \{ {}_r\mathbf{K}_E^{bar} + {}_r\mathbf{K}_E^{beam} + {}_r\mathbf{K}_G^{frame} \} d = f \quad (8.20b)$$

As shown in eqns (8.14) and (8.17), it is necessary to determine the axial forces in the individual elements of the unit cell in order to compute their geometrical stiffness matrices which are assembled into the global stiffness system of the unit cell. Details of computations of axial forces in the elements of the unit cell are presented in § 3.4.

As explained in § 3.4, the axial forces in the structural elements are composed of two terms: (i) t_f developed by the applied external loading, f , and (ii) S_G , developed by the imposed deformations into the redundant elements of the lattice structure. Both terms contribute to the structural geometrical stiffness. The current study focuses on the geometrical stiffness generated by the second term S_G as we are interested in studying ranges of stiffness characteristics offered by lattice materials and structures regardless of external loading. Once the applied external loading, in the form of macroscopic stress or strain fields, is determined, the term of the axial forces, t_f , can be obtained and a similar strategy can be followed to compute the additional geometrical stiffness developed by t_f .

The stiffness system of the unit cell finite structure can be easily extended to the stiffness system of the infinite lattice structure by applying the *Bloch's* theorem, see § 7.4. Details of the computation of the axial forces in the infinite lattice structure can also be found in § 3.4.

8.3 Macroscopic Stiffness of Lattice Material: the Homogenization Process of the Stiffness Properties of the Microscopic Lattice Structure:

The stiffness properties of the microscopic lattice structure are homogenized to generate the comprehensive, effective, macroscopic stiffness properties of the lattice material. This is done by using the *Cauchy-Born* hypothesis (Bhattacharya, K., 2003; Born, M., Huang, K., 1954; Maugin, G. A., 1992; Pitteri, M., & Zanzotto, G., 2003). Details of the application of the *Cauchy-Born* hypothesis are given in chapters four and seven.

Using the *Cauchy-Born* hypothesis, expressions of the nodal forces and deformations in terms of the macroscopic strain field are generated which can be expressed symbolically as:

$${}_p d_E^{bar} = {}_p^d \mathbf{M}_E^{bar} \bar{\boldsymbol{\epsilon}}, \quad {}_p f_E^{bar} = {}_p^f \mathbf{M}_E^{bar} \bar{\boldsymbol{\epsilon}} \quad (8.21a)$$

$${}_p d_G^{bar} = {}_p^d \mathbf{M}_G^{bar} \bar{\boldsymbol{\epsilon}}, \quad {}_p f_G^{bar} = {}_p^f \mathbf{M}_G^{bar} \bar{\boldsymbol{\epsilon}} \quad (8.21b)$$

$${}_r d_E^{bar} = {}_r^d \mathbf{M}_E^{bar} \bar{\boldsymbol{\epsilon}}, \quad {}_r f_E^{bar} = {}_r^f \mathbf{M}_E^{bar} \bar{\boldsymbol{\epsilon}} \quad (8.21c)$$

$${}_r d_E^{beam} = {}_r^d \mathbf{M}_E^{beam} \bar{\boldsymbol{\epsilon}}, \quad {}_r f_E^{beam} = {}_r^f \mathbf{M}_E^{beam} \bar{\boldsymbol{\epsilon}} \quad (8.21d)$$

$${}_r d_G^{frame} = {}_r^d \mathbf{M}_G^{frame} \bar{\boldsymbol{\epsilon}}, \quad {}_r f_G^{frame} = {}_r^f \mathbf{M}_G^{frame} \bar{\boldsymbol{\epsilon}} \quad (8.21e)$$

where \mathbf{M} matrices are transformation matrices from the vector of macroscopic strain field to the microscopic nodal forces and deformations. The superscripts, "d" and "f" indicate parameters corresponding to nodal displacements and nodal forces, respectively.

The generalized nodal forces and deformations, formulated in eqn (8.21), are used to derive the macroscopic stiffness properties of pin- and rigid-jointed lattice materials using the principle of virtual work (Timoshenko, S. P., & Young, D. H., 1945) and the *Hill-Mandel* principle (Maugin, G. A., 1992) of macro-homogeneity which result in:

$${}_p \mathbf{K}_{LE}^{bar} = \left(\frac{E}{2|Y|} \right) \left(\frac{\bar{\rho}_L}{c_T^\rho} \right) \left(\left({}_p^f \mathbf{M}_E^{bar} \right)^T \left({}_p^d \mathbf{M}_E^{bar} \right) \right) \quad (8.22a)$$

$${}_p \mathbf{K}_{LG}^{bar} = \left(\frac{E}{2|Y|} \right) \left(\frac{\bar{\rho}_L}{c_T^\rho} \right) \left(\left({}_p^f \mathbf{M}_G^{bar} \right)^T \left({}_p^d \mathbf{M}_G^{bar} \right) \right) \quad (8.22b)$$

$${}_r \mathbf{K}_{LE}^{bar} = \left(\frac{E}{2|Y|} \right) \left(\frac{\bar{\rho}_L}{c_T^\rho} \right) \left(\left({}_r^f \mathbf{M}_E^{bar} \right)^T \left({}_r^d \mathbf{M}_E^{bar} \right) \right) \quad (8.22c)$$

$${}_r\mathbf{K}_{LE}^{beam} = \left(\frac{E}{2|Y|} \right) \left(\frac{\rho_L}{c_T^\rho} \right) \left(\left({}^f_r\mathbf{M}_E^{beam} \right)^T \left({}^d_r\mathbf{M}_E^{beam} \right) \right) \quad (8.22d)$$

$${}_r\mathbf{K}_{LG}^{frame} = \left(\frac{E}{2|Y|} \right) \left(\frac{\rho_L}{c_T^\rho} \right) \left(\left({}^f_r\mathbf{M}_G^{frame} \right)^T \left({}^d_r\mathbf{M}_G^{frame} \right) \right) \quad (8.22e)$$

where c_T^ρ and $|Y|$ are, respectively, a density constant that depends on the topology of the unit cell and the in-plane area of the unit cell.

Using eqns (8.22), the comprehensive stiffness of a lattice material is formulated as:

$${}_p\mathbf{K}_{LC} = {}_p\mathbf{K}_{LE}^{bar} + {}_p\mathbf{K}_{LG}^{bar} \quad (8.23a)$$

$${}_r\mathbf{K}_{LC} = {}_r\mathbf{K}_{LE}^{bar} + {}_r\mathbf{K}_{LE}^{beam} + {}_r\mathbf{K}_{LG}^{frame} \quad (8.23b)$$

It worth mentioning that the ${}_p\mathbf{K}_{LE}^{bar} = {}_r\mathbf{K}_{LE}^{bar}$.

8.4 Classification of Lattice Material

Using eqn (8.23a), the comprehensive stiffness of pin-jointed lattice materials, it is possible to search for any macroscopic strain fields developed with zero macroscopic stress. A deformation with zero stress indicates failure of the lattice material as the strain field is developed due to inextensional periodic internal mechanisms in the infinite microstructure of the lattice. The failure macroscopic strain fields can be determined by computing the null space of the stiffness matrix. The existence of such strain fields is used as the criterion to classify lattice materials. Lattice materials can be classified into three classes, namely, Stretching Dominated Lattice Materials (SDLM), Bending Dominated Lattice Materials (BDLM) and Tensegrity Lattice Materials (TLM). Assume m_E^m and m_C^m are the numbers of macroscopic strain fields computed, respectively, from the null spaces of the material stiffness and the comprehensive stiffness matrices of the pin-jointed lattice material, the three classes can be determined as shown in table (8.1).

SDLMs are stable thanks to the material stiffness resistance of their pin-jointed versions. Although geometrical stiffness might be developed in SDLMs due to the static indeterminacy, however the role of the geometrical stiffness is limited in enhancing the material stiffness resistance rather than imparting stability. The secondary bending stiffness developed in SDLMs

due to the rigid-jointed nature of the materials' microstructures remains of a minor effect to the overall stiffness resistance of the SDLMs.

Table (8.1) Classification of lattice materials

Type	m_E^m	m_C^m	Class
I	$m_E^m = 0$	$m_C^m = 0$	SDLM
II	$m_E^m > 0$	$m_C^m > 0$	BDLM
III	$m_E^m > 0$	$m_C^m = 0$	TLM

In BDLMs, neither the material nor the geometrical stiffness resistances of the pin-jointed versions of the material microstructures can impart stability against macroscopic loadings. The only way to develop a loading carrying ability in the BDLM is to count for the bending stiffness of their microscopic constituents.

Pin-jointed versions of the TLMs are unstable under their material stiffness resistances. However they gain stability once their geometrical stiffness is superimposed to their material stiffness generating the material comprehensive stiffness.

This classification strategy is applied to the 13 lattice topologies, characterized in Appendix H, and the results are reported in table (8.2).

Recalling results of table (3.2) which summarizes the classification of infinite periodic lattice structures, it is realized that the Kagome and the SUBS infinite periodic structures are classified as BDLs while the Kagome and the SUBS lattice materials are classified as SDLM. We recall that such kind of topologies generate SDLMs that are structured by the concept of Periodicity Induced Stability (PIS). A lattice material structured by the concept of PIS, has a bending dominated infinite periodic microstructure, however, by considering the periodicity imposed by the *Cauchy-Born* kinematic boundary condition, the lattice material gains a macroscopic stable behavior as it fails extensionally under all modes of macroscopic loading.

Triangular - Triangular (TT) lattice materials received a considerable attention in literature (Hutchinson, R.G., 2004; Hutchinson, R.G. & Fleck, N.A., 2006). Hutchinson (2004) analyzed the infinite periodic lattice structure of the TT lattice and he found that this lattice does not

possess any microscopic internal mechanisms. This result is coincident with our result as we classified this periodic lattice structure as SDLS.

Table (8.2) Classification of lattice materials

Topology	ε_0	$m_E^m \& m_C^m$	Class
Square	-	$m_E^m > 0, m_C^m > 0$	BDLM
Triangular	-	$m_E^m = 0, m_C^m = 0$	SDLM
$3^3.4^2$	$\varepsilon_0 \in [-1,1] - \{0\}$	$m_E^m > 0, m_C^m = 0$	TLM
$3^4.6$	$\varepsilon_0 \in [-1,1] - \{0\}$	$m_E^m = 0, m_C^m = 0$	SDLM
DHT	$\varepsilon_0 \in [-1,1] - \{0\}$	$m_E^m = 0, m_C^m = 0$	SDLM
SUBS	$\varepsilon_0 \in [-1,1] - \{0\}$	$m_E^m = 0, m_C^m = 0$	SDLM
TT	$\varepsilon_0 \in [-1,1] - \{0\}$	$m_E^m > 0, m_C^m = 0$	TLM
SDBS	$\varepsilon_0 \in]0,1]$	$m_E^m = 0, m_C^m = 0$	SDLM
UBS	-	$m_E^m = 0, m_C^m = 0$	SDLM
DBS	$\varepsilon_0 \in [-1,1] - \{0\}$	$m_E^m = 0, m_C^m = 0$	SDLM
Patched Kagome	$\varepsilon_0 \in [-1,1] - \{0\}$	$m_E^m = 0, m_C^m = 0$	SDLM
SHT	$\varepsilon_0 \in [-1,1] - \{0\}$	$m_E^m = 0, m_C^m = 0$	SDLM
Kagome	$\varepsilon_0 \in [-1,1] - \{0\}$	$m_E^m = 0, m_C^m = 0$	SDLM

Hutchinson (2004) also studied the macroscopic behavior of the TT lattice and found this lattice deforms inextensionally under, macroscopic, hydrostatic, strain field as the TT microscopic topology of the TT lattice evolves to the Kagome lattice topology at which the lattice gains stability and develop SDLM. We reached to the same result once we consider only the material stiffness resistance of the TT lattice material. However, extending the analysis of the TT lattice to account for the geometrical stiffness of the lattice generates a stable TT lattice material as it generates a full rank comprehensive stiffness matrix capable of supporting all macroscopic strain fields. This result, classifies the TT lattice material as a TLM.

The last topology that we would like to highlight is the $3^3.4^2$ lattice, it is found that the infinite periodic lattice structure of the $3^3.4^2$ topology has tensegrity behavior and is classified as TLS; similarly, considering only the material stiffness resistance of the $3^3.4^2$ lattice material generates a

bending dominated behavior, however accounting for the macroscopic geometrical stiffness of the lattice generates a stable lattice material which classifies the $3^3.4^2$ lattice material as TLM. Another structuring concept can be introduced, namely, the Periodicity Induced Tensegrity (PIT). TLMs that are architected of BDLS are lattice materials structured by the PIT concept. So far, we did not determine a topology that has such behavior.

8.5 Effectiveness of the Geometrical Stiffness and its Contribution to the Lattice Material Stiffness Resistance:

We demonstrate the effectiveness of the geometrical stiffness and its contribution to the lattice material stiffness resistance by analysing the elastic properties of two lattice materials, the Kagome and the $3^3.4^2$ lattice materials.

8.5.1 The Kagome Lattice Material

Using the comprehensive stiffness properties of the Kagome lattice material, computed in Appendix H, it is possible to compute its relative elastic moduli (Elastic moduli of lattice material divided by the elastic modulus of the solid material used in manufacturing the lattice material) and Poisson's ratios as:

For pin-jointed Kagome lattice material:

$$\begin{aligned} \left({}_p\bar{E}_{LC} \right)_{xx} &= \left({}_p\bar{E}_{LC} \right)_{yy} = \bar{\rho}_L \frac{(\varepsilon_0 - 2)}{(\varepsilon_0 - 6)}, \quad {}_p\bar{G}_{LC} = \frac{1}{16} \bar{\rho}_L (2 - \varepsilon_0), \\ \left({}_p\nu_{LC} \right)_{xy} &= \left({}_p\nu_{LC} \right)_{yx} = -\frac{(\varepsilon_0 + 2)}{(\varepsilon_0 - 6)} \end{aligned} \quad (8.24a)$$

For rigid-jointed Kagome lattice material:

$$\begin{aligned} \left({}_r\bar{E}_{LC} \right)_{xx} &= \left({}_r\bar{E}_{LC} \right)_{yy} = \bar{\rho}_L \frac{(1250 + 208 \bar{\rho}_L - 375\varepsilon_0)}{3750 + 208 \bar{\rho}_L - 375\varepsilon_0}, \\ {}_r\bar{G}_{LC} &= \frac{\bar{\rho}_L}{10^4} (1250 + 208 \bar{\rho}_L - 375\varepsilon_0), \\ \left({}_r\nu_{LC} \right)_{xy} &= \left({}_r\nu_{LC} \right)_{yx} = -\frac{(-1250 + 208 \bar{\rho}_L - 375\varepsilon_0)}{3750 + 208 \bar{\rho}_L - 375\varepsilon_0} \end{aligned} \quad (8.24b)$$

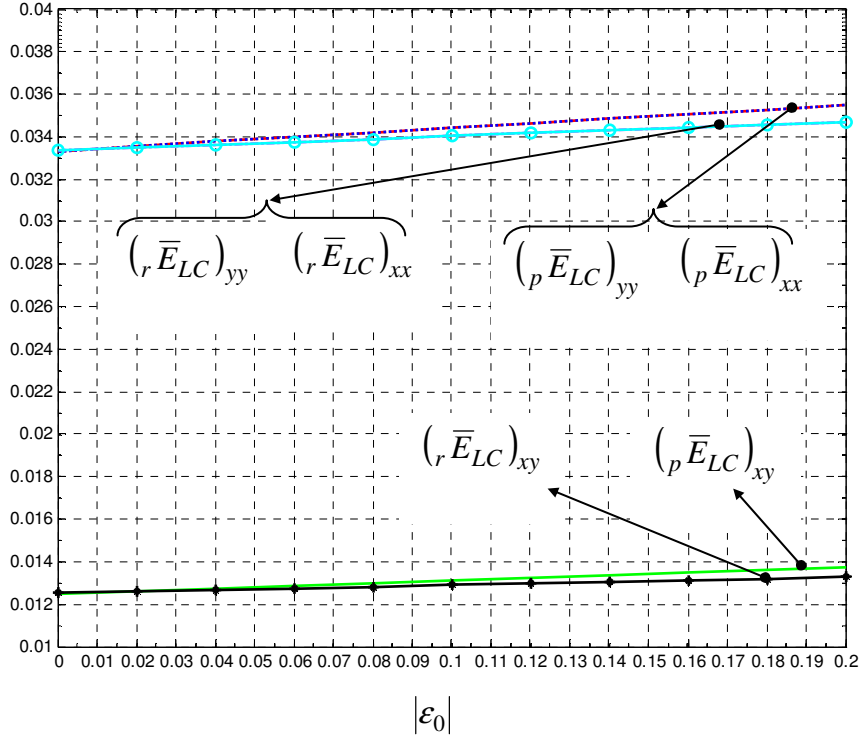


Fig (8.3) Variation of the elastic moduli of the Kagome lattice material with the nominal strain of the solid material

The effect of the geometrical stiffness can be ruled out by substituting $\epsilon_0 = 0$ in eqns (8.24) as it results in expressions of the elastic properties developed by material stiffness resistance rather than their comprehensive stiffness.

Considering a Kagome lattice material with relative density of $\bar{\rho}_L = 0.1$, and considering a nominal strain range of $\epsilon_0 = 0 : -0.2$, the variation of the lattice material elastic moduli against the solid material nominal strain is shown in Fig (8.3).

From Fig (8.3) it can be realized that the geometrical stiffness of the Kagome lattice material is of minor contribution to its comprehensive stiffness. Since the Kagome lattice material has a stretching dominated behavior then the material stiffness dominates the stiffness resistance of the lattice.

8.5.2 The $3^3.4^2$ Lattice Material

The relative elastic moduli and Poisson's ratios of the $3^3.4^2$ lattice material can be formulated as:

For pin-jointed $3^3.4^2$ lattice:

$$\begin{aligned} \left({}_p\bar{E}_{LC} \right)_{xx} &= 0.4045 \bar{\rho}_L, \left({}_p\bar{E}_{LC} \right)_{yy} = 0.4077 \bar{\rho}_L, {}_p\bar{G}_{LC} = -0.598 \bar{\rho}_L \varepsilon_0, \\ \left({}_p\nu_{LC} \right)_{xy} &= 0.15585, \left({}_p\nu_{LC} \right)_{yx} = 0.15462 \end{aligned} \quad (8.25a)$$

For rigid-jointed $3^3.4^2$ lattice:

$$\begin{aligned} \left({}_r\bar{E}_{LC} \right)_{xx} &= 0.4045 \bar{\rho}_L, \left({}_r\bar{E}_{LC} \right)_{yy} = 0.4077 \bar{\rho}_L, {}_r\bar{G}_{LC} = 3 \times 10^{-4} \left(93 \bar{\rho}_L^2 - 115 \varepsilon_0 \right), \\ \left({}_r\nu_{LC} \right)_{xy} &= 0.15585, \left({}_r\nu_{LC} \right)_{yx} = 0.15462 \end{aligned} \quad (8.25b)$$

From eqn (8.25) it can be realized that the geometrical stiffness of the $3^3.4^2$ contributes only to the material shear modulus as the Young's moduli are functions only in the lattice material relative density.

Considering a $3^3.4^2$ lattice material with relative density of $\bar{\rho}_L = 0.1$, and considering a nominal strain range of $\varepsilon_0 = 0 : -0.2$, the variation of the lattice material shear moduli against the solid material nominal strain is shown in Fig (8.4).

From Fig (8.4) it can be realized that the geometrical stiffness of the pin-jointed $3^3.4^2$ lattice material contributes significantly to its comprehensive stiffness. The geometrical stiffness becomes of less effect in the case of the rigid-jointed $3^3.4^2$ lattice material.

From Fig (8.5) it can be realized that the $3^3.4^2$ lattice material has Young's moduli that are better than those of the Kagome lattice material. On the other hand, the Kagome lattice material generates a better shear modulus at $\varepsilon_0 = 0$, than that developed by the $3^3.4^2$. By considering the geometrical stiffness, both lattice materials generate an equal shear stiffness resistance at $\varepsilon_0 = -0.234$ and the $3^3.4^2$ lattice material generates better shear resistances at $\varepsilon_0 < -0.234$.

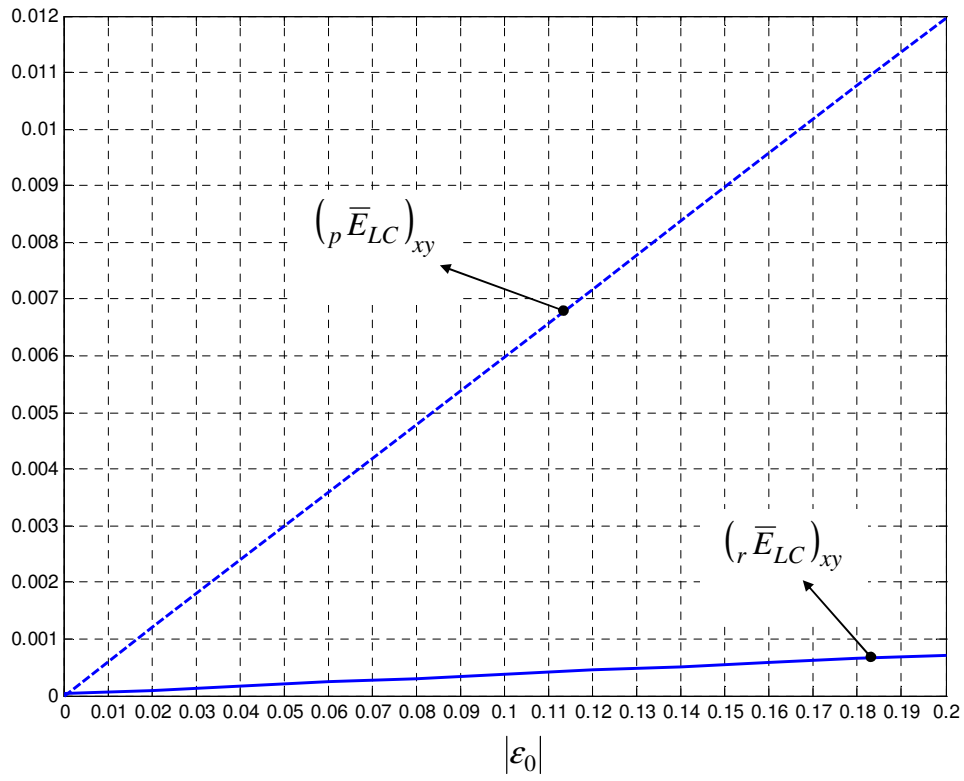


Fig (8.4) **Variation of the shear moduli of the $3^{3.4^2}$ lattice material with the nominal strain of the solid material**

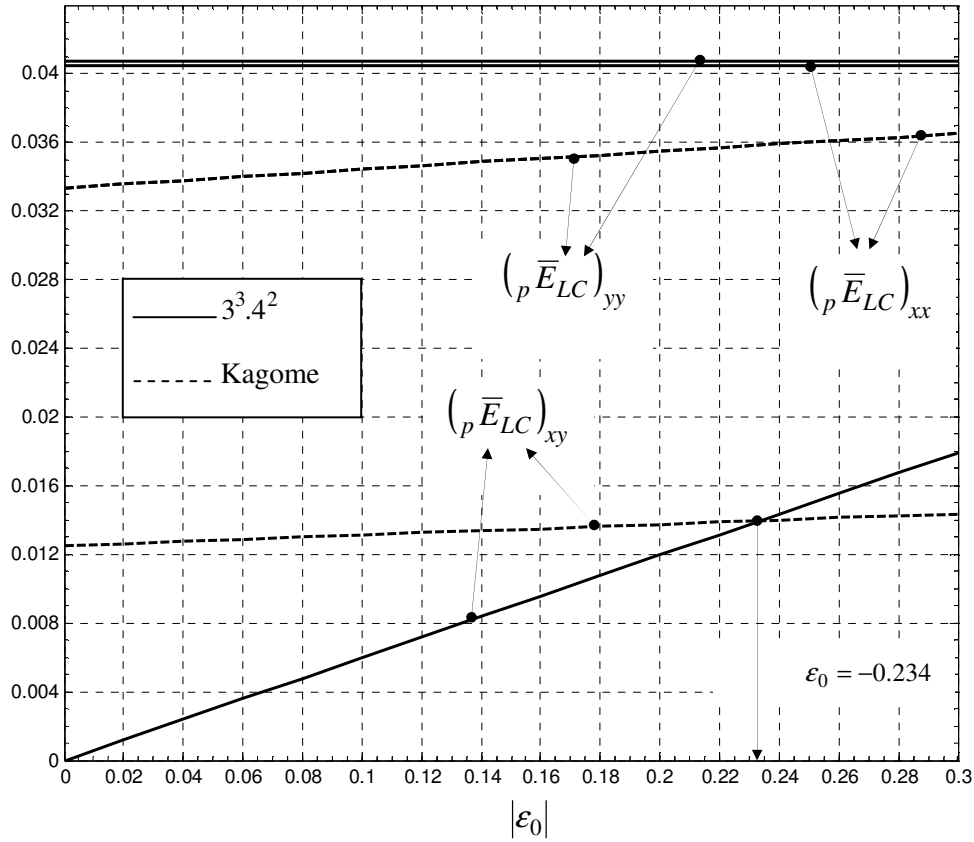


Fig (8.5) Comparison of the elastic moduli of the Kagome and the $3^3.4^2$ lattice materials

8.6 Conclusion

This chapter presented a matrix based approach to derive the comprehensive stiffness of periodic lattice structures and materials. The developed methodology is applied on pin- and rigid-jointed lattice structures. Homogenized stiffness characteristics of lattice materials are also derived. The effectiveness of the geometrical stiffness on the comprehensive stiffness of lattice materials is also discussed. Simple examples of deriving the comprehensive stiffness of the square and the $3^3.4^2$ lattice materials are reported and reported in Appendix H. The developed approach is applied to 11 lattice topologies where the homogenized comprehensive stiffness of lattice materials structured of pin- and rigid-jointed versions of those 11 topologies are reported in appendix H. The comprehensive stiffness properties of pin-jointed lattice materials are used for their classification. Three types of lattice materials are recognized, namely, SDLM, BDLM and TLM. TLMs are unstable under their material stiffness resistance where the materials possess

macroscopic strain fields generated by periodic internal mechanisms. Once the geometrical stiffness is superimposed to their material stiffness to formulate the lattice comprehensive stiffness, the lattice materials become stable and can support all macroscopic loadings, as the macroscopic kinematism is stiffened up by the geometrical stiffness developed by the tension fields in the lattice microstructure.

CHAPTER 9

Conclusions and Future work

9.1 Conclusions

1. An automated, systematic, matrix-based procedure for the determinacy analysis of infinite periodic structures with any arbitrary cell topology using the *Bloch*-wave method is developed. A new rule, namely, the Dummy Node Rule, supported by a simple scheme for its implementation, namely, the Dummy Node Scheme, is proposed to simplify and automate the analysis of infinite periodic structures that have unit cells with cell elements extending between adjacent cells.
2. The stiffening effect of the periodic states of self-stress to the periodic internal mechanisms is assessed using the Product Force Vector approach and the definiteness of the stress matrix developed by first-order, infinitesimal, periodic, internal mechanisms. The result of this analysis is used for the classification of periodic structures where three classes of periodic truss-like geometries are recognized, namely, stretching dominated, bending dominated and tensegrity lattice structures. It is found that the stretching dominated lattice structures are kinematically determinate. The bending dominated lattice structures are kinematically indeterminate and can be also statically indeterminate; however, the periodic states of self-stress fail in suppressing the internal mechanisms as the mechanisms are described as of a finite type. Tensegrity lattice structures are statically and kinematically indeterminate and the states of self-stress are capable of tightening-up the internal mechanisms as the mechanisms are classified as first-order infinitesimal mechanisms. The proposed analysis technique is applied to 19 2D lattice topologies and their determinacy analysis results are used for their classification. From the nineteen, two lattice topologies are classified as tensegrity lattice structures.
3. A systematic matrix-based procedure for the characterization of the specific stiffness and strength properties of lattice materials with any arbitrary microscopic topology is presented. The procedure makes use of the dummy node scheme to characterize lattice topologies with unit cells that have cell elements extending between adjacent unit cells. The elastic moduli of the stretching dominated topologies are plotted on design charts that can help select lattice materials that generate specific stiffness required by certain applications. It is found that lattice materials with the semi-uni-braced square and the semi-double-braced square topologies exhibit 11 % increase in the Young's moduli compared to the Kagome and the full triangulation lattice materials. On the

other hand, the lattice material with the double-braced square topology shows 17 % improvement in the specific shear modulus compared to the Kagome and the full triangulation lattice materials.

4. The developed characterization method is verified experimentally; the elastic and strength properties of the lattice material with the topology that has the Schläfli symbol of $3^4.6$ are tested. Three quasi-static tests are conducted to characterize the direct and the shear elastic and strength properties of the lattice material; the results are found in a good agreement with the theoretical ones. The maximum deviation of the experimental results from the theoretical computations is 15.2%, which is an acceptable error in the experimental studies on cellular solids.

5. Multiscale design charts for the selection of the geometric attributes of both the cell elements and columns made of octet-truss lattice material are presented. The charts help gain insight into the impact that the micro and macroscale geometry has on the overall strength of such columns. It is also a useful tool for designers to quickly determine the microscopic and the macroscopic geometrical details of their structural design. The design charts are developed by resorting to the method of shape transformers. It is demonstrated that shaping and sizing the cross-sections of the microscopic cell elements enhance the microscopic buckling resistance, which results in designing lattice materials with very low relative densities. Case studies are presented to demonstrate that the developed multiscale design strategy might save up to 50% of the structural weight as compared with the traditional design procedures.

6. An analytical approach to calculate the elastic properties of micro-truss lattice materials with rigid-jointed architectures is presented. Closed form expressions of the elastic moduli, Poisson's ratios and relative densities are obtained for 13 lattice topologies. The results for each topology are plotted into selection charts that illustrate the variation of the elastic moduli of the lattice material with respect to the material relative density. The contribution of the bending stiffness of the microscopic constituents of the stretching dominated lattice materials to their macroscopic homogenized stiffness properties is also analyzed. It is found that the closer the microscopic topology of the stretching dominated lattice material to the full triangulation, the less the microscopic bending stiffness contribution of the microscopic members. The contribution is negligible for lattice structures that possess no microscopic internal mechanisms in their pin-jointed counterpart. On the other hand, it is found that the Kagome lattice has constituent members whose bending resistant contribute up to 8% to the overall direct stiffness of the material. This is the highest contribution among the selected topologies. Although the semi-uni-

braced square lattice topology has internal mechanisms, the bending stiffness contribution of its microscopic constituents to the Young's moduli of the material is limited to 2.1%. The reason for this is that uni-directional loading in either x - and/or y - directions of the pin-jointed version of the semi-uni-braced square lattice does not excite its internal mechanism. On the other hand, the contribution of the bending stiffness to the homogenized shear stiffness is 17.5% for the semi-uni-braced square lattice since this topology has microscopic internal mechanisms that are excited by shear macroscopic loadings.

7. The anisotropic behavior of the lattice materials is also analyzed. The transformation of the material elastic properties through an angle $\theta \in [0^\circ, 360^\circ]$ is demonstrated on polar plots showing the variation of the lattice material elastic moduli with the direction of the applied load.

8. A matrix-based approach to derive the comprehensive stiffness of periodic truss-like structures and materials is presented. The developed methodology is applied to pin- and rigid-jointed lattice architectures. The effectiveness of the geometrical stiffness on the comprehensive stiffness of lattice materials is also discussed. The developed approach is applied to 13 lattice topologies where the homogenized comprehensive stiffness of lattice materials structured of pin- and rigid-jointed versions of those 13 topologies are reported.

9. The comprehensive stiffness properties of pin-jointed lattice materials are used for their classification. Three types of lattice materials are recognized, namely, stretching dominated, bending dominated and tensegrity lattice materials. Tensegrity lattice materials are unstable under their material stiffness resistance where the materials possess macroscopic strain fields generated by periodic internal mechanisms. Once the geometrical stiffness is superimposed to their material stiffness to formulate the lattice material comprehensive stiffness, the tensegrity lattice materials become stable and can support all macroscopic loadings, as the macroscopic kinematism is stiffened-up by the geometrical stiffness developed by the tension fields in the lattice microstructure. Two lattice materials with the $3^3.4^2$ and the Triangular-Triangular topologies are classified as tensegrity lattice materials. It is found that, at zero nominal strain, the pin-jointed $3^3.4^2$ lattice material has Young's moduli that are better than those of the pin-jointed Kagome lattice material. On the other hand, at nominal strain of $\varepsilon_0 = -0.234$, the $3^3.4^2$ lattice material generates a shear modulus that is equal to the shear modulus of the Kagome lattice material. This

analysis demonstrates the significance of the geometrical stiffness in enhancing the stiffness resistance of periodic lattice materials.

10. Two structuring concepts are introduced, the periodicity induced stability and the periodicity induced tensegrity. Bending dominated lattice structures are involved in both structuring concepts which develop stretching dominated lattice materials in the former and tensegrity lattice materials in the latter. Since the pin-jointed counterpart of a bending dominated lattice structure is not stable, the lattice material macroscopic stability is developed due to the periodic pattern of wave-functions propagation through the lattice microstructure. This feature is imposed in the characterization process by the application of the *Cauchy-Born* kinematic boundary condition.

9.2 Suggestions for Future Work

This study has shed some new light on the mechanics of lattice materials. Much remains to be done; the following are some suggestions.

1. Discrete Topology Optimization of Lattice Materials

Since this study has automated the analytical characterization process using the *Bloch*-wave method, it is possible to integrate the presented methodology to discrete topology optimization routines. For instance, a unit cell of a lattice material with a generic envelope can be generated by the ground-truss method (Da Silva Smith, O., 1996; 1998). This ground-truss unit cell can be optimized to maximize or minimize specific properties or can be tailored to meet specific design requirements.

2. Smart Lattice Materials, Adaptive Stiffness and Damping Characteristics

Pre-stressing has a significant effect on the stiffness and damping characteristics of structures (Elsayed, M.S.A. and Sherif, H.A., 2006). Statically indeterminate lattice materials have redundant microscopic cell elements. Embedding active members to replace these redundant elements enables the generation of different levels of pre-stressing within the lattice microstructure. The effect of pre-stress on the material stiffness and damping characteristics can be investigated.

Also, the redundant elements offer a multiple load paths within the microscopic architecture of the cellular solid which is a desirable feature in aerospace applications. The impact of adopting lattice

materials in aircrafts and vehicle structural designs can be investigated as well as their application in the field of vibration and acoustics.

3. Tensegrity Lattice Materials and Morphing Structures and Materials

Tensegrity structures are well known for their flexibility and adaptability especially for their use as morphing structures (Moored, K.W., and Bart-Smith, H., 2007). It is suggested to investigate the capabilities of tensegrity lattice materials as morphing materials where the control of the length of specific elements within the lattice microstructure could change the macroscopic geometry of the structural cellular components.

BIBLIOGRAPHY

- Abramowitz, M. and Stegun, I. A. (1970). *Handbook of Mathematical Functions with Formulas, Graphs, and Mathematical Tables*, New York: Dover Publications, Ninth printing.
- Aldrich, J. B. and Skelton, R. E. (2003a). Control/Structure Optimization Approach for Minimum-Time Reconfiguration of Tensegrity Systems. In *Proceedings of SPIE Smart Structures and Materials: Modeling, Signal Processing and Control*, vol. 5049, pp. 448:459, San Diego, CA, USA.
- Aldrich, J. B., Skelton, R. E. and Kreutz-Delgado, K. (2003b). Control Synthesis for a Class of Light and Agile Robotic Tensegrity Structures. In *Proceedings of the American Control Conf.*, pp. 5245:5251, Denver, CL, USA.
- Andrews, E.W., Gibson, L. J. and Ashby, M. F. (1999). The Creep of Cellular Solids, *Acta Mater.* Vol. 47, 10, pp. 2853:2863.
- Armstrong, M. A. (1988). *Groups and symmetry, Undergraduate texts in mathematics*, New York: Springer-Verlag.
- Aschbacher, M. (2000). *Finite group theory*, 2nd ed. Cambridge studies in advanced mathematics, 10, Cambridge: Cambridge University Press.
- Ashby, M. F., Evans, A. G., Fleck, N. A., Gibson, L. J., Hutchinson, J. W. and Wadley, H. N. G. (2000). *Metal Foams: A Design Guide, Butterworth Heinemann*. Oxford, UK: Butterworth Heinemann.
- Ashby, M.F. (2010). Materials and Shape, (1991), *Acta Metall Mater.* 39, 6, pp. 1025: 1039.
- Ashby, M.F. (2005). *Materials Selection in Mechanical Design*, 3rd ed., Elsevier, Butterworth-Heinemann.
- ASTM Standards, *Designation C363- 00, Standard Test Method for the Delamination Strength of Honeycomb Core Material*.
- ASTM Standards, *Designation C364- 99, Standard Test Method for Edgewise Compressive Strength of Sandwich Constructions*.
- ASTM Standards, *D 4255/D 4255M- 01, Standard Test Methods for In-Plane Shear Properties of Polymer Matrix Composite by the Rail Shear Method*.
- AULD, B. A. (1990). *Acoustic fields and waves in solids*, Krieger, Malabar.
- Banhart, J., Ashby, M. F. and Fleck, N. A. (1999). (eds) *Metal foams and foam metal structures*. Proc. Int. Conf. Metfoam 99. Bremen, Germany: MIT.

- Banhart, J., Ashby, M. F. and Fleck, N. A. (2001). (eds) *Metal foams and foam metal structures*. Proc. Int. Conf. Metfoam'01. Bremen, Germany: MIT.
- Banhart, J. and Fleck, N. A. (2003). (eds) *Metal foams and foam metal structures*. Proc. Int. Conf. Metfoam'03. Bremen, Germany: MIT.
- Bardenhagen, S. and Triantafyllidis, N. (1994). Derivation of higher order gradient continuum theories in 2,3-D non-linear elasticity from periodic lattice models. *J. Mech. Phys. Solids*, 42, 1, pp. 111:139.
- Bazant, Z.P. and Christensen, M. (1972). Analogy Between Micro-polar Continuum and Grid Frameworks under Initial Stress, *Int. J. Solids and Structures*, pp. 327:346.
- Beer, F.P. and Johnston, E.R. (1981). *Mechanics of Materials*, McGraw-Hill Int. Book Company.
- Bickford, W. B. (1998). *Advanced mechanics of materials*, Menlo Park: Addison- Wesley.
- Bhattacharya, K. (2003). *Microstructure of Martensite: Why it forms and how it gives rise to the shape-memory effect*. Oxford series on materials modeling, vol. 2. NY: Oxford U. Press.
- Bin, L. (2010). *Power and Energy Transduction in Piezoelectric Wafer Active Sensors for Structural Health Monitoring: Modeling and Applications*, PhD thesis, University of South Carolina.
- Bloch, F. (1928). Über die Quantenmechanik der Electronen in Kristallgittern, *Z Phys*, 53, 555:60.
- Bloch, F. (1976). Heisenberg and the early days of quantum mechanics, *Physics Today*, 29, 23.
- Born, M., Huang, K. (1954). *Dynamical Theory of Crystal Lattices*, Oxford: Clarendon Press.
- Bond, W. L. (1943), The Mathematics of the Physical Properties of Crystals, *Bell Sys. Tech. J.* 22, 1, (411).
- Brezny, R., Green, D. J. and Dam, C. Q. (1989). Evaluation of Strut Strength in Open-Cell Ceramics, *J. Am. Ceram. Soc.* 72, pp. 1145:1152.
- Brillouin, L. (1946). *Wave propagation in periodic structures: electric filters and crystal lattices*, Int. series in pure and applied physics. New York: McGraw- Hill.
- Brillouin, L. (1953). *Wave Propagation in Periodic Structures*, 2nd ed., Dover, New York.
- Byron, F. and Fuller, R. (1992). *Mathematics of Classical and Quantum Physics*, Dover Publications.
- Calladine, C.R. (1982). Modal stiffness of a pre-tensioned cable net, *Int. J. of Solids. Structures* 18, pp. 829:846.
- Calladine, C. R. (1978). Buckminster Fuller's Tensegrity Structures and Clerk Maxwell's Rules for the Construction of Stiff Frames. *Int. J. of Solids and Structures*, 14, pp.161:172.

- Calladine, C. R. and Pellegrino, S. (1991). First-Order Infinitesimal Mechanisms. *Int. J. of Solids and Fluids*, 27, 4, pp. 501:515.
- Calladine, C. R., and Pellegrino, S. (1992). Further remarks on First-Order Infinitesimal Mechanisms, *Int. J of solids and structures*, vol 29, 17, pp. 2119:2122.
- Calladine, C. R., and Pellegrino, S. (1991). Letter to the Editor, *Int. J of solids and structures*, vol 27, 4, pp. 517:519.
- Chiras, S., Mumm, D. R., Evans, A. G., Wicks, N., Hutchinson, J. W., Dharmasena, K., Wadley, H. N. G., and Fichter, S. (2002). The structural performance of near-optimized truss core panels. *Int. J. Solids. Structures*, 39, pp. 4093:4115.
- Christensen, R.M. (2000). Mechanics of cellular and other low-density materials, *Int. J. Solids. Structures*, 37, pp. 93:104.
- Colombo, P. and Scheffler, M. (2005) (eds) *Cellular ceramics*. Weinheim: Wiley–VCH.
- Connelly, R. and Whiteley, W. (1996). Second-Order Rigidity and Pre-stress Stability for Tensegrity Frameworks. *SIAM J. of Discrete Mathematics*, 9, 3, pp. 453:491.
- Cook, R.D., Malkus, D.S., Plesha, M.E., and Witt, R.J. (2001). *Concepts and Applications of Finite Element Analysis*, 4th ed. Wiley.
- Côté F., et.al. (2006). Dynamic fragmentation of brittle solids: a multi-scale model, *Int. J. Solids. Structures*, 43, pp. 6220:6242.
- Cundy, H. M. and Rolett, A. P. (1961). *Mathematical models*, Oxford: Clarendon Press.
- Da Silva Smith, O. (1998). Generation of ground structures for 2D and 3D design domains, *Engineering Computations*, Vol. 15, 4, pp. 462:500.
- Da Silva Smith, O. (1996). An interactive system for truss topology design, *Engineering Computations*, Vol. 27, 1-2, pp. 167:178.
- Davis, N.G, Teisen, J., Schuh, C., and Dunand ,D.C. (2001). Solid-state foaming of titanium by superplastic expansion of argon-filled pores. *J Mater Res*; 16, pp. 1508:1519.
- Deshpande, V. S., Ashby, M. F. and Fleck, N. A. (2001a). Effective properties of the octet-truss lattice material. *J. Mech. Phys. Solids*, 49, pp. 1724:1769.
- Deshpande, V. S., Ashby, M. F., Fleck, N. A. (2001a). Foam Topology Bending Versus Stretching Dominated Architectures, *J. Acta Materialia*, 49, 6, pp. 1035:1040.
- Deshpande, V.S., et.al. (2001). Effective properties of an octet truss lattice material, *J. of the Mechanics and Physics of Solids* 49, pp. 1747:1769.
- Deshpande, V. S. and Fleck, N. A. (2001). Collapse of truss core sandwich beams in 3-point bending, *Int. J. of Solids and Structures*, 38, pp. 6275:6305.

- De Oliveira, M. C. (2005). *Dynamics of Constrained Tensegrity Systems*. Technical report, Internal Report, Dynamic Systems Research, Inc., San Diego, CA, USA.
- De Oliveira, M. C. (2006). *Dynamics of Systems with Rods*. In Proceedings of the 45th IEEE Conf. on Decision and Control, San Diego, CA, USA.
- D'Estree Sterk, T. (2003). Using Actuated Tensegrity Structures to Produce a Responsive Architecture. In Proceedings of the 2003 Annual Conf. of the Association for Computer Aided Design In Architecture, pp 85:93, Indianapolis, IN, USA.
- D'Estree Sterk, T. (2006). The Office for Robotic Architectural Media and the Bureau for Responsive Architecture. URL www.oframbfra.com. Accessed September 4.
- R.H. Dieck, R.H. (1997). *Measurement Uncertainty: Methods and Applications: A Guide to Estimating and Understanding the Accuracy of Test and Experimental Data*. (2nd ed.), ISA, Research Triangle Park, NC.
- Douglas, T. Q. and Haydn, N.G.W. (2005). Cellular Metal Lattices with Hollow Trusses, *Acta Materialia* 53, pp. 303:313.
- El-Magd, E., Treppmann, C. and Korthäuer, M. (2003). Constitutive Modelling Of CK45N, Alznmgcu1.5 And Ti-6Al-4V in a Wide Range of Strain Rate and Temperature, *J. Phys. IV France* 110, 141.
- Elsayed, M.S.A., Pasini, D. (2008). Multiscale Model of the Effective Properties of the Octet-Truss Lattice Material, AIAA Technical Conferences, Victoria, BC, Canada, September 10-12, 2008.
- Elsayed, M.S.A., Pasini, D. (2009a). Mechanics of 2D Pin Jointed Lattice Structures, AES Technical Reviews, Part B: Int. J. of Advances in Mechanics and Applications of Industrial Materials, Vol. 1, 1, pp. 83:91.
- Elsayed, M.S.A., Pasini, D. (2009b). Characterization and Performance Optimization of 2D Lattice Materials with Hexagonal Bravais Lattice Symmetry, DETC2009-87540, Proceedings of the ASME Int. Design Engineering Technical Conferences and Computers and Information in Engineering Conf., IDETC/DAC-30, August 30 - September 2, San Diego, California, USA.
- Elsayed, M.S.A. (2009). The *Bloch's* Theorem, McGill University, Technical Report No. TR-MDOG-09-01.
- Elsayed, M.S.A., Pasini, D. (2010a). Multiscale Structural Design of Columns Made of Regular Octet-Truss Lattice Material, *Int. J. of Solids and Structures* Vol. 47, pp. 1764:1774.

- Elsayed, M.S.A., Pasini, D. (2010b). Analysis of the Elastostatic Specific Stiffness of 2D Stretching-Dominated Lattice Materials, *J. of Mechanics of Materials*, Vol. 42, 7, pp. 709:725.
- Elsayed, M.S.A., Pasini, D. (2010c). Stiffness Properties of Rigid-Jointed Periodic Cellular Solids, Submitted to the *Int. J. of Solids and Structures*, Manuscript Number: IJSS-D-10-00777.
- Elsayed, M.S.A. and Sherif, H.A. (2006). Pre-Tensioned Layer Damping as a New Approach for Vibration Control of Elastic Structures. *J. Vibration and Acoustics (ASME)*, Vol. 128, pp.338:346.
- Emmerich, D. G. (1996). Emmerich on Self-Tensioning Structures. *Int. J. of Space Structures*, 11, pp. 29:36.
- Emmerich, D. G. (1966). Reseaux. In *Proceedings of the Int. Conf. on Space Structures*, pp. 1059:1072, Guildford, England.
- Engel, B., Bourell, D.L. (2000). Titanium alloy powder preparation for selective laser sintering. *Rapid Prototyping J.*, Vol. 6, 2, pp. 97:106.
- Ericksen, J. L. (1984). In *Phase Transformations and. Material Instabilities in Solids*, edited by Gurtin, M. E., New York: Academic Press.
- Eringen, A.C. (1968). Theory of micro-polar elasticity, Chap. 7 of *Fracture* (ed. Liebowitz, H.), Vol. 2, pp. 621:729.
- Eringen, A.C. (1966) Theory of micro-polar fluids, *J. Math. Mech.*, 16, 1:18.
- Evans, A. G., Hutchinson, J. W., Fleck, N. A., Ashby, M. F., and Wadley, H. N. G. (2001). The topological design of multifunctional cellular metals, *Prog. Mater. Sci.*, 46, 3–4, pp. 309:327.
- Fan, H.L., Fang, D.N., and Jing, F.N. (2008). Yield surfaces and micro-failure mechanism of block lattice truss materials, *J. Material and Design*, 29, pp. 2038:2043.
- Fleck, N.A., Deshpande, V.S. and Ashby, M.F. (2010). *Micro-Architected Materials: Past, Present and Future*, Proceeding of the Royal Society A.
- Frederickson, G. N. (1997). *Dissections: plane and fancy*, Cambridge: Cambridge.
- Fuller, R. B. (1962).US Patent 3 063 521 Tensile Integrity Structures. United States Patent Office.
- Fuller, R. B. (1976). *And It Came to Pass - Not to Stay*, Macmillan, New York.
- Gent, A. N. and Thomas, A. G., *J. Appl. Polym. Sci.* 1, 107. (1959).
- Gibson, L. J. and Ashby, M. F. (1997). 2nd ed., *Cellular Solids: Structure and Properties*, Cambridge solid-state science series, Cambridge University Press.

- Gibson, L. J. (1989). Modeling the Mechanical Behavior of Cellular Materials, *Materials Science and Engineering*, A 110, pp. 1:36.
- Gough, M. (1998). In the Laboratory of Constructivism: Karl Ioganson's Cold Structures. *JSTOR*, 84, pp. 90:117.
- Greenberg, M. (1998). *Advanced Engineering Mathematics* (2nd ed.), Prentice Hall, ISBN 0-13-321431-1.
- Grosso, G., and Pastori-Parravicini, G. (2000). *Solid state physics*, London: Academic Press.
- Guest, S. (2006). The Stiffness of Prestressed frameworks: A unifying approach, *Int. J. of Solids. Structures*, 43, pp. 842:854.
- Guest, S.D. and Hutchinson, J.W. (2003). On the Determinacy of Repetitive Structures, *J. of Mechanics and Physics of Solids*, 51, 3, pp. 383:391.
- Hanaor, A. (1988). Prestressed Pin-Jointed Structures - Flexibility Analysis and Prestress Design. *Computers and Structures*, 28, pp. 757:769.
- Hanaor, A. (1994). Geometrically Rigid Double-Layer Tensegrity Grids. *Int. J. of Space Structures*, 9, pp. 227:238.
- Hanaor, A. (1992). Aspects of Design of Double-Layer Tensegrity Domes. *Int. J. of Space Structures*, 7, pp. 101:113.
- Hassani, B., and Hinton, E. (1998a). A review of homogenization and topology optimization I | homogenization theory for media with periodic structures. *Computers and Structures*, 69, pp. 707:717.
- Hassani, B., and Hinton, E. (1998b). A review of homogenization and topology optimization II | analytical and numerical solution of homogenization equations. *Computers and Structures*, 69, pp. 719:738.
- Hassani, B., and Hinton, E. (1998c). A review of homogenization and topology optimization III | topology optimization using optimality criterion. *Computers and Structures*, 69, 739:756.
- Hearmon, R. F. S. (1946). The Elastic Constants of Anisotropic Materials, *Rev. Mod. Phys.* 18, pp. 409:440.
- Hill, V. E. (2000). *Groups and characters*, Boca Raton: Chapman and Hall/CRC Press.
- Hinnerichs, T.D., Carne, T. G., Lu, Wei-Yang, Stasiunas, E. C., Neilsen, M. K., Scherzinger, W. and Rogillio, B. R. (2006). *Characterization of Aluminum Honeycomb and Experimentation for Model Development and Validation*, Vol. II: Honeycomb Experimentation for Model Development and Validation, Sandia Report.

- Hoff, N.J. and Fernandez-Sintes, J. (1980). *Kinematically unstable space frameworks* (2nd Edn). In: S. Nemat-Nasser, Editor, *Mechanics Today* **Vol. 5**, Pergamon Press, Oxford, Chap. 7.
- Hoffmeister, B. K., Smith, S. R., Handley, S. M., and Rho, J. Y. (2000). Anisotropy of Young's modulus of human tibial cortical bone, *J. of Medical and Biological Engineering and Computing*, Vol. 38, 3, pp. 333:338.
- Hollenberg, G. W. , G. R. Terwilliger, and R. S . Gordon. (1971). Calculation of Stresses and Strains in Four-Point Bending Creep Tests, *J. Am. Cerunz. Soc.*, 54, 4, pp. 196:199.
- Hongqing V. W., (2005), A Unit Cell Approach for Lightweight Structure and Compliant Mechanism, PhD thesis, Georgia Institute of Technology.
- Horn, Roger A. and Johnson, Charles R. (1985). *Matrix Analysis*, Cambridge University Press.
- Horn, Roger A. and Johnson, Charles R. (1991). *Topics in Matrix Analysis* , Cambridge University Press.
- Howard, D. Curtis, (1997). *Fundamentals of Aircraft Structural Analysis*, WCB McGraw- Hill.
- Huang, J. S. and Gibson, L. (1991a). Fracture toughness of brittle honeycombs. *J. Acta Metall. Mater.* 39, pp. 1617:1626.
- Huang, J. S. and Gibson, L. (1991b). Fracture toughness of brittle foams. *J. Acta Metall. Mater.* 39, pp. 1627:1636.
- Hutchinson, R. G. and Fleck, N.A. (2006). The structural performance of the periodic truss, *J. of the Mechanics and Physics of Solids*, 54, 4, pp. 756:782.
- Hutchinson R.G. (2004). *Mechanics of Lattice Materials*, Ph.D. thesis, Cambridge University.
- Hyun, S. and Torquato, S. (2002). Optimal and manufacturable two-dimensional Kagome-like cellular solids. *J. Mater. Res* 17, pp. 137:144.
- James, G., Liebeck, M. (2001). *Representations and characters of groups*, 2nd ed. Cambridge: Cambridge University Press.
- Jones, W., and March, N. H. (1973). *Theoretical solid state physics: perfect lattices in equilibrium*, Vol. 1. London: Wiley-Interscience.
- Joshi, S., Berglind, L., Jaehyung Ju, R., Summers, J. and Desjardins, J. (2010). Experimental Damage Characterization of Hexagonal Honeycombs Subjected to In-Plane Shear Loading; ASME Technical Publication. DETC2010-28549, IDETC/CIE Conf., Montreal, Quebec, Canada.
- Kebiche, K., Kazi-Aoual, M.N. and Motro, R. (1999). Geometrical Nonlinear Analysis of Tensegrity Systems. *J. of Engineering Structures*, 21, 9, pp. 864:876.
- Kelvin, (1887). The Optical Rotatory Power of Helical Molecules, *Philos. Mag.*, 24, pp. 503:514.

- Kollar, L., and Hegedus, I. (1985). *Analysis and design of space frames by the continuum method. Developments in civil engineering*, vol. 10. Amsterdam: Elsevier.
- Körner, C. (2008). *Integral Foam Molding of Light Metals: Technology, Foam Physics and Foam Simulation*, Springer-Verlag Berlin Heidelberg.
- Krempl, E. and Khan, F. (2003). Rate (Time)-Dependent Deformation Behavior: An Overview of Some Properties of Metals and Solid Polymers, *Int. J. of Plasticity* 19, pp. 1069:1095.
- Kruth, J.P., et.al. (2005). Benchmarking of Different SLS/SLM Processes as Rapid Manufacturing Techniques, *Int. Conf. of Polymers and Moulds Innovations (PMI) Gent*, Belgium, Apr 20-23, pp. 1:7.
- Kuznetsov, E. N. (1989). On immobile kinematic chains and a fallacious matrix analysis. *J. Appl. Mech.* 56, pp. 222:224.
- Kuznetsov, E. N. (2000). On the evaluation of statical-kinematic stiffness matrix for underconstrained structural systems, *Int. J. of Solids and Structures*, 37, 15, pp. 2215:2223.
- Kuznetsov, E.N. (1997). Orthogonal load resolution and statical-kinematic stiffness matrix, *Int. J. of Solids and Structures* 34, pp. 3657–3671.
- Lan, T. T. (1984). Recent trends and developments of space trusses in China. pp 22:35 of: Nooshin, H. (ed), 3rd Int. Conf. on Space Structures. London: Elsevier.
- Langley, R. S. (1993). A dynamic stiffness/boundary element method of the prediction of interior noise levels, *J. Sound Vib.* 167, pp. 377:381.
- Langley, R. S., Bardell, N. S., and Ruivo, H. M. (1997). The response of two-dimensional periodic structures to harmonic point loading: a theoretical and experimental study of a beam grillage, *J. Sound Vib.* 207, pp. 521:535.
- Lee, S., Barthelat, F., Moldovan, N., Espinosa, H.D. and Wadley, H.N.G. (2006). Deformation Rate Effects on Failure Modes of Open-Cell Al Foams and Textile Cellular Materials, *Int. J. of Solids and Structures* 43 (1), pp. 53:73.
- Levi-Civita, T., Amaldi, U., *Lezioni di Meccanica Razionale* (1930). 2nd ed., Vol. 1, Zanichelli, Bologna, (In Italian).
- Livesley, R. K. (1975). *Matrix methods of structural analysis*, 2nd edn. Pergamon int. library of science, technology, engineering and social studies. Oxford: Pergamon Press.
- Lockwood, E. H., Macmillan, R. H. (1978). *Geometric symmetry*, Cambridge: Cambridge University Press.
- Maiti, S. K., Gibson, L. J. and Ashby, M. F. (1984). Deformation and Energy Absorption Diagrams for Cellular Solids, *Acta Metall.* Vol. 32, II, pp. 1963:1975.

- Makowski, Z S (Editor). (1981). *Analysis, Design and Construction of Double Layer Grids*, Applied Science Publishers Ltd, (Obtainable from Chapman and Hall Publishers).
- Maugin, G. A. (1992). *Thermo-Mechanics of Plasticity and Fracture*, Cambridge texts in applied mathematics. Cambridge: Cambridge University Press.
- Maxwell, J. C. (1864). On the Calculation of the Equilibrium and Stiffness of Frames. *Phil. Mag.*, 27(294), Paper XXVI in *Collected Papers*, Cambridge University Press, Cambridge, U.K, (1890).
- McCormac, J.C. (2006). *Structural Analysis: Using Classical and Matrix Methods*, 4th ed., Wiley.
- McGuire, W., Gallagher, R.H., Ziemian, R.D. (2000). *Matrix Structural Analysis*, 2nd ed., John Wiley and Sons Publishers, New York, New York.
- Megson, T.H.G. (2003). *Aircraft Structures for Engineering Students*, 3rd ed, Butterworth-Heinemann.
- Mohr, O. (1885). Beitrag zur Theorie des Fackwerkes, *Der Civilingenieur* 31, pp. 289:310.
- Moored, K.W., and Bart-Smith, H. (2007). The Analysis of Tensegrity Structures for the Design of a Morphing Wing, *J. Appl. Mech.*, July, Vol. 74, 4, pp. 668:667.
- Motro, R. (2003). *Tensegrity: Structural Systems for the Future*. Kogan Page Science, London.
- Motro, R., Najari, S. and Jouanna, P. (1986). Static and Dynamic Analysis of Tensegrity Systems. In *Proceedings of ASCE Int. Symposium on Shells and Spatial Structures, Computational Aspects*, pp. 270:279, New York, NY, USA, Springer.
- Murakami, H. (2001). Static and Dynamic Analyses of Tensegrity Structures, Part 1. Nonlinear Equations of Motion. *Int. J. of Solids and Structures*, 38, pp. 3599:3613.
- Murakami, H. and Nishimura, Y. (2001a). Initial Shape Finding and Modal Analyses of Cycle Right-Cylindrical Tensegrity Modules. *Computers and Structures*, 79, pp. 891:917.
- Murakami, H. and Nishimura, Y. (2001b). Static and Dynamics Characterization of Some Tensegrity Modules. *J. of Applied Mechanics*, 68, pp. 19:27.
- Negroponte, N. (1975). *Soft Architecture Machines*. MIT Press, Cambridge, MA, USA.
- Noor, A.K. and Nemeth, M.P. (1980). Micro-polar Beam Models for Lattice Grids With Rigid Joints, *Computer Methods in Applied Mechanics And Engineering*, 21, pp. 249:263.
- Oppenheim, I.J. and Williams, W.O. (2000). Geometric Effects in an Elastic Tensegrity Structure. *J. of Elasticity*, 59, pp. 51:65.
- Parkes, E.W. (1974). *Braced Frameworks* (2nd Edn), Pergamon Press, Oxford.
- Parsons, R. T. (2009). *Experimental Characterization of the Compressive and Shear Behavior of Square Cell Titanium Honeycomb*, Msc Thesis, Kansas State University.

- Pasini, D. (2007). Shape Transformers for Material and Shape Selection of Lightweight Beams, , J. of Material and Design, Vol 28/7, pp. 2071: 2079.
- Pasini, D., et.al. (2003). Structural efficiency maps for beams subject to bending, J. of Material, Design and Applications, Vol. 217, pp. 207: 220.
- Pasini, D., et.al. (2006). A method for selecting macro-scale structures with axially loaded members, Int J Mech Mater Des, 3, 2, pp. 185: 199.
- Patel, M. R. and Finnie, I. (1970). Structural Features and Mechanical Properties of Rigid Cellular Plastics, J. Mater. 5, pp. 909:932.
- Paul, C., Roberts J. W., Lipson, H. and Valero-Cuevas, F. J. (2005). Gait Production in a Tensegrity Based Robot. In Proceedings of the Int. Conf. on Advanced Robotics (ICAR), Seattle, Seattle, WA, USA.
- Pellegrino, S. (1993). Structural computations with the singular value decomposition of the equilibrium matrix, Int. J. Solids. Structures, 34, 21, pp. 3025: 2035.
- Pellegrino, S. (1988). *Static response of prestressed mechanisms*, Cambridge University, Engineering Department, (Technical Report) CUED/D-Struct, n 120, var paging.
- Pellegrino, S. and Calladine, C. R. (1986). Matrix Analysis of Statically and Kinematically Indetermined Frameworks. Int. J. of Solids and Structures, 22, pp. 409:428.
- Pellegrino, S. (1990). Analysis of Prestressed Mechanisms, Int. J. of solids and Structures, Vol. 26, No 12, pp. 1329:1350.
- Pellegrino, S., Calladine, C.R. (1984). Two-Steps Matrix Analysis of Prestressed Cable Nets, Proceeding 3rd Int. Conf. Space Structure, Guildford, Elsevier Applied Science.
- Phan-Tien and Karihaloo (1994). 1993N. Phan-Tien and B.L. Karihaloo, Materials with negative Poisson's ratio: a qualitative micro-structural model, J. Appl. Mech. Vol. 61, 4, pp. 1001:1004.
- Phani, S.A., Woodhouse, J., and Fleck, N. A. (2006). Wave propagation in two-dimensional periodic lattices. J. of the Acoustical Society of America, 119, 4, pp. 1995:2005.
- Phani, S.A., Fleck, N. A., (2008). Elastic boundary layers in Two-Dimensional isotropic Lattices. J. Appl. Mech., Vol. 75.
- Prud'homme, C., Rovas, D., Veroy, K., Maday Y., Patera, A.T. and Turinici, G. (2002). Reliable real-time solution of parametrized partial differential equations: Reduced-basis output bound methods, J. Fluids Engrg. 124, 1, pp. 70:80.
- Pitteri, M., and Zanzotto, G. (2003). *Continuum Models for Phase Transitions and Twinning in Crystals*, Boca Raton: Chapman and Hall/CRC Press.

- Przemieniecki, J. S. (1968). *Theory of matrix structural analysis*, 2nd edn. New York: McGraw-Hill.
- Queheillalt, D. T. and Wadley, H. N. G. (2005a). Cellular material lattices with hollow trusses. *Acta Mater.* 53, pp. 303:313.
- Quirrant, J. , Kazi-Aoual, M. N. and Motro, R. (2003). Designing Tensegrity Systems: The Case of a Double Layer Grid. *Engineering Structures*, 25, pp. 1121:1130.
- Ramamurty, U., Paul, A. (2004). Variability in mechanical properties of a metal foam, *Acta Materialia*, 52, pp. 869:876.
- Reddy, J. N. (2002). *Energy principles and variational methods in applied mechanics*, New Jersey: John Wiley.
- Renton, J. D. (1984). The beam-like behavior of space trusses. *AIAA J.*, 22, pp. 273:280.
- Renton, J.D. (2002). *Elastic Beams and Frames*, 2nd ed., Horwood Publishing Limited, England.
- Rochus, P., et.al. (2007). New Applications of Rapid Prototyping and Rapid Manufacturing (RP/RM) Technologies for Space Instrumentation, *Acta Astronautica* 61, pp. 352:359.
- Sadao, S. (1996). Fuller on Tensegrity. *Int. J. of Space Structures*, 11, pp. 37:42.
- Sarsfield, H., Li Wang, Nikica Petrinic (2007). An Experimental Investigation of Rate-Dependent Deformation and Failure of Three Titanium Alloys, *J Mater Sci*, 42, pp. 5085:5093.
- Schraad, M. W., and Triantafyllidis, N. (1997a). Scale effects in media with nearly periodic microstructures, part I: macroscopic properties. *Trans. ASME: J. Appl. Mechanics*, 64, pp. 751:762.
- Schraad, M. W., and Triantafyllidis, N. (1997b). Scale effects in media with nearly periodic microstructures, part II: failure mechanisms. *Trans. ASME: J. Appl. Mechanics*, 64, pp. 763:771.
- Schwarzenbach, D. (1996). *Chrystallography*, England, John Wiley and Sons Ltd.
- Seitz, F. (1936). *Solid State Physics*, *Ann. Math.* 37, 17.
- Sener, M., Utku, S., Wada, B.K. (1994). Geometry control in prestressed adaptive space trusses, *J. of Smart Materials and Structures*, 3, 219.
- Shwartz, D. S., Shih, D. S., Evans, A. G. and Wadley, H. N. (1998). (eds) *Porous and cellular materials for structural applications*. Materials Research Society Proceedings, vol. 521. Warrendale, PA: MRS.
- Sigmund, O. (1994). Materials with prescribed constitutive parameters: an inverse homogenization problem. *Int. J. of Solids and Structures*, 31, 17, pp. 2313:2329.

- Simmons, A. H., Michal, C.A. and Jelinski. L. W. (1996). Molecular Orientation and Two-Component Nature of the Crystalline Fraction of Dragline Silk. *Science*, 271, pp. 84:87.
- Skelton, R. E. and Sultan, C. (1997). Controllable Tensegrity, A New Class of Smart Structures. In *Proceedings of the SPIE 4th Symposium on Smart Structures and Materials*, vol. 3039, pp. 166:177.
- Skelton, R. E. and Sultan, C. (2003). Deployment of Tensegrity Structures. *Int. J. of Solids and Structures*, 40, pp. 4637:4657.
- Skelton, R. E., Helton, J. W., Adhikari, R., Pinaud, J. P. and Chan, W. L. (2001a). An Introduction to the Mechanics of Tensegrity Structures. In *Proceedings of the 40th IEEE Conf. on Decision and Control*, Orlando, FL, USA.
- Skelton, R. E., Pinaud, J. P., and Mingori, D. L. (2001c). Dynamics of the Shell Class of Tensegrity Structures. *J. of the Franklin Institute*, 338(2-3), pp. 255:320.
- Skelton, R. E. (2005). Dynamics and Control of Tensegrity Systems. In *Proceedings of the IUTAM Symposium on Vibration Control of Nonlinear Mechanisms and Structures*, vol. 130, Munich, Germany.
- Snelson, K. (1996). Snelson on the Tensegrity Invention. *Int. J. of Space Structures*, 11, pp. 43:48.
- Snelson, K. (1965). US Patent 3 169 611 Continuous Tension Discontinuous Compression Structures. United States Patent Office.
- Song, B. , Ge, Y., Chen, W.W. and Weerasooriya, T. (2007). Radial Inertia Effects in Kolsky Bar Testing of Extra-Soft Specimens, *Experimental Mechanics*, 47, pp. 659:670 .
- Stewart (2008). J., *Vector Calculus*, *Calculus: Early Transcendentals*, 6th ed., Thomson Brooks Cole.
- Strang G. (1998). *Introduction to Linear Algebra*, 3rd ed., Wellesley-Cambridge Press.
- Sultan, C. (2006). Tensegrity Structures Research Evolution. In *Proceedings of the 45th IEEE Conf. on Decision and Control*, San Diego, CA, USA.
- Sultan, C. and Skelton, R. E. (1997). Integrated Design of Controllable Tensegrity Structures. In *Proceedings of the ASME Int. Congress and Exposition*, vol. 54, pp. 27:37.
- Syozaki, I. (1972). *Transformation of Ising models. In Phase transitions and critical phenomena* (eds C. Domb and M. S. Green). New York, NY: Academic Press.
- Tarnai, T. (1980). Simultaneous Static and Kinematic Interdeterminacy of Space Structures with Cyclic Symmetry. *Int. J. of Solids and Structures*, 16, pp. 347:359.
- Thomas F. (2005). Rationalising bubble trusses for batch production, *Automation in Construction*, 16, pp. 45:53.

- Thomas, George B. Jr.; Finney and Ross L. (1996). *Calculus and Analytic Geometry* (9th ed.), Addison Wesley.
- Tilbert, G. (2002). *Deployable Tensegrity Structures for Space Applications*, Doctoral thesis, Royal Institute of Technology, Department of Mechanics, Stockholm.
- Timoshenko, S.P. and Young, D.H. (1965). *Theory of Structures* (2nd Edn), McGraw-Hill, New York.
- Timoshenko, S.P., and Young, D.H. (1945). *Theory of Structures*, McGraw-Hill, New York.
- Timoshenko, S.P., Gere, J.M. (1961). *Theory of elastic stability*, McGraw-Hill.
- Triantafyllidis, N., and Bardenhagen, S. (1996). The influence of scale size on the stability of periodic solids and the role of associated higher order gradient continuum models. *J. Mech. Phys. Solids*, 44(11), pp. 1891:1928.
- Triantafyllidis, N., & Schnaidt, W. C. (1993). Comparison of microscopic and macroscopic instabilities in a class of two-dimensional periodic composites. *J. Mech. Phys. Solids*, 41(9), pp. 1533:1565.
- Triantafyllidis, N., and Schraad, M. W. (1998). Onset of failure in aluminum honeycombs under general in-plane loading. *J. Mech. Phys. Solids*, 46(6), pp. 1089:1124.
- Vassart, N. and Motro, R. (1999). Multiparametered Formfinding Method: Application to Tensegrity Systems. *Int. J. of Space Structures*, 14, 2, pp. 147:154.
- Vedula, V. R., Green, D. J. and Hellman, J. R. (1998a). *J. Eur. Ceram. Soc.* 18, pp. 2073:2080.
- Vedula, V. R., Green, D. J., Hellman, J. R. and Segall, A. E. (1998b). *J. Mater. Sci.* 33, pp. 5427:5432.
- Volokh, K.Yu., Vilnay, O. (1997). Natural, kinematic and elastic displacements of under constrained structures, *Int. J. of Solids. Structures*, 34, 8, pp. 911:930.
- Wadley, Hayden N.G. (2002). *Cellular Metals Manufacturing*, *Advanced Engineering Materials*, 10, pp. 726:733.
- Wallach, J. C., and Gibson, L. G. (2001). Mechanical behavior of a three dimensional truss material. *Int. J. Solids. Structures*, 38, pp. 7181:7196.
- Wang, J., Evans, A. G., Dharmasena, K., and Wadley, H. N. G. (2003). On the performance of truss panels with Kagome cores. *Int. J. Solids. Structures*, 40, pp. 6981:6988.
- Waterman, N. A., and Dickens, P. (1994). *Rapid Product Development in the USA, Europe and Japan*, *World Class Design to Manufacture*, Vol. 1, 3, pp. 27:36.
- Weaire, D. and Phelan, R. (1994). *A counterexample to Kelvin's conjecture on minimal surfaces*, *Phil. Mag., Lett.* 69, pp. 107:110.

- Weaver P. M. and Ashby M. F. (1997). Material limits for shape efficiency, *Progress in Materials Science*, 41, pp. 61:128.
- Wempner, G.A. (1981). *Mechanics of Solids with Applications to Thin Bodies*. , Sijthoff and Noordhoff, Alphen aan den Rijn.
- Wicks N. and Hutchinson, J.W. (2001). *Int. J. Solids. Structures*, 38, pp. 5165:5183.
- Wigner, E. and Seitz, F. (1933). On the Constitution of Metallic Sodium, *Phys. Rev.* 43, 804.
- Wright, D. T. (1965). Membrane forces and buckling in reticulated shells. *J. Struc. Div. Proc. ASCE*, 91(ST1), pp. 173:201.
- Wroldsen (2007), PhD thesis, *Modelling and Control of Tensegrity Structures*, Department of Marine Technology, Norwegian University of Science and Technology.
- Xiaogang, Chen¹, Ying Sun and Xiaozhou Gong, (2008a). Design, Manufacture, and Experimental Analysis of 3D Honeycomb Textile Composites Part I: Design and Manufacture, *Textile Research J.* Vol 78(9): pp. 771:781.
- Xiaogang Chen¹, Ying Sun and Xiaozhou Gong, (2008b). Design, Manufacture, and Experimental Analysis of 3D Honeycomb Textile Composites, Part II: Experimental Analysis *Textile Research J.* Vol 78(11): pp. 1011:1021.
- Zhang, L., Maurin, B. and Motro, R. (2006). Form-Finding of Nonregular Tensegrity Systems. *J. of Structural Engineering*, 132(9), pp. 1435:1440 .
- Zhou¹, Q., Mayer, R. R. (2002). Characterization of Aluminum Honeycomb Material Failure in Large Deformation Compression, Shear, and Tearing, *Transactions of the ASME*, Vol. 124, OCTOBER, pp. 412: 420.
- MTS: <http://www.mts.com/>. Accessed: October 4th 2010.
- MATLAB: <http://www.mathworks.com/>. Accessed: October 4th 2010.
- Arcam AB[®], URL: <http://www.arcam.com/index.aspx>. Accessed August, 19th (2010a).
- Ti6Al4V ELI Titanium Alloy: URL:
<http://www.arcam.com/CommonResources/Files/www.arcam.com/Documents/EBM%20Materials/Arcam-Ti6Al4V-ELI-Titanium-Alloy.pdf>. Accessed August, 19th (2010b).
- Arcam AB[®] Setting the standard for Additive Manufacturing, URL:
<https://www.dmace.net/FileDownload.aspx?FileId=25>. Accessed August, 19th (2010c).
- Hydro-Quebec Research Institute in Varennes, Canada: URL:
<http://www.hydroquebec.com/technology/index.html>. Accessed August, 19th 2010.

Appendix A

Bravais Lattices

A.1. 2D Bravais Lattices

In 2D, the location of every point in a Bravais lattice can be described as

$$\vec{R} = n_1 \vec{a}_1 + n_2 \vec{a}_2 \quad (\text{A.1})$$

where \vec{a}_1 and \vec{a}_2 are linearly independent two dimensional vectors called the primitive vectors and n_1 and $n_2 \in \mathbb{Z}$, the integer numbers group.

A.1.1. List of 2D Bravais Lattices

In 2D, there are five Bravais lattices,

1. Square Lattice:

The square lattice is symmetric under reflection about both x and y axes and with respect to 90° rotations.

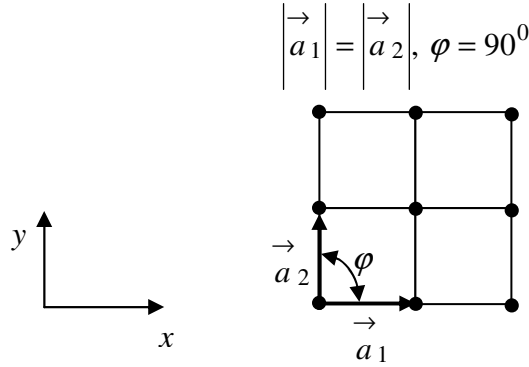


Fig (A.1) Square Lattice

2. Rectangular Lattice:

When compressed along one axis, the square lattice loses the 90° rotational symmetry and becomes the rectangular lattice.

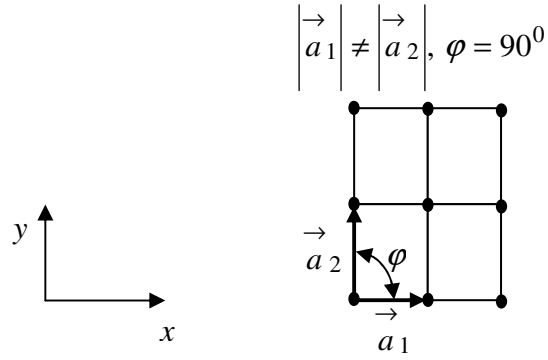


Fig (A.2) rectangular lattice

3. Hexagonal Lattice:

The hexagonal (or triangular) lattice is invariant under reflections about the x and y axes as well as with respect to 60° rotations.

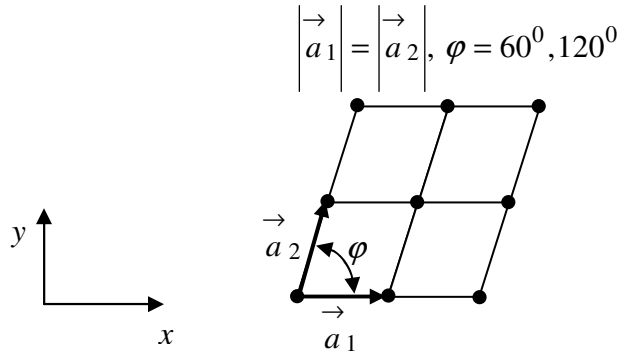


Fig (A.3) Hexagonal Lattice

4. Centered Rectangular Lattice:

The centered rectangular lattice results from a compression of the hexagonal lattice and loses the 60° rotational symmetries.

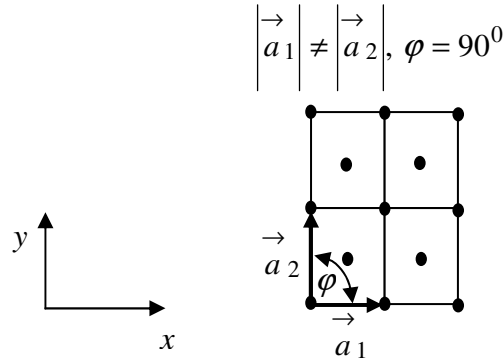


Fig (A.4) Centered Rectangular Lattice

5. Oblique Lattice:

An arbitrary choice of \vec{a}_1 and \vec{a}_2 with no special symmetry, results in an oblique lattice. This lattice still possesses inversion symmetry.

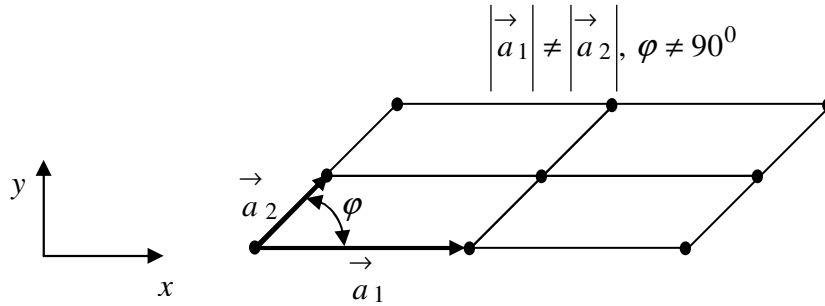


Fig (A.5) Oblique Lattice

A.2. 3D Bravais Lattices

In 3D, the location of every point in a Bravais lattice can be described as

$$\vec{R} = n_1 \vec{a}_1 + n_2 \vec{a}_2 + n_3 \vec{a}_3 \quad (\text{A.2})$$

where \vec{a}_1 , \vec{a}_2 and \vec{a}_3 are linearly independent three dimensional vectors called the primitive vectors and n_1, n_2 and $n_3 \in \mathbb{Z}$, the integer numbers group.

A.2.1. List of 3D Bravais Lattices

In 3D, there are fourteen Bravais lattices,

1. Triclinic cell

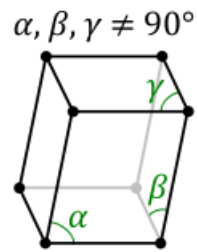
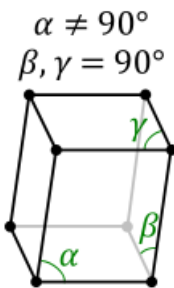
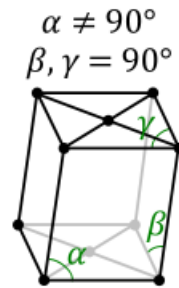


Fig (A.6) Primitive cell

2. Monoclinic cells



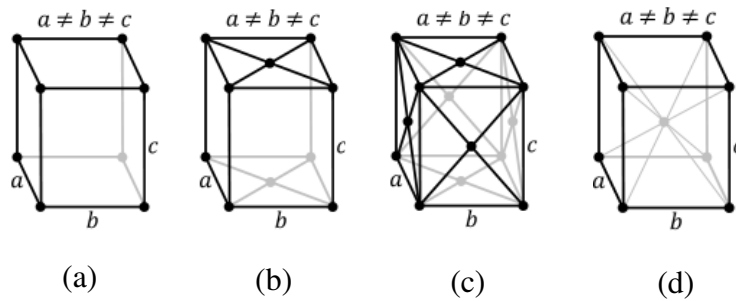
Primitive cell



Base centered cell

Fig (A.7) Monoclinic cells

3. Orthorhombic cells



(a) Primitive; (b) Base centered; (c) Face centered; (d) Body centered

Fig (A.8) Orthorhombic cells

4. Tetragonal Cell

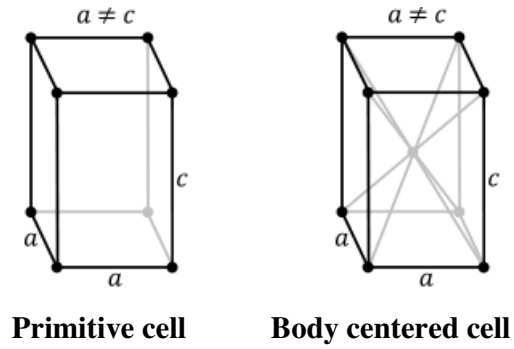
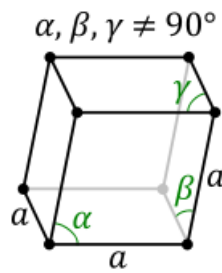


Fig (A.9) Tetragonal Cell

5. Rhombohedra Cell



Primitive cell

Fig (A.10) Rhombohedra Cell

6. Hexagonal Cell



Fig (A.11) Hexagonal Cell

7. Cubic Cell

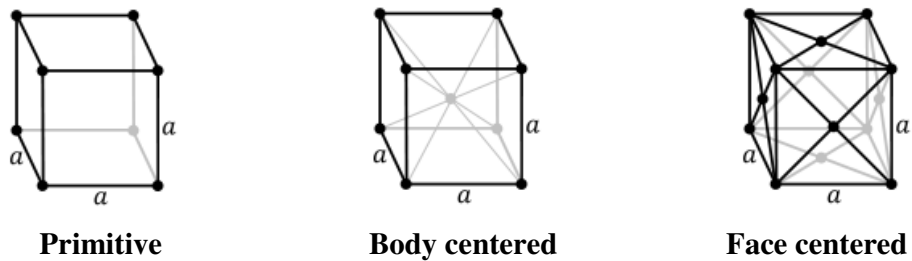


Fig (A.12) Cubic Cell

Appendix B

Definitions and Concepts of Solid State Physics and Quantum Mechanics Necessary for the Statement and Proof of the Bloch's Theorem

B.1 The Observable- Operators in Quantum Mechanics:

Associated with each measurable parameter in a quantum mechanical system is a quantum mechanical operator. Such operator arises because in quantum mechanics, real world is described by waves (the wave-functions) rather than with discrete particles whose motion and dynamics can be described with the deterministic equations of Newtonian mechanics. Part of the development of quantum mechanics is the establishment of the operators associated with the parameters needed to describe the system.

The observable associated with the total energy of the quantum system is the Hamiltonian. As with all observables, the spectrum of the Hamiltonian is the set of possible outcomes when the total energy of a system is measured.

The time dependent Hamiltonian is represented as:

$$H = i\hbar \frac{\partial}{\partial t} \quad (\text{B.1})$$

where i is the complex number, \hbar is the Plank's constant divided by 2π . The time independent Hamiltonian is represented as:

$$H = \frac{P^2}{2m} + V(x) \quad (\text{B.2})$$

where, P is the quantum particle momentum, m is the mass of the particle and $V(x)$ is the potential energy of the system.

B.2 The Schrödinger equation:

The Schrödinger equation in quantum mechanics plays the role of Newton's laws and conservation of energy in classical mechanics. It predicts the future behavior of a dynamic system by providing the probability of events outcome.

In classical mechanics, a single degree of freedom system contains a lumped mass m attached to a spring of stiffness K at one end while the other end of the spring is fixed to the foundation and in a harmonic oscillation, has a total energy E . This total energy is equal to:

$$\frac{1}{2}mv^2 + \frac{1}{2}Kx^2 = E \quad (\text{B.3})$$

where, v is the particle velocity. By using the concept of conservation of energy in classical mechanics, the total energy of the system is always a constant. Using Rayleigh's theorem, eqn (B.3) can be employed to derive the system equation of motion.

Using the Newtonian approach, the equation of motion of the single degree of freedom system can be derived as:

$$ma = -Kx \quad (\text{B.4})$$

where a is the particle acceleration.

In quantum mechanics, the total energy, E , of a particle is represented as:

$$E = T + V = \frac{1}{2} \frac{P^2}{m} + V \quad (\text{B.5})$$

where P is the particle's momentum, m is the mass of the particle. T and V are the kinetic and the potential energies of the particle, respectively.

By adopting Einstein's Light Quanta hypothesis (1905), the total energy of the quantum particle can be related to the frequency of its wave as follows:

$$E = hf = \frac{h}{2\pi} (2\pi f) = \hbar\omega \quad (\text{B.6})$$

where f is the frequency of the particle wave and ω is the angular frequency of the particle wave. Using the De Broglie hypothesis (1924), the momentum of particle is related to its wave length as follows:

$$P = \frac{h}{\lambda} = \frac{h}{2\pi} \frac{2\pi}{\lambda} = \hbar K \quad (\text{B.7})$$

where λ is the wave length of the particle's wave, k is its wave number.

Schrödinger expressed the wave-function of the particle as a complex plane wave which is expressed as:

$$\psi(x, t) = Ae^{i(Kx - \omega t)} \quad (\text{B.8})$$

Differentiating the wave-function with respect to time and position gives:

$$\frac{\partial \psi}{\partial t} = -i\omega\psi \quad (\text{B.9a})$$

$$\frac{\partial \psi}{\partial x} = iK\psi \quad (\text{B.9b})$$

By comparing eqns (B.9a) and (B.6) and eqns (B.9b) and (B.7), the following expressions can be obtained:

$$E\psi = i\hbar \frac{\partial \psi}{\partial t} \quad (\text{B.10a})$$

$$P^2\psi = -\hbar^2 \nabla^2 \psi \quad (\text{B.10b})$$

where $\nabla^2 = \left(\frac{\partial^2}{\partial x^2} + \frac{\partial^2}{\partial y^2} + \frac{\partial^2}{\partial z^2} \right)$. Substituting eqns (B.10a) and (B.10b) into eqn (B.5) gives

the Schrödinger Equation as:

$$i\hbar \frac{\partial \psi}{\partial t} = -\frac{\hbar^2}{2m} \nabla^2 \psi + V\psi \quad (\text{B.11})$$

B.3 The Translation Operator T_R :

In Euclidean geometry, a translation is moving every point a constant distance in a specified direction. A translation can also be interpreted as the addition of a constant vector to every point, or as shifting the origin of the coordinate system. A translation operator is an operator T_R such that:

$$T_R f\left(\vec{r}\right) = f\left(\vec{r} + \vec{R}\right) \quad (\text{B.12})$$

The translation operator can be represented in matrix form as:

$$T_R = \begin{bmatrix} 1 & 0 & 0 & R_x \\ 0 & 1 & 0 & R_y \\ 0 & 0 & 1 & R_z \\ 0 & 0 & 0 & 1 \end{bmatrix} \quad (\text{B.13})$$

If the function $f\left(\vec{r}\right)$ is a fixed vector such that $f\left(\vec{r}\right) = r_x \hat{i} + r_y \hat{j} + r_z \hat{k}$, then:

$$T_R f\left(\vec{r}\right) = \begin{bmatrix} 1 & 0 & 0 & R_x \\ 0 & 1 & 0 & R_y \\ 0 & 0 & 1 & R_z \\ 0 & 0 & 0 & 1 \end{bmatrix} \begin{bmatrix} r_x \\ r_y \\ r_z \\ 1 \end{bmatrix} = \begin{bmatrix} r_x + R_x \\ r_y + R_y \\ r_z + R_z \\ 1 \end{bmatrix} = f\left(\vec{r} + \vec{R}\right) \quad (\text{B.14})$$

B.4 The Wave-function, $\psi(x,t)$

In 1923, De Broglie had shown that electrons have wave-properties, in what is now called De Broglie hypothesis. Based on this hypothesis, each particle in quantum mechanics is represented by a wave-function $\psi(x,t)$, such that $\psi(x,t) \cdot \psi(x,t)$ gives the probability of finding that particle at a time “ t ” in a position “ x ”. These wave-functions are used in the Schrödinger equation (Jones, W., March, N. H., 1973).

The formulae for describing the behavior of electron waves might be expected to be similar to that describing classical waves. For instance, in continuum mechanics the equation of motion describing the wave on a stretched string can be expressed as:

$$\frac{\partial^2 y(x,t)}{\partial x^2} = \frac{\rho}{T} \frac{\partial^2 y(x,t)}{\partial t^2} \quad (\text{B.15})$$

where, $y(x,t)$ is the wave-function describing the spring lateral displacement at time t and position x along its axis; ρ and T are the mass per unit length and the tension force in the string, respectively.

In quantum mechanics, the plan electromagnetic wave is represented by the equation:

$$\frac{\partial^2 E(x,t)}{\partial x^2} = \frac{1}{C^2} \frac{\partial^2 E(x,t)}{\partial t^2} \quad (\text{B.16})$$

Where, $E(x,t)$ is the wave-function describing the total energy of the particle at a time t and a position x and C is the speed of light.

Comparing eqns (B.15) and (B.16), it can be seen that the equation of motion of a plan electromagnetic wave of a particle in quantum mechanics has a similar mathematical formulation of that in continuum mechanics. This can be justified by comparing eqn (B.16) to Rayleigh’s theorem, 1887 (Ashcroft, N., Mermin, N., 1976), for the derivation of the equation of motion of a one dimensional system in continuum mechanics.

B.4.1 Properties of the wave-function, $\psi(x,t)$

A wave-function, $\psi(x,t)$, must have the following properties:

1. $\psi(x,t)$ contains all the measurable information about the particle.
2. The sum of its square, $\psi(x,t) \cdot \psi(x,t)$, over the whole space is 1, i.e. the probability that the particle exists in its domain is 100%. In other words, the wave-function must possess the

ability of normalization which means that the sum of the probabilities over the whole space is unity. This is expressed mathematically as:

$$\int_r \psi \cdot \psi dr = 1 \quad (\text{B.17})$$

where, r is the spatial coordinate of the particle space. This property allows the wave-function calculated from the Schrödinger equation to be used to determine any physical observable.

3. It must be continuous over its boundaries.
4. It must be a solution of the Schrödinger equation.
5. It allows energy calculations via the Schrödinger equation.
6. It establishes the probability distribution in three dimensions.

Appendix C

The Bloch's theorem in Solid State Physics

C.1 The Bloch's Theorem

The Bloch's theorem for the description of electron motion in solids is a theory of non-interacting electrons. Instead of moving about in free space, the electrons now move about in a periodic potential, $U(\vec{r})$, which is generated by the periodic structure of the solid atomic lattice. The periodicity of the atomic lattice structure makes $U(\vec{r})$ obeys the periodic relation:

$$U(\vec{r} + \vec{R}) = U(\vec{r}) \quad (\text{C.1})$$

For all bases \vec{R} in a Bravais lattices that are mapped by translational symmetry.

The Bloch's theorem can be stated as:

The Eigen states of one dimensional Hamiltonian are expressed as:

$$H = -\hbar^2 \nabla^2 / 2m + U(\vec{r}) \quad (\text{C.2})$$

where $U(\vec{r} + \vec{R}) = U(\vec{r})$ for all \vec{R} in a Bravais lattice, can be chosen to have the form of a plane wave times a function with periodicity of the Bravais lattice which is expressed as:

$$\psi_{nk}(\vec{r}) = e^{ik \cdot \vec{r}} u_{nk}(\vec{r}) \quad (\text{C.3})$$

where $u_{nk}(\vec{r} + \vec{R}) = u_{nk}(\vec{r})$ for all \vec{R} in a Bravais lattice.

For details of the different parameters presented in this Appendix, see Appendix B.

From eqn (C.3), the Bloch's theorem can be stated in an alternative way as:

$$\psi(\vec{r} + \vec{R}) = e^{ik \cdot \vec{R}} \psi(\vec{r}) \quad (\text{C.4})$$

C.2 First Proof of the Bloch's theorem

A simple proof of the Bloch's theorem can be obtained by considering the special case of a one dimensional ring of lattice points as shown in Fig (C.1).

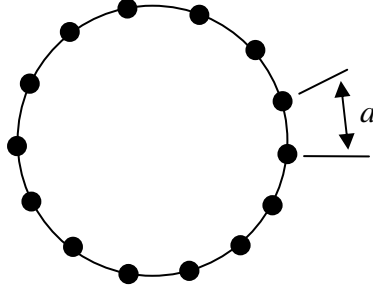


Fig. (C.1) One dimensional ring of lattice points

Assume that the number of points in the lattice, shown in Fig (C.1), is N . These lattice points are equally separated by distance a . A one dimensional lattice points can be represented as:

$$\vec{R} = na \hat{l} \quad (C.5)$$

where $0 \leq n \leq N$ is an integer number and \hat{l} is a unit vector in the circumferential direction of the circular lattice. The potential in this lattice, V , is periodic and can be formulated as:

$$V(\vec{r}) = V(\vec{r} + \vec{R}) \quad (C.6)$$

Since the potential is periodic, it is expected that any wave-function, $\psi(\vec{r})$, representing a physical property of a particle moving in this potential will differ from its value at $\left(\vec{r} + a \hat{l}\right)$ by a factor C . This can be formulated as:

$$\psi(\vec{r} + a \hat{l}) = C\psi(\vec{r}) \quad (C.7)$$

Similarly, the wave-function at $(\vec{r} + 2a \hat{l})$ can be formulated as:

$$\psi(\vec{r} + 2a \hat{l}) = C^2\psi(\vec{r}) \quad (C.8)$$

Following the same procedure, then, the wave function at $(x+Na)$ is formulated as:

$$\psi(\vec{r} + Na \hat{l}) = C^N\psi(\vec{r}) \quad (C.9)$$

After N steps the value of the wave-function is back to its original value, that means:

$$\psi(\vec{r} + Na \hat{l}) = \psi(\vec{r}) \quad (C.10)$$

By comparing eqns (C.9) and (C.10), then:

$$C^N = 1 \quad (C.11)$$

That means C has N values representing the N roots of unity. This is represented as:

$$C_n = e^{\frac{i2\pi n}{N}} \quad (C.12)$$

where $0 \leq n \leq N - 1$. Substituting eqn (C.12) into eqn (C.7) results in:

$$\psi(\vec{r} + \vec{R}) = e^{\frac{i2\pi n}{N}} \psi(\vec{r}) \quad (C.13)$$

Assume a periodic function $u(\vec{r})$ that has a periodicity similar to that of the lattice, such that:

$$u(\vec{r} + \vec{R}) = u(\vec{r}) \quad (C.14)$$

An expression for the wave-function in eqn (C.14) can be formulated as:

$$\psi(\vec{r}) = e^{\frac{i2\pi n}{Na} \vec{r}} u(\vec{r}) \quad (C.15)$$

The solution expressed in eqn (C.15) satisfies eqn (C.13), where:

$$\psi(\vec{r} + \vec{R}) = e^{\frac{i2\pi n}{Na} (\vec{r} + \vec{R})} u(\vec{r} + \vec{R}) \quad (C.16)$$

By substituting eqn (C.14) into eqn (C.16) and expanding the bracket in the exponent of eqn (C.16) results in:

$$\psi(\vec{r} + \vec{R}) = \psi(\vec{r}) e^{\frac{i2\pi n}{Na} \vec{R}} \quad (C.17)$$

Introducing $k = \frac{2\pi n}{Na}$ modifies eqn (C.17) into:

$$\psi(\vec{r} + \vec{R}) = \psi(\vec{r}) e^{ik \vec{R}} \quad (C.18)$$

Equation (C.18) is the Bloch's theorem for one dimensional lattice. Similarly, the proof can be expanded to the two and three dimensional cases.

C.3 Second Proof of the Bloch's theorem

For each Bravais lattice vector \vec{R} , a translation operator T_R is defined such that, when it operates on any function $f\left(\vec{r}\right)$, shifts the argument by \vec{R} , as shown in eqn (B.12, Appendix B).

Since the Hamiltonian is periodic, then:

$$T_R H\left(\vec{r}\right) \psi\left(\vec{r}\right) = H\left(\vec{r} + \vec{R}\right) \psi\left(\vec{r} + \vec{R}\right) = H\left(\vec{r}\right) \psi\left(\vec{r} + \vec{R}\right) = H\left(\vec{r}\right) T_R \psi\left(\vec{r}\right) \quad (\text{C.19})$$

From eqn (C.19), it can be stated that:

$$T_R H\left(\vec{r}\right) = H\left(\vec{r}\right) T_R \quad (\text{C.20})$$

From eqn (C.20), the result of applying two successive translations does not depend on the order in which they are applied, since for any wave-function, $\psi\left(\vec{r}\right)$, it can be stated that:

$$T_R T_{R'} \psi\left(\vec{r}\right) = T_{R'} T_R \psi\left(\vec{r}\right) = \psi\left(\vec{r} + \vec{R} + \vec{R}'\right) \quad (\text{C.21})$$

From eqn (C.21), the following expression is formulated:

$$T_R T_{R'} = T_{R'} T_R = T_{R+R'} \quad (\text{C.22})$$

From eqns (C.20) and (C.22), it can be deduced that T_R for all Bravais lattice vectors \vec{R} and the Hamiltonian H form a set of commuting operators. It follows from a fundamental theory of quantum mechanics that the eigen states of H can therefore be chosen to be simultaneous eigen states of all the T_R , such that:

$$H \psi\left(\vec{r}\right) = \epsilon \psi\left(\vec{r}\right) \quad (\text{C.23a})$$

$$T_R \psi\left(\vec{r}\right) = c\left(\vec{R}\right) \psi\left(\vec{r}\right) \quad (\text{C.23b})$$

The Eigenvalues $c\left(\vec{R}\right)$ of the translation operators are related because of the condition presented

in eqns (C.23a) and (C.23b), for on the one hand:

$$T_{R'} T_R \psi \left(\vec{r} \right) = c \left(\vec{R} \right) T_{R'} \psi \left(\vec{r} \right) = c \left(\vec{R} \right) c \left(\vec{R}' \right) \psi \left(\vec{r} \right) \quad (\text{C.24})$$

on the other hand, according to eqn (C.22):

$$T_{R'} T_R \psi \left(\vec{r} \right) = T_{R+R'} \psi \left(\vec{r} \right) = c \left(\vec{R} + \vec{R}' \right) \psi \left(\vec{r} \right) \quad (\text{C.25})$$

It follows that the Eigenvalues must satisfy:

$$c \left(\vec{R} + \vec{R}' \right) = c \left(\vec{R} \right) + c \left(\vec{R}' \right) \quad (\text{C.26})$$

Now, let a_i be three primitive vectors for the Bravais lattice. Then, $c(a_i)$ can be written as:

$$c(a_i) = e^{2\pi i x_i} \quad (\text{C.27})$$

By suitable choice of the x_i , it then follows by successive applications of eqn (C.26) that if \vec{R} is a general Bravais lattice vector given by:

$$\vec{R} = n_1 a_1 + n_2 a_2 + n_3 a_3 \quad (\text{C.28})$$

Then:

$$c \left(\vec{R} \right) = c(a_1)^{n_1} c(a_2)^{n_2} c(a_3)^{n_3} \quad (\text{C.29})$$

But this is precisely equivalent to:

$$c \left(\vec{R} \right) = e^{ik \vec{R}} \quad (\text{C.30})$$

$$\text{where } k = x_1 b_1 + x_2 b_2 + x_3 b_3 \quad (\text{C.31})$$

where b_i are the reciprocal lattice vectors.

From the previous derivation, it can be deduced that the Eigen states $\psi \left(\vec{r} \right)$ of H can be chosen

such that for every Bravais lattice vector \vec{R} :

$$T_R \psi \left(\vec{r} \right) = \psi \left(\vec{r} + \vec{R} \right) = c \left(\vec{R} \right) \psi \left(\vec{r} \right) = e^{ik \vec{R}} \psi \left(\vec{r} \right) \quad (\text{C.32})$$

Equation (C.32) is precisely the Bloch's theorem.

Appendix D

Mathematical Representation of Lattice Assemblies

In continuum mechanics, a lattice material can be characterized by adopting the notions of crystal physics (Grosso and Pastori-Parravicini, 2000). In the following sections we review the mathematical representation of atomic lattice structures of the condensed matter. Similar representation is used to model lattice materials in continuum mechanics.

D.1 Atomic Structure and Symmetries

Due to the complexity of the condensed matter, where it involves a huge number of atoms, the possibility of solving all underlying equations in full details is very expensive and might be impossible. Accordingly, the laws of greatest importance are the principles of symmetry. The first step to describe how atoms are arranged is to group them in crystal forms. A crystal consists of a small group of atoms that forms a unit cell. This unit cell repeats itself infinitely with specific symmetry either in one, two or three dimensional spaces in what is called crystalline order. This microscopic arrangement forms the macroscopic solid. That means the whole macroscopic matter behavior can be described by studying a few number of atoms on the microscopic level thanks to the microscopic structural symmetry. However, it should be noted that the real world matter is never perfect. Impurities play an important role in defining material properties.

As the nineteenth century progressed, an elaborate mathematical theory of symmetry was developed to show that the symmetries of natural crystals could be identified by the symmetries of regular lattices. For details of the different types of symmetry operators, the reader is referred to references (Brillouin, L., 1946; Schwarzenbach, D., 1996).

A lattice can be defined as a translational infinitely periodic arrangement of points. On the other hand, the crystal is a translational infinitely periodic arrangement of bases. In a crystal structure, the lattice governs the structural periodicity that defines the way the crystal is infinitely constructed in a translational symmetry, while the bases are responsible about what part of the structure repeats itself within each period. Therefore, a crystal structure can be formulated as:

$$\text{Crystal} = \text{Lattice} + \text{Basis} \quad (\text{D.1})$$

Figure (D.1) shows the two dimensional lattice of a square crystal structure. The unit cell of the lattice is shown in the middle of Fig (D.1) with the primitive bases \vec{a}_1 and \vec{a}_2 of the lattice translational symmetry. The primitive bases (vectors) of a lattice, $\vec{a}_i, i \in \{1,2,3\}$, where $i=1, i=2$ or $i=3$ in one, two or three dimensional space lattices, respectively, are a set of independent vectors in the space of the lattice that are used to identify the infinite crystal bases as their linear combinations. The crystal bases of the square lattice are shown on the right of Fig (D.1). These crystal bases include one point basis, \vec{j}_1 , and two connectivity lines bases, \vec{b}_1 and \vec{b}_2 . Applying the lattice translational symmetry on the crystal bases generates the infinite crystal structure.

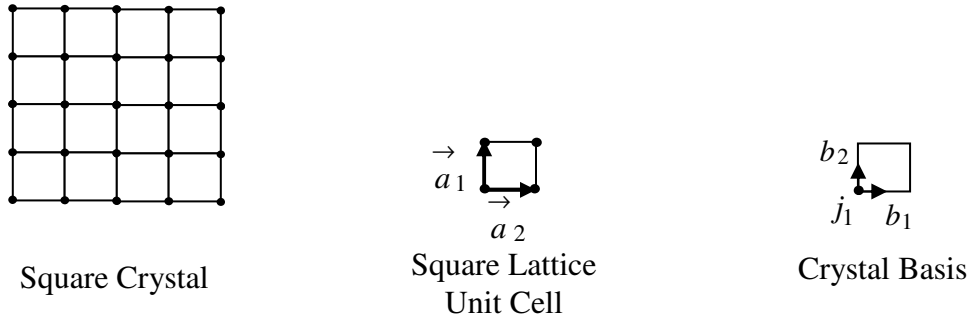


Fig (D.1) 2D Square Crystal Structure

To define the lattice translational symmetry, a unit cell is defined for each type of lattice. Two types of unit cells are available in literature, the primitive unit cell and the conventional unit cell, also known as the regular unit cell. In the following, the concepts of primitive and conventional cells are explained.

D.1.1 Primitive Unit Cell

The primitive unit cell of a lattice is a volume of space that, when translated by all the primitive vectors of the lattice, just fills the space without either overlapping itself or leaving voids. The primitive cell must have only one lattice point, or it may be adequately positioned to contain more lattice points on its circumference.

Assume \vec{a}_1, \vec{a}_2 and \vec{a}_3 are the primitive vectors of a three dimensional lattice, then the primitive cell of this lattice is always chosen as the set of points \vec{R} represented as:

$$\vec{R} = x_1 \vec{a}_1 + x_2 \vec{a}_2 + x_3 \vec{a}_3 \quad (\text{D.2})$$

where x_1, x_2 and x_3 are coefficients that have values in the range of $[0,1]$. This choice has sometimes the disadvantage that the primitive cell is not precisely representing the lattice symmetry. This problem is solved by choosing a different cell which is a conventional cell. In the following, the types of primitive unit cells are presented.

A. Bravais Lattices

There are two equivalent ways to define a Bravais lattice:

- (1) An infinite array of discrete points with arrangement and orientation to each other that appears exactly the same, from whichever of the points of the array is viewed.

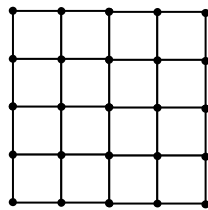
For example, in the hexagonal lattice, shown in Fig (D.2), points P and R have the same arrangement and the same orientation with respect to other points in the lattice, however, point Q has a different orientation, it is rotated 180° from points P and R. Accordingly, the Hexagonal lattice is not qualified as a Bravais lattice. On the other hand, all point of the square lattice, shown in Fig (D.2), have the same arrangement and orientation. Accordingly, the square lattice is a Bravais lattice.

The other definition of a Bravais lattice can be stated as:

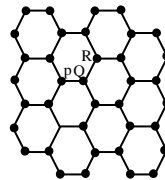
- (2) A Bravais lattice consists of all the points with position vectors \vec{R} of the form:

$$\vec{R} = \sum_{i=1}^m n_i \vec{a}_i \quad (\text{D.3})$$

where n_i is an integer number, \vec{a}_i is the lattice primitive vectors, and $i=1, 2$ or 3 corresponding to one, two or three dimensional Bravais lattices.



Square lattice
(a Bravais lattice)



Hexagonal lattice
(not a Bravais lattice)

Fig (D.2) A Bravais and a non-Bravais lattices

A comparison between definition one and two shows that the invariant geometry of the Bravais lattice is granted by translational symmetry presented by the position vector \vec{R} . Details of the different types of Bravais lattices available in literature, in 2D and 3D spaces, are reported in Appendix A.

B. Wigner-Seitz Primitive Cell

A technique to construct a primitive unit cell that has the symmetry of the Bravais lattice was presented by E. P. Wigner and Frederick Seitz (Wigner, E. and Seitz, F., 1933; Seitz, F., 1936; Brillouin, L., 1946) who developed what is called the Wigner-Seitz unit cell.

The cell may be chosen by first selecting a lattice point in the lattice space; then, lines are drawn from that point to all other nearby lattice points. At the midpoint of each constructed line, another line is drawn normal to each of them. In the case of a three-dimensional lattice, a perpendicular plane is drawn at the midpoint of the lines between the lattice points. By using this method, the smallest area or volume that is enclosed between the set of intersecting normal lines in 2D or intersecting normal planes in 3D is called the Wigner-Seitz primitive cell. All area or space within the lattice are filled by this type of primitive cell and leave no gaps.

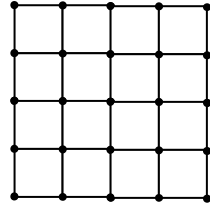
D.1.2 Conventional Unit Cells

Instead of using a primitive unit cell to generate the Bravais lattice, a better choice can be considered, where a different unit cell can be chosen which reflects the symmetry of the lattice. This type of cell is called the conventional unit cell. The conventional unit cell is always larger in size than that of the primitive unit cell and can contain more than one lattice point inside its envelope. The bases of the conventional unit cell are always a linear combination of the primitive cell bases.

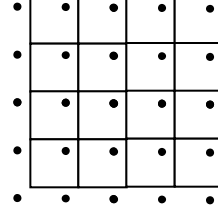
D.1.3 Lattices with Basis

The description of the crystal structure as a Bravais lattice is an idealization. Real lattice structure is far from the simple Bravais lattices representation. Instead, a real crystal structure can be described by its underlying Bravais lattice together with a description of the arrangement of the lattice points within the primitive cell envelope. These lattice points are represented by bases vectors.

In other words a crystal structure is a Bravais lattice with bases. Fig (D.3) illustrates the difference between a Bravais lattice and a lattice with bases. Both crystals and lattices are similar, however the left lattice is perfectly positioned that all the crystal points are located on the lattice points. On the right lattice, the crystal points have to be defined by additional bases which repeat itself with the lattice to construct the whole crystal structure.



Square Bravais
lattice



Square Bravais lattice
with a Basis

Fig (D.3) Square Lattice

D.2 Reciprocal Lattice

The reciprocal lattice plays a fundamental role in most studies of periodic structures. It is a mathematical tool to simplify the study of the behavior of the periodic function within a periodic lattice structure.

The reciprocal space, also called Fourier space, k- space, or momentum space, in contrast to the real space or the direct space, is a set of imaginary points constructed in such a way that:

1. The direction of a vector from one point to another coincides with the direction of a normal to the real space planes, where, in a specific direction within a lattice, all lattice points are on a series of equally separated planes called the crystal planes. The separation between these planes is called the interplanar distance.
2. The separation of the points in the reciprocal space (absolute value of its primitive vector) is equal to the reciprocal of interplanar distance of the real space (direct lattice).

Consider a set of points \vec{R} constituting a 2D Bravais lattice, also, consider a plane wave that

propagates through this lattice structure that has the wave-function of, $e^{ik \cdot \vec{r}}$, where $i = \sqrt{-1}$ is

the complex number, k is a wave number and \vec{r} is a spatial position vector (basis) in the plane of the lattice. At a specific value of k , such a plane wave has the periodicity of the Bravais lattice.

The set of wave vectors, k , that yields plane waves with the periodicity of a given Bravais lattice is derived from the lattice reciprocal space. k belongs to the reciprocal space of a Bravais lattice of

points \vec{R} , provided that the relation, given in eqn (D.4), holds for any basis \vec{r} , and for all \vec{R} in the Bravais lattice.

$$e^{ik\left(\vec{r}+\vec{R}\right)} = e^{ik\vec{r}} \quad (\text{D.4})$$

Factoring out $e^{ik\vec{r}}$, the reciprocal lattice can be expressed as the set of wave vectors k satisfying the relation:

$$e^{ik\vec{R}} = 1 \quad (\text{D.5})$$

for all \vec{R} in a Bravais lattice.

It should be noted that a reciprocal lattice is defined with a reference to a particular Bravais lattice. A Bravais lattice that determines a given reciprocal lattice is often referred to as the direct lattice.

If \vec{a}_1, \vec{a}_2 and \vec{a}_3 are the linearly independent three dimensional primitive vectors of the direct lattice, then, the reciprocal lattice can be constructed by the three primitive vectors \vec{b}_1, \vec{b}_2 and \vec{b}_3 that are defined as:

$$\vec{b}_i \cdot \vec{a}_j = 2\pi\delta_{ij} \quad (\text{D.6})$$

where $i, j \in \{1, 2, 3\}$ and δ_{ij} is the Kronecker delta symbol that satisfies:

$$\delta_{ij} = \begin{cases} 0 & \text{for } i \neq j \\ 1 & \text{for } i = j \end{cases} \quad (\text{D.7})$$

Using eqns (D.6) and (D.7), the reciprocal lattice primitive basis can be expressed as:

$$\vec{b}_1 = 2\pi \frac{\vec{a}_2 \times \vec{a}_3}{\vec{a}_1 \cdot (\vec{a}_2 \times \vec{a}_3)} \quad (\text{D.8a})$$

$$\vec{b}_2 = 2\pi \frac{\vec{a}_1 \times \vec{a}_3}{\vec{a}_2 \cdot (\vec{a}_1 \times \vec{a}_3)} \quad (\text{D.8b})$$

$$\vec{b}_3 = 2\pi \frac{\vec{a}_1 \times \vec{a}_2}{\vec{a}_1 \cdot \left(\vec{a}_2 \times \vec{a}_3 \right)} \quad (\text{D.8c})$$

The reciprocal lattice points can be expressed in terms of a vector \vec{K} which is a linear combination of \vec{b}_i , expressed as:

$$\vec{K} = k_1 \vec{b}_1 + k_2 \vec{b}_2 + k_3 \vec{b}_3 \quad (\text{D.9})$$

where k_1, k_2 and k_3 are integers.

To construct the reciprocal lattice, the following procedure is followed (Schwarzenbach, D., 1996):

- Select a point as an origin from the direct space.
- From this origin, lay out the normal to every family of parallel planes in the direct lattice.
- Set the length of each normal equal to 2π times the reciprocal of the interplanar distance for its particular set of planes.
- Place a point at the end of each normal.

D.3 Brillouin Zones

The Wigner-Seitz primitive cell of the reciprocal lattice is known as the First Brillouin Zone. The first Brillouin zone is a zone in which the behavior of the function is fully described. This can be shown by a one dimensional model example. The two and three dimensions can be derived easily from this case. The one dimensional model of a free electron within a periodic potential is shown in Fig (D.4). Here, the variation of free electron energy, E_n , is shown with respect to the wave number, k .

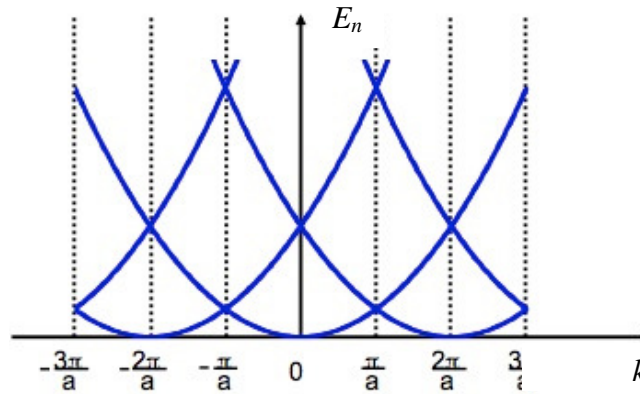


Fig (D.4) Variation of the free electron energy with respect to the wave number in a periodic potential

From Fig (D.4), it can be seen that the zone $[-\pi/a ; \pi/a]$ is fully sufficient to describe the value of the energy. This zone is called the First Brillouin zone. Because the other Brillouin zones are less used, the “First Brillouin Zone” is sometimes just named as the “Brillouin Zone”.

A further reduced zone in the reciprocal space of the lattice can be used to fully analyze the behavior of periodic wave-functions. This reduced zone is derived from the first Brillouin zone and is referred to as the Irreducible Brillouin Zone. The irreducible Brillouin zone is computed using point group symmetry. In the following, the basics of point group symmetry are described.

D.4 Point Group Symmetry and its application to the reduction of the first Brillouin Zone

The zone for the study of the properties of the periodic function can be further reduced due to the symmetry that exists in the direct lattice. One can notice that because of the reflection to the ‘ E_n (vertical)- axis’ in the example of the free electron, shown in Fig (D.4), the analysis can be further reduced to the zone $[0; \pi/a]$ which is the irreducible Brillouin zone for this case.

The point group symmetry of a lattice can be determined by resorting to the rotational and reflection symmetries that the lattice possesses. For example, Fig (D.3) shows that if any node is fixed in the plane of the lattice, the same lattice orientation can be maintained for any $\pi/2$ rotation or integer multiple thereof. Similarly, if the reflection of a lattice about either a horizontal, vertical, or $\pi/4$ -diagonal lattice lines, an identical lattice can be obtained. Thus the square lattice has four-fold rotational symmetry and two independent lines of reflection about the centre node. These symmetries are those of a regular square polygon and are labelled as D_4 in group-theoretic notation (Schwarzenbach, D., 1996). If one of the lattice bars is fixed at its midpoint and then the same exercise is performed, it can be found that the lattice now has two

folds rotational symmetry and one independent line of reflection. These symmetries are those of a rectangular polygon and are labelled D_2 in group-theoretic notation.

D.4.1 Point Group Theory of Lattice Symmetries

Point group symmetry is a mathematical group composed of the elements of the rotation and the reflection and sometimes a combination of the both. A structure belongs to point group symmetry is a structure that if one applies all the elements of the group to the structure it remains with the same geometrical orientation. The point group symmetry thus gives the equivalent directions within the direct lattice. Consequently it also gives the equivalent points in the reciprocal lattice, especially the points of the Brillouin zone. Knowing the point group symmetry of a structure, it is possible to reduce it to a smallest zone of the irreducible Brillouin zone. Each point of the irreducible Brillouin zone is representative of a set of points that is generated by the elements of the point group symmetry linked to the structure. This is commonly called equivalent class in mathematic.

The point group symmetry is easily determined once the primitive unit cell has been identified. Here, standard solid-state physics terminology, notation and the basic definitions of group theory are revised (Armstrong, M. A., 1988; Hill, V. E., 2000; Aschbacher, M., 2000; James, G. and Liebeck, M., 2001).

A. Mathematical Group

A mathematical group consists of a set G for which a product operation, acting on elements g and h of G and forming another element of G , is defined and written as $g.h$, such that this operation is associative and expressed as:

$$(g.h).k = g.(h.k) \quad \forall g, h, k \in G \quad (\text{D.10})$$

A group G contains an identity element e such that:

$$e.g = g.e \quad \forall g \in G \quad (\text{D.11})$$

and each element g has an inverse g^{-1} as a member of G , where:

$$g.g^{-1} = g^{-1}.g = e \quad \forall g \in G \quad (\text{D.12})$$

The product of an element g with itself is written as $g^2 = g.g$; similarly $g^3 = g^2.g$, $g^{-2} = (g^{-1})^2$ etc...

If the number of elements in G is finite, then G is finite where the number of elements in G is called the order of G and is written as $|G|$. Note that a group G is said to be Abelian if $g.h = h.g$ for all g and h in G .

In point group theory, we are concerned with two mathematical groups, the dihedral and the cyclic groups.

A.1 The Cyclic Group

In group theory, a cyclic group, also called a monogamous group, is a group that can be generated by a single element, in the sense that the group has an element “ a ”, called a “generator” of the group, such that, when written multiplicatively, every element of the group is a power of “ a ”. The Order of the cyclic group is “ n ” where “ n ” is a positive integer. Example of the cyclic groups is the n^{th} root of unity group which is denoted by C_n .

A.1.1 The n^{th} Root of Unity C_n

In mathematics, the n^{th} roots of unity, or de Moivre numbers, are all the complex numbers that yield 1 when raised to a given power n . They are located on the unit circle of the complex plane, and in that plane they form the vertices of an n -sided regular polygon with one vertex on 1.

Example of such group is the cyclic group C_n , such that:

$$C_n = \{1, a, a^2, \dots, a^{n-1}\} \quad (\text{D.13})$$

where C_n is formed by the products of “ a ” with restriction that powering “ a ” leads to unity. Here “ a ” can be formulated as:

$$a = e^{\frac{i}{n}} \quad (\text{D.14})$$

Where $i = \sqrt{-1}$. Normalizing “ a ” to the trigonometric functions cycle, by dividing it by $(1/2\pi)$, gives the form:

$$a = e^{\frac{2\pi i}{n}} \quad (\text{D.15})$$

From eqn (1.16), $a^n = 1 = e$, this can be proved by the Euler’s form representation in the complex plan.

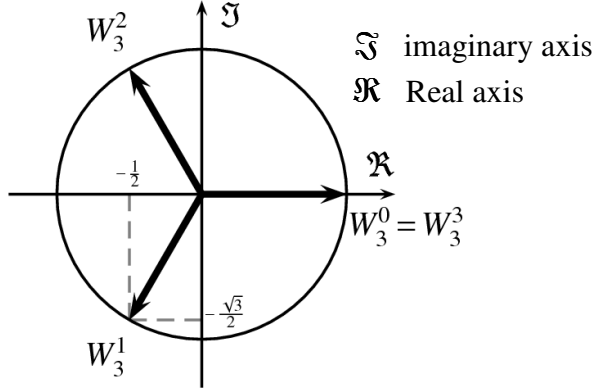


Fig (D.5) the third root of unity

Figure (D.5) shows the third root of unity in the complex plan. This can be formulated by Euler's rule, where:

$$e^{ix} = \cos(x) + i \sin(x) \quad (\text{D.16})$$

$$e^{-ix} = \cos(x) - i \sin(x) \quad (\text{D.17})$$

From eqns (D.16) and (D.17),

$$a^n = \left(e^{\frac{2\pi i}{n}} \right)^n = e^{2\pi i} = \cos(2\pi) + i \sin(2\pi) = 1 = e \quad (\text{D.18})$$

A.2 The dihedral group, D_n

In mathematics, a dihedral group is the group of symmetries of a regular polygon, including both rotations and reflections (mirroring). A regular polygon with “ n ” sides has $2n$ different symmetries, n rotational and n reflection symmetries. The associated rotations and reflections make up the dihedral group D_n .

Let “ a ” denotes the rotational symmetry element and “ b ” denoted the reflection symmetry element, then a dihedral group can be defined as

$$D_n = \langle a, b : a^n = e, b^2 = e, b^{-1}.a.b = a^{-1} \rangle \quad (\text{D.19})$$

Note that in executing the dihedral group operations, order is important, i.e. $a.b$ means do a then do b . i.e. rotate first then reflect second. The order of the dihedral group D_n is $2n$, where n elements for rotation and n for reflection, with $n \geq 3$. Example of a dihedral group is the point

group symmetry of the equilateral triangle which generates the fully triangulated lattice. As shown in Fig (D.6).

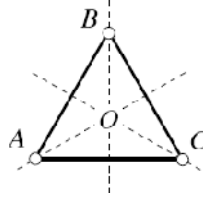


Fig (D.6) The equilateral triangle is D3-symmetric

In Fig (D.6), this is a D_3 dihedral group with order 6, 3 rotation elements and 3 reflection

elements. The rotational element is $a = e^{\frac{2\pi i}{n}} = e^{\frac{2\pi i}{3}}$, i.e. the three rotation elements can be constructed by three rotations of 120° counter clock wise around O . and the three reflection elements can be performed around OA , OB and OC .

Table (D.1) shows the point group symmetries of some 2D lattice structures that are analyzed throughout this thesis.

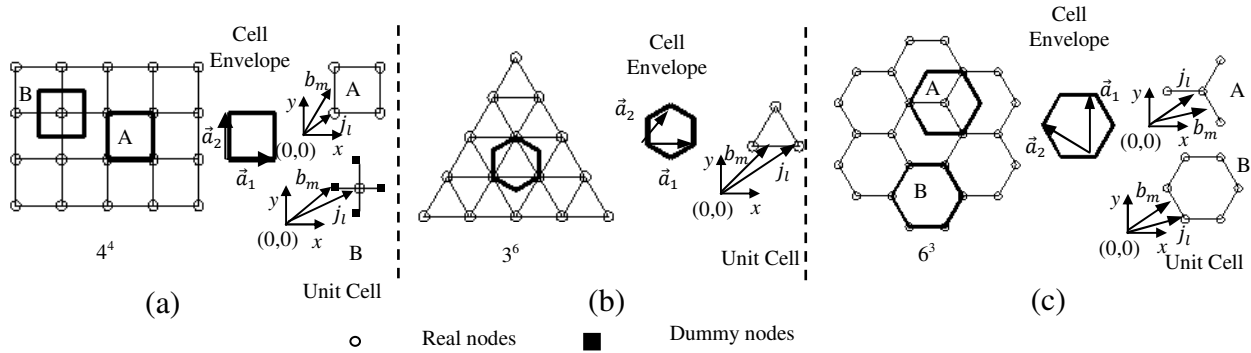
Table (D.1) Point group symmetries of 2D lattice materials

Name	Schlaflf Symbol	Connectivity	Point Group
Square	4^4	4	D_4
Hexagonal	6^3	3	D_6
Triangular	3^6	6	D_6
Kagome	$3.6.3.6$	4	D_6
Triangular- Triangular	$3_1.3_2.3_1.3_2$	4	D_3
Triangular- Square	$3^3.4^2$	5	D_2
Triangular- Hexagonal	$3^4.6$	5	C_6

APPENDIX E

Determinacy Analysis of 2D Infinite Lattice Structures: Applications

The determinacy analysis and the classification methodology, developed in chapter three, is applied to the nineteen lattice topologies, shown in Figs (E.1), (E.2) and (E.3) and their results are reported in this Appendix. Steps of the analysis for the square, the Kagome and the $3^3.4^2$ lattice topologies are demonstrated in details.

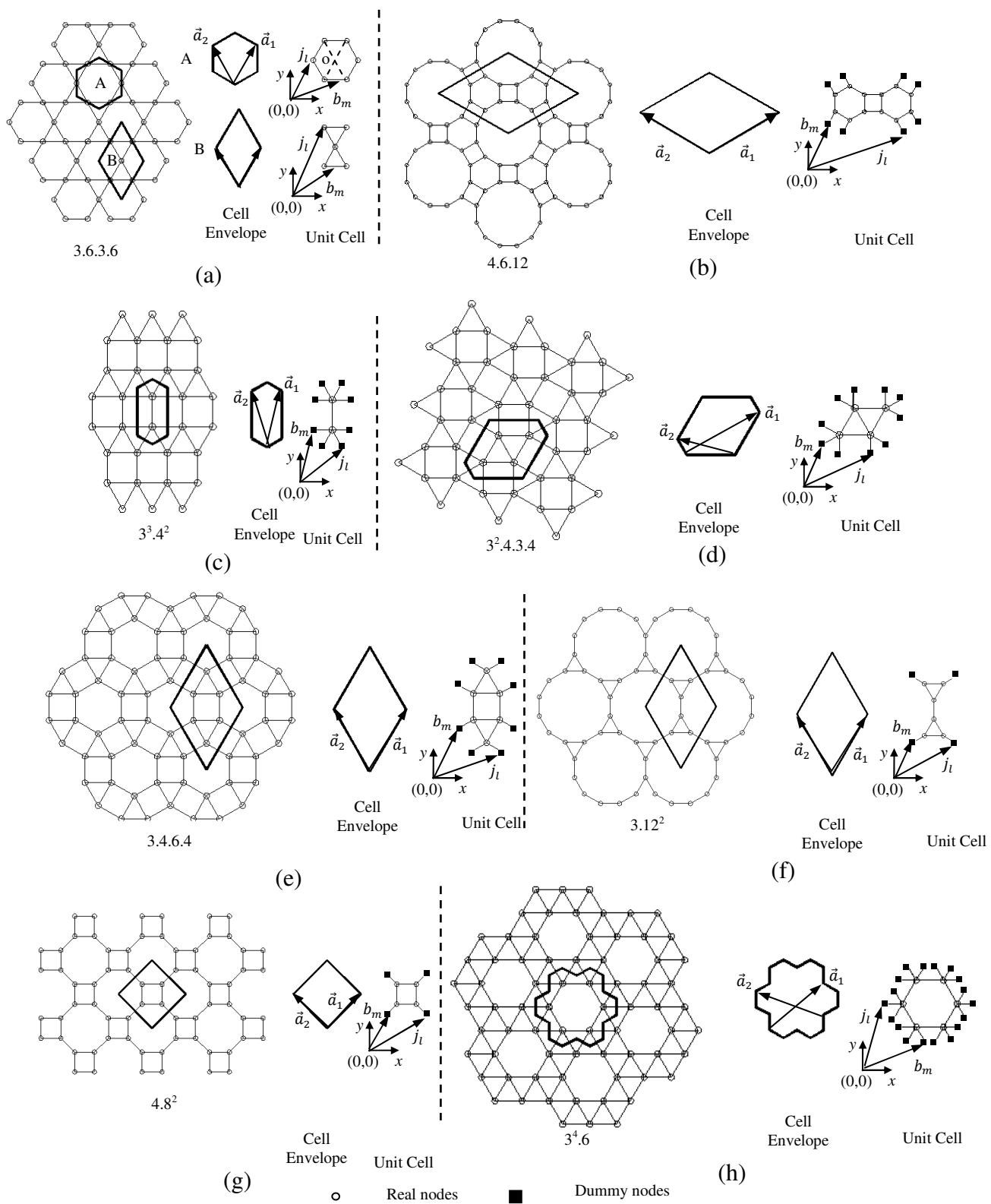


a- Square- 4^4 b- Triangular- 3^6 c- Hexagonal- 6^3

Fig. (E.1) 2D regular Lattice Structures

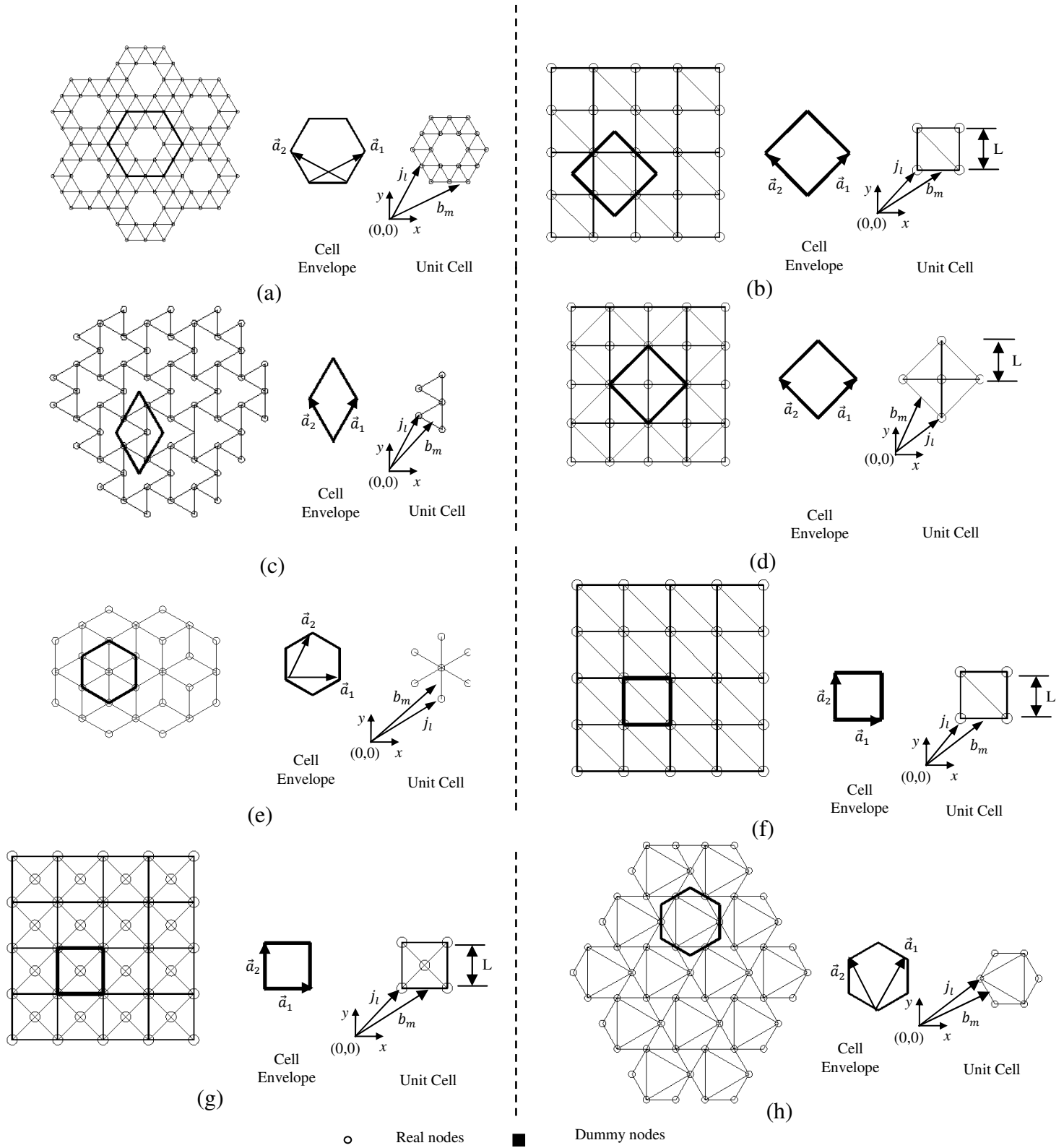
E.1 Square Lattice Structure

The analysis of the square lattice structure, shown in Fig (E.1a) is examined here. After the evaluation of the equilibrium and the kinematic systems (eqn (3.82)) of unit cell B of the square lattice, shown in Fig (E.1a), the technique described in §3.5 is applied to the real structure of the unit cell. The dependency relations of the bar and the node bases are computed, as shown in Table (E.1).



a- Kagome- 3.6.3.6 b- 4.6.12 c- $3^3.4^2$ d- $3^2.4.3.4$ e- 3.4.6.4 f- 3.12^2 g- 4.8^2 h- $3^4.6$

Fig (E.2) 2D semi-regular Lattice Structures



a- Double Hexagonal Triangulation; b- Semi-Uni- Braced Square (SUBS); c- Triangular-Triangular d- Semi-Double- Braced Square; e- Equilaterals- Hexagon; f- Uni- Braced Square; g- Double- Braced Square; h- Patched Kagome

Figure (E.3) 2D other lattice topologies

Table (E.1) Dependency analysis results for the square lattice unit cells

Cell A- nodes				Cell B- nodes			
Independent	Dependent	\hat{x}_1	\hat{x}_2	Independent	Dependent	\hat{x}_1	\hat{x}_2
j_1	j_4	1	0	-	-	-	-
j_1	j_2	0	1	-	-	-	-
j_1	j_3	1	1	-	-	-	-
Cell A- Bars				Cell B- Bars			
Independent	Dependent	\hat{x}_1	\hat{x}_2	Independent	Dependent	\hat{x}_1	\hat{x}_2
b_1	b_3	1	0	b_1	b_3	1	0
b_4	b_2	0	1	b_4	b_2	0	1

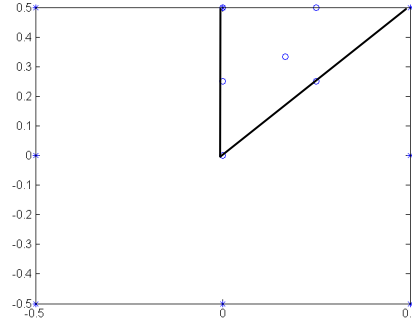


Fig (E.4) The first Brillouin zone and irreducible first Brillouin zone of the square lattice shown in Fig (3.5a)

The reciprocal lattice bases of the square lattice are computed as $\vec{b}_1 = (1,0)$ and $\vec{b}_2 = (0,1)$ which are used to construct the reciprocal lattice. The first Brillouin zone is determined and point group symmetry is used to determine the irreducible first Brillouin zone of the lattice. The irreducible first Brillouin zone of the square lattice along with its wave-numbers are shown in Fig (E.4) and table (E.2), respectively.

The periodicity information, given in table (E.1) is used to derive the transformation matrices of the bar and the node deformation vectors at the different wave-numbers, given in table (E.2). The transformation matrices are used for the reduction of the equilibrium and the kinematic systems of the unit cell to the irreducible forms of the infinite lattice at the different wave-numbers, as shown in eqns (E.1), for the analysis using unit cell B, shown in Fig (E.1a).

Table (E.2) Wave-numbers of the reciprocal space of the square lattice

No	ω_1	ω_2
1	0.25	0.5
2	0	0.5
3	0.5	0.5
4	0.1667	0.3333
5	0	0.25
6	0.25	0.25
7	0	0

$$\text{At } \omega = (0.25, 0.5), \tilde{\mathbf{A}} = \begin{bmatrix} 0.5+0.5i & 0 \\ 0 & -1-i \end{bmatrix}, \tilde{ss}_1 = \begin{bmatrix} 1 \\ 0 \end{bmatrix}, \tilde{d}_1 = \begin{bmatrix} 1 \\ 0 \end{bmatrix} \quad (\text{E.1a})$$

$$\text{At } \omega = (0, 0.5), \tilde{\mathbf{A}} = \begin{bmatrix} 0 & 0 \\ 0 & -1+i \end{bmatrix}, \tilde{ss}_1 = \begin{bmatrix} 1 \\ 0 \end{bmatrix}, \tilde{d}_1 = \begin{bmatrix} 1 \\ 0 \end{bmatrix} \quad (\text{E.1b})$$

$$\text{At } \omega = (0.5, 0.5), \tilde{\mathbf{A}} = \begin{bmatrix} 1 & 0 \\ 0 & -1 \end{bmatrix}, \tilde{ss}_1 = \begin{bmatrix} 1 \\ 0 \end{bmatrix}, \tilde{d}_1 = \begin{bmatrix} 1 \\ 0 \end{bmatrix} \quad (\text{E.1c})$$

$$\text{At } \omega = (0.1667, 0.333), \tilde{\mathbf{A}} = \begin{bmatrix} 0.25+0.43i & 0 \\ 0 & -0.75+0.43i \end{bmatrix}, \tilde{ss}_1 = \begin{bmatrix} 1 \\ 0 \end{bmatrix}, \tilde{d}_1 = \begin{bmatrix} 1 \\ 0 \end{bmatrix} \quad (\text{E.1d})$$

$$\text{At } \omega = (0, 0.25), \tilde{\mathbf{A}} = \begin{bmatrix} 0 & 0 \\ 0 & -0.5+0.5i \end{bmatrix}, \tilde{ss}_1 = \begin{bmatrix} 1 \\ 0 \end{bmatrix}, \tilde{d}_1 = \begin{bmatrix} 1 \\ 0 \end{bmatrix} \quad (\text{E.1e})$$

$$\text{At } \omega = (0.25, 0.25), \tilde{\mathbf{A}} = \begin{bmatrix} 0.5+0.5i & 0 \\ 0 & -0.5+0.5i \end{bmatrix}, \tilde{ss}_1 = \begin{bmatrix} 1 \\ 0 \end{bmatrix}, \tilde{d}_1 = \begin{bmatrix} 1 \\ 0 \end{bmatrix} \quad (\text{E.1f})$$

$$\text{At } \omega = (0, 0), \tilde{\mathbf{A}} = \begin{bmatrix} 0 & 0 \\ 0 & 0 \end{bmatrix}, \tilde{ss}_1 = \begin{bmatrix} 1 \\ 0 \end{bmatrix}, \tilde{ss}_2 = \begin{bmatrix} 0 \\ 1 \end{bmatrix}, \tilde{d}_1 = \begin{bmatrix} 1 \\ 0 \end{bmatrix}, \tilde{d}_2 = \begin{bmatrix} 0 \\ 1 \end{bmatrix} \quad (\text{E.1g})$$

For the determinacy analysis of the infinite square lattice using unit cell A, shown in Fig (E.1a), the following results are obtained:

$$\text{At } \omega = (0.25, 0.5), \tilde{\mathbf{A}} = \begin{bmatrix} 0 & 1-i \\ -2 & 0 \end{bmatrix}, \tilde{ss}_1 = \begin{bmatrix} 1 \\ 0 \end{bmatrix}, \tilde{d}_1 = \begin{bmatrix} 1 \\ 0 \end{bmatrix} \quad (\text{E.2a})$$

$$\text{At } \omega = (0, 0.5), \tilde{\mathbf{A}} = \begin{bmatrix} 0 & -2 \\ 0 & 0 \end{bmatrix}, \tilde{ss}_1 = \begin{bmatrix} 0 \\ 1 \end{bmatrix}, \tilde{d}_1 = \begin{bmatrix} 1 \\ 0 \end{bmatrix} \quad (\text{E.2b})$$

$$\text{At } \omega = (0.5, 0.5), \tilde{\mathbf{A}} = \begin{bmatrix} 0 & 2 \\ -2 & 0 \end{bmatrix}, \tilde{ss}_1 = \begin{bmatrix} 1 \\ 0 \end{bmatrix}, \tilde{d}_1 = \begin{bmatrix} 1 \\ 0 \end{bmatrix} \quad (\text{E.2c})$$

$$\text{At } \omega = (0.1667, 0.333), \tilde{\mathbf{A}} = \begin{bmatrix} 0 & -0.5 - 0.866i \\ -1.5 + 0.866i & 0 \end{bmatrix}, \tilde{ss}_1 = \begin{bmatrix} \cdot \\ \cdot \end{bmatrix}, \tilde{d}_1 = \begin{bmatrix} \cdot \\ \cdot \end{bmatrix} \quad (\text{E.2d})$$

$$\text{At } \omega = (0, 0.25), \tilde{\mathbf{A}} = \begin{bmatrix} 0 & 0 \\ -1 + i & 0 \end{bmatrix}, \tilde{ss}_1 = \begin{bmatrix} 0 \\ 1 \end{bmatrix}, \tilde{d}_1 = \begin{bmatrix} 1 \\ 0 \end{bmatrix} \quad (\text{E.2e})$$

$$\text{At } \omega = (0.25, 0.25), \tilde{\mathbf{A}} = \begin{bmatrix} 0 & -1 - i \\ -1 + i & 0 \end{bmatrix}, \tilde{ss}_1 = \begin{bmatrix} \cdot \\ \cdot \end{bmatrix}, \tilde{d}_1 = \begin{bmatrix} \cdot \\ \cdot \end{bmatrix} \quad (\text{E.2f})$$

$$\text{At } \omega = (0, 0), \tilde{\mathbf{A}} = \begin{bmatrix} 0 & 0 \\ 0 & 0 \end{bmatrix}, \tilde{ss}_1 = \begin{bmatrix} 1 \\ 0 \end{bmatrix}, \tilde{ss}_2 = \begin{bmatrix} 0 \\ 1 \end{bmatrix}, \tilde{d}_1 = \begin{bmatrix} 1 \\ 0 \end{bmatrix}, \tilde{d}_2 = \begin{bmatrix} 0 \\ 1 \end{bmatrix} \quad (3.2g)$$

where ss_i is the i^{th} mode of periodic states of self-stress as $i \in \{1, \dots, s\}$ and s is the number of periodic states of self-stress within the lattice at a specific wave-number. \tilde{d}_j is the j^{th} mode of periodic states of internal mechanism as $j \in \{1, \dots, im\}$ and im is the number of periodic states of internal mechanisms within the lattice at a specific wave-number.

Comparing eqns (E.1) and (E.2), taking into consideration the square symmetry of the lattice, one can realize that the two unit cells identically predict the microscopic determinacy state of the infinite periodic square lattice structure.

Extending the analysis to consider the stiffening effect of the periodic states of self-stress to the periodic states of internal mechanisms, indicates that the states of self-stress developed at wave-numbers $\omega = (0, 0.5)$, $\omega = (0, 0.25)$ and $\omega = (0, 0)$ are not capable of stiffening the corresponding periodic internal mechanisms. It is concluded that pin-jointed infinite periodic square lattice structure collapses by periodic internal mechanisms and thus classified as a bending dominated.

E.2 Lattice Structure with Schläfli symbol of $3^3.4^2$

The lattice structure with the Schläfli symbol of $3^3.4^2$, shown in Fig (E.2c) is analyzed here.

E.2.1 Unit Cell Equilibrium System

The finite structure of the unit cell has the following bases groups:

$$\text{The dummy node bases group: } G_D = \left\{ \begin{bmatrix} -0.25, 1 + \frac{\sqrt{3}}{4} \end{bmatrix}, \begin{bmatrix} 0.25, 1 + \frac{\sqrt{3}}{4} \end{bmatrix}, (0.5, 1), (0.5, 0), \right. \\ \left. \begin{bmatrix} 0.25, -\frac{\sqrt{3}}{4} \end{bmatrix}, \begin{bmatrix} -0.25, -\frac{\sqrt{3}}{4} \end{bmatrix}, (-0.5, 0), (-0.5, 1) \right\}$$

$$\text{The node bases group: } G_N = \left\{ \begin{array}{l} (0,0), (0,1), \left(-0.25, 1 + \frac{\sqrt{3}}{4}\right), \left(0.25, 1 + \frac{\sqrt{3}}{4}\right), (0.5,1), \\ (0.5,0), \left(0.25, -\frac{\sqrt{3}}{4}\right), \left(-0.25, -\frac{\sqrt{3}}{4}\right), (-0.5,0), (-0.5,1) \end{array} \right\}$$

$$\text{The bar bases group: } G_B = \left\{ \begin{array}{l} (0,0.5), \left(-0.25, 1 + \frac{\sqrt{3}}{4}\right), \left(0.25, 1 + \frac{\sqrt{3}}{4}\right), (0.5,1), \\ (0.5,0), \left(0.25, -\frac{\sqrt{3}}{4}\right), \left(-0.25, -\frac{\sqrt{3}}{4}\right), (-0.5,0), (-0.5,1) \end{array} \right\}$$

By applying the DNS, the equilibrium system of the unit cell, including the degrees of freedom of the dummy nodes, is computed as:

$$\begin{bmatrix} 0 & 0 & 0 & 0 & -1 & -0.5 & 0.5 & 1 & 0 \\ -1 & 0 & 0 & 0 & 0 & \sqrt{3}/2 & \sqrt{3}/2 & 0 & 0 \\ 0 & 0.5 & -0.5 & -1 & 0 & 0 & 0 & 0 & 1 \\ 1 & -\sqrt{3}/2 & -\sqrt{3}/2 & 0 & 0 & 0 & 0 & 0 & 0 \\ 0 & -0.5 & 0 & 0 & 0 & 0 & 0 & 0 & 0 \\ 0 & \sqrt{3}/2 & 0 & 0 & 0 & 0 & 0 & 0 & 0 \\ 0 & 0 & 0.5 & 0 & 0 & 0 & 0 & 0 & 0 \\ 0 & 0 & \sqrt{3}/2 & 0 & 0 & 0 & 0 & 0 & 0 \\ 0 & 0 & 0 & 1 & 0 & 0 & 0 & 0 & 0 \\ 0 & 0 & 0 & 0 & 0 & 0 & 0 & 0 & 0 \\ 0 & 0 & 0 & 0 & 1 & 0 & 0 & 0 & 0 \\ 0 & 0 & 0 & 0 & 0 & 0 & 0 & 0 & 0 \\ 0 & 0 & 0 & 0 & 0 & 0 & 0.5 & 0 & 0 \\ 0 & 0 & 0 & 0 & 0 & -\sqrt{3}/2 & 0 & 0 & 0 \\ 0 & 0 & 0 & 0 & 0 & 0 & -0.5 & 0 & 0 \\ 0 & 0 & 0 & 0 & 0 & 0 & -\sqrt{3}/2 & 0 & 0 \\ 0 & 0 & 0 & 0 & 0 & 0 & 0 & -1 & 0 \\ 0 & 0 & 0 & 0 & 0 & 0 & 0 & 0 & 0 \\ 0 & 0 & 0 & 0 & 0 & 0 & 0 & 0 & -1 \\ 0 & 0 & 0 & 0 & 0 & 0 & 0 & 0 & 0 \end{bmatrix} \begin{bmatrix} t_1 \\ t_2 \\ t_3 \\ t_4 \\ t_5 \\ t_6 \\ t_7 \\ t_8 \\ t_9 \end{bmatrix} = \begin{bmatrix} f_{1x} \\ f_{1y} \\ f_{2x} \\ f_{2y} \\ f_{d1x} \\ f_{d1y} \\ f_{d2x} \\ f_{d2y} \\ f_{d3x} \\ f_{d3y} \\ f_{d4x} \\ f_{d4y} \\ f_{d5x} \\ f_{d5y} \\ f_{d6x} \\ f_{d6y} \\ f_{d7x} \\ f_{d7y} \\ f_{d8x} \\ f_{d8y} \end{bmatrix} \quad (\text{E.3})$$

Eliminating the degrees of freedom associated with the dummy nodes results in:

$$\begin{bmatrix} 0 & 0 & 0 & 0 & -1 & -0.5 & 0.5 & 1 & 0 \\ -1 & 0 & 0 & 0 & 0 & \sqrt{3}/2 & \sqrt{3}/2 & 0 & 0 \\ 0 & 0.5 & -0.5 & -1 & 0 & 0 & 0 & 0 & 1 \\ 1 & -\sqrt{3}/2 & -\sqrt{3}/2 & 0 & 0 & 0 & 0 & 0 & 0 \end{bmatrix} \begin{bmatrix} t_1 \\ t_2 \\ t_3 \\ t_4 \\ t_5 \\ t_6 \\ t_7 \\ t_8 \\ t_9 \end{bmatrix} = \begin{bmatrix} f_{1x} \\ f_{1y} \\ f_{2x} \\ f_{2y} \end{bmatrix} \quad (\text{E.4})$$

E.2.2 Determinacy Analysis of Unit Cell Finite Structure

Computing the four fundamental subspaces of the equilibrium matrix of the unit cell indicates that this unit cell is statically determinate and kinematically indeterminate with eleven modes of mechanisms of which three are rigid-body mechanisms and eight are internal mechanisms.

E.2.3 Infinite Lattice Determinacy Analysis

The direct translational bases are computed as: $\vec{a}_1 = \left(0.5, 1 + \frac{\sqrt{3}}{2} \right)$ and

$\vec{a}_2 = \left(-0.5, 1 + \frac{\sqrt{3}}{2} \right)$. The dependency analysis results for the node and bar bases group

indicates that all real nodes are independent. The bar bases dependency relations are shown in table (E.3).

Table (E.3) Dependency analysis results for the bar bases of the $3^3.4^2$ lattice unit cell

Bar bases dependency			
Independent	Dependent	\hat{x}_1	\hat{x}_2
b_2	b_6	0	-1
b_3	b_7	-1	0
b_4	b_9	-1	1
b_5	b_8	-1	1

The reciprocal lattice bases are computed as: $\vec{b}_1 = (1, 0.2679)$ and $\vec{b}_2 = (-1, 0.2679)$. The reciprocal lattice bases are used to construct the reciprocal lattice, the first Brillouin zone is determined and point group symmetry is used to determine the irreducible first Brillouin zone, shown in Fig (E.5), and the wave-numbers are computed and reported in table (E.4).

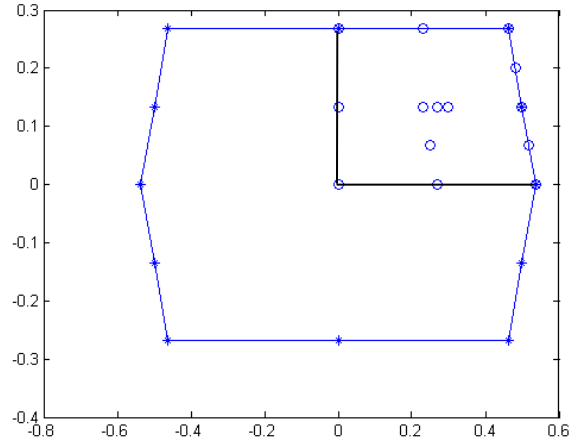


Fig (E.5) The first Brillouin zone and the irreducible first Brillouin zone of the $3^3.4^2$ lattice

Table (E.4) Wave-numbers of the reciprocal space of the $3^3.4^2$ lattice

No	ω_1	ω_2
1	0.61603	0.38397
2	0.61603	0.13397
3	0.38397	-0.13397
4	0.38397	0.11603
5	0.5	0.5
6	0.73205	0.26795
7	0.5	0
8	0.26795	-0.26795
9	0.4	0.1
10	0.25	0.25
11	0.36603	0.13397
12	0.25	0
13	0.13397	-0.13397
14	0	0

The dependency relations, given in table (E.3), are used to formulate the transformation matrices, necessary to reduce the equilibrium system of the unit cell to the irreducible form of the infinite lattice at each wave-number, given in table (E.4), which are used for the determinacy analysis of the infinite lattice structure. The results of the determinacy analysis of the infinite $3^3.4^2$ lattice are reported in table (E.5).

Table (E.5) Determinacy analysis of the semi-regular $3^3.4^2$ lattice

Wave-numbers		# SSS ¹	# SIM ²
ω_1	ω_2		
0.61603	0.38397	1	0
0.61603	0.13397	1	0
0.38397	-0.13397	1	0
0.38397	0.11603	1	0
0.5	0.5	2	1
0.73205	0.26795	1	0
0.5	0	1	0
0.26795	-0.26795	1	0
0.4	0.1	1	0
0.25	0.25	2	1
0.36603	0.13397	1	0
0.25	0	1	0
0.13397	-0.13397	1	0
0	0	3	2

¹SSS...States of Self-Stress; ²SIM...States of Internal Mechanisms

From table (E.5), it can be deduced that the $3^3.4^2$ infinite lattice is statically and kinematically indeterminate at wave-numbers $\omega = (0.25, 0.25)$, $\omega = (0.5, 0.5)$ and $\omega = (0, 0)$; and statically indeterminate and kinematically determinate at all other wave-numbers.

E.2.4 Stiffening Effect of Periodic States of Self-Stress to Periodic Internal Mechanisms

The $3^3.4^2$ lattice has only two mechanisms at wave number $\omega = (0, 0)$ which are translational rigid-body mechanisms. Thus, the lattice does not possess any internal mechanisms at $\omega = (0, 0)$. The stiffening effect of the periodic states of self-stress to the periodic states of internal mechanisms is examined at wave-numbers $\omega = (0.5, 0.5)$ and $\omega = (0.25, 0.25)$.

i. At Wave-Number $\omega = (0.5, 0.5)$

First, we test the necessary condition for the stiffening effect using the product force vector approach. The reduced equilibrium matrix of the infinite lattice and the associated periodic states of self-stress and periodic states of internal mechanisms at wave-number $\omega = (0.5, 0.5)$ are formulated as:

$$\tilde{\mathbf{A}} = \begin{bmatrix} 0 & 0.25 & -0.25 & 0 & 0 \\ -1 & -\sqrt{3}/4 & -\sqrt{3}/4 & 0 & 0 \\ 0 & 0.25 & -0.25 & 0 & 0 \\ 1 & -\sqrt{3}/4 & -\sqrt{3}/4 & 0 & 0 \end{bmatrix}, \tilde{ss}_1 = \begin{bmatrix} 0 \\ 0 \\ 0 \\ 1 \\ 0 \end{bmatrix}, \tilde{ss}_2 = \begin{bmatrix} 0 \\ 0 \\ 0 \\ 0 \\ 1 \end{bmatrix}, \tilde{d}_1 = \begin{bmatrix} -1 \\ 0 \\ 1 \\ 0 \end{bmatrix} \quad (\text{E.5})$$

To determine the non-pivotal columns in the reduced equilibrium matrix, we formulate the reduced row echelon form of the matrix as:

$$rref(\tilde{\mathbf{A}}) = \begin{bmatrix} 1 & 0 & 0 & 0 & 0 \\ 0 & 1 & 0 & 0 & 0 \\ 0 & 0 & 1 & 0 & 0 \\ 0 & 0 & 0 & 0 & 0 \end{bmatrix} \quad (\text{E.6})$$

The non-pivotal columns are the columns with indices 4 and 5. Considering a unit reference length, $L=1$ and a unit nominal strain, $\varepsilon_0=1$, the reduced imposed elongations vector and the reduced flexibility matrix are computed as:

$$\tilde{\mathbf{F}} = \frac{1}{EA} \begin{bmatrix} 1 & 0 & 0 & 0 & 0 \\ 0 & 0.5 & 0 & 0 & 0 \\ 0 & 0 & 0.5 & 0 & 0 \\ 0 & 0 & 0 & 0.5 & 0 \\ 0 & 0 & 0 & 0 & 0.5 \end{bmatrix}, \tilde{\varepsilon}_0 = \begin{bmatrix} 0 \\ 0 \\ 0 \\ 0.5 \\ 0.5 \end{bmatrix} \quad (\text{E.7})$$

which are used to compute the reduced vector of linear combination constants as:

$$\tilde{\gamma} = \begin{bmatrix} -0.5 \\ -0.5 \end{bmatrix} \quad (\text{E.8})$$

The reduced global state of self-stress is computed as:

$$\tilde{S}_G = \begin{bmatrix} 0 \\ 0 \\ 0 \\ -0.5 \\ -0.5 \end{bmatrix} \quad (\text{E.9})$$

The reduced periodic internal mechanism matrix is computed as:

$$\tilde{\mathbf{D}} = \begin{bmatrix} -1 \\ 0 \\ 1 \\ 0 \end{bmatrix} \quad (\text{E.10})$$

The reduced periodic internal mechanism matrix and the reduced global state of self-stress are expanded to include, respectively, the deformations of all nodes and axial forces of all elements of the unit cell, which results in:

$$\mathbf{D} = \begin{bmatrix} -1 \\ 0 \\ 1 \\ 0 \end{bmatrix}, S_G = \begin{bmatrix} 0 \\ 0 \\ 0 \\ -0.5 \\ -0.5 \\ 0 \\ 0 \\ -0.5 \\ -0.5 \end{bmatrix} \quad (\text{E.11})$$

The global state of self-stress and the global internal mechanism are used to derive the product force vector as:

$$\mathbf{PFV} = \begin{bmatrix} 2.1276 \\ 0 \\ -2.1276 \\ 0 \end{bmatrix} \quad (\text{E.12})$$

Columns 4 and 5 are eliminated from the reduced equilibrium matrix to generate the truncated reduced equilibrium matrix which is augmented to the product force vector matrix to generate the augmented reduced equilibrium matrix as:

$$\tilde{\mathbf{A}}_{\text{aug}} = \begin{bmatrix} 0 & 0.25 & -0.25 & 2.1276 \\ -1 & -\sqrt{3}/4 & -\sqrt{3}/4 & 0 \\ 0 & 0.25 & -0.25 & -2.1276 \\ 1 & -\sqrt{3}/4 & -\sqrt{3}/4 & 0 \end{bmatrix} \quad (\text{E.13})$$

Computing the four fundamental subspaces of the augmented equilibrium matrix indicates that this matrix is of full rank and the periodic internal mechanism is suppressed by the periodic states of self-stress; thus the structure becomes stable.

We test the sufficient stiffening condition; the result is in agreement with the necessary condition, as the periodic internal mechanism is tightened up by the periodic states of self-stress in a range of linear combination constants that span the whole range of $[-1,1]$.

The same computations are applied to the lattice at wave-number $\omega = (0.25, 0.25)$ which generates identical results to the analysis at $\omega = (0.5, 0.5)$. The determinacy analysis results of

the infinite lattice structure after the first-order infinitesimal deformation are reported in table (E.6).

Table (E.6) Determinacy analysis of the semi-regular $3^3.4^2$ lattice

Wave-numbers		# SSS	# SIM	PFV ¹	
ω_1	ω_2			# SSS	# SIM
0.61603	0.38397	1	0	-	-
0.61603	0.13397	1	0	-	-
0.38397	-0.13397	1	0	-	-
0.38397	0.11603	1	0	-	-
0.5	0.5	2	1	0	0
0.73205	0.26795	1	0	-	-
0.5	0	1	0	-	-
0.26795	-0.26795	1	0	-	-
0.4	0.1	1	0	-	-
0.25	0.25	2	1	0	0
0.36603	0.13397	1	0	-	-
0.25	0	1	0	-	-
0.13397	-0.13397	1	0	-	-
0	0	3	2	2	2

¹PFV...Product Force Vector.

E.3 Kagome Lattice Structure

Figure (E.2a) shows the Kagome periodic lattice structure along with the periodic structure unit cell and the cell envelope.

E.3.1 Determinacy Analysis of Unit Cell A of the Kagome Lattice Structure (Fig (E.2a))

For unit cell A, shown in Fig (E.2a), assuming the origin of the 2D Cartesian coordinate is located at point o, the node bases group of the unit cell of the Kagome lattice is formulated as:

$$G_N = \left\{ (-1,0), \left(-\frac{1}{2}, \frac{\sqrt{3}}{2}\right), \left(\frac{1}{2}, \frac{\sqrt{3}}{2}\right), (1,0), \left(\frac{1}{2}, -\frac{\sqrt{3}}{2}\right), \left(-\frac{1}{2}, -\frac{\sqrt{3}}{2}\right) \right\} \quad (E.14)$$

Similarly, the bar bases group is formulated as:

$$G_B = \left\{ \left(-\frac{3}{4}, \frac{\sqrt{3}}{4}\right), \left(0, \frac{\sqrt{3}}{2}\right), \left(\frac{3}{4}, \frac{\sqrt{3}}{4}\right), \left(\frac{3}{4}, -\frac{\sqrt{3}}{4}\right), \left(0, -\frac{\sqrt{3}}{2}\right), \left(-\frac{1}{4}, -\frac{\sqrt{3}}{4}\right) \right\} \quad (E.15)$$

Using the node and the bar bases groups, the equilibrium system of the unit cell of the Kagome lattice is formulated as:

$$\begin{bmatrix}
-0.5 & 0 & 0 & 0 & 0 & -0.5 \\
-\frac{\sqrt{3}}{2} & 0 & 0 & 0 & 0 & \frac{\sqrt{3}}{2} \\
0.5 & -1 & 0 & 0 & 0 & 0 \\
\frac{\sqrt{3}}{2} & 0 & 0 & 0 & 0 & 0 \\
0 & 1 & -0.5 & 0 & 0 & 0 \\
0 & 0 & \frac{\sqrt{3}}{2} & 0 & 0 & 0 \\
0 & 0 & 0.5 & 0.5 & 0 & 0 \\
0 & 0 & -\frac{\sqrt{3}}{2} & \frac{\sqrt{3}}{2} & 0 & 0 \\
0 & 0 & 0 & -0.5 & 1 & 0 \\
0 & 0 & 0 & -\frac{\sqrt{3}}{2} & 0 & 0 \\
0 & 0 & 0 & 0 & -1 & 0.5 \\
0 & 0 & 0 & 0 & 0 & -\frac{\sqrt{3}}{2}
\end{bmatrix}
\begin{bmatrix}
t_1 \\
t_2 \\
t_3 \\
t_4 \\
t_5 \\
t_6
\end{bmatrix}
=
\begin{bmatrix}
f_{1x} \\
f_{1y} \\
f_{2x} \\
f_{2y} \\
f_{3x} \\
f_{3y} \\
f_{4x} \\
f_{4y} \\
f_{5x} \\
f_{5y} \\
f_{6x} \\
f_{6y}
\end{bmatrix}
\quad (\text{E.16})$$

where t_i is the axial force in element i as $i \in \{1,2,3,4,5,6\}$. f_{jx} and f_{jy} are, respectively, the x and y components of the force of node j as $j \in \{1,2,3,4,5,6\}$.

The kinematic matrix of the unit cell of the Kagome lattice can be easily computed and the kinematic system of the unit cell finite structure can be formulated as:

$$\begin{bmatrix}
-0.5 & 0 & 0 & 0 & 0 & -0.5 \\
-\frac{\sqrt{3}}{2} & 0 & 0 & 0 & 0 & \frac{\sqrt{3}}{2} \\
0.5 & -1 & 0 & 0 & 0 & 0 \\
\frac{\sqrt{3}}{2} & 0 & 0 & 0 & 0 & 0 \\
0 & 1 & -0.5 & 0 & 0 & 0 \\
0 & 0 & \frac{\sqrt{3}}{2} & 0 & 0 & 0 \\
0 & 0 & 0.5 & 0.5 & 0 & 0 \\
0 & 0 & -\frac{\sqrt{3}}{2} & \frac{\sqrt{3}}{2} & 0 & 0 \\
0 & 0 & 0 & -0.5 & 1 & 0 \\
0 & 0 & 0 & -\frac{\sqrt{3}}{2} & 0 & 0 \\
0 & 0 & 0 & 0 & -1 & 0.5 \\
0 & 0 & 0 & 0 & 0 & -\frac{\sqrt{3}}{2}
\end{bmatrix}^T
\begin{bmatrix}
d_{1x} \\
d_{1y} \\
d_{2x} \\
d_{2y} \\
d_{3x} \\
d_{3y} \\
d_{4x} \\
d_{4y} \\
d_{5x} \\
d_{5y} \\
d_{6x} \\
d_{6y}
\end{bmatrix}
=
\begin{bmatrix}
e_1 \\
e_2 \\
e_3 \\
e_4 \\
e_5 \\
e_6
\end{bmatrix}
\quad (\text{E.17})$$

where e_i is the axial deformation in element i as $i \in \{1,2,3,4,5,6\}$. d_{jx} and d_{jy} are, respectively, the x and y components of the displacement of node j as $j \in \{1,2,3,4,5,6\}$.

For the determinacy analysis of the unit cell of the Kagome lattice, the four fundamental subspaces of the equilibrium and the kinematic matrices are computed which indicate that this unit cell is statically determinate, as it does not possess any states of self-stress, and kinematically indeterminate. The rank of the equilibrium and the kinematic matrices, formulated in eqns (E.16) and (E.17), respectively, is found as $r_A = 6$. The $Null(\mathbf{A}^T)$ generates six modes of mechanisms, of which three are planar rigid-body motion (two translation and one rotation) as the structure of the unit cell is not constrained into a foundation. The six modes of mechanisms are formulated as:

$$d_1 = \begin{bmatrix} \frac{\sqrt{3}}{2} \\ 0.5 \\ 0 \\ 1 \\ 0 \\ 0 \\ 0 \\ 0 \\ 0 \\ 0 \\ 0 \\ 0 \end{bmatrix}, d_2 = \begin{bmatrix} \frac{\sqrt{3}}{2} \\ 0.5 \\ \sqrt{3} \\ 0 \\ \sqrt{3} \\ 1 \\ 0 \\ 0 \\ 0 \\ 0 \\ 0 \\ 0 \end{bmatrix}, d_3 = \begin{bmatrix} -\sqrt{3} \\ -1 \\ -2\sqrt{3} \\ 0 \\ -2\sqrt{3} \\ 0 \\ -\sqrt{3} \\ 1 \\ 0 \\ 0 \\ 0 \\ 0 \end{bmatrix}, d_4 = \begin{bmatrix} \frac{\sqrt{3}}{2} \\ 0.5 \\ \sqrt{3} \\ 0 \\ \sqrt{3} \\ 0 \\ \sqrt{3} \\ 0 \\ 0 \\ 0 \\ 1 \\ 0 \end{bmatrix}, d_5 = \begin{bmatrix} 1 \\ 0 \\ 1 \\ 0 \\ 1 \\ 0 \\ 1 \\ 0 \\ 1 \\ 0 \\ 1 \\ 0 \end{bmatrix}, d_6 = \begin{bmatrix} -\frac{\sqrt{3}}{2} \\ 0.5 \\ 0 \\ 0 \\ 0 \\ 0 \\ 0 \\ 0 \\ 0 \\ 0 \\ 0 \\ 1 \end{bmatrix} \quad (E.18)$$

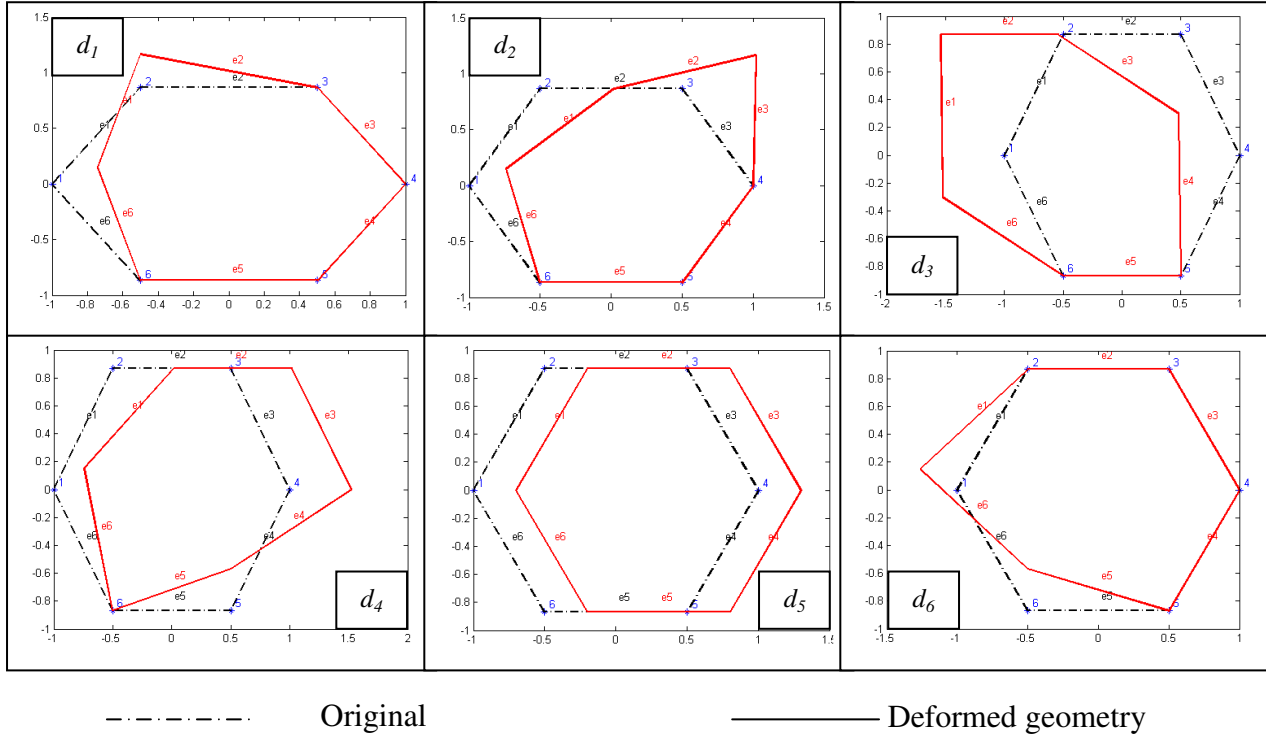


Fig. (E.6) Mechanisms experienced by the unit cell of the Kagome lattice (of which three are rigid body motions and three are internal mechanisms)

where d_i is the i^{th} mode of mechanism as $i \in \{1, \dots, m\}$ and m is the number of mechanisms within the framework. $m = 6$ in the case of the unit cell of the Kagome lattice.

The mechanisms, formulated in eqn (E.18), can be represented graphically, as shown in Fig (E.6). To distinguish between the rigid-body mechanisms and the internal mechanisms, Pellegrino & Calladine (1986) presented a simple strategy that is applicable for any finite framework.

Interested readers are referred to (Pellegrino, S., Calladine, C. R., 1986).

The unit cell A of the Kagome lattice, shown in Fig (E.2a) is statically determinate, as it does not possess any states of self-stress. Accordingly, the analysis of the stiffening effect of states of self-stress to the states of internal mechanisms is not applicable for such finite structure.

E.3.2 Determinacy Analysis of the Infinite Kagome Lattice Structure

For the unit cell envelope of the Kagome lattice, shown in Fig (E.2a), the direct translation bases are formulated as:

$$\vec{a}_1 = (1, \sqrt{3}) \text{ and } \vec{a}_2 = (-1, \sqrt{3}) \quad (\text{E.19})$$

The dependency relations of the bar and the node bases are computed using eqn (3.35). For unit cell A of the Kagome lattice, shown in Fig (E.2a), it is found that all bar bases of the unit cell are independent while the computed dependency relations for the nodes is listed in table (E.7).

Table (E.7) Dependency analysis results for the Kagome lattice unit cell A

Nodes dependency			
Independent	Dependent	\hat{x}_1	\hat{x}_2
j_1	j_4	1	-1
j_2	j_5	0	-1
j_3	j_6	-1	0

The reciprocal lattice bases are computed as:

$$\vec{b}_1 = (0.5, 0.2887) \text{ and } \vec{b}_2 = (-0.5, 0.2887) \quad (\text{E.20})$$

and the irreducible first Brillouin zone along with the wave-numbers are shown in Fig (E.7) and table (E.8), respectively.

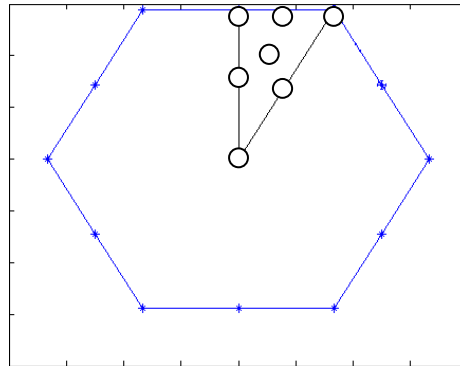


Fig (E.7) the first Brillouin zone and IBZ of the Kagome lattice

Table (E.8) wave-numbers of the reciprocal space of the Kagome lattice

No	ω_1	ω_2
1	0.1	0.2
2	0.2	0.3
3	0.125	0.125
4	0.3	0
5	0.25	0.25
6	0.5	0
7	0	0

Applying the Bloch's theorem, the dependency relations are used to compute the irreducible forms of the equilibrium system of the lattice at the different wave-numbers, computed from the irreducible first Brillouin zone of the reciprocal lattice. Once the irreducible form of the equilibrium system is computed, the corresponding periodic states of self-stress and periodic states of internal mechanisms can be computed from the fundamental subspaces of the reduced equilibrium matrix.

At wave-number $\omega = (0.1, 0.2)$:

$$\begin{bmatrix} -0.5 & 0 & a_8 - a_9i & a_8 - a_9i & 0 & -0.5 \\ -\frac{\sqrt{3}}{2} & 0 & -a_{10} + a_{11}i & a_{10} - a_{11}i & 0 & \frac{\sqrt{3}}{2} \\ 0.5 & -1 & 0 & -a_1 + a_2i & a_3 - a_4i & 0 \\ \frac{\sqrt{3}}{2} & 0 & 0 & -a_5 + a_6i & 0 & 0 \\ 0 & 1 & -0.5 & 0 & -a_{12} + a_{13}i & a_8 - a_9i \\ 0 & 0 & \frac{\sqrt{3}}{2} & 0 & 0 & -a_{10} + a_{11}i \end{bmatrix} \begin{bmatrix} t_1 \\ t_2 \\ t_3 \\ t_4 \\ t_5 \\ t_6 \end{bmatrix} = \begin{bmatrix} f_{1x} \\ f_{1y} \\ f_{2x} \\ f_{2y} \\ f_{3x} \\ f_{3y} \end{bmatrix} \quad (\text{E.21a})$$

$$\tilde{ss}_1 = \begin{bmatrix} \cdot \\ \cdot \end{bmatrix}, \quad \tilde{d}_1 = \begin{bmatrix} \cdot \\ \cdot \end{bmatrix}$$

At wave-number $\omega = (0.2, 0.3)$:

$$\begin{bmatrix} -0.5 & 0 & a_8 - a_9i & a_8 - a_9i & 0 & -0.5 \\ -\frac{\sqrt{3}}{2} & 0 & -a_{10} + a_{11}i & a_{10} - a_{11}i & 0 & \frac{\sqrt{3}}{2} \\ 0.5 & -1 & 0 & a_1 + a_2i & -a_3 - a_4i & 0 \\ \frac{\sqrt{3}}{2} & 0 & 0 & a_5 + a_6i & 0 & 0 \\ 0 & 1 & -0.5 & 0 & -a_3 + a_4i & a_1 - a_2i \\ 0 & 0 & \frac{\sqrt{3}}{2} & 0 & 0 & -a_5 + a_6i \end{bmatrix} \begin{bmatrix} t_1 \\ t_2 \\ t_3 \\ t_4 \\ t_5 \\ t_6 \end{bmatrix} = \begin{bmatrix} f_{1x} \\ f_{1y} \\ f_{2x} \\ f_{2y} \\ f_{3x} \\ f_{3y} \end{bmatrix} \quad (\text{E.21b})$$

$$\tilde{ss}_1 = \begin{bmatrix} \cdot \\ \cdot \end{bmatrix}, \quad \tilde{d}_1 = \begin{bmatrix} \cdot \\ \cdot \end{bmatrix}$$

At wave-number $\omega = (0.125, 0.125)$:

$$\begin{bmatrix} -\frac{0.5}{\sqrt{3}} & 0 & \frac{0.5}{2} & \frac{0.5}{\sqrt{3}} & 0 & -\frac{0.5}{2} \\ -\frac{\sqrt{3}}{2} & 0 & -\frac{\sqrt{3}}{2} & \frac{\sqrt{3}}{2} & 0 & \frac{\sqrt{3}}{2} \\ 0.5 & -1 & 0 & -\frac{1}{2\sqrt{2}} + \frac{1}{2\sqrt{2}}i & \frac{1}{\sqrt{2}} - \frac{1}{\sqrt{2}}i & 0 \\ \frac{\sqrt{3}}{2} & 0 & 0 & -a_7 + a_7i & 0 & 0 \\ 0 & 1 & -0.5 & 0 & -\frac{1}{\sqrt{2}} + \frac{1}{\sqrt{2}}i & \frac{1}{2\sqrt{2}} - \frac{1}{2\sqrt{2}}i \\ 0 & 0 & \frac{\sqrt{3}}{2} & 0 & 0 & -a_7 + a_7i \end{bmatrix} \begin{bmatrix} t_1 \\ t_2 \\ t_3 \\ t_4 \\ t_5 \\ t_6 \end{bmatrix} = \begin{bmatrix} f_{1x} \\ f_{1y} \\ f_{2x} \\ f_{2y} \\ f_{3x} \\ f_{3y} \end{bmatrix} \quad (\text{E.21c})$$

$$\tilde{ss}_1 = \begin{bmatrix} 0 \\ \frac{1}{\sqrt{2}} + \frac{1}{\sqrt{2}}i \\ 0 \\ 0 \\ 1 \\ 0 \end{bmatrix}, \quad \tilde{d}_1 = \begin{bmatrix} 0 \\ 0 \\ \sqrt{3} \\ -1 \\ \sqrt{3} \\ 1 \end{bmatrix}$$

At wave-number $\omega = (0.3, 0)$:

$$\begin{bmatrix} -\frac{0.5}{\sqrt{3}} & 0 & -a_1 + a_2i & -a_1 + a_2i & 0 & -\frac{0.5}{\sqrt{3}} \\ -\frac{\sqrt{3}}{2} & 0 & a_5 - a_6i & -a_5 + a_6i & 0 & \frac{\sqrt{3}}{2} \\ \frac{0.5}{\sqrt{3}} & -1 & 0 & -\frac{0.5}{\sqrt{3}} & 1 & 0 \\ \frac{\sqrt{3}}{2} & 0 & 0 & -\frac{\sqrt{3}}{2} & 0 & 0 \\ \frac{0.5}{2} & 0 & 0 & -\frac{0.5}{2} & 0 & 0 \\ 0 & 1 & -0.5 & 0 & a_3 + a_4i & -a_1 - a_2i \\ 0 & 0 & \frac{\sqrt{3}}{2} & 0 & 0 & a_5 + a_6i \end{bmatrix} \begin{bmatrix} t_1 \\ t_2 \\ t_3 \\ t_4 \\ t_5 \\ t_6 \end{bmatrix} = \begin{bmatrix} f_{1x} \\ f_{1y} \\ f_{2x} \\ f_{2y} \\ f_{3x} \\ f_{3y} \end{bmatrix} \quad (\text{E.21d})$$

$$\tilde{ss}_1 = \begin{bmatrix} 0 \\ 0 \\ -0.309 + 0.9511i \\ 0 \\ 0 \\ 1 \end{bmatrix}, \quad \tilde{d}_1 = \begin{bmatrix} 0.2676 + 0.8236i \\ -0.1545 - 0.4755i \\ 0 \\ 0 \\ 0 \\ 1 \end{bmatrix}$$

At wave-number $\omega = (0.25, 0.25)$:

(E.21e)

$$\tilde{ss}_1 = \begin{bmatrix} 0 \\ i \\ 0 \\ 0 \\ 1 \\ 0 \end{bmatrix}, \quad \tilde{d}_1 = \begin{bmatrix} 0 \\ 0 \\ \sqrt{3} \\ -1 \\ \sqrt{3} \\ 1 \end{bmatrix}$$

At wave-number $\omega = (0.5, 0)$:

(E.21f)

$$\tilde{ss}_1 = \begin{bmatrix} 0 \\ 0 \\ -1 \\ 0 \\ 0 \\ 1 \end{bmatrix}, \quad \tilde{d}_1 = \begin{bmatrix} \frac{\sqrt{3}}{2} \\ -0.5 \\ 0 \\ 0 \\ 0 \\ 1 \end{bmatrix}$$

At wave-number $\omega = (0, 0)$:

$$\begin{bmatrix} -\frac{0.5}{\sqrt{3}} & 0 & \frac{0.5}{\sqrt{3}} & \frac{0.5}{\sqrt{3}} & 0 & -\frac{0.5}{\sqrt{3}} \\ -\frac{2}{\sqrt{3}} & 0 & -\frac{2}{\sqrt{3}} & \frac{2}{\sqrt{3}} & 0 & \frac{2}{\sqrt{3}} \\ \frac{0.5}{\sqrt{3}} & -1 & 0 & -\frac{0.5}{\sqrt{3}} & 1 & 0 \\ \frac{2}{\sqrt{3}} & 0 & 0 & -\frac{2}{\sqrt{3}} & 0 & 0 \\ 0 & 1 & -\frac{0.5}{\sqrt{3}} & 0 & -1 & \frac{0.5}{\sqrt{3}} \\ 0 & 0 & \frac{\sqrt{3}}{2} & 0 & 0 & -\frac{\sqrt{3}}{2} \end{bmatrix} \begin{bmatrix} t_1 \\ t_2 \\ t_3 \\ t_4 \\ t_5 \\ t_6 \end{bmatrix} = \begin{bmatrix} f_{1x} \\ f_{1y} \\ f_{2x} \\ f_{2y} \\ f_{3x} \\ f_{3y} \end{bmatrix} \quad (\text{E.21g})$$

$$\tilde{ss}_1 = \begin{bmatrix} 1 \\ 0 \\ 0 \\ 1 \\ 0 \\ 0 \end{bmatrix}, \tilde{ss}_2 = \begin{bmatrix} 0 \\ 1 \\ 0 \\ 0 \\ 1 \\ 0 \end{bmatrix}, \tilde{ss}_3 = \begin{bmatrix} 0 \\ 0 \\ 1 \\ 0 \\ 0 \\ 1 \end{bmatrix}, \tilde{d}_1 = \begin{bmatrix} \frac{\sqrt{3}}{2} \\ 0.5 \\ 0 \\ 1 \\ 0 \\ 0 \end{bmatrix}, \tilde{d}_2 = \begin{bmatrix} 1 \\ 0 \\ 1 \\ 0 \\ 1 \\ 0 \end{bmatrix}, \tilde{d}_3 = \begin{bmatrix} -\frac{\sqrt{3}}{2} \\ 0.5 \\ 0 \\ 0 \\ 0 \\ 1 \end{bmatrix}$$

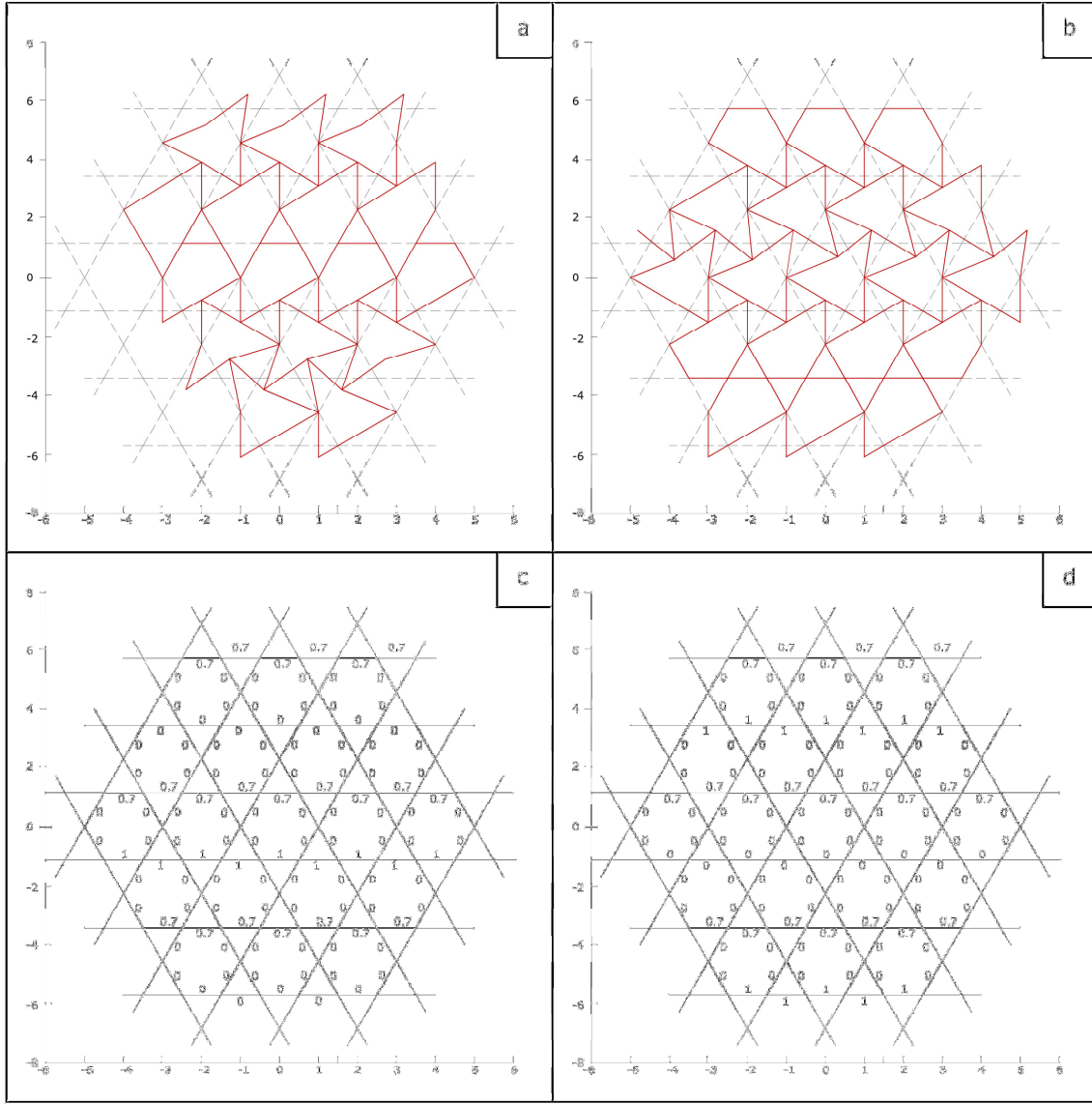
where $a_1 = 0.1545$, $a_2 = 0.4755$, $a_3 = 0.309$, $a_4 = 0.9511$, $a_5 = 0.2676$, $a_6 = 0.8236$,

$a_7 = 0.6124$, $a_8 = 0.4045$, $a_9 = 0.2939$, $a_{10} = 0.7006$, $a_{11} = 0.509$.

The determinacy analysis of the infinite periodic structure of the Kagome lattice indicates that the lattice is statically and kinematically determinate at wave-numbers $\omega = (0.1, 0.2)$ and $\omega = (0.2, 0.3)$, as shown in eqns (E.21a) and (E.21b), and statically and kinematically indeterminate at the rest wave-numbers, as shown in eqns (E.21c-g).

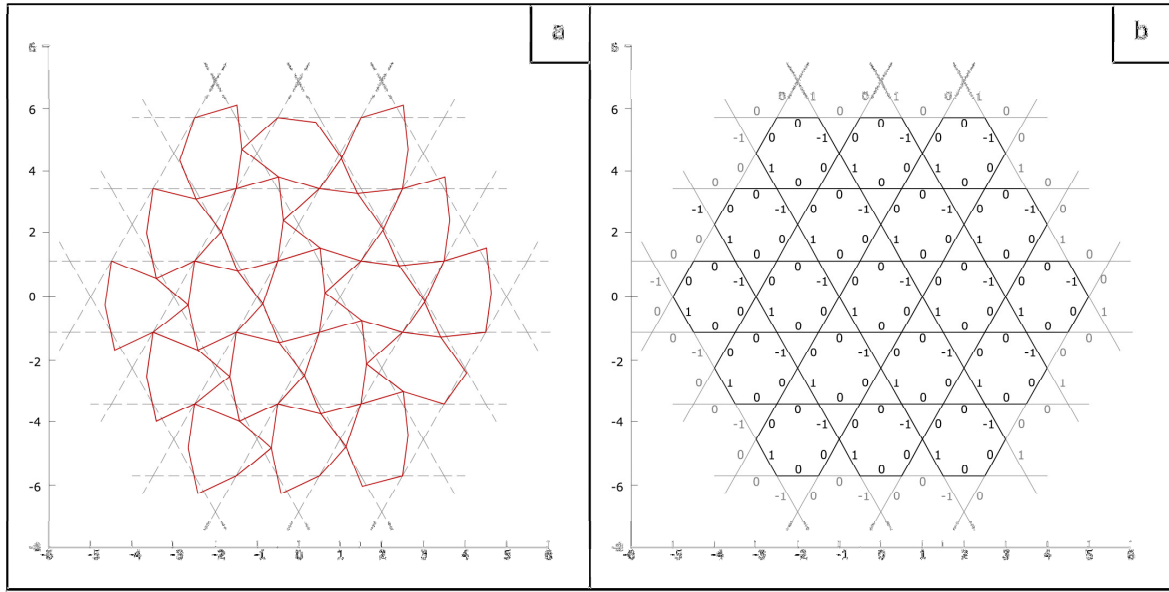
Accordingly, two of the three periodic mechanisms of the Kagome lattice at wave-number $\omega = (0, 0)$ are translational rigid-body motion and only one mode is internal mechanism.

The different states of self-stress and states of mechanisms experienced by the Kagome lattice at the different wave-numbers are represented graphically in Fig (E.8).



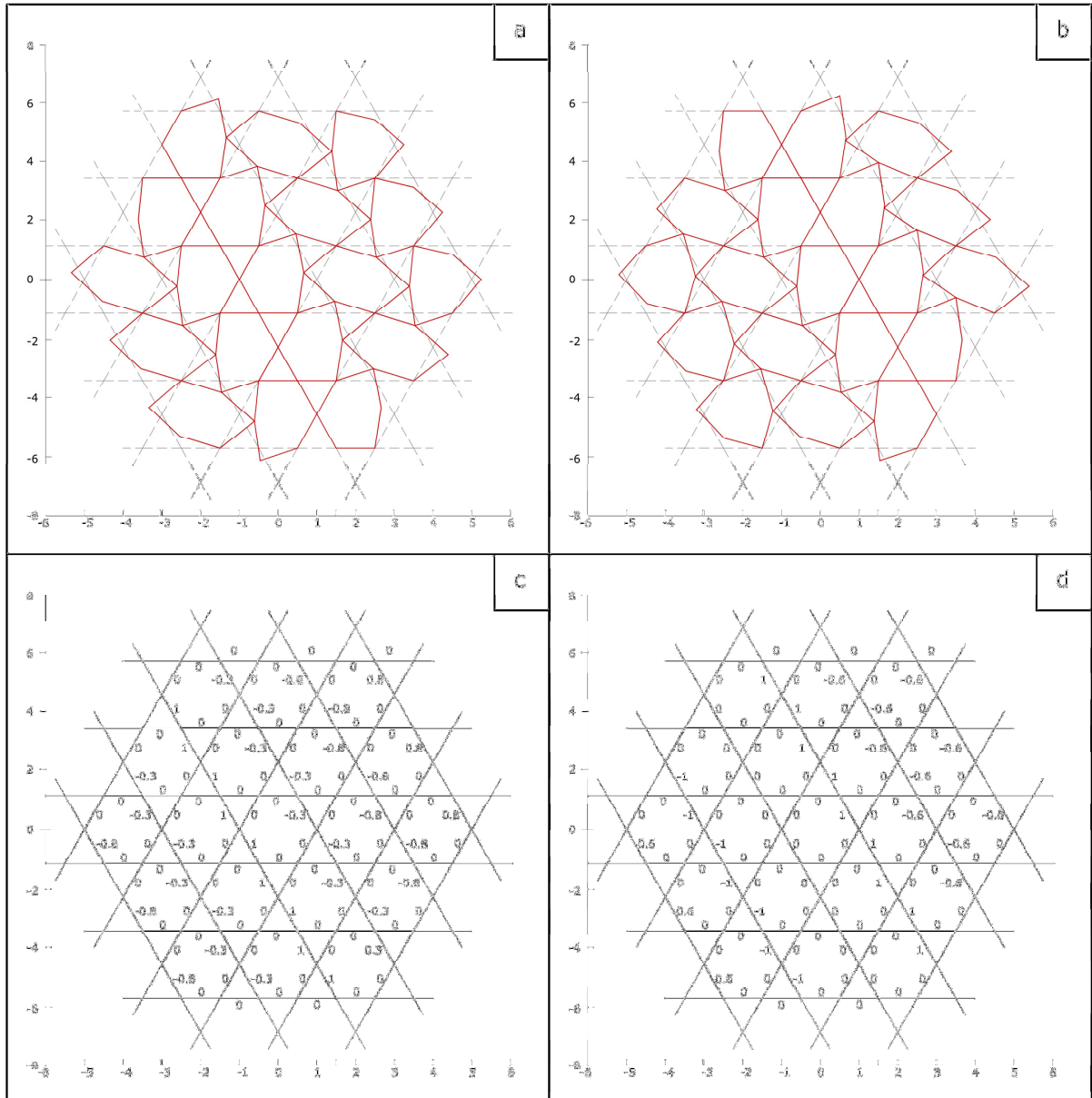
(a) Real part of internal mechanism; (b) imaginary part of internal mechanism; (c) real part of state of self-stress; (d) imaginary part of state of self-stress.

Fig (E.8a) Kagome lattice states of internal mechanisms and states of self-stress at wave-number $\omega = (0.125, 0.125)$



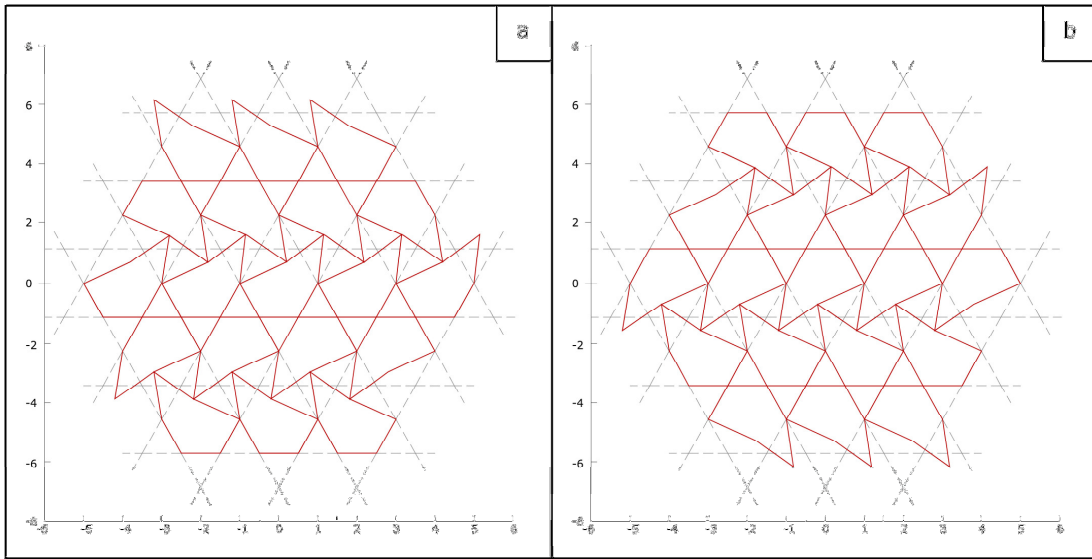
(a) Real part of internal mechanism; (b) real part of state of self-stress.

Fig (E.8b) Kagome lattice states of internal mechanisms and states of self-stress at wave-number $\omega = (0.5, 0)$



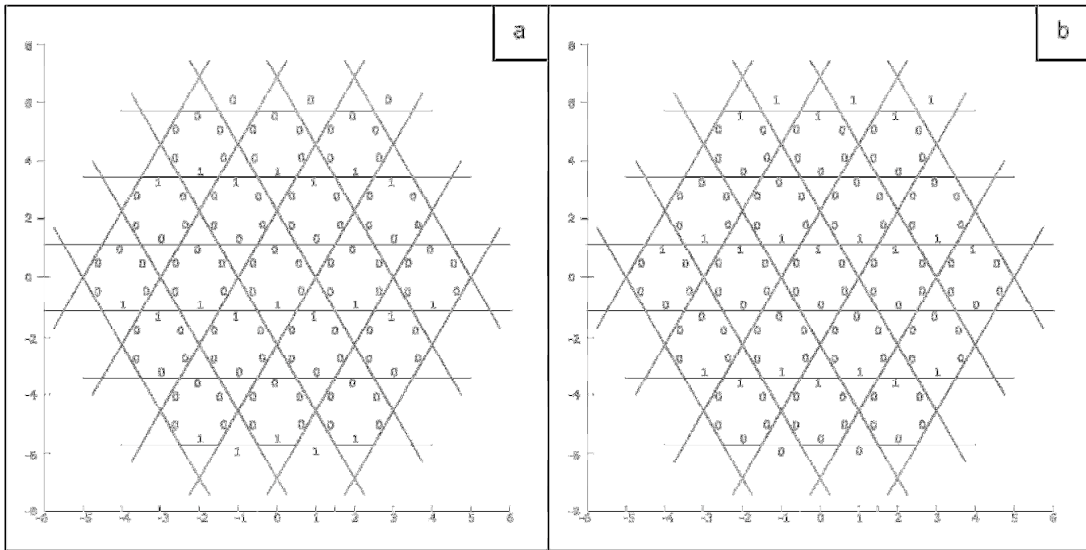
(a) Real part of internal mechanism; (b) imaginary part of internal mechanism; (c) real part of state of self-stress; (d) imaginary part of state of self-stress.

Fig (E.8c) Kagome lattice states of internal mechanisms and states of self-stress at wave-number $\omega = (0.3, 0)$



(a) Real part of internal mechanism; (b) imaginary part of internal mechanism.

Fig (E.8d) Kagome lattice states of internal mechanisms at wave-number $\omega = (0.25, 0.25)$



(a) Real part of state of self-stress; (b) imaginary part of state of self-stress.

Fig (E.8e) Kagome lattice state of self-stress at wave-number $\omega = (0.25, 0.25)$

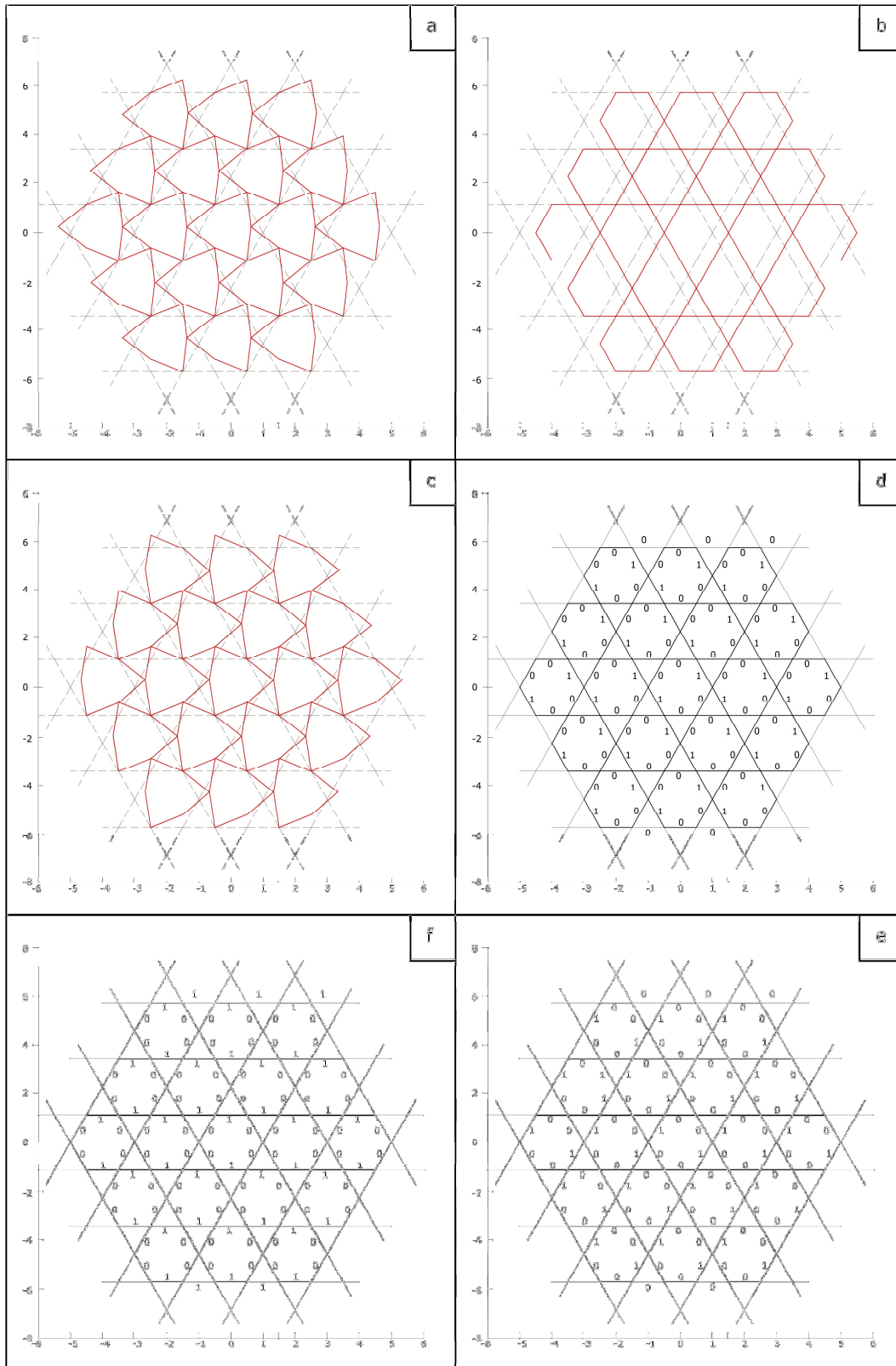


Fig (E.8f) Kagome lattice real parts of states of self-stress & states of mechanisms at $\omega = (0,0)$

E.3.3 Stiffening Effect Analysis of the Kagome Lattice at Wave-Number $\omega = (0.25, 0.25)$

Computing the reduced row echelon form (rref) of the reduced equilibrium matrix, at wave-number $\omega = (0.25, 0.25)$, shown in eqn (E.21e), results in:

$$\text{rref}(\tilde{\mathbf{A}}) = \begin{bmatrix} 1 & 0 & 0 & 0 & 0 & 0 \\ 0 & 1 & 0 & 0 & 0 & 0 \\ 0 & 0 & 1 & 0 & 0 & 0 \\ 0 & 0 & 0 & 1 & 0 & 0.309 - 0.9511i \\ 0 & 0 & 0 & 0 & 1 & 0 \\ 0 & 0 & 0 & 0 & 0 & 0 \end{bmatrix} \quad (\text{E.22})$$

From eqn (E.22), the non-pivotal column is found at the column of index number six.

Accordingly, the truncated reduced equilibrium system of the infinite Kagome lattice is expressed as:

$$\begin{bmatrix} -\frac{0.5}{\sqrt{3}} & 0 & \frac{0.5}{\sqrt{3}} & \frac{0.5}{\sqrt{3}} & 0 \\ -\frac{2}{\sqrt{3}} & 0 & -\frac{2}{\sqrt{3}} & \frac{2}{\sqrt{3}} & 0 \\ 0.5 & -1 & 0 & 0.5i & -i \\ \frac{0.5}{\sqrt{3}} & 0 & 0 & \frac{\sqrt{3}}{2}i & 0 \\ \frac{2}{\sqrt{3}} & 0 & 0 & \frac{2}{\sqrt{3}} & 0 \\ 0 & 1 & -0.5 & 0 & i \\ 0 & 0 & \frac{\sqrt{3}}{2} & 0 & 0 \end{bmatrix} \begin{bmatrix} t_1 \\ t_2 \\ t_3 \\ t_4 \\ t_5 \end{bmatrix} = \begin{bmatrix} f_{1x} \\ f_{1y} \\ f_{2x} \\ f_{2y} \\ f_{3x} \\ f_{3y} \end{bmatrix} \quad (\text{E.23})$$

Assuming a unit reference length, $L = 1$ and a unit nominal strain, $\varepsilon_0 = 1$, the reduced imposed elongation vector is computed at wave-number $\omega = (0.25, 0.25)$ as:

$$\tilde{e}_0 = [0 \quad 0 \quad 0 \quad 0 \quad 0 \quad 1]^T \quad (\text{E.24})$$

and the reduced flexibility matrix is computed as:

$$\tilde{\mathbf{F}} = \frac{1}{EA} \mathbf{I}(6,6) \quad (\text{E.25})$$

where $\mathbf{I}(6,6)$ is a unit matrix of dimension six by six; E and A are, respectively, the Young's modulus of the solid material and the nominal cross-section area of the lattice elements.

From eqn (E.21e), the reduced state of self-stress matrix of the Kagome lattice at wave-number $\omega = (0.25, 0.25)$ is the same as its state of self-stress as the lattice possesses only one state of self-stress at this wave-number.

Using the state of self-stress in eqn (E.21e), eqn (E.24) and eqn (E.25), the reduced vector of linear combination constants of the Kagome lattice at wave number $\omega = (0.25, 0.25)$ can be computed as:

$$\tilde{\gamma} = -0.5 \quad (\text{E.26})$$

Using the state of self-stress in eqn (E.21e) and eqn (E.26), the reduced global state of self-stress of the Kagome lattice at wave-number $\omega = (0.25, 0.25)$ can be computed as:

$$\tilde{S}_G = \begin{bmatrix} 0 \\ -0.5i \\ 0 \\ 0 \\ 0.5 \\ 0 \end{bmatrix} \quad (\text{E.27})$$

For the infinite periodic structure of the Kagome lattice, shown in Fig (E.2a), the product force vector as well as the reduced product force vector matrices at wave-number $\omega = (0.25, 0.25)$ are computed as:

$$\mathbf{PFV} = [0 \ 0 \ 0 \ i \ 0 \ -i \ 0 \ 0 \ 0 \ -i \ 0 \ i]^T \quad (\text{E.28a})$$

$$\tilde{\mathbf{PFV}} = [0.2992 - 0.4118i \ 0.1727 - 0.2378i \ 0 \ 0 \ -0.2992 - 0.4118i \ -0.1727 - 0.2378i]^T \quad (\text{E.28b})$$

The reduced product force vector matrix, given in eqn (E.28b), is now augmented into the truncated reduced equilibrium matrix, given in eqn (E.23), which results in the augmented reduced equilibrium matrix of the Kagome lattice at $\omega = (0.25, 0.25)$ as:

$$\tilde{\mathbf{A}}_{\text{aug}} = \begin{bmatrix} -\frac{0.5}{\sqrt{3}} & 0 & \frac{0.5}{\sqrt{3}} & \frac{0.5}{\sqrt{3}} & 0.2992 - 0.4118i \\ -\frac{2}{\sqrt{3}} & 0 & -\frac{2}{\sqrt{3}} & \frac{2}{\sqrt{3}} & 0.1727 - 0.2378i \\ \frac{0.5}{\sqrt{3}} & -1 & 0 & \frac{0.5i}{\sqrt{3}} & 0 \\ \frac{2}{\sqrt{3}} & 0 & 0 & \frac{\sqrt{3}}{2}i & 0 \\ 0 & 1 & -0.5 & 0 & -0.2992 - 0.4118i \\ 0 & 0 & \frac{\sqrt{3}}{2} & 0 & -0.1727 - 0.2378i \end{bmatrix} \quad (\text{E.29})$$

Computing the four fundamental subspaces of the augmented reduced matrix, given in (E.29),

produce an empty null space of the matrix transpose, i.e. ($\dim(\text{null}(\tilde{\mathbf{A}}_{\text{aug}}^T) = 0)$) which indicates

that the periodic states of self-stress is capable of stiffening the periodic internal mechanism at wave-number $\omega = (0.25, 0.25)$.

For the Kagome lattice, it is found that the periodic mechanisms tighten-up at all wave-numbers except at $\omega = (0.5, 0)$ as the periodic state of self-stress fails to stiffen the periodic mechanism.

E.3.4 Stiffening Effect Analysis of the Kagome Lattice at Wave-Number $\omega = (0.5, 0)$

The reduced row echelon form of the reduced equilibrium matrix, given in eqn (E.21f), of the Kagome lattice at wave-number $\omega = (0.5, 0)$ is computed as:

$$rref(\tilde{\mathbf{A}}) = \begin{bmatrix} 1 & 0 & 0 & 0 & 0 & 0 \\ 0 & 1 & 0 & 0 & 0 & 0 \\ 0 & 0 & 1 & 0 & 0 & 1 \\ 0 & 0 & 0 & 1 & 0 & 0 \\ 0 & 0 & 0 & 0 & 1 & 0 \\ 0 & 0 & 0 & 0 & 0 & 0 \end{bmatrix} \quad (\text{E.30})$$

and the non-pivotal column is found at the column of index number six. Accordingly, the truncated reduced equilibrium system of the lattice is computed as:

$$\begin{bmatrix} -\frac{0.5}{\sqrt{3}} & 0 & -\frac{0.5}{\sqrt{3}} & -\frac{0.5}{\sqrt{3}} & 0 \\ -\frac{2}{\sqrt{3}} & 0 & \frac{2}{\sqrt{3}} & -\frac{2}{\sqrt{3}} & 0 \\ 0.5 & -1 & 0 & -0.5 & 1 \\ \frac{\sqrt{3}}{2} & 0 & 0 & -\frac{\sqrt{3}}{2} & 0 \\ 0 & 1 & -0.5 & 0 & 1 \\ 0 & 0 & \frac{\sqrt{3}}{2} & 0 & 0 \end{bmatrix} \begin{bmatrix} t_1 \\ t_2 \\ t_3 \\ t_4 \\ t_6 \end{bmatrix} = \begin{bmatrix} f_{1x} \\ f_{1y} \\ f_{2x} \\ f_{2y} \\ f_{3x} \\ f_{3y} \end{bmatrix} \quad (\text{E.31})$$

Assuming a unit reference length, $L = 1$ and a unit nominal strain, $\epsilon_0 = 1$, the vector of imposed elongations and the flexibility matrix are generated as:

$$\tilde{e}_0 = [0 \quad 0 \quad 0 \quad 0 \quad 0 \quad 1]^T, \quad \tilde{\mathbf{F}} = \frac{1}{EA} \mathbf{I}(6 \times 6) \quad (\text{E.32})$$

Eqn (E.32) is used to compute the reduced vector of linear combination constants and the reduced global state of self-stress as:

$$\begin{bmatrix} \tilde{\gamma} \end{bmatrix} = -0.5, \quad \tilde{S}_G = \begin{bmatrix} 0 \\ 0 \\ -0.5 \\ 0 \\ 0 \\ 0.5 \end{bmatrix} \quad (\text{E.33})$$

which are used along with the reduced periodic internal mechanism to generate the product force vector as:

$$\mathbf{PFV} = \begin{bmatrix} -\frac{\sqrt{3}}{4} \\ -0.25 \\ 0 \\ 0 \\ \frac{\sqrt{3}}{4} \\ 0.25 \\ -\frac{\sqrt{3}}{4} \\ -0.25 \\ 0 \\ 0 \\ \frac{\sqrt{3}}{4} \\ 0.25 \end{bmatrix}, \quad \tilde{\mathbf{PFV}} = \begin{bmatrix} 0 \\ 0 \\ 0 \\ 1+i \\ 0 \\ -1-i \end{bmatrix} \quad (\text{E.34})$$

The reduced product force vector matrix, given in eqn (E.34), is augmented to the truncated reduced equilibrium matrix, given in eqn (E.31), which results in the augmented reduced equilibrium matrix as:

$$\tilde{\mathbf{A}}_{\text{aug}} = \begin{bmatrix} -\frac{0.5}{\sqrt{3}} & 0 & -\frac{0.5}{\sqrt{3}} & -\frac{0.5}{\sqrt{3}} & 0 & 0 \\ -\frac{2}{\sqrt{3}} & 0 & \frac{2}{\sqrt{3}} & -\frac{2}{\sqrt{3}} & 0 & 0 \\ 0.5 & -1 & 0 & -0.5 & 1 & 0 \\ \frac{0.5}{\sqrt{3}} & 0 & 0 & -\frac{\sqrt{3}}{2} & 0 & 1+i \\ \frac{2}{\sqrt{3}} & 0 & 0 & -\frac{2}{\sqrt{3}} & 0 & 0 \\ 0 & 1 & -0.5 & 0 & 1 & 0 \\ 0 & 0 & \frac{\sqrt{3}}{2} & 0 & 0 & -1-i \end{bmatrix} \quad (\text{E.35})$$

Computation of the four fundamental subspaces of the augmented equilibrium matrix, given in eqn (E.35), indicates that the periodic state of self-stress fails to stiffen the periodic internal mechanisms as the lattice still experiences the same periodic failure mechanism, given in eqn

(E.21f). This result indicates that the pin-jointed infinite Kagome lattice structure collapses with infinite periodic mechanisms at wave-number $\omega = (0.5, 0)$. Accordingly, the infinite periodic Kagome lattice structure is classified as a bending dominated lattice structure.

E.4 Determinacy Analysis of the Kagome Lattice at Wave-Number $\omega = (0, 0)$

From eqn (E.21g), the Kagome lattice experiences three states of self-stress and three states of mechanisms. Two out of three mechanisms are rigid-body translation and one is internal mechanisms. In the following we distinguish between the rigid-body motions and the internal mechanisms.

The set of reduced, periodic, states of self-stress of the Kagome lattice, given in eqn (E.21g), is used to generate the reduced state of self-stress matrix as:

$$\tilde{\mathbf{S}}\mathbf{S} = \begin{bmatrix} 1 & 0 & 0 \\ 0 & 1 & 0 \\ 0 & 0 & 1 \\ 1 & 0 & 0 \\ 0 & 1 & 0 \\ 0 & 0 & 1 \end{bmatrix} \quad (\text{E.36})$$

The reduced row echelon form of the reduced equilibrium matrix, given in eqn (E.21g), is computed to determine the non-pivotal elements in the infinite lattice, which results in:

$$rref\left(\tilde{\mathbf{A}}\right) = \begin{bmatrix} 1 & 0 & 0 & -1 & 0 & 0 \\ 0 & 1 & 0 & 0 & -1 & 0 \\ 0 & 0 & 1 & 0 & 0 & -1 \\ 0 & 0 & 0 & 0 & 0 & 0 \\ 0 & 0 & 0 & 0 & 0 & 0 \\ 0 & 0 & 0 & 0 & 0 & 0 \end{bmatrix} \quad (\text{E.37})$$

which indicates that the non-pivotal columns are the columns with indices 4, 5 and 6.

Assuming a unit reference length, $L = 1$ and a unit nominal strain, $\epsilon_0 = 1$, the reduced flexibility matrix, $\tilde{\mathbf{F}}$ matrix and the reduced vector of imposed elongations, $\tilde{\epsilon}_0$, are computed as:

$$\tilde{\mathbf{F}} = \frac{1}{EA} \begin{bmatrix} 1 & 0 & 0 & 0 & 0 & 0 \\ 0 & 1 & 0 & 0 & 0 & 0 \\ 0 & 0 & 1 & 0 & 0 & 0 \\ 0 & 0 & 0 & 1 & 0 & 0 \\ 0 & 0 & 0 & 0 & 1 & 0 \\ 0 & 0 & 0 & 0 & 0 & 1 \end{bmatrix}, \tilde{\mathbf{e}}_0 = \begin{bmatrix} 0 \\ 0 \\ 0 \\ 1 \\ 1 \\ 1 \end{bmatrix} \quad (\text{E.38})$$

Using eqns (E.38) and (E.36), the reduced vector of linear combination constants of the Kagome lattice, at wave-number $\omega = (0,0)$, can be computed as:

$$\tilde{\gamma} = \begin{bmatrix} -0.5 \\ -0.5 \\ -0.5 \end{bmatrix} \quad (\text{E.39})$$

The reduced global state of self-stress of the Kagome lattice at wave-number $\omega = (0,0)$ is computed as:

$$\tilde{S}_G = \begin{bmatrix} -0.5 \\ -0.5 \\ -0.5 \\ -0.5 \\ -0.5 \\ -0.5 \end{bmatrix} \quad (\text{E.40})$$

The set of mechanisms of the Kagome lattice, given in eqn (E.21g), is used to generate the reduced mechanisms matrix as:

$$\tilde{\mathbf{D}} = \begin{bmatrix} \frac{\sqrt{3}}{2} & 1 & -\frac{\sqrt{3}}{2} \\ 0.5 & 0 & 0.5 \\ 0 & 1 & 0 \\ 1 & 0 & 0 \\ 0 & 1 & 0 \\ 0 & 0 & 1 \end{bmatrix} \quad (\text{E.41})$$

Next, the reduced modes of mechanisms and the global states of self-stress are expanded to generate, respectively, the kinematical displacements of all nodes and the tension force of all elements within the unit cell, which results in:

$$\mathbf{D} = \begin{bmatrix} 0.866 & 1 & -0.866 \\ 0.5 & 0 & 0.5 \\ 0 & 1 & 0 \\ 1 & 0 & 0 \\ 0 & 1 & 0 \\ 0 & 0 & 1 \\ 0.866 & 1 & -0.866 \\ 0.5 & 0 & 0.5 \\ 0 & 1 & 0 \\ 1 & 0 & 0 \\ 0 & 1 & 0 \\ 0 & 0 & 1 \end{bmatrix}, \quad S_G = \begin{bmatrix} -0.5 \\ -0.5 \\ -0.5 \\ -0.5 \\ -0.5 \\ -0.5 \end{bmatrix} \quad (\text{E.42})$$

The expanded modes of mechanisms along with the expanded global state of self-stress are used to formulate the set of product force vectors corresponding to each individual mechanism. The developed product force vectors are concatenated into the product force vector matrix, \mathbf{PFV} . The product force vector matrix is then reduced to the irreducible product force vector matrix, $\tilde{\mathbf{PFV}}$, where $\tilde{\mathbf{PFV}}$ represents the product force vector of the infinite lattice structure. These computations results in:

$$\mathbf{PFV} = \begin{bmatrix} 0.866 & 1 & -0.866 \\ 0 & 0 & 0 \\ -0.433 & 0 & 0.433 \\ 0.75 & 0 & -0.75 \\ -0.433 & 0 & 0.433 \\ -0.75 & 0 & 0.75 \\ 0.866 & 0 & -0.866 \\ 0 & 0 & 0 \\ -0.433 & 0 & 0.433 \\ 0.75 & 0 & -0.75 \\ -0.433 & 0 & 0.433 \\ -0.75 & 0 & 0.75 \end{bmatrix}, \quad \tilde{\mathbf{PFV}} = \begin{bmatrix} 1.7321 & 0 & -1.7321 \\ 0 & 0 & 0 \\ -0.866 & 0 & 0.866 \\ 1.5 & 0 & -1.5 \\ -0.866 & 0 & 0.866 \\ -1.5 & 0 & 1.5 \end{bmatrix} \quad (\text{E.43})$$

The non-pivotal columns of the reduced equilibrium matrix of the infinite periodic Kagome lattice, at wave number $\omega = (0,0)$, given in eqn (E.21g), are eliminated to form the truncated

reduced equilibrium matrix $\hat{\tilde{\mathbf{A}}}$. The reduced product force vector matrix, given in eqn (E.43), is augmented to the matrix $\hat{\tilde{\mathbf{A}}}$ to form the augmented reduced equilibrium matrix as:

$$\tilde{\mathbf{A}}_{\text{aug}} = \left[\begin{array}{ccc|ccc} -0.5 & 0 & 0.5 & 1.7321 & 0 & -1.7321 \\ -0.866 & 0 & -0.866 & 0 & 0 & 0 \\ 0.5 & -1 & 0 & -0.866 & 0 & 0.866 \\ 0.866 & 0 & 0 & 1.5 & 0 & -1.5 \\ 0 & 1 & -0.5 & -0.866 & 0 & 0.866 \\ 0 & 0 & 0.866 & -1.5 & 0 & 1.5 \end{array} \right] \quad (\text{E.44})$$

The left-null space of the augmented reduced equilibrium matrix of the Kagome lattice, shown in eqn (E.44), is computed to determine the modes of the un-stiffened mechanisms along with their indices, these mechanisms are computed as:

$$\tilde{\mathbf{D}} = \begin{bmatrix} 1 & 0 \\ 0 & 1 \\ 1 & 0 \\ 0 & 1 \\ 1 & 0 \\ 0 & 1 \end{bmatrix} \quad (\text{E.45})$$

It can be realized that the first and the second columns of the mechanisms matrix, $\tilde{\mathbf{D}}$, of the Kagome lattice, given in eqn (E.45), are correspondent to translational rigid-body motion in the x and the y directions, respectively. Since there are only two mechanisms which both represent rigid-body motion, then, no additional filtration is required. The indices of these two mechanisms are determined as the 5th and 6th indices in the row space of the augmented reduced equilibrium matrix. The nodal degrees of freedom corresponding to these modes have to be eliminated from the reduced equilibrium matrix computed in eqn (E.21g) which results in:

$$\approx \tilde{\mathbf{A}} = \begin{bmatrix} -0.5 & 0 & 0.5 & 0.5 & 0 & -0.5 \\ -0.866 & 0 & -0.866 & 0.866 & 0 & 0.866 \\ 0.5 & -1 & 0 & -0.5 & 1 & 0 \\ 0.866 & 0 & 0 & -0.866 & 0 & 0 \end{bmatrix} \quad (\text{E.46})$$

Again the null space and the left-null space of the equilibrium matrix, defined in eqn (E.46), are computed to determine the final sets of states of self-stress and the states of internal mechanisms, respectively, which are computed as:

$$\tilde{\mathbf{D}} = \begin{bmatrix} 0.866 \\ 0.5 \\ 0 \\ 1 \end{bmatrix}, \tilde{\mathbf{SS}} = \begin{bmatrix} 1 & 0 & 0 \\ 0 & 1 & 0 \\ 0 & 0 & 1 \\ 1 & 0 & 0 \\ 0 & 1 & 0 \\ 0 & 0 & 1 \end{bmatrix} \quad (\text{E.47})$$

The set of states of self-stress can be used to check that the necessary condition for the stiffening effect of periodic states of self-stress to the periodic internal mechanism.

The analysis is expanded to consider the sufficient condition of the stiffening effect. It is found that, at wave-number $\omega = (0,0)$, the developed states of self-stress impart positive stiffness as the Kagome lattice structure deforms by a first-order periodic internal mechanism.

E.5 Summary of the Determinacy Analysis Results of the 19 Lattice Topologies

The infinite determinacy analysis results of the 19 lattice topologies shown in Figs (E.1), (E.2) and (E.3) are reported in tables (E9:E27). At each wave number, derived from the irreducible first Brillouin zone of the lattice, the States of Self-Stress (SSS) and the States of Internal Mechanisms (SIM) are computed. Also, the stiffening effect of the SSSs to the SIMs is checked using the Product Force Vector (PFV) approach as the necessary condition. For internal mechanisms that satisfy the necessary condition, we check the definiteness of the stress tensor to satisfy the sufficient condition of mechanisms to be classified as first-order infinitesimal mechanisms. The results obtained here, are used for the classification of the 19 topologies in chapter three.

Table (E.9) Determinacy analysis of the regular square lattice (Fig E.1a)

Wave-numbers		# SSS	# SIM	PFV	
ω_1	ω_2			# SSS	# SIM
0.25	0.5	0	0	-	-
0	0.5	1	1	1	1
0.5	0.5	0	0	-	-
0.1667	0.3333	0	0	-	-
0	0.25	1	1	1	1
0.25	0.25	0	0	-	-
0	0	2	2	2	2

Table (E.10) Determinacy analysis of the regular triangular lattice (Fig E.1b)

Wave-numbers		# SSS	# SIM	PFV	
ω_1	ω_2			# SSS	# SIM
0.1667	0.5833	1	0	-	-
0.4167	0.5833	1	0	-	-
0.25	0.5	1	0	-	-
0	0.5	1	0	-	-
0.3333	0.6667	1	0	-	-
0.5	0.5	1	0	-	-
0.2083	0.4167	1	0	-	-
0	0.25	1	0	-	-
0.1667	0.3333	1	0	-	-
0.25	0.25	1	0	-	-
0	0	3	2	3	2

Table (E.11) Determinacy analysis of the regular hexagonal lattice (Fig E.1c)

Wave-numbers		# SSS	# SIM	PFV	
ω_1	ω_2			# SSS	# SIM
0.5833	-0.1667	0	1	-	-
0.5	0	0	1	-	-
0.6667	-0.3333	0	1	-	-
0.3889	-0.1111	0	1	-	-
0.25	0	0	1	-	-
0.3333	-0.1667	0	1	-	-
0	0	1	2	2	2

Table (E.12) Determinacy analysis of the semi-regular (3.6.3.6) Kagome lattice (Fig E.2a)

Wave-numbers		# SSS	# SIM	PFV	
ω_1	ω_2			# SSS	# SIM
0.1	0.2	0	0	-	-
0.2	0.3	0	0	-	-
0.125	0.125	1	1	0	0
0.3	0	1	1	0	0
0.25	0.25	1	1	0	0
0.5	0	1	1	1	1
0	0	3	3	2	2

Table (E.13) Determinacy analysis of the semi-regular 4.6.12 lattice (Fig E.2b)

Wave-numbers		# SSS	# SIM	PFV	
ω_1	ω_2			# SSS	# SIM
0.4167	0.1667	7	13	2	2
0.5833	-0.1667	7	13	2	2
0.5833	-0.4167	7	13	2	2
0.4167	-0.0833	7	13	2	2
0.3333	0.3333	7	13	2	2
0.5	0	7	13	2	2
0.6667	-0.3333	7	13	2	2
0.5	-0.5	7	13	2	2
0.4	-0.1	7	13	2	2
0.1667	0.1667	7	13	2	2
0.25	0	7	13	2	2
0.3333	-0.1667	7	13	2	2
0.25	-0.25	7	13	2	2
0	0	7	13	2	2

Table (E.14) Determinacy analysis of the semi-regular $3^3.4^2$ lattice (Fig E.2c)

Wave-numbers		# SSS	# SIM	PFV	
ω_1	ω_2			# SSS	# SIM
0.61603	0.38397	1	0	-	-
0.61603	0.13397	1	0	-	-
0.38397	-0.13397	1	0	-	-
0.38397	0.11603	1	0	-	-
0.5	0.5	2	1	0	0
0.73205	0.26795	1	0	-	-
0.5	0	1	0	-	-
0.26795	-0.26795	1	0	-	-
0.4	0.1	1	0	-	-
0.25	0.25	2	1	0	0
0.36603	0.13397	1	0	-	-
0.25	0	1	0	-	-
0.13397	-0.13397	1	0	-	-
0	0	3	2	2	2

Table (E.15) Determinacy analysis of the semi-regular $3^2.4.3.4$ lattice (Fig E.2d)

Wave-numbers		# SSS	# SIM	PFV	
ω_1	ω_2			# SSS	# SIM
0.25	0.25	2	0	-	-
0.75	-0.25	2	0	-	-
0.75	-0.5	2	0	-	-
0.5	-0.5	2	0	-	-
0	0.5	2	0	-	-
0.5	0	2	0	-	-
1	-0.5	2	0	-	-
0.4	-0.1	2	0	-	-
0.25	-0.25	2	0	-	-
0	0.25	2	0	-	-
0.25	0	2	0	-	-
0.5	-0.25	2	0	-	-
0	0	4	2	2	2

Table (E.16) Determinacy analysis of the semi-regular 3.4.6.4 lattice (Fig E.2e)

Wave-numbers		# SSS	# SIM	PFV	
ω_1	ω_2			# SSS	# SIM
0.58333	0.41667	1	1	1	1
0.58333	0.16667	1	1	1	1
0.41667	-0.16667	1	1	1	1
0.41667	0.083333	1	1	1	1
0.5	0.5	1	1	1	1
0.66667	0.33333	1	1	1	1
0.5	0	1	1	1	1
0.33333	-0.33333	1	1	1	1
0.4	0.1	1	1	1	1
0.25	0.25	1	1	1	1
0.33333	0.16667	1	1	1	1
0.25	0	1	1	1	1
0.16667	-0.16667	1	1	1	1
0	0	3	3	2	2

Table (E.17) Determinacy analysis of the semi-regular 3.12² lattice (Fig E.2f)

Wave-numbers		# SSS	# SIM	PFV	
ω_1	ω_2			# SSS	# SIM
0.5833	0.4167	0	3	-	-
0.5833	0.1667	0	3	-	-
0.4167	-0.1667	0	3	-	-
0.4167	0.0833	0	3	-	-
0.5	0.5	0	3	-	-
0.6667	0.3333	0	3	-	-
0.5	0	0	3	-	-
0.3333	-0.3333	0	3	-	-
0.4	0.1	0	3	-	-
0.25	0.25	0	3	-	-
0.3333	0.1667	0	3	-	-
0.25	0	0	3	-	-
0.1667	-0.1667	0	3	-	-
0	0	1	4	2	2

Table (F.18) Determinacy analysis of the semi-regular 4.8² lattice (Fig E.2g)

Wave-numbers		# SSS	# SIM	PFV	
ω_1	ω_2			# SSS	# SIM
0.5	0.25	0	2	-	-
0.5	0.5	0	2	-	-
0.5	0	0	2	-	-
0.33333	0.16667	0	2	-	-
0.25	0.25	0	2	-	-
0.25	0	0	2	-	-
0	0	1	3	2	2

Table (E.19) Determinacy analysis of the semi-regular $3^4.6$ lattice (Fig E.2h)

Wave-numbers		# SSS	# SIM	PFV	
ω_1	ω_2			# SSS	# SIM
-0.41667	0.58333	3	0	-	-
-0.33333	0.66667	3	0	-	-
-0.5	0.5	3	0	-	-
-0.27778	0.38889	3	0	-	-
-0.16667	0.33333	3	0	-	-
-0.25	0.25	3	0	-	-
0	0	5	2	2	2

Table (E.20) Determinacy analysis of the semi-regular DHT lattice (Fig E.3a)

Wave-numbers		# SSS	# SIM	PFV	
ω_1	ω_2			# SSS	# SIM
0.6667	-0.3333	7	0	-	-
0.5	0	7	0	-	-
0.3333	0.3333	7	0	-	-
0	0.5	7	0	-	-
-0.3333	0.6667	7	0	-	-
-0.5	0.5	7	0	-	-
-0.6667	0.3333	7	0	-	-
-0.5	0	7	0	-	-
-0.3333	-0.3333	7	0	-	-
0	-0.5	7	0	-	-
0.3333	-0.6667	7	0	-	-
0.5	-0.5	7	0	-	-
0.3333	-0.1667	7	0	-	-
0.25	0	7	0	-	-
0.1667	0.1667	7	0	-	-
0	0.25	7	0	-	-
-0.1667	0.3333	7	0	-	-
-0.25	0.25	7	0	-	-
-0.3333	0.1667	7	0	-	-
-0.25	0	7	0	-	-
-0.1667	-0.1667	7	0	-	-
0	-0.25	7	0	-	-
0.1667	-0.3333	7	0	-	-
0.25	-0.25	7	0	-	-
0	0	9	2	2	2

Table (E.21) Determinacy analysis of the Semi-Uni- Braced Square (SUBS) lattice (Fig E.3b)

Wave-numbers		# SSS	# SIM	PFV	
ω_1	ω_2			# SSS	# SIM
0.25	0.5	1	0	-	-
0.5	0.25	1	0	-	-
0.5	-0.25	1	0	-	-
0	0.5	1	0	-	-
0.5	0.5	2	1	1	1
0.5	0	1	0	-	-
0.5	-0.5	2	1	1	1
0.3	0.1	1	0	-	-
0	0.25	1	0	-	-
0.25	0.25	1	0	-	-
0.25	0	1	0	-	-
0.25	-0.25	1	0	1	0
0	0	3	2	2	2

Table (E.22) Determinacy analysis of the Triangular- Triangular (T-T) lattice (Fig E.3c)

Wave-numbers		# SSS	# SIM	PFV	
ω_1	ω_2			# SSS	# SIM
-0.1667	0.4167	0	0	-	-
0.1667	0.5833	0	0	-	-
0.4167	0.5833	0	0	-	-
0.5833	0.4167	0	0	-	-
0.5833	0.1667	0	0	-	-
0.4167	-0.1667	0	0	-	-
-0.3333	0.3333	0	0	-	-
0	0.5	0	0	-	-
0.3333	0.6667	0	0	-	-
0.5	0.5	0	0	-	-
0.6667	0.3333	0	0	-	-
0.5	0	0	0	-	-
0.3333	-0.3333	0	0	-	-
0.2593	0.2963	0	0	-	-
0	0.25	0	0	-	-
0.1667	0.3333	0	0	-	-
0.25	0.25	0	0	-	-
0.3333	0.1667	0	0	-	-
0.25	0	0	0	-	-
0.1667	-0.1667	0	0	-	-
0	0	2	2	2	2

Table (E.23) Determinacy analysis of the Semi-Double- Braced Square lattice (Fig E.3d)

Wave-numbers		# SSS	# SIM	PFV	
ω_1	ω_2			# SSS	# SIM
0.5	0.25	2	0	-	-
0.5	0.5	2	0	-	-
0.5	0	2	0	-	-
0.3333	0.1667	2	0	-	-
0.25	0.25	2	0	-	-
0.25	0	2	0	-	-
0	0	4	2	2	2

Table (E.24) Determinacy analysis of the Equilaterals- Hexagon Square lattice (Fig E.3e)

Wave-numbers		# SSS	# SIM	PFV	
ω_1	ω_2			# SSS	# SIM
0.4167	0.1667	0	0	-	-
0.3333	0.3333	0	0	-	-
0.5	0	1	1	0	0
0.2778	0.1111	0	0	-	-
0.1667	0.1667	0	0	-	-
0.25	0	1	1	0	0
0	0	2	2	2	2

Table (E.25) Determinacy analysis of the Uni- Braced Square lattice (Fig E.3f)

Wave-numbers		# SSS	# SIM	PFV	
ω_1	ω_2			# SSS	# SIM
-0.25	0.5	1	0	-	-
0.25	0.5	1	0	-	-
0.5	0.25	1	0	-	-
-0.5	0.5	1	0	-	-
0	0.5	1	0	-	-
0.5	0.5	1	0	-	-
0.5	0	1	0	-	-
0.1	0.3	1	0	-	-
-0.25	0.25	1	0	-	-
0	0.25	1	0	-	-
0.25	0.25	1	0	-	-
0.25	0	1	0	-	-
0	0	3	2	5	2

Table (E.26) Determinacy analysis of the Double- Braced Square lattice (Fig E.3g)

Wave-numbers		# SSS	# SIM	PFV	
ω_1	ω_2			# SSS	# SIM
0.25	0.5	2	0	-	-
0	0.5	2	0	-	-
0.5	0.5	2	0	-	-
0.1667	0.3333	2	0	-	-
0	0.25	2	0	-	-
0.25	0.25	2	0	-	-
0	0	4	2	2	2

Table (E.27) Determinacy analysis of the Patched Kagome lattice (Fig E.3h)

Wave-numbers		# SSS	# SIM	PFV	
ω_1	ω_2			# SSS	# SIM
0.4167	0.5833	3	0	-	-
0.5833	0.4167	3	0	-	-
0.5833	0.1667	3	0	-	-
0.4167	0.3333	3	0	-	-
0.3333	0.6667	3	0	-	-
0.5	0.5	3	0	-	-
0.6667	0.3333	3	0	-	-
0.5	0	3	0	-	-
0.4	0.3	3	0	-	-
0.1667	0.3333	3	0	-	-
0.25	0.25	3	0	-	-
0.3333	0.1667	3	0	-	-
0.25	0	3	0	-	-
0	0	5	2	2	2

APPENDIX F

Effective Elastic and Strength Properties of Pin-Jointed Lattice

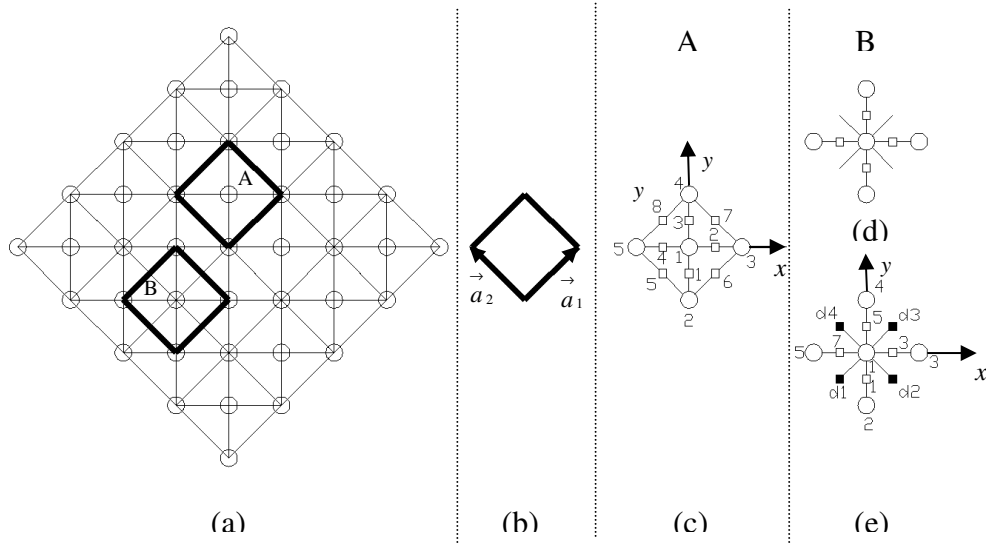
Materials: Applications

In this Appendix, we apply the characterization methodology, developed in chapter four, to ten lattice topologies. Details of the characterization process of the effective stiffness and strength properties are demonstrated for two lattice topologies, namely, the semi-double braced square lattice and the $3^4.6$ lattice. The former has a square Bravais lattice symmetry and the latter has a hexagonal Bravais lattice symmetry. Results of the effective stiffness characterization of the other eight lattice topologies are reported. Stretching-dominated characteristics of the lattices are determined and their elastic moduli and strength properties are computed.

F.1 Characterization of the Semi-Double-Braced Square Lattice

This section describes the characterization of the stiffness and strength properties of the semi-double braced square lattice topology that has a square Bravais lattice symmetry. We recall this lattice topology, shown previously in Fig (2.6d), into Fig (4.1) to describe its microscopic architecture in more details. This lattice structure can be generated by the candidate unit cells: A and B. Unit cell B, shown in Fig (F.1e) has eight cell elements of which four intersect the cell envelope extending to the adjacent unit cells and the other four are all contained within the cell envelope. Unit cell A, shown in Fig (F.1c) has also eight cell elements that are all contained within the cell envelope. Four dummy nodes, denoted as d1, d2, d3 and d4, are introduced to unit cell B at the intersection points between the cell envelope and the cell elements that extend between the adjacent cells.

The purpose of this example is to demonstrate the accuracy of the DNS as the characterization process is carried out by the two unit cells, A and B. Characterization using unit cell A is straight forward and does not require the application of the DNS, however, the characterization using unit cell B requires the application of the DNS. Both characterization approaches generate the same elastic properties for the lattice material, which proves the accuracy of the proposed method.



- ... Bar geometrical centroid
- ... Real node
- ... Dummy node

(a) Lattice structure, (b) Cell envelope, (c) Unit cell A, (d) Unit cell B without dummy nodes, (e) Unit cell B with dummy nodes

Fig. (F.1) The Semi-Double-Braced Square Lattice

The characterization process starts by defining the bar, the node and the dummy node bases groups of unit cells A and B as:

$$G_B^A = \{(0, -0.5), (0.5, 0), (0, 0.5), (-0.5, 0), (-0.5, -0.5), (0.5, -0.5), (0.5, 0.5), (-0.5, 0.5)\}$$

$$G_N^A = \{(0, 0), (0, -1), (1, 0), (0, 1), (-1, 0)\}, \quad G_D^A = \Phi$$

$$G_B^B = \{(0, -0.5), (0.5, -0.5), (0.5, 0), (0.5, 0.5), (0, 0.5), (-0.5, 0.5), (-0.5, 0), (-0.5, -0.5)\}$$

$$G_N^B = \{(0, 0), (0, -1), (1, 0), (0, 1), (-1, 0), (-0.5, -0.5), (0.5, -0.5), (0.5, 0.5), (-0.5, 0.5)\}$$

$$G_D^B = \{(-0.5, -0.5), (0.5, -0.5), (0.5, 0.5), (-0.5, 0.5)\}$$

The direct translational bases are formulated as: $\vec{a}_1 = (1, 1)$ and $\vec{a}_2 = (-1, 1)$

It should be noted that, $j_{d1} = b_8$, $j_{d2} = b_2$, $j_{d3} = b_4$ and $j_{d4} = b_6$.

Equation (3.35) is used to derive the node and the bar bases dependency relations as shown in table (4.1).

Table (F.1) Dependency analysis results for bases of candidate unit cells of the lattice shown in Fig (F.1a)

Cell A- nodes				Cell B- nodes			
Independent	Dependent	\hat{x}_1	\hat{x}_2	Independent	Dependent	\hat{x}_1	\hat{x}_2
j_2	j_4	1	1	j_2	j_4	1	1
j_2	j_3	1	0	j_2	j_3	1	0
j_2	j_5	0	1	j_2	j_5	0	1
-	-	-	-	j_{d2}	j_{d4}	0	1
-	-	-	-	j_{d3}	j_{d1}	-1	0
Cell A- Bars				Cell B- Bars			
Independent	Dependent	\hat{x}_1	\hat{x}_2	Independent	Dependent	\hat{x}_1	\hat{x}_2
b_5	b_7	1	0	b_2	b_6	0	1
b_6	b_8	0	1	b_4	b_8	-1	0

The bases groups are used to derive the equilibrium and the kinematic systems of the finite structure of the unit cells as:

For unit cell A:

$$\mathbf{A}^A = \begin{bmatrix} 0 & -1 & 1 & 0 & 0 & 0 & 0 & 0 \\ 1 & 0 & -1 & 0 & 0 & 0 & 0 & 0 \\ 0 & 0 & 0 & 0 & 1/\sqrt{2} & -1/\sqrt{2} & 0 & 0 \\ -1 & 0 & 0 & 0 & -1/\sqrt{2} & 1/\sqrt{2} & 0 & 0 \\ 0 & 1 & 0 & 0 & 0 & 1/\sqrt{2} & 1/\sqrt{2} & 0 \\ 0 & 0 & 0 & 0 & 0 & 1/\sqrt{2} & -1/\sqrt{2} & 0 \\ 0 & 0 & 0 & 0 & 0 & 0 & -1/\sqrt{2} & 1/\sqrt{2} \\ 0 & 0 & 1 & 0 & 0 & 0 & 1/\sqrt{2} & 1/\sqrt{2} \\ 0 & 0 & 0 & -1 & -1/\sqrt{2} & 0 & 0 & -1/\sqrt{2} \\ 0 & 0 & 0 & 0 & 1/\sqrt{2} & 0 & 0 & -1/\sqrt{2} \end{bmatrix}, \mathbf{B}^A = (\mathbf{A}^A)^T \quad (\text{F.1a})$$

For unit cell B:

$$\mathbf{A}_d^B = \begin{bmatrix}
0 & -1/\sqrt{2} & -1 & -1/\sqrt{2} & 0 & 1/\sqrt{2} & 1 & 1/\sqrt{2} \\
1 & 1/\sqrt{2} & 0 & -1/\sqrt{2} & -1 & -1/\sqrt{2} & 0 & 1/\sqrt{2} \\
0 & 0 & 0 & 0 & 0 & 0 & 0 & 0 \\
-1 & 0 & 0 & 0 & 0 & 0 & 0 & 0 \\
0 & 0 & 1 & 0 & 0 & 0 & 0 & 0 \\
0 & 0 & 0 & 0 & 0 & 0 & 0 & 0 \\
0 & 0 & 0 & 0 & 0 & 0 & 0 & 0 \\
0 & 0 & 0 & 0 & 1 & 0 & 0 & 0 \\
0 & 0 & 0 & 0 & 0 & 0 & -1 & 0 \\
0 & 0 & 0 & 0 & 0 & 0 & 0 & 0 \\
0 & 0 & 0 & 0 & 0 & 0 & 0 & -1/\sqrt{2} \\
0 & 0 & 0 & 0 & 0 & 0 & 0 & -1/\sqrt{2} \\
0 & 1/\sqrt{2} & 0 & 0 & 0 & 0 & 0 & 0 \\
0 & -1/\sqrt{2} & 0 & 0 & 0 & 0 & 0 & 0 \\
0 & 0 & 0 & 1/\sqrt{2} & 0 & 0 & 0 & 0 \\
0 & 0 & 0 & 1/\sqrt{2} & 0 & 0 & 0 & 0 \\
0 & 0 & 0 & 0 & 0 & -1/\sqrt{2} & 0 & 0 \\
0 & 0 & 0 & 0 & 0 & 1/\sqrt{2} & 0 & 0
\end{bmatrix}, \mathbf{B}_d^B = \left(\mathbf{A}_d^B\right)^T \quad (\text{F.1b})$$

Eliminating the degrees of freedom associated with the dummy nodes, generates the final forms of the equilibrium and the kinematic matrices as:

$$\mathbf{A}^B = \begin{bmatrix}
0 & -1/\sqrt{2} & -1 & -1/\sqrt{2} & 0 & 1/\sqrt{2} & 1 & 1/\sqrt{2} \\
1 & 1/\sqrt{2} & 0 & -1/\sqrt{2} & -1 & -1/\sqrt{2} & 0 & 1/\sqrt{2} \\
0 & 0 & 0 & 0 & 0 & 0 & 0 & 0 \\
-1 & 0 & 0 & 0 & 0 & 0 & 0 & 0 \\
0 & 0 & 1 & 0 & 0 & 0 & 0 & 0 \\
0 & 0 & 0 & 0 & 0 & 0 & 0 & 0 \\
0 & 0 & 0 & 0 & 0 & 0 & 0 & 0 \\
0 & 0 & 0 & 0 & 1 & 0 & 0 & 0 \\
0 & 0 & 0 & 0 & 0 & 0 & -1 & 0 \\
0 & 0 & 0 & 0 & 0 & 0 & 0 & 0
\end{bmatrix}, \mathbf{B}^B = \left(\mathbf{A}^B\right)^T \quad (\text{F.2})$$

where \mathbf{A} and \mathbf{B} are the equilibrium and the kinematic matrices, respectively. The superscripts A and B denote unit cells A and B , respectively; and the subscript d denotes a matrix system that includes the degrees of freedom associated with the dummy nodes. The dotted rectangle in the

formulation of the matrix \mathbf{A}_d^B , eqn (F.1b), denotes the modes in the row space of the equilibrium matrix that are associated with the degrees of freedom of the dummy nodes and that are eliminated to obtain the matrix \mathbf{A}^B , eqn (F.2). The superscript T denotes the transpose of the matrix, as the kinematic matrix is the transpose of the equilibrium matrix, as shown in §3.2.4. Once the kinematic and the equilibrium systems are formulated, the dependency relations (table (F.1)) are used to apply the Bloch's wave reduction at the different wave-numbers derived from the irreducible Brillouin zone, followed by the determinacy analysis of the infinite structure of the lattice. The determinacy analysis of the pin-jointed infinite structure of the lattice depicted in Fig (F.1a) shows that this lattice is kinematically determinate and statically indeterminate, which typifies this structure as stretching-dominated, as shown in §3.8.

In the following step, we formulate matrix \mathbf{E} of the Cauchy-Born kinematic boundary condition, eqn (4.5), as:

$$\mathbf{E}^B = \begin{bmatrix} 0 & 0 & 0 \\ 0 & 0 & 0 \\ 0 & 0 & 0 \\ 0 & 0 & 0 \\ 1 & 0 & 0.5 \\ 0 & 1 & 0.5 \\ 0 & 0 & 1 \\ 0 & 2 & 0 \\ -1 & 0 & 0.5 \\ 0 & 1 & -0.5 \\ 0 & 0 & 0 \\ 0 & 0 & 0 \\ 0 & 0 & 0 \\ 0 & 0 & 0 \\ 0 & 0 & 0 \\ 1 & 0 & 0.5 \\ 0 & 1 & 0.5 \\ -1 & 0 & 0.5 \\ 0 & 1 & -0.5 \end{bmatrix}, \quad \mathbf{E}^A = \begin{bmatrix} 0 & 0 & 0 \\ 0 & 0 & 0 \\ 0 & 0 & 0 \\ 0 & 0 & 0 \\ 1 & 0 & 0.5 \\ 0 & 1 & 0.5 \\ 0 & 0 & 1 \\ 0 & 2 & 0 \\ -1 & 0 & 0.5 \\ 0 & 1 & -0.5 \end{bmatrix} \quad (\text{F.3})$$

The above transformation matrix \mathbf{E} is used to derive the matrix system, formulated in eqn (4.9), as:

$$\begin{bmatrix} 0 & 1 & 0 & -1 \\ -1 & 0 & 1 & 0 \\ 0 & -1 & 0 & 1 \\ 1 & 0 & -1 & 0 \\ 0 & 0 & 0 & 0 \\ 0 & 0 & 0 & 0 \\ 0 & 0 & 0 & 0 \\ 0 & 0 & 0 & 0 \end{bmatrix} \begin{bmatrix} d_{1x} \\ d_{1y} \\ d_{2x} \\ d_{2y} \end{bmatrix}^A + \begin{bmatrix} 0 & 0 & 0 \\ 1 & 0 & 0.5 \\ 0 & 2 & 0 \\ 1 & 0 & -0.5 \\ 1/\sqrt{2} & 1/\sqrt{2} & -1/\sqrt{2} \\ 1/\sqrt{2} & 1/\sqrt{2} & 1/\sqrt{2} \\ 1/\sqrt{2} & 1/\sqrt{2} & -1/\sqrt{2} \\ 1/\sqrt{2} & 1/\sqrt{2} & 1/\sqrt{2} \end{bmatrix} \begin{bmatrix} - \\ \epsilon_{xx} \\ - \\ \epsilon_{yy} \\ - \\ \epsilon_{xy} \end{bmatrix} = \begin{bmatrix} e_1 \\ e_2 \\ e_3 \\ e_4 \\ e_5 \\ e_6 \\ e_7 \\ e_8 \end{bmatrix}^A \quad (\text{F.4a})$$

$$\begin{bmatrix} 0 & 1 & 0 & -1 \\ -1/\sqrt{2} & 1/\sqrt{2} & 0 & 0 \\ -1 & 0 & 1 & 0 \\ -1/\sqrt{2} & -1/\sqrt{2} & 0 & 0 \\ 0 & -1 & 0 & 1 \\ 1/\sqrt{2} & -1/\sqrt{2} & 0 & 0 \\ 1 & 0 & -1 & 0 \\ 1/\sqrt{2} & 1/\sqrt{2} & 0 & 0 \end{bmatrix} \begin{bmatrix} d_{1x} \\ d_{1y} \\ d_{2x} \\ d_{2y} \end{bmatrix}^B + \begin{bmatrix} 0 & 0 & 0 \\ 0 & 0 & 0 \\ 1 & 0 & 0.5 \\ 1/\sqrt{2} & 1/\sqrt{2} & 1/\sqrt{2} \\ 0 & 2 & 0 \\ 1/\sqrt{2} & 1/\sqrt{2} & -1/\sqrt{2} \\ 1 & 0 & -0.5 \\ 0 & 0 & 0 \end{bmatrix} \begin{bmatrix} - \\ \epsilon_{xx} \\ - \\ \epsilon_{yy} \\ - \\ \epsilon_{xy} \end{bmatrix} = \begin{bmatrix} e_1 \\ e_2 \\ e_3 \\ e_4 \\ e_5 \\ e_6 \\ e_7 \\ e_8 \end{bmatrix}^B \quad (\text{F.4b})$$

These matrix systems are then employed to write the element deformations in terms of the macroscopic strain field as:

$$\begin{bmatrix} e_1 \\ e_2 \\ e_3 \\ e_4 \\ e_5 \\ e_6 \\ e_7 \\ e_8 \end{bmatrix}^B = \begin{bmatrix} 0 & 1 & 0 \\ 1/(2\sqrt{2}) & 1/(2\sqrt{2}) & -1/(2\sqrt{2}) \\ 1 & 0 & 0 \\ 1/(2\sqrt{2}) & 1/(2\sqrt{2}) & 1/(2\sqrt{2}) \\ 0 & 1 & 0 \\ 1/(2\sqrt{2}) & 1/(2\sqrt{2}) & -1/(2\sqrt{2}) \\ 1 & 0 & 0 \\ 1/(2\sqrt{2}) & 1/(2\sqrt{2}) & 1/(2\sqrt{2}) \end{bmatrix} \begin{bmatrix} - \\ \epsilon_{xx} \\ - \\ \epsilon_{yy} \\ - \\ \epsilon_{xy} \end{bmatrix} \quad (\text{F.5a})$$

$$\begin{bmatrix} e_1 \\ e_2 \\ e_3 \\ e_4 \\ e_5 \\ e_6 \\ e_7 \\ e_8 \end{bmatrix}^A = \begin{bmatrix} 0 & 1 & 0 \\ 1 & 0 & 0 \\ 0 & 1 & 0 \\ 1 & 0 & 0 \\ 1/\sqrt{2} & 1/\sqrt{2} & -1/\sqrt{2} \\ 1/\sqrt{2} & 1/\sqrt{2} & 1/\sqrt{2} \\ 1/\sqrt{2} & 1/\sqrt{2} & -1/\sqrt{2} \\ 1/\sqrt{2} & 1/\sqrt{2} & 1/\sqrt{2} \end{bmatrix} \begin{bmatrix} - \\ \epsilon_{xx} \\ - \\ \epsilon_{yy} \\ - \\ \epsilon_{xy} \end{bmatrix} \quad (\text{F.5b})$$

Computing the null space of the right hand side matrices, given in eqn (F.5), generates an empty null spaces which indicates that this lattice structure constructs a stretching-dominated lattice material as there is no macroscopic strain field generated by inextensional deformations.

We use the element deformation vectors of the two unit cells, formulated in eqn (F.5), to derive the strain energy densities of the lattice. The strain energy densities are employed to obtain the homogenized stiffness matrix of the lattice material by applying Castigliano's theorem. It is found that the two deformation vectors generate identical homogenized, fourth order stiffness tensor for the lattice material, as:

$$\begin{bmatrix} \bar{\sigma}_{xx} \\ \bar{\sigma}_{yy} \\ \bar{\sigma}_{xy} \end{bmatrix} = \frac{EA}{L} \begin{bmatrix} 1+1/(2\sqrt{2}) & 1/(2\sqrt{2}) & 0 \\ 1/(2\sqrt{2}) & 1+1/(2\sqrt{2}) & 0 \\ 0 & 0 & 1/(2\sqrt{2}) \end{bmatrix} \begin{bmatrix} \bar{\epsilon}_{xx} \\ \bar{\epsilon}_{yy} \\ \bar{\epsilon}_{xy} \end{bmatrix} \quad (F.6)$$

This result demonstrates the accuracy of the DNS in the application of the Cauchy-Born hypothesis necessary to homogenize the stiffness properties of lattice materials.

A similar check for the stretching-dominated behavior of the material can be performed on the stiffness tensor, derived in eqn (F.6). This can be done by computing the null space of the stiffness tensor which search for any macroscopic strain fields generated by zero macroscopic stress fields, i.e. with no material resistance. Applying this check to the stiffness matrix developed in eqn (F.6) generates an empty null space which again indicates that this is a stretching-dominated lattice material.

Considering an out-of-plane unit length of the lattice, the relative density of the lattice material, shown in Fig (F.1a), can be simply formulated as:

$$\bar{\rho}_L = \frac{\rho_L}{\rho} = 3.41 \left(\frac{H}{L} \right) \quad (F.7)$$

Using eqn (F.7), the stiffness matrix in eqn (F.6) can be modified as:

$$\bar{\mathbf{K}}_L = \frac{\mathbf{K}_L}{E} = \bar{\rho}_L \begin{bmatrix} 0.3964 & 0.1036 & 0 \\ 0.1036 & 0.3964 & 0 \\ 0 & 0 & 0.1036 \end{bmatrix} \quad (F.8)$$

Inverting the stiffness matrix, given in eqn (F.8), the elastic moduli of the lattice material, shown in Fig (F.1a), can be derived as:

$$\begin{aligned} \left(\bar{E}_L \right)_{xx} &= \frac{(E_L)_{xx}}{E} = 0.3693 \bar{\rho}_L, \quad \left(\bar{E}_L \right)_{yy} = \frac{(E_L)_{yy}}{E} = 0.3693 \bar{\rho}_L, \\ \bar{G}_L &= \frac{G_L}{E} = 0.1036 \bar{\rho}_L \end{aligned} \quad (F.9)$$

To compute the strength properties of the lattice material, shown in Fig (F.1a), the matrix system in eqn (4.29) can be computed as:

$$\begin{bmatrix} \sigma_\mu^1 \\ \sigma_\mu^2 \\ \cdot \\ \cdot \\ \sigma_\mu^B \end{bmatrix} = \frac{1}{\bar{\rho}} \begin{bmatrix} 1 & 1 & -4.8284 \\ 1 & 1 & 4.8284 \\ 1 & 1 & -4.8284 \\ 1 & 1 & 4.8284 \\ 2.7071 & -0.7071 & 0 \\ -0.7071 & 2.7071 & 0 \\ 2.7071 & -0.7071 & 0 \\ -0.7071 & 2.7071 & 0 \end{bmatrix} \begin{bmatrix} \sigma_{xx} \\ \sigma_{yy} \\ \sigma_{xy} \end{bmatrix} \quad (F.10)$$

The matrix system in eqn (F.10) can be used to derive the critical strength of the lattice material, shown in Fig (F.1a), formulated in eqn (4.30), as:

$$\sigma_L^{cr} = \begin{bmatrix} 0.3694 \\ 0.3694 \\ 0.2071 \end{bmatrix} \sigma_\mu^{cr} \bar{\rho} \quad (F.11)$$

Using eqn (4.32) the plastic yield strength of the lattice material, shown in Fig (F.1a), can be computed as in:

$$\sigma_L^y = \begin{bmatrix} 0.3694 \\ 0.3694 \\ 0.2071 \end{bmatrix} \sigma_{ys} \bar{\rho} \quad \text{or} \quad \bar{\sigma}_L^y = \begin{bmatrix} 0.3694 \\ 0.3694 \\ 0.2071 \end{bmatrix} \bar{\rho} \quad (F.12)$$

Similarly, using eqn (4.36) the instability buckling strength of the lattice material, shown in Fig (F.1a), can be computed as in:

$$\sigma_L^b = \begin{bmatrix} 0.026 \\ 0.026 \\ 0.0146 \end{bmatrix} E \bar{\rho}^3 \quad \text{or} \quad \bar{\sigma}_L^b = \begin{bmatrix} 0.026 \\ 0.026 \\ 0.0146 \end{bmatrix} \left(\frac{E}{\sigma_{ys}} \right) \bar{\rho}^3 \quad (F.13)$$

F.2 Characterization of the $3^4.6$ Lattice Material

In this section we describe the characterization process to determine the stiffness and the strength properties of the lattice that has the Schläfli symbol of $3^4.6$ which has a hexagonal Bravais lattice symmetry. We recall the $3^4.6$ lattice topology, shown previously in Fig (2.5h), into Fig (F.2) to describe its microscopic architecture in more details.

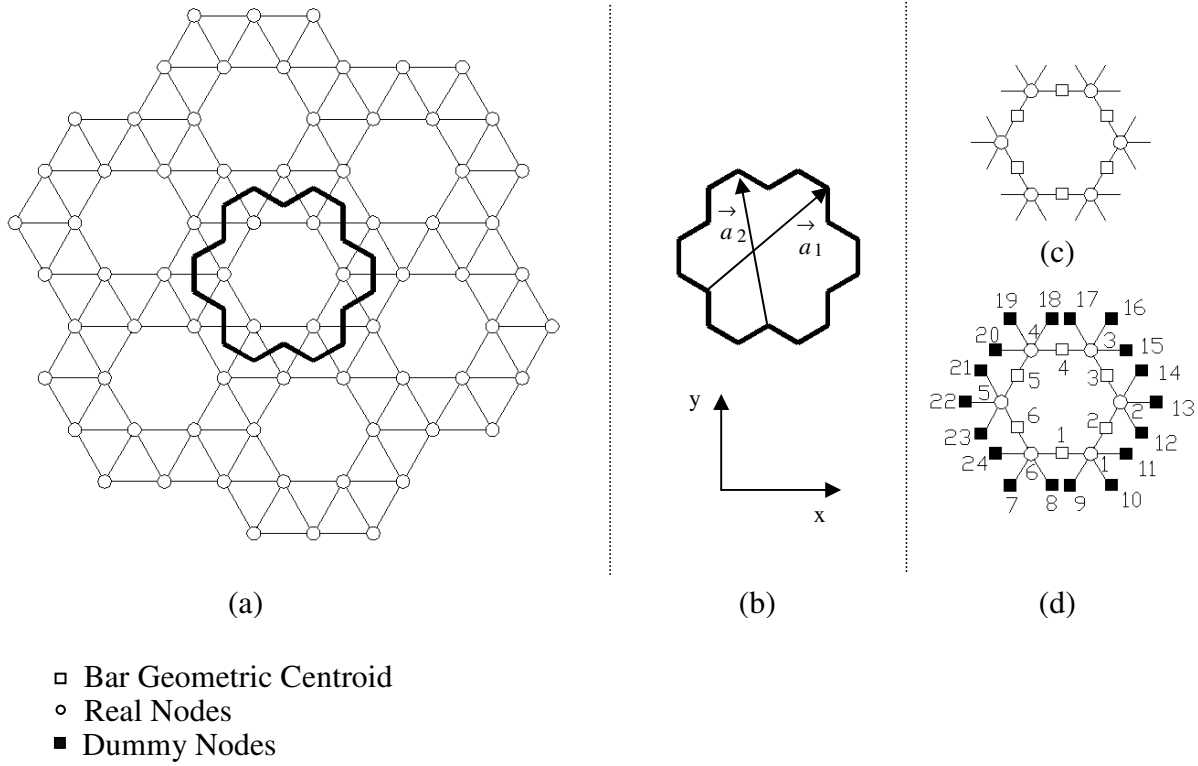


Fig. (F.2) (a) Lattice structure, (b) Cell envelope, (c) Unit cell without dummy nodes, (d) Unit cell with dummy nodes

The unit cell of the $3^4.6$ lattice contains 6 real nodes and 24 bars, as shown in Fig (F.2d). Since there are 18 intersection points between the cell envelope and the bar elements that extend between adjacent cells, we introduce a dummy node for each intersection. The groups of bar and node position vectors are used to formulate the kinematic and equilibrium matrices of the unit cell structure.

From the geometry of the unit cell envelope, the direct translational bases can be formulated as

$\vec{a}_1 = \left(-\frac{5}{2}, \frac{\sqrt{3}}{2} \right)$, $\vec{a}_2 = (-2, \sqrt{3})$. To determine the direct lattice bases, the dependency between

the unit cell bar and real node position vectors is computed on a unit cell bases using (eqn (3.35)). This test reveals that all the real nodes are independent whereas the bars exhibit dependencies, as shown in Table (F.2).

Table (F.2) Dependency relations of unit cell bars

Independent bars	Dependent bars	\hat{x}_1	\hat{x}_2
7	14	0	1
8	19	1	1
9	18	1	1
10	17	1	1
11	22	1	0
12	21	1	0
13	20	1	0
15	24	0	-1
16	23	0	-1

The numeric tags of the cell elements (table (F.2)) are used in Fig (F.2) to label the elements of the unit cell of the $3^4.6$ lattice. The dependency relations are used to generate the bars and the nodes transformation matrices, which are necessary to reduce the kinematic and the equilibrium systems to their periodic forms. The reduced equilibrium and kinematic matrices are computed at each wave-number, generated from the reciprocal lattice irreducible Brillouin zone, and the determinacy state of the infinite structure is computed.

The determinacy analysis shows that the infinite structure of the $3^4.6$ lattice is always kinematically determinate and statically indeterminate which indicates that this lattice material is a stretching dominated. The DNS is used to generate the matrix \mathbf{E} , which is necessary to formulate the kinematic boundary condition of the Cauchy-Born hypothesis. The singular value decomposition is used to formulate the microscopic element deformations in terms of the macroscopic strain field through the transformation matrix, \mathbf{M} . The null space of the matrix \mathbf{M} is finally computed to identify any special failure modes of macroscopic strain fields. The analysis shows that the $3^4.6$ lattice is stable under all macroscopic strain fields.

The computed element deformations are used to determine the strain energy density (eqn (4.20)) and then to compute the macroscopic stiffness (eqn (4.21)) of the lattice. Finally, the compliance matrix of the material and the material elastic moduli (eqn (4.23)) can be derived. For a lattice material with a unit out of plane thickness, the stiffness and the density are written, respectively, in eqns (F.14) and (F.15), as:

$$\bar{\rho}_L = 2.4744 \left(\frac{H}{L} \right) \quad (\text{F.14})$$

$$\mathbf{K}_L = \frac{EH}{L} \begin{bmatrix} 1.0998 & 0.5976 & 0 \\ 0.5976 & 1.0998 & 0 \\ 0 & 0 & 0.2511 \end{bmatrix} = E \bar{\rho}_L \begin{bmatrix} 0.4445 & 0.2415 & 0 \\ 0.2415 & 0.4445 & 0 \\ 0 & 0 & 0.1015 \end{bmatrix} \quad (\text{F.15})$$

where \mathbf{K}_L is the lattice material stiffness matrix. The relative stiffness can be computed as:

$$\bar{\mathbf{K}}_L = \frac{\mathbf{K}_L}{E} = \bar{\rho}_L \begin{bmatrix} 0.4445 & 0.2415 & 0 \\ 0.2415 & 0.4445 & 0 \\ 0 & 0 & 0.1015 \end{bmatrix} \quad (\text{F.16})$$

where $\bar{\mathbf{K}}_L$ is the lattice material relative stiffness matrix.

Once the stiffness tensor is computed, the compliance tensor can be computed as:

$$\mathbf{C}_L = \frac{1}{E \bar{\rho}_L} \begin{bmatrix} 3.1919 & -1.7342 & 0 \\ -1.7342 & 3.1919 & 0 \\ 0 & 0 & 9.8522 \end{bmatrix} \quad (\text{F.17})$$

This compliance tensor is used to compute the material elastic moduli as:

$$\left(\bar{E}_L \right)_{xx} = \frac{(E_L)_{xx}}{E} = 0.3133 \bar{\rho}_L, \left(\bar{E}_L \right)_{yy} = \frac{(E_L)_{yy}}{E} = 0.3133 \bar{\rho}_L$$

$$\bar{G}_L = \frac{G_L}{E} = 0.1015 \bar{\rho}_L \quad (\text{F.18})$$

The Poisson's ratios of the 3⁴.6 lattice material can also be computed as:

$$(v_L)_{xy} = (v_L)_{yx} = 0.5434 \quad (\text{F.19})$$

The critical strength properties are computed as:

$$\sigma_L^y = \begin{bmatrix} 0.2079 \\ 0.2468 \\ 0.1269 \end{bmatrix} \sigma_\mu^{cr} \bar{\rho} \quad (\text{F.20})$$

Equation (F.20) is used to compute the yield strength properties as:

$$\sigma_L^y = \begin{bmatrix} 0.2079 \\ 0.2468 \\ 0.1269 \end{bmatrix} \sigma_{ys} \bar{\rho} \quad \text{or} \quad \sigma_L^y = \begin{bmatrix} 0.2079 \\ 0.2468 \\ 0.1269 \end{bmatrix} \bar{\rho} \quad (\text{F.21})$$

and the buckling strength properties are computed as:

$$\sigma_L^b = \begin{bmatrix} 0.0279 \\ 0.0331 \\ 0.017 \end{bmatrix} E \bar{\rho}^3 \quad \text{or} \quad \bar{\sigma}_L^b = \begin{bmatrix} 0.0279 \\ 0.0331 \\ 0.017 \end{bmatrix} \left(\frac{E}{\sigma_{ys}} \right) \bar{\rho}^3 \quad (\text{F.22})$$

In the following we apply the same characterization process to determine the elastic properties of other eight lattice topologies. We use the elastic properties derived in this Appendix to develop the stiffness selection design charts, presented in chapter 4.

F.3 Double Hexagonal Triangulation (DHT), shown in Fig (2.6a)

$$K_L = \frac{EH}{L} \begin{bmatrix} 0.9575 & 0.388 & 0 \\ 0.388 & 0.9575 & 0 \\ 0 & 0 & 0.2595 \end{bmatrix} = E \bar{\rho}_L \begin{bmatrix} 0.3431 & 0.1391 & 0 \\ 0.1391 & 0.3431 & 0 \\ 0 & 0 & 0.093 \end{bmatrix}$$

$$\bar{K}_L = \frac{K_L}{E} = \bar{\rho}_L \begin{bmatrix} 0.3431 & 0.1391 & 0 \\ 0.1391 & 0.3431 & 0 \\ 0 & 0 & 0.093 \end{bmatrix}, \quad \bar{\rho}_L = 2.7905 \left(\frac{H}{L} \right)$$

$$\left(\bar{E}_L \right)_{xx} = \frac{(E_L)_{xx}}{E} = 0.2659 \bar{\rho}_L, \quad \left(\bar{E}_L \right)_{yy} = \frac{(E_L)_{yy}}{E} = 0.1972 \bar{\rho}_L, \quad \bar{G}_L = \frac{G_L}{E} = 0.0878 \bar{\rho}_L$$

F.4 Full Triangulation (3⁶), shown in Fig (2.4b)

$$K_L = \frac{EH}{L} \begin{bmatrix} 1.299 & 0.433 & 0 \\ 0.433 & 1.299 & 0 \\ 0 & 0 & 0.433 \end{bmatrix} = E \bar{\rho}_L \begin{bmatrix} 0.375 & 0.125 & 0 \\ 0.125 & 0.375 & 0 \\ 0 & 0 & 0.125 \end{bmatrix},$$

$$\bar{K}_L = \frac{K_L}{E} = \bar{\rho}_L \begin{bmatrix} 0.375 & 0.125 & 0 \\ 0.125 & 0.375 & 0 \\ 0 & 0 & 0.125 \end{bmatrix}, \quad \bar{\rho}_L = 3.4641 \left(\frac{H}{L} \right)$$

$$\left(\bar{E}_L \right)_{xx} = \frac{(E_L)_{xx}}{E} = 0.3333 \bar{\rho}_L, \quad \left(\bar{E}_L \right)_{yy} = \frac{(E_L)_{yy}}{E} = 0.3333 \bar{\rho}_L, \quad \bar{G}_L = \frac{G_L}{E} = 0.125 \bar{\rho}_L$$

F.5 Hexagonal Honeycombs, shown in Fig (2.4c)

$$K_L = \frac{EH}{L} \begin{bmatrix} 0.2887 & 0.2887 & 0 \\ 0.2887 & 0.2887 & 0 \\ 0 & 0 & 0 \end{bmatrix} = E \bar{\rho}_L \begin{bmatrix} 0.25 & 0.25 & 0 \\ 0.25 & 0.25 & 0 \\ 0 & 0 & 0 \end{bmatrix} \quad \bar{K}_L = \frac{K_L}{E} = \bar{\rho}_L \begin{bmatrix} 0.25 & 0.25 & 0 \\ 0.25 & 0.25 & 0 \\ 0 & 0 & 0 \end{bmatrix},$$

$$\bar{\rho}_L = 1.1547 \left(\frac{H}{L} \right)$$

From the stiffness matrix of the hexagonal lattice it can be realized that this lattice material is bending-dominated, the stiffness matrix of its pin-jointed lattice version is singular as the lattice has two modes of macroscopic strain fields that are developed with zero material resistance. These two modes can be generated by computing the null space of the stiffness matrix which generates:

$$\begin{bmatrix} \bar{\epsilon}_{xx} \\ \bar{\epsilon}_{yy} \\ \bar{\epsilon}_{xy} \end{bmatrix}_1 = \begin{bmatrix} -1 \\ 1 \\ 0 \end{bmatrix}, \quad \begin{bmatrix} \bar{\epsilon}_{xx} \\ \bar{\epsilon}_{yy} \\ \bar{\epsilon}_{xy} \end{bmatrix}_2 = \begin{bmatrix} 0 \\ 0 \\ 1 \end{bmatrix}.$$

The pin-jointed hexagonal honeycomb collapses by any macroscopic strain field generated as a linear combination of these two modes. Therefore, the compliance matrix and elastic moduli of the pin-jointed hexagonal honeycomb lose their significance. We do not present them here.

F.6 Kagome Lattice, shown in Fig (2.5a)

$$K_L = \frac{EH}{L} \begin{bmatrix} 0.6495 & 0.2165 & 0 \\ 0.2165 & 0.6495 & 0 \\ 0 & 0 & 0.2165 \end{bmatrix} = E \bar{\rho}_L \begin{bmatrix} 0.375 & 0.125 & 0 \\ 0.125 & 0.375 & 0 \\ 0 & 0 & 0.125 \end{bmatrix},$$

$$\bar{K}_L = \frac{K_L}{E} = \bar{\rho}_L \begin{bmatrix} 0.375 & 0.125 & 0 \\ 0.125 & 0.375 & 0 \\ 0 & 0 & 0.125 \end{bmatrix}, \quad \bar{\rho}_L = 1.7321 \left(\frac{H}{L} \right)$$

$$\left(\bar{E}_L \right)_{xx} = \frac{(E_L)_{xx}}{E} = 0.3333 \bar{\rho}_L, \quad \left(\bar{E}_L \right)_{yy} = \frac{(E_L)_{yy}}{E} = 0.3333 \bar{\rho}_L, \quad \bar{G}_L = \frac{G_L}{E} = 0.125 \bar{\rho}_L$$

F.7 Square Lattice, shown in Fig (2.4a)

$$\bar{K}_L = \frac{K_L}{E} = \bar{\rho}_L \begin{bmatrix} 0.5 & 0 & 0 \\ 0 & 0.5 & 0 \\ 0 & 0 & 0 \end{bmatrix}, \bar{\rho}_L = 2 \left(\frac{H}{L} \right)$$

The computation of the null space of the stiffness matrix indicates that this lattice material collapses at macroscopic strain field of $[0 \ 0 \ 1]^T$. Accordingly, the computation of the compliance matrix and the elastic moduli are not presented as the material is bending-dominated.

F.8 Semi-Uni-Braced Square Lattice, shown in Fig (2.6b)

$$\bar{K}_L = \frac{K_L}{E} = \bar{\rho}_L \begin{bmatrix} 0.4347 & 0.0653 & -0.0653 \\ 0.0653 & 0.4347 & -0.0653 \\ -0.0653 & -0.0653 & 0.0653 \end{bmatrix}, \bar{\rho}_L = 2.71 \left(\frac{H}{L} \right)$$

$$\left(\bar{E}_L \right)_{xx} = \frac{(E_L)_{xx}}{E} = 0.3694 \bar{\rho}_L, \left(\bar{E}_L \right)_{yy} = \frac{(E_L)_{yy}}{E} = 0.3694 \bar{\rho}_L, \bar{G}_L = \frac{G_L}{E} = 0.0482 \bar{\rho}_L$$

F.9 Uni- Braced Square Lattice, shown in Fig (2.6f)

$$\bar{K}_L = \frac{K_L}{E} = \bar{\rho}_L \begin{bmatrix} 0.3964 & 0.1036 & -0.1036 \\ 0.1036 & 0.3964 & -0.1036 \\ -0.1036 & -0.1036 & 0.1036 \end{bmatrix}, \bar{\rho}_L = 3.4142 \left(\frac{H}{L} \right)$$

$$\left(\bar{E}_L \right)_{xx} = \frac{(E_L)_{xx}}{E} = 0.2928 \bar{\rho}_L, \left(\bar{E}_L \right)_{yy} = \frac{(E_L)_{yy}}{E} = 0.2928 \bar{\rho}_L, \bar{G}_L = \frac{G_L}{E} = 0.0607 \bar{\rho}_L$$

F.10 Double- Braced Square Lattice, shown in Fig (2.6g)

$$\bar{K}_L = \frac{K_L}{E} = \bar{\rho}_L \begin{bmatrix} 0.3536 & 0.1464 & 0 \\ 0.1464 & 0.3536 & 0 \\ 0 & 0 & 0.1464 \end{bmatrix}, \bar{\rho}_L = 4.8284 \left(\frac{H}{L} \right)$$

$$\left(\bar{E}_L \right)_{xx} = \frac{(E_L)_{xx}}{E} = 0.293 \bar{\rho}_L, \left(\bar{E}_L \right)_{yy} = \frac{(E_L)_{yy}}{E} = 0.293 \bar{\rho}_L, \bar{G}_L = \frac{G_L}{E} = 0.1464 \bar{\rho}_L$$

The elastic properties of the stretching-dominated lattice materials are plotted on the design charts, shown in Figs (4.1), (4.2) and (4.3). These charts can help in the selection process of lattice topologies that generate specific stiffness properties required by certain applications.

Appendix G

Elastic Properties of Rigid Jointed 2D Lattice Materials: Applications

G.1 Example

In this section, we describe the characterization process, developed in chapter seven, to determine the stiffness properties and the elastic moduli of the 2D rigid-jointed lattice material that has a full triangulated topology. The full triangulated topology is represented by the Schläfli symbol of 3^6 which has a hexagonal Bravais lattice symmetry. We recall the full triangulated lattice topology, shown previously in Fig (2.4b), into Fig (G.1) to describe its microscopic architecture in more details.

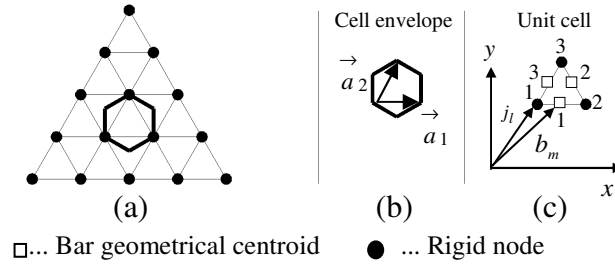


Fig. (G.1) (a) Triangular lattice structure, (b) Cell envelope, (c) Unit cell

The unit cell of the triangular lattice contains 3 real nodes and 3 bars, as shown in Fig (G.1c). Considering the origin of the Cartesian coordinate system to be located at node 1, the bar and the node bases groups can be formulated as:

$$G_B^A = \left\{ (0.5, 0), \left(0.75, \frac{\sqrt{3}}{4} \right), \left(0.25, \frac{\sqrt{3}}{4} \right) \right\}, G_N = \left\{ (0, 0), (1, 0), \left(0.5, \frac{\sqrt{3}}{2} \right) \right\}, G_D = \Phi \quad (G.1)$$

Following the nodal numbering shown in Fig (G.1c) and using eqn (G.1), the stiffness system of the rigid-jointed finite structure of the unit cell of the triangular lattice is written as:

$$EA \begin{bmatrix} 1.25 & 0.433 & 0 & -1 & 0 & 0 & -0.25 & -0.433 & 0 \\ 0.433 & 0.75 & 0 & 0 & 0 & 0 & -0.433 & -0.75 & 0 \\ 0 & 0 & 0 & 0 & 0 & 0 & 0 & 0 & 0 \\ -1 & 0 & 0 & 1.25 & -0.433 & 0 & -0.25 & 0.433 & 0 \\ 0 & 0 & 0 & -0.433 & 0.75 & 0 & 0.433 & -0.75 & 0 \\ 0 & 0 & 0 & 0 & 0 & 0 & 0 & 0 & 0 \\ -0.25 & -0.433 & 0 & -0.25 & 0.433 & 0 & 0.5 & 0 & 0 \\ -0.433 & -0.75 & 0 & 0.433 & -0.75 & 0 & 0 & 1.5 & 0 \\ 0 & 0 & 0 & 0 & 0 & 0 & 0 & 0 & 0 \end{bmatrix} \begin{bmatrix} d_{1x} \\ d_{1y} \\ \theta_1 \\ d_{2x} \\ d_{2y} \\ \theta_2 \\ d_{3x} \\ d_{3y} \\ \theta_3 \end{bmatrix} = \begin{bmatrix} f_{1x} \\ f_{1y} \\ m_1 \\ f_{2x} \\ f_{2y} \\ m_2 \\ f_{3x} \\ f_{3y} \\ m_3 \end{bmatrix}_{bar} \quad (G.2)$$

$$EI \begin{bmatrix} 0.75 & -0.433 & 0.433 & 0 & 0 & 0 & -0.75 & 0.433 & 0.433 \\ -0.433 & 1.25 & 0.25 & 0 & -1 & 0.5 & 0.433 & -0.25 & -0.25 \\ 0.433 & 0.25 & 0.6667 & 0 & -0.5 & 0.1667 & -0.433 & 0.25 & 0.1667 \\ 0 & 0 & 0 & 0.75 & 0.433 & 0.433 & -0.75 & -0.433 & 0.433 \\ 0 & -1 & -0.5 & 0.433 & 1.25 & -0.25 & -0.433 & -0.25 & 0.25 \\ 0 & 0.5 & 0.1667 & 0.433 & -0.25 & 0.6667 & -0.433 & -0.25 & 0.1667 \\ -0.75 & 0.433 & -0.433 & -0.75 & -0.433 & -0.433 & 1.5 & 0 & -0.866 \\ 0.433 & -0.25 & 0.25 & -0.433 & -0.25 & -0.25 & 0 & 0.5 & 0 \\ 0.433 & -0.25 & 0.1667 & 0.433 & 0.25 & 0.1667 & -0.866 & 0 & 0.6667 \end{bmatrix} \begin{bmatrix} d_{1x} \\ d_{1y} \\ \theta_1 \\ d_{2x} \\ d_{2y} \\ \theta_2 \\ d_{3x} \\ d_{3y} \\ \theta_3 \end{bmatrix} = \begin{bmatrix} f_{1x} \\ f_{1y} \\ m_1 \\ f_{2x} \\ f_{2y} \\ m_2 \\ f_{3x} \\ f_{3y} \\ m_3 \end{bmatrix}_{beam} \quad (G.3)$$

where the stiffness systems presented in eqns (G.2) and (G.3) are for the triangular unit cell bar and beam stiffness resistances, respectively.

From the geometry of the unit cell envelope, the direct translational bases can be formulated as:

$\vec{a}_1 = (1,0)$, $\vec{a}_2 = \left(0.5, \frac{\sqrt{3}}{2}\right)$. To determine the direct lattice bases, the dependency between the

unit cell bar and node position vectors is computed on a unit cell bases using (eqn (3.35)). This test reveals that all bars are independent whereas the nodes exhibit dependencies, as shown in Table (G.1).

Table (G.1) Dependency Relations of Unit Cell Nodes

Independent nodes	Dependent nodes	\hat{x}_1	\hat{x}_2
1	2	1	0
1	3	0	1

The dependency relations are used to generate the transformation matrices, which are necessary to reduce the kinematic and the equilibrium systems to their periodic forms.

For the triangular lattice shown in Fig (G.1), the nodal displacements and the nodal forces transformation matrix systems are formulated respectively, in eqns (G.4) and (G.5), as:

$$\begin{bmatrix} d_{1x} \\ d_{1y} \\ \theta_1 \\ d_{2x} \\ d_{2y} \\ \theta_2 \\ d_{3x} \\ d_{3y} \\ \theta_3 \end{bmatrix} = \begin{bmatrix} 1 & 0 & 0 & e^{2\pi\omega_1 i} & 0 & 0 & e^{2\pi\omega_2 i} & 0 & 0 \\ 0 & 1 & 0 & 0 & e^{2\pi\omega_1 i} & 0 & 0 & e^{2\pi\omega_2 i} & 0 \\ 0 & 0 & 1 & 0 & 0 & e^{2\pi\omega_1 i} & 0 & 0 & e^{2\pi\omega_2 i} \end{bmatrix}^H \begin{bmatrix} d_{1x} \\ d_{1y} \\ \theta_1 \end{bmatrix} \quad (G.4)$$

$$\begin{bmatrix} f_{1x} \\ f_{1y} \\ m_1 \end{bmatrix} = \begin{bmatrix} 1 & 0 & 0 & e^{2\pi\omega_1 i} & 0 & 0 & e^{2\pi\omega_2 i} & 0 & 0 \\ 0 & 1 & 0 & 0 & e^{2\pi\omega_1 i} & 0 & 0 & e^{2\pi\omega_2 i} & 0 \\ 0 & 0 & 1 & 0 & 0 & e^{2\pi\omega_1 i} & 0 & 0 & e^{2\pi\omega_2 i} \end{bmatrix} \begin{bmatrix} f_{1x} \\ f_{1y} \\ m_1 \\ f_{2x} \\ f_{2y} \\ m_2 \\ f_{3x} \\ f_{3y} \\ m_3 \end{bmatrix} = 0 \quad (G.5)$$

Using the transformation matrices, formulated in eqns (G.4) and (G.5) at wave-number $\omega = (0,0)$ the reduced stiffness system for the triangular lattice, shown in Fig (G.1), can be written as:

$$\left\{ EA \begin{bmatrix} 0 & 0 & 0 \\ 0 & 0 & 0 \\ 0 & 0 & 0 \end{bmatrix} + EI \begin{bmatrix} 0 & 0 & 0 \\ 0 & 0 & 0 \\ 0 & 0 & 3 \end{bmatrix} \right\} \begin{bmatrix} d_{1x} \\ d_{1y} \\ \theta_1 \end{bmatrix} = \begin{bmatrix} f_{1x} \\ f_{1y} \\ m_1 \end{bmatrix} = 0 \quad \text{or}$$

$$\{\mathbf{K}^{bar} + \mathbf{K}^{beam}\} \tilde{d} = \tilde{f} = 0 \quad (G.6)$$

The Cauchy-Born kinematic boundary condition of the full triangulated lattice is derived as:

$$\begin{bmatrix} d_{1x} \\ d_{1y} \\ \theta_1 \\ d_{2x} \\ d_{2y} \\ \theta_2 \\ d_{3x} \\ d_{3y} \\ \theta_3 \end{bmatrix} = \begin{bmatrix} 1 & 0 & 0 \\ 0 & 1 & 0 \\ 0 & 0 & 1 \\ 1 & 0 & 0 \\ 0 & 1 & 0 \\ 0 & 0 & 1 \\ 1 & 0 & 0 \\ 0 & 1 & 0 \\ 0 & 0 & 1 \end{bmatrix} \begin{bmatrix} d_{1x} \\ d_{1y} \\ \theta_1 \end{bmatrix} + \begin{bmatrix} 0 & 0 & 0 \\ 0 & 0 & 0 \\ 0 & 0 & 0 \\ 1 & 0 & 0 \\ 0 & 0 & 0.5 \\ 0 & 0 & 0 \\ 0.5 & 0 & 0.433 \\ 0 & 0.866 & 0.25 \\ 0 & 0 & 0 \end{bmatrix} \begin{bmatrix} - \\ - \\ - \\ \varepsilon_{xx} \\ \varepsilon_{yy} \\ \varepsilon_{xy} \end{bmatrix} \quad (G.7)$$

Substituting eqn (G.6) into eqns (G.2) and (G.3) and inverting the stiffness matrices after eliminating all modes related to rigid-body motion and internal mechanisms, the reduced form of the nodal deformations can be formulated for the beam and the bar stiffness resistances. The reduced forms of the nodal deformations can be easily expanded into the full nodal deformations vector of the unit cell using eqn (G.7). The full vectors of nodal deformations are now substituted into eqn (G.2) and (G.3) to compute the vectors of nodal forces. The microscopic nodal deformations and forces are computed in terms of the macroscopic strain field as:

$$\begin{bmatrix} d_{1x} \\ d_{1y} \\ \theta_1 \\ d_{2x} \\ d_{2y} \\ \theta_2 \\ d_{3x} \\ d_{3y} \\ \theta_3 \end{bmatrix}_{bar} = \begin{bmatrix} -2 & 0 & 0 \\ 0 & 0 & 0 \\ 0 & 0 & 0 \\ -1 & 0 & 0 \\ 0 & 0 & 0.5 \\ 0 & 0 & 0 \\ -1.5 & 0 & 0.433 \\ 0 & 0.866 & 0.25 \\ 0 & 0 & 0 \end{bmatrix} \begin{bmatrix} - \\ - \\ - \\ \varepsilon_{xx} \\ \varepsilon_{yy} \\ \varepsilon_{xy} \end{bmatrix}, \quad \begin{bmatrix} f_{1x} \\ f_{1y} \\ m_1 \\ f_{2x} \\ f_{2y} \\ m_2 \\ f_{3x} \\ f_{3y} \\ m_3 \end{bmatrix}_{bar} = \begin{bmatrix} -1.125 & -0.375 & -0.2165 \\ -0.2165 & -0.6495 & -0.375 \\ 0 & 0 & 0 \\ 1.125 & 0.375 & -0.2165 \\ -0.2165 & -0.6495 & 0.375 \\ 0 & 0 & 0 \\ 0 & 0 & 0.433 \\ 0.433 & 1.299 & 0 \\ 0 & 0 & 0 \end{bmatrix} \begin{bmatrix} - \\ - \\ - \\ \varepsilon_{xx} \\ \varepsilon_{yy} \\ \varepsilon_{xy} \end{bmatrix}$$

or $d_{bar} = \mathbf{M}_{bar}^d \bar{\varepsilon}$, $f_{bar} = \mathbf{M}_{bar}^f \bar{\varepsilon}$ (G.8)

$$\begin{aligned}
& \begin{bmatrix} d_{1x} \\ d_{1y} \\ \theta_1 \\ d_{2x} \\ d_{2y} \\ \theta_2 \\ d_{3x} \\ d_{3y} \\ \theta_3 \end{bmatrix}_{beam} = \begin{bmatrix} 0 & 0 & 0 \\ 0 & 0 & 0 \\ 0 & 0 & 0.333 \\ 1 & 0 & 0 \\ 0 & 0 & 0.5 \\ 0 & 0 & 0.333 \\ 0.5 & 0 & 0.433 \\ 0 & 0.866 & 0.25 \\ 0 & 0 & 0.333 \end{bmatrix} \begin{bmatrix} - \\ - \\ - \\ \bar{\epsilon}_{xx} \\ - \\ \bar{\epsilon}_{yy} \\ - \\ \bar{\epsilon}_{xy} \\ - \end{bmatrix} \\
& \begin{bmatrix} f_{1x} \\ f_{1y} \\ m_1 \\ f_{2x} \\ f_{2y} \\ m_2 \\ f_{3x} \\ f_{3y} \\ m_3 \end{bmatrix}_{beam} = \begin{bmatrix} -0.375 & 0.375 & 0.0722 \\ 0.2165 & -0.2165 & -0.2083 \\ -0.2165 & 0.2165 & -0.0417 \\ 0.375 & -0.375 & 0.0722 \\ 0.2165 & -0.2165 & 0.2083 \\ 0.2165 & -0.2165 & -0.0417 \\ 0 & 0 & -0.0417 \\ -0.433 & 0.433 & 0 \\ 0 & 0 & 0.0833 \end{bmatrix} \begin{bmatrix} - \\ - \\ - \\ \bar{\epsilon}_{xx} \\ - \\ \bar{\epsilon}_{yy} \\ - \\ \bar{\epsilon}_{xy} \\ - \end{bmatrix}
\end{aligned}$$

$$\text{or} \quad d_{beam} = \mathbf{M}_{beam}^d \bar{\epsilon}, \quad f_{beam} = \mathbf{M}_{beam}^f \bar{\epsilon} \quad (\text{G.9})$$

Equations (G.8) and (G.9) are now used to compute the macroscopic fourth order stiffness tensor as:

$$\begin{aligned}
\bar{\mathbf{K}}_L &= \frac{\mathbf{K}_L}{E} = \bar{\rho}_L \begin{bmatrix} 0.375 & 0.125 & 0 \\ 0.125 & 0.375 & 0 \\ 0 & 0 & 0.125 \end{bmatrix} \\
&+ \left(\bar{\rho}_L \right)^3 \begin{bmatrix} 0.0052 & -0.0052 & 0 \\ -0.0052 & 0.0052 & 0 \\ 0 & 0 & 0.0006 \end{bmatrix}
\end{aligned} \quad (\text{G10})$$

where the relative density of the triangulated lattice material can be easily computed as

$$\bar{\rho}_L = 3.4641 \left(\frac{H}{L} \right).$$

The compliance matrix can be computed using eqn (G.10) and the elastic moduli and Poisson's ratios of the rigid-jointed triangular lattice are written as:

$$\begin{aligned}
(\bar{E}_L)_{xx} = (\bar{E}_L)_{yy} &= \frac{\bar{\rho}_L(625 + 26\bar{\rho}_L)}{1875 + 26\bar{\rho}_L}, \quad \bar{G}_L = \frac{\bar{\rho}_L(625 + 3\bar{\rho}_L)}{5000}, \\
(\nu_L)_{xy} = (\nu_L)_{yx} &= \frac{625 - 26\bar{\rho}_L}{1875 + 26\bar{\rho}_L}
\end{aligned} \tag{G.11}$$

The characterization method, developed in chapter seven, is applied to other 12 lattice topologies and their results are reported in the following sections.

G.2 Square Lattice Material

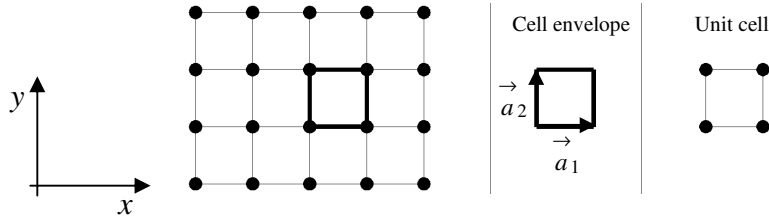


Fig (G.2) Microstructure of the 2D square lattice material

$$\bar{\mathbf{K}}_L = \frac{\mathbf{K}_L}{E} = \bar{\rho}_L \begin{bmatrix} 0.5 & 0 & 0 \\ 0 & 0.5 & 0 \\ 0 & 0 & 0 \end{bmatrix} + \left(\bar{\rho}_L \right)^3 \begin{bmatrix} 0 & 0 & 0 \\ 0 & 0 & 0 \\ 0 & 0 & 0.0625 \end{bmatrix}, \quad \bar{\rho}_L = 2 \left(\frac{H}{L} \right)$$

$$(\bar{E}_L)_{xx} = (\bar{E}_L)_{yy} = \frac{1}{2} \bar{\rho}_L, \quad \bar{G}_L = \frac{1}{16} \bar{\rho}_L^3, \quad (\nu_L)_{xy} = (\nu_L)_{yx} = 0$$

G.3 Kagome Lattice Material

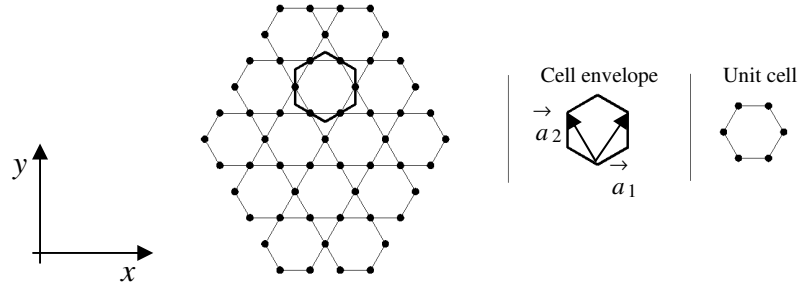


Fig (G.3) Microstructure of the 2D Kagome' lattice material

$$\bar{\mathbf{K}}_L = \frac{\mathbf{K}_L}{E} = \bar{\rho}_L \begin{bmatrix} 0.375 & 0.125 & 0 \\ 0.125 & 0.375 & 0 \\ 0 & 0 & 0.125 \end{bmatrix} + \left(\bar{\rho}_L \right)^3 \begin{bmatrix} 0.0208 & -0.0208 & 0 \\ -0.0208 & 0.0208 & 0 \\ 0 & 0 & 0.0208 \end{bmatrix},$$

$$\bar{\rho}_L = 1.7321 \left(\frac{H}{L} \right)$$

$$(\bar{E}_L)_{xx} = (\bar{E}_L)_{yy} = \frac{\bar{\rho}_L (625 + 104 \bar{\rho}_L^2)}{1875 + 104 \bar{\rho}_L^2}, \quad \bar{G}_L = \frac{\bar{\rho}_L (625 + 104 \bar{\rho}_L^2)}{5000},$$

$$(v_L)_{xy} = (v_L)_{yx} = \frac{625 - 104 \bar{\rho}_L^2}{1875 + 104 \bar{\rho}_L^2}$$

G.4 Lattice Material with Schlafl Symbol of $3^3.4^2$

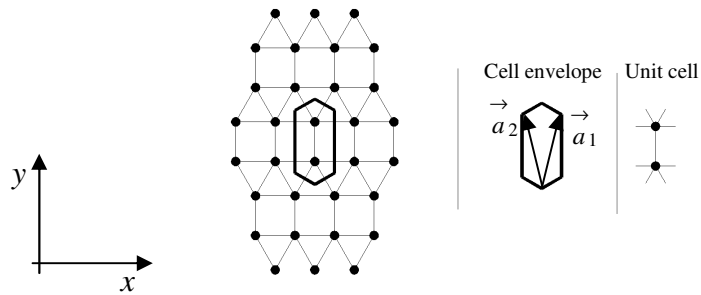


Fig (G.4) Microstructure of the 2D lattice material with Schlafl symbol of $3^3.4^2$

$$\bar{\mathbf{K}}_L = \frac{\mathbf{K}_L}{E} = \bar{\rho}_L \begin{bmatrix} 0.41 & 0.0646 & 0 \\ 0.0646 & 0.4178 & 0 \\ 0 & 0 & 0 \end{bmatrix} + \left(\bar{\rho}_L \right)^3 \begin{bmatrix} 0 & 0 & 0 \\ 0 & 0 & 0 \\ 0 & 0 & 0.0279 \end{bmatrix}, \bar{\rho}_L = 2.6795 \left(\frac{H}{L} \right)$$

$$(\bar{E}_L)_{xx} = (\bar{E}_L)_{yy} = 0.4 \bar{\rho}_L, \bar{G}_L = 0.0279 \bar{\rho}_L^2, (\nu_L)_{xy} = (\nu_L)_{yx} = 0.156$$

G.5 Lattice Material with Schafli Symbol of 3⁴.6

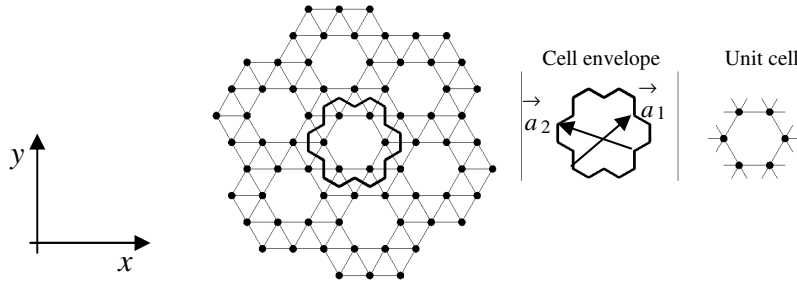


Fig (G.5) Microstructure of the 2D lattice material with Schafli symbol of 3⁴.6

$$\bar{\mathbf{K}}_L = \frac{\mathbf{K}_L}{E} = \bar{\rho}_L \begin{bmatrix} 0.4445 & 0.2415 & 0 \\ 0.2415 & 0.4445 & 0 \\ 0 & 0 & 0.1015 \end{bmatrix} + \left(\bar{\rho}_L \right)^3 \begin{bmatrix} 0.0095 & -0.0095 & -0.0019 \\ -0.0095 & 0.0095 & 0.0019 \\ -0.0019 & 0.0019 & 0.0124 \end{bmatrix},$$

$$\bar{\rho}_L = 2.4744 \left(\frac{H}{L} \right)$$

$$(\bar{E}_L)_{xx} = (\bar{E}_L)_{yy} = 1.372 \bar{\rho}_L \left(\frac{90.2 + 19.5 \bar{\rho}_L^2 + \bar{\rho}_L^4}{395 + 56.7 \bar{\rho}_L^2 + \bar{\rho}_L^4} \right), \bar{G}_L = \bar{\rho}_L \left(\frac{20.6 + 4.4 \bar{\rho}_L^2 + 0.228 \bar{\rho}_L^4}{203 + 19 \bar{\rho}_L^2} \right),$$

$$(\nu_L)_{xy} = (\nu_L)_{yx} = \left(\frac{214.6 + 17.8 \bar{\rho}_L^2 - \bar{\rho}_L^4}{395 + 56.7 \bar{\rho}_L^2 + \bar{\rho}_L^4} \right)$$

G.6 Double Hexagonal Triangulation (DHT) Lattice Material

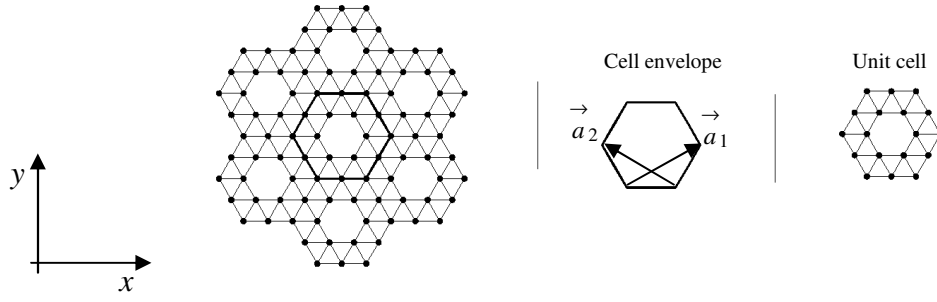


Fig (G.6) Microstructure of the DHT lattice material

$$\bar{\mathbf{K}}_L = \frac{\mathbf{K}_L}{E} = \bar{\rho}_L \begin{bmatrix} 0.3431 & 0.1391 & 0 \\ 0.1391 & 0.3431 & 0 \\ 0 & 0 & 0.093 \end{bmatrix} + \left(\bar{\rho}_L \right)^3 \begin{bmatrix} 0.0041 & -0.0041 & 0 \\ -0.0041 & 0.0041 & 0 \\ 0 & 0 & 0.004 \end{bmatrix}$$

$$\bar{\rho}_L = 2.7905 \left(\frac{H}{L} \right)$$

$$(\bar{E}_L)_{xx} = (\bar{E}_L)_{yy} = 0.964 \bar{\rho}_L \left(\frac{-2}{41 \bar{\rho}_L + 1020} \right), \bar{G}_L = \frac{\bar{\rho}_L}{1000} \left(93 + 4 \bar{\rho}_L^{-2} \right),$$

$$(\nu_L)_{xy} = (\nu_L)_{yx} = \left(\frac{1391 - 41 \bar{\rho}_L^{-2}}{3431 + 41 \bar{\rho}_L} \right)$$

G.7 Semi-Uni- Braced Square (SUBS) Lattice Material

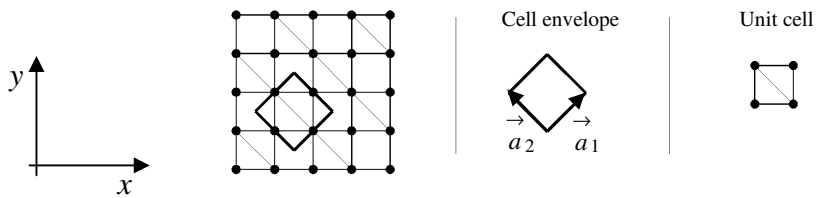


Fig (G.7) Microstructure of the SUBS lattice material

$$\bar{\mathbf{K}}_L = \frac{\mathbf{K}_L}{E} = \bar{\rho}_L \begin{bmatrix} 0.4347 & 0.0653 & -0.0653 \\ 0.0653 & 0.4347 & -0.0653 \\ -0.0653 & -0.0653 & 0.0653 \end{bmatrix} + \left(\bar{\rho}_L \right)^3 \begin{bmatrix} 0 & 0 & 0 \\ 0 & 0 & 0 \\ 0 & 0 & 0.0126 \end{bmatrix}$$

$$\bar{\rho}_L = 2.7071 \left(\frac{H}{L} \right)$$

$$(\bar{E}_L)_{xx} = (\bar{E}_L)_{yy} = 0.3694 \bar{\rho}_L \left(\frac{1.15 \bar{\rho}_L + 4.4}{\bar{\rho}_L + 4.4} \right), \bar{G}_L = \bar{\rho}_L \left(0.0482 + 0.0126 \bar{\rho}_L \right),$$

$$(\nu_L)_{xy} = (\nu_L)_{yx} = \left(\frac{\bar{\rho}_L}{29.3 + 6.65 \bar{\rho}_L} \right)$$

G.8 Triangular- Triangular (TT) Lattice Material

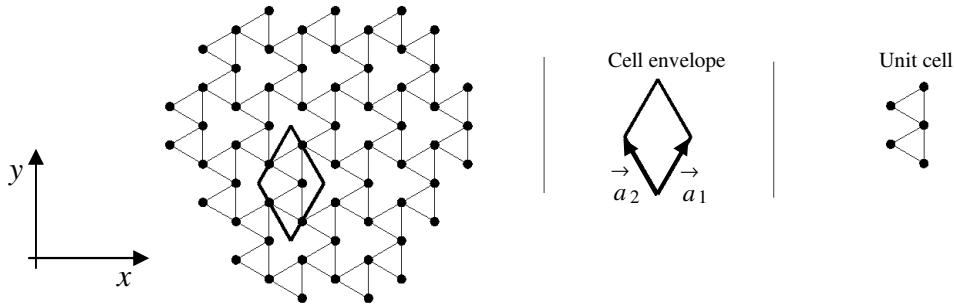


Fig (G.8) Microstructure of the TT lattice material

$$\bar{\mathbf{K}}_L = \frac{\mathbf{K}_L}{E} = \bar{\rho}_L \begin{bmatrix} 0.0937 & -0.0937 & 0 \\ -0.0937 & 0.0937 & 0 \\ 0 & 0 & 0.0938 \end{bmatrix} + \left(\bar{\rho}_L \right)^3 \begin{bmatrix} 0.0053 & -0.0053 & -0.003 \\ -0.0053 & 0.0053 & 0.003 \\ -0.003 & 0.003 & 0.0018 \end{bmatrix}$$

$$\bar{\rho}_L = 2.3094 \left(\frac{H}{L} \right)$$

$$(\bar{E}_L)_{xx} = (\bar{E}_L)_{yy} \approx 0.3956 \bar{\rho}_L, \bar{G}_L = 0.0954 \bar{\rho}_L, (\nu_L)_{xy} = (\nu_L)_{yx} = 1$$

G.9 Semi-Double Braced Square (SDBS) Lattice Material

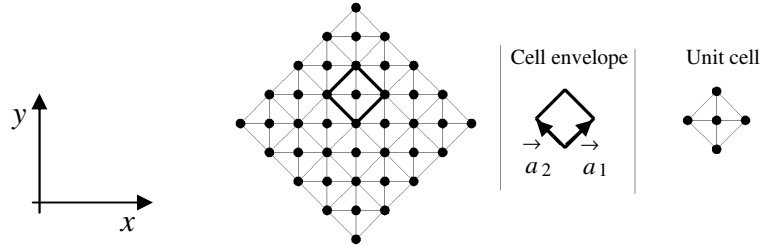


Fig (G.9) Microstructure of the SDBS lattice material

$$\bar{\mathbf{K}}_L = \frac{\mathbf{K}_L}{E} = \bar{\rho}_L \begin{bmatrix} 0.3964 & 0.1036 & 0 \\ 0.1036 & 0.3964 & 0 \\ 0 & 0 & 0.1036 \end{bmatrix} + \left(\bar{\rho}_L \right)^3 \begin{bmatrix} 0.0022 & -0.0022 & 0 \\ -0.0022 & 0.0022 & 0 \\ 0 & 0 & 0.0063 \end{bmatrix}$$

$$\bar{\rho}_L = 3.4142 \left(\frac{H}{L} \right)$$

$$(\bar{E}_L)_{xx} = (\bar{E}_L)_{yy} = \bar{\rho}_L \left(\frac{11\bar{\rho}_L + 732}{11\bar{\rho}_L + 1982} \right), \quad \bar{G}_L = \frac{7\bar{\rho}_L}{10^4} \left(148 + 9\bar{\rho}_L \right),$$

$$(\nu_L)_{xy} = (\nu_L)_{yx} = \left(\frac{518 - 11\bar{\rho}_L}{11\bar{\rho}_L + 1982} \right)$$

G.10 Uni- Braced Square (UBS) Lattice Material

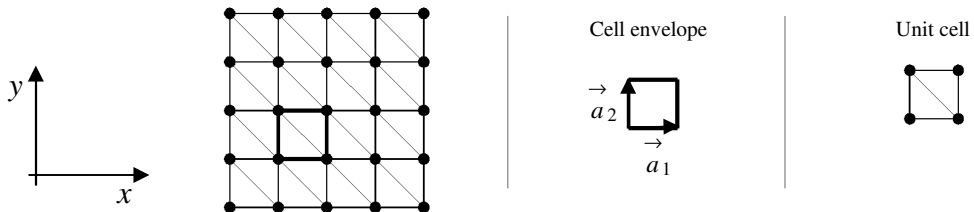


Fig (G.10) Microstructure of the UBS lattice material

$$\bar{\mathbf{K}}_L = \frac{\mathbf{K}_L}{E} = \bar{\rho}_L \begin{bmatrix} 0.3964 & 0.1036 & -0.1036 \\ 0.1036 & 0.3964 & -0.1036 \\ -0.1036 & -0.1036 & 0.1036 \end{bmatrix} + \left(\bar{\rho}_L \right)^3 \begin{bmatrix} 0.0016 & -0.0016 & 0 \\ -0.0016 & 0.0016 & 0 \\ 0 & 0 & 0.0063 \end{bmatrix}$$

$$\bar{\rho}_L = 3.4142 \left(\frac{H}{L} \right)$$

$$(\bar{E}_L)_{xx} = (\bar{E}_L)_{yy} = \bar{\rho}_L \left(\frac{881.1 + 101.1 \bar{\rho}_L + \bar{\rho}_L}{3009.3 + 264.2 \bar{\rho}_L + \bar{\rho}_L} \right), \bar{G}_L = \bar{\rho}_L \left(0.06 + 0.0063 \bar{\rho}_L \right),$$

$$(\nu_L)_{xy} = (\nu_L)_{yx} = \bar{\rho}_L \left(\frac{48.3 - \bar{\rho}_L}{3009.3 + 264.2 \bar{\rho}_L + \bar{\rho}_L} \right)$$

G.11 Double-Braced Square (DBS) Lattice Material

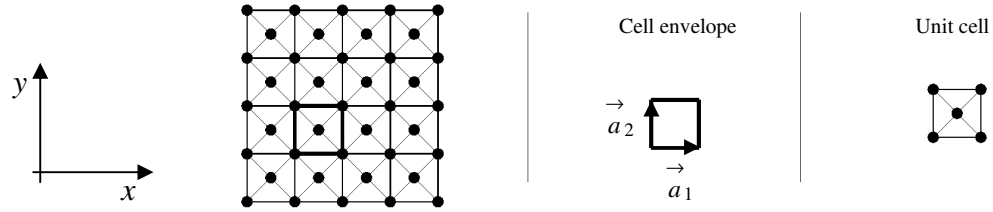


Fig (G.11) Microstructure of the DBS lattice material

$$\bar{\mathbf{K}}_L = \frac{\mathbf{K}_L}{E} = \bar{\rho}_L \begin{bmatrix} 0.3536 & 0.1464 & 0 \\ 0.1464 & 0.3536 & 0 \\ 0 & 0 & 0.1464 \end{bmatrix} + \left(\bar{\rho}_L \right)^3 \begin{bmatrix} 0.0063 & -0.0063 & 0 \\ -0.0063 & 0.0063 & 0 \\ 0 & 0 & 0.0022 \end{bmatrix}$$

$$\bar{\rho}_L = 4.8284 \left(\frac{H}{L} \right)$$

$$(\bar{E}_L)_{xx} = (\bar{E}_L)_{yy} = 7 \bar{\rho}_L \left(\frac{148 + 9 \bar{\rho}_L^{-2}}{3536 + 63 \bar{\rho}_L^{-2}} \right), \bar{G}_L = \frac{\bar{\rho}_L}{5000} \left(732 + 11 \bar{\rho}_L^{-2} \right),$$

$$(\nu_L)_{xy} = (\nu_L)_{yx} = 3 \left(\frac{488 - 21 \bar{\rho}_L^{-2}}{3536 + 63 \bar{\rho}_L^{-2}} \right)$$

G.12 Patched Kagome' Lattice Material

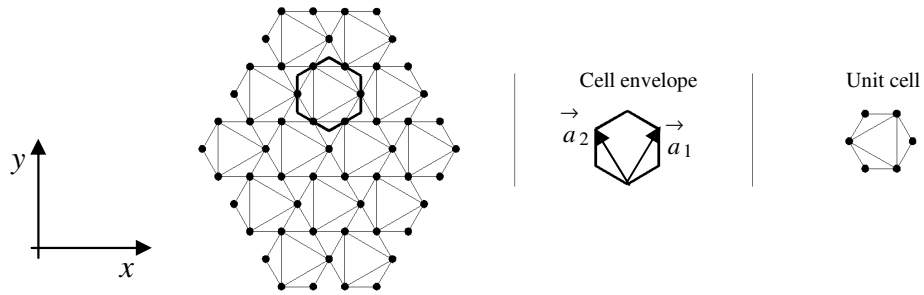


Fig (G.12) Microstructure of the patched Kagome' lattice material

$$\bar{\mathbf{K}}_L = \frac{\mathbf{K}_L}{E} = \bar{\rho}_L \begin{bmatrix} 0.246 & 0.022 & 0 \\ 0.022 & 0.246 & 0 \\ 0 & 0 & 0.112 \end{bmatrix} + \left(\bar{\rho}_L \right)^3 \begin{bmatrix} 0.0037 & -0.0037 & -0.0003 \\ -0.0037 & 0.0037 & 0.0003 \\ -0.0003 & 0.0003 & 0.0034 \end{bmatrix}$$

$$\bar{\rho}_L = 3.2321 \left(\frac{H}{L} \right)$$

$$(\bar{E}_L)_{xx} = (\bar{E}_L)_{yy} = \bar{\rho}_L \left(\frac{538.3 + 34.1 \bar{\rho}_L^{-2} + \bar{\rho}_L^{-4}}{2206 + 100.1 \bar{\rho}_L^{-2} + \bar{\rho}_L^{-4}} \right), \bar{G}_L = \bar{\rho}_L \left(\frac{125.44 + 7.952 \bar{\rho}_L^{-2} + 0.1249 \bar{\rho}_L^{-4}}{1120 + 37 \bar{\rho}_L^{-2}} \right),$$

$$(\nu_L)_{xy} = (\nu_L)_{yx} = \left(\frac{197.3 - 27.2 \bar{\rho}_L^{-2} - \bar{\rho}_L^{-4}}{2206 + 100.1 \bar{\rho}_L^{-2} + \bar{\rho}_L^{-4}} \right)$$

G.13 Semi-Hexagonal Triangulation (SHT) Lattice Material

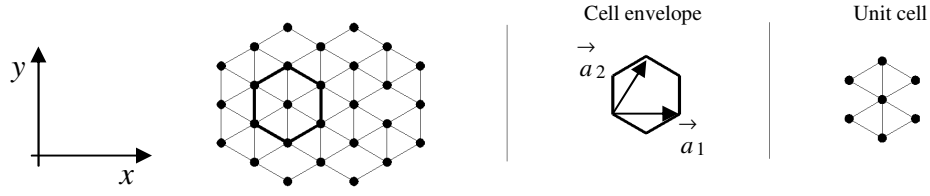


Fig (G.13) Microstructure of the SHT lattice material

$$\bar{\mathbf{K}}_L = \frac{\mathbf{K}_L}{E} = \bar{\rho}_L \begin{bmatrix} 0.4219 & 0.1406 & 0 \\ 0.1406 & 0.1969 & 0 \\ 0 & 0 & 0.1406 \end{bmatrix} + \left(\bar{\rho}_L \right)^3 \begin{bmatrix} 0.005 & -0.005 & 0.0002 \\ -0.005 & 0.005 & -0.0002 \\ 0.0002 & -0.0002 & 0.013 \end{bmatrix}$$

$$\bar{\rho}_L = 3.0792 \left(\frac{H}{L} \right)$$

$$(\bar{E}_L)_{xx} = \bar{\rho}_L \left(\frac{137 + 22.4 \bar{\rho}_L + 0.9 \bar{\rho}_L}{426.2 + 50.2 \bar{\rho}_L + \bar{\rho}_L} \right), (\bar{E}_L)_{yy} = \bar{\rho}_L \left(\frac{137 + 22.4 \bar{\rho}_L + 0.9 \bar{\rho}_L}{913.1 + 95.254 \bar{\rho}_L + \bar{\rho}_L} \right),$$

$$\bar{G}_L = \bar{\rho}_L \left(\frac{1.98 + 0.323 \bar{\rho}_L + 0.013 \bar{\rho}_L}{14.06 + \bar{\rho}_L} \right), (v_L)_{xy} = \left(\frac{304.3 + 17.3 \bar{\rho}_L - \bar{\rho}_L}{913.1 + 95.254 \bar{\rho}_L + \bar{\rho}_L} \right),$$

$$(v_L)_{yx} = \left(\frac{304.3 + 17.3 \bar{\rho}_L - \bar{\rho}_L}{426.2 + 50.2 \bar{\rho}_L + \bar{\rho}_L} \right)$$

Appendix H

Comprehensive Stiffness Properties of 2D Pin- and Rigid-Jointed Lattice Materials: Application

Following the approach developed in chapter 8, we derive the comprehensive stiffness properties to two types of planar lattice materials, the square lattice and the lattice material with Schläfli symbol of $3^3.4^2$.

H.1 Square Lattice Material

The material stiffness properties of the pin-jointed and the rigid-jointed square lattice material are derived in Appendix G as:

$${}_p\bar{\mathbf{K}}_{LE} = \frac{{}_p\mathbf{K}_{LE}}{E} = \bar{\rho}_L \begin{bmatrix} 0.5 & 0 & 0 \\ 0 & 0.5 & 0 \\ 0 & 0 & 0 \end{bmatrix} \quad (\text{H.1a})$$

$${}_r\bar{\mathbf{K}}_{LE} = \frac{{}_r\mathbf{K}_{LE}}{E} = \bar{\rho}_L \begin{bmatrix} 0.5 & 0 & 0 \\ 0 & 0.5 & 0 \\ 0 & 0 & 0 \end{bmatrix} + \left(\bar{\rho}_L \right)^3 \begin{bmatrix} 0 & 0 & 0 \\ 0 & 0 & 0 \\ 0 & 0 & 0.0625 \end{bmatrix} \quad (\text{H.2b})$$

where the relative density of the square lattice is formulated as: $\bar{\rho}_L = 2 \left(\frac{H}{L} \right)$.

To formulate the geometrical stiffness, the axial forces in the microscopic elements of the infinite lattice are computed. First we formulate the equilibrium matrix of the pin-jointed unit cell of the square lattice as:

$$\mathbf{A} = \begin{bmatrix} 0 & 0 & 0 & -1 \\ -1 & 0 & 0 & 0 \\ 0 & -1 & 0 & 0 \\ 1 & 0 & 0 & 0 \\ 0 & 1 & 0 & 0 \\ 0 & 0 & 1 & 0 \\ 0 & 0 & 0 & 1 \\ 0 & 0 & -1 & 0 \end{bmatrix} \quad (\text{H.3})$$

The equilibrium matrix of the unit cell, eqn (H.3), is used to formulate the reduced equilibrium matrix of the infinite lattice at wave-number $\omega = (0,0)$, using the Bloch's theorem, as:

$$\tilde{\mathbf{A}} = \begin{bmatrix} 0 & 0 \\ 0 & 0 \end{bmatrix} \quad (\text{H.4})$$

The reduced kinematic matrix of the infinite square lattice can be derived as $\tilde{\mathbf{B}} = \tilde{\mathbf{A}}^T$ which generates a typical matrix to eqn (H.4). Using the reduced equilibrium and kinematic matrices of the square lattice at wave-number $\omega = (0,0)$, the states of self-stress and the states of mechanisms of the lattice can be derived as:

$$\tilde{\mathbf{S}}\mathbf{S} = \begin{bmatrix} 1 & 0 \\ 0 & 1 \end{bmatrix} \quad (\text{H.5a})$$

$$\tilde{\mathbf{D}} = \begin{bmatrix} 1 & 0 \\ 0 & 1 \end{bmatrix} \quad (\text{H.5b})$$

From eqn (H.5b), it can be realized that there are only two mechanisms. It can be concluded, without applying the product force vector approach, that the two modes of mechanisms are rigid-body motion of the lattice. Eliminating the modes of rigid-body motion from the row space of the reduced equilibrium matrix generates the empty matrix:

$$\tilde{\tilde{\mathbf{A}}} = [] \quad (\text{H.6})$$

Again, the null space of the matrix, derived in eqn (H.6), is computed to generate the states of self-stress of the infinite square lattice that are associated only with modes of states of internal mechanisms which generates an empty null space. This is interpreted as zero element forces.

Using this result, the comprehensive stiffness of the square lattice material is computed as:

$${}_p\bar{\mathbf{K}}_{LC} = \frac{{}_p\mathbf{K}_{LE}}{E} = \bar{\rho}_L \begin{bmatrix} 0.5 & 0 & 0 \\ 0 & 0.5 & 0 \\ 0 & 0 & 0 \end{bmatrix} + \bar{\rho}_L \varepsilon_e \begin{bmatrix} 0 & 0 & 0 \\ 0 & 0 & 0 \\ 0 & 0 & 0 \end{bmatrix} \quad (\text{H.7a})$$

$${}_r\bar{\mathbf{K}}_{LC} = \frac{{}_r\mathbf{K}_{LE}}{E} = \bar{\rho}_L \begin{bmatrix} 0.5 & 0 & 0 \\ 0 & 0.5 & 0 \\ 0 & 0 & 0 \end{bmatrix} + \left(\bar{\rho}_L \right)^3 \begin{bmatrix} 0 & 0 & 0 \\ 0 & 0 & 0 \\ 0 & 0 & 0.0625 \end{bmatrix} + \bar{\rho}_L \varepsilon_e \begin{bmatrix} 0 & 0 & 0 \\ 0 & 0 & 0 \\ 0 & 0 & 0 \end{bmatrix} \quad (\text{H.7b})$$

Using eqn (H.7), the elastic moduli and Poisson's ratios can be computed only for the rigid-jointed square lattice material as:

$$({}_r\bar{E}_{LC})_{xx} = ({}_r\bar{E}_{LC})_{yy} = \frac{1}{2} \bar{\rho}_L, \bar{G}_{Lr} = \frac{1}{16} \bar{\rho}_L^3, ({}_r\nu_{LC})_{xy} = ({}_r\nu_{LC})_{yx} = 0 \quad (\text{H.8})$$

H.2 The $3^3.4^2$ Lattice Material

The material stiffness properties of the pin-jointed and the rigid-jointed $3^3.4^2$ lattice material are derived in Appendix G as:

$${}_p\bar{\mathbf{K}}_{LE} = \frac{{}_p\mathbf{K}_{LE}}{E} = \bar{\rho}_L \begin{bmatrix} 0.41 & 0.0646 & 0 \\ 0.0646 & 0.4178 & 0 \\ 0 & 0 & 0 \end{bmatrix} \quad (\text{H.9a})$$

$${}_r\bar{\mathbf{K}}_{LE} = \frac{{}_r\mathbf{K}_{LE}}{E} = \bar{\rho}_L \begin{bmatrix} 0.41 & 0.0646 & 0 \\ 0.0646 & 0.4178 & 0 \\ 0 & 0 & 0 \end{bmatrix} + \left(\bar{\rho}_L \right)^3 \begin{bmatrix} 0 & 0 & 0 \\ 0 & 0 & 0 \\ 0 & 0 & 0.0279 \end{bmatrix} \quad (\text{H.9b})$$

where the relative density of the $3^3.4^2$ lattice is formulated as: $\bar{\rho}_L = 2.6795 \left(\frac{H}{L} \right)$.

To formulate the geometrical stiffness, the axial forces in the microscopic elements are computed. We first formulate the equilibrium matrix of the unit cell of the lattice using the DNR where the DNS is employed for this analysis. The equilibrium matrix is used to generate the reduced equilibrium matrix of the infinite lattice at wave-number $\omega = (0,0)$, using the *Bloch's* theorem, as:

$$\tilde{\mathbf{A}} = \begin{bmatrix} 0 & -0.25 & 0.25 & 0 & 0 \\ -1 & \frac{\sqrt{3}}{4} & \frac{\sqrt{3}}{4} & 0 & 0 \\ 0 & 0.25 & -0.25 & 0 & 0 \\ 1 & -\frac{\sqrt{3}}{4} & -\frac{\sqrt{3}}{4} & 0 & 0 \end{bmatrix} \quad (\text{H.10})$$

The reduced kinematic matrix of the infinite lattice can be derived as $\tilde{\mathbf{B}} = \tilde{\mathbf{A}}^T$ which is used along with the equilibrium matrix to derive the states of self-stress and the states of mechanisms of the lattice, at wave-number $\omega = (0,0)$, as:

$$\tilde{\mathbf{S}}\mathbf{S} = \begin{bmatrix} \frac{\sqrt{3}}{2} & 0 & 0 \\ 1 & 0 & 0 \\ 1 & 0 & 0 \\ 0 & 1 & 0 \\ 0 & 0 & 1 \end{bmatrix}, \quad \tilde{\mathbf{D}} = \begin{bmatrix} 1 & 0 \\ 0 & 1 \\ 1 & 0 \\ 0 & 1 \end{bmatrix} \quad (\text{H.11})$$

The two mechanisms in eqn (H.11) are translational rigid-body motion and no need for the application of the product force vector analysis. Also, the non-pivotal columns in the reduced kinematic matrix are determined as columns number 3 and 4. The next step is to eliminate the

third and the fourth rows in the reduced equilibrium matrix to generate the truncated equilibrium matrix as:

$$\tilde{\mathbf{A}} = \begin{bmatrix} 0 & -0.25 & 0.25 & 0 & 0 \\ -1 & \frac{\sqrt{3}}{4} & \frac{\sqrt{3}}{4} & 0 & 0 \end{bmatrix} \quad (\text{H.12})$$

Again, the null space of the equilibrium matrix, derived in eqn (H.12), is computed to generate the states of self-stress of the infinite lattice that are associated only with modes of states of internal mechanisms which generates a state of self-stress matrix typical to the one derived in eqn (H.11). Next, the vector of imposed elongations and the flexibility matrix are derived which are used to derive the reduced global state of self-stress as:

$$\tilde{S}_G = (\epsilon_0) \begin{bmatrix} -0.1237 \\ -0.1429 \\ -0.1429 \\ -0.5 \\ -0.5 \end{bmatrix} \quad (\text{H.13})$$

The reduced global state of self-stress, eqn (H.13), is expanded to the unit cell level to compute the axial forces in all microscopic cell elements which are used to derive the geometrical stiffness of the $3^3.4^2$ lattice material.

The comprehensive stiffness of the $3^3.4^2$ lattice material is derived as:

$${}_p\bar{\mathbf{K}}_{LC} = \frac{{}_p\mathbf{K}_{LE}}{E} = \bar{\rho}_L \begin{bmatrix} 0.41 & 0.0646 & 0 \\ 0.0646 & 0.4178 & 0 \\ 0 & 0 & 0 \end{bmatrix} + \bar{\rho}_L \epsilon_0 \begin{bmatrix} 0 & 0 & 0 \\ 0 & 0 & 0 \\ 0 & 0 & -0.0598 \end{bmatrix} \quad (\text{H.14a})$$

$$\begin{aligned} {}_r\bar{\mathbf{K}}_{LE} &= \frac{{}_r\mathbf{K}_{LE}}{E} = \bar{\rho}_L \begin{bmatrix} 0.41 & 0.0646 & 0 \\ 0.0646 & 0.4178 & 0 \\ 0 & 0 & 0 \end{bmatrix} + \\ &\left(\bar{\rho}_L \right)^3 \begin{bmatrix} 0 & 0 & 0 \\ 0 & 0 & 0 \\ 0 & 0 & 0.0279 \end{bmatrix} + \bar{\rho}_L \epsilon_0 \begin{bmatrix} 0 & 0 & 0 \\ 0 & 0 & 0 \\ 0 & 0 & -0.0345 \end{bmatrix} \end{aligned} \quad (\text{H.14b})$$

The comprehensive stiffness matrices of other eleven 2D rigid-jointed lattice topologies are computed and reported in the following sections.

H.3 Triangular Lattice Material

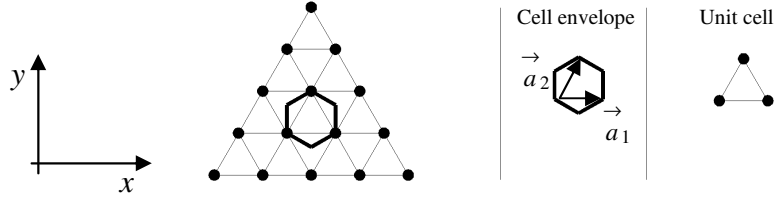


Fig (H.3) Microstructure of the 2D triangular lattice material

$$\begin{aligned}
 {}_p\bar{\mathbf{K}}_{LC} &= \frac{{}_p\mathbf{K}_{LC}}{E} = \bar{\rho}_L \begin{bmatrix} 0.375 & 0.125 & 0 \\ 0.125 & 0.375 & 0 \\ 0 & 0 & 0.125 \end{bmatrix} + \bar{\rho}_L \varepsilon_0 \begin{bmatrix} 0 & 0 & 0 \\ 0 & 0 & 0 \\ 0 & 0 & 0 \end{bmatrix} \\
 {}_r\bar{\mathbf{K}}_{LC} &= \frac{{}_r\mathbf{K}_{LC}}{E} = \bar{\rho}_L \begin{bmatrix} 0.375 & 0.125 & 0 \\ 0.125 & 0.375 & 0 \\ 0 & 0 & 0.125 \end{bmatrix} + \left(\bar{\rho}_L \right)^3 \begin{bmatrix} 0.006 & -0.006 & 0 \\ -0.006 & 0.006 & 0 \\ 0 & 0 & 0.006 \end{bmatrix}, \\
 &+ \bar{\rho}_L \varepsilon_0 \begin{bmatrix} 0 & 0 & 0 \\ 0 & 0 & 0 \\ 0 & 0 & 0 \end{bmatrix} \\
 \bar{\rho}_L &= 3.4641 \left(\frac{H}{L} \right)
 \end{aligned}$$

H.4 Lattice Material with Schläfli Symbol of $3^3.4^2$

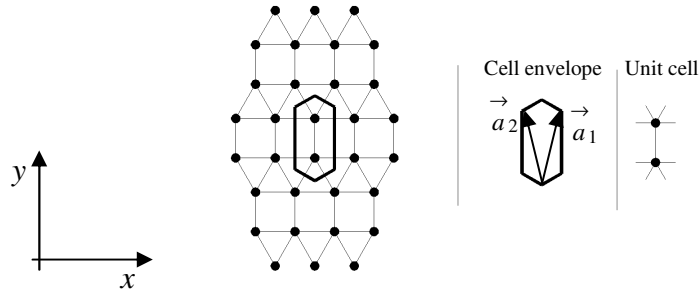


Fig (H.4) Microstructure of the 2D lattice material with Schläfli symbol of $3^3.4^2$

$${}_p\bar{\mathbf{K}}_{LC} = \frac{{}_p\mathbf{K}_{LC}}{E} = \bar{\rho}_L \begin{bmatrix} 0.41 & 0.0646 & 0 \\ 0.0646 & 0.4178 & 0 \\ 0 & 0 & 0 \end{bmatrix} + \bar{\rho}_L \varepsilon_0 \begin{bmatrix} 0 & 0 & 0 \\ 0 & 0 & 0 \\ 0 & 0 & -0.0598 \end{bmatrix}$$

$$\begin{aligned}
{}_r\overline{\mathbf{K}}_{LC} &= \frac{{}_r\mathbf{K}_{LC}}{E} = \bar{\rho}_L \begin{bmatrix} 0.41 & 0.0646 & 0 \\ 0.0646 & 0.4178 & 0 \\ 0 & 0 & 0 \end{bmatrix} + \\
&\left(\bar{\rho}_L\right)^3 \begin{bmatrix} 0 & 0 & 0 \\ 0 & 0 & 0 \\ 0 & 0 & 0.0279 \end{bmatrix} + \bar{\rho}_L \varepsilon_0 \begin{bmatrix} 0 & 0 & 0 \\ 0 & 0 & 0 \\ 0 & 0 & -0.0345 \end{bmatrix}, \\
\bar{\rho}_L &= 2.6795 \left(\frac{H}{L} \right)
\end{aligned}$$

H.5 Lattice Material with Schläfli Symbol of $3^4.6$

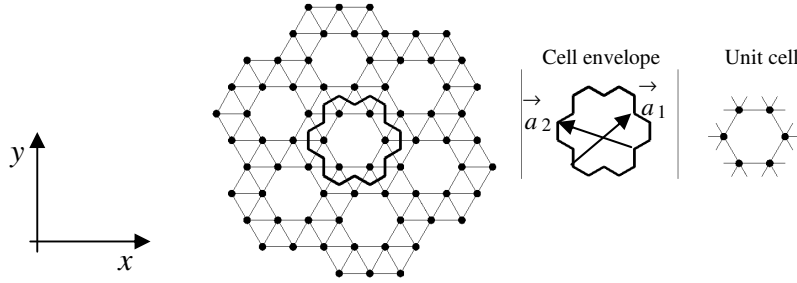


Fig (H.5) Microstructure of the 2D lattice material with Schläfli symbol of $3^4.6$

$$\begin{aligned}
{}_p\overline{\mathbf{K}}_{LC} &= \frac{{}_p\mathbf{K}_{LC}}{E} = \bar{\rho}_L \begin{bmatrix} 0.4445 & 0.2415 & 0 \\ 0.2415 & 0.4445 & 0 \\ 0 & 0 & 0.1015 \end{bmatrix} + \\
&\bar{\rho}_L \varepsilon_0 \begin{bmatrix} -0.0034 & 0.0034 & 0.012 \\ 0.0034 & -0.0034 & -0.012 \\ 0.012 & -0.012 & 0.0271 \end{bmatrix},
\end{aligned}$$

$$\begin{aligned}
{}_r\bar{\mathbf{K}}_{LC} &= \frac{{}_r\mathbf{K}_{LC}}{E} = \bar{\rho}_L \begin{bmatrix} 0.4445 & 0.2415 & 0 \\ 0.2415 & 0.4445 & 0 \\ 0 & 0 & 0.1015 \end{bmatrix} + \\
&\left(\bar{\rho}_L\right)^3 \begin{bmatrix} 0.0095 & -0.0095 & -0.0006 \\ -0.0095 & 0.0095 & 0.0006 \\ -0.0006 & 0.0006 & 0.0124 \end{bmatrix} \quad \bar{\rho}_L = 2.4744 \left(\frac{H}{L}\right) \\
&+ \bar{\rho}_L \varepsilon_0 \begin{bmatrix} -0.0035 & 0.0035 & 0.0032 \\ 0.0035 & -0.0035 & -0.0032 \\ 0.0032 & -0.0032 & 0.0045 \end{bmatrix}
\end{aligned}$$

H.6 Double Hexagonal Triangulation (DHT) Lattice Material

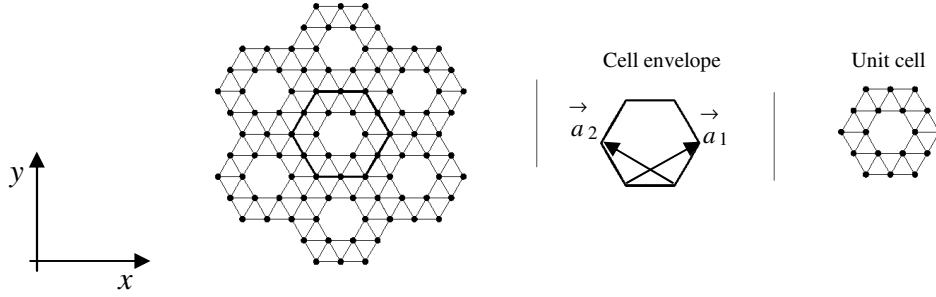


Fig (H.6) Microstructure of the DHT lattice material

$$\begin{aligned}
{}_p\bar{\mathbf{K}}_{LC} &= \frac{{}_p\mathbf{K}_{LC}}{E} = \bar{\rho}_L \begin{bmatrix} 0.3431 & 0.1391 & 0 \\ 0.1391 & 0.3431 & 0 \\ 0 & 0 & 0.093 \end{bmatrix} + \\
&\bar{\rho}_L \varepsilon_0 \begin{bmatrix} -0.0095 & 0.0095 & -0.0056 \\ 0.0095 & -0.0095 & 0.0056 \\ -0.0056 & 0.0056 & -0.0334 \end{bmatrix} \\
{}_r\bar{\mathbf{K}}_{LC} &= \frac{{}_r\mathbf{K}_{LC}}{E} = \bar{\rho}_L \begin{bmatrix} 0.3431 & 0.1391 & 0 \\ 0.1391 & 0.3431 & 0 \\ 0 & 0 & 0.093 \end{bmatrix} + \left(\bar{\rho}_L\right)^3 \begin{bmatrix} 0.0041 & -0.0041 & 0 \\ -0.0041 & 0.0041 & 0 \\ 0 & 0 & 0.004 \end{bmatrix} \\
&+ \bar{\rho}_L \varepsilon_0 \begin{bmatrix} -0.0056 & 0.0056 & -0.0033 \\ 0.0056 & -0.0056 & 0.0033 \\ -0.0033 & 0.0033 & -0.0198 \end{bmatrix}
\end{aligned}$$

$$\bar{\rho}_L = 2.7905 \left(\frac{H}{L} \right)$$

H.7 Semi-Uni- Braced Square (SUBS) Lattice Material

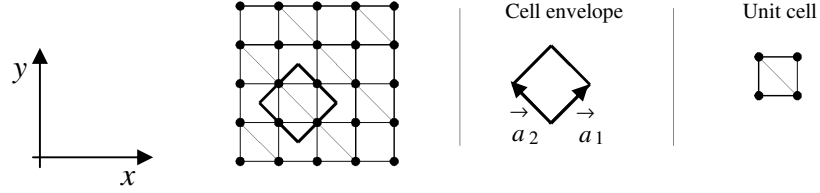


Fig (H.7) Microstructure of the SUBS lattice material

$${}_p \bar{\mathbf{K}}_{LC} = \frac{{}_p \mathbf{K}_{LC}}{E} = \bar{\rho}_L \begin{bmatrix} 0.4347 & 0.0653 & -0.0653 \\ 0.0653 & 0.4347 & -0.0653 \\ -0.0653 & -0.0653 & 0.0653 \end{bmatrix} +$$

$$\bar{\rho}_L \varepsilon_0 \begin{bmatrix} -0.0923 & 0.0923 & 0 \\ 0.0923 & -0.0923 & 0 \\ 0 & 0 & -0.0923 \end{bmatrix}$$

$${}_r \bar{\mathbf{K}}_{LC} = \frac{{}_r \mathbf{K}_{LC}}{E} = \bar{\rho}_L \begin{bmatrix} 0.4347 & 0.0653 & -0.0653 \\ 0.0653 & 0.4347 & -0.0653 \\ -0.0653 & -0.0653 & 0.0653 \end{bmatrix} + \left(\bar{\rho}_L \right)^3 \begin{bmatrix} 0 & 0 & 0 \\ 0 & 0 & 0 \\ 0 & 0 & 0.0126 \end{bmatrix}$$

$$+ \bar{\rho}_L \varepsilon_0 \begin{bmatrix} -0.043 & 0.043 & 0 \\ 0.043 & -0.043 & 0 \\ 0 & 0 & -0.0554 \end{bmatrix}$$

$$\bar{\rho}_L = 2.7071 \left(\frac{H}{L} \right)$$

H.8 Triangular- Triangular (TT) Lattice Material

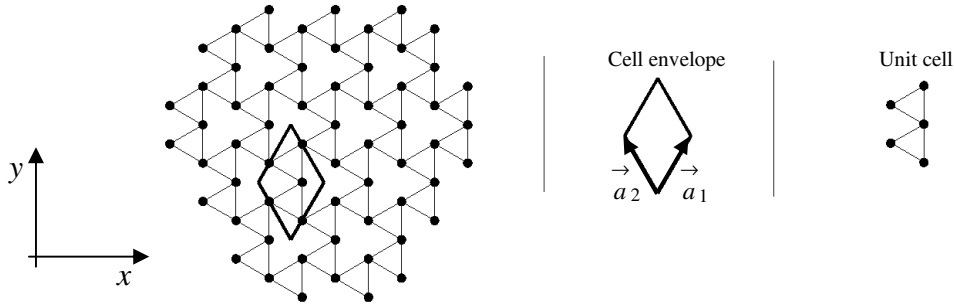


Fig (H.8) Microstructure of the TT lattice material

$$\begin{aligned}
 {}_p\bar{\mathbf{K}}_{LC} &= \frac{{}_p\mathbf{K}_{LC}}{E} = \bar{\rho}_L \begin{bmatrix} 0.0937 & -0.0937 & 0 \\ -0.0937 & 0.0937 & 0 \\ 0 & 0 & 0.0938 \end{bmatrix} + \\
 &\bar{\rho}_L \varepsilon_0 \begin{bmatrix} 0.0781 & -0.1094 & -0.0722 \\ -0.1094 & 0.1406 & 0.0541 \\ -0.0722 & 0.0541 & 0.0156 \end{bmatrix} \\
 {}_r\bar{\mathbf{K}}_{LC} &= \frac{{}_r\mathbf{K}_{LC}}{E} = \bar{\rho}_L \begin{bmatrix} 0.0937 & -0.0937 & 0 \\ -0.0937 & 0.0937 & 0 \\ 0 & 0 & 0.0938 \end{bmatrix} + \left(\bar{\rho}_L \right)^3 \begin{bmatrix} 0.0053 & -0.0053 & -0.003 \\ -0.0053 & 0.0053 & -0.003 \\ -0.003 & 0.003 & 0.0018 \end{bmatrix} \\
 &+ \bar{\rho}_L \varepsilon_0 \begin{bmatrix} 1.8685 & -1.8685 & -0.9442 \\ -1.8685 & 1.8685 & 0.9442 \\ -1.298 & 1.298 & 0.3623 \end{bmatrix} \\
 \bar{\rho}_L &= 2.3094 \left(\frac{H}{L} \right)
 \end{aligned}$$

H.9 Semi-Double Braced Square (SDBS) Lattice Material

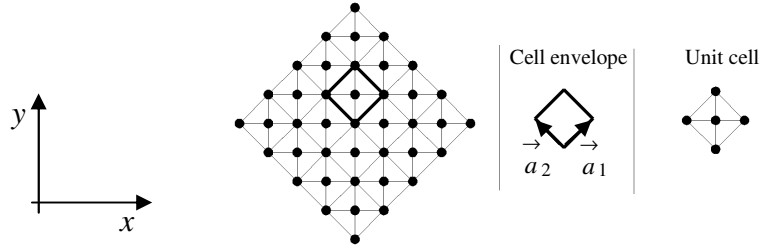


Fig (H.9) Microstructure of the SDBS lattice material

$$\begin{aligned}
 {}_p\bar{\mathbf{K}}_{LC} &= \frac{{}_p\mathbf{K}_{LC}}{E} = \bar{\rho}_L \begin{bmatrix} 0.3964 & 0.1036 & 0 \\ 0.1036 & 0.3964 & 0 \\ 0 & 0 & 0.1036 \end{bmatrix} + \\
 &\bar{\rho}_L \varepsilon_0 \begin{bmatrix} -0.1464 & 0.1464 & 0 \\ 0.1464 & -0.1464 & 0 \\ 0 & 0 & -0.0732 \end{bmatrix} \\
 {}_r\bar{\mathbf{K}}_{LC} &= \frac{{}_r\mathbf{K}_{LC}}{E} = \bar{\rho}_L \begin{bmatrix} 0.3964 & 0.1036 & 0 \\ 0.1036 & 0.3964 & 0 \\ 0 & 0 & 0.1036 \end{bmatrix} + \left(\bar{\rho}_L \right)^3 \begin{bmatrix} 0.0022 & -0.0022 & 0 \\ -0.0022 & 0.0022 & 0 \\ 0 & 0 & 0.0063 \end{bmatrix} \\
 &+ \bar{\rho}_L \varepsilon_0 \begin{bmatrix} -0.0879 & 0.0879 & 0 \\ 0.0879 & -0.0879 & 0 \\ 0 & 0 & -0.0439 \end{bmatrix} \\
 \bar{\rho}_L &= 3.4142 \left(\frac{H}{L} \right)
 \end{aligned}$$

H.10 Uni- Braced Square (UBS) Lattice Material

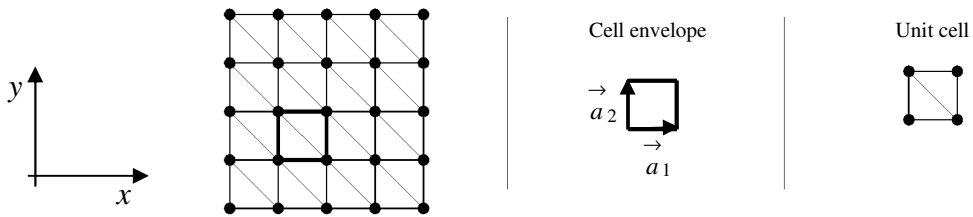


Fig (H.10) Microstructure of the UBS lattice material

$$\begin{aligned}
{}_p\bar{\mathbf{K}}_{LC} &= \frac{{}_p\mathbf{K}_{LC}}{E} = \bar{\rho}_L \begin{bmatrix} 0.3964 & 0.1036 & -0.1036 \\ 0.1036 & 0.3964 & -0.1036 \\ -0.1036 & -0.1036 & 0.1036 \end{bmatrix} + \bar{\rho}_L \varepsilon_0 \begin{bmatrix} 0 & 0 & 0 \\ 0 & 0 & 0 \\ 0 & 0 & 0 \end{bmatrix} \\
{}_r\bar{\mathbf{K}}_{LC} &= \frac{{}_r\mathbf{K}_{LC}}{E} = \bar{\rho}_L \begin{bmatrix} 0.3964 & 0.1036 & -0.1036 \\ 0.1036 & 0.3964 & -0.1036 \\ -0.1036 & -0.1036 & 0.1036 \end{bmatrix} + \\
&\left(\bar{\rho}_L \right)^3 \begin{bmatrix} 0.0016 & -0.0016 & 0 \\ -0.0016 & 0.0016 & 0 \\ 0 & 0 & 0.0063 \end{bmatrix} \\
&+ \bar{\rho}_L \varepsilon_0 \begin{bmatrix} 0 & 0 & 0 \\ 0 & 0 & 0 \\ 0 & 0 & 0 \end{bmatrix} \\
\bar{\rho}_L &= 3.4142 \left(\frac{H}{L} \right)
\end{aligned}$$

H.11 Double-Braced Square (DBS) Lattice Material

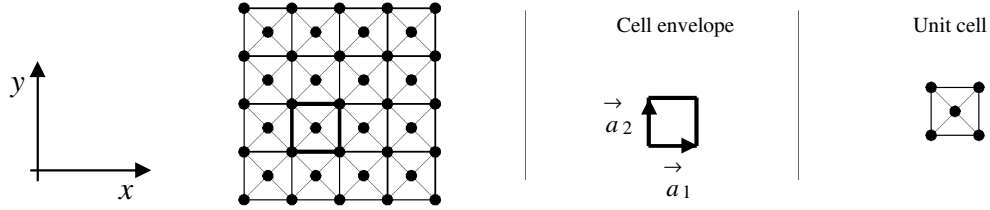


Fig (H.11) Microstructure of the DBS lattice material

$$\begin{aligned}
{}_p\bar{\mathbf{K}}_{LC} &= \frac{{}_p\mathbf{K}_{LC}}{E} = \bar{\rho}_L \begin{bmatrix} 0.3536 & 0.1464 & 0 \\ 0.1464 & 0.3536 & 0 \\ 0 & 0 & 0.1464 \end{bmatrix} + \\
&\bar{\rho}_L \varepsilon_0 \begin{bmatrix} -0.00518 & 0.00518 & 0 \\ 0.00518 & -0.00518 & 0 \\ 0 & 0 & -0.1036 \end{bmatrix}
\end{aligned}$$

$$\begin{aligned}
{}_r\bar{\mathbf{K}}_{LC} &= \frac{{}_r\mathbf{K}_{LC}}{E} = \bar{\rho}_L \begin{bmatrix} 0.3536 & 0.1464 & 0 \\ 0.1464 & 0.3536 & 0 \\ 0 & 0 & 0.1464 \end{bmatrix} \\
&+ \left(\bar{\rho}_L\right)^3 \begin{bmatrix} 0.0063 & -0.0063 & 0 \\ -0.0063 & 0.0063 & 0 \\ 0 & 0 & 0.0022 \end{bmatrix} \\
&+ \bar{\rho}_L \varepsilon_0 \begin{bmatrix} -0.0311 & 0.0311 & 0 \\ 0.0311 & -0.0311 & 0 \\ 0 & 0 & -0.0621 \end{bmatrix} \\
\bar{\rho}_L &= 4.8284 \left(\frac{H}{L} \right)
\end{aligned}$$

H.12 Patched Kagome Lattice Material

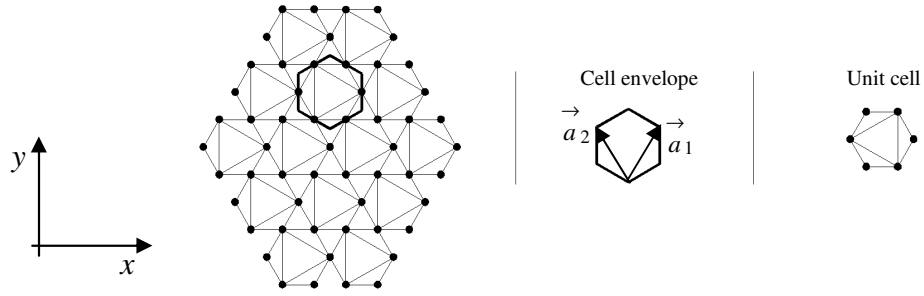


Fig (H.12) Microstructure of the patched Kagome lattice material

$$\begin{aligned}
{}_p\bar{\mathbf{K}}_{LC} &= \frac{{}_p\mathbf{K}_{LC}}{E} = \bar{\rho}_L \begin{bmatrix} 0.246 & 0.022 & 0 \\ 0.022 & 0.246 & 0 \\ 0 & 0 & 0.112 \end{bmatrix} \\
&+ \bar{\rho}_L \varepsilon_0 \begin{bmatrix} -0.0621 & 0.0621 & 0.0319 \\ 0.0621 & -0.0621 & -0.0319 \\ 0.0319 & -0.0319 & -0.0823 \end{bmatrix}
\end{aligned}$$

$$\begin{aligned}
{}_r\bar{\mathbf{K}}_{LC} &= \frac{{}_r\mathbf{K}_{LC}}{E} = \bar{\rho}_L \begin{bmatrix} 0.246 & 0.022 & 0 \\ 0.022 & 0.246 & 0 \\ 0 & 0 & 0.112 \end{bmatrix} \\
&+ \left(\bar{\rho}_L\right)^3 \begin{bmatrix} 0.0037 & -0.0037 & -0.0003 \\ -0.0037 & 0.0037 & 0.0003 \\ -0.0003 & 0.0003 & 0.0034 \end{bmatrix} \\
&+ \bar{\rho}_L \varepsilon_0 \begin{bmatrix} -0.036 & 0.036 & 0.0195 \\ 0.036 & -0.036 & -0.0195 \\ 0.0195 & -0.0195 & -0.0538 \end{bmatrix} \\
\bar{\rho}_L &= 3.2321 \left(\frac{H}{L} \right)
\end{aligned}$$

H.13 Semi-Hexagonal Triangulation (SHT) Lattice Material

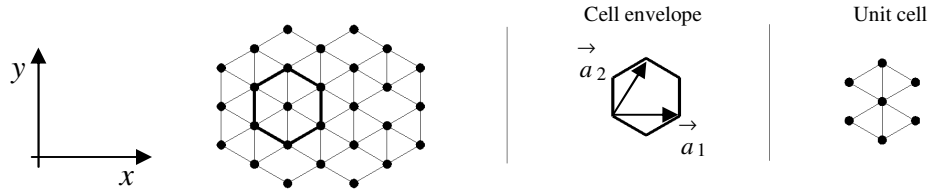


Fig (H.13) Microstructure of the SHT lattice material

$$\begin{aligned}
{}_p\bar{\mathbf{K}}_{LC} &= \frac{{}_p\mathbf{K}_{LC}}{E} = \bar{\rho}_L \begin{bmatrix} 0.4219 & 0.1406 & 0 \\ 0.1406 & 0.1969 & 0 \\ 0 & 0 & 0.1406 \end{bmatrix} \\
&+ \bar{\rho}_L \varepsilon_0 \begin{bmatrix} -0.092 & 0.092 & 0 \\ 0.092 & -0.092 & 0 \\ 0 & 0 & -0.0125 \end{bmatrix}
\end{aligned}$$

$$\begin{aligned}
{}_r\bar{\mathbf{K}}_{LC} &= \frac{{}_r\mathbf{K}_{LC}}{E} = \bar{\rho}_L \begin{bmatrix} 0.4219 & 0.1406 & 0 \\ 0.1406 & 0.1969 & 0 \\ 0 & 0 & 0.1406 \end{bmatrix} \\
&+ \left(\bar{\rho}_L \right)^3 \begin{bmatrix} 0.005 & -0.005 & 0.0002 \\ -0.005 & 0.005 & -0.0002 \\ 0.0002 & -0.0002 & 0.013 \end{bmatrix} \\
&+ \bar{\rho}_L \varepsilon_0 \begin{bmatrix} -0.0546 & 0.0546 & 0.0002 \\ 0.0546 & -0.0546 & -0.0002 \\ 0.0002 & -0.0002 & -0.0077 \end{bmatrix} \\
\bar{\rho}_L &= 3.0792 \left(\frac{H}{L} \right)
\end{aligned}$$

H.14 Kagome lattice material

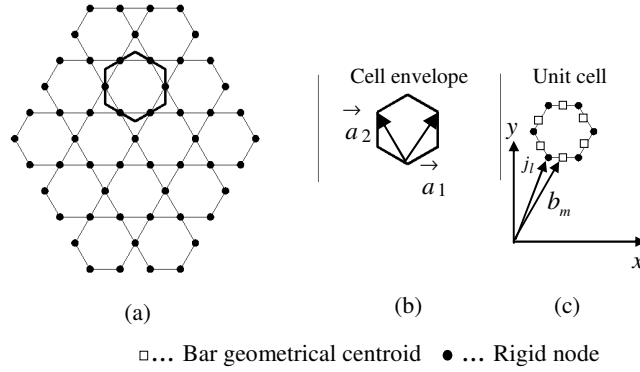


Fig (H.14) Kagome lattice structure

$$\begin{aligned}
{}_p\bar{\mathbf{K}}_{LC} &= \frac{{}_p\mathbf{K}_{LC}}{E} = \bar{\rho}_L \begin{bmatrix} 0.375 & 0.125 & 0 \\ 0.125 & 0.375 & 0 \\ 0 & 0 & 0.125 \end{bmatrix} \\
&+ (\varepsilon_0) \left(\bar{\rho}_L \right) \begin{bmatrix} -0.0625 & 0.0625 & 0 \\ 0.0625 & -0.0625 & 0 \\ 0 & 0 & -0.0625 \end{bmatrix}
\end{aligned}$$

$$\begin{aligned}
{}_r\overline{\mathbf{K}}_{LC} &= \frac{{}_r\mathbf{K}_{LC}}{E} = \bar{\rho}_L \begin{bmatrix} 0.375 & 0.125 & 0 \\ 0.125 & 0.375 & 0 \\ 0 & 0 & 0.125 \end{bmatrix} \\
&+ \bar{\rho}_L^3 \begin{bmatrix} 0.0208 & -0.0208 & 0 \\ -0.0208 & 0.0208 & 0 \\ 0 & 0 & 0.0208 \end{bmatrix} \\
&+ (\varepsilon_0) \left(\bar{\rho}_L \right) \begin{bmatrix} -0.0375 & 0.0375 & 0 \\ 0.0375 & -0.0375 & 0 \\ 0 & 0 & -0.0375 \end{bmatrix}
\end{aligned}$$

where $\bar{\rho}_L = 1.7321 \left(\frac{H}{L} \right)$.